AD-A184 047 FATIGUE '87 VOLUME 3(U) VIRGINIA UNIV CHARLOTTESVILLE SCHOOL OF ENGINEERING AND APPLIED SCIENCE R O RITCHIE ET AL. JUN 87 ARO-24134.3-MS-CF 1/6

UNCLASSIFIED N00014-87-G-0008 F/G 20/11 NL

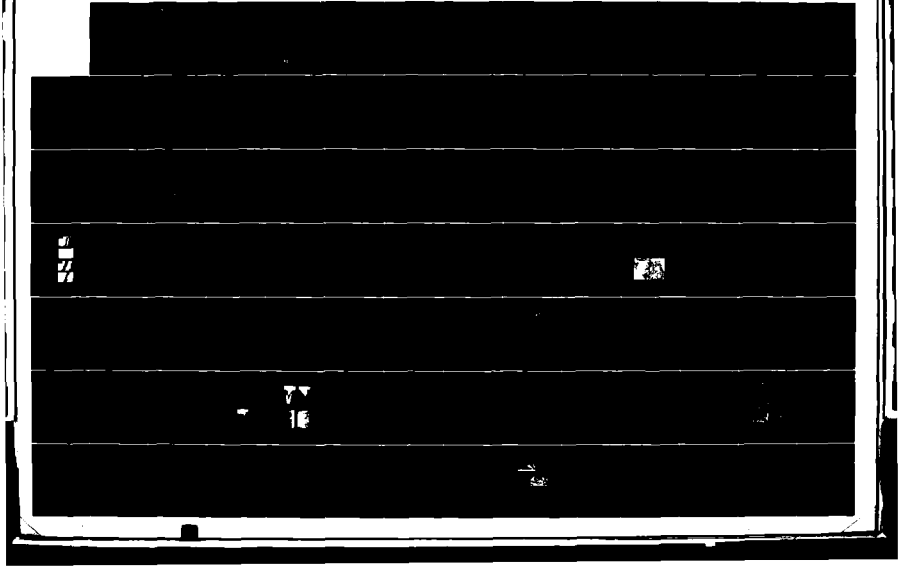

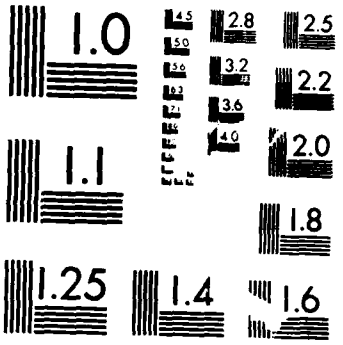

FATIGUE '87

VOLUME III

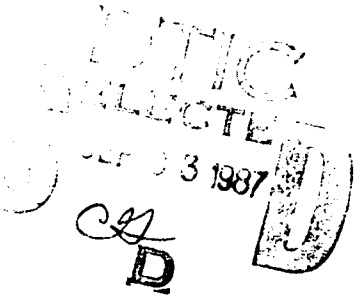

Papers present at the Third International Conference
on Fatigue and Fatigue Thresholds
held at the University of Virginia, Charlottesville, Virginia
June 28 – July 3, 1987

UNCLASSIFIED AD-A184047 MASTER COPY - FOR REPRODUCTION PURPOSES

SECURITY CLASSIFICATION OF THIS PAGE

REPORT DOCUMENTATION PAGE

1a REPORT SECURITY CLASSIFICATION: Unclassified	1b. RESTRICTIVE MARKINGS
2a. SECURITY CLASSIFICATION AUTHORITY	3 DISTRIBUTION / AVAILABILITY OF REPORT: Approved for public release; distribution unlimited.
2b. DECLASSIFICATION / DOWNGRADING SCHEDULE	
4. PERFORMING ORGANIZATION REPORT NUMBER(S)	5. MONITORING ORGANIZATION REPORT NUMBER(S): ARO 24134.3-MS-CF
6a. NAME OF PERFORMING ORGANIZATION: Univ. of Virginia; 6b OFFICE SYMBOL (If applicable)	7a. NAME OF MONITORING ORGANIZATION: U. S. Army Research Office
6c. ADDRESS (City, State, and ZIP Code): Charlottesville, VA 22904	7b. ADDRESS (City, State, and ZIP Code): P. O. Box 12211, Research Triangle Park, NC 27709-2211
8a. NAME OF FUNDING / SPONSORING ORGANIZATION: U. S. Army Research Office; 8b. OFFICE SYMBOL (If applicable)	9. PROCUREMENT INSTRUMENT IDENTIFICATION NUMBER: DAAL03-87-G-0102
8c. ADDRESS (City, State, and ZIP Code): P. O. Box 12211, Research Triangle Park, NC 27709-2211	10 SOURCE OF FUNDING NUMBERS: PROGRAM ELEMENT NO. / PROJECT NO. / TASK NO. / WORK UNIT ACCESSION NO.

11. TITLE (Include Security Classification): Fatigue "87", Volume III

12 PERSONAL AUTHOR(S): R. O. Ritchie, E. A. Starke, Jr. (Editors)

13a. TYPE OF REPORT	13b. TIME COVERED	14. DATE OF REPORT (Year, Month, Day)	15. PAGE COUNT
Final	FROM 6/1/87 TO 5/1/88	August 1987	

16. SUPPLEMENTARY NOTATION: The view, opinions and/or findings contained in this report are those of the author(s) and should not be construed as an official Department of the Army position, policy, or decision, unless so designated by other documentation.

17 COSATI CODES		
FIELD	GROUP	SUB-GROUP

18. SUBJECT TERMS (Continue on reverse if necessary and identify by block number): Fatigue, Cyclic Deformation, Crack Initiation, Crack Propagation, Crack Closure

19 ABSTRACT (Continue on reverse if necessary and identify by block number)

The current proceedings (3 volumes) of the third conference, "Fatigue 87" which was held at the University of Virginia, Charlottesville, covered a wide range of diverse views of the fundamental and applied aspects of fatigue. This includes questions of cyclic deformation, crack initiation and propagation, small cracks, crack closure, variable amplitude effects, and environmentally-influenced behavior. The proceedings should provide a comprehensive state-of-the-art review of the field, suitable for student, researchers and practising engineers alike. (Volume III)

20 DISTRIBUTION / AVAILABILITY OF ABSTRACT: ☐ UNCLASSIFIED/UNLIMITED ☐ SAME AS RPT ☐ DTIC USERS	21. ABSTRACT SECURITY CLASSIFICATION: Unclassified
22a NAME OF RESPONSIBLE INDIVIDUAL	22b. TELEPHONE (Include Area Code) / 22c. OFFICE SYMBOL

DD FORM 1473, 84 MAR 83 APR edition may be used until exhausted. All other editions are obsolete

SECURITY CLASSIFICATION OF THIS PAGE

UNCLASSIFIED

FATIGUE '87

VOLUME III

EDITORS:
R.O. Ritchie and E.A. Starke, Jr.

Papers presented at the
Third International Conference on Fatigue and Fatigue Thresholds
held at the University of Virginia, Charlottesville, Virginia.
June 28 – July 3, 1987

EMAS ENGINEERING MATERIALS ADVISORY SERVICES LTD.
339, Halesowen Road, Cradley Heath,
Warley, West Midlands, B64 6PH, U.K.

PREFACE

Fracture by the progressive growth of incipient flaws under cyclically varying loads, i.e., by fatigue, must now be considered as the principal cause of in-service failures of engineering structures and components, whether associated with mechanical sliding and friction (fretting fatigue), rolling contact, aggressive environments (corrosion fatigue), or elevated temperatures (creep-fatigue). Of particular importance are the early stages of fatigue damage, involving the initial extension of microcracks and their subsequent growth at very low velocities, as these processes tend to dominate overall lifetime. This has been reflected by trends in fatigue research over the past five years, which have focused largely on so-called "small cracks," of dimensions comparable with the scale of microstructure or local plasticity, and on crack growth in the near-threshold regime, i.e., at stress intensities approaching the fatigue threshold below which cracks are presumed dormant. In addition, associated mechanistic studies have highlighted the critical role of crack tip shielding in fatigue, which arises predominantly from crack closure and deflection, and this has proved to be important in modeling aspects of environmentally-assisted cracking and behavior under variable amplitude loads, and in rationalizing the classical stress/strain-life and defect-tolerant design approaches.

The series of internationl conferences on Fatigue and Fatigue Thresholds, although devoted to all aspects of fatigue, has emphasized these topics of small cracks and near-threshold behavior, and consequently, has become an international forum for the exchange of information in this field. The series, which has been run under the auspices of a steering and international committee with representatives from Australia, Austria, Canada, China, Czechoslovakia, France, Holland, Japan, Norway, Sweden, U.K., W. Germany and the U.S.A., began in Stockholm, Sweden, in 1981, and continued at the University of Birmingham in England in 1984.

The current proceedings of the third conference, "Fatigue '87," which was held at the University of Virginia, Charlottesville, covered a wide range of diverse views of the fundamental and applied aspects of fatigue. This includes questions of cyclic deformation, crack initiation and propagation, small cracks, crack closure, variable amplitude effects, and environmentally-influenced behavior. The proceedings should provide a comprehensive state-of-the-art review of the field, suitable for students, researchers and practising engineers alike.

The Editors would like to thank the Editorial Committee, particularly Professors R.P Gangloff and J.A. Wert, the International Committee and the University of Virginia for their help over the past couple of years. We express our sincere thanks to Dr. A.H. Rosenstein of the Air Forces Office of Scientific Research, Dr. G. Mayer of the Army Research Office, Dr. B.A. MacDonald of the Office of Naval Research, and Dr. G. Hartley of the National Science Foundation for their financial support, and to Ms. Tana B. Herndon for her sterling efforts as the conference secretary.

R.O. Ritchie
E.A. Starke, Jr.
June 1987.

RECOMMENDED SYMBOLS

a	Crack-Length - One-Half the Total Length of an Internal Crack or Depth of a Surface Crack
Δa	Crack Growth Increment
a.c.	Alternating Current
B	Test Piece Thickness
C	Compliance
C_1 - C_5 & D	Constants
da/dN	Rate of Fatigue Crack Propagation
$\Delta\frac{da}{dN}$	Additional Growth Rate due to Environment
$\left[\frac{da}{dN}\right]_{CTB}$	Growth Rate Retarded by Crack Tip Blunting
$\left[\frac{da}{dN}\right]_{LHE}$	Growth Rate Enhanced by Localised Hydrogen Embrittlement
$\left[\frac{da}{dN}\right]_{TCF}$	Overall Growth Rate for 'True Corrosion Fatigue'
$\left[\frac{da}{dN}\right]_{SCF}$	Stress Corrosion Fatigue Crack Growth Rate
$\left[\frac{da}{dt}\right]_{P}$	Stress Corrosion Plateau Growth Rate Per Second
da/dt	Crack Extension Rate
d.c.	Direct Current
δ	Value of Crack Opening Displacement (see British Standard BS5762)
δ_c	Critical Crack Opening Displacement, being One of the Following: (1) Crack Opening Displacement at Fracture (2) Crack Opening Displacement at First Instability or Discontinuity (3) Crack Opening Displacement at which

	an Amount of Crack Growth Commences
δ_m	Crack Opening Displacement at First Attainment of Maximum Force
D_H	Diffusion Coefficient for Hydrogen in Iron
E	Young's Modulus of Elasticity
exp	Exponential Base of Natural Logarithms
ε	Creep Strain
$\dot{\varepsilon}_S$	Secondary Creep Rate
ε_T	Transient Creep Strain
F	Cyclic Frequency
G	Strain Energy Release Rate
$G_I G_{II} G_{III}$	Crack Extension Forces for Various Modes of Crack Opening
I	Current
i_a	Anodic Current Density
K	Stress Intensity Factor - a Measure of the Stress-Field Intensity Near the Tip of a Perfect Crack in a Linear-Elastic Solid
K_c	Fracture Toughness - The Largest Value of the Stress-Intensity Factor that exists Prior to the Onset of Rapid Fracture
K_{cl}	K in Fatigue Cycle Below which Crack is Closed
K_I	Opening Mode Stress Intensity Factor
K_{IC}	Plane-Strain Fracture Toughness as Defined by ASTM Standard Designation E 399-74 or British Standard BS 5447
K_{Ii}	Elastic Stress-Intensity Factor at the Start of a Sustained-Load Flaw-Growth Test
K_{ISCC}	Plane-Strain K_I Threshold Above which Sustained Load Flaw-Growth Occurs

K_{IH_2S}	Value of K_{ISCC} in Dry H_2S Gas
K_Q	Provisional Fracture Toughness Value Corresponding to a 5% Deviation of the Load/Displacement Relationship from Linearity
K_{max}	Maximum Stress-Intensity Factor
K_{min}	Minimum Stress-Intensity Factor
ΔK	Stress Intensity Range
ΔK_{th}	Threshold Stress Intensity Factor Below which Fatigue Crack Growth will not occur
ΔK_i^o	ΔK_i to just cause Fatigue Initiation
ΔK_n	Next Value of ΔK
ΔK_{th}^o	Value of ΔK_{th} at R = O
ΔK_o	Constant Value of ΔK_{th}
$d\Delta K$	Notional Extra Stress Intensity due to Environment
k_T, k_N	Stress Concentration Factor, Neuber Correction Factor
ln	Natural Logarithm
log	Common Logarithm
m	Power Exponent in Paris-Erdogen Expression $\frac{da}{dN} = A\ \Delta\ K^m$
N	Cycles
N_i	Cycles to Initiate
N_F	Cycles to Failure
ΔN	Cycles Increment
n	Strain Hardening Exponent
ΔP	Load Range
ν	Poisson's Ratio

Q	Flaw Shape Parameter
σ	Stress
$\Delta\sigma$	Stress Range
σ_{max}	Maximum Stress
σ_{ps}	Proof Stress
σ_{min}	Minimum Stress
σ_u	Ultimate Tensile Strength
σ_y	Yield Stress under Uniaxial Tension
$\Delta\sigma_{net}$	Stress Range on Net Section
R	Minimum Load/Maximum Load
R_{cl}	R below which Crack Closure Occurs
r_p	Plastic Zone Size
ρ	Crack Tip Radius
ρ_o	Notional Minimum Value of ρ
T	Temperature
t	Time
t_h	Hold Time in Load Cycle
t_r	Rise Time in Load Cycle
t_r^o, t_r^{max}	Values of t_r at Minimum and Maximum Environmental Enhancement
V	Potential Difference
V_o	Reference Potential Difference
$V(a)$	Potential Difference at Crack Length, a
W	Test Piece Width
ϕ	Electric Potential
x, y	Cartesian Co-ordinates

Y	Compliance Function
Ω	Ohms

RECOMMENDED ABBREVIATIONS

BFS	Back Face Strain
BRF	Blunting Retardation Factor
CCP	Centre Cracked Plate
COD	Crack Opening Displacement
CT	Compact Tension
CTB	Crack Tip Blunting
DCPD	Direct Current Potential Drop
EEF	Environmental Enhancement Factor
LHE	Localised Hydrogen Embrittlement
PD	Potential Drop
SENB	Single Edge Notched Bend
SENT	Single Edge Notched Tension
SCC	Stress Corrosion Cracking
SCF	Stress Corrosion Fatigue
TCF	True Corrosion Fatigue
T-Type WOL	T-Type Wedge Open Loading
UTS	Ultimate Tensile Strength

CONTENTS

VOLUME III

ENVIRONMENTAL ASSISTED FATIGUE

MODELING AND EXPERIMENTAL TECHNIQUES

OVERVIEWS

ENVIRONMENTAL ASSISTED FATIGUE

A STUDY OF CORROSION FATIGUE CRACK INITIATION, GROWTH AND THE THRESHOLD CONDITION UNDER VARIABLE AMPLITUDE LOADING

I.M. Austen* and E.F. Walker*

Variable amplitude corrosion fatigue is the major cause of service failures and fatigue life is dominated by crack initiation and growth at low rates. Life predictions require research into mechanisms and modelling and this paper describes work on three areas. These are initiation from notches, crack growth rates and threshold ΔK each under constant and variable amplitude loading. Results are considered in terms of quantitative models based on mechanistic understanding.

INTRODUCTION

Fatigue is still the major cause of failure in metal structures or components and in virtually every case the situation is complicated in terms of investigation and prevention by at least one of the following features:- (i) a corrosive environment which accelerates failure rate, (ii) a stress history that is not simple constant amplitude, (iii) a stress concentration, notch or crack-like defect.

Thus, understanding of variable amplitude corrosion fatigue crack growth becomes the most important task in improving the integrity of components and structures in service.

Quantitative information for preventative design and life prediction can come either from modelling or from laboratory tests which simulate the service condition. Accurate simulation of the service environment implies not accelerated but real time testing. Data acquisition rates are then directly related to the expected or design life, typically tens of years. Accurate prediction from models which can extrapolate to realistic fatigue life requirements

* British Steel Corporation, Swinden Laboratories, Rotherham, UK.

necessitate precise mechanistic models which in the first instance require validation against experimental data.

EXPERIMENTAL PROGRAMME

A comprehensive experimental programme has been carried out and full details and results will be published elsewhere (1). The research addressed three areas of corrosion fatigue crack growth and employed constant amplitude (CAL), block loading (BL) and random loading (RL). The areas, with the total number of experiments in each, were:- (i) initiation from notches (116), (ii) crack growth rate (48), (iii) crack growth thresholds (32).

Steels Three steels were used in the research, two high strength steels with tempered martensitic microstructures and a structural steel with a ferrite/pearlite microstructure. The analysis and properties of these steels are given in Tables 1 and 2.

TABLE 1 - Chemical Analyses (Wt, %)

Steel	C	Si	Mn	P	S	Cr	Mo	Ni	V	Cu	Nb
BS4360-50D	0.155	0.36	1.24	0.019	0.025	0.045	0.025	0.04	-	0.06	0.03
835M30	0.29	0.16	0.47	0.016	0.012	1.2	0.19	4.22	-	-	-
817M40	0.38	0.29	0.67	0.04	0.017	1.26	0.28	1.50	0.20	0.21	-

TABLE 2 - Basic Properties

	σy MPa	σu MPa	Elongation %	R of A %	K_{IC} MPa $\sqrt{m}$	K_{IH_2S} MPa $\sqrt{m}$
BS4360-50D	353	504	31	65	62*	63
835M30	1291	1686	11	41	80	17.6
817M40	1166	1277	14	49	66	23.6

* not valid K_{IC}

Computer Controlled Testing All tests used the DCPD technique for monitoring initiation and growth of fatigue cracks. Calibrations were derived experimentally and represented as third order polynomials (2,3). Most of the tests were controlled and monitored using a multi-tasking computer system developed at BSC Swinden Laboratories (4). This system controls eight servohydraulic fatigue machines simultaneously where each can perform a different test type from a choice of eleven. Facilities are available for CAL, BL and three types of narrow band random loading with testing modes of increasing ΔK, constant ΔK or reducing ΔK. In addition, strain controlled low cycle fatigue (LCF) testing is performed using this system.

Initiation From Notches Three point bend specimens of 817M40 steel, 10 x 30 x 140 mm, were used which contained notches 7.5 mm deep with 0.076, 1.59, 3 and 11.75 mm root radius in addition to fatigue pre-cracks. Fatigue tests were performed under CAL and narrow band RL at stress ratios of 0.05 to 0.7 in air and in 3.5% NaCl. For each combination, up to five tests were used to define the minimum driving force for initiation, the cycles to initiate cracks discernible by the 50 μm resolution DCPD system and the subsequent crack growth rates.

With a view to prediction of initiation life, LCF parameters were established for this steel using both smooth and precorroded specimens.

Crack Growth Rate The history effects of RL and BL on crack growth rate as a function of ΔK were assessed using 20 mm thick CT specimens of 835M30 and BS4360-50D steels in air and aqueous environments.

The block loading consisted of simple single overloads repeated after intervals of constant amplitude loading and also more complex overload/underload and repeated overload sequences were used. The random loading had clipping on both peaks and trough with turning points linked by a ramp waveform with a constant time period. The clipping necessarily altered the specified mean and rms so each sequence was cycle counted by the 'Rainflow' method to produce accurate parameters for calculation of ΔK_{rms} for data presentation. Crack growth rate, da/dN, was calculated using a five point sliding polynomial method using logarithmic increments of crack length (1, 2).

Crack Growth Thresholds Automated threshold testing was carried out using a constant K gradient, constant R, step load reduction technique to establish ΔK_{th} values at a growth rate of 2×10^{-11} m/c. This method is one of four outlined in a British Standard Draft for Development to be published in the near future (5). The ΔK level was reduced according to:-

$$\Delta K = \Delta K_s \exp [C_K (a-a_s)] \quad \ldots (1)$$

where C_K, the normalised K gradient, was calculated from:-

$$C_K = -0.35 \left[\frac{(1-R)\sigma_y}{\Delta K_s}\right]^2 \quad \ldots (2)$$

This provides a 10% reduction in the first step over an increment of three times the maximum crack tip plastic zone size (1,5).

RESULTS, ANALYSIS AND MODELLING

Initiation From Notches

Fracture Mechanics Approach Traditionally, initiation life, N_i, has been correlated with the notional stress parameter $\Delta K_i/\sqrt{\rho}$ where ΔK_i is calculated assuming the notch depth is part of the crack (2). This approach was shown to provide inadequate statistical correlation for prediction purposes with a typical scatter band width of two orders of magnitude on life (1). An alternative fracture mechanics approach has been developed with the derivation of a K solution for short cracks emanating from notches. The form of short crack correction has been demonstrated by Smith and coworkers (6,7) as:-

$$\frac{\Delta K_{calc}}{\Delta K_i} = \left[\frac{a_n + H\,(D/\rho)^{\frac{1}{2}} + l_o}{a_n + D}\right]^{\frac{1}{2}} \qquad \ldots (3)$$

where values of the constant, H, are quoted as 7.09 (6) and 4.76 (7). The short crack parameter, l_o is given by:-

$$l_o = \frac{1}{\pi}\left[\frac{\Delta K_{th}}{\Delta \sigma_o}\right]^2 \qquad \ldots (4)$$

An alternative form to Equation (3) is now proposed which allows H to be uniquely defined, independent of l_o, by setting the correction to unity for the case of a fatigue precrack; this gives:

$$\frac{\Delta K_{calc}}{\Delta K_i} = \left[\frac{a_n + H \cdot \frac{a_n}{l_o} \cdot \left(\frac{D}{\rho}\right)^{\frac{1}{2}}}{a_n + D}\right]^{\frac{1}{2}} \qquad \ldots (5)$$

Substitution at a_n equal to l_o gives H simply as $\sqrt{D\rho_c}$, where ρ_c is the root radius of a real fatigue crack. This correction factor applies only when it is greater than unity and for crack lengths less than l_o, a_n is set equal to l_o. Using this approach, Fig. 1 shows the correlation with initiation life. Note that there are some data points for initiation and subsequent arrest which could also be predicted from Equation (5) with a knowledge of the propagation threshold, ΔK_{th}, for the appropriate environment and loading mode. The lower bound to the data in Fig. 1, excluding arrest points is:-

$$N_i = 3.92.10^7\ \Delta K_{calc}^{-4.29} \text{ for } \Delta K_{calc} > 2 \text{ MPa } \sqrt{m} \qquad \ldots (6)$$

Local Stress Approach As an alternative to the fracture mechanics approach, a local stress approach may be adopted so that initiation life can be predicted from LCF parameters. Using Neuber's Rule, it can be shown that:-

$$\Delta\sigma_{local} = \Delta\sigma_{net} \cdot k_N = \left[4\,\sigma_f'^2\,(2N_i)^{2b} + 4\,E.\varepsilon_f'(2N_i)^{b+c}\right]^{\frac{1}{2}} \quad \ldots(7)$$

A comparison is made in Fig. 2 between the data expressed in terms of local stress, which has much reduced scatter, with the prediction from LCF properties which gives an adequate lower bound prediction.

Crack Growth Rate

As an illustrative example of the results obtained comparing CAL, BL and RL corrosion fatigue crack growth rates, Fig. 3 shows data for BS4360-50D steel in seawater at 1 Hz with a stress ratio of 0.05.

Random Loading The RL results in Fig. 3 were obtained using a Gaussian sequence with complete cycles. The crack growth behaviour, when plotted in terms of ΔK_{rms}, fall just to the left of the CAL data. The rms representation is not strictly valid as exact coincidence can only occur when an equivalent ΔK parameter based on the mth root of the mth moment of the RL sequence is used where m is the slope of the Paris Law for CAL. The correction factor for narrow band random loading is (8)

$$\frac{\Delta K_h}{\Delta K_{rms}} = \sqrt[m]{\Gamma\left(\frac{m}{2} + 1\right)} \quad \ldots (8)$$

(where Γ is the gamma function from statistical tables).

In this particular case, the correction is to increase ΔK_{rms} values by 13.4% which would result in exact coincidence. This implies that there are no net history effects and that all cycles are damaging. In this sequence, the smallest cycles have the highest stress ratio so most, if not all, of them are above their respective ΔK_{th} values. This conclusion further implies that Miner's Rule of linear damage accumulation may be applied to predict RL growth rates from CAL behaviour.

Block Loading Whilst narrow band RL with complete cycles appears to produce no net history effects, the crack growth results in Fig. 3 for periodic overloads clearly show retardations in growth rate. In this case, single overloads 70% higher than the CAL maximum were applied every 25 000 cycles.

Modelling of crack growth retardation due to overloads may be tackled quantitatively using the residual stress intensity approach (9) where the overload induces a compressive K_R at the crack tip which must be subtracted from the K_{max} and K_{min} to leave ΔK_{eff} for calculation of growth rate. The original formulation of the model due to Willenborg (10) has

$$K_R = K_{OL}\left[1 - \frac{\Delta a}{Z_{OL}^{max}}\right]^{\frac{1}{2}} - K_{max} \qquad \ldots (9)$$

In this research, this model has been refined to incorporate so called 'delayed retardation' and 'overshoot' as follows:-

$$K_R = K_{OL}\left[1 - \frac{\Delta a}{Z_{OL}^{max} - Z_{CA}^{max}}\right]^{\frac{1}{2}} - (K_{OL} - K_{max})\left[1 - \frac{\Delta a}{Z_{OL}^{rev}}\right]^{\frac{1}{2}}$$

$$- K_{max}\left[1 - \frac{\Delta a}{Z_{OL}^{max}}\right]^{\frac{1}{2}} \qquad \ldots (10)$$

A full derivation is given elsewhere (1). The first term in Equation 13 describes the decay in the overload effect which becomes zero when the CAL maximum plastic zone boundary crosses that due to the overload (Fig. 4c). The second term controls delayed retardation where K_R is in fact zero at the point of overload (Fig. 4a) and realises its greatest effect when the moving crack tip crosses the reversed plastic zone boundary due to the overload (Fig. 4b). The third term describes the overshoot phenomena where growth rates surpass those expected in CAL (Fig. 4c and d). During this period K_R is in fact negative and hence increases both K_{max} and K_{min} thus raising the stress ratio. An overshoot of growth rate than occurs if there is a strong stress ratio effect in CAL growth rate response.

Prediction based on Equation 13 is compared to measured growth rates in Fig. 3 where agreement is good. However this model remains simplistic in that threshold and crack closure aspects are not yet included. Current research is considering this and also considering multiple overload effects and the reduced retardation effects from overload-underload combinations. Even the single overload case is not fully resolved as not only beneficial retardation and even arrest can occur, but also bursts of ductile crack extension which dramatically increase crack length and reduce life can result from overloads. These may be modelled from CAL behaviour close to fracture and a J integral resistance curve can be used to provide a basis.

Crack Growth Thresholds The ΔK_{th} values obtained by CAL and RL testing of 835M30 and BS4360-50D steels are given in Table 4.

These results show that in the low strength BS4360-50D steel, thresholds at low R are higher in seawater due to corrosion blunting (2) and thresholds under RL are higher than under CAL due to history effects. By contrast, thresholds in the high strength 835M30 steel are low in corrosion fatigue presumably because environmentally enhanced growth lowers the ΔK at the cut off growth

rate. The RL results for this steel are not so affected by history effects as the plastic zone sizes are smaller and growth rates out of affected zones are faster.

TABLE 4 - Threshold ΔK Value (in MPa$\sqrt{m}$) For 835M30 And BS4360-50D Steels

Steel	Loading	Environment	Stress Ratio 0.05	0.25	0.5	0.75
835M30	CAL	Air	4.53	3.90	3.48	2.89
		Water	2.84	2.74	2.36	1.57
	RL	Air	7.28	5.41	2.60	1.98
		Water	4.95	3.82	2.61	
BS4360-50D	CAL	Air	6.29	4.57	5.48	3.95
		Water	8.75	6.57	5.25	3.76
	RL	Air	8.69	8.24	8.50	6.81
		Seawater	7.67	7.21	7.75	6.05

Under RL, ΔK_{th} values are characterised by a single value of ΔK_{rms}. Conceptually, growth will proceed if the one largest cycle in the test block is damaging, but at a growth rate equal to the CAL growth rate divided by the block length. Consequently, RL threshold testing should either be continued to very much lower cut off growth rates, which is impracticable, or should be carried out over a range of block lengths to determine ΔK_{th} by extrapolation.

It is known that ΔK_{th} tends towards 2 MPa $\sqrt{m}$ in steels as R tends towards unity in CAL testing and since random sequences contain all R values, this value may be assumed for life prediction purposes. However, this assumes a complete lack of history effects which are particularly prevalent at near threshold growth rates leading to high ΔK_{th} values which depend on both the RL sequence and on crack length.

The existence of a positive threshold for non-propagating cracks implies that the driving force for crack advance is zero and that this only occurs when the crack is closed throughout the fatigue cycle by various mechanisms of crack closure (1). Plastically induced closure occurs at a constant K (K_{cl}); oxide induced closure occurs at a constant ΔK (ΔK_{ox}) at the threshold. Toughness induced closure occurs as the result of a change in propagation mechanism below a K_{max} level (K^*_{max}) and thereafter at a fixed proportion (α) of K_{max} at a constant stress. Thorough consideration of the interaction of these closure mechanisms (1) reveals that there are only four relations governing the dependence of ΔK_{th} on stress ratio depending on the combination of the parameters K_{cl}, ΔK_{ox}, K^*_{max}, α and R:-

$$\Delta K_{th} = (K_{cl} + \Delta K_{ox})(1-R) \text{ or } \Delta K_{ox}$$

$$\text{or } \Delta K_{ox}\ (1-R)/(1-\alpha) \text{ or } K^*_{max}\ (1-R) \qquad \ldots (11)$$

The appropriate boundary conditions for each relation are given in (1).

To illustrate the complexity of closure mechanisms, Fig. 5 shows a schematic illustration of the course of a ΔK decreasing threshold test where ΔK is modified to ΔK_{eff} which becomes zero at threshold.

Clearly, acquisition of threshold data is time consuming and expensive so a database has been compiled of over 1000 ΔK_{th} values for steels ranging in yield strength from 114 to 2050 MPa and in various environments. This is mounted on an IBM-XT computer and has interactive interrogation and facilities for graphical display and hard copy. It incorporates the steels data from (11) together with more recently published information and it is periodically updated.

CONCLUDING REMARKS

Variable amplitude corrosion fatigue life consists notionally of four phases:- (i) initiation - an incubation period of cycles for crack formation, (ii) initial growth - where growth at ΔK levels above a threshold is discontinuous, not all cycles are damaging and growth rate can be significantly influenced by history effects, (iii) propagation - where the Paris Law governs continuous growth and da/dN correlates with ΔK_h for narrow band RL, (iv) failure - rapid increase in growth rate as instability is approached though ductile crack extension and even premature failure can be caused by high peak loads.

This paper serves to demonstrate the extent to which research has been successful in quantitative modelling within these categories. Attention has necessarily been focussed on the first two as most cycles accumulate here and dominate total life. The current position is that:- (i) initiation can be predicted from LCF properties, (ii) initial growth can be modelled using short crack ΔK corrections and measurements (or predictions) of threshold ΔK and near propagation threshold growth rates, (iii) corrosion fatigue enhancement of crack propagation can be modelled predictively (1, 2, 4, 12, 13), (iv) narrow band RL can be assessed using CAL information and Miner's Rule, (v) simple overload effects on growth rate can be quantitatively modelled.

Several problems remain. One is the requirement to model complex history effects, via plastic zone interactions, on a cycle by cycle basis. This must also include predicting the crack extensions during fatigue with large peak loads. A second major problem is cycle counting and the subsequent ordering of cycles in

a RL sequence as all history effects are dependent on K and hence crack size so the order in which cycles occur can significantly influence response and hence total life.

Prediction of variable amplitude corrosion fatigue life is therefore a real possibility provided that research continues to generate the appropriate models or data. Then prediction of each phase of life becomes a matter of appropriate computer programming.

ACKNOWLEDGEMENT

The authors are indebted to Dr. R. Baker, Research Director, British Steel Corporation for permission to publish this paper. The research was financially supported by the European Coal and Steel Community through Contract Number 7210.KE/810. The technical assistance of K. Holdsworth, M. Large and C. Lindley is also acknowledged.

ADDITIONAL SYMBOLS

a_s = starting crack length (m)

a_n = crack length from a notch (m)

b = fatigue strength component

c = fatigue ductility exponent

C_K = normalised K gradient (m^{-1})

D = notch depth, (m)

H = constant (m)

k' = cyclic strain hardening coefficient (MPa)

K^*_{max} = minimum K for roughness induced closure (MPa $\sqrt{m}$)

K_R = residual K due to overload (MPa $\sqrt{m}$)

K_{OL} = K_{max} at overload (MPa $\sqrt{m}$)

ΔK_{calc} = ΔK corrected for short cracks (MPa $\sqrt{m}$)

ΔK_{eff} = effective ΔK (MPa $\sqrt{m}$)

ΔK_h = equivalent ΔK in RL (MPa $\sqrt{m}$)

ΔK_i = initial value of ΔK (MPa $\sqrt{m}$)

ΔK_{ox} = ΔK at threshold due to oxide induced closure (MPa $\sqrt{m}$)

ΔK_{rms} = root mean square ΔK (MPa $\sqrt{m}$)

l_o = short crack parameter (m)

n' = cyclic strain hardening exponent

R = stress ratio

Z_{CA}^{max} = maximum plastic zone diameter for CAL

Z_{CA}^{rev} = reversed plastic zone diameter for CAL

Z_{OL}^{max} = overload maximum plastic zone diameter

Z_{OL}^{rev} = overload reversed plastic zone diameter

α = closure factor

ε_f' = fatigue ductility coefficient

ρ_c = fatigue crack tip radius (m)

σ_f = fatigue strength coefficient (MPa)

$\Delta\sigma_{local}$ = local stress range (MPa)

$\Delta\sigma_o$ = fatigue limit (MPa)

REFERENCES

(1) Austen, I.M. 'Quantitative Assessment of Corrosion Fatigue Crack Growth Under Variable Amplitude Loading', ECSC Contract 7210.KE/810 Final Report, to be published in 1987.

(2) Austen, I.M. 'Quantitative Understanding of Corrosion Fatigue Crack Growth Behaviour', ECSC Contract 7210.KE/806 Final Report EUR 8560 July 1982 (HMSO).

(3) Lindley, C. and Austen, I.M. BSC Technical Note EM/2/86/A (7687) Feb. 1986.

(4) Austen, I.M. and Holdsworth, K. in Proc. Int. Conf. 'Fatigue of Engineering Material and Structures', Sheffield, Sept. 1986 (I.Mech.E) p 485.

(5) 'Draft British Standard Method for the Measurement of Threshold Stress Intensity Values and Fatigue Crack Growth Rates in Metallic Materials' to be published in 1987.

(6) Smith, R.A. and Miller, K.J. Int. Jnl. Mech. Sci. 19, 1977 p 11.

(7) Cameron, A.D. and Smith, R.A. Int. Jnl. Fatigue, 3, 1981, p 9.

(8) Hancock, J.W. et al in Proc. Int. Conf. 'Fatigue and Crack Growth in Offshore Steels', London April 1986 (I.Mech.E) p 49.

(9) Chang, B. and Hudson, C.M. (Eds) 'Methods and Models for Predicting Fatigue Crack Growth Under Random Loading', ASTM SPT 748, 1981, (ASTM).

(10) Willenborg, J.D. et al 'A Crack Retardation Model Using an Effective Stress Intensity Concept,' AFFDL Report TM-71-1-FBR, 1971.

(11) Taylor, D. 'A Compendium of Fatigue Thresholds and Growth Rates', (EMAS), Warley, UK 1985.

(12) Austen, I.M. et al in Proc. Int. Conf. 'Steel in Marine Structures', Paris, October 1981, (CEC/IRSID) Paper 5.4.

(13) Austen, I.M. et al in Proc. Int. Conf. 'Prediction of Materials Performance in Plants Operating with Corrosive Environments' Cranfield, February 1986 (Ellis Horwood) to be published.

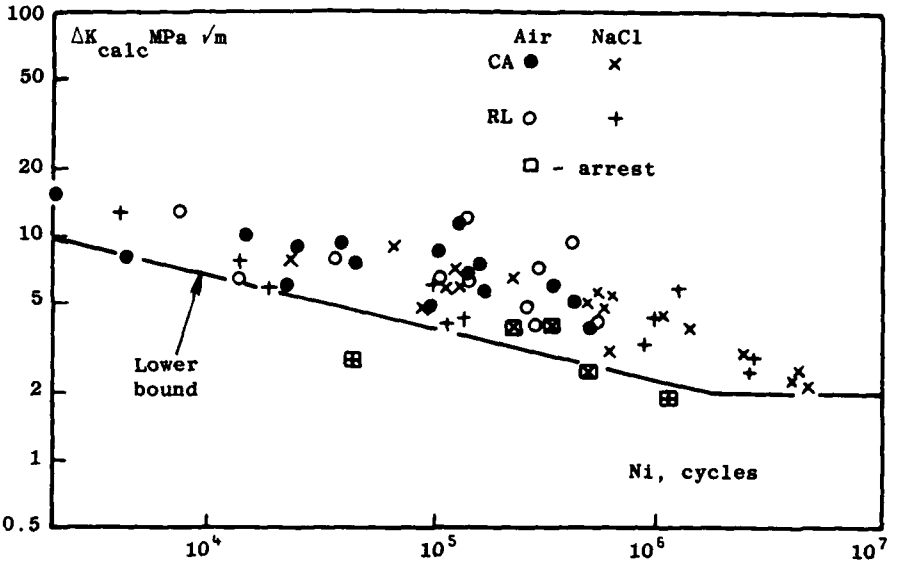

Figure 1 Correlation of Initiation Life with Geometric ΔK for 817M40 Steel

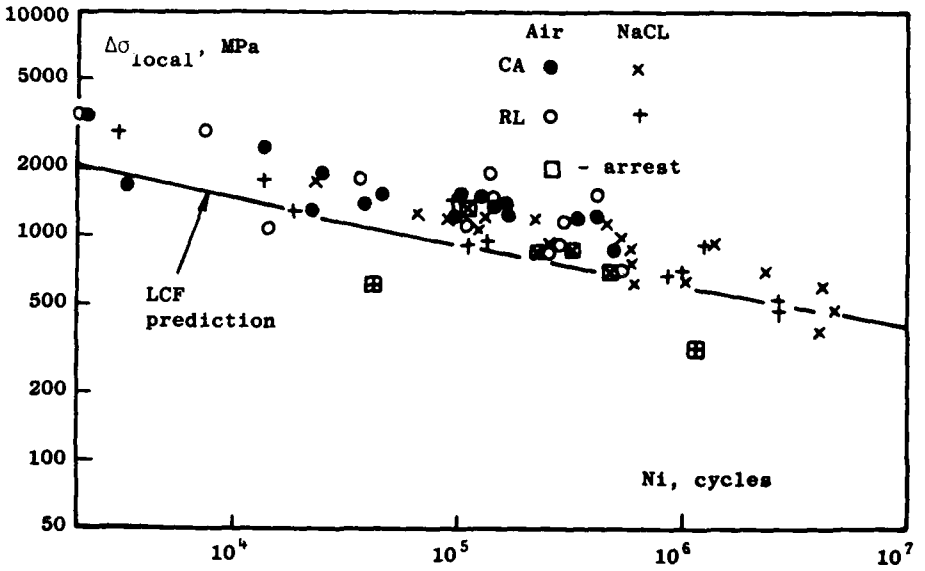

Figure 2 Prediction of Initiation Life from LCF Properties for 817M40 Steel

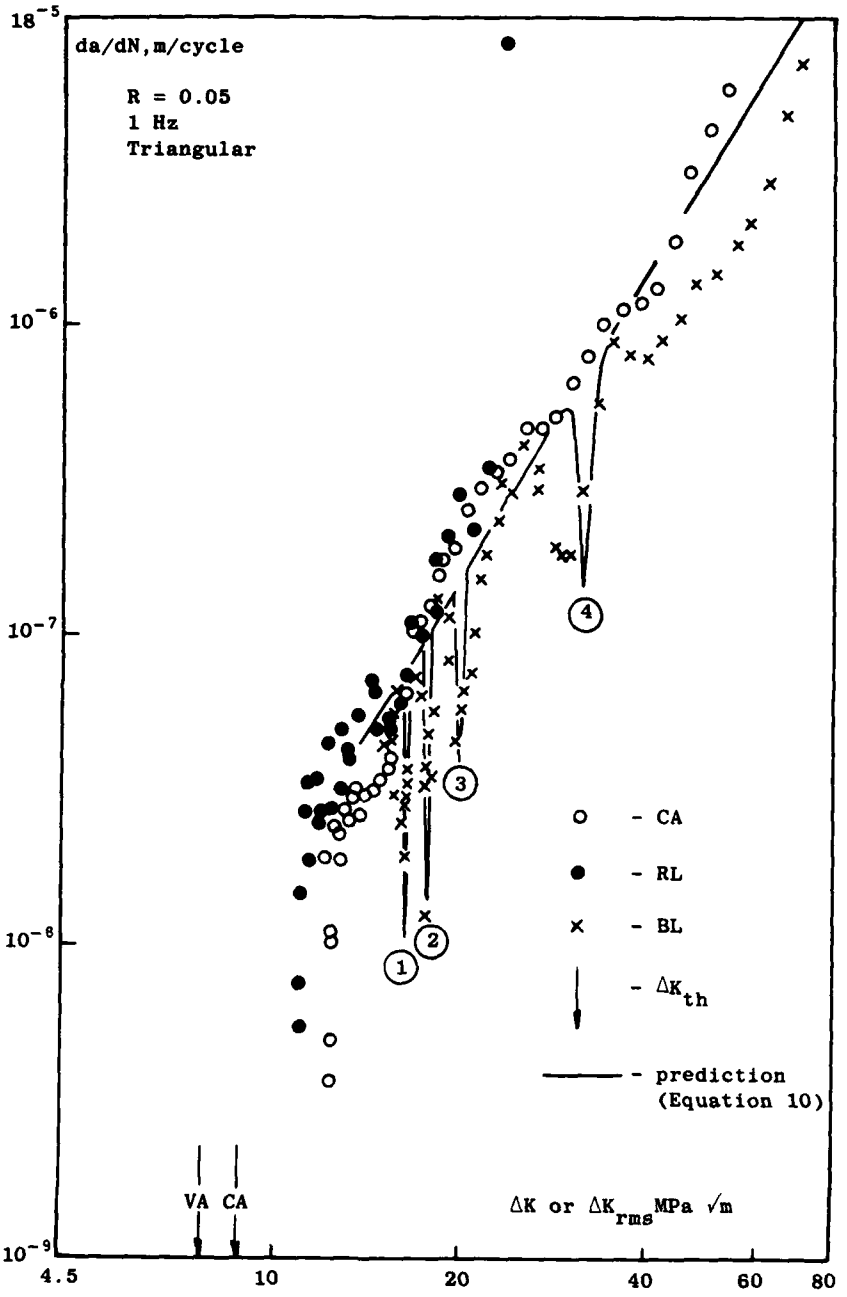

Figure 3 Crack Growth Rates in BS4360-50D in Seawater

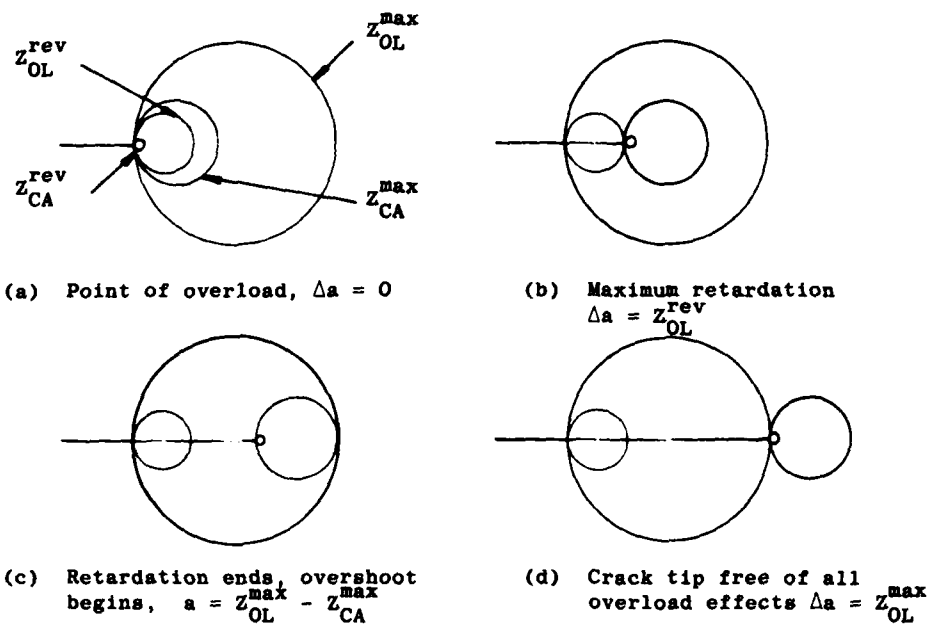

(a) Point of overload, $\Delta a = 0$

(b) Maximum retardation $\Delta a = Z_{OL}^{rev}$

(c) Retardation ends, overshoot begins, $a = Z_{OL}^{max} - Z_{CA}^{max}$

(d) Crack tip free of all overload effects $\Delta a = Z_{OL}^{max}$

Figure 4 Crack Tip Plastic Zone Interaction Following an Overload

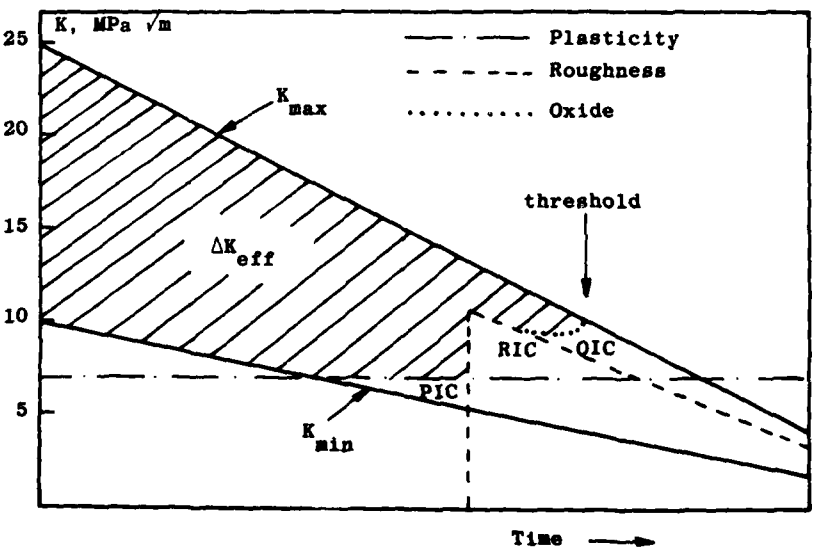

Figure 5 Development of ΔK_{eff} During a Threshold Test

EFFECTS OF CORROSION AND CATHODIC PROTECTION ON CRACK GROWTH IN OFFSHORE PLATFORM STEELS IN SEA WATER:

EINAR BARDAL*

Corrosion fatigue of steel for offshore platforms has been studied at SINTEF since 1973. Particularly, the following subjects have been given much attention: Near threshold crack growth, measurement of very low crack growth rates, effects of corrosion and cathodic protection at different crack growth levels, mechanisms of the effects of cathodic protection and the total effects of corrosion and cathodic protection on fatigue crack growth life. The paper gives a review of the most important of these results, which are compared with results reported in the literature.

INTRODUCTION

Due to long service lives required from offshore steel structures and the uncertainties involved with acceleration of fatigue tests in corrosive environments, realistic endurance data for these conditions cannot be obtained by conventional SN tests (1). For welded joints, however, fracture mechanics methods and crack growth data offer a possibility of extrapolation of SN-curves into the high cycle region. In this connection there is a need for very slow crack growth data, and an experimental program was established in 1975 to obtain such data.

Two main features have characterized the experimental efforts to obtain sufficient amount of data from the low crack growth rate region:

i) The application of multi single edge notch (MSEN) specimens, each of which contains 6 cracks to be studied simultaneously. The specimen, the experimental rig and the set up have been described elsewhere (2).

ii) The development and application of a crack growth measuring method and equipment, based on the potential drop technique with pulsed direct current, by which a particularly high accuracy and stability was obtained (3)(4)(5).

*) The Corrosion Centre/Division of Materials and Processes, SINTEF, N-7034 Trondheim-NTH. Norway

In addition to the experiments with MSEN-specimens, some special tests have been carried out with CT-specimens in order to study the effects of calcareous deposits formed on the crack surfaces (6).

When results from experiments with natural sea water are compared with corresponding results obtained in synthetic sea water, no significant difference is found (7). Most of the experiments referred to in this review are carried out with synthetic sea water. The investigated steel is BS 4360-50D.

In early experiments at SINTEF, no significant difference between the crack growth rates at a frequency of 0.167 Hz (representing an average wave frequency in the North Sea) and those at 1 Hz was found in the low growth rate region investigated ($da/dN < 2 \times 10^{-8}$ m/cycle) (2). This result applies to conditions of free corrosion as well as of cathodic protection. Because of this, most experiments in synthetic sea water have been carried out with a frequency of 1 Hz in order to reduce the test time. Results from other laboratories show, however, that the frequency has a remarkable effect at high growth rates (8).

In the early experimental work, effects of crack depth were also investigated (2). The strongest effect of crack depth on growth rate was found in the case of free corrosion and low stress ratio. The growth rates under these conditions are higher in shallow (1-3 mm) than in deep (3-7 mm) cracks. The effects of crack depth were further described and discussed in refs. (2) and (3).

EFFECTS OF CORROSION AND CATHODIC PROTECTION ON CRACK GROWTH RATES AND THRESHOLD VALUES.

Fig. 1 shows an example of crack growth results in the low growth rate region under free corrosion. The stress ratio R = 0.5 in this case. A curve representing the average results in Fig. 1 is shown in Fig. 2 in comparison with similar curves from MSEN-tests under other conditions.

Fig. 2 shows that the crack growth rate increases with increasing stress ratio R under free corrosion. The effect of R is less clear under cathodic protection. In both cases the threshold value of stress intensity range, ΔK_{th}, decreases with increasing stress ratio. It is well known that this is also the case in air, as shown in the figure.

Fig. 2 shows the effects of corrosion and cathodic protection on growth rates $< 2 \times 10^{-8}$ m/cycle at two different R-levels. At R = 0.02-0.1 there are only small differences between the results for air, free corrosion and cathodic protection. Taking into consideration that the shown results are mainly from deep cracks (3-10 mm), this is in agreement with results published earlier (2). At R = 0.5, however, free corrosion in sea water gives considerably higher crack growth rates and lower threshold value than air

exposure, while cathodic protection has the opposite effects compared with air. This is also shown in Fig. 10 and found in other investigations (9).

The reason for the higher threshold value under cathodic protection compared with air was studied by means of special tests with CT - specimens in air as well as in 3 % NaCl-solution and synthetic sea water under cathodic protection (-800 mV SCE) (6).

The purpose of the three different environmental conditions was to obtain three different conditions on the crack surfaces i) a relatively thin oxide layer (air), ii) no deposit (3 % NaCl solution and cathodic protection) and iii) a thicker calcareous deposit (synthetic sea water and cathodic protection).

The results are to be compared with the crack closure models (10) (11). The model developed by Suresh and Richie (10) analyses the effect of a wedge inside the crack. The important parameters are shown to be the thickness, d, of the wedge (thickness of deposit) and its distance, l, from the crack tip. More sophisticated models also take into account the rigidity of the wedge (11). The output from the models is the effect of the wedge upon the stress intensity factor at which closure occurs, expressed as $K_{cl} = f(l, d, E ---)$, where E is Youngs modulus. The driving force for crack growth thus will be reduced from the nominal ΔK to an effective $\Delta K_{eff} = K_{max} - K_{cl}$.

The specimens were tested at a frequency of 10 Hz, with a stress ratio of 0.1 and t = 20°C. Load shedding (succesive reduction of ΔK in small steps in order to avoid any effect of load history upon crack growth rate) was done in accordance with ASTM E647-78T. The load shedding was performed in the same environment as the following main test. The main test was run at constant load amplitude. For the specimen tested in synthetic sea water, it was, however, necessary to increase the load in three steps of 5 % in order to obtain a steady crack growth. In agreement with the model of crack closure and observations reported below, this indicates growth of a calcareous deposit on the crack surfaces.

The results of this is shown by the obtained crack growth data in Fig. 3. The just mentioned growth of the deposit during the experiment in seawater with cathodic protection leads to a scatter of the data points for this case. The curve suggested to the right is assumed to represent the final stage of this process.

After the crack growth tests were finished the specimens were broken open and crack surface deposits were analysed in SEM by use of EDAX. Examples of analysis at two different distances from the crack tip are shown in Figs. 4 and 5.

It is shown that the Ca/Mg ratio increases with increasing distance from the crack tip. Realizing that increasing distance means increasing exposure time, this result is in accordance with several reported analyses of calcareous deposits formed under cathodic polarization.

Thickness measurements of the deposits were also carried out, in the following way: Nickel was deposited on the crack surfaces with the aim to isolate the calcareous deposits between the nickel layer and the steel. Then the crack with the deposit was cross sectioned and the cross section was studied in optical and scanning electron microscopes. Examples of micrographs with corresponding EDAX analysis with respect to Ca at two different distances from the crack tip are shown in Figs. 6, 7, 8 and 9. The thickness of the deposit between steel and Ni a few mm from the crack tip is typically of the order of 10μm, and the existence of Ca in the deposit is evident.

The crack growth results in Fig. 3 show a good correspondance with the crack closure model. The anticipated thin oxide layer on the air exposed specimens (spec. 1 and 2) gives some increase in the threshold value compared with the spec. 3, which ideally should be free of any crack surface layer. The thick calcareous deposit (spec. 4), however, gives a much greater increase. Inserting our thickness observations in Fig. 8 in the crack closure model developed by Suresh and Richie (12) we obtain a K_{cl} value of 7-8 MPa$\sqrt{m}$, which can explain most of the difference in the nominal threshold value indicated in Fig. 3.

The above results support the crack closure model and indicate that the numinal ΔK_{th} is strongly affected by surface deposits. The calculation results in ref. (10) shows that K_{cl} is rather sensitive to variation in deposit thickness in the actual region. Therefore, the crack closure concept also can explain the large variation in experimentally determined threshold values.

In Fig. 10 mean crack growth curves from tests at R = 0.5 in air, under free corrosion in sea water and with cathodic protection at two different potentials are shown. The curves are based on crack growth data from our work at SINTEF combined with comparable data from UKAEA, Harwell, UK (8). It is seen that free corrosion in sea water gives higher growth rates than exposure in air at all growth levels. On the other hand, the effect of cathodic protection at high growth rates are quite opposite to that at low rates. The increased crack growth due to cathodic protection at high growth rates is explained by hydrogen development and embrittlement. The various effects of corrosion and cathodic protection are further discussed in ref. (7).

PREDICTION OF EFFECTS OF CORROSION AND CATHODIC PROTECTION ON FATIGUE LIFE BY MEANS OF CRACK GROWTH DATA.

It has been shown (7)(12) that the effects of cathodic protection

compared with free corrosion as well as with air exposure can be completely different for conditions resulting in fatigue lives of 40-300 years, as compared to conditions producing lives of 1-10 years. Such differences can not be disclosed by SN tests, where the whole life is spent in the test. However, long time effects of environmental conditions can be shown by fatigue life calculations based on fracture mechanics and crack growth data, assuming that reliable data are available at low stress intensity ranges near to the threshold value ΔK_{th}. That procedure is based on the knowledge that the major part of the fatigue life of welded joints in plates and tubulars is spent on crack growth under conditions that can be described by linear elastic fracture mechanics.

Some results of fatigue life calculations are presented in this section. Appropriate data for tests conducted with variable amplitude loading are scarce. Therefore a linear load distribution has been assumed, and the crack growth was calculated based on the constant amplitude growth rate curves in Fig. 10. It should be observed that by using this approach, possible sequence effects escape attention.

The loading and geometrical conditions for the calculations are shown in ref. (7). Examples of results for two different cases are shown in Figs. 11 and 12.

Fig. 11 represents a case with a small initial defect and a constant nominal stress spectrum as the crack propagates. With such a small initial defect, the crack growth data in the low growth rate region in the da/dN - ΔK diagram (Fig. 10) dominate. The result is that free corrosion decreases the life by a factor of three, while a normal and a high degree of cathodic protection increases life by the same factor. Both comparisons refer to life in air.

Fig. 12 on the other hand represents a case with a larger initial defect, pertinent to a practical situation where the defect has escaped detection after fabrication. In addition, redistribution of stresses during crack growth is assumed, so that ΔK does not increase with time (time independent ΔK-spectrum). In this case (Fig. 12) it is seen that the relative effect of free corrosion compared with air exposure is the same as for the small initial defect (Fig. 11). The consequence of the larger defect is, however, that a moderate degree of cathodic protection does not increase the life above that of free corrosion, and overprotection reduces the fatigue life furtner (in the example by a factor of 2 compared with free corrosion, but this may be a rather extreme case (7).

These results tally with SN results from other investigations concerning the effect of free corrosion. Further, they indicate that catnodic protection is no better and some times worse than free corrosion at higher stress intensity levels possible in real struc-

tures, but even better than air exposure at low stress intensity levels (small initial defects). The latter result is due to the higher threshold value which is obtained under formation of calcareous deposits. In practice, one can probably not rely upon these deposits, and design fatigue life in sea water under cathodic protection should not be assumed higher than in air under any circumstances.

The applied geometrical model is simplified, but the calculation is thought to be relevant for other geometries as well (7)(12). Possible sequence effects which are not included in the calculation, are not expected to affect the main trend in the results.

CONCLUSIONS

Application of multi single edge notched (MSEN) specimens and development of a crack growth measuring method and equipment with particularly high accuracy and stability made it possible to obtain considerable amounts of crack growth data at low growth rates ($2x10^{-11}$ - $2x10^{-8}$ m/cycle).

The threshold value, ΔK_{th}, decreases with increasing stress ratio both in air and in sea water with and without cathodic protection.

At a stress ratio R = 0.5, free corrosion in sea water gives considerably higher crack growth rates and lower threshold value than does air exposure, while cathodic protection has the opposite effects compared with air (in the low growth rate region). The reason for the higher threshold value under cathodic protection is most probably the existence of calcareous deposits formed on the crack surfaces. The results support the crack closure model. Crack surface deposits and crack closure may also explain the large variation in experimentally determined threshold values under cathodic protection.

Free corrosion in sea water gives higher crack growth rates than air exposure at all levels of crack growth. The effect of cathodic protection at high growth rates is to accelerate the growth further, and thus it is quite opposite to that at low growth rates. In accordance with these results, free corrosion in sea water reduces fatigue life compared to air exposure under different conditions, while cathodic protection affects fatigue life in completely different ways depending on geometrical and loading conditions. Under long life conditions (small initial defects) cathodic protection may give longer life than air exposure. With larger initial defects, cathodic protection may give even shorter life than free corrosion.

ACKNOWLEDGEMENT

The author wish to thank his colleagues at SINTEF who have taken part in the corrosion fatigue research work. The financial support and the permission to publish this paper from The Royal Norwegian

Council for Scientific and Industrial Research (NTNF), Phillips Petroleum CO. Norway, Statoil, Norsk Hydro, The Norwegian Petroleum Directorate, Kværner Brug,Oxelösunds Järnverk,Det norske Veritas, SINTEF and The Norwegian Institute of Technology (NTH) is gratefully acknowledged.

REFERENCES

(1) Bardal, E., Proc. 7. Scand. Corros. Congress, SINTEF, Trondheim, 1975, pp. 259-278.

(2) Bardal, E., Søndenfor, J.M. and Gartland, P.O., Proc. European Offshore Steel Research Seminar, Welding Institute, Cambridge, Nov. 1978, pp. V1/P16-1-V1/P16-12.

(3) Bardal,E., Berge, T., Grøvlen, M., Haagensen, P.J. and Førre, B., Proc. Int. Conf. Fatigue Thresholds, Stockholm 1981, EMAS 1982, vol. 1, pp. 471-487.

(4) Grøvlen, M.K., Berge, T. and Bardal, E., Conf. on Steel in Marine Structures, IRSID, Paris, Oct., 1981, Paper no. 5.6.

(5) Bardal, E., Berge, T., Grøvlen, M., Haagensen, P.J. and Førre, B., "A Pulsed d.c. Method for the Measurement of Low Rates of Fatigue Crack Growth", "Advances in Crack Length Measurement," Ed. C.J. Beevers, EMAS, 1982, pp. 139-158.

(6) Grøvlen, M. and Bardal, E., Proc. 10. Scand. Corros. Congress, Swedish Corrosion Institute, Stockholm, 1986, pp. 431-434.

(7) Bardal,E., "Effects of Marine Environment and Cathodic Protection on Fatigue of Structural Steels", "Fatigue Handbook", Ed. A. Almar-Næss, TAPIR, Trondheim, 1985.

(8) Morgan, H.G., Thorpe, T.W., Rance, A., Sylvester, D.R.V. and Scott, P.M., Conf. on steel in Marine Structures, IRSID, Paris Oct. 1981, Paper no. 5.1.

(9) Havn, T., "Corrosion Fatigue of Steel in Sea Water", Thesis for the Dr.ing.-degree at the Norwegian Institute of Technology, Trondheim, 1983 (in Norwegian).

(10) Suresh, S and Ritchie, R.O., Scripta Metallurgica, vol. 17, 1983, pp. 575-580.

(11) Beevers, C.J., Bell, K., Carlson, R.L., Starke, E.A.; Eng. Fract. Mech., Vol. 19, No. 1, pp. 93-100, 1984.

(12) Bardal, E., Haagensen, P.J., Grøvlen, M. and Sæther, F.: Proc. Fatigue 1984, University of Birmingham, Ed. C.J. Beevers, EMAS 1984, pp. 1541-1552.

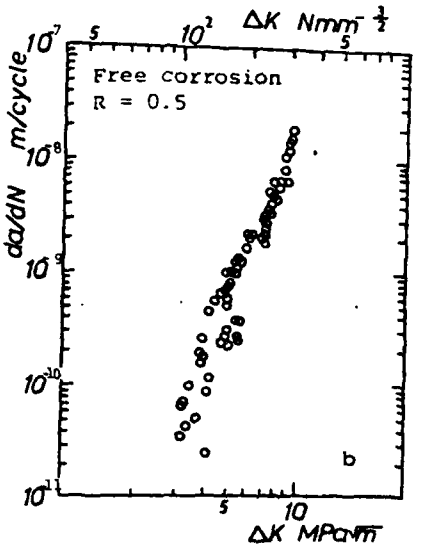

Figure 1. Crack growth data. Artificial sea water. f=1 Hz.

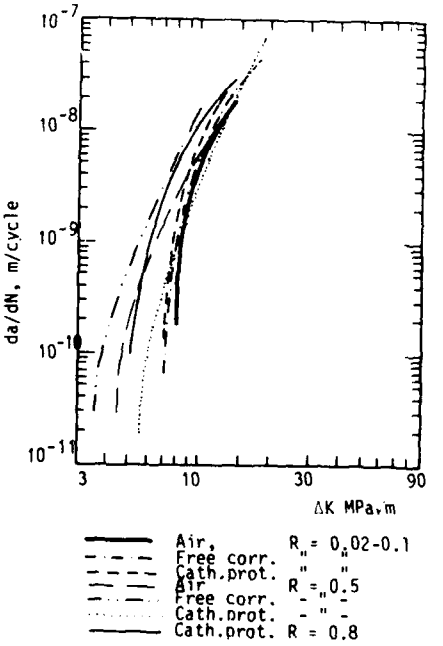

Figure 2. Mean crack growth curves for different experimental conditions.

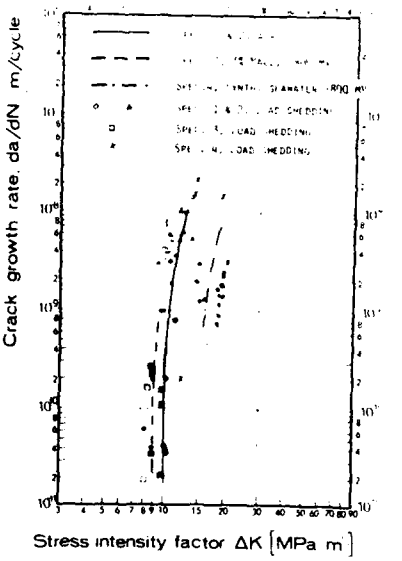

Figure 3. Results from crack growth tests with CT-specimens (6).

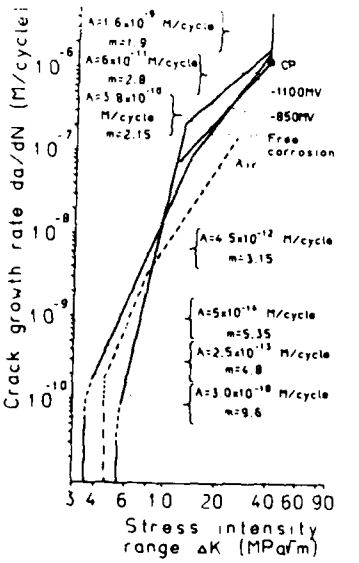

Figure 10. Mean crack growth curves for different conditions R=0.5 (7).

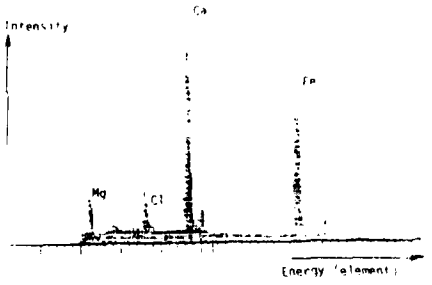

Figure 4. Analysis of crack surface deposits close to the crack tip, specimen 4 (6).

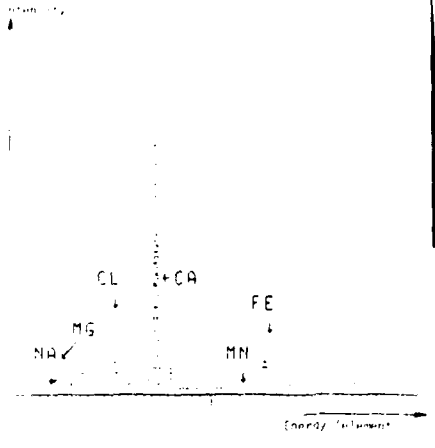

Figure 5. Analysis of crack surface deposits near the crack mouth, specimen 4. (6).

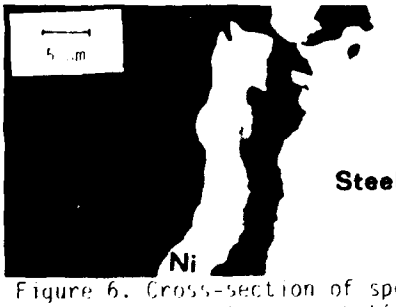

Figure 6. Cross-section of specimen 4, 0.5 mm from crack tip. SEM.(6).

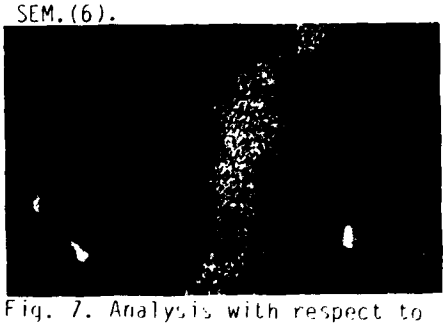

Fig. 7. Analysis with respect to Ca. Same area as shown in fig. 6. (6).

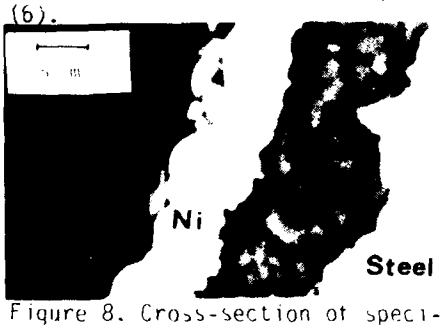

Figure 8. Cross-section of specimen 4, 2.6 mm from crack tip. SEM

Fig. 9. Analysis with respect to Ca. Same area as shown in fig.8.

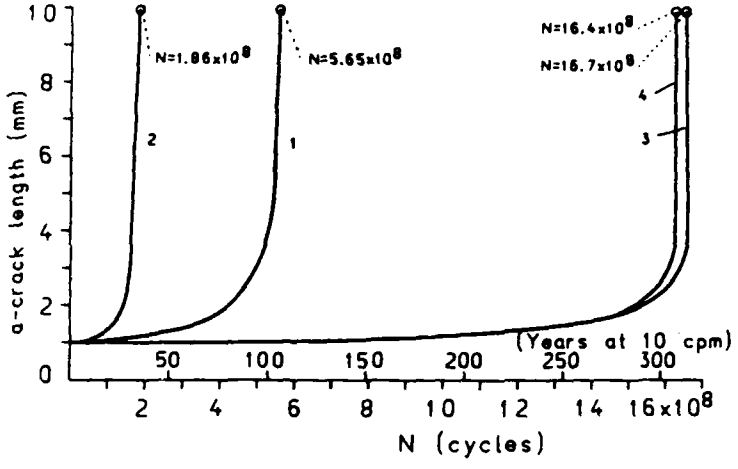

Figure 11.a-N curves for a crack of initial length 1 mm under long life conditions. Crack from a plane surface in air (1), under free corrosion in sea water (2), and with cathodic protection at -850 mV (3) and -1100 mV (4) (Ag/AgCl/sea water). $\Delta\sigma_{rms}$=28.4 MPa.

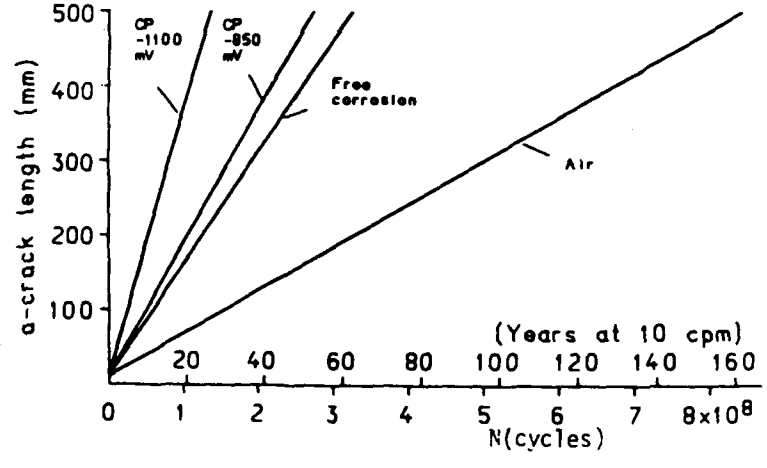

Figure 12.a-N curves for a crack of initial length 10 mm, grown from a plane surface. Constant ΔK-spectrum with ΔK_{max}≈37.5 MPa√m.

THE INFLUENCE OF CRACK CONDITIONS ON HYDROGEN UPTAKE BY STEELS

R.A. Cottis, E.A. Taqi and M. Haji-Ghassemi*

Investigations into the chemical conditions existing within simulated cracks have shown that an increased hydrogen overpotential may be obtained when the external surface of a sample is anodically polarized. This work has examined the hydrogen uptake by the steel directly, using a conventional hydrogen permeation electrode set into the wall of a simulated crack. This has confirmed that high hydrogen uptake rates may be obtained with anodic polarization. Additional tests using an occluded cell around a slow strain rate test-piece have demonstrated the possibility of hydrogen embrittlement under anodic polarization, the fractographic features observed at -500 mV (SCE) and -1200 mV (SCE) being essentially identical.

INTRODUCTION

It is generally accepted that the enhanced growth rate of corrosion fatigue cracks in steels in seawater is due to the effect of hydrogen produced by the corrosion reaction. Furthermore it is clear that the chemical and electro-chemical conditions in the crack and on the external surface of the steel will control the rate of the hydrogen evolution reaction. The chemical changes occurring within real and simulated corrosion fatigue cracks have been investigated by several workers [1-11]. Their work suggests that the pH and potential within the crack changes in a co-ordinated fashion such that the hydrogen overpotential remains relatively small at intermediate potential ranges, a significant driving force for hydrogen evolution only being obtained at external potentials below -1000 mV (SCE). However, there was an indication in work by Alavi and Cottis [10] that a significant driving force for hydrogen evolution might also occur at more positive external potentials, typically in the range -600 mV (SCE) and above. This was clearly of great significance for the interpretation of the results of fatigue tests performed at more positive potentials, since the electrochemical measurements implied that enhanced corrosion fatigue crack growth rates might be attributable to hydrogen embrittlement, rather than the more obvious explanation of anodic dissolution. The argument that hydrogen embrittlement can occur at anodic potentials is not

* Corrosion and Protection Centre, UMIST, P.O. Box 88, Manchester M60 1QD, UK.

a new one, and Barth et al. [12] have demonstrated the occurrence of hydrogen embrittlement on plane surfaces in aerated solution, although the electrochemical processes responsible for the embrittlement were not explained. Despite this evidence the role of hydrogen embrittlement at anodic potentials has not been taken very seriously, and the work reported here was intended to obtain more direct evidence of the relationship between crack electrochemistry, hydrogen uptake and hydrogen embrittlement. Both static and fatigue-cycled simulated cracks have been studied, and the results validated using the constant extension rate test in an occluded cell.

MATERIAL

The experiments were performed on a structural steel to BS 4360 Grade 50E.

EXPERIMENTAL PROCEDURES

Simulated-crack hydrogen permeation measurement

The experiments used a simulated crack formed between a steel block and a Perspex (poly-methyl methacrylate) cover plate. The crack was parallel-sided with a width determined by the thickness of a PTFE gasket which was used to seal the sides of the crack. A recess was machined in the block and the cover-plate which provided a solution reservoir at the mouth of the crack, and also allowed for the insertion of secondary and reference electrodes for the control of the external potential. Miniature glass pH electrodes were mounted in the cover plate, together with Ag/AgCl electrodes for the measurement of chloride concentration and Agar gel/KCl salt bridges. The latter connected to saturated calomel reference electrodes for the measurement of local potential, and to act as references for pH and chloride measurements. In addition to these measurements of electrochemical conditions within the crack, the rate of hydrogen permeation through a region of the crack wall was also measured. This was achieved by machining a recess 12 mm in diameter in the rear of the steel block, leaving a membrane approximately 0.4 mm thick in the crack wall. The exterior surface of this membrane was electroplated with palladium. A polypropylene electrochemical cell was inserted into the recess and sealed against the membrane with an O-ring. This cell contained 0.1 M NaOH solution together with a nickel oxide electrode extracted from a nickel-cadmium rechargeable cell. The nickel oxide electrode was electrically connected to the steel block via a zero-resistance ammeter. This maintained the potential of the palladium-plated surface of the membrane at approximately +360 mV (SCE), which ensured that all dissolved hydrogen reaching the membrane was oxidized to hydrogen ions. Consequently the current flowing in the external circuit was directly related to the flux of hydrogen leaving the membrane.

Fatigue-cycled simulated crack

In order to ensure that the crack mouth-opening displacement was realistic, the dimension and displacement of the simulated crack were based on the calculated values for a fatigue crack in steel. The relevant notional test conditions used were: crack length 60 mm, stress intensity factor range (ΔK)

38 MPa √m and cyclic frequency 0.25 Hz. The design of the simulated crack was similar to that of the static crack described above, except that the Perspex cover-plate was sealed onto the steel block by means of side-mounted strips of silicone rubber. The compliance of the rubber allowed the mouth of the crack to be opened by means of a cam attached to a small electric motor. The crack shape was essentially triangular, the Perspex cover plate remaining in contact with the steel block at the crack tip throughout the cycle. As with the static crack, facilities were provided for the measurement of pH, chloride concentration and potential within the crack, and the rate of hydrogen permeation through the crack wall.

Constant extension rate test with occluded cell

A third simulated crack was produced in which the crack geometry was less clearly defined, but in which the metal could be strained to simulate the conditions occurring at the tip of a fatigue or stress corrosion crack. It was not possible to undertake hydrogen permeation measurements in this case, but the effect of the hydrogen on the mechanical properties of the steel provided an indirect measure of the rate of hydrogen generation. The CERT test used a conventional test machine developed at Newcastle University. The specimen configuration is shown in Figure 1. This used a silicone rubber tube mounted around the gauge length of the specimen. pH, potential and chloride electrodes were sealed into this tube using cold-curing silicone rubber compound, while a small hole in the tube provided reasonably reproducible mass transport conditions.

RESULTS

Static crack

The electrochemical conditions in the crack and the rate of hydrogen permeation through the crack wall is shown in Figure 2, together with the overpotential for hydrogen evolution, calculated from the pH and potential within the crack. It can be seen that the rate of hydrogen permeation tends to follow the hydrogen overpotential in a reasonably consistent fashion. Furthermore the hydrogen overpotential becomes more negative and the rate of hydrogen permeation increases as the potential is made more positive. The effect of small additions of sulphide to the solution varies according to the applied potential and the concentration of sulphide. In contrast with expectations from work in acid solution the effect of sulphide is not always to increase the rate of hydrogen permeation, and even when it does increase, the magnitude of the increase is relatively modest.

Fatigue-cycled crack

Unfortunately, problems were experienced with high and variable background currents in the hydrogen permeation measurements in the fatigue-cycled crack. In Figure 3 the majority of the hydrogen permeation values have been estimated from the hydrogen overpotential calculated from the crack pH and potential values. In general it can be seen that the behaviour in terms of crack potential and pH is changed relatively little compared to the static crack. This is consistent with the predictions of the model developed by

Turnbull [13]. However, when viewed in terms of the hydrogen overpotential, it is clear that the slightly higher pH in the fatigue-cycled crack at anodic potentials leads to a significantly more positive hydrogen overpotential, and hence (presumably) a lower hydrogen uptake. The pH will presumably fall closer to that observed in the static crack at lower cyclic frequencies, and it may be significant that the test frequency was in the middle of the range where frequency is found to affect crack growth rates. It can also be seen that the estimated permeation current does not match with the measured current. Where measurements were able to be made, the estimated current is of the order of ten times that which was measured. This may simply be an indication of the difficulty of extrapolating from hydrogen overpotential measurements, since these are particularly sensitive to errors in the measurement of pH and potential. Alternatively it may indicate that hydrogen recombination poisons, such as hydrogen sulphide, are building up in the static crack.

CERT tests

The effect of applied external potential on the reduction of area in the CERT test is shown in Figure 4. It can be seen that the steel is embrittled both with cathodic and anodic polarization, and the change in reduction of area is consistent with the hydrogen permeation current measured in the static simulated crack. The fractographic features observed at extreme anodic and cathodic potentials (Figures 5 and 6) appear virtually identical, and it is clear that hydrogen embrittlement is occurring at the anodic potential.

DISCUSSION

The behaviour of the crevice and the specimen in the CERT test with cathodic polarization is consistent with intuitive expectations and with much other work, consequently this aspect of the behaviour will not be explicitly considered here.

The behaviour observed with anodic polarization is somewhat more unexpected, despite previous observations by others [12]. The results of the hydrogen permeation measurements, the observed hydrogen overpotential and the failure times and fractography of the CERT tests all imply that hydrogen embrittlement is occurring at the anodic potentials. In terms of the electrochemical conditions in the crack the increased hydrogen overpotential results from the pH continuing to fall while the external potential is raised, whereas the crack potential appears to be limited to around 600 mV (SCE). To consider the significance of this observation we must first see why the overpotential tends to remain relatively constant in the intermediate potential range. In the quasi-equilibrium conditions which develop in the crack after a few hours the oxygen concentration within the crevice is negligeable, and the primary reactions occurring are :

$$Fe \rightarrow Fe^{2+} + 2e^{-} \qquad 1.$$

$$Fe^{2+} + H_2O \rightarrow Fe(OH)_2 + H^{+} \qquad 2.$$

$$2H^+ + 2e^- \rightarrow H_2 \qquad 3.$$

In the intermediate potential range, where the hydrogen overpotential remains relatively constant, it is proposed that the pH in the crack is controlled by the precipitation of ferrous hydroxide, the net reaction being:

$$Fe + 2H_2O \rightarrow Fe(OH)_2 + 2H^+ + 2e^- \qquad 4.$$

This reaction has a potential/pH relationship which follows that of the hydrogen equilibrium, the potential at any given pH being about 50 mV above the 1 atmosphere hydrogen equilibrium.

As the potential rises and the pH falls an additional reaction must take over in order to explain the tendency of the crevice pH/potential to fall below the hydrogen equilibrium line. A possible hydrolysis reaction is :

$$Fe^{2+} + H_2O + Cl^- \rightarrow Fe(OH)Cl + H^+ \qquad 5.$$

giving a net reaction

$$Fe + H_2O + Cl^- \rightarrow Fe(OH)Cl + H^+ + 2e^- \qquad 6.$$

Because of the 2:1 ratio of electrons to hydrogen ions in this reaction the slope of the line on the E−pH diagram is half that of the hydrogen equilibrium line, giving the overall behaviour indicated in Figure 7.

Whatever the cause of the observed potential−pH behaviour, there can be little doubt of the resultant hydrogen embrittlement with anodic polarization. While this work relates to conditions in cracks or simulated cracks, similar behaviour for plain specimens in aerated solution has been observed by Barth et al. [12]. Consequently very great care must be taken in using observations of enhanced crack growth rates at anodic potentials as an argument against a hydrogen embrittlement mechanism of crack growth.

CONCLUSIONS

Enhanced hydrogen uptake and hydrogen embrittlement in steel can occur with both anodic and cathodic applied potentials.

The enhanced hydrogen uptake in conditions of anodic polarization occurs because the crack becomes acid more rapidly than the potential rises, thereby increasing the overpotential for hydrogen evolution.

REFERENCES

1. Barsom, J.M., *Corrosion Fatigue*, ed. Deveraux, O.F., McEvily, A.J. and Staehle, R.W., NACE, 1972.

2. Duquette, D.J., *ibid.*

3. Ritchie, R.O., *Proc. Environment Sensitive Fracture of Engineering Materials*, ed. Foroulis, Z.A., TMS–AIME, 1977.

4. Barsom, J.M., *Int. J. Fracture Mechanics*, **7**, 1971, p.163.

5. Hodgekiess, T., *Proc. Mechanisms of Environment Sensitive Fracture of Materials*, Metals Society, 1977, p.348.

6. Dolphin, A.S. and Turnbull, A., *Proc. Corrosion Chemistry Within Pits, Crevices and Cracks*, NPL, 1984.

7. Edwards, R.A.H., *ibid.*

8. Hart, W.H., *Corrosion 83*, Paper No. 62, NACE, 1983.

9. Landles, K., Congleton, J. and Parkins, R.N., *Embrittlement by the Localized Crack Environment*, ed. Gangloff, R.P., AIME, 1983, p.59.

10. Alavi, A. and Cottis, R.A., *ibid*, p.75.

11. Turbull, A. and Gardener, M.K., *Br. Corr. J.*, **16**, 1980.

12. Barth, C.F., Steigerwald, E.A. and Troiano, A.R., *Corrosion*, **28**, 1972, p.259.

13. Turnbull, A., *Embrittlement by the Localized Crack Environment*, ed. Gangloff, R.P., TMS–AIME, Warrendale, 1984, p.3.

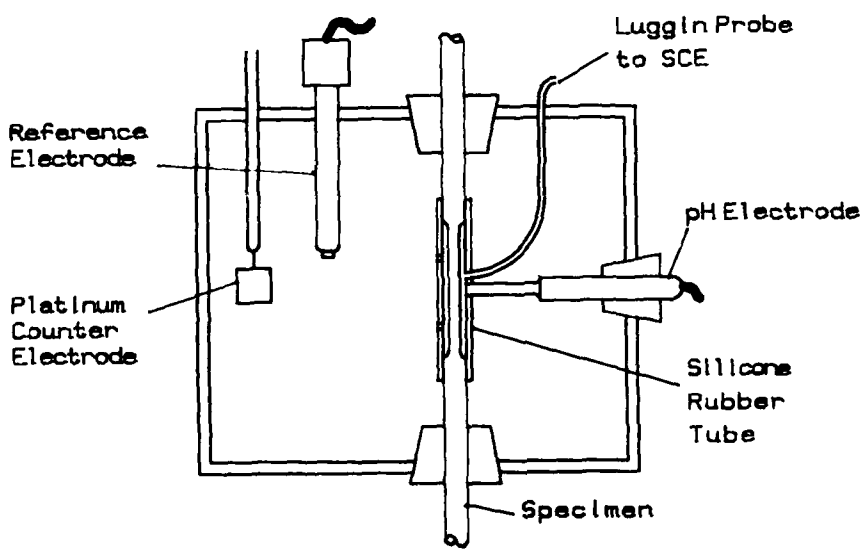

Figure 1. Configuration of CERT Test with Occluded Cell.

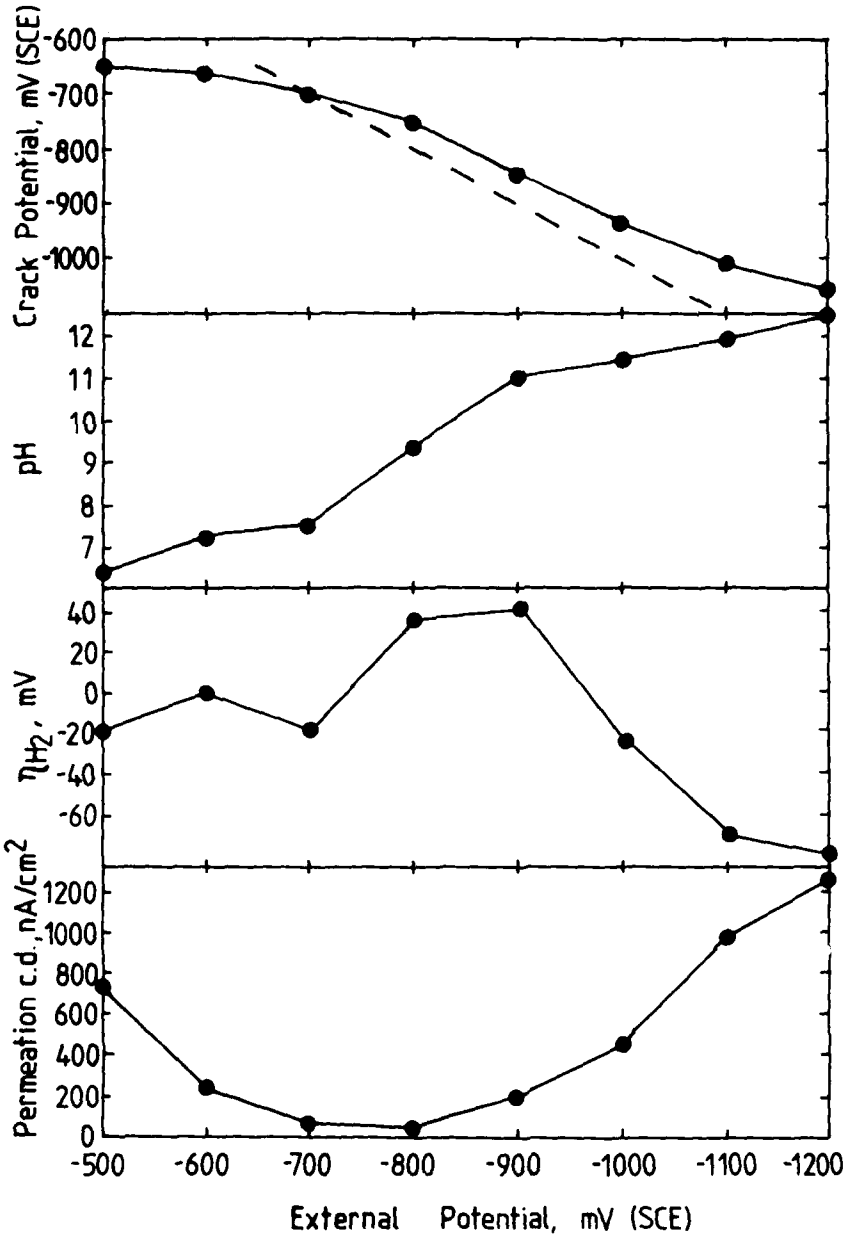

Figure 2. Electrochemical Conditions and Rate of Hydrogen Permeation in the Static Simulated Crack.

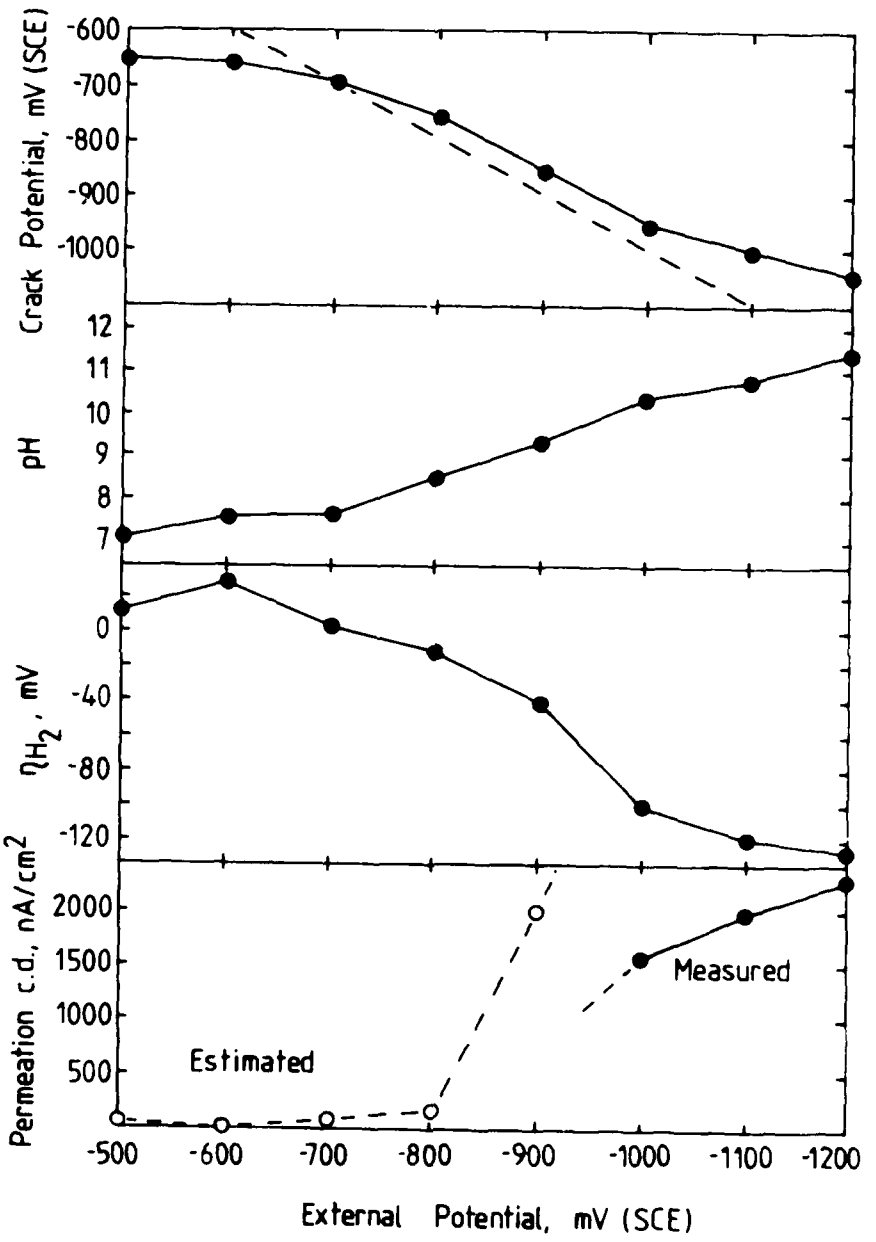

Figure 3. Electrochemical Conditions and Estimated Rate of Hydrogen Permeation in the Simulated Fatigue Crack.

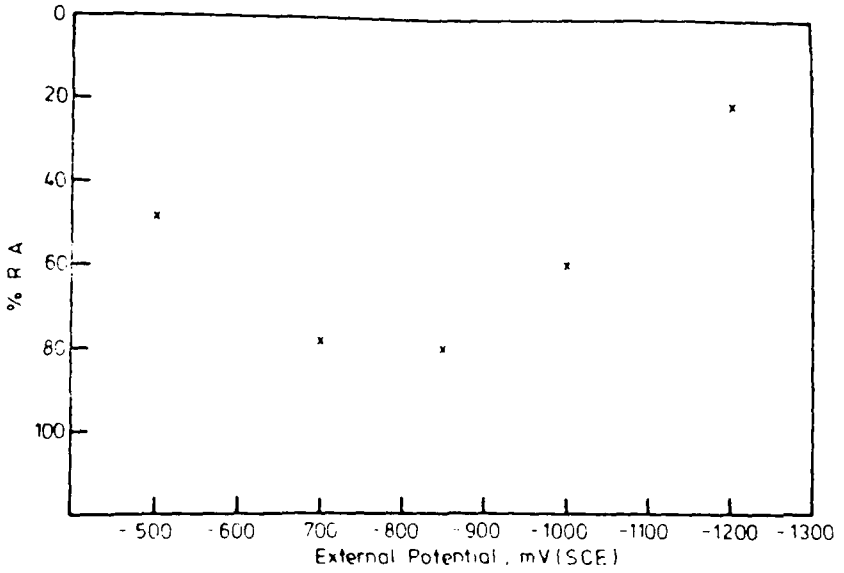

Figure 4. Effect of External Potential on Reduction of Area for the CERT Test in an Occluded Cell.

Figure 5. Fracture Surface Observed at −1200 mV (SCE).

Figure 6. Fracture Surface Observed at −500 mV (SCE).

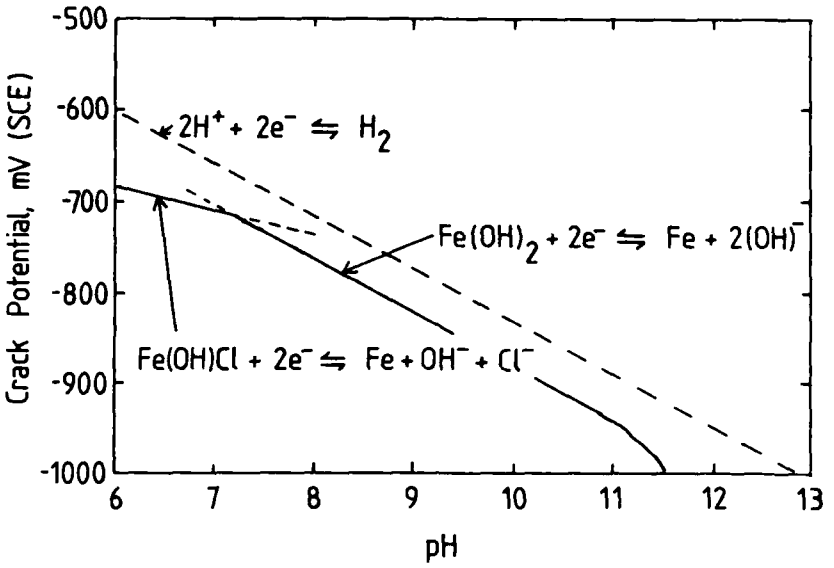

Figure 7. Schematic E−pH Behaviour in a Crack.

MODELING THE EFFECT OF SULFUR ON THE THRESHOLD ENVIRONMENTAL CRACKING RATE OF STEELS IN HIGH TEMPERATURE WATER

Peter L. Andresen*

The effect of metallurgical sulfur on the environmental crack growth rates of steels in high temperature water is modeled based on crack tip transport considerations. Contributions of sulfide dissolution are integrated with the effects of water chemistry (corrosion potential, solution conductivity, and convection) to determine the crack tip chemistry. This knowledge is coupled with oxidation kinetics measurements for various materials and calculated crack tip strain rates to provide predictions of steady state and threshold crack growth rates. The model provides a unified understanding of water and material chemistry effects in low alloy, carbon, and stainless steels as well as Inconels.

INTRODUCTION

The sub-critical, environmental crack growth rate of low alloy and carbon steels in high temperature water is dependent on numerous variables, including mechanics parameters (stress intensity, load ratio, waveform and frequency) and water and material chemistry parameters (dissolved oxygen / corrosion potential, external solution conductivity, fluid velocity and number, type, orientation and morphology of MnS inclusions) (1-3). These parameters are also known to influence growth rates in high temperature aqueous environments of stainless steels and Inconels (4-10), suggesting that a generalized model may exist to account for water and material chemistry effects.

In deaerated environments, crack growth rate enhancement can occur in steels containing more than about 0.015% sulfur (11) (Figure 1), resulting in rates above the ASME XI wet (1980) code evaluation curves. The 'high sulfur' rates are not sustained as the stress intensity range or frequency is progressively lowered, giving rise to threshold behavior which varies with system parameters and exhibits hysteresis (i.e., the threshold is dependent on whether it is approached by decreasing or increasing K, frequency, etc) (1-3).

A quantitative model developed to account for these observations has been formulated on the hypothesis that the primary influence of metallurgical sulfur (segregated to inclusions or grain boundaries)

* General Electric CRD, PO Box 8 Room 3A43, Schenectady, NY 12301

is, in combination with water chemistry parameters, to establish the crack tip chemistry. The concept implies an inter-relationship between growth rate and crack tip chemistry and inherently predicts hysteresis since the threshold condition is related to crack tip chemistry and growth rate, not loading parameters per se. Thus compared to an initially 'high' sulfur crack tip condition, starting from a 'low' sulfur condition requires a higher stress intensity or frequency to achieve the critical growth rate / chemistry.

This paper will describe a framework for integrating the effects of various water chemistry parameters to determine the crack tip chemistry. The effect of material chemistry (i.e., sulfur) will then be incorporated into this framework via an iterative solution. Other alloy composition / processing effects (e.g., chromium content or depletion in stainless steels) are independently accounted for via the oxidation / passivation kinetics as a function of crack tip chemistry. The material and environment contributions are expressed in the form of a single parameter, 'n', which is consistent with theoretical considerations (4,9). Coupling of 'n' with crack tip strain rate, calculated from engineering mechanics parameters, permits prediction of crack growth rates (9,10).

DESCRIPTION OF EXPERIMENTS

Purely analytical solutions to 2- and 3-dimensional mass transport equations which incorporate the effects of ordinary (Fickian) diffusion, ionic migration and convection are complex and critically dependent on assumptions of arguable validity. Thus crack tip chemistry studies were undertaken to experimentally simulate the effects of the three components of liquid mass transport:

$$J_i = - D_i \cdot \nabla C_i - Z_i \mu_i F C_i \cdot \nabla \phi + C_i \cdot V \qquad (1)$$

where J_i is the flux, D_i is the diffusion coefficient, C_i is the concentration, Z_i is the charge per ion, μ_i is the ionic mobility, F is Faraday's constant, $\nabla\phi$ is the potential gradient, and V is the velocity field.

The room temperature simulation experiments were performed using a Teflon® specimen of dimension similar to a 25 mm compact tension specimen with the crack simulated by a 0.46 mm or 0.076 mm machined slot 23.6 mm long (9). Crack chemistry was monitored using an array of 20, 2 mm diameter chloride ion sensitive probes, which fit snugly into vertical holes in the specimen and were positioned flush with the top surface of the crack.

The experiments examined the effects of mass transport by determining the chloride ion activity versus time at various locations in the simulated crack. Two basic types of experiments were performed. Ordinary diffusion and convection were studied by placing the specimen into a large reservoir of dilute KCl (typically 0.001 N), then introducing a more concentrated KCl solution (typically 0.3 N) into the crack and observing the decay in concentration in the crack with time. The effects of density induced flow were overcome by equalizing the solution densities using a non-ionic solute in the reservoir.

$$\dot{a} = f(n) \cdot \dot{\epsilon}_{ct}^{n} \quad (3)$$

The goal of this paper is to establish a fundamental, quantitative basis for determining 'n' as a function of corrosion potential, solution conductivity, fluid velocity, metallurgical sulfur content, alloy type, etc. The basis for and formulation of the crack tip strain rate as a function of stress intensity, frequency, load ratio, etc has been developed primarily by Ford (3,9,10).

Crack Tip Chemistry - Water Chemistry Effects

The results of the experimental simulation of crack tip chemistry are voluminous and presented in detail elsewhere (9). In the absence of convective transport, the effect on the crack tip chemistry (anion concentration) of external solution conductivity and the potential gradient is summarized in Figure 3 (lower left). The external solution conductivity, C_{ext}, establishes a minimum crack tip chemistry, C_{ct}, condition which is enhanced by a factor which is exponentially related to the potential difference, $\Delta\phi$, via:

$$C_{ct} = C_{ext} \cdot 10^{\frac{\Delta\phi}{0.4}} = C_{ext} \cdot 316^{\Delta\phi} \quad (4)$$

This prediction of crack tip chemistry assumes a critical crack length to height aspect ratio (>10 - 50), based primarily on the requirement that no oxygen be present at the crack tip. It is also assumed to scale to actual crack geometries and higher temperatures, since the effects of aspect ratio, crack length, path tortuosity, etc tend to be normalized for 'symmetrical' transport (where [1] the competing elements of transport, e.g., ordinary diffusion and ionic migration, are similarly influenced (via the Einstein relationship between diffusivity and mobility) by variations in the transport path and [2] where the source and sink for, e.g., sulfur anions are identical). Thus transport crack tip, or when convection contributes to transport since factors which influence the velocity field in crack may not similarly affect the diffusivity.

The potential gradient is established by the difference in corrosion potential between the crack mouth (the corrosion potential as normally measured) and tip (which, since oxygen is absent, is -0.5 to -0.7 V_{she} for the pH range / anion levels of interest). The anion enhancement at the crack tip results from ionic current flow in the crack, which is reasoned to be iR limited and is a simple function of the potential gradient, $\nabla\phi$, times the solution conductivity, κ. For dilute solutions, the anion enhancement factor for a given potential gradient can be assumed to be independent of conductivity; at higher conductivities, the ionic current flow for a fixed potential gradient increases and, to a first approximation, is balanced by the increased flux due to ordinary diffusion.

There are alternative explanations for the mechanism which determines the ionic current flow in the crack, including polarization at the anode or cathode, and its direct determination by the faradaically equivalent metal oxidation current density resulting from crack growth. However, [1] these factors lead to decreased accuracy in the growth rate predictions, [2] the ionic current flow calculated from iR considerations can be supplied by passive currents within the crack,

and [3] at moderately high growth rates, the equivalent crack tip metal oxidation current would create an iR drop in excess of 100 V. Instead, a significant fraction of the oxidation at the crack tip occurs by spontaneous (local) corrosion with generation of hydrogen:

$$3Me + 4H_2O = Me_3O_4 + 4H_2 \quad (5)$$

The factor of enhancement (Figure 3, lower left) is decreased by convection so that, at sufficiently high fluid velocities, little anion enhancement at the crack tip may be observed. The effect of fluid velocity is critically dependent on crack orientation, with the experimentally observed effect adequately accounted for via a pressure gradient which develops along the crack mouth and induces fluid flow within the crack (9). For an idealized crack perpendicular to the direction of flow with no variations in surface roughness or morphology along the crack mouth, fluid flow simply moves the boundary condition into the crack. For high aspect ratio cracks, this is a negligible effect. However, since the effect of fluid velocity was experimentally observed at very low fluid velocities (pressure gradients), small variations in crack orientation (from perpendicular) or surface roughness could result in significant convective effects. Thus, without detailed knowledge of the crack orientation, etc., fluid velocity effects are difficult to predict quantitatively, although their effects have been observed in the laboratory (15,16) and inferred from field data (17). By contrast, the simulation experiments showed that, except at high displacement rates where the growth rate is dominated by mechanical (inert) fatigue, the contribution of cyclic-enhanced convective transport is comparatively small.

Evaluation of Water Chemistry Predictions

The goal of crack tip chemistry modeling is ultimately to provide accurate predictions of crack growth rate over a wide range of water and material chemistries. Also, no adequate high temperature crack tip chemistry data are available for comparison, although experiments are planned. The overall, strain rate based model of crack growth rate prediction (Eqn 3) has been previously validated for low alloy, carbon and sensitized stainless steels (9,10), solution annealed stainless steel (8) and Inconels (7). Those predictions relied upon empirical fits of sensitization (EPR), which are mathematically complex. Thus, a reasonable basis for determining the accuracy of the crack tip chemistry modeling by comparing it with existing formulations of 'n'.

The basis for determining 'n' is shown graphically in Figure 3, where the predicted crack tip chemistry (lower left) is used to determine the oxidation current density at time t (upper left). This value is inversely proportional to 'n', since 'n' is simply the slope on a log-log plot of the oxidation current density vs time. The result of the graphical projection of the water chemistry curves (lower left to upper right) is a plot of the variation of 'n' with corrosion potential and solution conductivity. The predicted values, shown in dotted lines, compare very well with the empirically derived curves for low alloy steel (Figure 4) except at low potential and high conductivity, where no data was available for the empirical fit. Similar agreement is obtained for sensitized (EPR = 15 C/cm^2, Figure 3) and solution annealed stainless steel (EPR = 0, Figure 4).

Oxidation Kinetics - Critical Sulfur Level and Anion Specificity

The oxidation current density curves shown in the upper left of Figure 3 were based on measurements of Ford and Combrade (9,18). The 'critical' sulfur level (at which large changes in the oxidation current density were observed) differed by about 3 orders of magnitude, although the shapes of the curves were similar. The difference is probably attributable to the molybdate carrier electrolyte used by Ford, an influence which also may exist in borate solutions. For example, Kassner (6) observed that the 'critical' sulfur concentration (as H_2SO_4) for an increase in the growth rate of sensitized stainless steel was approximately linearly related to the sodium borate concentration.

Borate has a pH buffering effect, which tends to maintain the crack tip solution near the minimum in oxide solubility. Thus its effect is consistent with Andresen's (4) hypothesis that a primary mechanism for the effect of anions is their influence on oxide solubility (via pH shifts and complexing), particularly in establishing the transport-limited oxidation kinetics at the crack tip. While other factors may undoubtedly influence the oxidation kinetics, this hypothesis is consistent with numerous observations, including: [1] the increase in growth rate (paralleled by the oxide solubility curves) both for solutions which become acidic and those which can only become basic (eg., NaOH) (4), [2] the general similarity in enhancing growth rates (4-6) of numerous anions (sulfate, chloride, nitrate, carbonate, fluoride, etc), [3] crack velocity can be maintained as the potential is decreased if the anion content is sufficiently high (4-6), [4] the continuum in cracking kinetics from pure to impure water, and [5] the observation that two fundamental parameters, oxidation / passivation and liquid mass transport kinetics, which incorporate water and material chemistry effects, distill into a single parameter, 'n' (4,9). It also provides a basis for using oxidation kinetics measurements on smooth specimens to predict those at the crack tip, based on near-surface transport control of oxidation kinetics.

For the water and material chemistry predictions in this paper, curves similar to the Combrade data were used, with variations as a function of chromium content similar to that observed by Ford (9,18). Differences in overall alloy composition (9,10) can be adequately accounted for by altering the dependency of the oxidation current density on the crack tip sulfur level (i.e., the curve shape). Anions such as borate and molybdate apparently shift the 'critical' sulfur level, while other (aggressive) anions (eg., chloride, nitrate, carbonate, fluoride, etc) can be treated in a similar fashion to sulfur. In the latter group, correction for the contribution of the cation to solution conductivity should be made (eg., HCl vs NaCl), since it is the anion concentration which is important.

Crack Tip Chemistry - Incorporation of Metallurgical Sulfur Effects

The incorporation of metallurgical sulfur effects into the crack tip chemistry model requires some assumptions regarding the rates of sulfur anion generation and transport in the crack. Assumptions are necessary since insufficient data are available to adequately characterize the rate of generation which is a function of the distribution

of sulfur (e.g., length, aspect ratio, etc) and kinetics of dissolution (e.g., intersection rate, extent and rate of dissolution, etc). Similarly, the transport rates are difficult to determine analytically or experimentally since factors such as path tortuosity (esp., resulting from oxide precipitation) in high temperature water are difficult to characterize and are dependent on the chemistry in the crack (oxide solubility is pH dependent). In contrast to external anion sources, where transport path effects tend to be normalized by their offsetting effect on diffusivity (out) and mobility (into the crack, Eqn 1), a crack tip anion source can't be as readily modeled or extrapolated using room temperature experiments.

Thus, at this point in the research, the following working assumptions are employed. For steady state conditions, there is a linear relationship between: [1] the crack growth rate and sulfur dissolution rate in the crack, and [2] the sulfur dissolution rate and the crack tip sulfur concentration. To establish a quantitative relationship between the growth rate and (the metallurgical sulfur contribution to) the crack tip sulfur concentration, a single fitting point must be used. This is graphically shown in the lower part of Figure 5, where an arbitrary growth rate / crack tip sulfur content coordinate has been used to establish the position of the lines. For deaerated solutions (no potential gradient), the horizontal positioning of the lines is linearly related to the sulfur content (although deviations may result from non-linear relationships, e.g., of nominal S content versus MnS volume fraction, aspect ratio, distribution (banding), etc).

Apart from agreement with growth rate observations, the fitting point can be justified by calculations which employ reasonable values for the path length (1 cm), the diffusion coefficient at 300 C (19) (0.0002 cm^2/s), and the amount of sulfur dissolved per unit of crack advance, although this latter value is difficult to estimate. A sulfur 'magnification' factor, representing the ratio of the zone from which overall alloy dissolution occurs (< crack tip opening displacement) to the zone from which sulfur (MnS) can be dissolved (effective active volume), can be used to account for the non-uniform distribution of sulfur in the matrix. However, not all of the several types of MnS dissolve readily (20). Additionally, studies of the effect of sulfide stringer orientation relative to the direction of crack growth (1-3,21) show that the L-S orientation (sulfide stringers oriented perpendicular to the cracking plane) induces lower growth rates than either the T-L or L-T orientations, which are similar. Since the L-S orientation represents the largest volume of contiguous MnS intersected by the crack (volume ratio) but the smallest area of MnS (area ratio), it is reasonable to assume that incomplete dissolution of contiguous MnS occurs and therefore that the area ratio intersected by the crack is the dominant factor.

Thus the transport calculation was based on uniform sulfur distribution with dissolution from the entire (1 micron) crack tip opening displacement. At 10^{-6} cm/s and 0.02% nominal sulfur level, the sulfur anion generation rate is $-2x10^{-15}$ moles S/s. In the absence of a potential gradient and for an average crack opening displacement of 20 microns, an approximate solution for ordinary diffusion ($J_i = -D_i \cdot \Delta C_i/\Delta x$) yields a crack tip anion concentration of 0.13 ppm S^{-1} in good agreement with Figure 3 (upper left). The curve in Figure

4 (lower part) is shifted to the left for lower sulfur alloys, and to the right when a potential gradient exists (displacement to the right is assumed to be proportional to the enhancement factor in Eqn 4).

The crack tip chemistry curves (Figure 5, lower part) can be graphically projected as shown in Figure 3 using the oxidation current density curves for low alloy steel (Figure 3, upper left) to obtain the relationship between 'n' and the growth rate (Figure 5, upper part). Very high purity water (low external solution conductivity) is assumed in Figure 5. To determine 'n' and thereby the growth rate (Eqn 3) for a given loading condition (crack tip strain rate), an iterative approach is used whereby an initial growth rate estimate is used to determine the crack tip chemistry and thus 'n', which is then used to re-calculate the growth rate (Eqn 3). For a 0.02% S steel, the relationship for crack tip sulfur concentration, C_{ct}, in ppm is:

$$C_{ct} \cong C_{ext} \cdot 316^{\Delta\phi} + 10^{8} \cdot \dot{a} \qquad (6)$$

where $\dot{a}$ is the growth rate in m/s. In the absence of a potential gradient, only the second term is required. From this, 'n' can be estimated from the following fit to the oxidation current density curves:

$$'n' \cong \frac{0.55}{C_{ct} + 3.0} + 0.45 \qquad (7)$$

Substitution from Eqns 6 and 7 into Eqn 3 leads to a complex equation with three separate a terms which must be solved numerically.

In all instances, the resulting solution for growth rate is stable, as shown in Figures 6 and 7 for a high sulfur (0.02% S) steel in deaerated water and for a medium sulfur (0.01%) steel in aerated water. With decreasing strain rate, where the upper ('high' crack tip sulfur) and lower ('low' sulfur) lines diverge, two effects are predicted: [1] the sharpness of the threshold is increased and [2] the hysteresis in strain rate is increased. This model also predicts that below the 'threshold' the growth rate decreases and the dependency (slope) of growth rate versus strain rate increases, but the cracking does not cease.

Figures 6 and 7 compare the model prediction and observation for a wide range of data (see Ref 9), indicating good agreement for both the threshold and steady state predictions of the crack growth rate. The model predicts similar metallurgical sulfur effects for stainless steels, although they are of less practical consequence since the 'critical' crack tip sulfur content varies with alloy composition (Figure 3, upper left), so that much higher growth rates / sulfur intersection rates are necessary to achieve an equivalent effect. Additional factors include possible differences in the sulfide intersection rate for intergranular versus transgranular cracking and preliminary evidence that grain boundary carbide precipitation may be competitive with sulfur segregation to the boundaries.

CONCLUSIONS

1. A model for predicting the crack tip chemistry as a function of water and material chemistry is presented which provides a unified approach for understanding and predicting the effects of water chemistry (corrosion potential, solution conductivity, and fluid velocity) and material chemistry (sulfur content).

2. The model provides a mechanism for accounting for differences in alloy composition (e.g., among low alloy steel, stainless steel and Inconel) and accordingly predicts different 'critical' crack tip sulfur levels for each material.

3. Used crack tip strain rate calculations and a film rupture / slip dissolution mechanism for crack advance, quantitative predictions of threshold and steady state crack growth rates can be made which are in good agreement with observation.

REFERENCES

(1) Proc IAEA Specialists Mtg on Subcritical Crack Growth, Ed. WH Cullen, Freiburg, May 1981, NUREG/CP-0044, NRC, May 1983.

(2) Aspects of Fracture Mechanics in Pressure Vessels and Piping, Eds SG Sampath and SS Palusamy, June 1982, PVP-Vol 58, ASME, NY, 1982.

(3) Proc 2nd IAEA Specialists Meeting on Subcritical Crack Growth, Ed. WH Cullen, Sendai, Japan, May 1985, NUREG/CP-0067, NRC, April 1986.

(4) PL Andresen, Paper #101, Corrosion/85, Boston, NACE, Houston.

(5) WE Ruther, WK Soppet, and TF Kassner, Paper #102, Corrosion/85, Boston, NACE, Houston.

(6) WJ Shack, TF Kassner, PS Maiya, JY Park and WE Ruther, NUREG/CR-4667, Vol I & II, NRC, 1986.

(7) PL Andresen, Paper #84, Corrosion/87, San Francisco, NACE, Houston.

(8) PL Andresen, Paper #85, Corrosion/87, San Francisco, NACE, Houston.

(9) FP Ford, DF Taylor, PL Andresen and RN Ballinger, Final Report, Project RP2006-6, EPRI, June 1986.

(10) PL Andresen and FP Ford, Predictive Capabilities in Env Asstd Cracking, Ed. R Rungta, Nov 1985, PVP-Vol.99, ASME, NY, 1985, p 17-38.

(11) C Amzallag and JL Bernard, "Proc, IAEA Specialists Mtg on Subcritical Crack Growth", Freiburg, May 1981, NUREG/CP-0044, Vol 2, NRC, May 1983, p 127-142.

(12) HL Logan, J Research NBS, 48, 99, 1985.

(13) Int Conf on "Stress Corrosion Cracking and Hydrogen Embrittlement of Iron Base Alloys," Ed. RW Staehle, June 1973, NACE, 1977.

(14) K Sieradski and RC Newman, Phil Mag A, Vol 51, 1985, p 95-132.

(15) DR Tice, JD Atkinson and PM Scott, Proc 2nd IAEA Specialists Mtg on Subcritical Crack Growth, Ed. WH Cullen, Sendai, Japan, May 1985, NUREG/CP-0067, NRC, April 1986, p 251-282.

(16) H Choi, FH Beck, Z. Szklarska-Smialowska and DD Macdonald, Corrosion, Vol 38,p 76-84, 1982. See also Paper#249, Corrosion/86, NACE, Houston.

(17) J Hinckling and D Blind, Nucl Eng and Design, 91, 1986, p 305-330.

(18) FP Ford and P Combrade, Proc 2nd IAEA Specialists Mtg on Subcritical Crack Growth, Ed. WH Cullen, Sendai, Japan, May 1985, NUREG/CP-0067, NRC, April 1986, p 231-268.

(19) JW Cobble, Science, 152 (1966), p 1479-1485.

(20) JD Atkinson and JE Forrest, Proc 2nd IAEA Specialists Mtg on Subcritical Crack Growth, Ed. WH Cullen, Sendai, Japan, May 1985, NUREG/CP-0067, NRC, April 1986, p 153-178.

(21) WH Bamford, Aspects of Fracture Mechanics in Pressure Vessels and Piping, Eds SG Sampath and SS Palusamy, June 1982, PVP-Vol 58, ASME, NY, 1982, p209-228.

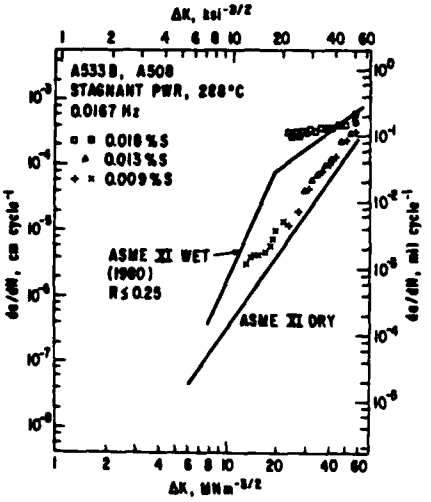

Figure 1. Effect of S content on da/aN vs ΔK, R=0.2, triangle (11).

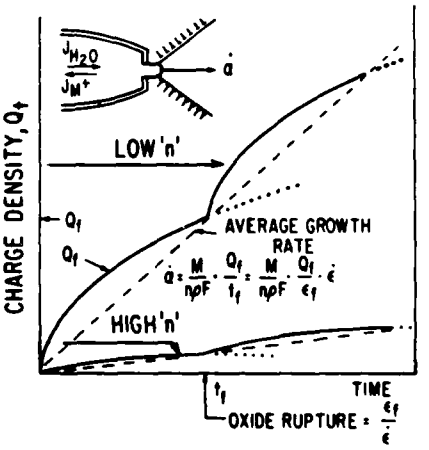

Figure 2. Oxidation charge vs time for two chemistry conditions.

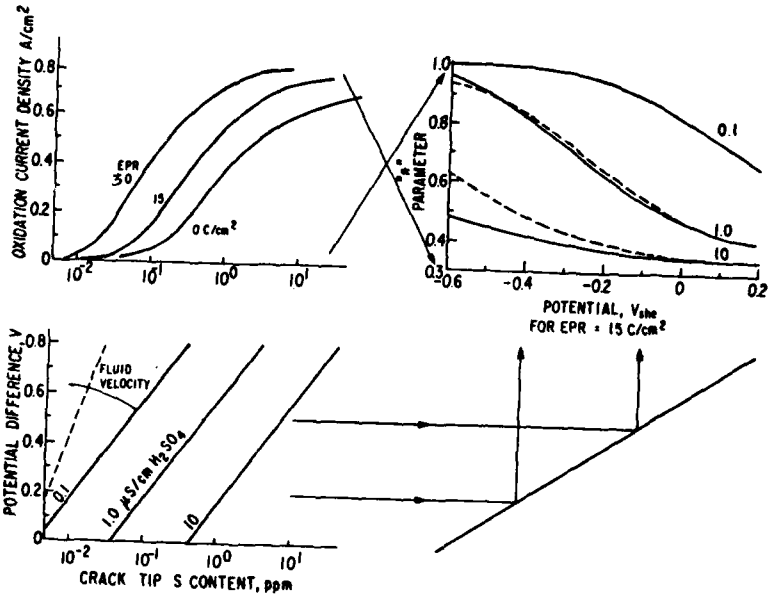

Figure 3. 'n' determination via water (lower left predicts crack tip chemistry) & material (upper left, oxidation kinetics) chemistries.

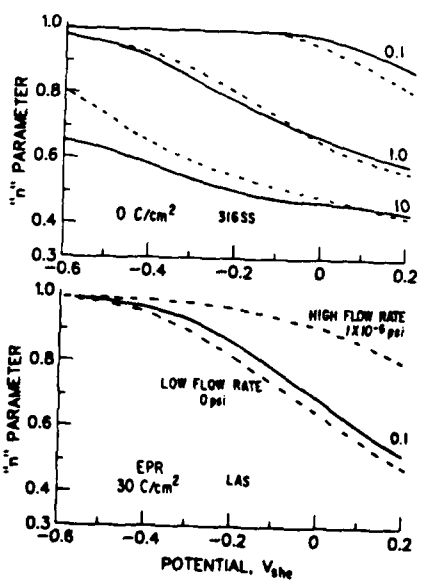

Figure 4. Comparison of predictions and empirical fits of 'n'.

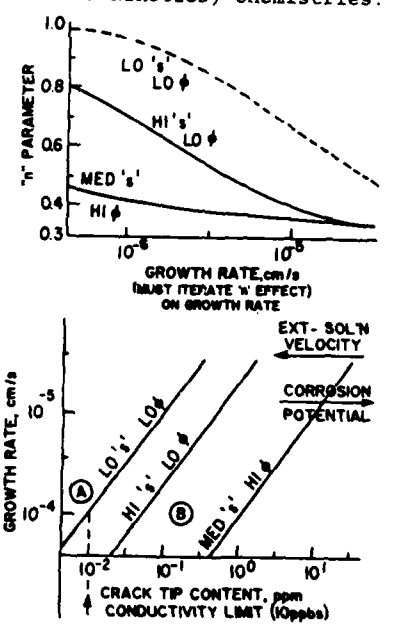

Figure 5. Predicted effect of metall. S on crack tip chemistry.

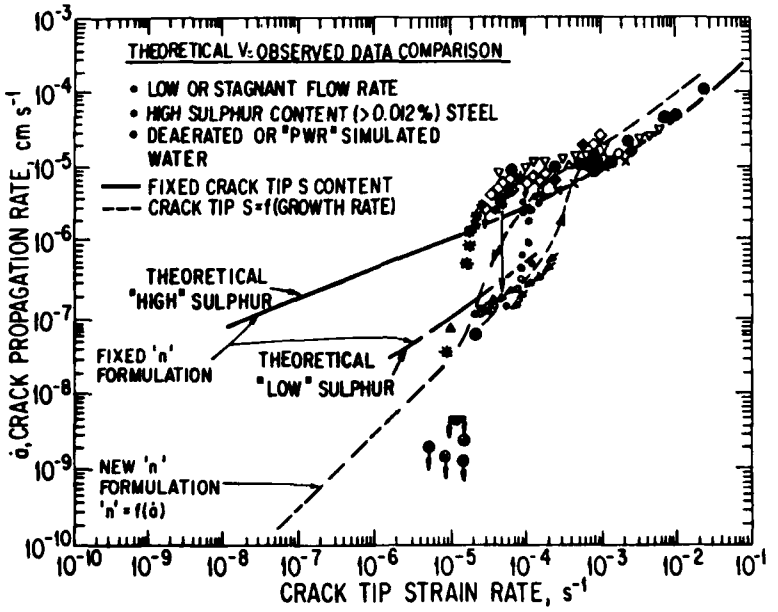

Figure 6. Comparison of predicted and observed steady state and threshold crack growth rates in deaerated water.

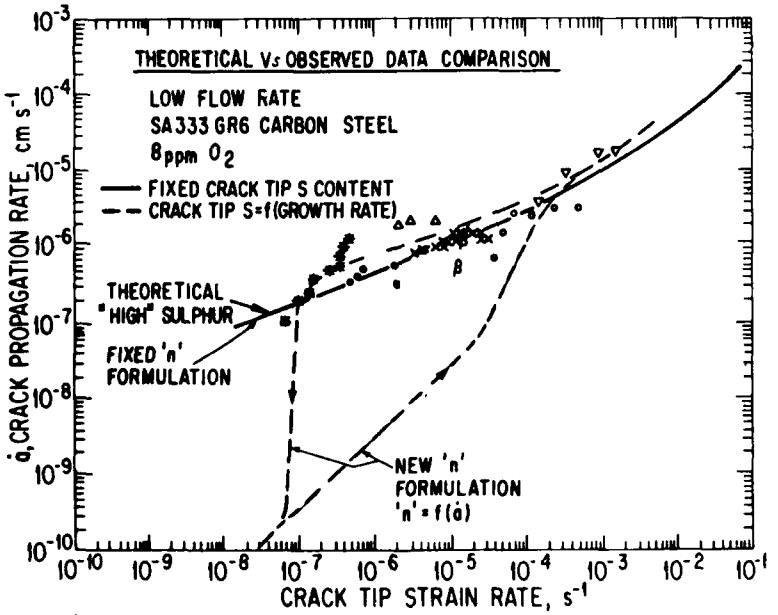

Figure 7. Comparison of predicted and observed steady state and threshold crack growth rates in aerated water.

OCCURRENCE AND GROWTH OF FATIGUE CRACKS IN CORROSION ENVIRONMENT

F.Kosel*, L.Kosec**

This contribution explains the mechanism of the development and growth of defects occurring due to metal oxidation at the conditions of changing temperature field. The analysis is made on two examples: the breaking of a growing oxide wedge, and crack closure by a composite layer between the metal and the oxide. Finally the effect of the number of cracks on their growth is also analyzed.

INTRODUCTION

In chemically active environment metal surfaces get covered by corrosion product coatings whose adhesion to the base metal is variously firm. Firmly adhered and thick corrosion product coatings can slow down or even completely prevent the progress of corrosion processes. However, thermal and/or mechanical loads of metal/oxide systems can failure corrosion product coatings. The latter can no longer protect the base metal or can do so only to a certain extent. The defects of the failured coatings can be of various kinds like cracks, splitting of corrosion products on parts of the surface, on the boundary to the base metal or inside the corrosion product layer etc. One of the most frequently found kind of corrosion is the oxidation of metals.

This contribution treats the effects of thermal stresses and metal oxidation on the occurrence and development of defects leading to failure. An analysis is made of a case where due to mechani-

* Faculty of Mechanical Engineering, University in Ljubljana, YU
** Faculty of Nature Science and Technology, Dept. of Metallurgy, University in Ljubljana, YU

cal instability, the oxide surface coating broke, and through the created cracks the corrosion medium came into contact with the metal. On such places an intensified oxidation took place. Due to the special way of transfer of the oxidizing agent through the broken oxide layer, on these places the oxides grew in the form of a wedge. Corrosion products differ essentially from metals so by their physical as well as their mechanical properties. As a result the properties inside such a system are very non-uniform, so the stress-strain states which occur at temperature changes cause the deformation of the corrosion products, and change their geometric characteristics.

The results of a general analysis of the model representing the discussed system are illustrated by three examples: an element of tool for die casting of brass, pipes of a steam superheater from a thermal power plant, and anode sticks of an accumulator. These examples should point to the relative frequency of the phenomenon. In the literature very few references are to be found about it. The effect of the oxide wedge phenomenon on crack propagation was analysed by P.T. Heald |1| who found out that, when no load is applied, a crack cannot start growing unstably only because of the oxide wedge. The importance of the oxide wedge phenomenon was described qualitatively and partly quantitatively also by Kosel, Kosec, Vodopivec et al:, |2| and |3|.

OCCURRENCE AND GROWTH OF OXIDE WEDGE

The oxide wedge occurs after a previous uniform oxidation of the metal surface at a correspondingly high temperature. The newly occurred oxide on the surface has a different thermal expansion coefficient than the metal. It is also important that this new corrosion product has a considerably larger specific volume than the metal. Under changing temperature conditions, the physical and mechanical properties of the oxide and the metal do not change in the same way. An equally important parameter for the discussed phenomenon is also the strength of the link between the oxide and the metal.

Occurrence of Oxide Wedge

We will discuss a case where the occurrence and growth of the oxide wedge are possible because of changing thermal loads. At a correspondingly high temperature and within a certain time a continuous oxide layer occurs on the metal surface. During the cooling process of the metal/oxide system compressive stresses occur in the oxide due to the different thermal expansion coefficients. At higher temperatures the oxide and the metal plastisize because of the compressive stresses, but when the temperature lowers, and the system passes from the plastic into elastic region, the compressive stresses in the oxide start increasing. Now, the oxide layer on the surface undergoes elastic deformation. During the

process of cooling the compressive stresses in the oxide can reach the plastic limit. If the strength of the adhesion to the metal is strong enough, the oxide starts flowing plastically. Otherwise, it can bend locally or split in case that the breaking shear strength on the metal boundary is smaller than the tangential stresses. Generally, however, both these two processes are going on simultaneously.

At reheating of the system at a certain temperature the possible remaining compressive stresses in the oxide become annulled because of the difference in expansion of the metal and the oxide. If heating is continued, the tensile stresses appear and increase in the oxide. Due to mechanical defects that occurred in the oxide during the process of cooling, different stress concentration areas can be found in the oxide. With continued heating on these areas, a relatively brittle oxide can break with a crack running rectangularly to the metal surface. Several such cracks might occur. These cracks enable a free and fast transfer of the oxidant (air) to the metal, inducing a limited local oxidation. This tiny oxide flaw means the beginning of the oxide wedge.

Growth of Oxide Wedge

The newly formed oxide has a much larger volume than the metal. The volume deformation due to chemical reaction is so extensive that the stress state would by far exceed the rupture strength of the metal and the oxide. Therefore both of them (the metal/oxide system) plasticize. The stress state in the oxide flaw (wedge embryo) is equal to the lower yield point of one of the system's components as follows

$$\sigma_{y_{min}} = \min \left(\sigma^{OK}_{y_{min}}, \sigma^{M}_{y_{min}} \right) \qquad (1)$$

By cooling from T_{max}, compressive stresses would appear in the oxide due to which the system plasticizes. The plastification continues down to the temperature of the transition of the system from the plastic into elastic state, T_p (temperature of the system's transition into elastic state under pressure). The stress state in the oxide flaw at this temperature is:

$$\sigma_{y_{min}}(T_p) = \min(\sigma^{OK}_{y}(T_p), \sigma^{M}_{y}(T_p)) \qquad (2)$$

With continued cooling the compressive stresses increase. If they attain the yield point $\sigma_{y\,min}$, this induces a repeated plastic flow of the system.

At changing temperature conditions, the next stage is heating up the system from T_{min} onto T_{max}. Here, at the beginning, the

compressive stresses reduce and at a certain temperature the system is free of any stresses. By further heating, up, tensile stresses increasing with temperature, appear in the system. In the event that the stress attains the strength of the flaw below the temperature of the transition from the elastic into plastic state (T_p^+ under tensile load) the flaw breaks. The newly occurred crack is the continuation of the crack in the primary surface layer of the oxide. In this manner a fast way for the transfer of the oxidant to the metal reopens, enhancing the growth of the flaw in the direction of the crack. After several repetitions of the temperature cycle (T_{max} - T_{min} - T_{max}) the flaw grows into a wedge of microscopic dimensions.

STRESSES INDUCED BY THE OXIDE WEDGE

The growth of the oxide wedge in the metal is governed, in the first place, by the fast transfer of the oxidant to the metal along the crack and, in the direction normal to the wedge wall, by the diffusion through the oxide. In this manner a triangular form of wedge is created and maintained. Any crack through the primary oxide layer can mean the onset of an oxide flaw or wedge. As a result, on metal parts which are exposed to changing temperature conditions, a great number of microscopic defects in the form of oxide wedges can be found.

The stress state occurring in the system during the process of oxide wedge development, is investigated on a simplified model by choosing a thin layer of semi-space, representing the semi-plane with several oxide wedges. The stress state as function of thermal loads will be analysed only at three characteristic limiting temperatures.

Stress State at the Highest Temperature, T_{max}

At this temperature the oxide wedge grows the most rapidly. Compressive stresses appear in it, attaining the minimum yield point of one of the system's components $\sigma_{y_{min}}$. But since the oxide and the metal differ also in other properties additional thermal stresses appear too. On the back face of the oxide wedge, i.e. on the semiplane boundary, these stresses are compressive, and relatively high, acting in the direction parallel to the semi-plane. Under the semi-plane boundary considerable shear and normal stresses act on the wedge in the direction rectangular to the semi-plane [5]. The comparative stress in the metal-oxide system is considerably higher than the yield point, therefore, the rate of plastic deformation is high, and the stress state does not exceed the $\sigma_{y_{min}}$. The resultant of the forces arising from compressive stress on the wedge faces ($\sigma_{y_{min}}$), acts in the direction towards the semi-plane boundary . Because of this and due to temperature stresses, the system undergoes a typical deformation. The oxide wedge on the semi-plane boundary narrows, and by plastic

flaw the metal takes its place. The consequence of the resulting stresses is the buckling of the semi-plane boundary around the oxide wedge, (Fig.1). Very distinct cases of plastic deformation of the system can be observed if on the back face of the wedge a tiny piece of the oxide splits and destroys the equilibrium stress-state on this part of the semi-plane.

The oxide wedge has an influence on the stable or unstable crack growth in the metal owing to compressive stresses being equal to the yield point $\sigma_{y_{min}}(T_{max})$:

The actual width of the crack tip is |2|

$$\emptyset(c) = \frac{c(1-\nu)}{4\pi\mu\,\sigma_u(T_{max})}\left[\frac{\mu}{1-\nu}\tan\theta + \pi\sigma_{y_{min}}(T_{max})\right] \qquad (3)$$

where θ is the wedge angle of the crack in the metal, ν Poisson's number and μ shear module.

And the critical width of the crack tip at unstable growth is:

$$\emptyset_c = 2\gamma / \sigma_u(T_{max}) \qquad (4)$$

where γ is the surface stress. Crack growth is stable if $\emptyset_c > \emptyset(c)$, and unstable and leading to failure if $\emptyset_c < \emptyset(c)$.

Stress State at the Temperature of the Transition from the Plastic into Elastic State T_p

In this case the compressive stresses in the oxide wedge are increased, but not beyond the yield point. We can define the maximum stress state as well as the stress concentration factor around the oxide wedge tip. The stress in the oxide wedge is equal to $\sigma_{y_{min}}(T_p)$, and the stress concentration factor is

$$K_I = 1.1209\ \sigma_{y_{min}}(T_p)\sqrt{c} \qquad (5)$$

where c is the length of the oxide wedge. In case there are several wedges on the surface, then the stress concentration factor in the metal around the wedge tip is smaller (Fig.2).

If there are several wedges in the semi-plane, with different distances between them (d) and of different lengths (c) the stress concentration factor is as follows

$$K_I = \beta_I\ \sigma_{y_{min}}(T_p)\sqrt{c}$$

λ	0	0,2	0,4	0,6	0,8	1,0	2,0	3,0
β_I	1,1209	0,87186	0,62535	0,51046	0,4446	0,39866	0,28206	0,2303

(6)

where $\lambda = c/d$

The rupture resistance of the system is better if there are several equally sized oxide wedges in the semi-plane than when there is only one single wedge of the same size.

Stress State at the Lowest Temperature, T_{min}

The compressive stresses in the wedge increase, and at a certain minimum temperature (T_{min}), attain the value which exceeds the stress state at all higher temperatures. The stress concentration factor is therefore increased, and can be defined in the same way as above.

Similarly as for T_{max}, we are also for T_{min} interested in the answer to the question of stable or unstable crack growth.

The rate of crack propagation c(t) |2| is:

$$c(t) = \frac{\mu w(t)}{\pi(1-\nu)\sigma}\left\{\left[1 - \frac{w(t)\sigma}{2\gamma}\right]^{-0,5} - 1\right\} \qquad (7)$$

Wherefrom the condition for the unstable crack growth is obtained: $w = 2\gamma/\sigma$ where w is the width of the oxide wedge back face. In this case the rate of crack propagation is infinite.

RETARDATION IN THE GROWTH OF THE OXIDE WEDGE

Retardation in the growth of the oxide wedge occurs at certain time intervals when the crack enabling a fast transfer for the oxidant to the metal at the wedge tip, does not reopens. In some cases it can happen that the corrosion products close the crack from the outside so that even at temperature variation this closure does not break. In this case the oxidation goes on only by the aid of diffusion through the oxide. Owing to this the growth of the wedge slows down, especially at the tip, which changes also its morphology. A very solid closure for the transfer of oxygen represents for example a composite layer of oxide and metal, which is created at specific operating conditions. This layer is resistant to changing temperature loads, especially in the phase of heating up (tension), and is a cause for a long retardation in the oxide wedge growth. Such a composite closure can,however, be less resistant to compressive and shear loads due to which it can split from the surface, and the wedge starts growing again. (Fig. 3).

SOME ILLUSTRATIVE EXAMPLES OF THE OXIDE WEDGE OCCURRENCE

The Plunger of a Die Casting Machine

The plunger of a die casting machine for brass is made from hot work tool steel (0.4% C, 5% Cr, 1,3% Mo and 0.4% v) |5|. At stable operating conditions the temperature on the plunger surface varies from 780°C (T_{max}) to 600°C in approx. 11 seconds, while at work stoppage, the plunger surface cools down below 200°C, or even down to the ambient temperature (T_{min}). After a certain time of operation, heat checking occurs on the working surface of the plunger. These defects can be seen as a network of more or less deep cracks - channels - extending into the metal in the form of oxide wedges. On the axial cross section of the plunger it is thus possible to observe practically all the above described phenomena: cracks in the wedges, deformation of wedges and the surrounding metal, crack closure and retardation in the growth of the oxide wedge etc. (Fig. 4,5,6).

Steam Superheater

On the outer wall of the steam superheater, operating at a lower temperature level than the plunger, oxide wedges were observed under a relatively thin layer of oxide scale. In some cases the defects arising from these wedges developed into total failure of the pipe wall. Besides the agressive effect of the environment (flue gases), the piping system is subjected also to loads arising from temperature variation (Fig. 7).

Accumulator Battery

The same kind of defects in the form of corrosion product wedges were found on positive electrodes of an accumulator battery. These defects resulted in local breaking of anode sticks and total failure of the battery. The anode sticks, which are made from a low-alloyed Pb-alloy, are hung onto the battery box. They are thus constantly under tension load. During battery filling and discharging a chemical reaction takes place. Its products differ very much in specific volume, so the $PbSO_4$ probably cannot bear the weight of the anode stick and breaks. The exchanging cycles of discharing and filling at constant tensile load enable the growth of corrosion products in the form of wedges (Fig.8) resulting in a sudden brittle, catastrophic failure.

CONCLUSION

On the basis of analytical and experimental investigation this contribution explains the mechanism of an oxide wedge growth at changing temperature field and the presence of the oxidant. At

these specific conditions a wedge is capable of growth leading to a catastrophic failure. In metal/oxide wedge systems very typical stress-strain states occur. These have an influence on the formation of the wedge and on the final failure of the system. Two examples are analyzed: one when the oxide layer on the semi-plane boundary breaks, and the other when corrosion products close the crack from the outside despite temperature variation. This prevention of the fast transfer for the oxidant to the metal retards the growth of the oxide wedge, and the normal development of their morphology. It is also found out that the oxide wedges grow more slowly if there are several of them on the surface than in the case when there in only one wedge of the same size.

SYMBOLS USED

T = temperature

σ = stress

σ_u = ultimate tensile strength

σ_y = yield stress under uniaxial tension

c = length of the oxide wedge

w = width of the oxide wedge

γ = surface stress

REFERENCES

|1| Heald P.T., "The Oxide Wedging of Surface Cracks", Material Science and Engineering, No. 35, 1978, pp. 165-169, Lausanne, Swiss.

|2| Kosel F. and Kosec L., "Toplotno razpokanje orodij za delo v vročem", Strojniški vestnik, No. 7-9, 1983, pp. 151-159, Ljubljana, Yugoslavia.

|3| Vodopivec F., Ralič B. and Dobovišek B., "Poškodbe na cevah visokotlačnega parnega kotla zaradi kombiniranega vpliva mehanske in kemijske obremenitve", Strojniški vestnik, No.1-3, 1985, pp. 6-12, Ljubljana, Yugoslavia.

|4| Berežnickij L.T., Panasjuk V.V. and Staščuk N.G., "Vzaimodejstvie žestkih linejnih uključenij i treščin', Naukova Dumka, 1983, Kiev, USSR.

|5| Kosel F. and Kosec L., "High Temperature Fatigue in Nonhomogeneous continuum", Fatigue and Fatigue Thresholds, Vol. I, 1984, pp. 613-623, Birmingham, England.

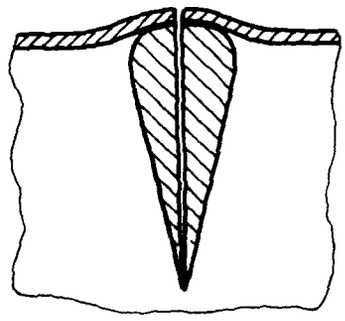

Fig.1 Cracks through the oxide layer into the wedge

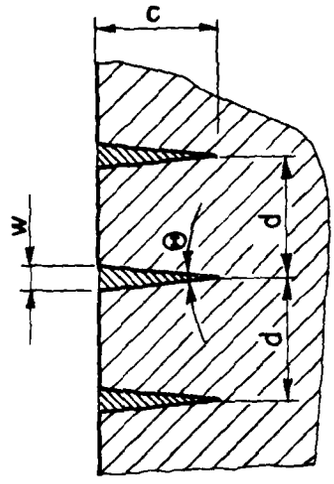

Fig.2 Schematic presentation of the metal surface with several oxide wedges

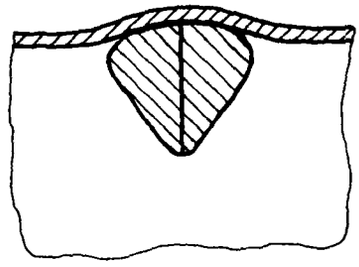

Fig.3 Oxide wedge under the unaffected layer of the metal/oxide composite

Fig.4 Metal deformation alongside the oxide wedge. A crack through the surface composite and the wedge

Fig.5 Deformation of the metal and the oxide wedge due to splitting of the oxide on the wedge back face

Fig.6 Retarded growth of the oxide wedge under the unaffected layer of the oxide/metal composite

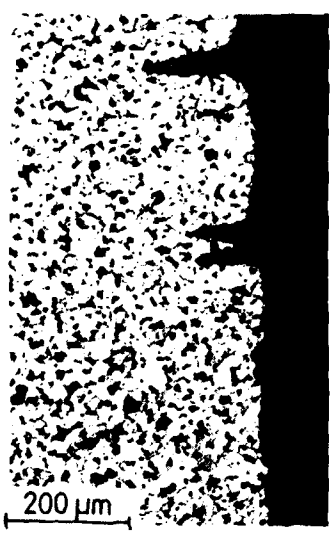

Fig.7 Oxide wedge on the outer side of the pipe of a steam superheater

Fig.8 Oxide wedge on the anode stick of an accumulator battery

THE EFFECT OF ENVIRONMENT ON LOW CYCLE FATIGUE PROPERTIES IN HSLA STEEL

W.J. Lee*, S.P. Bhat**, Y.W. Chung* and M.E. Fine*

The influence of gaseous environment on low cycle fatigue properties and microcrack initiation mechanisms has been studied in 0.11 wt.% Nb HSLA steel. Completely reversed push-pull fatigue tests at various plastic strain amplitudes were performed both in air and in ultrahigh vacuum (UHV). A two-stage surface replication technique for transmission electron microscopy was used to determine the initial microcracks which when formed are less than one μm in length. Microcracks are initiated along slip lines both in air and in UHV. The increase in fatigue resistance in UHV is attributed to a delay in microcrack initiation and, more importantly, decrease in the microcrack growth rate. The environmental effect becomes more severe as the plastic strain amplitude decreases.

INTRODUCTION

It has been known since the pioneering work of Gough and Sopwith (1,2) that the fatigue resistance of metals increases as the ambient pressure decreases. Since the fatigue life in vacuum is, in some cases, more than ten times longer than in air (3,4,5), the study of the effect of these ambient gases on the fatigue behavior is of great importance. Fatigue test results obtained in vacuum experiments can be used as a reference to elucidate the ambient effects on fatigue properties. However, the vacuum employed by most investigators was not lower than 1×10^{-4} Pa. At these pressures, an initially clean surface can be contaminated within a few seconds assuming a sticking probability of unity, and this may affect the fatigue properties in a major way. Therefore, experiments in ultrahigh vacuum (UHV) under which environmental effects are either minimized or eliminated are required to understand gaseous effects on fatigue properties of metals.

* Department of Materials Science and Engineering and Materials Research Center, Northwestern University
** Inland Steel Company Laboratories, East Chicago, IN

Earlier research (6,7) on the fatigue deformation of commercially pure iron in a reverse bending mode revealed significant differences in the surface morphology and crack initiation modes in UHV and oxygen. To obtain a uniform strain and stress distribution across the section of the specimen and to compare results with most existing literature data, axial-loading experiments are required. To this end, an axial-loading closed-loop electrohydraulic fatigue apparatus was constructed and installed in a UHV scanning Auger microprobe (SAM). A detailed description of the apparatus and electronics was presented elsewhere (8).

The objective of this research is to gain a better understanding of the influence of the ambient environment on the fatigue behavior in a high-strength low-alloy (HSLA) steel. Low cycle fatigue properties and fatigue crack initiation mechanisms have been carefully characterized both in air and in UHV over a wide range of plastic strain amplitudes.

EXPERIMENTAL

The HSLA steel used in this research was found to contain the following elements (wt. pct): 0.06 C, 0.11 Nb, 1.25 Mn, 0.22 Si, 0.011 P, 0.004 S, 0.048 Al, 0.012 Ce and 0.006 Ca. The average grain size measured by the linear intercept method was 7 μm. The mechanical properties are provided in Table 1. Sheet-type fatigue specimens with gage section dimensions of 5x2.5x5 mm were machined such that the loading axis was parallel to the rolling direction and polished to a 0.25 μm diamond finish. All experiments were done under plastic strain control using a triangular strain waveform and a constant total strain rate of $1x10^{-3}$ sec^{-1}. The cyclic plastic strain was measured and controlled with an axial MTS sub-miniature extensometer mounted on the gage section of the specimen. Fully reversed push-pull strain cycling ($R' = \varepsilon_{min} / \varepsilon_{max} = -1$) was performed with a constant plastic strain amplitude $\Delta\varepsilon_p/2$ ranging from $5x10^{-4}$ to $1x10^{-2}$ both in air and in UHV. The routine base pressure during fatigue testing in UHV was $6.5x10^{-8}$ Pa, obtained by an ion pump and a titanium sublimator. During evacuation of the chamber, a zero strain condition was maintained by applying a tensile load to counteract the atmospheric pressure. After the desired vacuum condition was achieved, the applied tensile load (0.18 KN, which is less than 4% of the peak load at the smallest plastic strain amplitude tested) was set equal to a reference level of zero. Surface deformation was observed in situ with a secondary electron detector in the vacuum chamber and the specimen surface was replicated at selected intervals using cellulose films. The replicas were shadowed with a platinum-paladium alloy at an angle of 30 deg, parallel to the straining axis, and then coated with amorphous carbon.

TABLE 1 - Mechanical Properties

Young's Modulus	203 GPa
Upper Yield Strength	535 MPa
Lower Yield Strength	506 MPa
Ultimate Tensile Strength	603 MPa
Uniform Elongation	15.0 %
Total Elongation	23.5 %
Reduction in Area	66 %
Vickers Hardness, 500 g Load	161 Kg/mm^2

Tensile tests were conducted at a cross-head speed of 3 mm/min (which is approximately equal to the total strain rate of $1x10^{-3}$ sec^{-1}) using standard 50 mm gage length longitudinal sheet specimens.

Examination of the two-stage surface replicas using the transmission electron microscope allowed detection of the very early stage of microcrack initiation where cracks were less than one μm in length. Microcrack initiation life N_i was defined as the number of cycles when a crack of length less than one μm was found. Specimens were cycled until failure. Specimen failure was defined as the point at which a measurable change in the ratio of maximum stress in tension to maximum stress in compression was detected.

RESULTS

In tests carried out at $\Delta\varepsilon_p/2$ of $3x10^{-3}$ in air, as an example, very narrow and deep fatigue microcracks developed inside a grain after 1100 cycles, as shown in Fig. 1(a). With continued cycling, more microcracks initiated and they coalesced or lined up to form a long crack (Fig. 1(b)). The deformation was quite localized and integrity of grain boundaries was maintained even at the very late stages of fatigue. Fatigue in UHV at $\Delta\varepsilon_p/2$ of $3x10^{-3}$ produced wavy slip lines with occasional microcracks along them (Fig. 1(c)). Little environment-induced differences were observed in the microcrack initiation features. At a later stage of fatigue (Fig. 1(d)), numerous and uniform slip bands appeared because of the higher accumulated plastic strain resulting from the longer fatigue life in UHV.

Over the range of plastic strain amplitudes tested, both in air and UHV, microcracks were initiated along slip lines, whereas grain boundaries showed great resistance to fatigue damage and acted as an effective barrier to the spreading of microcracks. Only at $\Delta\varepsilon_p/2$ of 1×10^{-2}, grain boundary cracking was observed but considerably later than slip line cracking. Contrary to the present finding, working with commercially pure iron, Majumdar and Chung (6,7) observed grain boundary cracking in UHV and slip line cracking in oxygen. It was observed that the surface deformation in vacuum was suppressed relative to that in air after the same number of cycles, especially at the lowest plastic strain amplitude (5×10^{-4}). When an initial microcrack was detected, no significant differences in the morphology of microcracks between air and UHV were observed except that the deformation was a little more uniformly distributed in UHV.

In Fig. 2, the change in the average stress amplitude as a function of the number of cycles N in air and in UHV is shown for HSLA steel specimens fatigued in UHV and air at various plastic strain amplitudes. The cyclic stress response shows mixed softening and hardening depending on the plastic strain amplitude: cyclic hardening above 0.3%, cyclic softening below 0.3%, and a nearly constant stress response at 0.3%. It should be noted that the macroscopic cyclic stress response curves are mainly defined by deformation amplitude and are not affected by the environment even though deformation markings on the surface are affected by the environment.

In Fig. 3, the number of reversals to microcrack initiation ($2N_i$) and fatigue failure ($2N_f$) in air and in UHV are plotted as functions of plastic strain amplitude on a log-log diagram. Microcrack initiation life, N_i, is represented as a range-bar whose magnitude is dependent on how often replicas are taken. Since the relations seem to be approximated by straight lines for the range of strain amplitudes tested, they can be expressed by the Coffin-Manson formula:

$$\Delta\varepsilon_p/2 = \varepsilon_i' (2N_i)^{c_i} \quad \ldots\ldots(1)$$

$$\Delta\varepsilon_p/2 = \varepsilon_f' (2N_f)^{c_f} \quad \ldots\ldots(2)$$

where ε_i', c_i, ε_f' and c_f are experimentally determined constants. The plastic strain-life data follow a single set of parameters to a reasonable approximation over the entire plastic strain range investigated. Similar results were reported by Bhat (9): no break in plastic strain-fatigue life plots for three different HSLA steels tested in air. The values of the constants determined in the present study are listed in TABLE 2. It is apparent that microcrack initiation life and fatigue life in UHV are larger than those in air over the whole plastic strain amplitude range.

TABLE 2 - Coffin-Manson Parameters

relation	parameter	(in air)	(in UHV)
$(\Delta\varepsilon_p/2)$ vs. $(2N_i)$	ε_i'	0.231	0.136
	c_i	-0.606	-0.484
$(\Delta\varepsilon_p/2)$ vs. $(2N_f)$	ε_f'	1.085	< 0.442
	c_f	-0.682	>-0.492

The smaller absolute values of the slopes in UHV indicate that both microcrack initiation life and fatigue life in UHV are enhanced as the plastic strain amplitude decreases.

DISCUSSION

In air, the microcrack initiation process occupies approximately 15-30% of the total lifetime depending on the plastic strain amplitude, as compared to 10% in UHV, as shown in Fig. 4. This results from the fact that the microcrack growth stage is more extended in UHV as compared to the initiation stage. It is known that the crack initiation stage usually becomes more important as the deformation amplitude decreases. We found the same trend in air; i.e. the ratio of crack initiation life to fatigue life (N_i/N_f) increases as the strain amplitude decreases. Such a trend, however, was not observed in UHV: the fraction of the lifetime for microcrack initiation was almost constant for all plastic strain amplitudes. It indicates that as the strain amplitude decreases, environmental effects in the crack growth stage become even more severe in comparison with those in the crack initiation stage. Therefore in air at low strain amplitudes, the crack initiation stage becomes more important. In consequence, it is suggested that the increase of the ratio N_i/N_f with the decrease of the deformation amplitude in air is due to the gaseous environmental effect.

To illustrate the effect of gaseous environment on fatigue damage, it was assumed that the fatigue damage in air is a sum of the intrinsic cyclic damage and the damage associated with the gaseous environment. In the microcrack initiation stage, the fraction of the environmental damage to the total fatigue damage in air F_i is expressed as

$$F_i = 1 - N_{i,air}/N_{i,UHV} \quad \cdots\cdots (3)$$

where $N_{i,air}$ = microcrack initiation life in air (cycles)

$N_{i,UHV}$ = microcrack initiation life in UHV (cycles).

Similarly the fraction of the environmental damage in air during the microcrack growth stage F_g is given by

$$F_g = 1 - N_{g,air}/N_{g,UHV} \quad \cdots\cdots (4)$$

where $N_{g,air}$ = microcrack growth life in air (cycles)

$N_{g,UHV}$ = microcrack growth life in UHV (cycles).

Microcrack growth life is obtained by subtracting microcrack initiation life from fatigue life. In Fig. 5, fractions of environmental damage in the microcrack initiation and growth stages are plotted as functions of plastic strain amplitude. It is clearly shown that the environmental effect is greater in the microcrack growth stage than in the microcrack initiation stage and that it becomes more severe for both stages as strain amplitude decreases. During the microcrack growth stage at low strain amplitude, the gaseous environment is responsible for most of the fatigue damage. It is emphasized that in determining the effect of environment the plastic strain amplitude must be specified.

CONCLUSIONS

Low cycle fatigue behavior and fatigue crack initiation in Nb HSLA steel were characterized at plastic strain amplitudes ranging from 5×10^{-4} to 1×10^{-2} both in air and in UHV under the plastic strain control mode.

(1) The number of cycles to initiate a fatigue microcrack and the fatigue life in UHV are larger than those in air over the range of plastic strain amplitudes tested.

(2) Microcracks are initiated along slip lines over the range of plastic strain amplitudes tested both in air and in UHV and not on grain boundaries except at the highest plastic strain amplitude.

(3) Cyclic stress response curves are defined mainly by the deformation amplitude and are not affected by the environment.

(4) Coffin-Manson relations are reasonably satisfied for both microcrack initiation and fatigue life in air and in UHV.

(5) In air, the fraction of lifetime for microcrack initiation increases as the plastic strain amplitude decreases. This trend, however, was not observed in UHV.

(6) The environmental effect is more important in the microcrack growth stage than in the microcrack initiation stage and becomes more severe for both stages as plastic strain amplitude decreases.

REFERENCES

(1) H. J. Gough and D. G. Sopwith, J. Inst. Metals, Vol.49, 1932, p.93

(2) H. J. Gough and D. G. Sopwith, J. Inst. Metals, Vol.52, 1935, p.55

(3) N. J. Wadsworth and J. Hutchings, Phil. Mag. Vol.3, 1958, p.1154

(4) D. J. Duquette, in Proceedings on Environment-Sensitive Fracture of Engineering Materials, 1977, edited by Z. A. Foroulis (Metallurgical Society of AIME, Warrendale, Pa., 1979), p.521.

(5) R. Wang, H. Mughrabi, S. McGovern and M. Rapp, Mater. Sci. Eng. Vol.65, 1984, p.219

(6) D. Majumdar and Y. W. Chung, Script. Met. Vol.16, 1982, p.791

(7) D. Majumdar and Y. W. Chung, Met. Trans. Vol.14A, 1983, p.1421

(8) W.J. Lee, J.P. Baker, Y.W. Chung and M.E. Fine, Rev. Sci. Instrum. Vol.57, (11), 1986, p.2854

(9) S.P. Bhat, in Proceedings on HSLA Steels, Technology and Applications, 1983 (American Society for Metals, Metals Park, Ohio, 1984), p.579

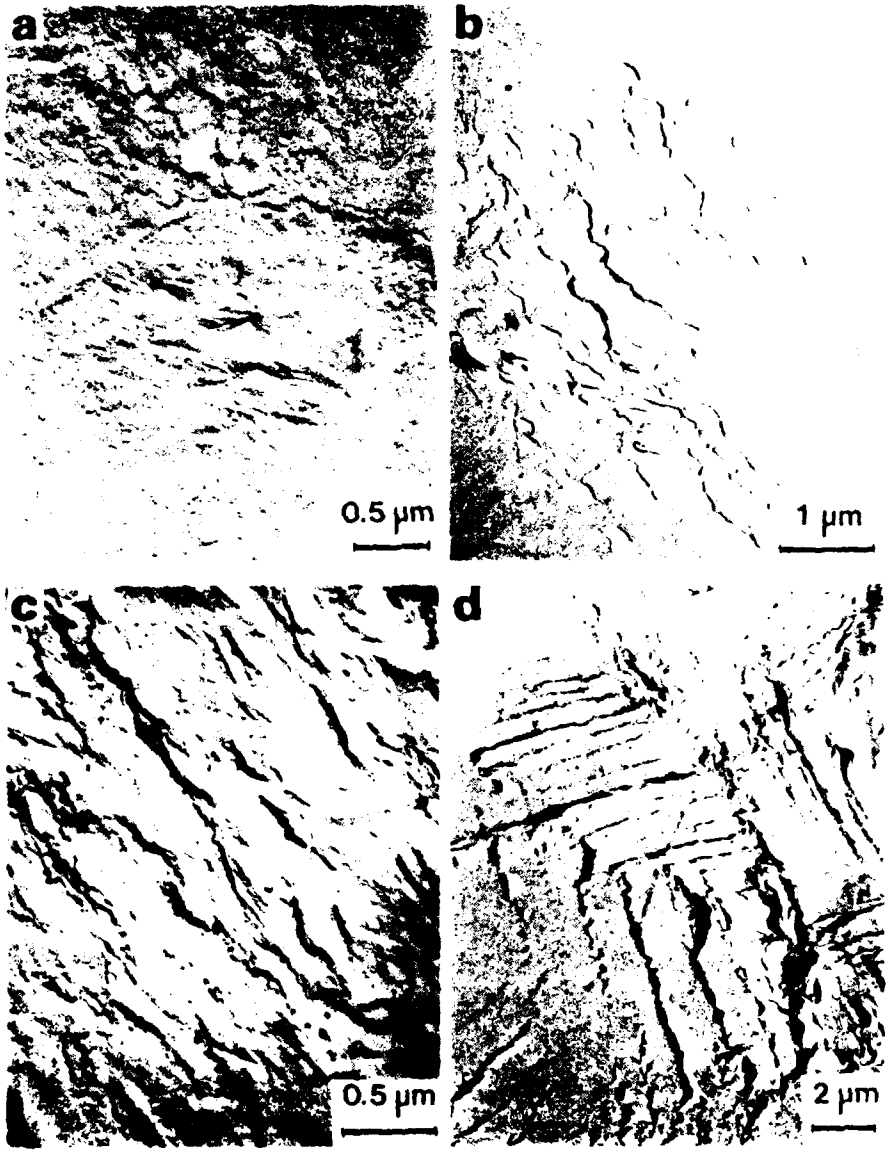

Fig. 1. Transmission electron micrographs of surface replicas at a plastic strain amplitude of 3×10^{-3}. $N_{f,air}$= 3,300 cycles, $N_{f,UHV}$= 13,500 cycles (a) 1,100 cycles in air, (b) 2,200 cycles in air, (c) 2,000 cycles in UHV, (d) 9,700 cycles in UHV.

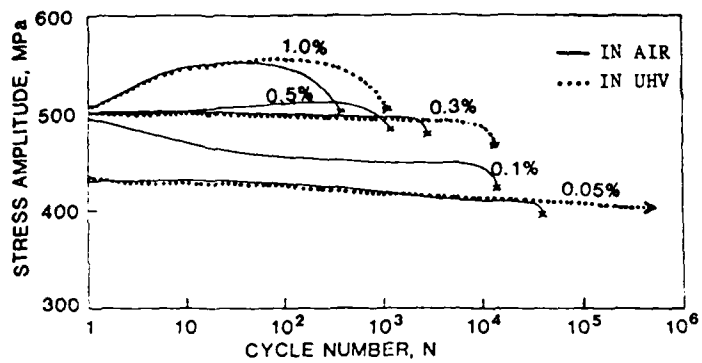

Fig. 2. Cyclic stress response curves for Nb steel in air (solid lines) and UHV (dashed lines). The percent numbers indicate the plastic strain amplitudes. The arrow means that the specimen did not fail at the indicated cycles.

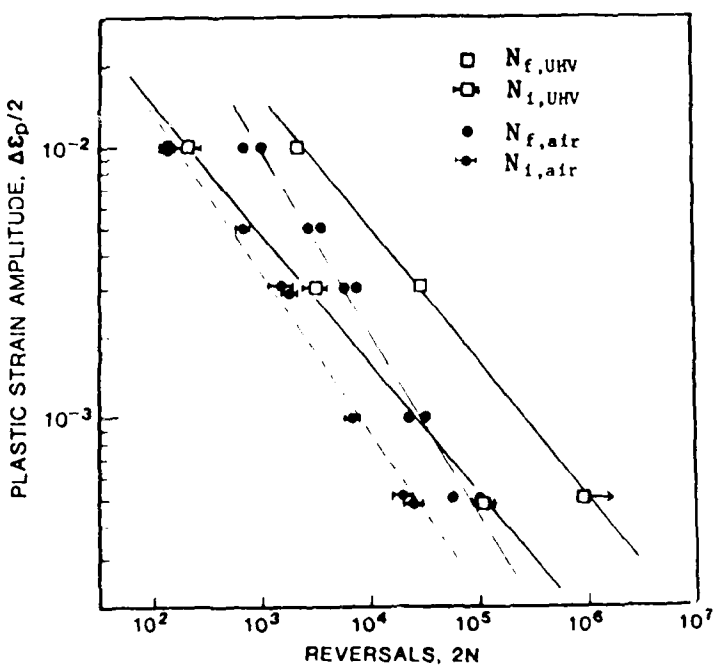

Fig. 3. Coffin-Manson plots of plastic strain amplitude vs. number of reversals to microcrack initiation and fatigue failure in air and UHV.

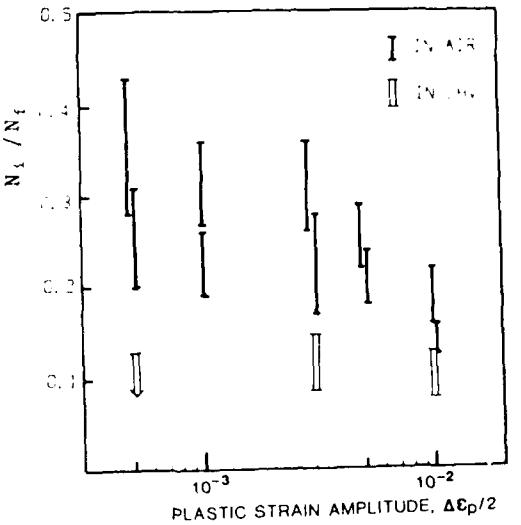

Fig. 4. Fraction of lifetime for microcrack initiation in air and UHV as a function of plastic strain amplitude.

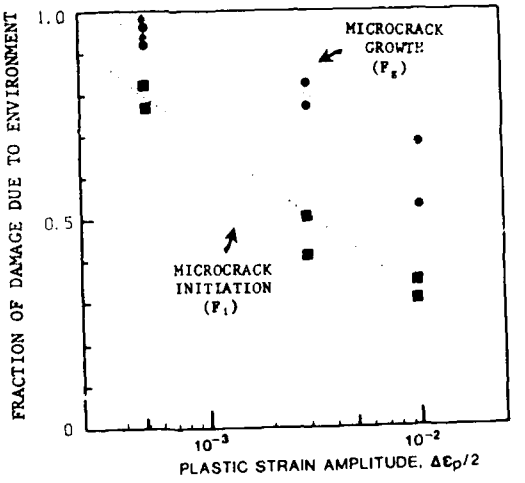

Fig. 5. Fraction of environmental damage in the fatigue damage in air for microcrack initiation and growth stages as a function of plastic strain amplitude.

COUPLING EFFECTS BETWEEN THE α AND γ PHASES DURING CORROSION FATIGUE OF AN α/γ DUPLEX STAINLESS STEEL

T. Magnin*, J.M. Lardon* and C. Amzallag**

The corrosion fatigue behaviour in a 3.5 % NaCl solution at pH 2 of an α/γ duplex stainless steel with 50 % ferrite content is studied and compared with those of the α and γ phases considered separately. The better resistance to corrosion fatigue of the duplex alloy in comparison to those of its individual phases is emphasized and explained by both mechanical and electrochemical coupling effects between the α and γ phases in the duplex alloy.

INTRODUCTION

Duplex austenitic-ferritic stainless steels have been developed for their good resistance to intergranular corrosion and chloride stress corrosion cracking and for their high strength at room temperature (1). The stress corrosion cracking properties of the duplex alloys have been related to complex electrochemical and mechanical coupling effects between their α (ferrite) and γ (austenite) phases (2,3). Thus, in chloride solutions and at free corrosion potential, the austenite which can be deformed more easily than the ferrite, is cathodically protected by the ferrite (3), and the stress corrosion properties of the duplex alloy are then closely dependent on the ferrite content.

In practical applications, duplex stainless steels are often exposed to both electrochemical and mechanical damages, the latter being usually fatigue. Thus the corrosion fatigue properties of the duplex alloys must be also analysed since the mechanical damage has been shown to be very different in fatigue and in monotonic

*Ecole des Mines, Saint-Etienne, France

**Société UNIREC, Firminy, France.

deformation (4). Nevertheless only a few studies have been published on this field (5,6). Moreover they are devoted to the influence of an aqueous environment on the fatigue crack propagation properties of the duplex alloys, and nothing is known about their corrosion fatigue crack initiation resistance.

Thus the aim of the present paper is to analyse the crack initiation mechanisms during corrosion fatigue in a chloride solution of a duplex stainless steel with 50 % ferrite, paying a particular attention to the mechanical and electrochemical coupling effects between the α and γ phases.

EXPERIMENTAL

A sensitive testing equipment is used to record simultaneously the cyclic evolution of the electrochemical and mechanical parameters. This method has been described in detail elsewhere (7). Smooth specimens (10 mm gauge length and 5 mm diameter) are symmetrically cycled in tension-compression at a prescribed plastic strain amplitude $\Delta\varepsilon_p/2$ and at constant strain rate $\dot{\varepsilon}$ on a servohydraulic machine. Tests are conducted at room temperature in dry air and in an aerated and replanished 3.5 % NaCl solution at pH 2 under potentiostatic control. During cycling the evolution of either the electrochemical potential E or the current transient characteristics at imposed electrochemical potential is recorded.

To quantitatively determine the crack initiation, the number of cycles N_a corresponding to a rapid 1 % decrease of the cyclic peak stress in tension σ has been selected. It has been shown elsewhere that N_a corresponds to the formation of cracks able to propagate through the volume of the specimen,which is not always the case of shorter cracks (4).

Tests were performed on an α/γ URANUS 50 duplex stainless steel with 50 % ferrite. It contains (in wt%) 20.6 Cr, 5.97 Ni, 2.45 Mo, 1.64 Cu, 0.009 P, 0.01 S, 0.018 C, 0.07 N. Elongated ferritic bands are observed in an austenitic matrix (3). All the specimens are waterquenched, but some of them were also aged at 400°C for two hours (after waterquenching). This usual treatment induces a large hardening of the α phase by formation of chromium-rich zones in the iron-rich matrix.

RESULTS

Electrochemical behaviour of the duplex alloy

The polarization curve (E = f(J), where J is the current density)of the duplex α/γ alloy have been determined in the 3.5 % NaCl solution at pH 2. Figure 1 indicate the obtained result for $\Delta E/\Delta t$ = 90 mV/h. The corresponding values of the dynamic free potential E_{od} of the α and γ phases considered separately have been

determined using ferritic and austenitic stainless steels the composition of which are similar to those of the α and γ phases of the duplex alloy. On Figure 1, the cathodic protection of the γ phase by the α phase in the duplex alloy is confirmed for J = 0. This clearly illustrates the electrochemical coupling effect between the α and γ phases of the α/γ alloy. Moreover it can be observed that the pitting potential of the duplex alloy is about E = 400 mV (E is refered to a saturated calomel electrode).

Fatigue behaviour in air

This behaviour, which has been described in details elsewhere (8),can be summurized by the Figure 2 which shows the Coffin-Manson curves of the duplex (α/γ) alloy and of its individual phases α and γ. It has been shown (8) that : (i) at low strain amplitudes ($\Delta\varepsilon_p/2 < 10^{-3}$), the cyclic deformation of the austenitic phase controls the fatigue properties of the duplex alloy. Because of the large reversibility of the cyclic strain in the fcc γ phase, a good fatigue resistance of the duplex alloy is observed (as for the γ phase considered separately). Crack nucleation in the duplex alloy takes place in the γ phase. (ii) At high strain amplitudes ($\Delta\varepsilon_p/2 > 10^{-3}$), the cyclic deformation of the ferritic phase (which occurs by twinning and pencil glide) controls the fatigue properties of the duplex alloy. Because of twinning and pencil glide in the α phase, an early crack initiation takes place in the ferritic phase of the duplex alloy. The fatigue life is then reduced and a marked change in the slope of the Manson Coffin curve is observed.

Corrosion Fatigue behaviour in the passive region

Tests have been conducted for two different values of the electrochemical potential : $E = E_o = -120$ mV where E_o is the rest potential and $E = E_{anodic} = +150$ mV (E is refered to the saturated calomel electrode). For a given strain rate $\dot{\varepsilon} = 10^{-2} s^{-1}$, the Coffin Manson curves have been determined in each case as shown on Figure 3. It can be observed that : (i) the corrosive solution at $E = E_{anodic}$ strongly reduces the fatigue life in comparison to air (and also to the behaviour at $E = E_o$), particularly at low strain amplitudes : N_a is reduced by a factor 10 at $\Delta\varepsilon_p/2 = 7.10^{-4}$ in comparison to air. (ii) At $E = E_o$, the reduction of the fatigue life is only significant at high strain amplitudes ($\Delta\varepsilon_p/2 > 10^{-3}$). A reduction by a factor 2 is observed at $\Delta\varepsilon_p/2 = 4.10^{-3}$ (and at very low strain amplitudes which is so significant in this latter case) but no reduction is observed at $\Delta\varepsilon_p/2 = 10^{-3}$.

To analyse the observed effect of the electrochemical potential in the passive region, the crack initiation sites have been observed. At $E = E_o$ (Figures 4 and 5) the observations are similar to those in air. At high strain amplitude ($\Delta\varepsilon_p/2 > 10^{-3}$) cracks initiate principally in the α phase (Figure 4), either at α/α grain boundaries or in the twins. The corrosive solution at $E = E_o$ acce-

lerates the mechanical damage in this case by localisation of the anodic dissolution at twins and α/α grain boundaries. However, at $\Delta\varepsilon_p/2 \leqslant 10^{-3}$ for which only the γ phase is plastically deformed, cracks initiate in the slip bands of the γ phase (Figure 5) for nearly the same number of cycles than in air. Such results indicate a strong influence of the deformation mode of the α phase on the corrosion fatigue resistance of the duplex alloy. To confirm this effect, tests have been conducted on specimens aged at 400°C for two hours. This heat treatment is known to harden the duplex alloy and to promote twinning in the α phase (3). The influence of this heat treatment is that the corrosion fatigue resistance of the aged specimens at $E = E_o$, $\Delta\varepsilon_p/2 = 4.10^{-3}$ and $\dot{\varepsilon} = 10^{-2}s^{-1}$ is twice lower than the resistance of non aged specimens.

At $E = E_{anodic}$, it has been observed that cracks initiate principally from pits which are formed in the γ phase whatever the applied strain amplitude. Pitting starts during the first cycles in the γ phase which induces a rapid increase of the current density : $J = 1\ \mu A/cm^2$ at $N = 1$ and $5\ mA/cm^2$ at $N = 100$ for $\Delta\varepsilon_p/2 = 4.10^{-3}$ for instance.

Finally, it has been shown (9) that, whatever the applied electrochemical potential, the fatigue lifetimes of the duplex alloy are always longer than those of the α and γ phases considered separately.

Corrosion fatigue behaviour in the cathodic region

Tests have been conducted at E = - 500 mV (refered to the saturated calomel electrode) to analyse the effect of the hydrogen entry on the corrosion fatigue behaviour of the duplex alloy. For this test, the potential is first imposed at E = - 800 mV during some minutes to destroy the passive film (9) and then is imposed at E = - 500 mV. On the Coffin-Manson curves at $\dot{\varepsilon} = 10^{-2}s^{-1}$ (Figure 6) it can be observed that a reduction of the fatigue life in comparison to the behaviour at $E = E_o$ occurs only for $\Delta\varepsilon_p/2 > 10^{-3}$. At lower strain amplitudes the behaviour at E = - 500 mV is similar to the behaviour at $E = E_o$.

Tests have been also conducted at imposed cathodic potential on aged specimens. The same effect than at $E = E_o$ is encountered. When $\Delta\varepsilon_p/2 > 10^{-3}$, the corrosion fatigue life of the duplex alloy is twice shorter on aged specimens than on non aged specimens, but no difference is observed at $\Delta\varepsilon_p/2 \leqslant 10^{-3}$.

DISCUSSION AND CONCLUSIONS

All the obtained results concerning the corrosion fatigue behaviour of the duplex stainless steel can be analysed in terms of coupling effects between the α and γ phases. In particular, the behaviour of the duplex alloy is very sensitive to the plastic deformation mode of the α phase. At low strain amplitudes ($\Delta\varepsilon_p/2 \leqslant 10^{-3}$) the

α phase is not plastically deformed (8) and the corrosion fatigue resistance of the duplex alloy is then completely different than at $\Delta\varepsilon_p/2 > 10^{-3}$ for which the cyclic plastic deformation of the α phase is of prior importance. So the corrosion fatigue damage mechanisms of the duplex alloys can be classified in two different types according to the applied plastic strain :

(i) At low strain amplitudes ($\Delta\varepsilon_p/2 \leqslant 10^{-3}$), the plastic deformation principally takes place in the γ phase of the duplex alloy. Thus the fatigue behaviour in air of the duplex stainless steel is controlled by the cyclic properties of the γ phase. In corrosion fatigue, when the duplex alloy is in the passive region, the depassivation and the localized dissolution take place principally at the slip band emergence in the γ phase, and sometimes at α/γ grain boundaries. At $E = E_\rho$, the localized anodic dissolution in the γ phase is limited because of the cathodic protection of the γ phase by the α phase in this case (see Figure 1). Thus, the corrosion fatigue resistance of the duplex alloy in such conditions is very good and similar to the resistance in air. However, it must be noticed that, when the tests are very long as for very low strain amplitudes, a localized corrosion at inclusions can occur which induces small reduction of the fatigue life as indicated on Figure 3. These effects may be also sensitive to strain rate as discussed elsewhere (9).

At $E = E_{anodic} = + 150$ mV, the cyclic deformation promotes pitting in the γ phase even if the pitting potential of the duplex alloy is + 400 mV. Cracks can then initiate at pits inducing a reduction of the fatigue life which will be very sensitive to the duration of tests : at very low strain amplitudesthis reduction is then very marked (by a factor 10 or more).

When the specimens are aged at 400°C, the corrosion fatigue resistance of the duplex alloy at low strain amplitude is not modified because the main influence of ageing occurs in the ferrite which is not plastically deformed.

(ii) At high strain amplitudes ($\Delta\varepsilon_p/2 > 10^{-3}$), the plastic deformation mode of the ferritic phase is of prior importance. Thus the fatigue behaviour in air of the duplex stainless steel is controlled by the cyclic properties of the α phase which deforms by twinning and pencil glide. In corrosion fatigue, when the duplex alloy is in the passive region, the depassivation takes place both in the α and γ phases. At $E = E_\rho$, because of the cathodic protection of the γ phase by the α phase, the dissolution is principally localized in the α phase, at twins and at α/α grain boundaries. This effect induces a reduction of the fatigue lifetime in comparison to the behaviour in air. However, it has been noticed (9) that, for a given value of $\Delta\varepsilon_p/2$, the reduction of the fatigue life described above is lower in the duplex alloy than in the ferritic alloy representing the α phase of the α/γ alloy. This is related to the presence of the γ phase in the duplex alloy which can adapt a part of the plastic deformation.

The role of the α phase at high strain amplitudes is confirmed by the results obtained at cathodic potential. At E = - 500 mV, only the ferritic phase is sensitive to hydrogen embrittlement (9). The strong reduction of the duplex stainless steel fatigue life in this case and the negligible reduction of this fatigue life at low strain amplitudes in the same electrochemical conditions, clearly emphasize the role the α phase and of its plastic deformation mode. Moreover, a marked reduction of the fatigue life at $E = E_0$ and at E = - 500 mV has been observed on aged specimens. The ageing at 400°C has been shown to promote twinning in the α phase, which induces a marked localization of the dissolution and/or the hydrogen reduction reaction in the α phase and which leads to an early crack initiation. The role of the α phase at high strain amplitude is confirmed again.

In conclusion, the mechanical and electrochemical coupling effects between α and γ phases have been shown in this paper to be the key to understand the better resistance to corrosion fatigue of the duplex alloys than those of its individual phases considered separately.

REFERENCES

(1) Lula, R.A., "Duplex stainless steels", Edited by ASM, 1983.

(2) Desestret, A. and Oltra, R., Corrosion Science, 20, 1980, p. 799.

(3) Magnin, T., LE COZE, J. and DESESTRET, A., Metals Materials Technology Series, ASM Metals Congress, St-Louis, USA, 1982, p. 1.

(4) Magnin, T., Coudreuse, L. and Lardon, J.M., Scripta Met., 19, 1985, p. 1487.

(5) Amzallag, C., Rabbe, P. and Desestret, A., "Corrosion Fatigue Technology", ASTM STP 642, 1978, p. 117.

(6) Bassidi, M.A., Masounave, J., Dickson, J.I. and Baïlon, J.P., Can. Met. Quaterly, 23, 1, 1984, p. 17.

(7) Magnin, T. and Coudreuse, L., Mater. Sci. Eng., 72, 2, 1985, p. 125.

(8) Magnin, T., Lardon, J.M. and Coudreuse, L., Proc. Conf. Low Cycle Fatigue, Lake George, USA, 1985 (to be published in an ASTM STP).

(9) Lardon, J.M., Thesis, Ecole des Mines de St-Etienne, 1986.

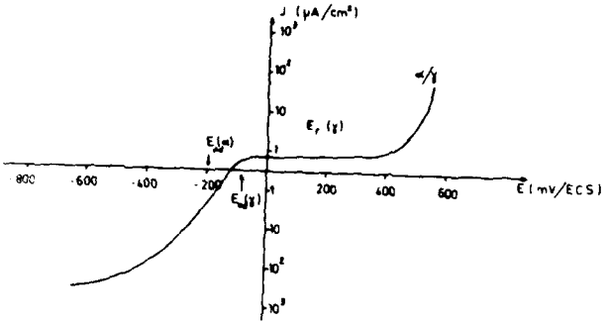

Figure 1 Polarization curve of the α/γ duplex alloy in the 3.5 % NaCl solution at pH 2 and $\Delta E/\Delta t$ = 90 mV/h.

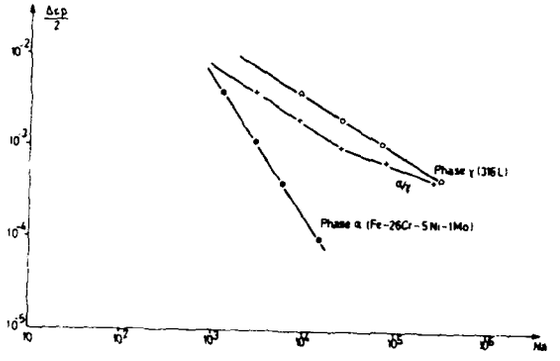

Figure 2 Coffin-Manson curves in air at $\dot{\varepsilon} = 10^{-2} s^{-1}$ of the α/γ duplex alloy and of its α and γ phases considered separately.

Figure 3 Coffin-Manson curves at $\dot{\varepsilon} = 10^{-2} s^{-1}$ of the duplex alloy at $E = E_0$ and $E = +150$mV (ECS = saturated calomel electrode)

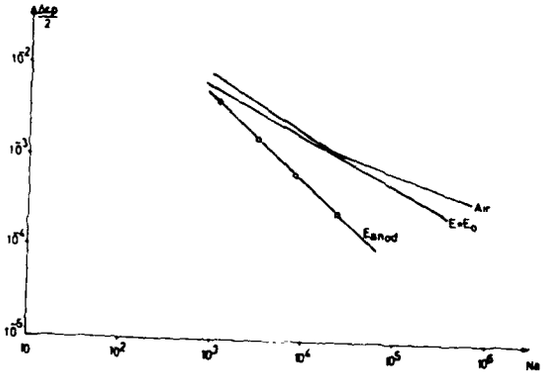

Figure 4 Corrosion fatigue crack initiation in the duplex stainless steel at $E = E_o$, $\Delta\varepsilon_p/2 = 4.10^{-3}$ and $\dot{\varepsilon} = 10^{-2}s^{-1}$.

Figure 5 Corrosion fatigue crack initiation in the duplex alloy at $E = E_o$, $\Delta\varepsilon_p/2 = 10^{-3}$ and $\dot{\varepsilon} = 10^{-2}s^{-1}$

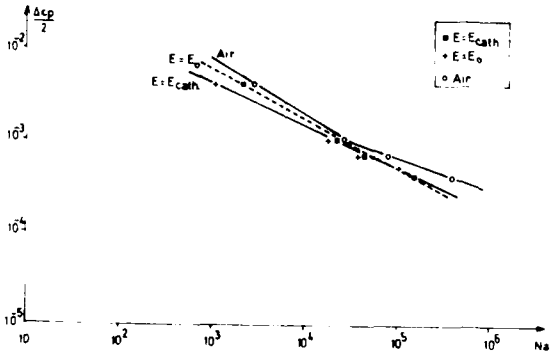

Figure 6 Coffin-Manson curves at $\dot{\varepsilon} = 10^{-2}s^{-1}$ of the duplex alloy at $E = E_o$ and $E = -500$ mV/ECS.

FATIGUE CRACK PROPAGATION IN Al-Zn-Mg BICRYSTALS AND ITS DEPENDENCE ON THE ENVIRONMENT

A. Niegel, H.-J. Gudladt and V.Gerold*

High cycle fatigue crack propagation has been studied in precipitation hardened Al-Zn-Mg specimens containing a single grain boundary perpendicular or at 45° to the load axis. In peak-aged bicrystals tested in laboratory air as well as in wet nitrogen the crack propagates intergranular. In dry nitrogen and wet atmospheres containing less than 0.8 kPa wetness the crack initiation and propagation becomes transgranular and is 100 times slower than intercrystalline crack propagation. The influence of moisture affecting the intergranular crack propagation will be discussed in terms of SCC and SCF.

INTRODUCTION

Several types of stress corrosion cracking (SCC) and hydrogen embrittlement mechanisms were discovered during the 1970's, which explained the mechanical behavior for commercial aluminium alloys (1,2,3). More recently, attention has been paid to the transition from cracking under monotonic loading and different environmental conditions to the phenomena of corrosion fatigue under dynamic loading conditions (4,5). Starting from the investigation of environmental effects of crack propagation in single crystals (6,7,8) this study concentrates on the crack propagation in grain boundaries.

In order to get a better insight into micromechanisms controlling fatigue crack growth in a "corrosive" environment experiments have been undertaken using specimens which contain only a single grain boundary (gb).

* Max-Planck-Institut für Metallforschung, Institut für Werkstoffwissenschaften and Institut für Metallkunde der Universität Stuttgart, D-7000 Stuttgart, F.R.Germany

EXPERIMENTAL DETAILS

The material used for this study was a high purity Al-4.5wt%Zn-1.25wt%Mg alloy provided by VAW, Bonn. Bicrystals with a single grain boundary in the middle of the specimen were prepared by a modified strain annealing technique. The cylindrical bicrystals were machined by spark erosion into flat specimens having a rectangular cross-section of 1.5 x 6 mm^2.

Usually, the specimen axes were oriented for single slip in one of the two grains with the broad surface parallel to the Burgers vector of the primary slip system. In most cases, the grain boundary plane was normal to the long direction of the specimen and, therefore, to the load axis. For some fatigue tests, specimens were prepared having a grain boundary at nearly 45° to the load direction. The grain boundaries prepared by the strain-annealing technique had no special symmetry. First analyses (Laue pattern) showed that the orientation of the two grains differed by less than 10°. The exact determination of the grain boundary orientations and structures are in progress.

All samples were homogenized for 30 min at 480°C, water quenched and electrolytically polished. To initiate cracks into the grain boundary notches having a depth of about 500 µm were spark machined into the small face of the specimens. These were then aged at 135°C for 100 hours to peak-hardness. Thereafter, they were fatigued either in laboratory air or in nitrogen atmospheres with different moisture content. The latter was controlled by a capacitance method throughout the experiment. All bicrystals were fatigued electrodynamically using cyclic tension-compression loading with a minimum to maximum load ratio of R = -1 at frequencies of 100 Hz (sometimes 1 Hz).

Crack initiation and propagation were measured with a travelling microscope at 200 times magnification in the x and y direction with a detection limit better than 5 µm. Threshold measurements were also made using this optical method as well as a 10 amp d.c potential drop method which was capable of measuring changes in crack length better than 10 µm for a crack to width ratio a/w greater than 0.2 (9). To account for different orientations of the cracks, the stress intensity factor ΔK for crystallographic stage I cracks as well as for gb cracks oriented about 45° to the load axis was calculated using mode I and mode II stress intensities to obtain an average ΔK (10):

$$\Delta K^2 = (\Delta K_I)^2 + (\Delta K_{II})^2 \qquad (1)$$

For non-crystallographic cracks as well as for gb cracks propagating normal to the load axis, only mode I is dominant and a correction function for fixed grips after Rooke et al. (11) has been used.

For all ΔK-calculations it was assumed that the crack propagates only in tension mode and the ΔK-factor for R = -1 was described by $\Delta K = K_{max}$. Special effects of crack closure induced by roughness of the crack surface or by plastic work were not considered (12).

EXPERIMENTAL RESULTS

Influence of the Grain Boundary Orientation

It is possible that the grain boundary direction, relative to the load axis, has an influence on the crack propagation. In order to study this influence bicrystals were fatigued in a wet nitrogen atmosphere containing a water vapor pressure of 3.1 kPa. The fatigue crack propagation behavior for specimens containing a 45° grain boundary is shown in Fig.1. For wet nitrogen the crack propagates in an intercrystalline manner. In order to compare the cyclic crack propagation rate with that of transgranular cracks, the stage I crack propagation in a similar direction as that of the intergranular crack is also presented in the figure. In the intermediate ΔK-region smaller than 1.5 MPa$\sqrt{m}$ the gb crack propagates more than ten times faster than the crystallographic crack. The threshold value was measured to be ΔK_{th} = 0.3 MPa$\sqrt{m}$ which is three times smaller than that for stage I cracks (8). In the intermediate ΔK region da/dN satisfies the general crack propagation relationship for a given mean stress

$$da/dN = c \cdot (\Delta K)^m \qquad (2)$$

where c and m are material constants. The coefficient m for gb cracks was calculated as m = 2. For stage I cracks m = 4 was found according to Liang et al. (8). For high ΔK-values the curves for trans- and intergranular cracks approach each other and meet at a crack propagation rate of $5 \cdot 10^{-8}$ m/cycle for ΔK = 3 MPa$\sqrt{m}$. In this range the slope m of the curves are nearly the same.

Fig.2 shows the cyclic crack propagation rate for bicrystals with a grain boundary orientation of 90° to the load axis in comparison to that of stage II cracks. In the wet atmosphere, the crack propagates intergranularly but leaves the grain boundary for ΔK-values greater than 10 MPa$\sqrt{m}$. In this region both curves of trans- and intercrystalline cracks meet each other at da/dN-values of about 1 μm/cycle. At lower ΔK values the crack propagates in an intercrystalline manner and at ΔK = 5 MPa$\sqrt{m}$ its propagation rate is more than 100 times greater than that for stage II cracks. In the intermediate ΔK-region, the slope m for intergranular cracks was calculated to be again m = 2. For stage II cracks, however, m was calculated to be m = 4. The threshold value for intergranular Mode I cracks measured as ΔK_{th} = 0.65 MPa$\sqrt{m}$ was three times smaller than for stage II cracks. The crack transition shown in Fig. 2 is

caused by a stage II crack running against a curved grain boundary. After reaching it the crack continues in an intercrystalline manner.

The Influence of the Environment

The influence of three different partial water vapor pressures, 3.1, 1.2 and less than 0.8 kPa on the crack propagation behavior is shown in Fig.3. For the two higher pressures the ΔK_{th}-value for intergranular cracking increased with decreasing pressure from 0.65 to 1.3 MPa$\sqrt{m}$.

For a water vapor pressure lower than 0.8 kPa, however, the crack initiation becomes more and more transgranular and the crack propagates as a stage I or a stage II crack. In a dry nitrogen atmosphere only transgranular crack propagation could be observed.

The cyclic grain boundary crack propagation rates as well as the ΔK_{th}-values, depend on the water vapor pressure and increase with increasing moisture. For ΔK-values greater than 2 MPa$\sqrt{m}$ all curves approach each other and meet at a crack propagation rate of 0.2 µm/cycle for ΔK = 5 MPa$\sqrt{m}$.

The influence of moisture on grain boundary cracking has also been investigated by changing the moisture in the specimen chamber during the fatigue test. For most of these tests, a crack was initiated in wet nitrogen. Thereafter, the environment was changed to dry nitrogen with a water vapor pressure of less than 35 Pa. Surprisingly, the crack propagation in the new atmosphere always remained intergranular. For further understanding of this phenomenon, the specimens were heat treated (10 h at 135°C) before the fatigue tests were continued in the dry nitrogen atmosphere. This procedure showed the same result as before, i.e., the crack propagation remained intergranular. Only after a full heat treatment (homogenisation at 480°C and ageing to peak-hardness) the crack did continue in a transcrystalline manner in the dry environment.

DISCUSSION

As has been shown by different investigators stress corrosion phenomena occur in commercial Al-Zn-Mg alloys in the presence of water vapor (1-3). But even for monotonic loading conditions it is often difficult to resolve the difference between what might be dissolution controlled SCC and true hydrogen embrittlement. Under cyclic loading conditions the effect of hydrogen embrittlement on crack propagation has been observed using single crystal specimens and has been discussed in previous papers (6-8). For bicrystals intercrystalline crack propagation must be affected by SCC as well as by stress corrosion fatigue (SCF).

It is well known that Al-Zn-Mg specimens aged to peak-hardness tend to form precipitation free zones (PFZ) which contain incoherent grain boundary precipitates (13,14). TEM examinations of the grain boundaries reveal the existence of oblated grain boundary precipitates with visible dimensions 110 and 25 nm which were surrounded by a PFZ having a width of 80 nm (Fig.4). These incoherent $MgZn_2$ precipitates were also observed on grain boundary crack surfaces by REM if the applied ΔK-value was greater than 1.5 MPa$\sqrt{m}$, as seen in Fig.5. The intercrystalline crack surface is very smooth and shows no sign of any striation which otherwise are typical for stage II cracks. In this case, it is suggested that the plasticity in front of the crack tip is very small compared to stage II - cracks.

For the case of monotonic loading, this grain boundary embrittlement due to hydrogen has been observed and discussed by Speidel as well as by Gruhl (1,3). It is referred to SCC and depends on the water vapor pressure and the applied stress intensity (2). If it is assumed that the hydrogen acts in a similar way under cyclic loading conditions, it must enter the grain boundary during the tensile half cycles where probably K_{max} is the controlling parameter which is identical with ΔK in the present case. Then SCC only occurs if a critical water vapor pressure p_c and a critical stress intensity ΔK_{SCC} is exceeded. This critical ΔK_{SCC} represents the threshold value and depends on the water vapor pressure p as

$$\Delta K_{SCC} = \Delta K_{th} \cdot (p_c/p)^{1/2} \qquad \text{for } p \geq p_c \qquad (3)$$

where ΔK_{th} is supposed to be that for stage II cracks.

TABLE 1 - Comparison of Characteristic Values for Trans- and Intergranular Cracks in Al-Zn-Mg Bicrystals

Crack	Intergranular (3.1 kPa)	Transgranular (3.1 kPa)
Cyclic crack propagation rate (da/dN) (m/cycle)	Mode I (ΔK=4 MPa$\sqrt{m}$) 1.5×10^{-7} Mixed Mode (ΔK=1 MPa$\sqrt{m}$) 1×10^{-8}	Mode I (ΔK=4 MPa$\sqrt{m}$) 2×10^{-9} Mixed Mode (ΔK=1 MPa$\sqrt{m}$) 1×10^{-9}
ΔK-dependence (MPa$\sqrt{m}$)	Mode I, Mixed Mode $da/dN = C_{gb} \cdot (\Delta K)^m$, m=2	Mode I, Mixed Mode $da/dN = C \cdot$
Threshold-value ΔK_{th}(MPa$\sqrt{m}$)	Mode I: 0.65 ± 0.05 Mixed Mode: 0.3 ± 0.1	
Influence of moisture $p(H_2O)$	> 80% if p > 1.2 kPa	

AD-A184 047 FATIGUE '87 VOLUME 3(U) VIRGINIA UNIV CHARLOTTESVILLE 2/6
SCHOOL OF ENGINEERING AND APPLIED SCIENCE
R O RITCHIE ET AL. JUN 87 ARO-24134.3-MS-CF
UNCLASSIFIED N00014-87-G-0008 F/G 20/11 NL

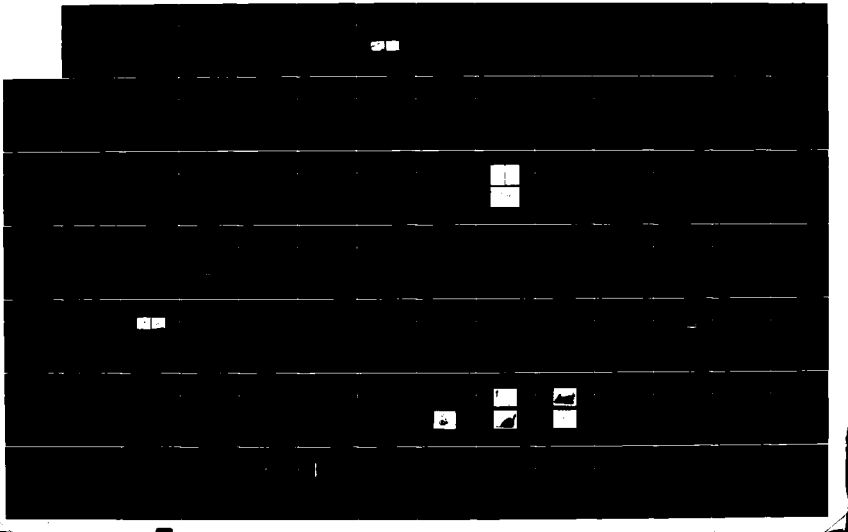

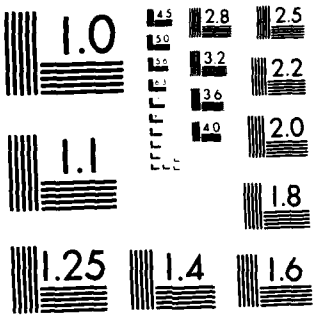

The upper limit for p_c has been determined to be 0.8 kPa from experimental results. In order to initiate intercrystalline crack growth, the threshold value ΔK_{SCC} must be smaller than the ΔK_{th} value for stage II cracks, which is 2 MPa$\sqrt{m}$. For a vapor pressure of 3.1 kPa, the calculated ΔK_{SCC} is smaller than 1 MPa$\sqrt{m}$. This represents an upper limit for ΔK_{SCC} and is comparable to the 0.65 MPa$\sqrt{m}$ obtained from experimental results shown in Table 1. The discrepancy between measured and calculated ΔK_{SCC} may be derived from the uncertainty in p_c determination. Preliminary experiments with coarse grained specimens at a vapor pressure p = 0.5 MPa revealed a portion of 30% intercrystalline cracks. Thus, the assumption p_c =0.8 kPa may be an overestimation.

Under monotonic loading conditions SCC is characterized by a plateau range for intermediate ΔK-values, e.g. the crack extension rate $[da/dt]_p$ is nearly constant (1,13). For cyclic loading cases, however, the crack extension rate da/dN for SCC becomes frequency dependent and an additional SCF term has to be included (16):

$$da/dN = F^{-1}[da/dt]_p + \{c(\Delta K)^m\}_{SCF} \qquad (4)$$

In order to study the two parts quantitatively, the test frequency F was changed to 1 Hz. The cyclic crack propagation rate showed a plateau range for intermediate ΔK-values as it is expected for SCC. If it is assumed that the crack growth rate is mainly determined by $[da/dt]_p$ the upper limit was calculated to be $5 \cdot 10^{-8}$ m/cycle or $5 \cdot 10^{-8}$ m/s for 1 Hz, respectively. For 100 Hz, however, the calculated value of $[da/dt]_p$ represents a cyclic crack growth rate of $5 \cdot 10^{-10}$ m/cycle which is about 100 times smaller than the measured crack growth rates. Therefore, the second term of Equ.(4) appears to control intercrystalline crack propagation. It could be that SCC determines the threshold-value ΔK_{SCC}, but another mechanism must control intercrystalline crack propagation, where $\Delta K > \Delta K_{SCC}$.

For SCF it is assumed that the hydrogen dissolved in the grain boundary has been trapped in form of bubbles which induce the crack propagation. It is possible that for crack propagation rates greater than 0.1 µm/cycle it is the trapped hydrogen which governs the crack propagation. Christodoulou et al. show in their work that $MgZn_2$ precipitates on the grain boundary act as traps for the embrittling hydrogen (15) and they suppose that bubbles filled with hydrogen gas will nucleate around the precipitates. Bubbles produced by trapped hydrogen atoms has been observed by other workers using TEM.

Preliminary TEM investigations stated the existence of bubbles in the grain boundary of bicrystals after fatiguing in wet nitrogen. During the fatigue test, hydrogen produced by the dissociation of water vapor on the newly created crack surface can be dissolved in the grain boundary. The incoherent gb precipitates probably act

as nuclei for bubbbles where the hydrogen can be trapped. Compared to the dissolved hydrogen, which is in equilibrium with the water vapor pressure, the amount of trapped hydrogen increases during cycling. After a certain number of cycles it is the trapped hydrogen that governs the crack propagation rate and da/dN becomes independent of the water vapor pressure p and, therefore, of the environment. This assumption has been tested by changing the atmosphere during a fatigue test from wet to dry nitrogen. A crack which propagates in a grain boundary in wet N_2 atmosphere, continues to do so even when the environment is changed to dry N_2 because the crack propagation is controlled by the trapped hydrogen. However, if the trapped hydrogen is removed by a full heat treatment (homogenizing and ageing to peak-hardness) prior to continuing the experiment in dry N_2, the intergranular crack will change to a transgranular one.

CONCLUSIONS

Fatigue tests with peak-aged Al-Zn-Mg bicrystals have shown intergranular crack growth in wet nitrogen or laboratory air due to stress corrosion fatigue (SCF). The threshold value ΔK_{SCC} may be controlled by SCC and depends on the partial water vapor pressure p. In atmospheres with a pressure p less than 0.8 kPa the crack propagates only transgranularly. It is suggested that the threshold is controlled by hydrogen dissolved in the grain boundaries during cyclic loading.

Intercrystalline cracks produced in wet atmospheres continue to propagate in this mode even if the environment has been changed to a dry atmosphere. This may be caused by hydrogen which has been trapped in bubbles at the grain boundary precipitates during cycling at medium ΔK values in wet environment. These bubbles remain after changing the atmosphere and can be annealed out only at temperatures far above 150°C.

ACKNOWLEDGEMENT

The authors gratefully acknowledge the financial support of the Deutsche Forschungsgemeinschaft.

REFERENCES

(1) Speidel, M.O., "The Theory of Stress Corrosion Cracking in Alloys". Published by: NATO Scientific Affairs Division Brussels 1971, pp. 289-344.

(2) Speidel, M.O., Hydrogen in Metals, ASM 1973. Edited by Bernstein, I.M., Thompson, A.W., pp. 249-271.

(3) Gruhl, W., Z. Metallkde., Vol. 75, 1984, pp. 819-826.

(4) Wei, R.P. and Simmons, G.W., Int. J. Fract., Vol. 17, No.2, 1981, pp. 235-247.

(5) Jacko, R.J., Duquette, D.J., Hydrogen Effects in Metals, Ed. Bernstein, I.M., Thompson, A.W., 1981, pp. 477-484.

(6) Nageswararao, M. and Gerold, V., Met.Trans., Vol. 7A, 1976, pp. 1847-1855.

(7) Affeldt, E. and Gerold, V., Proceedings of ICF6, New Delhi, 1984, pp. 1579-1588.

(8) Liang, P., Gudladt, H.-J., Gerold, V., Proc. of ECF6, Amsterdam, 1986, Vol. III, pp. 1493-1502.

(9) Gudladt, H.-J., Nagy, P., "The Cyclic Crack Propagation Behaviour of a Hardenable Polycrystalline Ag-Mg-Sc-Alloy". In: Age-Hardenable Aluminium Alloys. Proc. 4th Int. Conf., Budapest 1986, Eds. I. Kovacs & J. Lendvai, Materials Science Forum Vols.13/14, 1986 (Trans Tech Publ. Ltd Adermannsdorf, Switzerland).

(10) Knott, J.F., Fatigue and Microstructure, American Soc. of Metals, Metals Park, Ohio, 1978, p. 149.

(11) Rooke, D.P. and Cartwright, D.J., Compendium of stress intensity factors, Her Majesty's Stationary Office London, 1976.

(12) Elber, W., Eng. Fract. Mech., Vol. 2, 1970, p. 37.

(13) Rippstein, K., Baumgartner, M., Konys, J., Kaesche, H., Z. Metallkde., Vol. 75, 1984, pp. 291-298.

(14) Embury, J.D. and Nicholson, R.B., Acta Met., Vol.13, 1965, pp. 403-417.

(15) Christodoulou, L., Flower, H.M., Hydrogen Effects in Metals, Ed. Bernstein, I.M., Thompson, A.W., 1981, pp. 493-501.

(16) Wei, R.P., in Fatigue Mechanisms, ASTM Symposium, Kansas City, May 1978, ASTM STP 675 pp.816-840.

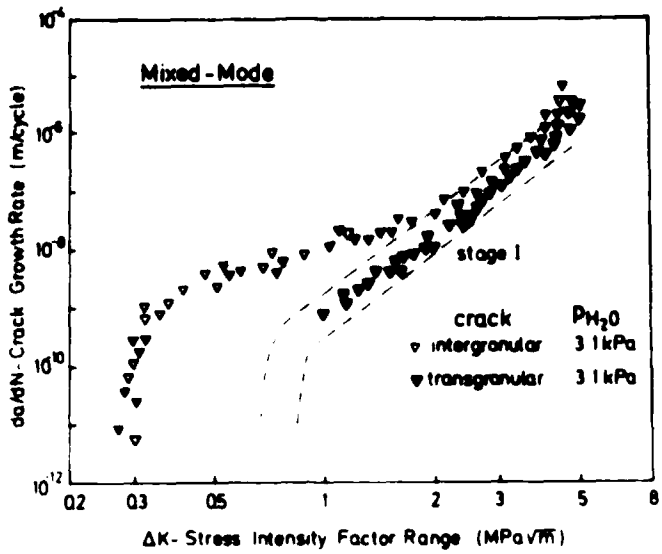

Figure 1 Crack propagation rate vs ΔK for stage I and intergranular cracks. Scatter band after Liang et al. (8).

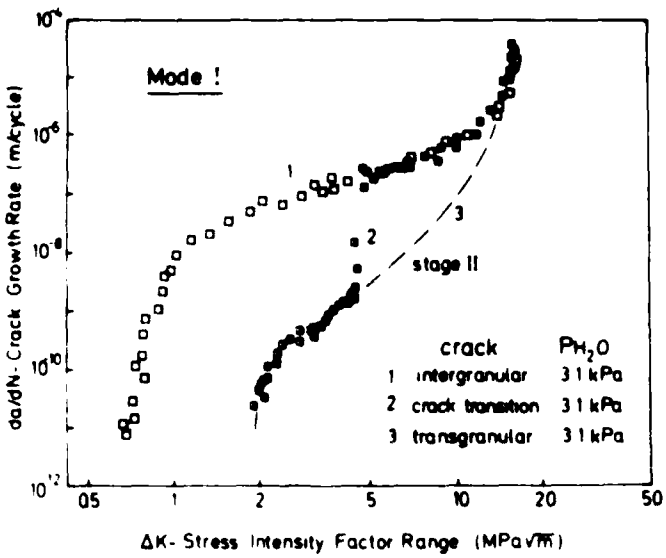

Figure 2 Crack propagation rate vs ΔK for stage II and intergranular cracks.

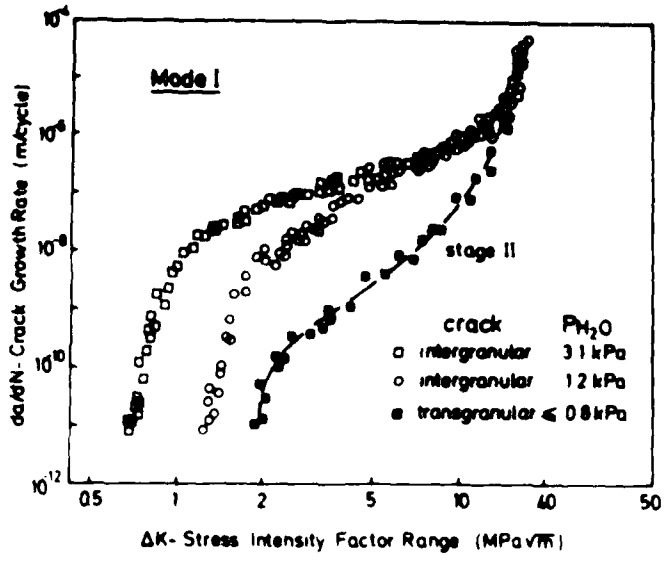

Figure 3 Crack propagation rate vs ΔK for intergranular cracks fatigued in atmospheres with different water vapor pressures.

Figure 4 TEM observation of a precipitation free zone for an Al-Zn-Mg bicrystal. The PFZ contains incoherent $MgZn_2$ precipitations for the peak-aged condition.

Figure 5 REM examination of a grain boundary crack plane for specimens fatigued in wet nitrogen. The incoherent precipitates, shown in Fig.4 has been observed on the crack plane if ΔK is greater than 1.5 MPa√m.

FRACTURE KINETICS OF CORROSION FATIGUE

F. Krausz* and A.S. Krausz**

Thermally activated threshold effects in fatigue originate from atomic vibration-induced rebonding and crack closure-induced growth rate reduction. Fracture kinetics analyses of fatigue carried out for a wide range of metals and some polymers indicate that in about two thirds of these materials the threshold effect is controlled by thermal-vibration rebonding and the rest by closure effects. The interrelations among mechanical and corrosion fatigue, and stress corrosion cracking are recognized.

INTRODUCTION

It is well recognized that environment assisted fatigue cracking is controlled by several thermally activated processes. Crack growth is time and temperature dependent. Wei [1], Weir et al [2], Wei and Simmons [3], and Wei and Shim [4], considered that in gaseous environment the rate of crack growth is described as

$$\left(\frac{da}{dN}\right)_e = \left(\frac{da}{dN}\right)_r + \left(\frac{da}{dN}\right)_{cf} + \left(\frac{da}{dN}\right)_{SCC} \qquad (1)$$

The terms have the following meaning:

- $(da/dN)_r$ is the rate of fatigue crack growth in an inert environment. This process is not thermally activated and is referred to as "mechanical" or "reference" fatigue (Figure 1, curve A).
- $(da/dN)_{cf}$ is the corrosion fatigue term representing the combined action of cyclic loading and degrading environment (curve

*300 The Driveway, Ottawa.
**Department of Mechanical Engineering, University of Ottawa

B in Figure 1);

- $(da/dN)_{SCC}$ is the crack growth rate under sustained loading in a degrading environment (curve C in Figure 1).

Equation (1) is a typical expression of parallel (independent) processes. Consequently, it is always the fastest process that is rate controlling; when two are of about equal magnitude the combination of the two terms is effective. In the following, these remarks will acquire a special significance.

In addition to the complex kinetics of the mechanical fatigue, the environment-influenced terms are affected by chemical and transport processes as well, each forming time and temperature dependent consecutive and parallel processes (Brown (5), Krausz (6) and Brown (7). Some details of these will be elaborated upon, but by no means all: environment assisted fatigue is an intricate system of mechanisms.

An analysis on the effect of cycling frequency was reported before (Krausz and Krausz (8). Partial rebonding in each cycle is an important cause of threshold effects; it decelerates the net crack growth. There are two sources of rebonding: the thermal vibration-induced, atomic scale partial rebonding of newly generated surfaces (Krausz and Krausz (9), and the crack closure-induced, thermally activated growth retardation (Krausz and Krausz (8), McEvily (10). This communication is concerned with some aspects of the threshold behavior, particularly with the role of thermal activation associated with crack closure.

DISCUSSION

In Region I and II stress corrosion cracking occurs under the combined effects of diffusion, chemical reaction, and the atomic bond breaking processes of crack growth. It was shown (5),(6),(7),(8), and Wiederhorn (11), that these two regions are related in a sequential combination and, therefore, the slower process controls crack growth in each region. Again, a combination of various mechanisms are effective, but for the present purpose it is sufficient to model SCC in terms of the overall rate of each. It must also be recognized that due to the random vibration of atoms, thermally activated processes always occur in the forward as well as in the backward direction. These terms mean that the forward occurrences are observed macroscopically, while the backward,being of a slower rate, are in the direction opposite to the overall process. These concepts are used in common with chemical kinetics and thermally activated fracture kinetics (Krausz (10), Glasstone et al (12) and Laidler (13).

It was shwon by Krausz (6) that the crack velocity, v, in SCC is expressed in the threshold zone, and in Regions I and II as

$$v \propto L \frac{k_{If}k_{IIf} - k_{Ib}k_{IIb}}{k_{If} + k_{IIf} + k_{Ib} + k_{IIb}} \tag{2}$$

where L is the distance the crack travels after activation over the consecutive barrier system composed of the two (overall) mechanisms that control Region I and II; the rate constants, k, are labelled according to their association with the indicated Region; the second subscript signifies that the rate constant is that of forward (f) or backward (b) activation. Whichever type it is, the rate constant is described as

$$k = \frac{kT}{h} \exp\left[-\frac{\Delta G^{\ddagger}(W)}{kT}\right] \tag{3}$$

In this k and h are universal constants, Boltzmann's and Planck's respectively, and T is the absolute temperature. In the exponent $\Delta G^{\ddagger}(W)$ is the apparent activation free energy, a function of the mechanical energy, W, as defined by fracture mechanics. Accordingly, $\Delta G^{\ddagger}(W)$ for the four cases of Equation (2) is expressed as

$$\begin{aligned} &\Delta G^{\ddagger}_{If}(W) = \Delta G^{\ddagger}_{If} - W_{If} \; ; \quad \Delta G^{\ddagger}_{IIf}(W) = \Delta G^{\ddagger}_{IIf} - W_{IIf} \; ; \\ &\Delta G^{\ddagger}_{Ib}(W) = \Delta G^{\ddagger}_{Ib} + W_{Ib} \; ; \quad \Delta G^{\ddagger}_{IIb}(W) = \Delta G^{\ddagger}_{IIb} + W_{IIb} \; . \end{aligned} \tag{4}$$

Some comments are in place here. The description of the apparent activation energy by the true activation energy, $\Delta G^{\ddagger}$, and the mechanical energy, W, is a standard procedure. For some processes, such as many diffusion mechanisms, the apparent activation energy is substantially independent of the mechanical energy and thus

$$\Delta G^{\ddagger}(W) = \Delta G^{\ddagger} \; .$$

Usually the mechanical energy is a linear function of the stress intensity factor, K, or the strain energy release rate, G, or the strain energy density factor, S, for mixed mode loading (Sih (14) and Badaliance (15). Other effects, such as the Hillig and Charles (16) geometrical relation, or the environmental and hydrostatic pressure effects are readily accommodated in this expression. The appropriate form and numerical values must be established through a rigorous fracture kinetics analysis, as shown by Krausz and Krausz (9).

By definition, at the threshold $v = 0$; accordingly, from Equation (2)

$$k_{If}k_{IIf} = k_{Ib}k_{IIb} \; . \tag{5}$$

The consequences of this relation and conclusions were discussed by Krausz (6), and by Krausz and Krausz (9). As it was shown, the relation is valid when no other effects than those, identified above are involved, and the model used for Equation (2) is appropriate.

In corrosion fatigue a different mechanism can be forcefully present as well: the crack closure effect with its consequent "crack rewelding". In a previous publication, it was reported (8) that the consideration of crack closure and the associated effective cycle time (that is, the cycle time, less the period over which the crack surfaces are in contact), leads to valid conclusions when rewelding was described by thermal activation theory (9).

To elucidate the influence of crack closure on the threshold it is considered that according to Equation (1) the stress corrosion cracking threshold mechanism and the thermally activated corrosion fatigue terms are parallel mechanisms. Consequently, in environment assisted fatigue, the threshold is controlled by the faster process.

To describe rebonding during closure, the rate constant, k_{rb}, is defined from thermal activation theory as

$$k_{rb} \quad \frac{kT}{h} \exp\left[-\frac{\Delta G^{\ddagger}_{rb}(W)}{kT}\right]. \tag{6}$$

Crack closure, and thus rebonding, occurs because during load decrease the elastic matrix compresses the plastically deformed crack-tip zone, thereby promoting rebonding. Accordingly, the apparent free energy is

$$\Delta G^{\ddagger}_{rb}(W) \quad \Delta G^{\ddagger}_{rb} - W_{rb}$$

where $\Delta G^{\ddagger}_{rb}$ is the true activation free energy of rebonding. Because the pressure exerted by the elastically contracted surrounding zone promotes rebonding, the work reduces the thermal energy need. Following established principles and practices, corrosion fatigue is modelled in the threshold zone and beyond as

$$\left(\frac{da}{dN}\right)_{cf} \quad L_f k_f - L_{rb} k_{rb} \quad L_f \frac{kT}{h} \exp\left[-\frac{\Delta G^{\ddagger}_f - \alpha_f \Delta K}{kT}\right]$$

$$- L_{rb} \frac{kT}{h} \exp\left[-\frac{\Delta G^{\ddagger}_{rb} - \alpha_{rb} \Delta K}{kT}\right] \tag{7}$$

where α is the work factor corresponding to the crack growth mechanism identified with the subscript f, and rebonding with rb.

As before, L is the distance of crack growth on each activation. The two rate constants are representing opposite directions of crack tip movement, hence their opposite signs. At this stage the physical or chemical mechanism of the first term is not identified: this is the task of fracture kinetics analysis that has to be carried out for the material composition and microstructure, temperature range, frequency, wave-form, R value (Bamford (17), and for the investigated degrading environmental conditions. The specific mechanism of rebonding may also be determined by some of these factors.

When the effect of the closure process on rebonding is negligible the typical reverse step of thermally activated processes may still occur. The functioning of this healing step was demonstrated in SCC (5),(6),(9). Accordingly, corrosion fatigue is described as

$$\left(\frac{da}{dN} \right)_{cf} \quad L_f k_f - L_h k_h \tag{8}$$

where the healing rate constant, being a reverse process, is

$$k_h \quad \frac{kT}{h} \exp\left(- \frac{\Delta G_h^{\ddagger}(W)}{kT}\right) \quad \frac{kT}{h} \exp\left(- \frac{\Delta G_h^{\ddagger} + \alpha_h \Delta K}{kT}\right) .$$

A wide range of published results were analyzed using the techniques of fracture kinetics (9). These included SM1 1010, 25 Mn-5 Cr-1Ni, SUS 304, 10 Ni, A 302B, A 561, HSLA steels, NIMONIC 105; Ti-8 Al-1 Mo-IV, Al-2219-T 851, Ti-6 Al-4V, 7475-T 761 alloys; polymers; AgCl; Mg, Al, Ag, Cu, Zr, Ti, Fe, Ni,alloys ; frequencies in the range of 3.3 to 100 Hz; R values of 0.05 to 0.08 and in ambient, seawater and other environments. Several of these were obtained over a temperature range. All were well reprsented by the relations described by Equations (7) or (8). This result indicates that fracture kinetics can provide useful guidance for the establishment of some of the mechanisms of threshold effects. Because the rate constants identify the influence of the various factors that control threshold quantitatively, including the microstructure, the thermal activation relations provide indications for the improvement of corrosion fatigue behavior.

Figures 2 and 3 are typical representations of crack closure-induced "rewelding", and reverse activation-induced healing behaviors, respectively. Semilog coordinates were used because these represent best the exponential function relations of thermally activated processes. It is clear from the figures that in the high ΔK zone, where the $(da/dN)_{cf}$ vs. ΔK relation is a straight line, the $L_f k_f$ term is rate controlling, while in the

threshold zone the closure, or healing mechanisms are also effective.

Fracture kinetics analysis of the behavior in Figure 2 revealed that closure by rewelding is indeed the process in the low-ΔK region: Equation (7) was used to calculate the curve, with the constants $(da/dN) = 7 \times 10^{-4} \exp(0.033\ \Delta K) - 1 \times 10^{-3} \exp(0.0126\ \Delta K)$. The analysis of the steel of Figure 3, on the other hand, revealed bond healing in the threshold zone. The corresponding constants of Equation (8) are $(da/dN) = 6 \times 10^{-5} \exp(0.062\ \Delta K) - 1 \times 10^{-3} \exp(-0.067\ \Delta K)$. The method of the calculation and the kinetics analyses are elaborated upon in reference (9).

The study of threshold behavior can be extended by considering the effective stress intensity range, ΔK_{eff}, as considered by Esaklul and Gerberich (18) for the internal hydrogen degredation of fatigue thresholds in HSLA steels, and by other investigators. Particularly relevant information can be expected from tests carried out over wide temperature ranges. These are the only appropriate tests to measure the true activation energies, $\Delta G^{\ddagger}$. They provide important guidance to the identification of the mechanisms. The corresponding experimental, analytical, and theoretical program is quite involved and time consuming. No fast and hard answers can be expected. However, the usual methods employed for the determination of the true activation energy, $\Delta G^{\ddagger}$, can be significantly simplified by the following technique of fracture kinetics.

Fracture kinetic diagrams are developed in the logarithm rate vs. linear driving force (ΔK, ΔG, or ΔS) coordinate systems. Each of the two mechanisms (Carlson and Beevers (19), Vincent and Remy (20), and Speidel (21), (crack growth by bond breaking and crack healing by closure "welding") is described by a relation of the type

$$\dot{L}k = L \frac{kT}{h} \exp\left(-\frac{\Delta G^{*} - \alpha \Delta K}{kT}\right) .$$

In the semi-log plot of fracture kinetics they are represented by a straight line. True activation energy can be obtained by extending the linear behavior, measured at different temperatures, to $\Delta K \to 0$. The intercept of crack velocity values are then replotted in an Arrhenius plot; the slope of the resultant straight line gives the true activation energy ΔG^{*}. This, being independent of the mechanical energy input, is the actual energy needed to rearrange the atomic configuration in order to operate the specific thermally activated process of crack growth or healing. This type of study is now in progress.

The fracture kinetics evaluations were carried out on the corrosion fatigue behavior in a wide range of metals, ceramics, and polymers. An extensive account will be published elsewhere; here the principles and the conceptual developments are reported.

SUMMARY AND CONCLUSIONS

(1) Corrosion fatigue is recognized as a thermally activated process and its relation to SCC is indicated.

(2) Crack closure leads to partial healing by thermally activated rebonding in typical corrosion fatigue processes. Similarly, atomic vibration effects reduce crack growth rates.

(3) Fracture kinetics analysis leads to the establishment of the mechanism, and the effect of microstructure through the quantitative evaluation of the work factor, α, and the true activation energy, $\Delta G^{\ddagger}$.

(4) For the analysis of corrosion fatigue behavior the semi-log plot of fracture kinetics holds essential advantages over the more conventional double-log coordinates: it reveals the mechanisms and facilitates the establishment of physically based corrosion fatigue constitutive equations. It provides an advantageous technique for the direct determination of the true activation energy.

ACKNOWLEDGEMENT

One of the authors (A.S. Krausz) thanks the Natural Sciences and Engineering Research Council for the grant that facilitated this project.

REFERENCES

(1) Wei, R.P. in "Fatigue Mechanisms", ASTM STP 675. American Society for Testing and Materials, 1979, pp. 816-831.

(2) Weir, T.W., Simmons, G.W., Hart, R.G., and Wei, R.P.,Scripta Met., Vol. 14, No. 3, March 1980, pp. 357-364.

(3) Wei, R.P. and Simmons, G.W., "Surface Reactions and Fatigue Crack Growth", in Proceedings, 27th Army Materials Research Conference, Bolton Landing, N.Y., July 1980.

(4) Wei, R.P. and Shim, G., in Corrosion Fatigue, ASTM STP 801, American Society for Testing and Materials, 1982, pp. 5-25.

(5) Brown, S.D., J. Am. Cer. Soc., Vol. 62, 1979, pp. 515-524.

(6) Krausz, A.S., Eng. Fract. Mech., Vol. 11, 1979, pp. 33-42.

(7) Brown, S.C., Am. Cer. Soc. Bull.,Vol. 55, 1976, pp. 395.

(8) Krausz, K. and Krausz, A.S., "A Fracture Kinetics Representation of Fatigue Crack Propagation Rate", Proceedings of the 2nd International Conference on "Fatigue and Fatigue Thresholds", Editors C.J. Beevers, J. Bachlund, P. Lukas, J. Schijve, R.O. Ritchie, Birmingham, England, 1984.

(9) Krausz, K., and Krausz, A.S., "Fracture Kinetics of Crack Growth", Martinus Nijhoff, in press.

(10) McEvily, A.J., in "Fatigue Mechanism", ASTM STP 811, American Society for Testing and Materials, 1983, p. 347.

(11) Wiederhorn, S.M., J. Am. Cer. Soc., Vol. 50, 1967, pp. 407-414.

(12) Glasstone, S., Laidler, K.J. and Eyring, H., "The Theory of Rate Processes", McGraw-Hill, 1941.

(13) Laidler, K.J., "Chemical Kinetics", McGraw-Hill, 1965.

(14) Sih, G.C. in Methods of Analysis and Solution of Crack Problems, G.C. Sih, Ed., Noordhoff International Publishing, Leyden, The Netherlands, 1973, pp. XXI-XLV.

(15) Badaliance, R., Engineering Fracture Mechanics, Vol. 13, No. 3, 1980, pp. 657-666.

(16) Hillig, W.B., and Charles, K.J., "High Strength Materials", Edited by Z. Zakay, Wiley-Interscience, 1964.

(17) Bamford, W.H., in Corrosion Fatigue, ASTM STP 801, American Society for Testing and Materials, 1982, pp. 405-422.

(18) Esaklul, K.A. and Berberich, W.W., in Fracture Mechanics, ASTM STP 868, American Society for Testing and Materials, 1985, pp. 131-148.

(19) Carlson, R.L., and Beevers, C.J., "Fatigue '84", Proceedings of the 2nd International Conference on "Fatigue and Fatigue Thresholds". Edited by C.J. Beevers, J. Backlund, P. Lukas, R.O. Ritchie, Engineering Materials Advisory Services Ltd., 1984.

(20) Vincent, J.N., and Remy, L. "Fatigue '84", Proceedings of the 2nd International Conference on "Fatigue and Fatigue Thresholds". Edited by C.J. Beevers, J. Backlund, P. Lukas, R.O. Ritchie, Engineering Materials Advisory Services Ltd.,1984.

(21) Speidel, M.O., "Stress Corrosion Cracking and Hydrogen Embrittlement in Iron Base Alloys", National Association of Corrosion Engineers-5, 1977.

α fracture mechanical work factor

$\Delta G^{\dagger}$ true activation energy

$\Delta G^{\dagger}(W)$ apparent activation free energy

h Planck's constant (6.6×10^{-39} J-sec)

k Boltzmann constant (1.38×10^{-23} J K^{-1})

k rate constant (sec^{-1})

L crack growth per activation

v crack growth velocity

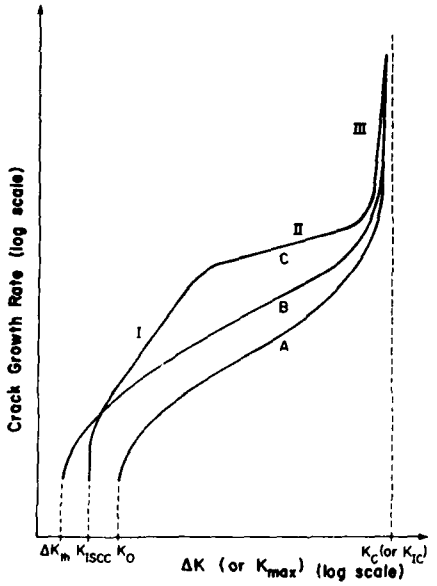

Figure 1. Schematic representation of the three crack growth processes of Equation (1).

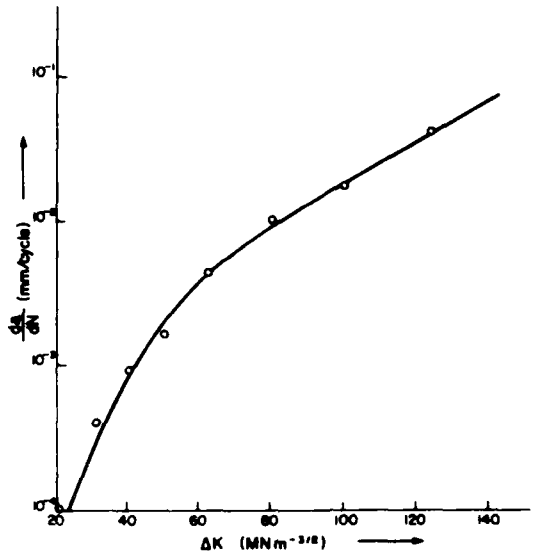

Figure 2. Fatigue of a Ti-alloy in seawater.

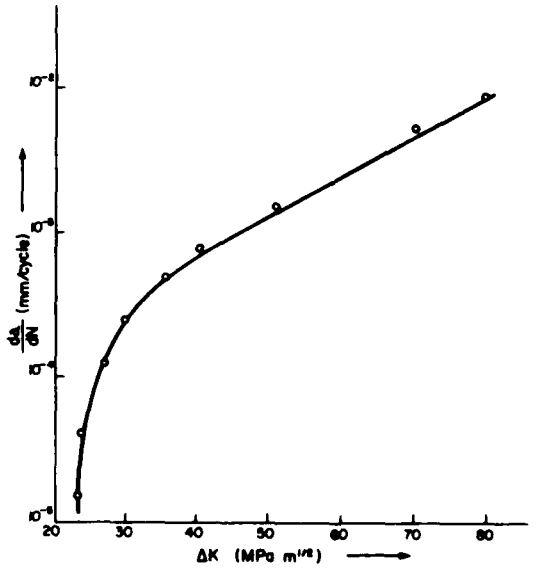

Figure 3. Fatigue of an austenitic ferritic steel in 3% NaCl solution.

THE INFLUENCE OF TEMPER EMBRITTLEMENT ON FATIGUE CRACK GROWTH IN HYDROGEN

C.A. Hippsley*

The effects of temper embrittlement on fatigue crack growth in gaseous hydrogen have been examined for 2.25Cr 1Mo steel. A range of tempered and aged conditions was examined, using vacuum as the control environment. In the unembrittled state, hydrogen encouraged intergranular cracking at intermediate ΔK and transgranular cracking at high ΔK. Reversible temper embrittlement promoted the intergranular mode, and one-step temper embrittlement promoted the transgranular mode, thus reflecting lower-shelf fracture mechanisms.

INTRODUCTION

Medium and low strength steels (i.e. yield stress <700MPa) are generally considered resistant to stable crack growth under static loading in gaseous hydrogen (Birth (1)). However, a number of examples are given in the literature of gaseous hydrogen affecting crack propagation in such steels under conditions of cyclic loading in fatigue (Ritchie (2) and Nakanasa et al (3)). In high strength steels, in which hydrogen assisted cracking under static loads can occur, an increase in susceptibility to the intergranular form of hydrogen assisted cracking has been observed after reversible temper embrittlement (Bandyopadhyay et al (4)). It is possible therefore that temper embrittlement could also affect hydrogen assisted fatigue crack growth in lower strength steels, although little information is available regarding this possibility.

*Materials Physics and Metallurgy Division, AERE Harwell Oxfordshire OX11 ORA, England

The current investigation (Hippsley (5,6)) has examined fatigue cracking in 2.25Cr 1Mo steel tempered to a range of strengths in vacuum and hydrogen environments, and the influences of both reversible and one-step temper embrittlement. This paper summarises the most significant results, paying particular attention to temper embrittlement effects.

EXPERIMENTAL

A commercial melt of 2.25Cr 1Mo steel of the following composition was employed (wt.%) 2.12Cr, 0.95Mo, 0.17Si, 0.20Ni, 0.15Cu, 0.13C 0.021S, 0.015P. Compact tension specimens of 25mm thickness were machined and given an austenitisation treatment of 960°C for 2h, followed by a water quench. The following tempering and embrittling treatments were then applied:

CODE	TEMPERING TREATMENT	HARDNESS (VPN)
A	As quenched	400
M	600°C for 10h	265
I	600°C for 500h	190
	ONE-STEP TEMPER EMBRITTLEMENT (OSTE)	
300I	A+300°C for 30h	390
500I	A+500°C for 64h	370
	REVERSIBLE TEMPER EMBRITTLEMENT (RTE)	
MI	M+500°C for 1000h	255
II	I+500°C for 1000h	190

The microstructure resulting from each treatment was characterised both optically and in the transmission electron microscope. In RTE samples the degree of grain boundary segregation was evaluated using Auger electron spectroscopy.

Load-shedding fatigue crack growth tests were performed for each condition in a vacuum of 3×10^{-4}Pa, and in laboratory-grade hydrogen at a pressure of 9.5×10^{4}Pa. The loading ratio (R) and test frequency were fixed at 0.3 and 10Hz respectively. All crack lengths were obtained from potential-drop measurements. Cyclic yield behaviour was determined using cylindrical

tension/compression testpieces which were heat treated and cycled at 0.1Hz to a total strain amplitude of +/-1%. Tests were interrupted when the resulting stress/strain hysteresis curves had stabilised, and the equilibrium cyclic yield stress measured from their final shape. Charpy impact tests were also used to characterise the effects of temper embrittlement on the ductile/brittle transition in the temperature range -200°C to +200°C.

Detailed fractography was performed on all the fatigue crack growth testpieces using a scanning electron microscope. Reference to the potential drop calibration of crack length, and the load shedding schedule enabled fractographic features to be characterised as a function of applied alternating stress-intensity (ΔK). The surfaces of cyclic yield specimens were also examined for the emergence of persistent slip bands, together with Charpy fracture-surfaces to establish the effects of embrittlement on impact fracture.

RESULTS

The microstructure in the as-quenched condition (A) was fully martensitic, with a prior austenite grain size of 22μm (mean linear intercept), and a few autotempered carbides. One-step temper embrittlement (OSTE) produced a fine dispersion of Fe_3C carbides, increasing in density from the 300T to the 500T condition. The temper at 600°C (M-10h, L-500h) produced a mixture of M_2C and M_7C_3 alloy carbides. The overall density of these carbides was relatively stable during reversible temper embrittlement (RTE) at 500°C, particularly in conditions L/LE. Auger electron spectroscopy indicated an enrichment of phosphorus at grain-boundaries in the RTE specimens, producing levels of 12atom% in condition ME and 24atom% in condition LE.

The basic influence of hydrogen on fatigue crack growth relative to vacuum is illustrated by data for condition L shown in Figure 1. First, the threshold alternating stress-intensity (ΔK_{th}) was reduced in hydrogen. Secondly, after a region of constant Paris exponent, a sudden rise in growth rates and Paris exponent occurred above a ΔK of approximately 10MNm$^{-3/2}$. These observations are consistent with those first demonstrated by Ritchie (2).

Reversible temper embrittlement produced no change in vacuum growth behaviour for either M/ME or L/LE

conditions (Figure 1). However, crack propagation in hydrogen was significantly affected: ΔK_{th} was further lowered, and growth rates were elevated at intermediate ΔK, but not at high ΔK levels (Figure 1). The effect of hydrogen on crack growth rates relative to the vacuum control behaviour is best illustrated by plotting the ratios of growth rate in hydrogen to that in vacuum as a function of ΔK. Figure 2(a) shows a distinct increase in rate ratios after RTE in condition LE up to a ΔK of approximately $20MNm^{-3/2}$. Condition ME exhibited similar but less pronounced effects.

One-step temper embrittlement produced a change in growth rates in both vacuum and hydrogen environments. Using the 'unembrittled' as-quenched condition, A, as a reference, the effects of OSTE on crack growth rate ratios (hydrogen/A-vacuum) are shown in Figure 2(b). Both OSTE conditions (300T and 500T) exhibited an increase in rate ratios at high ΔK ($>17MNm^{-3/2}$) which diminished as ΔK decreased through intermediate to threshold levels.

Cyclic work softening was found in all material conditions. RTE treatment produced no significant change in cyclic yield stress for either M/ME or L/LE specimens. However, the 500T OSTE condition showed a greater resistance to softening than either the 300T or A conditions.

Fractographic investigation showed that the failure mode for all conditions tested in vacuum was 100% transgranular. However, when tested in hydrogen, the unembrittled conditions A,M and L exhibited transgranular fracture at low ΔK, a peak in intergranular fracture at intermediate ΔK, and transgranular fracture at high ΔK (Figure 3). The transgranular fracture at high ΔK levels was less rough in hydrogen than in vacuum. The main influence of RTE was to increase the height of the intergranular peak at intermediate ΔK in conditions ME and LE (Figure 3(a)). OSTE had little effect on the height of the intergranular peak (Figure 3(b)), but did further reduce the roughness of the transgranular fracture mode at high levels of ΔK, as determined by sections and stereo microscopy.

Persistent slip bands (PSB's) were observed emerging onto the surfaces of cyclic yield specimens in all conditions. RTE had no detectable effect on their morphology. However, after OSTE, the short and diffuse PSB's in condition A became longer and much narrower in conditions 300T and 500T.

Observation of Charpy impact specimen fracture surfaces indicated that RTE promoted intergranular failure on the lower shelf, while OSTE promoted transgranular failure.

DISCUSSION

The basic effects of hydrogen on unembrittled materials, A,M and L were to reduce ΔK_{th}, promote intergranular fracture at intermediate ΔK, and facilitate transgranular fracture at high ΔK. The apparent reduction in ΔK_{th} is probably due to crack tip rewelding in vacuum, rather than a true enhancement in hydrogen (2).

It is important to note that the peak in intergranular fracture did not coincide with the greatest enhancement of growth rates, as has been suggested (2) (Figure 2). Fransden and Marcus (7) have argued that this peak occurs when the size of the forward plastic zone equals the grain size, due to a dislocation transport mechanism. However, this would require the ΔK at which the intergranular peak occurs to scale with cyclic yield stress, since the grain size for all conditions was constant. Figure 3 indicates very little difference in peak ΔK, despite a wide range of material strengths. An alternative theory is proposed, therefore, which is based on diffusional transport of hydrogen to the region of maximum hydrostatic stress ahead of the crack tip. A recent model of this process (6,8) predicts that the concentration of hydrogen available to embrittle the crack falls with increasing ΔK. If grain boundary embrittlement by hydrogen takes place by a decohesion mechanism, and follows a form similar to that observed for other embrittling species (e.g. phosphorus) (Kameda and McMahon (9)), the situation described by Figure 4(a) results. Only at intermediate ΔK is there sufficient hydrogen at the crack to satisfy the requirements for intergranular fracture.

The highest growth rate enhancement was associated with transgranular fracture at high ΔK. A reduction in surface roughness was observed and it is suggested that this is due to the promotion of dislocation emission from the crack tip by hydrogen (Tabata and Birnbaum (10)), which increases the efficiency of the fatigue fracture process.

The major effect of RTE was to promote higher levels of intergranular fracture together with increased growth

rates at intermediate ΔK, for tests performed in hydrogen only. Since no other significant parameter (e.g. microstructure, cyclic yield stress) except grain boundary phosphorus segregation was altered by RTE, it is clear that a synergism exists between intergranular impurity segregation and hydrogen embrittlement in fatigue of medium strength 2.25Cr 1Mo steel. In terms of the proposed theory of intergranular fracture, the segregated phosphorus would have lowered levels of hydrogen required for intergranular fracture, as described by Figure 4(b), producing a wider and higher intergranular fracture peak. A comparison of behaviour between conditions ME and LE shows that this effect scales with the degree of phosphorus embrittlement.

The major effect of OSTE was to increase the hydrogen/vacuum growth rate ratios at high ΔK, and further reduce the fracture surface roughness. In contrast to RTE, no segregation or change in the degree of intergranular fracture was observed, but carbide precipitation did occur due to an inherently unstable microstructure. It is suggested that the fine dispersion of Fe_3C carbides in 300T and 500T conditions promotes the intensification of slip at the crack tip into narrow bands, as observed on cyclic yield specimens (6). This process will work together with the influence of hydrogen to increase further the efficiency of the fatigue crack growth mechanism.

In summary it is apparent that temper embrittlement does interact with hydrogen embrittlement during fatigue of 2.25Cr 1Mo steel. RTE promotes intergranular fracture, while OSTE promotes transgranular fracture. Both types of temper embrittlement therefore reflect in their fatigue/hydrogen interactions their basic influences on impact fracture.

ACKNOWLEDGEMENT

Work described in this paper was undertaken as part of the Underlying Research Programme of the UKAEA.

REFERENCES

(1) Hirth J P, Met Trans, Vol 11A, 1980, p861.

(2) Ritchie R O, 'Analytical and Experimental Fracture Mechanics,' Rome 1980, p81.

(3) Nakanasa K, Takei H, Itoh H and Kobayashi M, Trans Jpn Inst Met, Vol 27, 1986, p260.

(4) Bandyopadhyay N, Kameda J and McMahon C J, Met Trans, Vol 14A, 1983, p7.

(5) Hippsley C A, AERE Report No. R-11472, 1984.

(6) Hippsley C A, AERE Report No. R-12322, 1986.

(7) Fransden J D and Marcus H L, Met Trans, Vol 18A, 1977, p265.

(8) Hippsley C A and Briant C L, Scripta Met, Vol 19, 1985, p1203.

(9) Kameda J and McMahon C J, Met Trans, Vol 14A, 1983, p777.

(10) Tabata T and Birnbaum H K, Scripta Met, Vol 18, 1984, p231.

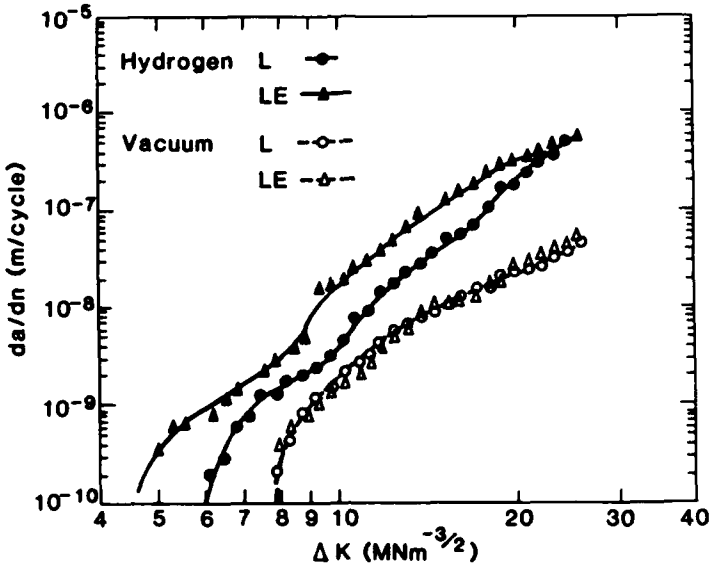

Figure 1. Influence of RTE on crack growth rates in vacuum and hydrogen (conditions L/LE)

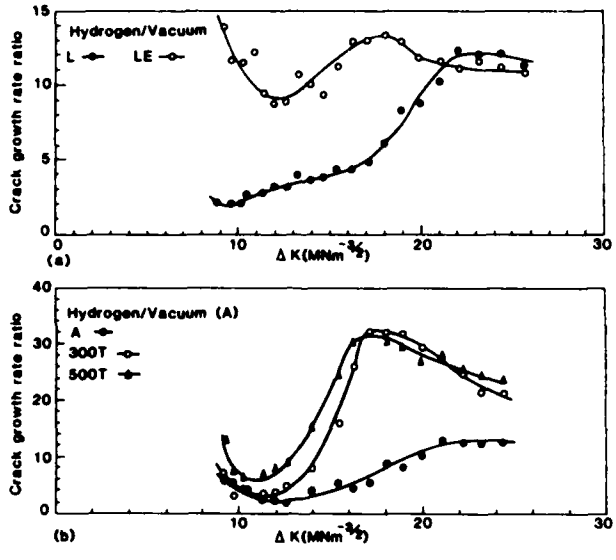

Figure 2. Influence of (a) RTE and (b) OSTE on hydrogen/vacuum growth rate ratios

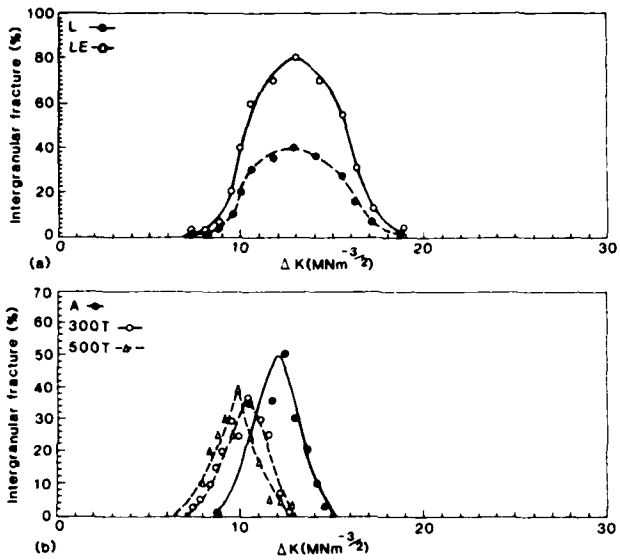

Figure 3. Influence of (a) RTE and (b) OSTE on intergranular fracture

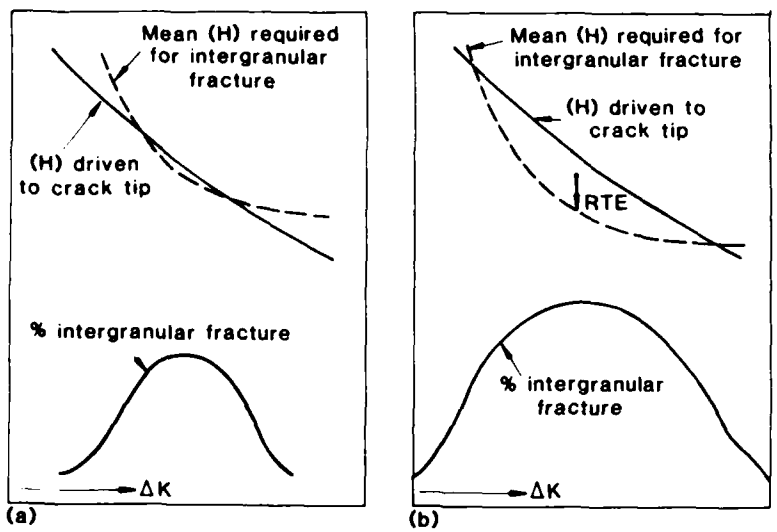

Figure 4. Schematic illustration of mechanism for intergranular fracture peak, (a) unembrittled and (b) after RTE

CRACK INITIATION STUDIES IN HYDROGEN EMBRITTLED SPRING STEEL STRIP

L. W. Lack,* R. Brook*, G. W. Greenwood* and I. C. Howard +

Fatigue tests in bending are described on high carbon spring steels over a frequency range from 2 to 0.02 Hz on material with and without an electro deposited zinc coating. It is shown that the hydrogen embrittlement introduced through the zinc plating had a particularly severe effect at the lowest frequency and its effect was further enhanced by increase in the content of residual elements. Fracture initiation appeared to be influenced by impurity particles, notably, MnS, and by defects at the strip surface produced by arcing in the electroplating barrel. Conversely elongated stringers in the strip interior tended to arrest and deflect the crack path.

INTRODUCTION

Hydrogen embrittlement has long been recognised (Tetelman (1)) and, amongst its many manifestations it has been a matter of serious concern for the spring industry for more than fifty years (Jackson (2)). High strength steels are frequently used in thin strip form, which may be bent into various shapes for numerous applications, some of which take the form of retaining clips whereas others work in mechanisms involving repeated spring loading.

High strength steel strip used in these applications is often electroplated with zinc to protect against corrosion in storage or during service, and this plating also improves the general appearance.

It has long been appreciated that such a plating process however can have the serious consequence of introducing hydrogen into the steel which is then subject to embrittlement. To over-

* Department of Metallurgy, University of Sheffield
+ Department of Mechanical Engineering, University of Sheffield

come this problem, baking treatments have been proposed for times up to 24 hours and temperatures up to 230°C, to remove substantial amounts of hydrogen and thus decrease the extent of embrittlement. The optimisation of such treatments and the variability of their effects in steels even of marginally different compositions, has lead to the need to investigate in further detail, the sources of crack initiation and failure in embrittled and unembrittled high strength steels.

In practice, most thin strip springs in dynamic operation work under conditions of repeated constant strain rather than under given stress cycles. In the present work therefore, a jig was devised whereby six strips could be loaded with each end clamped in freely moving pivots with coupling to a servohydraulic machine, such that a constant displacement of the jig subjected each of the strips to similar parabolic bending.

The experiments permitted gross comparisons to be obtained of the performance of both plated and unplated steels, and allowed the comparison of two different steels of identical strengths, but with one having a slightly higher concentration of residual elements than the other. Both steels were also studied after two heat treatments to determine the further effect that this may have on their behaviour.

The experiments also allowed the effect of cyclic frequency to be determined over a range of two orders of magnitude and extensive metallography was carried out to determine the form of cracking that occurred.

MATERIALS USED

The two electroplated steels that were compared had their designations S4 and S7 and their compositions together with that of an unplated reference steel S5, are given in Table 1. These compositions are within the general range of spring steels and as seen from Table 2, the two steels had identical hardness, and similar yield strength. The specimens for test were in the form of cold rolled strip of 0.8 mm thickness, 12 mm width and 120 mm length.

Prior to plating, some batches of the steels were in the quenched and tempered condition, having the structure of tempered martensite. Both steels had similar microstructures but manganese sulphide stringers aligned with the rolling direction were more numerous in steel S4. The other form of heat treatment was by austempering, which involved quenching from a temperature of 860°C, into a salt bath at 330°C and holding at that temperature for 20 minutes.

Etching revealed a prior austenite grain size after these heat treatments of between 30 and 40 μm with rather larger grains at the

TABLE 1 - Designation and Analysis of Spring Steels used in the Investigations

Elements present	Steel Designation S4	S5	S7
C	0.63	0.80	0.64
Si	0.27	0.20	0.25
Mn	0.71	0.70	0.66
S	0.03	0.003	0.012
P	0.02	0.011	0.012
Al	0.028	0.018	0.009

TABLE 2 - Hardness, Yield Stress and Modulus Values

Property	Steel Designation S4	S7
Hardness	501 HV	501 HV
Yield stress	1495 N/mm^2	1385 N/mm^2
Youngs Modulus	208 kN/mm^2	208 kN/mm^2

specimen edges.

The electroplating by zinc produced a relatively uniform layer of zinc of about 8μm thickness. The zinc grains were mainly columnar, with length perpendicular to the interface with the steel. The zinc plating was carried out in a cyanide bath within a rotating barrel, which also formed one of the electrodes. Occasionally it was possible for some sparking to occur between pieces of strip in the plating barrel and, as will be mentioned later, this appeared to be related to some of the forms of cracking.

These strips of steel, both in plated and unplated form and with the two types of heat treatment, were of almost identical dimensions: the final operation was to holes at either end to facilitate their mounting in the test rig.

FATIGUE TESTING

The criteria adopted in the design of fatigue test rig was that the

loading mechanisms should ensure a constant strain amplitude, that the frequency should be variable and that six specimens should be capable of simultaneous test with three specimens of each of the two types of steels arranged randomly amongst six test stations. This specially-made fatigue testing rig was used in the 250 kN servohydraulic testing machine under strain control so that the strain amplitude was independent of specimen response and did not vary when any of the specimens developed fatigue damage and cracking. Electrical resistance monitors were connected to each of the six specimen testing stations so that the number of cycles at which any specimen failed could be determined. This also meant that the test could be stopped whilst some of the specimens remained intact and a search for fatigue damage and cracking could be undertaken before complete failure of the specimens. This arrangement also ensured that exactly identical treatments were given to all six simultaneously tested specimens.

The deflection of the specimens was approximately parabolic in form and the stroke of the servohydraulic machine was arranged so that the specimen deflection varied from near zero strain up to a strain of about 1%. This value was maintained constant in each of the tests so that strain amplitude was eliminated as a variable in all of the experiments. With this arrangement, comparisons could be directly made of the effects of plating, of the differences between the austempered and the quenched and tempered steels and the effect of marginally different compositions in comparing steels with similar strengths. Moreover, this type of test provided similar conditions to those of operational performance to which many high strengths strip steel springs are subjected in practice.

FATIGUE TEST RESULTS

First, data was obtained on the fatigue life of steel S5 in the hardened and tempered condition but without electroplating. The test range of frequency was varied between 0.2 and 2.0 Hz. In Table 3 it is seen that there is a slight but noticeable increase in the number of cycles to failure at the high testing frequencies.

Contrasting results were obtained from studies of the effect of frequency on the fatigue lives of the hardened and tempered specimens of steels S4 and S7 when tested in the plated condition, presented in Table 4. For both these steels it was noted that there was a marked decrease in the number of cycles to failure with decrease in frequency. The interpretation of this effect must lie in the rate of movement of hydrogen in the region of the crack tip in relation to the appropriate strain rate in this region Thomson and Lin (1985) (3). The situation was most striking in the case of steel S4 which had the higher residual element content. This steel had about half the number of cycles to failure of that shown by S7 at the 2.0 Hz frequency but, at a frequency two orders

TABLE 3 - The Average Number of Cycles to Failure of Unplated Steel S5 with 12 Specimens tested at each Frequency

Cycles to Failure (x 10^{-})	Frequency (Hz)
110	0.2
100	0.5
111	0.8
118	1.0
115	1.3
147	1.5
128	1.7
124	2.0

TABLE 4 - Average Number of Cycles to Failure of Two Plated Steels at Three Frequencies

Steel	Cycles to Failure	Frequency (Hz)
S4	160	0.02
S7	1396	0.02
S4	615	0.20
S7	2929	0.20
S4	2557	2.00
S7	5242	2.00

of magnitude below this value, the mean life of steel S4 was reduced to a mere 160 cycles which was only about 11% of the value shown by steel S7. These results demonstrated the influence of hydrogen embrittlement on both steels, but in particular, the greater deleterious effect in the steel with higher impurity content.

In order to identify the effects of heat treatment and its subsequent influence on both unplated and plated steels, specimens of steel S5 were selected and, to obtain a significant number of results in a reasonable period of time, a frequency of 2 Hz was chosen. The results of these tests are shown in Table 5 which clearly indicates the deleterious effect of hydrogen in each case,

TABLE 5 - Effect of Heat Treatment and Plating on the Number of Cycles to Failure of Steel S5 at a Test Frequency of 2 Hz

Condition	Cycles to Failure ($\times 10^{-3}$)
Hardened and Tempered (Unplated)	145
Hardened and Tempered (Plated)	38
Austempered (Unplated)	212
Austempered (Plated)	110

resulting from the plating process, with the further indication of the benefits of the austempering form of treatment.

To summarize briefly the results of fatigue tests, it is clear that over the frequency range in the tests, the number of cycles to failure of the unplated steel was effectively independent of frequency. Compared with this behaviour, zinc plating substantially reduced the fatigue lives through hydrogen embrittlement. This form of embrittlement was particularly dependent upon frequency (5). At 2 Hz, there appeared to be only a small effect of residual elements on the number of cycles to fatigue failure. At a frequency of 0.02 Hz however, there was substantial reduction in the number of cycles to failure with the largest effect being in the steel with higher residual elements.

CRACK INITIATION AND GROWTH

Extensive microstructure examinations were carried out both on fracture surfaces and on polished sections. Optical microscopy and scanning electron microscopy were both used, the latter using a Philips PSEM 500 instrument.

Most observations suggested that cracks were initiated at the surface of the strips which were subjected to the highest tensile stress component, (5). A frequent site for the origin of fracture was near a corner of the strip so that the cracks propagated both through the thickness of the strip and along the tensile surface. The initial angle of many of the cracks was close to 45° to the tensile stress, indicating the occurrence of shear-type processes. These cracks did not originate in the zinc plated layer but at or near to the steel surface. After their beginning at this angle, the crack path was soon deflected to a position approximately normal to the tensile stress, and the fracture propagated in this way, largely in an intergranular manner in the specimens that were subject to hydrogen embrittlement. The fracture gradually progressed through the thickness and along the width of the strip, until

finally there was a further region of shear fracture to complete the separation of surfaces on the side of the strip where the tensile stress was a minimum.

A search was made for stress raisers and factors that could assist in crack initiation. The complex nature of the microstructure made such a search difficult, but certain features were noted.

One of the problems implicit in the barrel method of electroplating, is that arcing can take place as the strips come into contact and separate within the rotating barrel. Such arcing may cause pitting in the steel surface and possibly also cause a small region where the steel is overheated and the rapid cooling gives a martensite which is not subsequently tempered. An example of such a feature is shown in Figure 1 and the crack path is clearly related to the presence of this disturbed region near the surface.

In some instances inclusions were found to be associated with cracks, and these were particularly noted on fracture surfaces, Figure 2. The energy dispersive X-ray analysis attachment to the scanning electron microscope enabled a chemical identification of particles to be made and it appeared that MnS inclusions were often associated with a local separation of surfaces which interacted with the growing fatigue crack in a complex way.

It was often found that fatigue failure did not simply result from one initiation site, but from several of these. Moreover, the morphology of the cracks showed considerable irregularity and the elongated stringers of inclusions caused by the initial rolling process of the steel could apparently act as temporary arrestors to the progress of the crack growth. Such an example is shown in Figure 3.

The interaction of the precipitate stringers, lying with their major dimensions along the strip, in diverting the crack from its initial transverse path was no doubt responsible for a certain improvement in the material toughness. Indeed, Figure 3 shows that in many respects the failure mode of the material is somewhat similar to that of a composite material in which cracks can be deflected away from a most deleterious path.

It thus appeared that the morphology of precipitates and not simply their type was important in determining the number of cycles to fatigue failure. There was evidence that voids could be nucleated ahead of the advancing crack and this was one of the mechanisms whereby crack propagation could occur.

The role of hydrogen in such complicated structures probably lies in its trapping at inclusions Lee et al (1984) (4), thereby weakening their interface with the matrix. There must also be a capability for hydrogen to diffuse to the region of the tip

of the crack, otherwise it seems unlikely that the marked effect of frequency would arise.

CONCLUSIONS

The steels examined showed that there was a marked deterioration in their fatigue performance when they were electroplated by zinc, resulting from the introduction of hydrogen which caused embrittlement. The extent of embrittlement was dependent upon three factors. One was the frequency of testing from which it was shown that there was a steady decrease in the number of cycles to fatigue failure as the frequency was reduced from 2 Hz down to 0.02 Hz. Secondly, the embrittlement was sensitive to the heat treatment of the steels. The austempered treatment reduced the susceptibility of the steels to fatigue failure, when compared with the effects of hardening and tempering. This was true in both the unplated and in the plated steels. Thirdly, there appeared to be an effect of residual elements. This was most particularly marked in the plated specimens at the low end of the frequency range 0.02 Hz.

The general characteristics of the fatigue failure were approximately similar in all the tests with fracture surfaces having an increased intergranular area as the fatigue embrittlement increased. However, in addition to this intergranular fracture on the prior austenite grain boundaries, areas of dimpled rupture, of quasi-cleavage and of shear fracture were also noted.

The evidence for crack initiation suggests that this occurred at regions of high strain, sometimes associated with inclusions or with damage by arcing processes during the plating operation. Such features were often related to the early stages of the crack path. The results were complicated however by many observations of changes in crack direction. There were many instances of crack arrest by longitudinal stringers whereby the plane of the crack path was changed by about 90°. Thus in steels with these complicated microstructures, as well as their susceptibility to hydrogen embrittlement, it is clear that chemical composition, including residual elements, details of heat treatment and control of precipitate morphology are of considerable significance.

REFERENCES

(1) Tetelman, A.S., 'The Hydrogen Embrittlement of Ferrous Alloys' Fracture of Solids, Proc. of International Conf. 1962, pp. 671-708.

(2) Jackson, J.S., 'Hydrogen Embrittlement of Steel - A Review of Available Information,' Coiled Spring Journal, 12 and 13, 1948.

(3) Thomson, R. and Lin, Ing-Hour, 'Hydrogen Degradation in Ferrous Alloys,' edited by Oriani, R.A., Hirth, J.P. and Smislowski, M., Noyes Publications, New Jersey, U.S.A. 1985 p.507.

(4) Lee, K.Y., Lee, Jai-Y. and Kim, D.R., Materials Science and Engineering, 67, 1984, p.213.

(5) Lack, L.W. To be published.

ACKNOWLEDGEMENTS

The authors are grateful to the Science and Engineering Research Council, UK, for financial support.

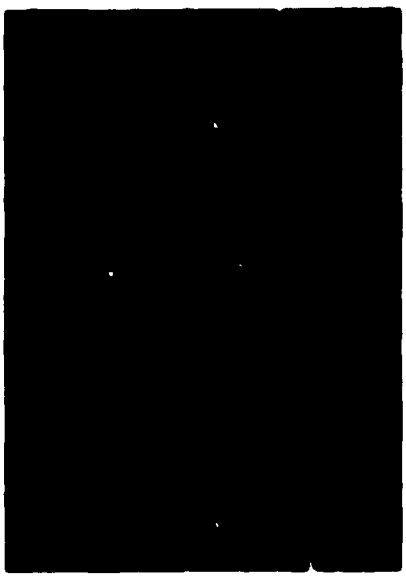

Figure 1 Crack associated with arcing damage (x 150)

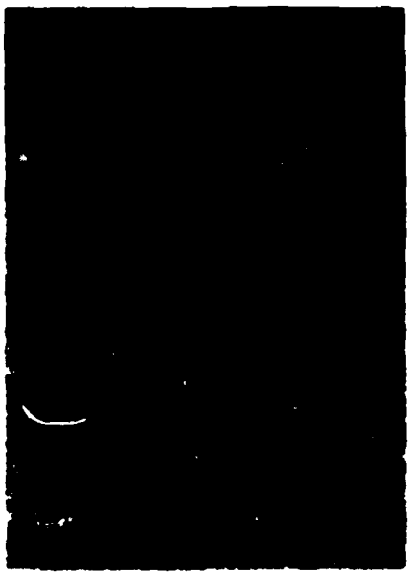

Figure 3 Crack deflection at MnS stringers (x 150)

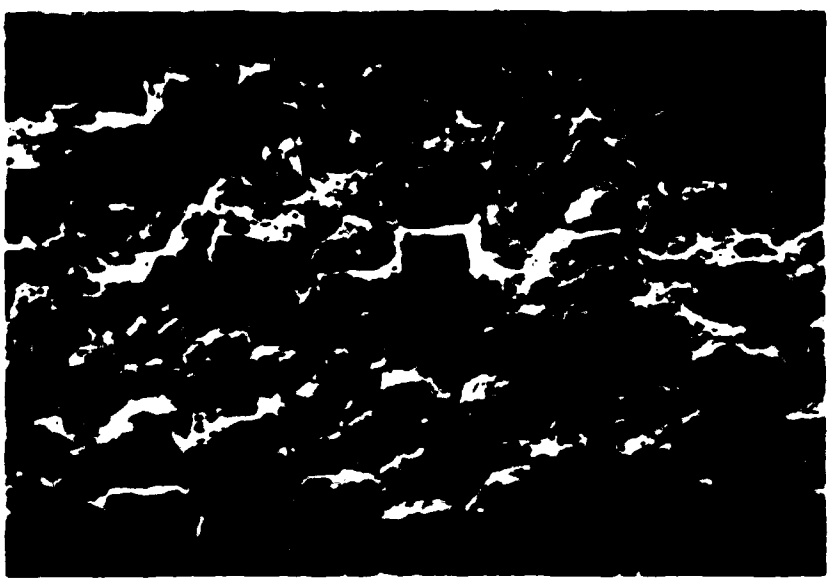

Figure 2 Scanning electron fractograph of micro-cracks associated with MnS particles (x 200)

FATIGUE OF NON METALIC AND ADVANCED MATERIALS

FATIGUE MECHANISMS IN ARALL, A FATIGUE RESISTANT HYBRID ALUMINIUM ARAMID COMPOSITE MATERIAL

R. Marissen*

ARALL (Aramid Reinforced Aluminium Laminates) is a hybrid composite containing thin high strength aluminium alloy sheets, which are laminated using a structural epoxy adhesive containing about 50 % aramid fibres. ARALL shows an excellent resistance against fatigue crack growth, due to intact fibres bridging fatigue cracks in the aluminium sheet material.

INTRODUCTION

The high resistance of ARALL against fatigue allows for weight savings up to 30 % as compared to monolithic aluminium alloys for fatigue critical structural components of aircraft. However, the technological properties of ARALL are similar to those of monolithic sheet material. All conventional workshop techniques as they are applied for the manufacturing of aircraft, including a cold bending process may also be performed on ARALL.

The general properties of ARALL as a material for primary aircraft structure are discussed in a considerable amount of papers by investigators at the Technical University of Delft, the ALCOA company, and the DFVLR (1) to (10), and it will not be repeated here. The fatigue mechanisms in ARALL are briefly discussed in the next section. Then one mechanism is considered separately and some experimental and analytical results will be discussed for this mechanism.

* DFVLR, Institute for Materials Research, Fatigue Department, D 5000 Köln 90, F.R.G.

FATIGUE MECHANISMS IN ARALL

ARALL consists of thin aluminium alloy sheets (thickness 0.3 - 0.5 mm) laminated with about 0.2 mm thick adhesive layers containing about 50 % of aramid fibres (see Figure 1). The fibre direction coincides with the direction of the main fatigue load.

If fatigue cracks occur in the aluminium sheets (e.g. at notches), the fibres remain intact and bridge the crack. The crack bridging reduces the crack opening displacement and the stress intensity factor at the crack tip. Consequently the crack growth rate is reduced. The crack bridging mechanism is shown schematically in Figure 2.

The efficiency of the crack bridging mechanism is influenced by a large amount of parameters. However, these influences become active mainly by their effect on two mechanisms only:

1. The crack bridging stresses are transferred from the fibres to the aluminium by adhesive shear stresses. The resulting adhesive shear deformation allows for some crack opening displacement, and consequently, for some crack growth.

2. The local cyclic adhesive shear stresses result in a limited fatigue debonding between fibres and aluminium in the cracked region. This debonding reduces the stiffness of the connection between the crack flanks, and the efficiency of the crack bridging mechanism is reduced.

Figure 3 shows schematically, how these two mechanisms act in a cracked ARALL sheet.

In a previous paper the author (7) showed, how the mechanical situation of Figure 3 may be characterized, and a prediction model based on linear elastic material behaviour was proposed. Further investigations showed that linear elastic behaviour is indeed representative for the main deformation component. However, plasticity and time dependent deformations of the adhesive have a significant effect on the crack opening displacement COD due to adhesive deformation. The COD behaviour as caused by adhesive deformation is discussed in more detail in the following sections.

DEFORMATION BEHAVIOUR OF THE INTERFACIAL ADHESIVE LAYER

Experimental

The crack opening displacement as a function of the crack bridging stresses was determined on special specimens. The specimens consisted of two aluminium sheets and one fibre-adhesive layer. A narrow slot was produced by spark erosion in both aluminium layers at the specimen centre (see Figure 4).

No load transfer through the aluminium sheets is possible at the location of the slot, and the entire load is carried by the fibres. Consequently, the crack bridging forces (for the slot) are exactly known. A clip gauge with a small measuring length was put over the slot, and the COD values were measured as a function of the load level. A correction on these measurements was derived for the strain of the fibres within the width of the slot and for the (small) strain of the aluminium sheets within the gauge length.

Analytical

Calculations of COD as a function of the external load and the laminate parameters are performed on the basis of a schematized laminate build-up, as shown in Figure 4. The fibre-adhesive layer is divided into three individual layers. The tensile stiffness is concentrated in the central layer and the shear compliance is present in two layers between the aluminium sheets and the central layer.

Hart-Smith (11) presented an analytical solution which may be used for the calculation of the crack opening displacement. For linear elastic material is:

$$COD = B_{al}\,\sigma_{al} \cdot \sqrt{\frac{2}{S_{al}\,S_{ad}} + \frac{2}{S_{ar}\,S_{ad}}} \qquad (1)$$

where σ_{al} is the stress in the aluminium layers. S_{al} and S_{ar} are the tensile stiffness of the aluminium and aramid fibres, respectively (Young's modulus E times thickness B). S_{ad} is the shear stiffness of the interfacial adhesive layer (shear modulus G_{ad} divided by thickness B_{ad}). The definition of the thickness of the different layers is also presented in Figure 4.

The adhesive shear stress as a function of the dis-

tance y from the crack flanks is an exponential function of -y and the stiffness parameters. If the maximum adhesive shear stress at the crack flanks exceeds the elastic limit of the adhesive, stress redistribution occurs. Homan (12) proposed an analytical technique assuming that the stresses exceeding the elastic limit near the crack flanks are carried by elastic stresses more remote from the crack flanks (see Figure 5). Ideal elastic-plastic adhesive behaviour is assumed. The result for the adhesive plastic zone size y_p is:

$$y_p = \frac{B_{al}\,\sigma_{al}}{2\,\tau_p} - \sqrt{\frac{S_{ar}\,S_{al}}{2\,S_{ad}\,(S_{al} + S_{ar})}} \qquad (2)$$

where τ_p is the yield shear stress of the adhesive. If the equation above yields $y_p \leq 0$ as a result, the adhesive yield stress is not exceeded. The result for COD is (if $y_p > 0$):

$$COD = \frac{\tau_p}{S_{ad}} + \frac{(B_{al}\,\sigma_{al})^2 \cdot (S_{al} + S_{ar})}{2\,\tau_p\,S_{ar}\,S_{ald}} \qquad (3)$$

Some values of the present parameters are given below:

B_{al} = 1 mm
B_{ar} = 0.2 mm
S_{al} = 72 000 N/mm
S_{ar} = 12 400 N/mm
S_{ad} = 16 000 N/mm^3
τ_p = 38 MPa

Results

Figure 6 shows experimental COD values as compared to calculated values. The calculation is performed for the first uploading only. The respective S_{ad}, S_{al} and S_{ar} values are given above. S_{al} and S_{ar} were determined by tensile tests on single layers. S_{ad} was based on an estimation of the thickness of the interfacial adhesive layer, B_{ad}, according to:

$$B_{ad} = (0.8\,v_m\,B_{ar})/2 \qquad (4)$$

The factor 0.8 is an empirical factor, which accounts for the circumstance that a part of the adhesive in the fibre-adhesive layer is located near to the symmetry axis, where no shear stresses are present. v_m is the

matrix volume content of the fibre-adhesive combination layer.

Figure 6 shows that the main displacement component is due to elastic deformation. However, the influence of plasticity during uploading is significant. Some reversed plasticity occurs, but the significance of plasticity for the cyclic deformations is further reduced. Some time dependent deformation can also be seen in Figure 6. The loading cycle causes a shifted COD hysteresis loop. However, this creep component stabilizes quickly, as it is shown in Figure 7, where COD is plotted against time. Creep is promoted during the test in this figure by the application of 30 seconds hold time. The stabilizing of the creep deformation is also due to stress redistributions. The redistributed stress field also acts as a driving force for the reversed creep, which occurs after unloading.

CONCLUSIONS

The fatigue behaviour of ARALL was summarized. Crack opening due to adhesive deformation is one important fatigue mechanism in this material. A detailed analysis of this mechanism shows that elastic adhesive deformation is of major importance. However, adhesive plasticity significantly contributes to the crack opening displacement. The influence of plasticity may be considered quite well, using analytical methods. A further experimental influence on the COD behaviour was found due to time dependent adhesive behaviour. The displacements due to adhesive creep stabilize after a short period of time, and they appear to be reversed some time after unloading.

ACKNOWLEDGMENT

The DFG (Deutsche Forschungsgemeinschaft) supported the ARALL research at the DFVLR financially and is gratefully acknowledged.

REFERENCES

(1) Marissen, R. and Vogelesang, L.B., "Development of a New Hybrid Material: Aramid Reinforced Aluminium Laminate (ARALL)", Int. SAMPE Meeting, Cannes, France, Jan. 1981.

(2) Gunnink, J.W., Vogelesang, L.B. and Schijve, J., "Application of a New Hybrid Material (ARALL) in Aircraft Structures", ICAS Conference, Seattle,USA, ICAS Paper No. 3.4, August 1982.

(3) Vogelesang, L.B. and Paalvast, C.G., "The Application of Briles Rivets for Mechanical Jointing of ARALL", Delft University of Technology, Dept. of Aerospace Engineering, Netherlands, Report LR-387, June 1983.

(4) Vogelesang, L.B. and Gunnink, J.W., "ARALL, a Material for the Next Generation of Aircraft. A State of the Art", Delft University of Technology, Dept. of Aerospace Engineering, Netherlands, Report LR-400, August 1983.

(5) Marissen, R., "Flight Simulation Behaviour of Aramid Reinforced Aluminium Laminates (ARALL)", Engineering Fracture Mechanics Vol. 19, No. 2, 1984, pp. 261-277.

(6) Marissen, R., Trautmann, K.H., Foth, J. and Nowack, H., "Microcrack Growth in Aramid Reinforced Aluminium Laminates (ARALL)", Proceedings Fatigue 84 Conference, Birmingham, UK, Vol. II, August 1984, pp. 1081-1091.

(7) Marissen, R., "Fatigue Crack Growth in Aramid Reinforced Aluminium Laminates (ARALL), Mechanisms and Predictions", DFVLR, Institut für Werkstoff-Forschung, DFVLR-FB-84-37, 1984.

(8) Verbruggen, M.L.C.E., "Investigation on Fatigue Crack Growth in Fibre Adhesive Bondlines", Delft University of Technology, Dept. of Aerospace Engineering, Netherlands, Report LR-478, Oct. 1985.

(9) Marissen, R., "Fatigue Crack Growth Predictions in Aramid Reinforced Aluminium Laminates (ARALL)", Proceedings 15th ICAS Conference, London, England, 7-12 Sept. 1986, pp. 801-807.

(10) Bucci, R.J., Mueller, L.N., Schultz, R.W. and Prohaska, J.L., "Results from a Cooperative Test Program on ARALL Aramid Aluminium Laminate", 18th SAMPE Conf., Materials for Space - The Gathering Momentum, Seattle, USA, 7-9 Oct. 1986.

(11) Hart-Smith, L.J., "Analysis and Design of Advanced Composite Bonded Joints. Report NASA CR-2218, 1974.

(12) Homan, J., "Crack Opening Behaviour in ARALL as a Consequence of Adhesive Deformation", Thesis, Delft University of Technology, Dept. of Aerospace Engineering, Dec. 1984.

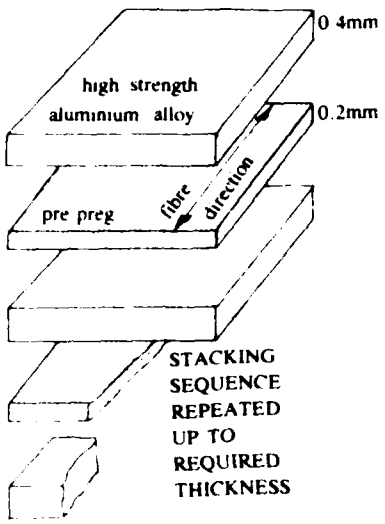

Figure 1 Laminating order of ARALL

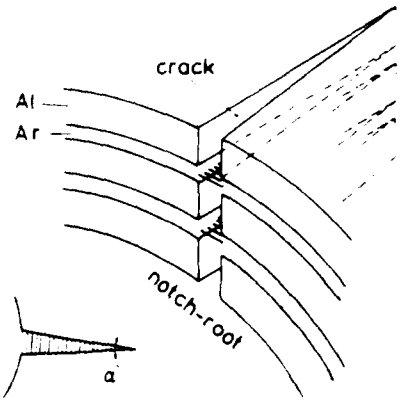

Figure 2 Crack bridging in ARALL (schematic)

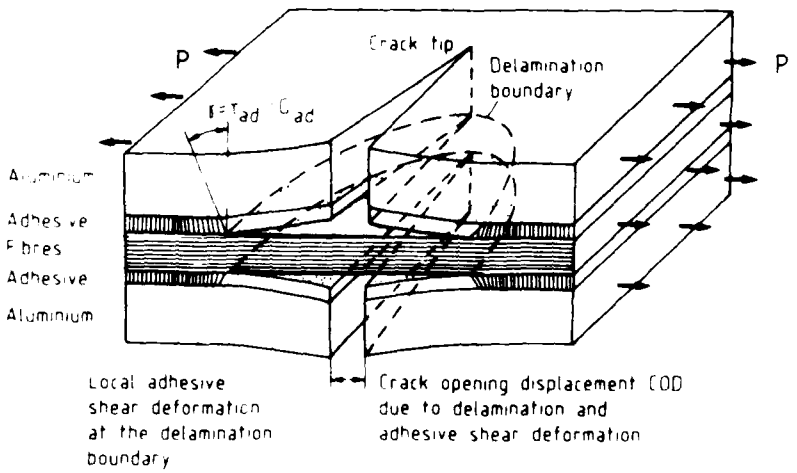

Figure 3 Schematic illustration of the influence of delamination and adhesive shear deformation in cracked ARALL

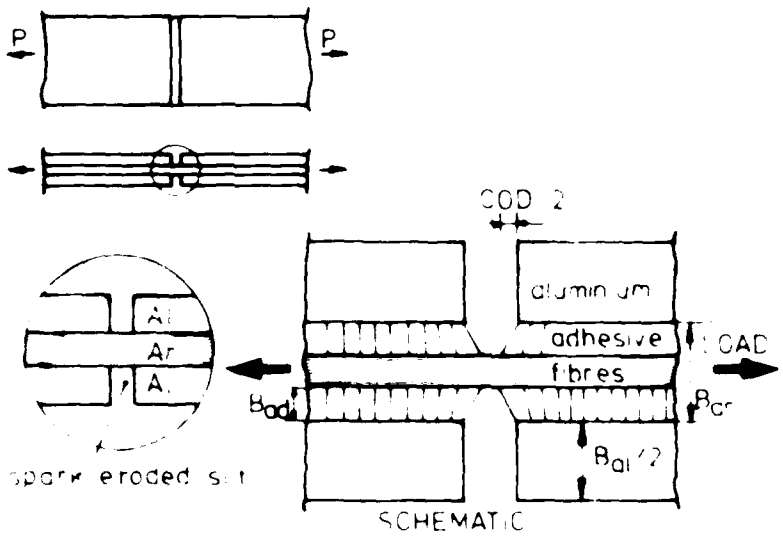

Figure 4 Specimen for the measurement of the crack opening displacement due to adhesive deformation

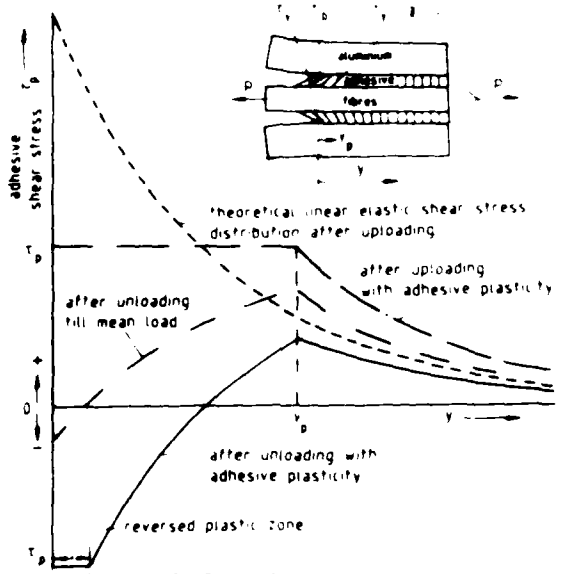

Figure 5 Model for the influence of adhesive plasticity on the COD

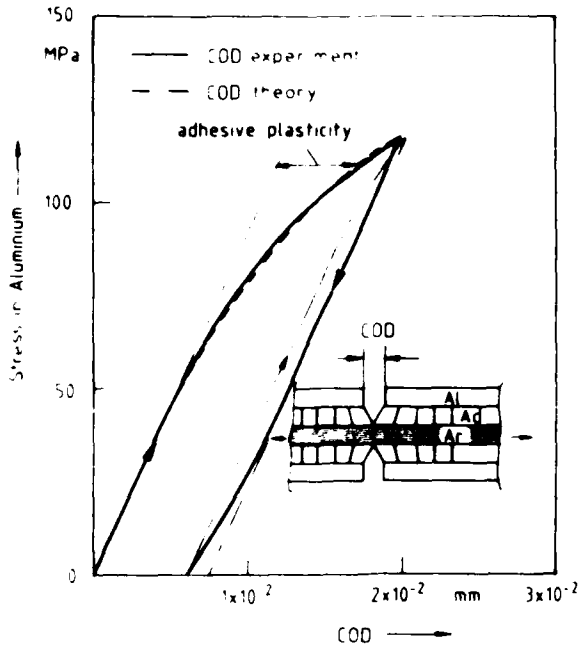

Figure 6 Comparison of experimental and calculated COD values as a function of the load level

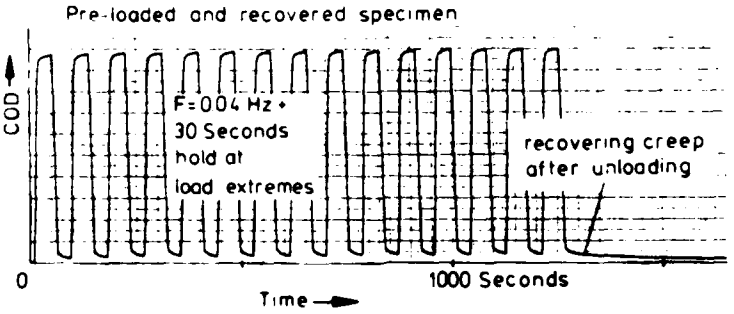

Figure 7 Time dependent behaviour of the COD due to adhesive shear deformation

LOW CYCLE FATIGUE BEHAVIOUR OF NOTCHED SPECIMENS OF NICKEL BASED SUPERALLOY SINGLE CRYSTAL

A. [illegible] SEMS*

ABSTRACT. The low cycle fatigue behaviour of notched specimens was studied for two nickel superalloy single crystals MAR-M 200 and CMSX 2 at 650°C in the life range 10^3 to 10^5 cycles. The initiation and growth of cracks were monitored throughout cycling using a replication technique at the notch root as well as the potential drop technique. Initiation was found to occur in the early cycles. Cracking in CMSX 2 involves the development of a single crack whereas several cracks grow and coalesce in MAR-M 200. Low cycle fatigue data on smooth specimens were shown to be unable to account for an engineering definition of life to crack initiation on notched specimens. The fatigue life of notched specimens was computed therefore using fatigue crack growth data. The calculated life was found to be in pretty good agreement with experimental data and a fatigue limit was actually predicted.

INTRODUCTION

The efficiency of gas turbines for jet engines relies in part on the temperature capability of turbine blade and vane materials. These components are submitted to severe thermal and mechanical loading in hot combustion gases. The design of advanced jet engines with improved performance has led to the development of single crystal components. The anisotropy of elastic constants may have a considerable influence on fatigue properties of such materials. This can be of paramount importance for the root of the blade where the blade is attached to the turbine disc. This part of the blade is primarily a notched member which is submitted to low cycle fatigue loading at medium temperatures say about 650°C. The behaviour of notched members in polycristals is usually accounted through empirical rules such as Neuber's rule and using data from smooth fatigue specimens. A study was thus undertaken to investigate the low cycle fatigue behaviour of notched specimens of nickel base superalloy single crystals.

Two superalloys were used : MAR-M 200 and CMSX 2. This work reports on the stress dependence of the life time for both materials using notched and unotched specimens.

* **Centre des Matériaux de l'école des Mines de Paris, UA CNRS 866, BP 87 91003 EVRY CEDEX, FRANCE.**

[illegible]

MATERIALS AND EXPERIMENTAL PROCEDURES

Two [illegible] nickel base superalloys were used in this study MAR M [illegible] (MAR M 200 + Hf) and CMSX 2. Their nominal composition is reported as follows :

Material	C	Cr	Co	W	Nb	Ti	Al	B	Zr
MAR-M200	0.14	8.44	9.68	11.93	0.82	1.80	4.84	0.014	0.038
CMSX2	28ppm	7.90	4.70	7.90	0.01	0.99	5.69	10ppm	50ppm

MAR M 200 is a first generation single crystal superalloy which bears 1.5 wt % of carbon. It has a dendritic structure. The dendrites are constituted by a nickel rich matrix which is strengthened by a high volume fraction of small γ' precipitates. γ-γ' eutectics and MC carbides precipitate on casting in the interdendritic areas. Specimens were machined from cast cylinders 20 mm in diameter. Three heat treatments were done : first, the bars were heat-treated at 1210°C during 2 hrs. During this treatment the γ' precipitates are taken into solution. They look like small disordered cubes a few tenth of microns in size. The second heat treatment is at 1100°C during 5 hrs. It simulates the treatment of aluminisation in vapour phase which protects the blades from environmental effects. The γ' precipitates are then well ordered in the matrix. The size of the small γ' precipitates is about 0,3 µm. The latest treatment, at 870°C during 16 hrs, is a tempering treatment which improves the alloy properties at low temperatures.

CMSX 2 is a new single crystal superalloy which has a low carbon content. This alloy is fully solutionized and bears out a still higher volume fraction of γ' precipitates. Three heat treatments were respectively done at 1315°C during 3 hrs, 1050°C during 16 hrs and 870°C during 16 hrs.

The mechanical properties of both materials are given in tab. 1 ([1], HARRIS et al [2]). Young's modulus is calculated using available anisotropic elastic constants of a similar nickel base superalloy (DALAL et al [3]) tab. 2.

The cylinders were cast as single crystals within 10 degres of [001] direction. Smooth specimens were cylindrical, 6 mm in diameter and 10 mm in gauge length. Notched specimens had a rectangular cross section with two symmetrical edge notches on opposite faces which give an elastic stress concentration factor K_t = 2.3 (as computed under an isotropic assumption). The notched specimen geometry is reported in fig.1. Each specimen was oriented by X ray Laue diffraction before machining the gauge length, so that notch orientation could be chosen at will. The orientation chosen was a [110] direction for the experiments reported here.

Low cycle fatigue tests were carried out under load control at [illegible] in laboratory air. Specimens were heated by a radiation furnace. The tests were conducted on a modified screw-driven tensile testing machine. The load was continuously recorded as well as stress-strain hysteresis loops occasionally. The smooth specimens were tested with a stress ratio of -1 and the notched specimens with one of 0. A saw tooth load wave was used at a frequency about [illegible] Hz for smooth specimens and in the range [illegible] 0.6 Hz for notched specimens. In both cases, crack growth was monitored continuously using a D.C. potential drop technique. Tests were interrupted at regular intervals and plastic replicas were taken from the notch root.

EXPERIMENTAL RESULTS

Tests were done on both materials in the life range 10^3 to 10^5 cycles on smooth and on notched specimens at 650°C in air. In fig. 2, the stress range is reported for notched specimens <001> [011] as a function of the number of cycles for a given variation in potential drop that corresponds to a surface crack length of 0.3 mm. The data of MAR-M 200 and CMSX 2 are on the same curve with a narrow scatter. This curve exhibits a fatigue limit of about 580 MPa.

Some observations at the root of the notch were made on a scanning electron microscope. Cracks were seen to be perpendicular with the loading axis in the whole life range investigated for both materials. Plastic replicas give the aspect of the root of the notch at a given number of cycles. So, the crack propagation can be analysed during the life when the initiation occurs at the specimen surface. In fig. 3 the crack length on the surface is reported as a function of the number of cycles for a total life of 11000 cycles and a nominal stress range of ±70 MPa for CMSX 2. On every replica, the crack length on the surface was measured for a given number of cycles. The measured length is the length of the crack projected on the notch axis (perpendicular to the loading axis). This curve in fig. 3 is typical of the crack evolution on CMSX 2. We can see that life is only a crack propagation phenomenon. A single crack appears within a few of cycles. In fig. 4, we can observe a surface crack

about 15 µm in width, after the first 100 cycles. During the first half life time the fatigue crack growth rate does not increase very quickly. The crack grows symmetrically : we can see in the fig.5 the crack after 2 000 cycles. During the second half of the total life, the fatigue crack growth rate rises up to about 10^{-6} m/cycle. From 10 500 cycles we can observe a cristallographic crack propagation. And after 10 950 cycles some slip bands can be observed.

For a lower nominal stress range of 620 MPa, an internal initiation probably on a porosity, had occured. The crack reaches the surface for 45 000 cycles with a crack length on surface of 180 µm, for a total life of about 56 000 cycles.

For MAR-M 200 several cracks appear within a few of cycles on the surface for the higher and the lower stresses. The coalescence of those several cracks leads to the final crack which propagates in the later tenths of the total life. We did not found out a cristallographic crack aspect such as for the CMSX 2 but some slip bands appear in the latest part of the life.

DISCUSSION

In polycrystals, the endurance of notched specimens is usually accounted through empirical rules such as Neuber's rule and using data from smooth specimens (NEUBER [4]). The stress concentration of notched specimens could be described by the stress concentration factor K_t. So the effective stress intensity range becomes equal to $K_t\Delta\sigma$. We assume that the calculation of K_t ($K_t = 2.3$) based on anisotropic elasticity assumption remains valid in a first approximation in anisotropic single crystals.

The number of cycles to crack initiation, as defined on an engineering basis to 120 µm crack depth is plotted in Fig. 6 versus the stress range at the notch root $K_t\ \Delta\sigma$ or Neuber's factor $K\sigma\Delta\sigma$ for the higher stresses. We used in the latter case Neuber's hyperbola and the cyclic stress-strain curve $\Delta\sigma - \Delta\varepsilon_t$ ($\Delta\sigma$ stress range, $\Delta\varepsilon_t$ total strain range) to compute Neuber's factor $K\sigma$. However the high cyclic elastic limit in these materials results in a $K\sigma$ value which is at most within a few percent of K_t. The life to macroscopic crack initiation, i.e. to 120 µm crack depth, in smooth specimens has been included in Fig. 6. It turns out that the fatigue life of smooth specimens of CMSX 2 is two to three times lower than that of notched specimens. The difference between smooth and notched specimens of MAR-M 200 can reach two orders of magnitude. This definitely shows in the latter material that Neuber's rule using crack initiation data on smooth specimens cannot account for the fatigue life of notched specimens.

The discrepancy between smooth and notched specimens was not unexpected : indeed observations on replicas have shown that fatigue life of notched specimens is almost completely spent in crack propagation. An approach based on crack growth should yield therefore better predictions than an initiation based method such as Neuber's one. Fatigue crack growth rate curves da/dN - ΔK were previously determined using <001> compact tension (CT) specimens of MAR-M 200 (DEFRESNE [5]). The fatigue life spent in crack propagation can thus be computed using such data and an appropriate estimate of the range of the stress intensity factor ΔK. As initial defects are present in these alloys in the form of casting pores (CHIERAGATTI [6], ABDELMAGSIH [7]), the "crack initiation" period can be computed as the number of cycles to propagate a crack from an initial size a_0 to final size a_f = 120 µm :

$$Np = \int_{a_0}^{a_f} \frac{da}{da/dN[\Delta K(a)]} \qquad (1)$$

The initial crack depth was taken as a_0 = 25 µm. The average size of subsurface porosities is about 20 µm. It was assumed that within a few cycles the largest subsurface porosity can give rise to a semi-elliptical part through crack with an equilibrium shape and a crack depth a about 25 µm.

The range of stress intensity factor ΔK was derived as follows. SCHIJVE [8] has shown that the presence of a notch gives rise to a rapid variation ΔK for an edge crack in the vicinity of the notch root say for a crack depth smaller than the notch radius ρ. He derived the following expression for an edge through crack :

$$\Delta K_e = K_t \, \Delta\sigma . \sqrt{\pi a} \, . \, C(a/\rho) \qquad (2)$$

where

$$C(a/\rho) = 1.1215 - 3.21(a/\rho) + 5.16(a/\rho)^{1.5} - 3.73(a/\rho)^2 + 1.14(a/\rho)^{2.5}$$

where a is the physical crack depth at the notch root, ρ the root radius and $\Delta\sigma$ the nominal tensile stress range in the minimum section.

A correction factor was used to account for the fact that cracks in the present case are semi-elliptical through cracks. A study of a large number of small surface cracks in these alloys has shown that the crack depth a of equilibrium surface cracks was 0.76 times half the crack length at the surface. Therefore the ratio of ΔK for a semi-elliptical surface crack to ΔK_e for an edge through

crack ΔKe was taken from Irwin's formula [9] as :

$$\Delta K = \Delta\sigma \sqrt{\pi \frac{a}{Q}} \left[\sin^2\Phi + \left(\frac{a}{c}\right)^2 \cos^2\Phi\right]^{1/4} / E(k) \qquad (3)$$

where a is the crack depth, c half the crack length on the surface, Φ the angle with the surface and E(k) the elliptic integral of the second kind which can be approximated as (ABOTT and THORFF [10]) :

$$E(k) = \frac{\pi}{2}\left[1 + \frac{1}{4}k^2 + \frac{3}{64}k^4 + \frac{5}{256}k^6 + \frac{175}{16384}k^8 + \frac{441}{65536}k^{10}\right] \qquad (4)$$

An average stress intensity factor M was derived by integration of Eq. 3 along the crack front in the width direction. This computation yields :

$$M = \Delta K / \Delta\sigma \sqrt{\pi a / Q} \qquad (5)$$

The fatigue crack growth curve in da/dN - ΔK of MAR-M 200 at 950°C in air exhibits a threshold about 5 MPa.m$^{1/2}$. Therefore this curve was described by Paris equation :

$$da/dN = C\,\Delta K^n \qquad (6)$$

for fatigue crack growth rates higher than 6.10^{-9} m/cycle and by :

$$da/dN = B(\Delta K - \Delta K_{th})^p \qquad (7)$$

where B, p are two constants and where ΔK_{th} is the threshold value at lower crack growth rates.

The life to crack initiation was computed from Eq. 1 using Eqs. 2 and 5 for ΔK as well as Eqs. 6 and 7 to describe the material behaviour. The predicted curve is compared with experimental results in Fig. 2. In the limited life range a good agreement is observed with experimental data on MAR-M 200 within a factor of two. A fatigue limit for a net stress range about 580 MPa is predicted due to the threshold for crack propagation. This is in fairly good agreement with the trend of experimental results. Therefore in this material the engineering life to crack initiation in notched specimens can be only accounted by crack propagation. This conclusion reached in this high strength single crystal superalloy is in good agreement with other results obtained on fine grained materials (BREAT et al. [11]). Such a crack propagation rationale could explain why the notch fatigue life of the two studied alloys is less sensitive to composition than fatigue life of smooth specimens' since crack propagation is expected to be less structure sensitive. Experiments are currently under way to check this point.

CONCLUSIONS

The present investigation of the low cycle fatigue behaviour of <001> oriented single crystal notched specimens of CMSX 2 and MAR-M 200 at 650°C has shown the following points :

Crack initiation was found to occur early in fatigue life for both materials using plastic replicas of the notch root. Fatigue failure in CMSX 2 occurs by the growth of a single crack which initiates at a surface or subsurface porosity. In MAR-M 200 several cracks initiate and coalesce.

An engineering definition of crack initiation i.e. to 120 µm crack depth results in a fatigue life which cannot be accounted for using crack initiation data on smooth specimens. This life to crack initiation however can be computed as being solely spent in crack propagation using data from CT specimens. The life thus calculated is in good agreement with experimental data and a fatigue limit is predicted as actually observed.

ACKNOWLEDGEMENTS

The authors are indebted to Turbomeca and SNECMA for provision of research facilities, and the DRET for financial support.

SYMBOLS USED

a	: crack depth (m)
c	: half of the crack length on surface (m)
ρ	: root radius (m)
Δσ	: nominal tensile stress range (MPa)
ΔK	: range of stress intensity factor (MPa.m$^{1/2}$)
ΔK$_{th}$	: threshold stress intensity range (MPa.m$^{1/2}$)

REFERENCES

[1] J.Y. GUEDOU, 1984, Private Communication

[2] K. HARRIS, G.L. ERICKSON, R.E. SCHWER : "Development of the CMSX" series of single crystal alloys for advanced technology turbine components", TMS-AIME High temperature Alloys Committee Session on Recent Advances in Superalloy Technology, 1982 TMS AIME Fall Meeting St LOUIS, MISSOURI

[3] R.P. DALAL, C.R. THOMAS, L.E. DARDI : "The effect of crystallographic orientation on the physical and mechanical properties of an investment cast single crystal nickel-base superalloy", Superalloys 1984, pp.185-197.

[4] H. NEUBER, KFONSTRUKTION, 1968, N°8, p.245.

[5] A. DEFRESNE, 1985, Unpublished results, Centre des Matériaux

[6] R. CHIERAGATTI : "Influence of the crystalline orientation of the low cycle fatigue behaviour of single crystal MAR-M 200",in French, Doctor's Thesis, Ecole des Mines de Paris, 1987.

[7] A. ABDELMASSIH, L. REMY, 1982, Unpublished Results, Centre des Materiaux

[8] J. SCHIJVE : "The stress intensity factor of small cracks at notches", Fat. of Eng. Mat. and struct., 1982 vol.5, n°1, pp.77-90.

[9] G.R. IRWIN : "Crack extension force for a part through crack in a plate , J. Appl. Mech. Trans. ASME, 1984, 651-654.

[10] P.M. SCOTT and T.W. THORPE : "A critical review of crack tip stress intensity factors for semi-elliptic cracks , Fat. of Eng. Mat. and struct. 1981, vol.4, n°4, pp.291-309.

[11] J.L. BREAT, F. MUDRY and A. PINEAU : "Initiation and propagation of fatigue cracks in stress concentration areas", in French, Journees de Printemps 1984, pp.143-158.

Material	Temperature °C	0.2% Y.S. MPa	U.T.S. MPa
MAR-M200	R.T.	936	1120
(1)	650	928	1073
CMSX2	R.T.	1136	1187
(2)	760	1246	1296

TABLE.1 Mechanical properties of MAR-M200 and CMSX2.

Temperature °C	<001> MPa	<011> MPa	<111> MPa
R.T.	132000	221000	285000
650	115000	194000	252000

TABLE.2 Young's modulus of MAR-M200 and CMSX2.

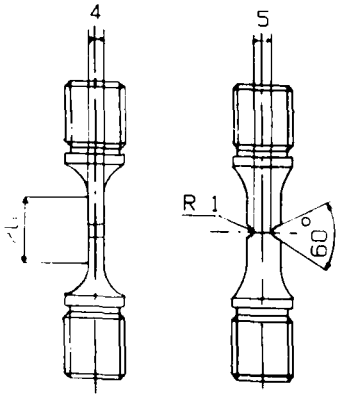

Fig.1 Notched specimen geometry.

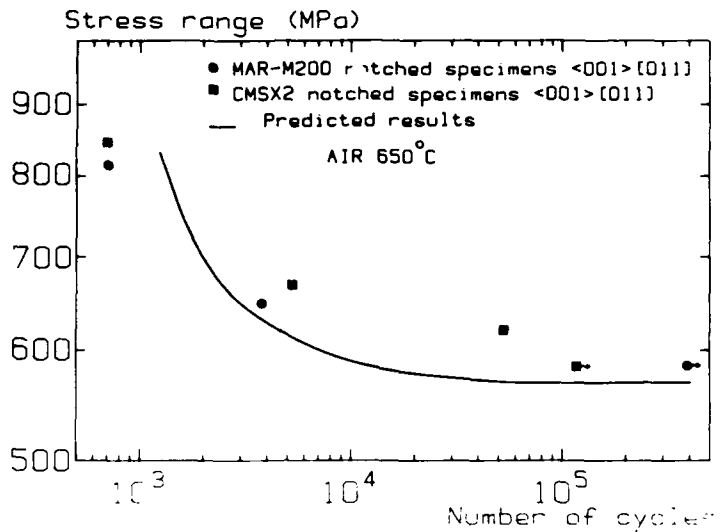

Fig.2 Stress range versus the number of cycles associated to a crack length of 0.3 mm for notched specimens.

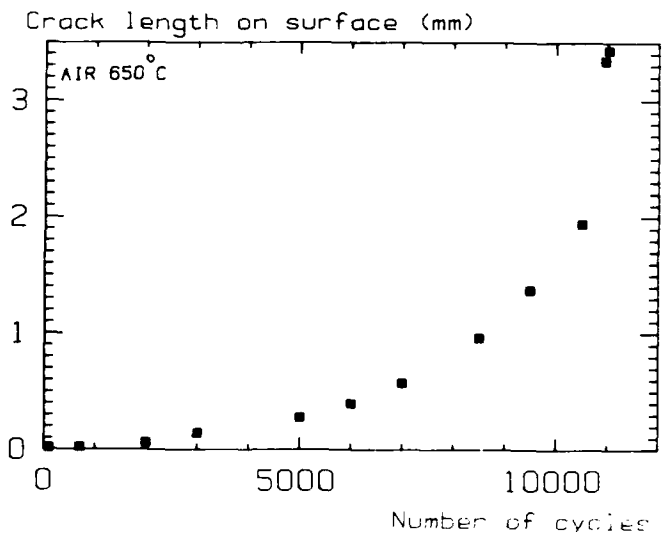

Fig.3 Crack length on surface versus the number of cycles for CMSX2 on a notched specimen ($\Delta\sigma$ = 670 MPa).

Fig.4 Plastic replica of CMSX2
N = 100 cycles, $\Delta\sigma$ = 670 MPa

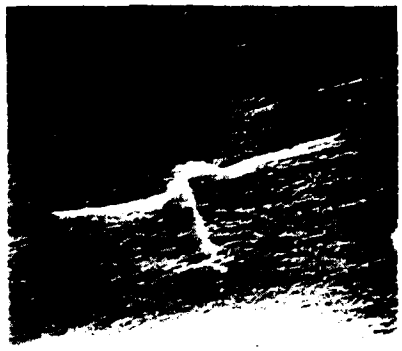

Fig.5 Plastic replica of CMSX2
N = 2000 cycles, $\Delta\sigma$= 670 MPa

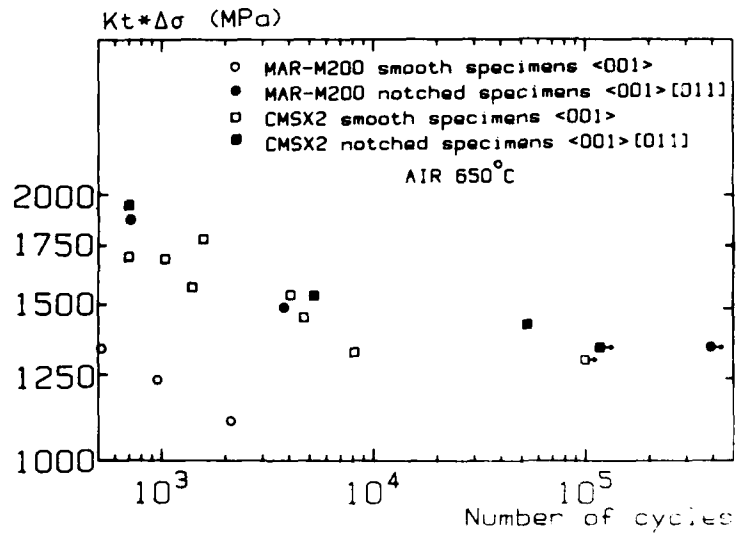

Fig.6 Effective stress intensity $K_t \Delta\sigma$ versus the number of cycles for notched and unotched specimens for CMSX2 and MAR-M200.

FATIGUE CHARACTERISTICS OF ION TREATED SURFACES

R. Krishnamurthy* and H.V. Somasundar**

Surface technologists aim to develop suitable surface coatings to enhance the fatigue life of engineering materials. Most of the coatings would influence the substrate material with undesirable effects such as thermal softening, interface transitions, and other substrate defects. Of late, Ion treatments have found increasing applications. These include Ion-nitriding and Ion implantation. Where Ion nitriding is plating of surfaces with N^+ ion bombardment, resulting in formation of compound surfacial layers, Ion implantation is a cool surface treatment resulting in little change in surface characteristics. The paper discusses the fatigue characteristics of Ion implanted and Ion nitrided HSLA steel.

INTRODUCTION

Majority of engineering designs lay emphasis on 'tribological' features of engineering surfaces. The general trend in design of sliding and rolling elements such as gears, cams, tappets and bearing elements has been to reduce the damage caused by working conditions enhancing their life. For this, various surface treatments have been resorted to [1]. Surface treatments could be broadly classified as

(i) Treatments adding material to surfaces,
ex: Thermal spraying, cladding and vapour deposition.
(ii) Treatments altering surface chemistry,
ex: Interstitial hardening such as carburising, nitriding, tuffriding and sur-soft.
(iii) Mechanical treatments,
ex: Peening, rolling and thermo-mechanical treatment.

Though all these treatments have been used for enhacing the wear resistance, selection of an unique process for a 'special' application is as difficult as material selection. The most recent technique used in enhacing surface quality for 'tribological'

* Asst. Professor, Mech. Engg. Dept., I.I.T., Madras-600 036, INDIA
**Dept. of Prodn. & Ind. Engg., NIE, Mysore, India.

applications is ion treatment. Surfaces are treated with suitable ion-species or plated with ion beams. Ion-implantation of chosen species into a variety of technologically important metals and carbides has brought about striking changes in their behaviour [2]. Chosen atomic species are first ionised and their accelerated to energies of around 90 - 150 Kev. The ions penetrate the surface layer of the workpiece, forming an ion-concentrated layer.

The penetrated depth of ions depends on the atomic number, mass of the ions and of the target atoms and the rate of energy transfer. The implantation of ions into target materials can produce both amorphous and metastable alloys [3]. The implanted ions are mobile during implantation and precipitation may occur. This precipitation produces a high density of point defects, developing compressive stresses [4]. All these processes tend to enhance the physical properties of engineering materials. The published wear data on implanted materials have illustrated both merits and demerits of implantation process. A review through could reveal certain contradictions on the influence of implantation on wear of engineering materials. The present paper presents data on contact fatigue of implanted high strength low alloy (HSLA) steels.

EXPERIMENT

Rolling contact fatigue trials were carried out in a block on disc machine provided with splash lubrication. The test samples were made with N^+ and B^+ ions. The material specification, the implantation details and the experiment details are given in Table 1. The samples were removed from the machine at regular intervals of time, thoroughly cleaned, dried and were weighed in a single pan electronic balance to calculate the wear. The observations include surface texture recording during testing and element study with Auger Emission Spectrometer and X-ray photon spectroscopy.

RESULTS AND DISCUSSION

The HSLA test samples were heat treated to maintain an average grain size of 8 microns. During ion implantation, ion fluence of the order 1×10^{15} ions.cm^2 was used. With higher dosages, the implantation process took considerably longer times. So the experiments were restricted to only 1×10^{15} ions/cm^2. There was considerable improvements in the micro hardness values due to implantation (Table 1).

Ion implantation on surface Texture.

During ion implantation, the injection of defects and of ions imparts to the surface a tendency to swell. This is restrained by the substrate resulting in generation of intense compressive stresses. This is analogous to the shot peening process. Thus the tribological characteristics of the implanted surface depends on

the surface texture its hardness and the ion species. The influence of ion implantation on surface texture remains a controversy. It has been reported that(5) the surface roughness of the implanted surface decreased due to implantation, while it has been contradicted (6).

Fig.1 illustrates typical texture study on implanted surfaces. It is seen that ion-implantation produces surface roughening to some extent. As seen in the figure, the increase in R_t value, indicates that during implantation, while the asperities might be folded due to ion-impingement, there could be considerable deepening of the valleys. The higher energy ions bombarded the surface during implantation, heating the target material (Reported temperature around 330-370 K). This could reduce in the yield strength of the surface materials, causing asperity folding; however the valleys were deepened due to ion sputtering. The bearing area (Abott) curves obtained shows that after implantation, there is some improvement in the bearing area of surface layer TP(1) - 5% after implantation against 1% before implantation, TP(2) - 29% as against 10% before implantation. The increase in bearing area due to asperity folding could enhance the fatigue life of implanted surfaces to some extent. Hartley (6) has reported the presence of three distinct regions of surface appearance. The surface was reported to show blistering at dosage approaching 1×10^{17} ions/cm^2 and eventually bursted out resulting in craterisation. At medium dosages, there was a mild modification of the surface texture.

Implantation on Contact Fatigue.

Wear performance. Most of the material properties such as friction, wear, hardening, fatigue, corrosion resistance, adhesion and lubrication characteristics are influenced mostly by the surface composition. Ion-implantation influences considerably the surface qualities and thereby the above mentioned characteristics. It is well known that contact between two surfaces occurs at a large number of very small regions called surface interactive junctions. Surface coating technologists frequently aim to improve friction properties by hardening the surface so that very little local plastic yielding occurs, resulting in reduced work input to maintain relative motion between surfaces. Traditional methods to achieve this is to incorporate elements into the original surface which will reduce diffusional movement. These methods are thermally based techniques such as carburising, carbonitriding, nitriding. Ion-implantation falls into the category of surface engineering however they are different from the traditional diffusion coating in that a high degree of atomic [illegible] with the tendency to minimise [illegible] wear. [illegible] enhance the fatigue [illegible] engineering materials.

TABLE 1 - Material specification, implantation and experiment details

Test Material : HSLA Steel

C	Mn	Si	S	P	Nb
0.18	1.55	0.24	.033	.034	.04

Grain size: 8 microns (average)

Implantation Details

Species	Fluence ions/cm^2	Energy Kev	Microhardness (after implantation) Kp/mm^2
N^+	1×10^{15}	90 - 120	290 - 300
B^+	1×10^{15}	120 - 180	340 - 360

Test Details : Falex Block-Disc Test machine

Test Specimen : i) Untreated HSLA steel
ii) N^+ implanted HSLA steel
iii) B^+ implanted HSLA steel
iv) Ion nitrided HSLA steel

Surface Finish : Ground, R_a = 0.05 - 0.07 microns

Disc : 0.2% C steel - Carburised

Hardness : 60 - 64 Rc

Surface Finish : R_a 0.3 microns

Test Load : 10 N/mm width of contact

Lubrication : Tellus 27 oil (Splash lubricated)

Contact fatigue (sliding wear) tests were conducted on HSLA steel specimen both un treated and ion-implanted in a test setup similar to the modified Falex testing machine. The test setup consisted of a carburised and ground steel disc, establishing sliding contact with the flat test sample held in a nest work holder. The wear qualities of the test samples were assessed by weight loss measurement using a single pan electronic balance and recording wear tack profiles. Fig.2 shows typical influence of implantation on wear performance of HSLA steel. This is a considerable improvement in wear resistance due to ion implantation.

Fig.3 shows the influence of B^+ and N^+ implantation wear performance. It is seen that N^+ implantation considerably increases the wear resistance compared to the B^+ ion-implantation. It is significant to note that in spite of the higher microhardness,

B^+ implanted surfaces wore out more than N^+ implanted. It is known that the atomic number of Nitrogen is greater than that of carbon and boron; however the atomic volume of B^+ is very much larger than that of N^+ ion (volume ratio around 13.6:4.5). The impingement of B^+ ions (lighter and larger volume) has resulted in appreciable surface hardening than that of N^+ ions impingement; however the mobility of B^+ ions could not be higher than that of N^+ ions. This could be expected owing to the smaller size of the N^+ ions and increased solubility of N^+ ions than B^+ ions in steel,

Ion migration. Published literature on N^+ and B^+ ion implanted stainless steels (7) illustrated the marked difference in the performance and attributed it to the difference in roles between atomic species which could migrate relatively easily during surface contact (N^+) and those which cannot (B^+) Picraux (8) has reported that Amco iron implanted with N^+ ions exhibited marginal increase in wear resistance, in spite of appreciable surface hardening. This could be attributed to the increased solubility of N^+ in iron than in Amco iron. Thus it could be seen that the higher wear resistance of N^+ implanted specimen could be mostly due to migration and allied processes, rather than surface hardening. For understanding the migration process, Auger Electron Spectrum were obtained for both implanted and tested samples. Fig.4 shows typical AES records illustrating N^+ migration during wear process. The records were taken after sputtering, the etching was repeated several times at the same region to study the N^+ presence in the depth direction. Presence of N^+ ion, both on the unused and worn out portion of the test samples at depths greater than the depth of implantation, indicated the migration of N^+ ion during the wear process.

The literature on ion-implantation has reported on the formation of compounds (9) such as nitrides and migration of implanted ions enhancing wear resistance. Hartley found that during implantation, the stress rise could be partly due to the injection of an excess quantity of ions and partly due to the disturbed lattice caused by the material mobility during implantation. It is reported by Robert Bolster (10) that this disordered zone could be as much as 10-15 times deeper into the material, than the implanted range. Implanted ions or combinations of them are known to be mobile interstitial species in steel and are known to form harder compounds possibly as a fine dispersion of precipitates. In the present study, this mechanism could be much more effective in HSLA steel owing to its fine grained structure. The presence of N^+ peaks around 383 Kev energy levels indicate the N^+ presence and no compound formation could be traces.

Wear track profiles. The wear trials were conducted (Partially conforming flat specimen contacting a cylindrical disc. During the tests, certain amount of conformity would be established by the formation of wear track with certain curvature. Typical wear

track profiles recorded are presented in Fig.5. After conforming the contact between mating surfaces could become dry Hertzian, resulting in local welds and plowing. This is very much seen with unimplated surfaces. Compared to the unimplanted and B^+ implanted surfaces, the N^+ implanted surfaces exhibited smooth wear tack, with minimum plowing. This might be due to the reduced adhesion caused by N^+ implantation, minimising the friction and reducing the possibilities for local welding and subsequent plowing.

Wear characteristics of Ion Nitrided HSLA steel. Ion nitrided HSLA steel specimen were tested under conditions identical to the Ion-implanted specimen. Typical wear characteristics of ion nitrided samples is illustrated in Fig.6. It is seen that both the samples of having 550 Hv and 700 Hv exhibited a steady wear upto about 300 Kev of sliding distance; afterwards 550 Hv samples exhibited increased wear rate. During ion nitriding a thin brittle layer of γ - Fe_3N or ϵ - Fe_4N would form depending upon the temperatures and duration of ion-nitriding (Fig.7). With the larger duration, thicker layer of Fe_4N could have been formed, resulting in spalling during the test. This has resulted in larger initial wear, subsequently the harder layer perform better. Fig.8 shows the propagation of wear scar depth. It is seen that Ion nitriding performed better than ion implanted samples. Hence it is worth mentioning that probably with higher ion fluence, it may be possible to achieve comparable performance for ion-implanted specimen as well.

CONCLUSIONS

From the present study, the following major conlusions could be drawn.

1. The contact fatigue performance of HSLA steels could be considerably enhanced by Ion implantation.
2. Better performance of N^+ implanted steels than the B^+ implanted) illustrated that more than the surface hardening, other mechanism such as migration could significantly contribute to the enhancement in contact fatigue behaviour.
3. Ion implantation modified the surface texture; the bearing area improved with asperity folding, while the valley porosity due to ion sputtering.
4. with implanted surface, the wear track was smoother, while the nonimplanted surface presented rough wear track with severe ploughed craters.
5. with the fine grained material, such as the HSLA steel used, it was possible to enhance the contact fatigue characteristics with lower dosages, which were not recommended in the available literature.

REFERENCES

(1) Dearnaley, G. and Hartley, N.E.W., Thin Solid Films, 54, 1978, pp.215-232.

(2) Hartley, N.E.W., J. Vac. Science Technology, 12, 1, 1975, pp.485-489.

(3) Hartley, N.E.W., Tribology, 8 (2), 1975, 65.

(4) Hartley, N.E.W., Thin Solid Films, 64, 1979, pp.177-190.

(5) James, D.H., Smart, R.F. and Reynolds, J.A., Wear, 34, 3, 1975, pp.373-382.

(6) Longworth, G. and Hartley, N.E.W., Thin Solid Films, 48, 48, 1977, pp.95-104.

(7) Picraux, S.T., Myers, S.M. and Foolstaeat, D.M., Thin Solid Films, 63, 1979, pp.1-2.

(8) Picraux, S.T., Annual reviews of materials science, 14, 1984, pp.1-14.

(9) Poate, J.M., Thin Solid Films, 58, 1979, pp.133 143.

(10) Robert N. Bolster and Irwin L. Singer, ASLE Trans. 24, 4, 1981, pp.526-532.

(11) Shepard, S.R. and Suh, N.P., Trans. ASME JL. Lub. Tech., 104, 1982, pp.29-37.

(12) White, S. and Dearnaley, G., Wear, 64, 1980, pp.327-332.

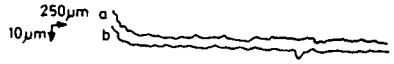

Profile	R_a	R_{max}	R_t	R_z
	Across grinding marks			
a	0.56	5.69	5.69	3.89
b	0.69	9.42	8.42	4.87
	Indentation			
c	9.9	91.1	91.1	24.1
d	9.4	96.7	96.7	25.9
a, c - before ion implantation b, d - after implantation				

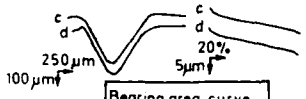

Bearing area curve		
	d	c
TP (7)	100%	100%
TP (6)	96	98
TP (5)	80	95
TP (4)	58	81
TP (3)	30	58
TP (2)	10	29
TP (1)	1	5

Figure 1 Bearing area improvement & valley deepening on implantation

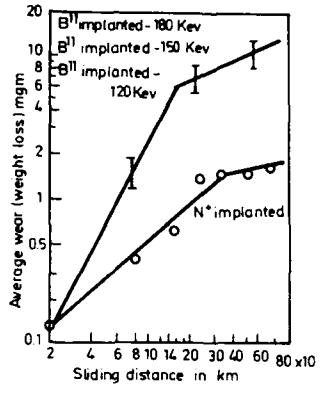

Figure 3 Superiority of N^+ implantation on wear resistance

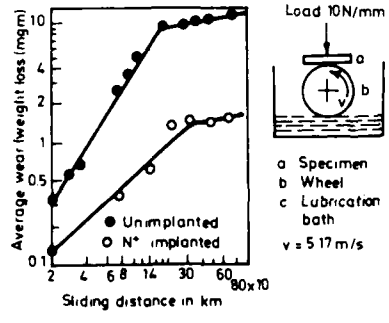

Figure 2 Implantation enhances contact fatigue resistance

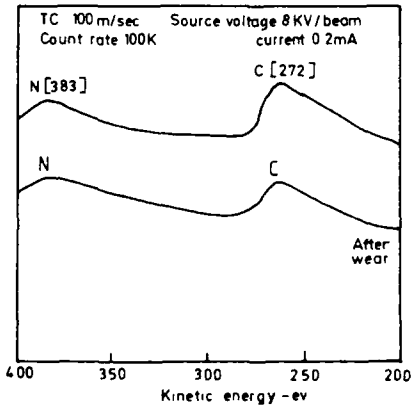

Figure 4 AES profiles illustrating N^+ migration

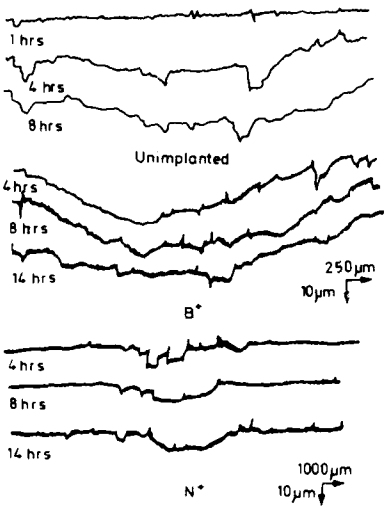

Figure 5 Typical wear track profiles

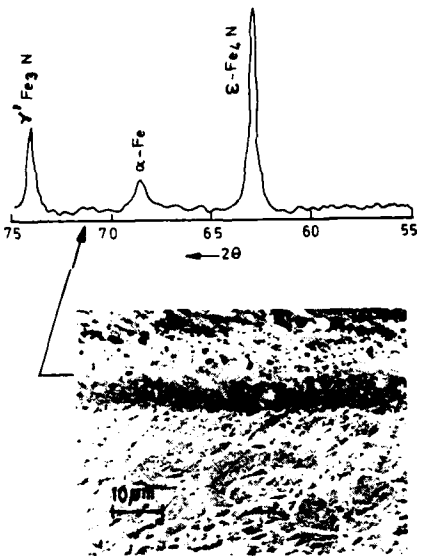

Figure 7 X-ray profile of Ion nitrided HSLA Steel

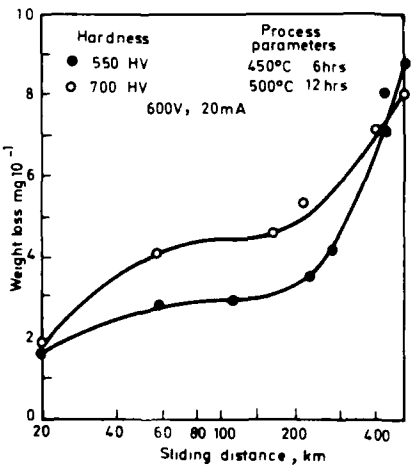

Figure 6 Wear characteristics of Iron nitrided HSLA steel

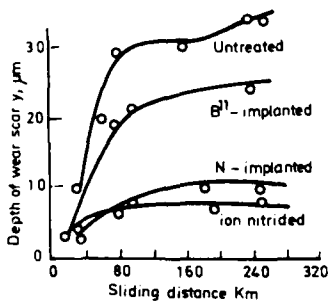

Figure 8 Influence of Ion treatment on wear scar propagation

THE EFFECT OF HEAT TREATMENT ON FATIGUE CRACK GROWTH IN POLYCARBONATE

L. E. Hornberger and K. L. DeVries*

Residual stresses are known to have pronounced effects on the mechanical properties of materials. Previous studies have shown that the quenching of polycarbonate from above its glass transition temperature produced sizeable surface stresses and these stresses were accompanied by a tenfold increase in Izod impact strength and a twentyfold increase in the mean fatigue life of the material at a maximum flexural stress of 62 MPa. More recently, studies on the effect of heat treatment on fatigue crack growth have been undertaken. Heat treatment was accomplished either prior to or subsequent to the introduction of a crack and the crack growth then monitored as a function of the number of fatigue cycles.

INTRODUCTION

The fatigue behavior of polymers, such as polycarbonate, has attracted much interest during recent years due to the increased use of these materials in structural applications. The fatigue life of these materials under cyclic loads has been studied extensively (1-7). In general, the fatigue life of polycarbonate is a function of the maximum tensile stress, the thermal and chemical environment and the thermal and mechanical history of the particular component.

Recent studies, in this laboratory, have demonstrated that the fatigue life of polycarbonate has been significantly extended by thermal treatments (8). When beam samples of polycarbonate were heated above their glass transition temperature and then rapidly quenched in either liquid nitrogen or ice water compressive residual stresses were introduced into the surface of the material and improvements in fatigue life resulted. The mean bending fatigue life of ice quenched samples was extended over six times that of untreated samples while the life of the liquid nitrogen quenched samples was increased by a factor of ten.

The thermal tempering process used in this study produced a gradient of residual stresses throughout the material. With the aid of photoelastic and material removal techniques (9) the average residual stress at the surface of the water quenched samples was evaluated as -14 MPa (-2100 psi), while that for liquid

*Department of Mechanical and Industrial Engineering, University of Utah.

nitrogen quenched samples was -20 MPa (2800 psi). In the initial stress-life tests on treated samples, it was determined that samples with larger surface residual compressive stresses generally exhibited longer fatigue lifes.

In the study reported here, the rate of crack growth in the material was measured as a function of heat treatment in order to gain more extensive insight into the effects of heat treatment on the processes of fatigue.

The effect of thermal treatment on crack growth in a beam sample exposed to cyclic loading was examined in two test series. In the first test series, beam samples of polycarbonate were exposed to a variety of thermal treatments after a 1.0 mm crack had been grown in the material by cyclic loading. The subsequent growth of this pre-existant crack under cyclic loading was monitored after heat treatment. In the second series of tests, the material was first thermally treated and then cracks were grown from a notch in the material that had been produced by a razor blade. In these latter tests, the resistance of treated material to crack development was monitored. Similiar tests were conducted on untreated, dried and annealed beam samples in order to separate the effects of thermal exposure from those of surface residual stresses.

PROCEDURE

Sample Preparation

Beam samples, 12.5 x 80 mm x 6.4 mm, were machined from commercially available 6.4 mm thick Lexan polycarbonate sheet. The samples were milled flat on the cut surfaces and sanded with 600 grit paper with the sample sides left as cast.

For the first test series, untreated polycarbonate samples were notched immediately after removal from the nitrogen bath by scoring the center section of the base of the beam with a razor blade across the 6.4 mm depth of the sample. The notched samples were then placed in a three point load bending fixture and cycled at 15 Hz in an MTS testing machine with a sinusoidal wave form. A maximum flexural stress of 41 MPa (6000 psi) with an R factor (the ratio of minimum to maximum cyclic stress) of 0.2 was applied until a detectable (approximately 0.4 mm) crack had grown across the beam. Crack length was measured with the aid of a cathetometer. When the crack appeared to have developed a uniform crack front across the face of the sample, the maximum cyclic stress was reduced to 33 MPa and the crack allowed to grow until it was approximately 1.0 mm long. The sample was then removed from the test fixture and given one of the following prescribed thermal treatments:

a) untreated: tested as received from the manufacturer b) dried: heated at 125°C for 48 hours in an air circulating oven and cooled to room temperature c) annealed: dried, then heated to 160°C for a minimum of an hour and cooled slowly in the oven to room temperature d) water quenched: dried, heated to 160°C for one hour and cooled by rapidly quenching in ice water e) liquid nitrogen quenched: dried, heated to 160°C for one hour and cooled by rapidly quenching in liquid nitrogen.

Samples given one of the above treatments were again mounted in the flexural fixture and cycled to failure at a maximum bending stress of 33 MPa with an R factor of 0.2. Crack length was monitored at 2000 cycle intervals.

For the second series of tests, samples were subjected to one of the following heat treatments: a) untreated, b) dried, c) annealed, d) water quenched, or e) liquid nitrogen quenched. Treated samples were then cooled to liquid nitrogen temperatures and "notched" by a razor blade. These notched samples were then tested in cyclic three point bending as previously described at a maximum flexural stress of 41 MPa (6000 psi) until a detectable crack was established and growing relatively evenly across the depth of the sample. At this point the maximum stress level was reduced to 33 MPa and the crack length monitored at 2000 cycle intervals.

RESULTS

Reinitiated Crack Growth after Thermal Treatment

Thermal treatment, whether drying, annealing or quenching, had little effect on the growth of large (1.0 mm) existing cracks. This can be observed in the collection of typical growth curves for various heat treatments compiled in Figure 1. Quenching in liquid nitrogen did delay the restart of crack growth significantly in two of the three samples tested as shown in more detail in Figure 2.

Initiated Crack After Thermal Treatment

There also appears to be little difference in fatigue crack growth behavior in cracks which were developed and propagated in untreated, annealed or dried polycarbonate (See Figure 3). It was, however, very difficult to develop a crack from the razor notch in the quenched material. Over 500,000 fatigue cycles were required to develop a detectable crack at an elevated maximum stress of 41 MPa in the water quenched sample. It was much more difficult to develop a perceptible crack from a razor notch in liquid nitrogen quenched polycarbonate. After exposing the sample to 1 million cycles at 41 MPa without any detectable growth, the maximum stress level was increased to 48 MPa (7000 psi). A crack finally began to grow after an additional 40,000 cycles at this greater stress level. The crack which formed was narrow and looked like a vein or tube growing through the sample. It did not grow across the thickness of the sample (i.e., in the direction of the razor scratch) until it had extended to approximately half the height of the sample. A second sample of liquid nitrogen quenched material was razor scored and cycled under a maximum stress of 52 MPa (7500 psi) Two narrow, hairline cracks were detected in this sample after 75,000 cycles. The two cracks eventually merged but the sample failed before a uniform crack front through the thickness of the sample was established.

The most noticeable difference in the fatigue behavior among the samples notched both before and after thermal treatment was observed in the microscopic texture of their fracture surfaces. The fracture surfaces of the annealed, dryed, and untreated samples appear rough and stringy both in the "initiated and the "reinitiated" crack growth samples. The scanning micrograph of Figure 4 is typical of the fracture surface of annealed and dried samples. The stringy material which covers the fracture surface of this annealed material and to a lesser extent the

untreated material shown in Figure 5 appears to be composed of fibrils or crazes which have been torn in the fracture process. There is little of this rough fibrous material on the fracture surfaces of the liquid nitrogen and ice quenched samples. The fracture surfaces of these samples, exhibited in Figure 6 and 7, appear flat and smooth. Fracture apparently initiated from the side and corners of these quenched samples rather than the razor notch located on the base. The early growth of the crack in the quenched samples seems to have been limited to a very small area near the edge. As the crack grew it appears to have expanded into the center of the beam. There is also evidence of a shear lip on the razor notched edges in both the quenched samples. In the unquenched samples the cracks appear to have grown evenly over the entire cross section of the samples. The fracture surfaces are homogeneous without any indication of local crack development.

Distinct, discontinuous crack growth bands (as described by Takemori (2) and Skibo et al. (4)) are evident in the micrograph of the fracture surface of quenched material shown in Figure 8. These bands were observed in the smooth section of the fracture surface near the notched edge of the sample in the liquid nitrogen and water quenched fracture samples. These bands were also present, but rather blurred, in the fracture surfaces of untreated, dried and annealed samples. Neither the length of these bands in the direction of crack propagation nor the stripped appearance of the bands varied with heat treatment. These crack arrest bands were typical for all the samples; treated or untreated.

DISCUSSION

The quenching and annealing processes used in this study had only minor effects on the growth rate of established, propagating cracks in polycarbonate. The heat treatment processes employed did, however, produce noticeable changes in the patterns on the fracture surfaces. As can be observed in the photographs of Figure 6 and 7 the bulk of the fracture surface of the samples notched after the quenching process is composed of a smooth, flat, "mirror" region marked with concentric rings or bands. Fibrous strands are also present on the fracture surface of quenched materials (See Figures 6) but are fewer in number, less distinct, and are located farther away from the notched edge of the sample than the stringy structures which spread across the fracture surface of the annealed samples (See Figure 4)

The fracture surface of the untreated polycarbonate (Figure 5) also exhibited a smooth "mirror" area with concentric rings which transformed into a rough stringy "mist" area. These smooth and rough features were analyzed by MacKay, Teng and Schultz (10) in their work on the role of crazes in the fatigue of polycarbonate. They suggested that the smooth area evident at the edge of an untreated sample is a remnant of a single craze which first formed during cyclic loading at a point of high local surface stress. Under cyclic loading, this craze grew, as did the number of voids within the craze. According to this model, a crack propagated, eventually, from inside this weakened craze and grew until the stress level was no longer sufficient to rupture the partially voided craze and the crack was arrested. With continued cycling, the remaining portion of the craze in front of this crack increased in void content and again reached a level at which crack growth was reinitiated. Accordingly, the growth of the crack through this single expanding craze produced the flat glassy surface noted in the fracture pattern while the discontinuous crack growth process formed the ringed pattern on the surface of

the material. MacKay et al. proposed, further, that at some point in this process the stress field in front of the crack increased to such a magnitude as to produce multiple crazes ahead of the crack. As the crack front accelerated it intersected this extensive craze field and was diverted from its previous flat path as it stepped its way through various weak crazes located on the planes close to the crack tip. This growth of the crack from craze to craze and plane to plane caused the rough textured "mist" area on the fracture surface. Chudnovsky (11) adds to this model by suggesting that while fatigue crack extension in polycarbonate begins with growth through a single root craze a "simultaneous dissemination of microcrazing" is occurring in the bulk of the sample surrounding the crack-root craze. At some critical crack length, crack extension occurs by fracture through the field of microcrazes rather than through the continued growth of the root craze.

In the context of this model of the fracture surface features and their relationship to failure mechanisms, it appears that quenching alters the material in such a way as to supress the formation of microcrazes while annealing tends to increase the formation of microcrazes. The fatigue life of quenched material far exceeds that of annealed material because the probability of craze and subsequent crack formation is significantly reduced in quenched samples. The authors believe that the retardation of craze formation is in large part a consequence of the presence of compressive residual stresses (produced in the quenching process) on the surface of the material and perhaps to a lesser extent morphological changes including free volume changes. These stresses which are in the order of -14 to -21 MPa (-2 to -3 ksi) lower the local stress field on the outer surface of the material and consequently decrease the sensitivity of the material to stress risers which activate the formation of crazes. These stresses delay the formation of the root craze and suppress microcrazing. This delay appears to be a function of the magnitude of the residual compressive surface stresses as crack suppression was far greater in the samples quenched in liquid nitrogen (which produces -21 MPa surface stress) than in those quenched in ice water (which produces -14 MPa surface stress).

The role of compressive residual stresses in extending fatigue behavior was predicted by Chen, Chheda and Sauer (12) who suggested that any modification of the surface of the material which delayed craze formation or inhibited craze rupture would enhance fatigue life. In their extensive and informative work on polystyrene and HIPS, these investigators extended the fatigue life of their materials by as much as a factor of 20 by various surface coating and polishing treatments which they conducted to decrease the probability of craze initiation and growth. The retardation of craze formation by compressive residual stresses produced by thermal quenching was noted by Rabinowitz and Beardmore (4) in their study of the fatigue process in quenched PMMA. Takemori (2), in his study on fatigue crack growth in polycarbonate, also observed a retardation of initial crack growth occurred in injection molded samples due to the presence of surface residual stresses.

The role of the annealing and drying processes is the opposite to that of quenching. These processes increase the probability of craze and subsequent crack formation. The results of the present study on fatigue crack growth rate in annealed material are consistent with those of Manson et al. (1) who observed few differences in the crack growth rates of untreated samples relative to those annealed at 125°C or 160°C. The authors propose, in agreement with an earlier suggestion by Broutman and Kirshnakumar (13), that although annealing may cause some form of structural change within the material, its primary effect in this fatigue study

was to lower the surface residual stresses and/or orientation which were present in the material as a residue from sheet forming and sample machining processes. These stresses may be present to some extent in the untreated and dried samples and may increase their resistance to crack formation. Although no clear delay of crack initiation in untreated or dried samples relative to annealed samples was detected in this study, the mean fatigue life of unnotched annealed beam samples was determined to be 10% lower than that of untreated samples in fatigue tests at a maximum flexural stress of 62 MPa.

CONCLUSIONS

Fatigue crack growth results on beam samples of polycarbonate which were heat treated both prior to and after fatigue crack initiation show little evidence that heat treatment affects the rate of crack growth within the material. However, heat treatment was determined to significantly affect the time for fatigue crack initiation and/or growth to a perceptible size. For example, quenching processes which produced compressive residual stresses in the surface of the material delayed the formation of fatigue cracks up to 1 million cycles over that of untreated material. Annealing processes which may relax existing residual stresses and/or the orientation in the material, appear to increase the probability of craze and subsequent crack formation in the material.

REFERENCES

1 Hertzberg, R. W., and Manson, J. A. "Fatigue of Engineering Materials, Academic Press, New York, 1980

2 Takemori, M. T., Polymer Engr. Sci.Vol. 22, 1982, pp. 937-945

3 Rabinowitz, S., and Beardmore, P., J. Mater. Sci. Vol 9, 1974, pp 81-99

4 Skibo, M. D., Hertzberg, R.W., Manson, J. A. and Kim, S.L., J. Mater. Sci.,12, 1977, pp. 531-542

5 Mills, N. J., and Walker, N., J. Mater. Sci., Vol. 15, 1980, pp 1832-1840

6 Radon, J.C., Arad, S., and Culver, L.E.,Engineering Fracture Mechanics, Vol. 6, 1974, pp. 195-208

7 Pitman, G., and Ward, I. M., J. Mater. Sci., Vol. 15, 1980, pp 635-645

8 L. E. Hornberger and K. L. DeVries, paper submitted to Polymer Engr. Sci.

9 L. E. Hornberger and K. L. DeVries, paper submitted to Experimental Mechanics.

10 Mackay, M. E., Teng, T. E., and Schultz, J. M., J. Mater. Sci., Vol 14, 1979, pp. 221-227

11 Chudnovsky, A., Moet, A., Palley, I. and Baer, E., J. Org. Coat. Plast. Chem., Vol. 44, 1981, pp. 309-318

12 Chen, C C , Chheda, N , and Sauer, J A ,J Macromol Sci-Phys , Vol B19, 1981, pp 565-588

13 Broutman, L J , and Krishnakumar, S M , Polymer Engr Sci , Vol 16, 1976, pp 74-81

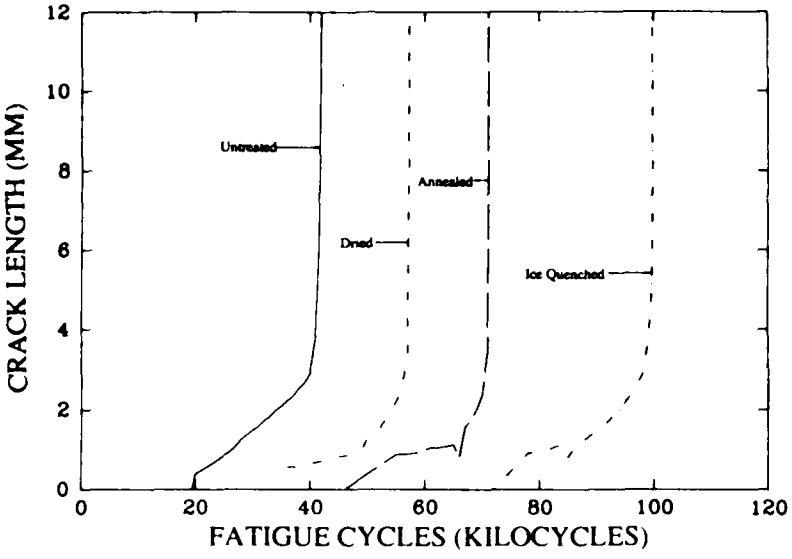

Figure 1 Crack growth behavior in samples heat treated after crack growth has been established

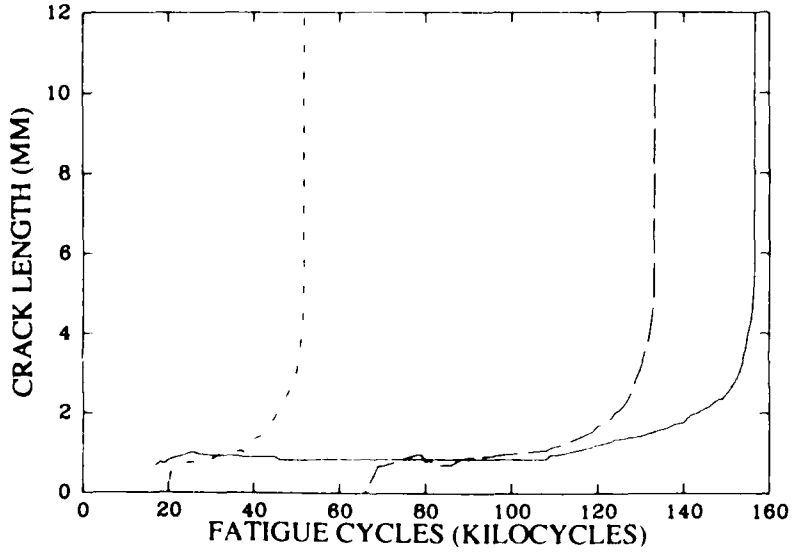

Figure 2. Crack growth behavior in samples quenched in liquid nitrogen after crack growth has been established.

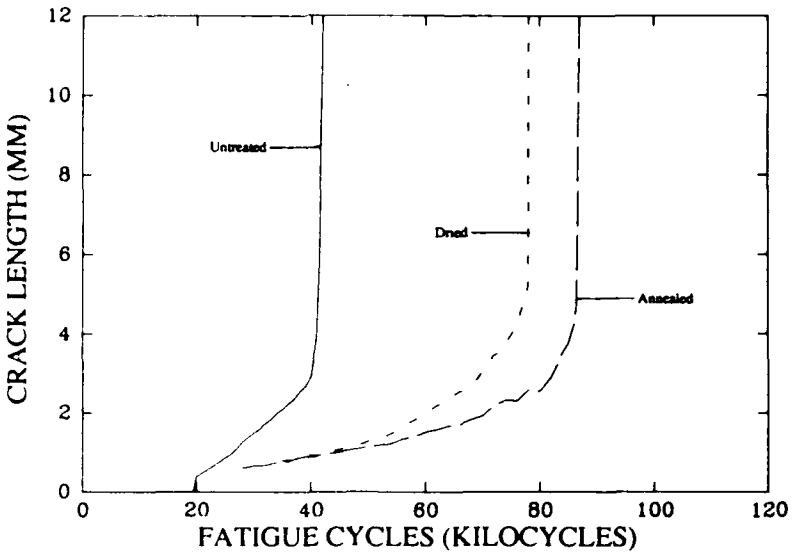

Figure 3. Crack growth behavior in samples notched after heat treatment.

Figure 4. Fracture surface of sample notched after annealing.

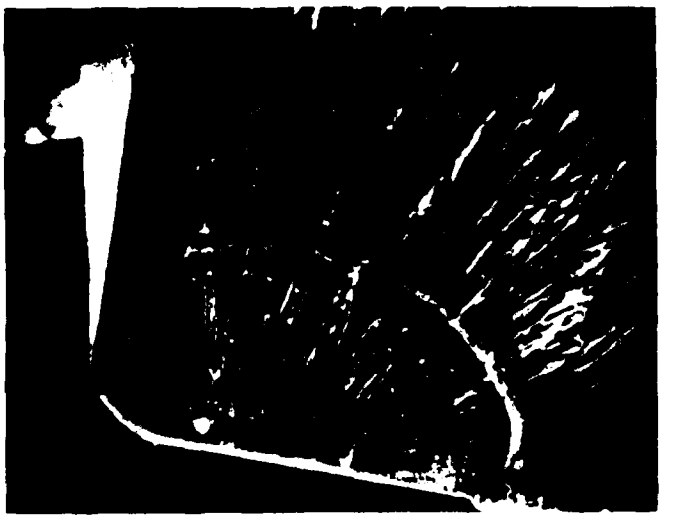

Figure 5. Fracture surface of untreated polycarbonate.

Figure 6. Fracture surface of sample notched after quenching in ice water

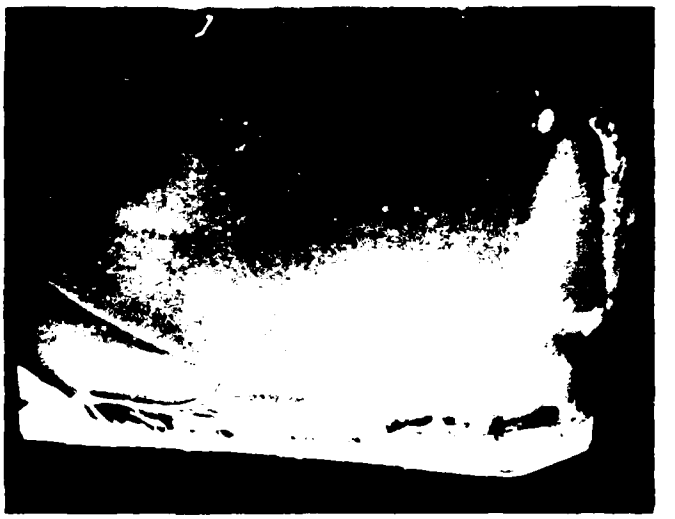

Figure 7. Fracture surface of sample notched after quenching in liquid nitrogen

Figure 8. Discontinuous growth bands in sample notched after liquid nitrogen quenching. Magnification: 1100X.

EFFECT OF TEST TEMPERATURE AND FREQUENCY ON FATIGUE CRACK PROPAGATION IN PVC

J. D. Phillips, R. W. Hertzberg, and J. A. Manson*

The effect of frequency and temperature on the fatigue crack propagation (FCP) behavior of poly(vinyl chloride) was studied. An Arrhenius relationship between the crack growth rate and the reciprocal of the absolute temperature was found, leading to an estimate of the activation energy for the FCP propagation process. Examination of the fracture surfaces revealed the presence of discontinuous growth bands, which correspond to the size of the crack tip plastic zone during each test. Dimensions of the stretch zones separating these bands coincide with to calculated values of the crack opening displacement. Also, J-integral values, inferred from stretch zone size measurements, agree with values calculated from material properties.

INTRODUCTION

Engineering plastics are finding increased usage in pipeline systems and other structural applications. Consequently, increasing attention has been given to the material's mechanical properties, including its fatigue behavior, at various service conditions. Since many components may be expected to contain flaws, notched specimens are often used to study the fatigue crack propagation (FCP) process. Such information permits the design engineer to predict the fatigue life of a given component. For many polymeric materials, linear elastic fracture mechanics concepts can be used to describe FCP behavior (1,2), with the crack growth rate being related to the crack driving force parameter K according to equation (1) (3):

$$da/dN = A\Delta K^{m} \qquad (1)$$

where a = crack length
N = number of loading cycles
A,m = test and material variable constants
K = stress intensity factor range

*Department of Materials Science and Engineering, Lehigh University, Bethlehem, PA 18015.

In turn, $\Delta K = Y\Delta\sigma\sqrt{a}$ (2)

where $\Delta\sigma$ = cyclic stress range
Y = geometry-dependent calibration factor.

Due to the viscoelastic nature of polymers, their fatigue behavior is sensitive to the test variables of frequency and temperature. An increase in the test frequency has often been shown to increase the resistance of the material to fatigue crack propagation and has been attributed to local crack tip heating and/or strain rate effects (4-6). Fatigue crack growth rates have also been observed to increase with increasing temperature (7) consistent with time-temperature equivalence (8).

Two different fractographic features have been found on the fatigue fracture surfaces of engineering plastics--fatigue striations and discontinuous growth bands (DGBs). Fatigue striations, oriented normal to the direction of crack growth, represent the successive position of the crack front after each load excursion. The striation spacing increases with ΔK, and in polymers, correspond to the macroscopic growth rate, da/dN (1,9). DGBs also lie normal to the direction of crack growth and increase in length with K, but represent instead the discrete positions of the crack tip after many loading increments (9-12). These bands form by rupture of a craze zone* at the crack tip after several hundred to several thousand loading cycles, and correspond in width to the size of the crack tip plastic zone whose size has been frequently described by the Dugdale plastic strip model (13):

$$\text{Band width} = \text{plastic zone size} = \frac{\pi}{8}(K_{max}/\sigma_{ys})^2 \quad (3)$$

where K_{max} = the maximum stress intensity factor
σ_{ys} = the yield strength.

It has been suggested that discontinuous crack extension occurs when the equilibrium crack opening displacement (COD) (14) (eq. 4) exceeds the maximum length of the craze fibrils for that ΔK level. For most polymers, this occurs under conditions where craze thickening takes place by orientation hardening of fibrils rather than by viscous flow processes involving surface drawing of matter into the craze.

$$COD = K^2_{max}/E\sigma_{ys} \quad (4)$$

where E = elastic modulus
σ_{ys} = yield strength.

Separating each DGB is a stretch zone, which is thought to represent the region of crack tip blunting produced when the crack arrests at the tip of the craze. Since the stretch zone represents the size of the crack tip radius, it follows that the

*A craze is a lenticular damage zone consisting of many microvoids and slender fibrils oriented parallel to the tensile stress axis.

crack opening displacement should be equal to twice the value of the stretch zone width.

To date, little attention has been given to a combined study of the effects of temperature and frequency on the kinetics of the fatigue crack propagation process and an identification of the fracture mechanisms operative over a wide range of test temperatures and cyclic frequencies. This study addresses these issues for the case of poly(vinyl chloride) (PVC).

EXPERIMENTAL PROCEDURE

Mechanical properties were determined for a commercial sheet grade of poly(vinyl chloride) (PVC), produced by Dynamit Nobel (tradename Trovidor, ASTM D1784-8, Class 11452-B). The dynamic mechanical spectrum for the material was determined with the use of an automated Rheovibron DDV-III-C with a scan rate of 1°C per minute. Yield strength of the material was determined as a function of temperature.* Tensile specimens were brought to temperature through the use of heating tape and tested according to ASTM D638. Single edge notch (SENT) specimens 50.8 mm in width were machined from the 4.76 mm thick sheet, and fatigue crack propagation tests conducted under manual load control on an Instron servohydraulic unit. The tests were run under constant load-range conditions using a sinusoidal wave form and a load ratio of R = 0.1. Precracking of the specimens was done in accordance with ASTM Specification E647-81. Frequency and temperature conditions were varied with specimens being tested at frequencies of 1, 10, 50 and 100 Hz at temperatures between 20°C and 55°C; 100 Hz tests were also conducted at 0°C and -30°C. Fatigue tests were conducted inside an Applied Test Systems oven with a Series 2010 control system; subambient temperature tests were conducted in a flowing nitrogen gas environment.

The stress intensity factor was calculated from the equation:

$$K=\sigma\sqrt{a}[1.99-0.41(a/W)+18.7(a/W)^2-38.48(a/W)^3+53.85(a/W)^4] \quad (5)$$

where σ = applied stress
B = specimen thickness
W = specimen width
a = crack length.

Crack length measurements were made at approximately 0.2 mm intervals with a Gaertner traveling microscope and a modified secant method used to calculate the crack growth rate da/dN:

$$(da/dN)_n = (a_{n+1}-a_{n-1})/(N_{n+1}-N_{n-1}) \quad (6)$$

where a is the crack length and N is the total number of cycles for that crack tip measurement.

*Test results provided by Steffanie Sunday, Lehigh University.

Macroscopic examination of the fracture surfaces and measurement of the discontinuous growth band (DGB) sizes were made with the use of a Zeiss Axiomat microscope. Microscopic examination of the fracture surfaces and measurement of the DGB stretch zone sizes were performed using an ETEC Scanning Electron Microscope at 20kV. All samples were coated with a Au-Pd alloy prior to viewing. During measurement of the stretch zone widths, the specimen was oriented such that the stretch zones were positioned normal to the tilt axis; accordingly, it was not necessary to correct the measurements for the angle of viewing.

EXPERIMENTAL RESULTS AND DISCUSSION

The FCP response of the current PVC material supply is shown in Figure 1 as a function of test frequency and temperature. As noted previously with many other polymeric solids as well as PVC, FCP rates are found to decrease with increasing cyclic frequency (Figure 1a) as a result of complex interactions associated with the viscoelastic response of the material (5,16). Fatigue crack propagation rates are also seen to decrease markedly with decreasing temperature with the ΔK-dependence of da/dN changing only slightly except at ~30°C, where a much stronger dependence is noted (Fig. 1b). Mai and Williams (7) noted similar behavior for FCP studies conducted on polystyrene. Note that the influence of cyclic frequency and test temperature on FCP response is consistent with the equivalence of time and temperature. To explore further the influence of test temperature on crack growth behavior, crack growth rates shown in Figure 1b were plotted versus reciprocal absolute temperature. Figure 2 clearly demonstrates a strong Arrhenius relationship (eq. 7) with a single value of activation energy computed to be approximately 30 kJ/mole for tests conducted at 100Hz.

$$da/dN = C \exp(-Q+v\sigma)/RT = C \exp(Q'/RT) \quad (7)$$

where Q = activation energy
Q' = apparent activation energy
= activation volume
σ = effective stress
R = gas constant
T = absolute temperature

This apparent activation energy for the fatigue process in PVC is approximately half that value corresponding to molecular motions associated with the beta peak in this material and less than 10% of for the alpha peak [i.e. glass transition temperature (T_g)] (17,18). The significance of Q' corresponding to testing at 10^6 Hz is not clear at this time though it surely reflects that the fatigue fracture process is not controlled by main chain segmental movements associated with T_g. On the other hand, if one were to equate Q solely with processes associated with the beta

peak, then either the computed value of activation volume or effective stress acting on the craze fibrils would prove to be several orders of magnitude too large. It should be noted, however, that the single value of Q' assigned to the fatigue process, based upon the present data, is consistent with the fact that only one fracture mechanism (DGB formation) was observed over the entire test temperature range (see below).

The fracture surface appearance of the PVC samples was examined over a broad range of ΔK, cyclic frequency an test temperature levels. For every condition examined, discontinuous crack extension took place with discontinuous growth bands being the only observed fracture surface feature (Fig. 3) As noted by others (10) each band contained a gradient of microvoid sizes with the largest microvoids found near the craze mouth, associated with the location of highest tensile triaxiality (19), and the smallest microvoids being found at the end of the DGB. The narrow band separating each DGB corresponds to the blunted crack contour resulting from arrest of the crack after it traversed the craze zone. Discontinuous growth band widths increased with increasing test temperature and ΔK level (Fig. 4) and decreasing cyclic frequency, each finding being consistent with the fact that DGBs usually correspond to the crack tip plastic zone dimension, as described by the Dugdale model (eq. 8) (13). That is,

$$\text{DGB size} = \frac{\pi}{8} \frac{K^2}{\sigma_{ys}} 2 \qquad (8)$$

σ_{ys} decreases with increasing temperature and decreasing test frequency. Since the DGB spacing in the current material supply varied with less than the second power of K, it was not possible to infer yield strength values for this material at each frequency-temperature condition. However, tensile test results confirmed that σ_{ys} decreased with increasing temperature.

Assuming that the stretch zone area that separates each DGB represents the profile of the blunted crack, comparison was made between the width of the stretch zone (SZW) and computed values of the crack opening displacement (COD) at each stretch zone location As suggested by others (20), half of the total COD may be approximated by the width of the stretch zone. Fig. 5 reveals an encouraging one-to-one correlation between fracture surface measurements of stretch zone widths and computed values of COD/2 for samples tested at 100Hz and at temperatures between 22 and 55°C. Linear correlations between these SZW and COD values were also noted for tests conducted at 1 and 10Hz, respectively, though stretch zone widths were approximately two times greater than their corresponding COD/2 computed values.

Based on this encouraging correlation between SZW and COD/2, efforts were made to compare values of J computed from the

Griffith energy criteria ($J=G=\frac{K^2}{(1-\nu^2)E}$) and from COD considerations (21):

$$J \sim m\sigma_{flow} \cdot COD \quad (9)$$

where J = J integral
m = 1 (plane stress conditions)
m = 1.3-2.0 (plane stress conditions)
$\sigma_{flow} = (\sigma_{ys}+\sigma_{TS})/2$ (σ_{ys} was used in the calculations)
COD = total crack opening displacement

If one assigns decreasing values of m from 2 to 1 with increasing test temperature to account for changes in stress state (based on a similar method employed by Hashemi and Williams (22), good correlation is noted between the J values computed by the two different methods (Fig. 6).

CONCLUSIONS

The fatigue resistance of PVC improved under conditions of decreasing test temperature and increasing cyclic frequency, in accordance with time-temperature superposition principles.

An Arrhenius relationship between the crack growth rate and the reciprocal of the absolute temperature was found. Although the significance of the calculated value for the apparent activation energy is not clear, the single value observed over the temperature range corresponded with the presence of only one fracture mechanism--discontinuous crack extension.

Measurements of the discontinuous growth bands over the observed stress intensity range indicates that the Dugdale model is invalid for this material supply. However, the data indicates that sizes of the discontinuous growth bands do increase with increasing temperature and decreasing frequency, as expected.

The size of the DGB stretch zones corresponded to COD-based calculated values for the radius of the crack tip. Likewise, the value of the J-integral can be inferred from values calculated using stretch zone size measurements. These findings imply that the stretch zone is indeed a measure of the crack tip radius and equivalent to half the value of the crack opening displacement.

ACKNOWLEDGEMENTS

The authors appreciate the financial support of the Polymer Program, NSF, Grant DMR-8412357.

REFERENCES

1. Manson,J.A., Hertzberg,R.W., CRC Crit.Rev.Macromol.Sci., Vol.1,No.4,1973,p.433.

2. Sauer,J.A.,Richardson,G.C.,Int.J.Fracture,Vol.16,No.6,1980, p 449.

3. Paris,P.C.,Proc.Sagamore Army Mater.Res.Conf.,10th,1964,p.107.

4. Hertzberg,R.W., Manson,J.A. and Skibo,M.D., Poly.Eng.Sci., Vol.15,No.4,1975,p.252.

5. Hertzberg,R.W.,Manson,J.A. and Skibo,M.D., Polymer, Vol.19, 1978,p.358.

6. Skibo,M.D., Hertzberg,R.W. and Manson,J.A., J.Mater.Sci., Vol.11,1976,p.479.

7. Mai,Y.W. and Williams,J.G., J.Mater.Sci.,Vol.14,No.8,1979, p.1933.

8. Ferry,J.D., "Viscoelastic Properties of Polymers," Wiley, New York, 1961.

9. Hertzberg,R.W. and Manson,J.A., "Fatigue of Engineering Platics," Academic Press, New York, 1980.

10. Skibo,M.D., Hertzberg,R.W., Manson,J.A., and Kim,S.L., J.Mater.Sci.,Vol.12,1977,p.531.

11. Rimnac,C.M., Hertzberg,R.W. and Manson,J.A., J.Mater.Sci., Vol.19,1984,p.1116.

12. Rimnac,C.M., Hertzberg,R.W. and Manson,J.A., ASTM STP 733, 1981,p.291.

13. Dugdale,D.S., J.Mech.Phys.Sol.,Vol.8,1960,p.100.

14. Goddier,J.N. and Field,F.A., "Fracture of Solids," Interscience, New York, 1963.

15. Hertzberg,R.W. and Manson,J.A., "Materials Experimentation and Design in Fatigue," Edited by F.Sherratt and J.B.Sturgeon, Westbury House, Surrey, England, 1981.

16. Hertzberg,R.W., Manson,J.A. and Skibo,M.D., Poly.Eng.Sci., Vol.15,No.4,1975,p.252.

17. McCrum,N.G., Read,B.E. and Williams,G., "Anelastic and Dielectric Effects in Polymeric Solids," Wiley, NY, 1967.

18. Kausch,H.H.,"Polymer Fracture,"Springer-Verlag, Berlin, 1978.

19. McMeeking,R.M., J. Mech. Phys. Sol., Vol.25, 1977, p. 357.

20. Amouzouvi,K.F.and Bassim,M.N.,Mater.Sci.Eng.,Vol.55,1982,p.257.

21. Hashemi,S. and Williams,J.G., Polymer,Vol.27,1986,p.384.

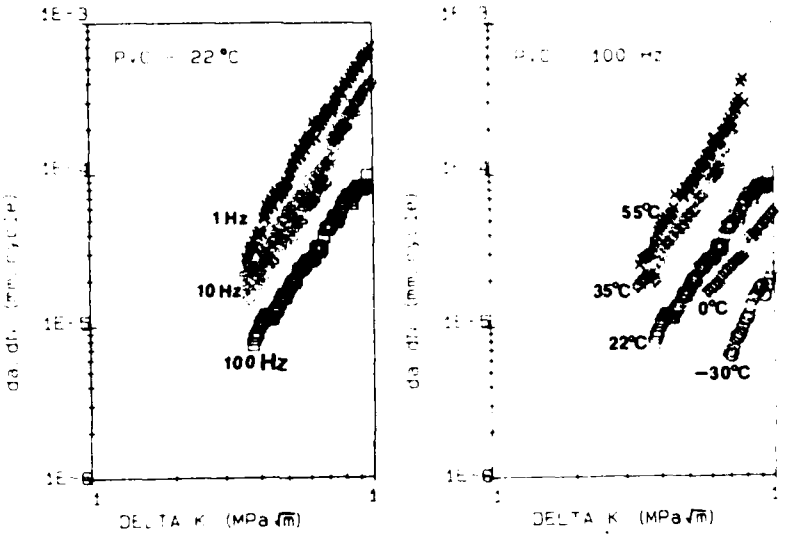

Figure 1a,b. Variation in FCP Response in PVC With Changing (a) Frequency and (b) Temperature

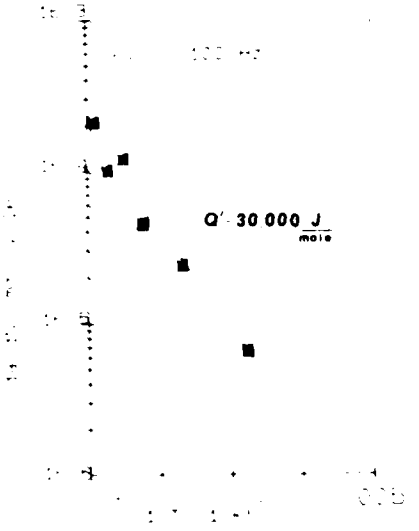

Figure 2. Arrhenius Relationship Between the Fatigue Crack Growth Rate and Inverse Absolute Temperature in PVC.

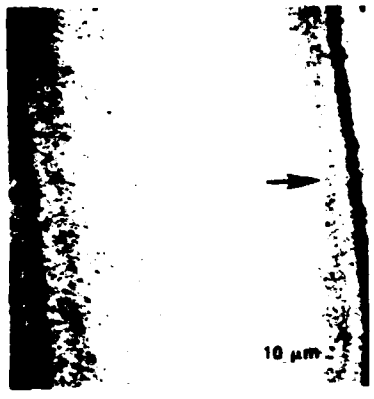

ΔK = .4 MPa√m, 50 Hz, 45°C

Figure 3. Fractograph Showing Discontinuous Growth Band Morphologies. Arrow indicates direction of crack growth.

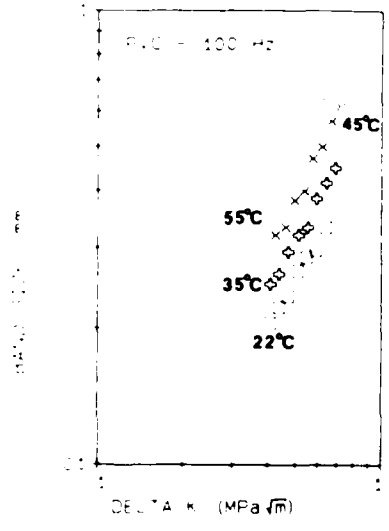

Figure 4. Discontinuous Growth Band Sizes in PVC as a Function of ΔK and Temperature.

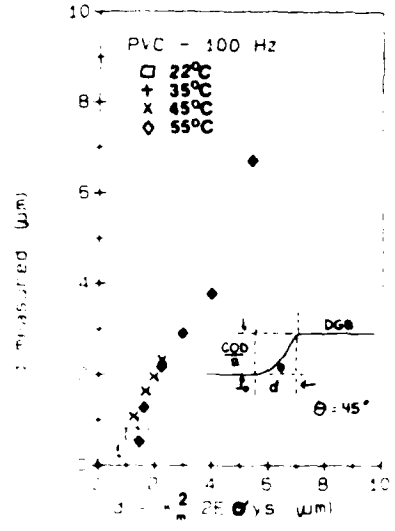

Figure . Correspondence of Measured and Calculated [illegible] Values.

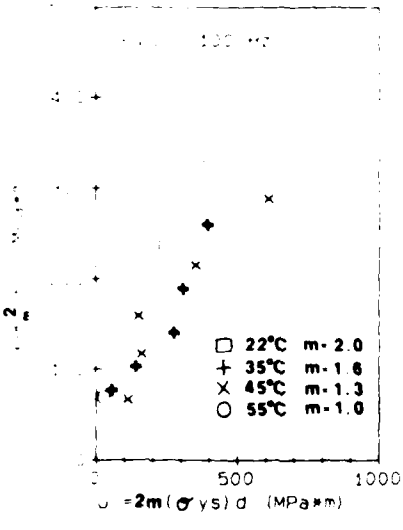

Figure 6. Relationship Between Calculated and Fractographically Inferred Values of the J-integral.

ENVIRONMENTAL FRACTURE TOUGHNESS AND STATIC FATIGUE CRACK PROPAGATION OF SILICA GLASS

Y. Sawaki*, K. Kobayashi**, S. Sakaguchi*** and T. Kawasaki****

The region 1 static fatigue crack growth curve, da/dt- K, of silica glass determined by pre-cracked CT specimen can be characterized by the parallel curves each other, shifting into higher stress intensity region with decreasing the humidity in an air. This can be rationalized by introducing the newly proposed parameter, environmental fracture toughness, Kie, which is the measure of the degree of degradation of the material at the crack tip caused by the interaction with water. This Kie is linearly related to the water vapour pressure on the log-log paper and successfully explains the fatigue cracking behaviour.

INTRODUCTION

Optical fibers have been developed for optical communications utilizing the very low loss transmission and high strength properties of silica glass. Both of the tensile strength and fatigue lifetime are dependent on the macroscopic flaw present in the fibers (1). So in order to assure the long-term reliability of the fibers, it is necessary to thoroughly understand the fundamental cracking behaviour of the silica glass.

Therefore, much of the work (2), (3), (4) has been carried out on this material to analyse the crack growth based on the fracture mechanics. However the crack grow-

* Department of Mechanical Engineering II, Tohoku University, Sendai, Japan
** Canon Inc., Ohta-ku, Tokyo, Japan
*** Nippon Telegraph and Telecommunication Corporation, Tokai, Ibaraki, Japan
**** Hiroshima Denki Institute of Technology, Hiroshima, Japan

th rate, da/dt, tested in these studies, were mostly in the range between 10^{-7} - 10^{-5} mm/sec. and not yet been sufficiently clarified on the threshold stress intensity and the behaviour of final catastrophic fracture.

On the other hand, recently the importance of fracture toughness value at final fracture in fatigue (Fatigue Fracture Toughness) is pointed out to clear the crack propagation behaviour (5), (6). Although these findings are for the metallic materials, the situation is thought to be the same also for glass materials.

So in the present study, static fatigue cracking behaviour of silica glass, was investigated covering the entire range of stress intensity, from nealy threshold to final fracture, by carefully pre-cracked CT specimens under the condition of various environments. And its correlation with the stress intensity at final fracture was examined.

EXPERIMENTAL PROCEDURE

Material and Specimen

Fused silica was used in the failure test. The specimen is a WOL type compact tension specimen (7), and its configuration is shown in Fig. 1.

Pre-cracking

In the preliminary test, it is proved that the condition of the pre-cracking exertes considerable effects on the test results, such as crack propagation rate, stress intensity K calculation and the fracture toughness value, for these brittle materials. So the introduction of the pre cracking constitutes the key technique for these investigations.

Therefore, the following technique is developed in this study. First, ahead of the machined slit, the straight line, about 1.5 mm length and 0.005 mm depth, was scribed on both surfaces of the specimen using diamond pyramidal indentor. Then, the specimen was mounted on the fatique testing machine and cyclic tensile loading was applied. The crack initiation occured at one corner of the tip of the machined slit and then extended towards the other corner. After that, it's extention was well alongside the line scribed on the surface. This behaviour was monitored carefully on the CRT video display connected with a CCD camera and the range of cyclic loading was reduced stepwisely with the extension of the

crack. In this manner, the pre-cracking having accurately vertical to the loading direction and almost the same in geometrical configuration could be introduced.

Static Fatigue

Tensile load is applied to the pre-cracked specimen mounted in an environment chamber made of transparent acryc board. Compressed air of commercial purity was introduced into the chamber through a humidity generator. The extremely dry environment (relative humidity = 0.01*) was attained by flowing the temperature controlled evaporated liquid nitrogen into the chamber.

The crack length measurment was made through traveling microscope with a magnification of 20. Specifically, in higher crack growth region, a CCD camera with 135 mm telescope lense and video recorder system was used for this measurement. Then, the data were converted into the da/dt and stress intensity factor (7), K.

RESULTS AND DISCUSSIONS

Fatigue Crack Propagation

Crack growth rates in an air at 298 K, relative humidities of 75, 20, 4 and 0.08*, and in nitrogen gas (r.h.= 0.01*), are shown in Fig. 2 as a function of the stress intensity factor. The growth rate tends to decrease with decreased humidity.

Also Fig. 3 shows the similar result obtained by changing the temperature of the constant humidity air. The higher the test temperature, the higher growth rate is cleared.

These results suggest that the crack growth behavior can be devided into three regions. In region 1, the data trend is found to be characterized by the parallel curves each other, shifting into higher stress intensity region with decreasing the humidity. In region 2, the K dependency of the growth rate becomes more moderate. The transition from region 1 to region 2 tend to occur also at larger value of K in lower humidity environment. There are not enough data in region 3, however, the presence of this region can be anticipated (2) and will be much cleared in the following section.

Critical Stress Intensity Factor at Fracture, Kix

The fracture surface of these specimens were observ-

ed under the differential interference contrast microscope. The crack front, corresponding to the final fracture can be well identified as a single line, probably due to the slight inclination of the fracture plane. Then, the final crack length can be measured and the critical stress intensity factor, Kix, were calculated. These values were found to be independent to the environment tested and the average of Kix is to be 0.89 MPa $\sqrt{m}$, which compares favourably with the fracture toughness of 0.81 MPa$\sqrt{m}$ reported by Wiederhorn (8).

Since this Kix is independent to the environment, the existence of the region 3 in da/dt-K curve can be presumed where the crack extension is completely governed by mechanical cracking.

Fatigue Crack Propagation Curve

The crack propagation behaviour in region 1 is the conjoint phenomena of mechanical cracking and the chemical reaction with water molecule. In the region 2, the rate of mechanical cracking becomes faster than that of the chemical reaction taking place, because of the relatively higher stress intensity applied at the crack tip. Then the chemical reaction will be reduced gradually with K and finally the cracking is governed completely by the mechanical one. This is the region 3, where no effect of environment is observed.

From the present method of crack length measurement, enough data, in the region 3, could not be obtained, however, the critical stress intensity, Kix, was independent to the environment. Therefore, crack growth with no chemical reaction, namely that of mecahanical one, should be represented by the curve, shifting the region 1 line (solid line in Fig. 2) to higher K up to the upper limit of K coinciding with the Kix. This result is shown by a broken line in the figure.

Schönert et al.(9) has reported that the crack growth curve of soda-lime glass measured in vacuum (1.3×10^{-4} Pa) is placed just onto the extraoporated region 3 air data curve to the lower da/dt region. In such a high vacuum condition, little effect of humidity being present, it is supported that the mechanical crack growth should be expressed as broken line, mentioned above.

Recently, it has been reported (5),(6) that the fatigue crack propagation rate of steel can be well expressed by the four parameter Weibull function and that the fatigue fracture toughness, corresponding to the

final fracture in fatigue, is one of the four parameters in this function.

Then the curve fitting for the broken line in Fig. 2 was carried out based on the following four parameter Weibull function,

$$da/dt = e + (v-e)[-\ln(1-K/K_{1x})]^{1/k} \quad \ldots\ldots\ldots (1)$$

where, k = shape parameter, e = threshold value, v = characteristic value, and K_{1x} is the critical stress intensity at fracture, 0.89 MPa m. This result showed a meaningful coefficient of correlation factor of 0.998. Therefore, in the following discussions, thus determined da/dt -K relation can be regarded to show the mechanical crack growth behaviour without any chemical reaction and forms the base line discussing the chemical effect.

Environmental Fatigue Fracture Toughness, K_{1e}

From the test results in Fig. 2, the higher crack growth in region 1 is revealed with the lower humidity, in case of the constant temperature. And in case of constant humidity, the crack growth is accelerated with temperature (Fig. 3).

The chemical reaction (10) between the silica and water is represented as,

$$\text{-Si-O-Si-} + H_2O \rightarrow 2[\text{-Si-OH}]$$

This results in the breakage of Si-O bond and produces microscopic flaws ahead of the crack. This situation corresponds to the material having low critical stress intensity, K_{1x}, at the crack tip. The above reaction can proceeds with higher water vapour pressure and hence the reduced K_{1x} at the crack tip causes higher growth rate. This behaviour can be expressed as the shift of crack growth curve to lower stress intensity region on the da/dt - K plot. In another words, the cracking behaviour in the moist environment is observed as if that in material with low K_{1x}.

The mechanical crack growth is assumed as Eq. (1). The reducing K_{1x} means the parallel translation in negative direction of the abscissa. So in Figs. 2 and 3 (the broken line in Fig. 3 is the same as that in Fig. 2), the parallel translated curves were drawn to fit the region 1 data, which reflects the chemical reaction, by solid lines. The K_{1x} value of these curves, namely the upper limit K value of the curve, is named as environmental fracture toughness, K_{1e}. That is, the crack growth rate, considering the chemical reaction can be writ-

ten as changing the Kix to environmental fracture toughness, Kie,

$$da/dt = e + (v-e)\{-\ln(1- K/Kie)\}^{1/k} \quad \ldots\ldots\ldots (2)$$

Thus determined Kie are plotted against water vapour pressure in Fig. 4. This figure also contains the results of soda lime glass, determined by the same procedure for the published data (9),(11). It is clealy found that the Kie decreases linearly with increasing the water vapour pressure. This toughness reduction is thought to be the result of debonding Si-O by the water molecule, namely the creations of sub-micro-cracks and accordingly the degradation of the material at the crack tip. The Kie is the measure of this toughness reduction.

Furthermore, in the case of extremely low humidity condition, mechanical crack growth governs the entire region. This limits the upper value of Kie as Kix. This is well verified as in the soda-lime glass.

On the other hand, Fig. 5 shows the results in distilled water. The acceleration of crack growth rate with temperature of distilled water is clearly seen. The broken line in the figure is the calculated mechanical crack growth da/dt - K relation (Eq. (1)). This curve is the same as that in Fig. 2, since the mechanical crack growth is thought to be independent to the environment. The solid lines show the result of moving parallel of this mechanical crack growth curve. One can see that even in a distilled water, the data also fall onto these parallely shifted curves. Therefore, the environmental fracture toughness, Kie, in distilled water could be determined.

The temperature dependence of thus determined Kie is presented in Fig. 6 as a function of reciprocal of the absolute temperature. The Kie values, determined by the same manner for the data in literatures (9), (11), are also contained. A linear relation can be well established for each glass material. The functional form of this relation is similar to that of rate process but the detailes are left for further studies.

Time to Failure

Since the crack propagation rate of region 1, is given as Eq. (2), the time to failure, tf, can be calculated by integral of this equation over initial crack length, ai, to that at final fracture, af, corresponding to the Kie.

In practice, the region 1 crack propagation is followed by those in regions 2 and 3. Therefore, the decreased crack growth in these regions should be considered. However, the effect of this discrepancy on the prediction of lifetimes is negligible, since the crack propagation in these regions are comparatively high and constitutes only a minor fraction of the total lifetime.

This calculated results are shown in Fig. 7 as a relation between the initial stress intensity, Kii, and time to failure, tf, for various environments. Since the environmental fracture toughness, Kie, value in an extremely dry environment is much higher than those in humid ones (see Fig.4). Accordingly the time to failure in dry environment calculated to be much longer than that in humid air and distilled water. This tendency well coincides with test data, suggesting that dry atmosphere is very favourable for silica glass.

CONCLUSIONS

Crack propagation behaviour in silica glass is studied over the entire range of stress intensity in various environments. The main results are as follow;

(1) The region 1 static fatigue crack propagation curve, da/dt-K, of silica glass is characterized by the parallel curves each other, shifting into higher stress intensity region with decreasing the humidity in an air.

(2) This behaviour can be rationalized by introducing newly proposed parameter, environmental fracture toughness, Kie, which is the measure of the degree of degradation of the material at the crack tip caused by the interaction with water molecule.

(3) This Kie is found to be linearly related with the water vapour pressure on the log-log paper. In case of the distilled water environment, the Kie decreases with temperature.

(4) The Kie is closely correlated with the crack propagation rate da/dt, in the so called region 1.

ACKNOWLEDGEMENT

Financial support by the Grants-in-Aid for Scientific Research through the Japan ministry of education (Project No. 61550051) is gratefully acknowledged.

The authors are grateful to Professor Stef[illegible]

AD-A184 047 FATIGUE '87 VOLUME 3(U) VIRGINIA UNIV CHARLOTTESVILLE SCHOOL OF ENGINEERING AND APPLIED SCIENCE 3/6
R O RITCHIE ET AL. JUN 87 ARO-24134.3-MS-CF
UNCLASSIFIED N00014-87-G-0008 F/G 20/11 NL

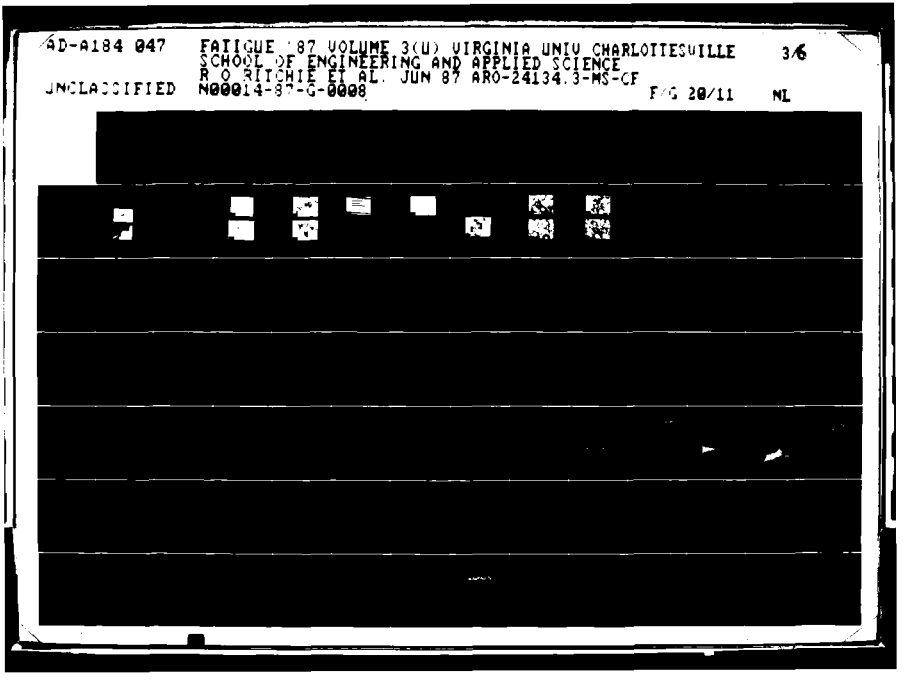

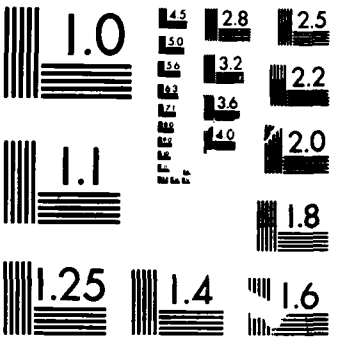

MICROCOPY RESOLUTION TEST CHART
NATIONAL BUREAU OF STANDARDS-1963-A

STANZl of University of Wien and Professor Elmer TSCHEGG of Technical University Wien, Austria for their stimulating discussions during their stay at Tohoku University, Japan. Thanks are also due to Mr. S. Honda, graduate student of Tohoku University, for experimental assistance.

REFERENCES

(1) Sakaguchi, S. and Hibino, T., J. Mater. Sci., Vol. 19., 1984, pp. 3416-3420.

(2) Wiederhorn, S. M., "Mechanisms of Subcritical Crack Growth in Glass", "Fracture Mechanics of Ceramics", Edited by R. C. Brandt, P. P. H. Hasselmann and F. F. Lange, Plenum Press, New York, U.S.A., 1978.

(3) Sakaguchi, S., Sawaki, Y., Abe, Y. and Kawasaki, T. J. Mater. Sci., Vol. 17., 1982, pp. 2878-2886.

(4) Sawaki, Y., Sakaguchi, S., Abe, Y. and Kawasaki, T. Trans. IECE Japan., Vol.E65., 1982, pp. 310-317.

(5) Sawaki, Y. and Kawasaki, T., "Determination of Fatigue Characteristic Values by Conventional Rotary Bending Specimen", "Fatigue 84", Edited by C.J. Beevers, EMAS, U.K., 1984.

(6) Sawaki, Y., Tada, S., Hashimoto, S. and Kawasaki, T to be appeared in Int. J. Fracture.

(7) Newman, J. C. Jr., "Stress Analysis of the Compact Specimen Including the Effect of Pin Loading", ASTM STP 560, "Fracture Analysis", Edited by P.C. Paris and G.R. Irwin, 1974.

(8) Wiederhorn, S. M., J. Ameri. Ceramic Soc., Vol.52., 1969, pp. 95-105.

(9) Schönert, K., Umhauer, H. and Klemm, W., "The Influence of Temerature and Environment on the Slow Crack Propagation in Glass", "Fracture 1969", Edited by P.L. Platt, Chapman and Hall, U.K., 1969.

(10) Charles, R. J., J. Appl. Phys., Vol.29., 1958, pp. 1549-1553.

(11) Wiederhorn, S.M. and Bolz, L.H., J. Ameri. Ceramic Soc., Vol.53., 1970, pp.543-548.

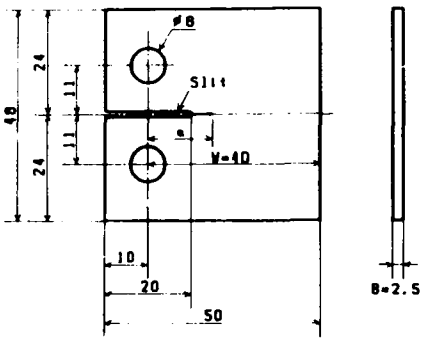

Figure 1 Size and dimensions of the specimen

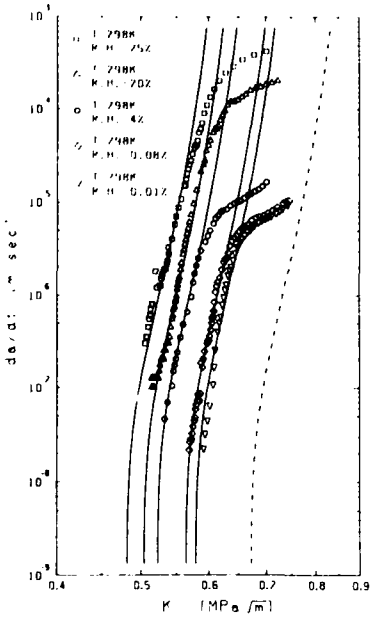

Figure 2 da/dt-K in an air Effect of humidity

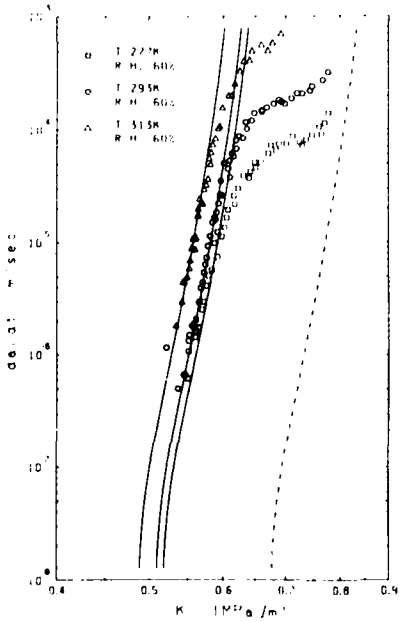

Figure 3 da/dt-K in an air Effect of temperature

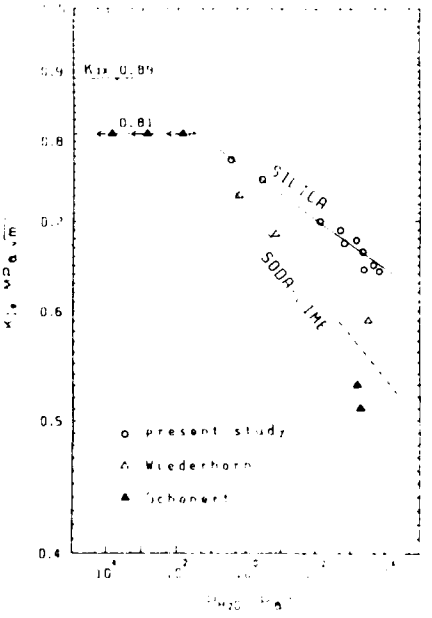

Figure 4 Environmental fracture toughness, K_{Ie}

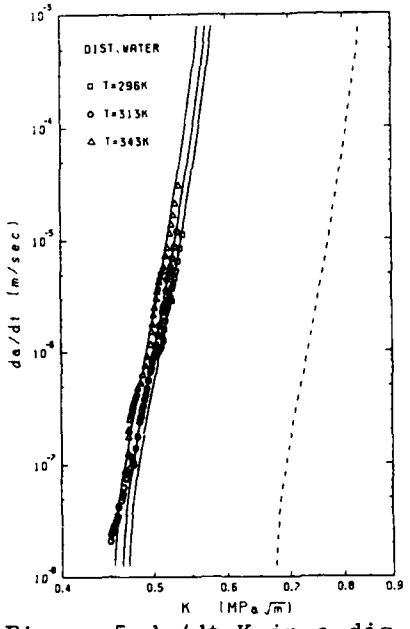

Figure 5 da/dt-K in a distilled water

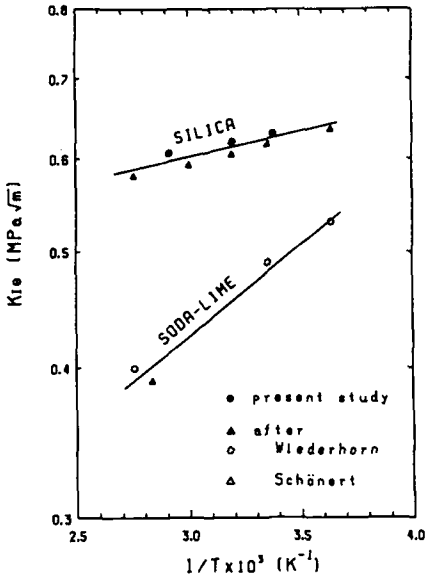

Figure 6 Environmental fracture toughness, Kie

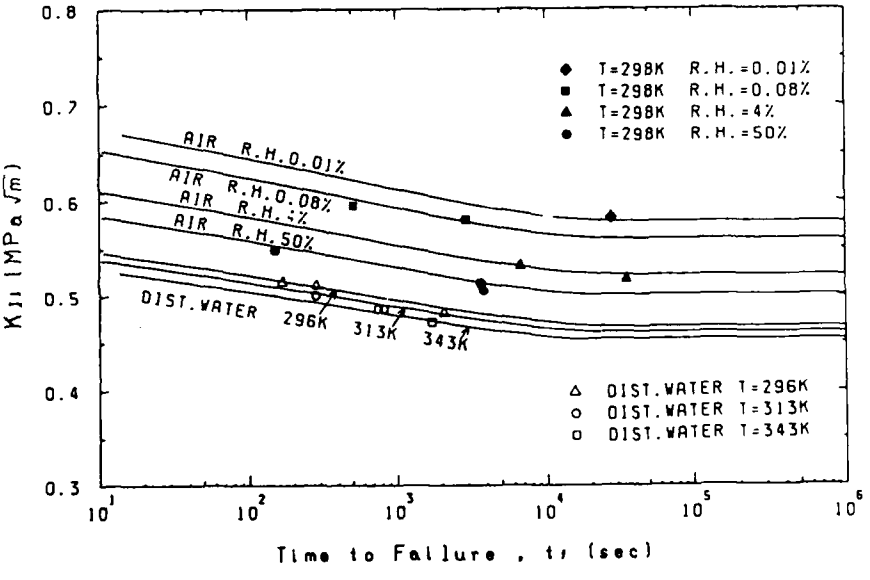

Figure 7 Initial stress intensity factor, Kii, vs. time to failure, tf

EFFECT OF INTERFACE ON MECHANICAL PROPERTIES OF GRAPHITE / 201 ALUMINUM COMPOSITES

J. Seyyedi*, H. Nayeb - Hashemi* and J. Blucher*

The effect of interface on mechanical properties of Gr/201 Al composite material, was investigated after being heat treated in vacuum for 24 hours at 450°C, 500°C and 545°C. The longitudinal tensile and compressive strengths declined as a result of heat treatment. However, an increase in the interfacial shear strength was observed through a steady decrease in the amount of fiber pullout with increasing the heat treatment temperature. Transmission electron microscopic studies revealed the formation and growth of Al_4C_3 and Al_4O_4C in the interface which degraded the fiber surface. This fiber surface appears to be responsible for a decrease in strength at elevated temperatures. Tension -tension fatigue behavior of these composites were evaluated. The results showed that the failure was controlled by a combination of matrix and interfacial zone properties.

INTRODUCTION

Advanced fiber reinforced composites consist of fibers, such as carbon, glass, aramid and boron, which are most often embedded in a polymeric matrix. However, polymeric composites exhibit quasi-brittle behavior, and are also not suitable for high temperature applications. Consequently, considerable interest has been shown in the development of metal-matrix composites, in particular, graphite fiber reinforced aluminum composites. The difference in chemical potential between graphite and aluminum provides a driving force for diffusion or chemical reaction when these composites are subjected to high temperatures, either during manufacturing or while in service. An interfacial reaction zone of some thickness (usually ranging from several nanometers to a few microns) then may develop which can effect the fiber-matrix bond and hence the mechanical behavior of the composite.

Blankenburgs (1) showed that aluminum carbide, Al_4C_3, forms on the surface of carbon fibers at temperatures above 500°C. The tensile strength of the composite improved considerably after development of relatively small amounts of carbide. However, further formation of carbide did not degrade the composite

*Dept. Mech. Eng. Northeastern University, Boston, Ma 02115.

strength. Similarly, Harrigan (2) reported that even prolonged exposure at high temperatures did not significantly change the interface, and the strength of the composite was not degraded. In contrast, Jackson (3) and Khan (4) showed that up to 500°C, little degradation of strength occurred while for composites exposed to higher temperatures the strength declined rather significantly. The formation of aluminum carbide at the fiber-matrix interface was also considered to be the cause for poor composite properties observed by Pepper and Penty (5), Okura et al. (6) and Xiangun et al. (7).

Although all research results are in agreement about the formation and growth of carbide, but not all show similar carbide influence on mechanical properties. The fabrication methods of graphite reinforced aluminum composites as well as the inherent properties of the matrix are expected to influence both monotonic and fatigue behaviors. Amateau and Hanna (8) observed that composites produced by liquid metal infiltration had superior fatigue properties as compared to those of composites prepared by hot-pressing. It was also found that the fatigue behavior was controlled by the matrix properties. Baker et al. (9) obtained poor fatigue properties for composites produced at high pressing temperatures. This was attributed to increased aluminum carbide formation. The mechanism of fatigue failure was described as a process of matrix cracks propagating along the path of previously broken fibers.

Despite the cited articles and a number of other works, the literature is rather meager on the effect of interfacial reaction zone on bond strength (interfacial shear strength), on compressive and fatigue behaviors of this class of composites. The present study was undertaken to explore the effect of prolonged high temperature exposure on formation and growth of the interfacial reaction zone and its impact on the overall properties of Gr/201Al composite.

EXPERIMENTAL DETAILS

Material

The graphite/201 aluminum composite (41 vol pct fiber) used in this investigation was fabricated by DWA Composite Specialties, Inc., using liquid metal infiltrated graphite fibers obtained from Materials Concepts, Inc. The graphite fibers used were Thornel P-55, with the following characteristics: diameter 10 μm, tensile strength 1720 MPa and modulus 380 GPa. Pitch 55 fiber tows were drawn through a Ti-B coating chamber and then through a molten bath of 201 aluminum alloy. The coating is to promote wetting and to reduce fiber - melt chemical interaction. The diameter of the resultant graphite/201 Al wire (precursor wire) was typically 0.064 cm.

Fabrication of the precursor wire into panels was done by DWA Composite Specialties, Inc., using the solid-state diffusion bonding technique. This process involved pressing of packed wires within two cover foils for 40 minutes at 21 MPa at about 555°C. The consolidated unidirectional two-ply panel was then trimmed and cleaned in a HNO3/HF/H20 solution. After being cut into strips of appropriate size, they were encapsulated in vacuums of better than 1.34×10^{-4} Pa (10^{-6} torr) and then heat treated at 450°C, 500°C and 545°C (solidus temperature of the matrix is 565°C).

Experimental Procedure

Tensile specimens were cut from unidirectional composite strips using a low speed diamond cutter. The specimens dimensions were : 15.24cm long, 1.27cm wide, and 0.11cm thick. The specimens were tabbed with 0.15cm thick aluminum using CY-1000 methyl-2-cyanoacrylate adhesive. Figure 1 shows the specimen configuration. Test were performed on an Instron 1350 hydraulic testing machine at an actuator velocity of 0.15 cm/min. The stress-strain curves to failure were obtained using an extensometer with 2.54cm gage length. A universal joint was used to align specimens with the center line of the loading train.

Tensile tests were also conducted along the transverse direction on rectangular sided specimens of 10.16cm x 1.27cm x 0.11cm dimensions. After tabbing the specimens, they were pulled to failure on an Instron 1122 screw type mechanical testing machine outfitted with hydraulic grips and a 500-kg load cell. The crosshead velocity was 0.10 cm/min. The stress-strain curves were determined using an extensometer with a gage length of 1.27cm.

Tension-tension fatigue behavior was measured on rectangular sided specimens of 10.16cm x 1.27cm x 0.11cm size, at stress ratio of about zero. Testing was performed on Instron 1350 machine under load control with a sinusoidal wave form and a frequency of 20 Hz. Tests which did not result in failure in 2 to 6×10^6 cycles were terminated.

Compression tests were performed along the axial direction on rectangular sided specimens of 5.08cm x 1.27cm x 0.11cm dimensions. The specimen ends were reinforced with 1.90cm long by 0.15cm thick aluminum tabs. Electrical resistance strain gages were mounted at the center of each specimen on one side along the loading direction and strain was measured throughout the test by means of a strain recorder unit. An Instron 1350 testing machine with an actuator velocity of 0.15cm/min was utilized. Upon completion of each test, fracture surfaces were studied by scanning electron microscopy (SEM).

The interfacial shear strengths were determined from measurement of the critical fiber lengths produced as a result of

tensile testing. A partial dissolution of the 201 alloy matrix, using a few drops of 1 molar sodium hydroxide, was followed by a gentle removal of the separated fibers. Using a microscope equipped with a filar micrometer eyepiece, a critical fiber length was then established by finding the statistical distribution of the broken fibers and evaluating the mean value.

As a qualitative step for identification of the interfacial constituents, the graphite fibers were separated from composite specimens. This was carried out using a solution of sodium hydroxide in absolute methanol. Absolute methanol was used instead of water to avoid the dissolution of aluminum carbide in water (Kosolapora (10)). The specimens were soaked in the alkali solution for one week. The loose fibers were then removed and cleaned in absolute methanol. Interfacial regions still attached to separate fibers were analyzed by using the selected area diffraction technique, with an applied voltage of 120KV, in a transmission electron microscope (TEM).

Finally, microhardness tests were performed on the matrix alloy for both as received and heat treated composites. A Kentron AK8 microhardness tester was utilized with a Knoop indenter and an applied load of 0.05 kgf.

RESULTS AND DISCUSSION

Analysis of Interfacial Microstructure

Transmission electron microscopic studies of the loose fibers were carried out as a first step in determining the identity of interfacial constituents. Figure 2 reveals a diffraction pattern for an interfacial particle shown in Fig. 3. An examination of the pattern identifies the compound particle as Al_4C_3. The spotty nature of the diffraction pattern seems to indicate the presence of relatively coarse grains. Some degree of texture is also apparent in the pattern. This type of patterns usually were observed for composite specimens heat treated at 500°C and 545°C temperatures. Al_4O_4C, γ-Al_2O_3 and TiB_2 compounds were found in the interface region of as-received and 450°C heat treated specimens. Work is currently in progress for a more rigorous investigation of the nature and the size of interfacial constituent layers using specimens that are being thinned to electron transparency and subsequently examined in a scanning transmission electron microscope.

The Effect of Heat Treatment on 201 Al Alloy Matrix

Microhardness tests were carried out in conjunction with metallographic examinations in order to evaluate the effect of heat treatment on the matrix material. Table 1 shows the results of microhardness tests.

TABLE 1 - Microhardness data for 201 Al alloy matrix

Specimen	Measured Knoop Hardness No.(kgf/mm^2)
as received	78.8
$450^{o}c$-24h	62.0
$500^{o}c$-24h	55.0
$545^{o}c$-24h	68.2

The results indicate that the matrix material of the as-received composite is stronger than that of heat treated at $545^{o}C$. Considering the manufacturing temperature ($555^{o}C$), and natural aging (2 years) of the as-received material, as compared to the composite heat treated at $545^{o}C$ and naturally aged for one year, one anticipates a strength difference of about 5% between them. Repetition of microhardness tests did not produce any different results. Currently experiment is in progress (using TEM specimens) to analyze the microstructure of the matrix, and to find possible sources of strengthening of the as-received matrix material. A relatively lower strengths observed with matrix alloy heat treated at $450^{o}C$ and $500^{o}C$ is due to overaging effect.

Tensile Behavior

Figure 4 depicts typical longitudinal tensile stress-strain curves for Gr/201 Al composite specimens. The observed strengths are lower than rule of mixtures (ROM) strengths. The effect of prior high-temperature exposure on the room temperature tensile properties are summarized in Fig. 5. As can be seen, thermal exposure has a drastic effect on the tensile strength. This reduction in the composite strength can be related to the chemical reaction at the fiber-matrix interface. The primary reaction product at the interface is Al_4C_3 which is formed on lateral sides of the fibers. The development of brittle aluminum carbide will strengthen the fiber-matrix bond and will degrade the surface of the fiber. The fiber surface degradation appears to get enhanced with increasing temperature. Consequently, the fibers develop sites of enhanced stress concentrations resulting in deterioration of the longitudinal tensile strength. Furthermore, the brittle carbide phase formed at the interface is ineffectual in transferring loads to the fibers. This in turn can yield lower strengths for heat treated composite specimens.

The failure modes of all specimens were identical. The failure consisted of fiber fracture and propagation of the cracks along the interface (shear cracks). These cracks are likely to have been initiated at the point of maximum stress concentration and propagate along the fiber-matrix interface before the specimen

fails. SEM examinations of the fracture surface revealed brittle fracture of fibers and considerable plastic deformation in the matrix between the fibers (Fig. 6). Detailed examination of the fracture surfaces showed a declining trend in the amount of fiber pullouts with increasing the heat treatment temperature. Less pullout in turn implies stronger bond between fiber and matrix and thus higher strengths for heat treated specimens as compared to as-received. This conclusion is contradictory to the observed composite strengths. However, the ineffectiveness of the brittle intermetallic interfacial constituents in transferring loads to the fibers and the fiber surface degradation are principally responsible for lower strengths observed with the heat treated materials.

Figure 7 shows a close-up view of the lateral surface of the fibers failed in tension for as-received and heat treated specimens at 545^{o}C, respectively. The apparent roughening of the fiber surface with heat treatment is attributed to heterogeneous reaction of aluminum matrix and graphite fiber, therefore, it is considered that stress concentration occurs at some regions of rough surface and tensile strength decreases accordingly.

The modulus of elasticity (averaged over initial and secondary moduli) seemed (Fig.5) to be virtually unchanged after the high-temperature treatment, implying that the fiber modulus was unaffected despite the observed surface damage and consequent degradation in fiber strength.

The transverse tensile strength of the composites was much lower than expected. The strength was independent of the degree of heat treatment and averaged about 18.2 MPa for all the specimens. Figure 8 illustrates a typical fractograph for a representative transverse tensile specimen. The surfaces of the graphite fibers are clearly visible with little or no interfacial/matrix material adhering to them. Failure is along the fiber direction and seems to occur at fiber-matrix interface for both as-received and the heat treated specimens.

Compressive Behavior

Representative compressive stress-strain diagrams are shown in Fig. 9. The curves demonstrated an initial linear region followed by a non-linear behavior. The initial modulus of elasticity seemed to vary slightly among different specimens, and was found to average about 150 GPa. The bilinear behavior of the stress-strain curves may be attributed to the yielding of the matrix (Majidi et al. (11)) and the formation of micro-cracks along the interface. The compressive strengths were generally lower than tensile strengths and appeared to be little sensitive to heat treatment.

The mechanism of failure in compression was found to be by the

formation and linkage of micro-cracks along the fiber-matrix interface. This is followed by shearing of the fibers at 45° to the loading direction. Figure 10 is a typical micrograph showing several micro-cracks formed along the axial direction of the composite failed in compression.

Interfacial Shear Strength

The effective interfacial shear strength was estimated from measured mean fiber segments lengths, and using the equation developed by Kelly and Davis (12). Figure 11 depicts the results for all Gr/201 Al composite specimens. The fiber-matrix interfacial shear strength appears to rise with increasing the heat treatment temperature. This can be attributed to the formation of intermetallics which improve the fiber-matrix bond. Confidence in the accuracy of the preceding results may be gained when one observes that the calculated shear strengths do not exceed the shear strengths of the matrix alloy.

Fatigue Behavior

The fatigue test results are presented in Fig. 12 in the form of stress-cycle life (S-N) curves for both as-received and heat treated composites. A S-N curve, adopted from reference (8), for as-cast 201 Al alloy is also shown for comparison. The fatigue experiments were performed at stress ratio ($\sigma_{min}/\sigma_{max}$) of zero and at maximum stress ranging from 0.7 to 0.9 of the corresponding ultimate tensile strength. The results showed that the fatigue strengths of the composites are far superior to that of unreinforced alloy material over the range of life cycle from 1 to 10^7 cycles.

The fatigue strength of the as-received composite material is greater than those of the heat treated ones. The fatigue strength declines significantly with increasing heat treatment temperature. These results are in contradiction to those of Dvorak and Tarn(13), and Christian(14), who reported that heat treatment had very little effect on fatigue behavior of the composites. They concluded that the fatigue characteristic of Borsic aluminum composites are controlled by the matrix properties alone. Similar conclusions have been drawn by Amateau and Hanna (8), from their fatigue work on graphite/aluminum composites. On the other hand, the current research results show that if the matrix was the sole controlling factor of the fatigue behavior (assuming that the fatigue life is controlled by the number of cycles to initiate cracks in matrix, and propagation life is independent of the microstructure of matrix) then the fatigue strength degradation should have increased in the following order: as-received, 545°C, 450°C, and 500°C, respectively. Conversely, if the fatigue strength (crack initiation) is based on the degradation of the interface, then the lowest fatigue properties should be anticipated from 545°C

specimens, which is consistent with experimental results. However, it may be argued that the crack initiation at the interface may result in fracturing the fibers and hence yields very low fatigue properties for these materials. This might have been prevented by formation of branch cracks along the fiber-matrix interface, because of extremely low transverse bond strengths. A low transverse strength causes fiber-matrix debonding. Cracks can, nonetheless, still propagate in the matrix and be arrested at other fiber-matrix interfaces and thus preventing fiber fracture. Final failure of the composite is as a result of interaction of these cracks and loss of fiber-matrix bond, leading to nonuniform loading (tensile overload) of composite structure. Figures 13 through 15 show the micro-mechansim of fatigue failure in this composite. The fractography shows cracks initiation at the interface and their subsequent propagation in the matrix (Figs.14 and 15.)

CONCLUSIONS

The following conclusions can be derived from the present investigation:

1. The longitudinal tensile strength for Gr/201 Al composite decreases with an increase in the heat treatment temperature. The observed strengths and elastic modulii are lower than those predicted by the rule of mixtures.

2. The formation of brittle intermetallic constituents at the interface in conjunction with fiber surface degradation are the principal parameters in the degradation of composite strength.

3. The transverse tensile strengths were generally much lower than expected. Failure appeared to occur as a result of fiber-matrix debonding for all of the specimens.

4. Under compressive loading, the Gr/201 Al specimens appeared to fail by formation and linkage of longitudinal microcracks at fiber-matrix interface. The measured strengths and elastic modulii were lower than those measured in tensile testing.

5. The interfacial shear strength showed a gradual improvement with increasing heat treatment temperatures. The estimated interfacial shear strengths were lower than of the matrix.

6. The longitudinal fatigue strength decreases significantly with increasing heat treatment temperature. The mechanism of fatigue failure is perceived to be the initiation of cracks in the fiber-matrix interfacial zone and their subsequent propagation within the matrix, and along the interface, leading to a nonuniform load transfer from matrix to fibers, and causing tensile overload failure.

ACKNOWLEDGMENT

The authors are indebted to Professor D.M. Parks, Mechanical Engineering Department, M.I.T. and Professor J. Rossettos, Mechanical Engineering Department, Northeastern University for their valuable suggestions and encouragements. Furthermore, the authors are very thankful to Messrs. John Noon and Wayne Bethoney from the Army Materials and Mechanics Research Center for their constructive criticism and guidance. Financial supports from the U.S. National Science Foundation, the Army Materials and Mechanics Research center, and the Engineering Foundation are gratefully acknowledged.

REFERENCES

(1) Blankenburgs, G., J. Australian Inst. Mets., Vol.14, No.4, 1969, pp., 236-241.

(2) Harrigan, W. C., Jr., Metall. Trans. A, Vol 9A, 1978, pp. 503-507.

(3) Jackson, P. W., Mets. Eng. Quart., August 1969, pp. 22-30.

(4) Khan, I. H., Metall. Trans. A, Vol. 7A, 1976, pp. 1281-1289.

(5) Pepper, R. T. and Penty, R. A., J. Compos. Mats., Vol.8, 1974, pp. 29-37.

(6) Okura, A., Nakata, E. and Sakai, S., J. Japan Inst. Mets., Vol.47, No. 3, 1983, pp. 271-279.

(7) Xiangun, L., Hanlin, Z. and Renjie, W., "The Effect of Long Period Heat-Treatment on Carbon Fiber Reinforced Aluminum Composite," Proc. of the Fifth Intl. Conf. on Composite Materials, (ICCM-V). Edited by W. C. Harrigan, Jr. et al. AIME Publication 1985, pp. 623-629.

(8) Amateau, M. F. and Hanna, W. D., "Fatigue Behavior of Aluminum Alloy - 30% Graphite Fiber Composites," Proc. of the First Intl. Conf. on Composite Materials, (ICCM-I). Edited by E. Scala et al. Vol.1, AIME Publication, 1976, pp. 586-601.

(9) Baker, A. A., Braddick, D. M. and Jackson, P. W., J. Mats. Sci., Vol.7, 1972, pp. 747-762.

(10) Kosolapora, T. Y., "Carbides", translated by N. B. Vangham, Plenum Press, New York, USA, 1971.

(11) Majidi, A. P., Yang, J. M., Pipes, R. B. and Chou, T. W., "Mechanical Behavior of Three-Dimensional Woven Fiber Composites," Proc. of the Fifth Intl. Conf. on Composite Materials, (ICCM -V). Edited by W.C. Harrigan, Jr. et al. AIME Publication, 1985, pp. 1247-1265.

(12) Kelly, A. and Davis, G. J., Metall. Rev., Vol.10, No.37, 1965, pp. 1-75.

(13) Dvorak, G. J. and Tarn, J. Q., "Fatigue and Shakedown in Metal Matrix Composites," Fatigue of Composite Materials, ASTM STP 569, 1975, pp. 145-168.

(14) Christian, J. L, "Axial Fatigue Properties of Metal Matrix Composites," Fatigue of Composite Materials, ASTM STP 569, 1975, pp. 280-294.

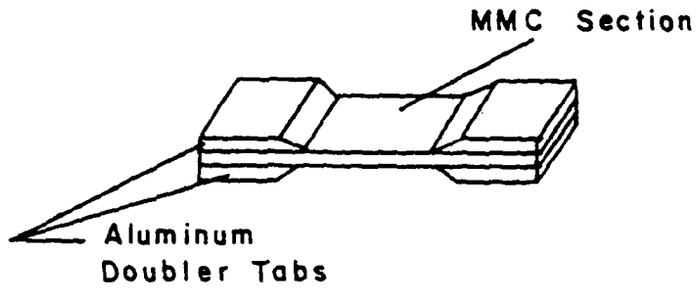

Figure 1 Composite specimen configuration

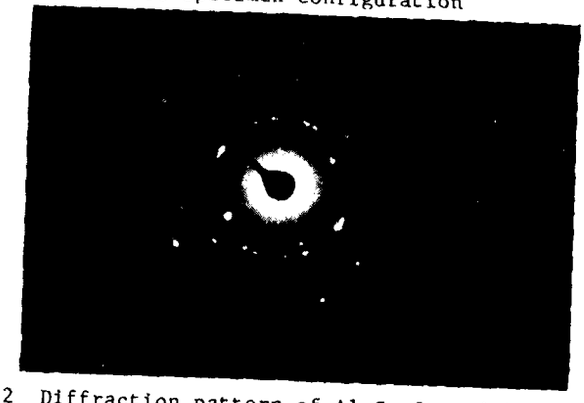

Figure 2 Diffraction pattern of Al_4C_3 formed in the interface of specimen heat treated at 545°C

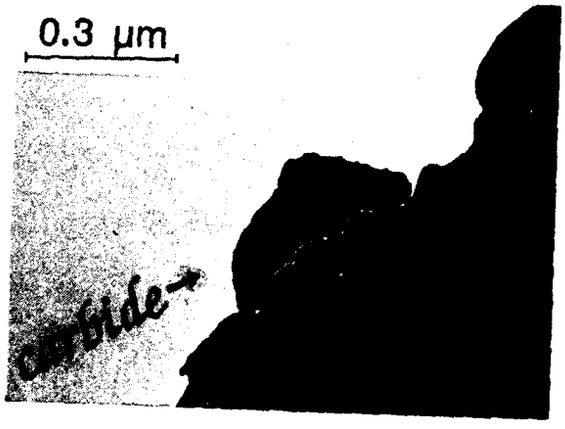

Figure 3 Micrograph revealing the presence of an Al_4C_3 particle for specimen heat treated at 545°C

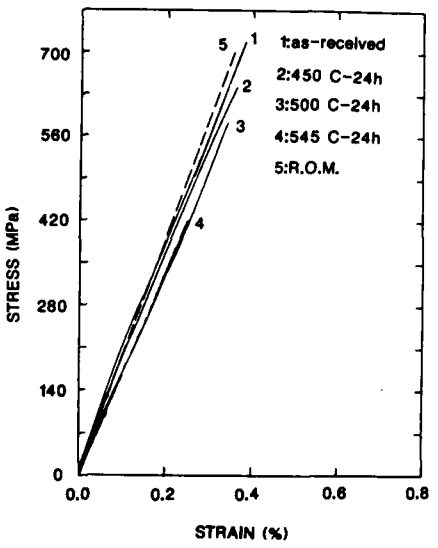

Figure 4 Representative tensile stress-strain curves obtained for Gr/201 Al composite specimens

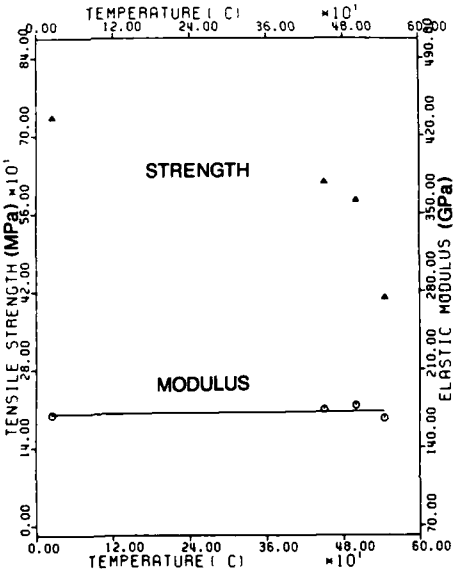

Figure 5 Tensile properties of Gr/201 Al composite as a function of exposure temperature

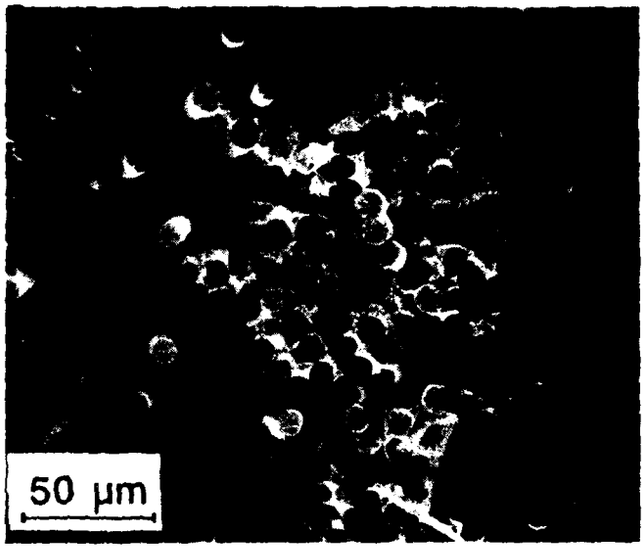

Figure 6 Typical SEM fractographs of Gr/201 Al specimens failed in tension; (a) as-received and (b) heat treated at 545°C

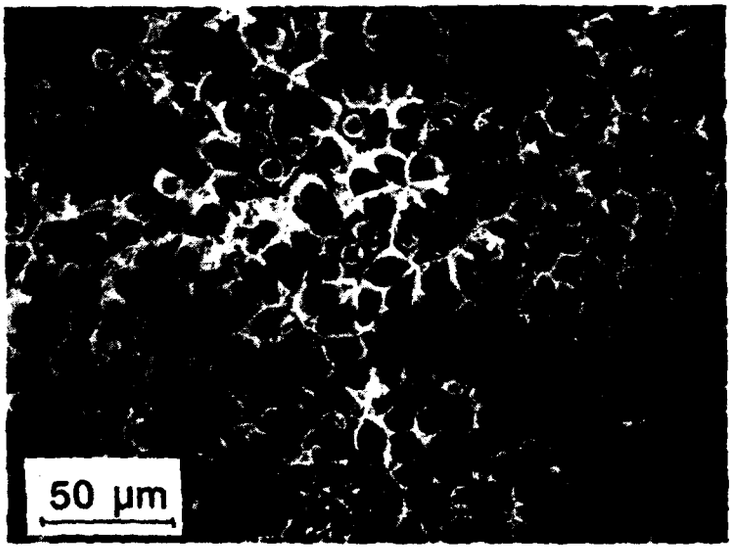

Figure 6 Continued (b)

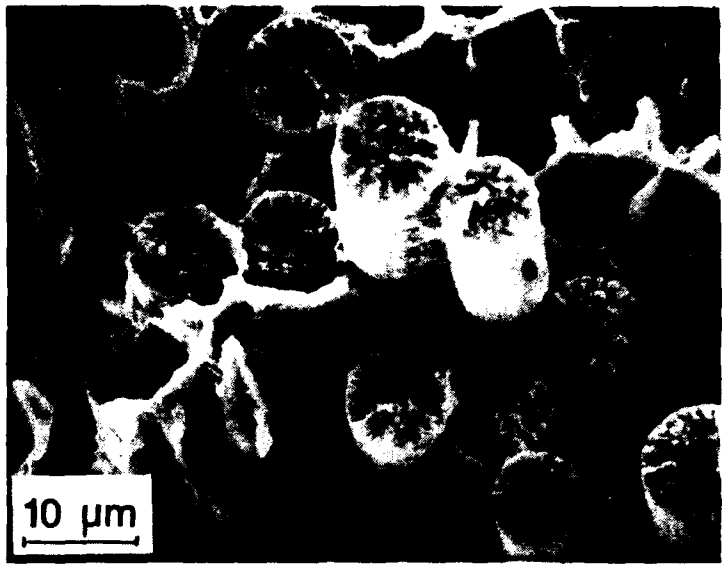

Figure 7 SEM fractographs of Gr/201 Al specimens failed in tension showing the condition of fiber surface for (a) as-received and (b) 545°C heat treated material

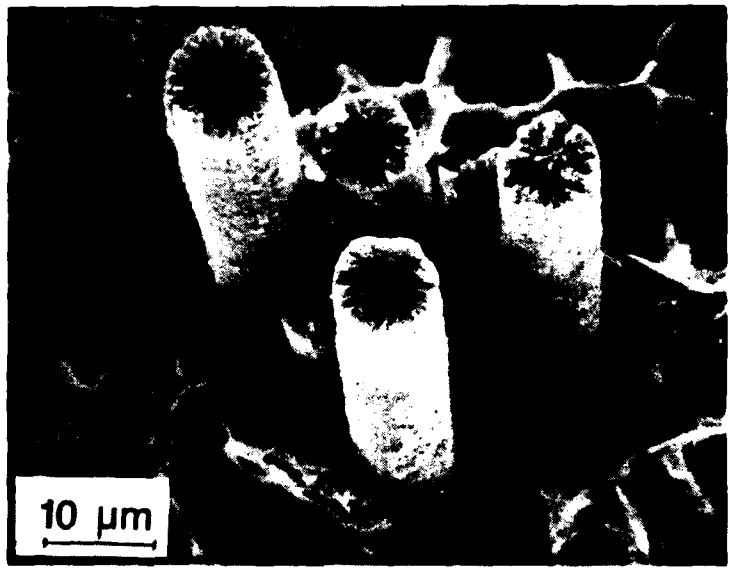

Figure 7 Continued (b)

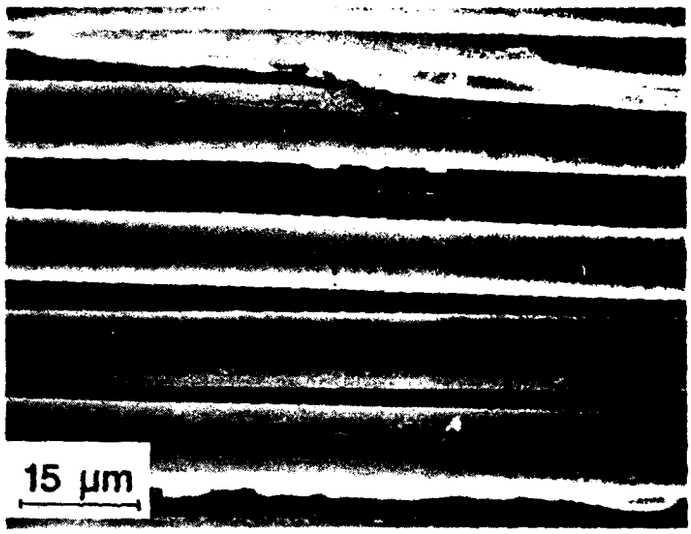

Figure 8 A transverse tensile fractograph for composite heat treated at 545°C

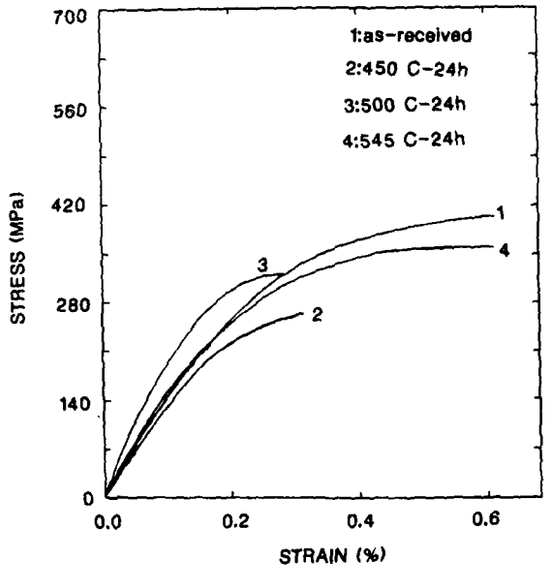

Figure 9 Representative compressive stress-strain curves obtained for Gr/201 Al composite specimens

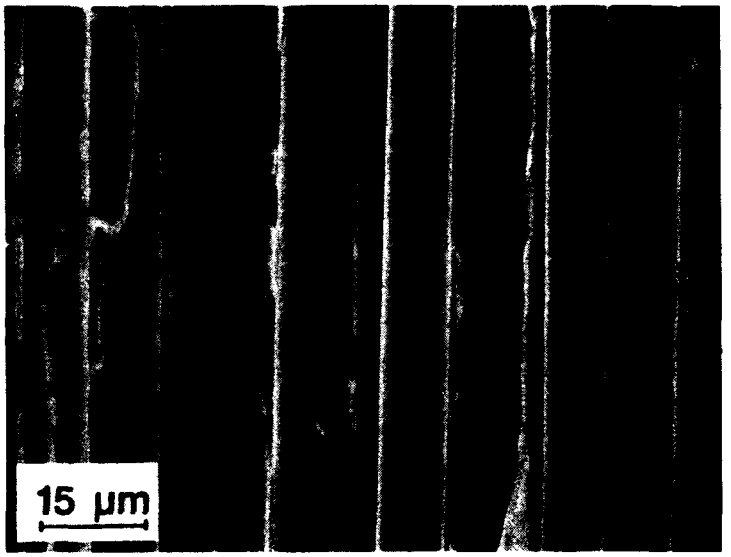

Figure 10 Scanning electron micrograph of a typical compression test specimen (450°C-24h) failed by development of longitudinal cracks

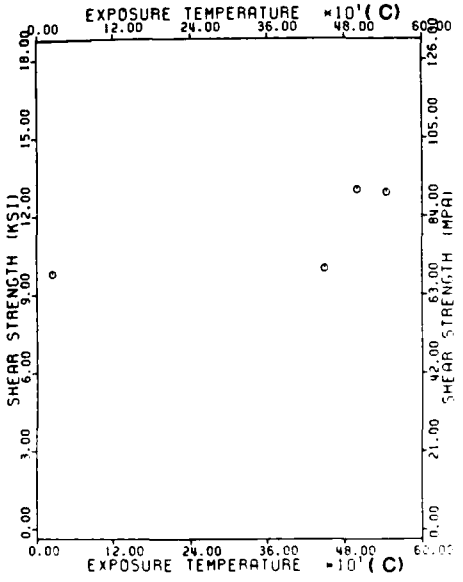

Figure 11 The effect of heat treatment on interfacial shear strength of Gr/201 Al composite

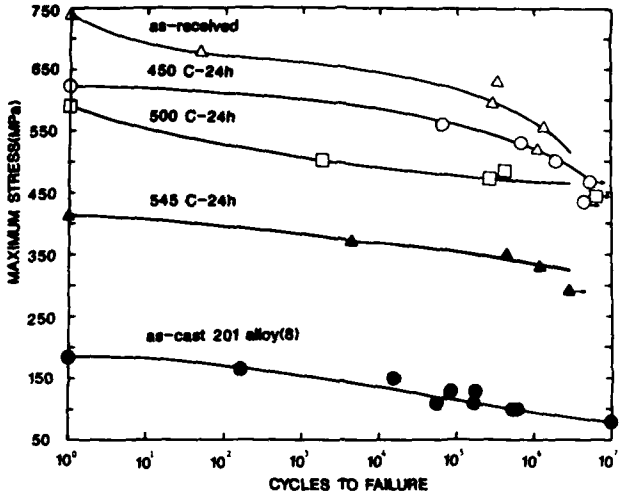

Figure 12 The effect of heat treatment on longitudinal fatigue properties of Gr/201 Al composite

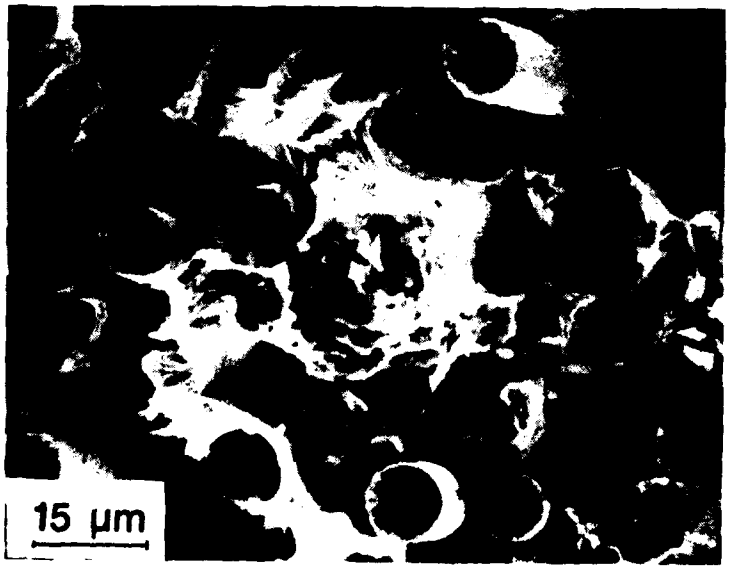

Figure 13 SEM fractograph showing region of tensile overload for as-received composite

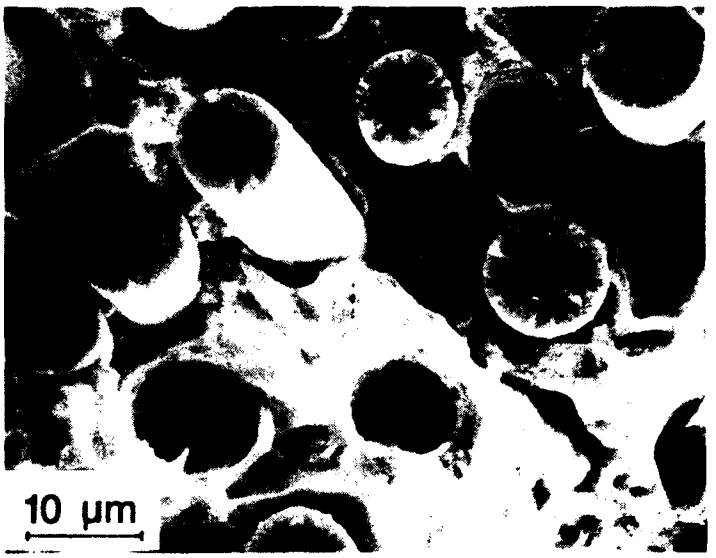

Figure 14 SEM fractographs showing crack propagation through the matrix for specimens heat treated at 500°C

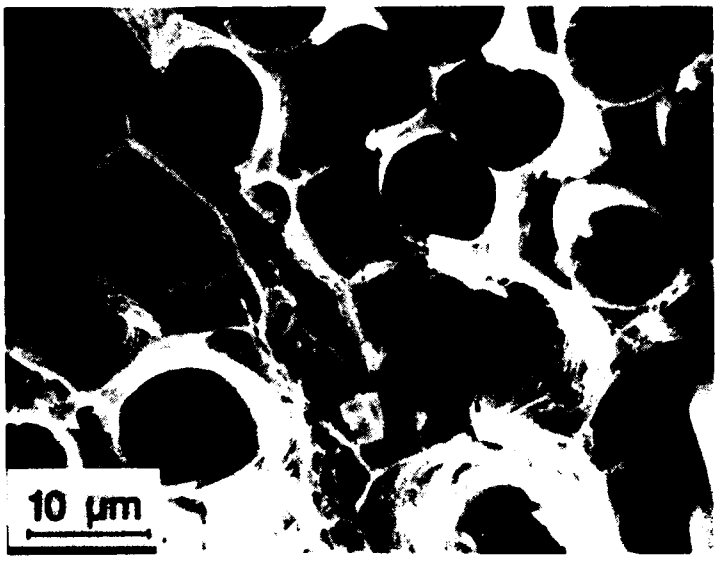

Figure 14 Continued

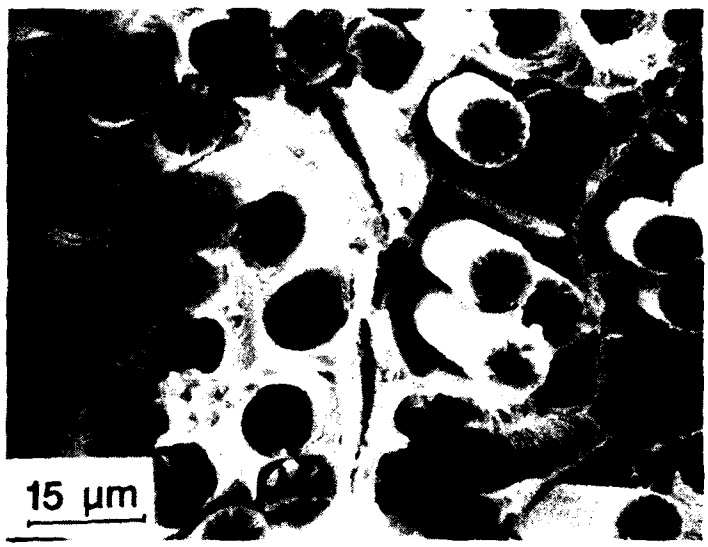

Figure 15 SEM fractographs revealing crack propagation through the matrix for specimens heat treated at 545°C

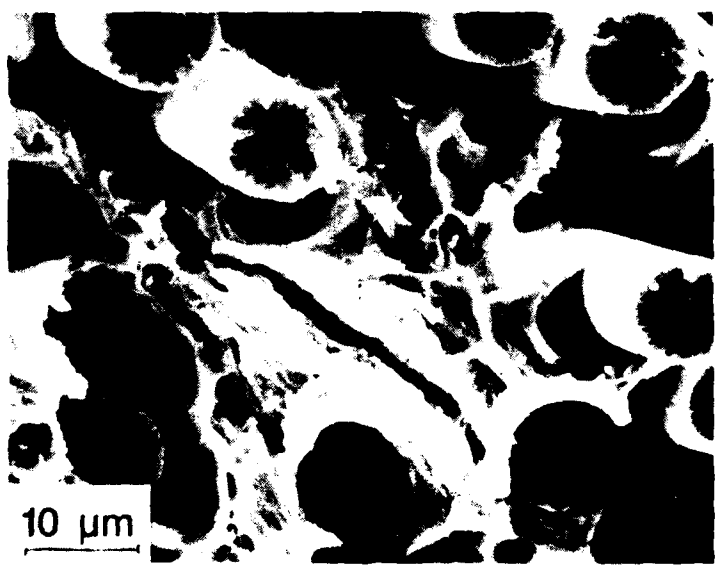

Figure 15 Continued

FATIGUE FAILURE IN BONE CEMENTS FOR HIP JOINT IMPLANTS

D.Taylor *

A method of analysis is developed for predicting fatigue failure of bone cements in use in hip joint prostheses. A stress-intensity-based approach is used to describe failure from pre-existing defects; this compares favourably with results on brittle fracture strengths for specimens with similar types of defects. The analysis is then combined with fatigue data and with the results of stress analyses. It is concluded that fatigue failure of the cement is predictable under present conditions. Possible improvements to mechanical properties can be envisaged which would make the material sufficiently defect tolerant for this application.

INTRODUCTION

Bone cements, based on polymethylmethacrylate (PMMA) are widely used in orthopaedic surgery, especially in the implantation of prostheses such as hip and knee joints. The present work is part of a study into the long term integrity of bone cements in the femoral part of the hip joint prosthesis. Fig.1 shows the arrangement of prosthesis, cement and bone; the cement acts as a filler material to ensure smooth stress transfer from the metal stem to the femur. The use of cement has greatly increased the performance for these prostheses over the last twenty years, but at present there are still an unacceptable number of failures in service (1-3). In many cases failure can be traced to loosening of the stem following cracking in the cement (4,5); at present the cement is considered to be the weak link in the total structure.

The present paper develops a method for predicting fatigue failure of the cement in this application. Defect tolerant approaches are developed, tested on their ability to describe brittle fracture in test specimens, and then combined with fatigue data and with estimates of the stresses present in service.

* Dublin Centre for Biomaterials Research, Mechanical Engineering Department, Trinity College, Dublin, Republic of Ireland.

STRESS ANALYSIS RESULTS

A number of attempts have been made to estimate the stresses in the prosthesis, using both finite element methods (6,7) and strain gauge measurements (8). Unfortunately the number of degrees of freedom required is large and comparison between finite element and strain gauge results shows large differences even for models with as many as 700 elements (8). For our purposes, results will be used from two sources:
a) Crowninshield et al (7), using a finite element method, recorded maximum tensile stresses in the cement which varies between 2.8 MPa and 5.5MPa for the highest likely applied load.
b) Yettram and Wright (8) carried out both finite element and strain gauge measurements, recording the stress in the metal stem. Using the same applied load as in a) and assuming good metal/cement adhesion, the maximum cement stress is expected to be 3.4MPa, caused by bending stresses in the stem around the mid section.

Since the estimate from b) falls within the range of estimates from a), this range, 2.8-5.5MPa, will be taken to be the range of possible maximum stresses in the cement. In normal operation the cement will experience about one million cycles per year, so a fatigue life in excess of ten million cycles is required.

DEFECTS IN THE BONE CEMENT

Two types of defects can be identified:
a) "Intrinsic" Defects: a large number of small, spherical bubbles caused by air entrapment and monomer evaporation which are always present when the polymer is prepared at atmospheric pressure for surgical use. The population of intrinsic defects was measured for the present material under study, Palacos R; as fig.2 shows, this population can be decreased by mixing under vacuum. As well as acting as potential sites for crack growth, these defects increase the effective stress by reducing the cross sectional area by up to 30%.
b)"Introduced"Defects: larger defects which arise when the cement is inserted into the bone. These include cavities, blood and fluid entrapment and laminations caused by premature solidification. In practice, cavities up to 3mm may occur, this being the maximum thickness of the cement layer.

DEFECT TOLERANCE OF BONE CEMENT

PMMA is known to fail in a brittle manner under normal testing conditions, so some form of defect tolerance approach would seem to suggest itself. Fracture toughness values have been measured by various workers (9,10); a value of 1.6MPa$\sqrt{m}$ being the appropriate one for Palacos R.

At an early stage in this work it was noted that a simple LEFM approach could approximately predict the failure strengths of specimens which contained only intrinsic defects, taking the defect

to be a penny-shaped crack of the same size. However, the same approach underestimated the failure strengths of specimens containing large, introduced defects. A possible reason for this was found in the work of Berry (11) who showed, in tests on Perspex, that crazes will arise in initially defect-free material during loading, final fracture being characterised by propagation of these crazes in an LEFM manner. The craze size was 70-100μm in this case. It seemed likely that similar crazes would occur in the vicinity of stress concentrators such as intrinsic or introduced defects, hence a method of analysis was developed based on LEFM fracture by propagation of a small craze/crack in the stress field of a larger, spherical defect.

OUTLINE OF THE ANALYSIS

Fig.3 shows schematically how the application was reduced to a simple model. In use, the material is in the form of a tapered tube of variable thickness up to 3mm, containing defects of various types, the largest being through-thickness cavities. In the model the tube is opened out to form a plate of finite width and constant thickness. Two cases are considered:
a) Small Defects: since there are many small defects it is assumed that the worst case is a defect which breaks the surface whilst retaining an approximately spherical shape.
b) Large Defects: these are modelled as uniform, through-thickness holes of circular section.

Using the approach mentioned above, it is assumed that these defects have small crack-like extensions as shown in fig.4. The value of K for these cracks can be approximated (12) by:

$$K = F\sigma_{0.6a}\sqrt{\pi a} \qquad (1)$$

... where $\sigma_{0.6a}$ is the stress at a point 0.6a along the crack, measured from the tip of the defect, and F is a constant which depends on a/ρ , ρ being the defect radius.

For the case of large cracks a simple Airy stress function was used and modified by the finite plate width. For small defects the Airy function was modified to allow for the spherical shape as well as for the finite plate thickness. The most damaging small defect (see fig.4b) is taken to be a sphere which just breaks the surface, from which a semi-circular crack develops.

This approach was used to predict fracture stress as a function of defect radius for all defect radii up to 3mm. The small defect case is only expected to be valid for defects less than 0.5mm radius, and the large defect case for defects greater than 1.5mm, but in practice it was found that the two solutions merged at the intermediate sizes. For comparison purposes the fracture stress was also calculated on the assumption that the defects can be treated as sharp cracks of the same radius.

COMPARISON OF ANALYSIS WITH EXPERIMENTAL RESULTS

Since the above analysis involved a number of assumptions it was decided to test it against results from simple tensile specimens of thickness similar to that in the application. Flat plate, waisted specimens of cross section 10mm x 4mm and gauge length 100mm were produced by casting Palacos R into metal moulds in such a way as to introduce cavities similar to those in the application. A total of 26 specimens was fractured; after failure the cross sectional area of the defect on the fracture surface was measured and an effective radius calculated assuming the defect to be spherical.

Fig.5 shows the comparison between experimental results and the predictions described above. The following points can be noted:

1) The great majority of results lie between the two lines, implying that typical defects have a geometry which is intermediate between that of a crack and that of a spherical or circular hole.
2) For very small, intrinsic defects the solutions merge to a point which predicts well the fracture stress.
3) Though the defect-and-crack analysis predicts too high a failure stress for large defects, it predicts well the fact that failure stress is virtually independant of defect size in the range 1-3mm. The finite-width correction factor is important in this prediction.
4) The simple crack approach forms a good lower bound for defects smaller than 1mm radius.
5) A small number of results (shown as full data points) gave failure stresses which were the same as those for defect-free material, when corrected for net section stress. It is assumed that these defects had very low stress concentration factors.

PREDICTION OF FATIGUE PROPERTIES

Considering the methods of analysis developed and the fracture strength results obtained, the following policy was evolved for the consideration of fatigue in this material:

a) Failure from defects can be well-described using LEFM analysis, deriving an effective K value.
b) For defects less than 1mm radius, the defect can be treated as a sharp crack.
c) For defects of radius 1-3mm the best model is that of a blunt cavity with a small craze crack at its tip. The model of a spherical cavity can be used if the result is reduced by a factor of 1.4; the result obtained is not sensitive to the value of the cavity radius.
d) It can be assumed that a K-based analysis will be valid for the description of fatigue crack growth as well as of brittle fracture.

Crack growth rate data have been generated for various bone cements (10,13), but not for growth rates in the near-threshold region, which is the region of interest for the present high-cycle application. Fig.6 summarises existing results, showing for comparison

purposes some data on epoxy (14). As fig.6 shows, the attempt to extrapolate this data down to the threshold region leads to large errors - the value of ΔK_{th} could be as low as 0.15MPa$\sqrt{m}$, or as high as 0.4MPa$\sqrt{m}$ if the data curves down to parallel the epoxy results.

More confidence in a threshold estimate can be obtained by examining results from S/N fatigue tests on bone cements (15-18). A large amount of data is available for lives up to one million cycles, so that a value of 7MPa can be estimated to be the endurance limit for the present material at R ratios close to zero. Assuming that the specimens used contained only intrinsic defects, and using the methods described above, one arrives at a threshold value of 0.16MPa$\sqrt{m}$ for the material, which agrees well with the lowest estimate made using fig.6.

PREDICTION OF SAFE STRESSES IN THE APPLICATION

For the case of the prosthesis itself it will be assumed that defects in the size range 1-3mm are always present. Using the methods developed above, and assuming a threshold stress intensity of 0.16MPa$\sqrt{m}$, the stress range corresponding to threshold conditions is found to be 2.2MPa. This is slightly less than the lowest of the values obtained from stress analyses (see above), implying that fatigue failure by the mechanism of crack growth from defects is likely in this application.

COMPLICATING FACTORS

A number of other factors have not been considered in this analysis, largely because there is insufficient information on them at present. Firstly, it is known that the material is sensitive to strain rate and frequency, hence all experimental fatigue data was used at the same frequency as envisaged for the application (about 1Hz). Secondly, the material is known to be temperature sensitive in the range 20-40^{o}C, which has consequences for its behaviour at body temperature (19), and to exhibit slight reductions in strength after periods of exposure to in vivo conditions (20). Concerning the stress conditions, it should be remembered that the figures quoted above from the stress analyses are the maximum values, which only occur in limited locations in the structure; on the other hand, no attempt has been made to correct for the conditions of complex stress which certainly arise in practice.

CAN THE MATERIAL BE MADE TO BE DEFECT TOLERANT?

It is interesting to consider whether the properties of bone cement could be improved so as to bring the endurance limit for 3mm defects above the maximum assumed stress of 5.5MPa, and thus making the material defect-tolerant in this application. Using the present analysis this would require the threshold value to be increased to 0.4MPa$\sqrt{m}$, which is certainly within the capabilities of other

polymers, such as the epoxy shown in fig.6, and may be possible for fibre-reinforced versions of PMMA cement, though as yet the improvements which have been achieved with reinforcement are smaller than this (13).

REFERENCES

(1) Beckenbaugh, R.D. and Ilstrup, D.M., J.Bone Joint Surg. Vol.60A, 1978, pp306-312.
(2) Muller, M.E., Proc.2nd Meeting, The Hip Soc., St.Louis, 1974.
(3) Moreland, J.R., Gruen, T.A., Mai, L. and Amstutz, H.C., The Hip, Chapter 13, 1980, pp281-290.
(4) McBeath, A.A. and Foltz, R.N., Clin.Orthop. Vol.141, 1979, pp66-70.
(5) Pellici, P.M., Salvati, E.A. and Robinson, H.J., J.Bone Joint Surg. Vol.61A, 1979, pp28-33.
(6) Huiskes, R. and Chao, E.Y.S., J.Biomechanics Vol.16, 1983, pp385-409.
(7) Crowninshield, R.D., Brand, R.A., Johnston, M.D. and Milroy, J.C., Clin.Orthop. Vol.146, 1980, pp71-77.
(8) Yettram, A.L. and Wright, K.W.J., J.Biomed.Eng. Vol.1, 1979, pp281-285 and Vol.2, 1980, pp54-59.
(9) Saha, S. and Pal, S., J.Biomed.Mater.Res., Vol.18, 1984, pp435-462.
(10) Rimnac, C.M., Wright, T.M. and McGill, D.L., J.Bone Joint Surg. Vol.68A, 1986, pp281-287.
(11) Kinloch, A.J. and Young, R.J., "Fracture Behaviour of Polymers" 1983, Applied Science Publishers.
(12) Pickard, A.C., "The Application of Three-Dimensional Finite Element Methods to Fracture Mechanics", 1986, EMAS Publishers.
(13) Wright, T.M., Connelly, G.M., Rimnac, C.M., Hertzberg, R.W. and Burstein, A.H., Biomat.and Biomech., 1983, Elsevier Publ.
(14) Taylor, D. "A Compendium of Fatigue Thresholds and Crack Growth Rates", 1985, EMAS Publishers.
(15) Pilliar, R.M., Blackwell, R., MacNab, I. and Cameron, H.U., J.Biomed. Mater.Res. Vol.10, 1976, pp893-906.
(16) Freitag, T.A. and Cannon, S.L., J.Biomed.Mater.Res. Vol.10, 1976, pp805-28.
(17) Stark, C.F., ibid. Vol.13, 1979, pp339-342.
(18) Pilliar, R.M., Bratina, W.J. and Blackwell, R., ASTM-STP 636, 1977, pp206-227, The Amer.Soc.for Testing and Materials.
(19) Hertzberg, R.W. and Manson, J.A., "Fatigue of Engineering Plastics", 1980, Academic Press.
(20) Wright, T.M., Sullivan, D.J. and Arnaczky, S.P., Meeting of the Orthop.Res.Soc., Anaheim, California, March 1983.

ACKNOWLEDGEMENTS

The Dublin Centre for Biomaterials Research acknowledge the continued support of the National Board for Science and Technology, Ireland, and the Institute of Industrial Research and Standards, Ireland, in this research programme.

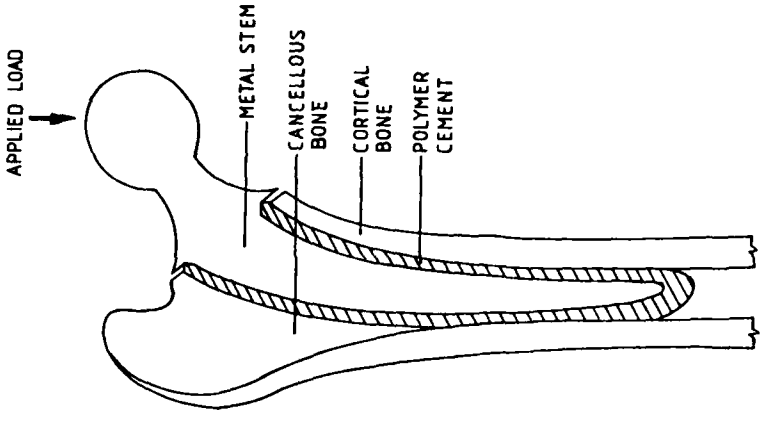

Figure 1 Components of the Hip Joint Prosthesis

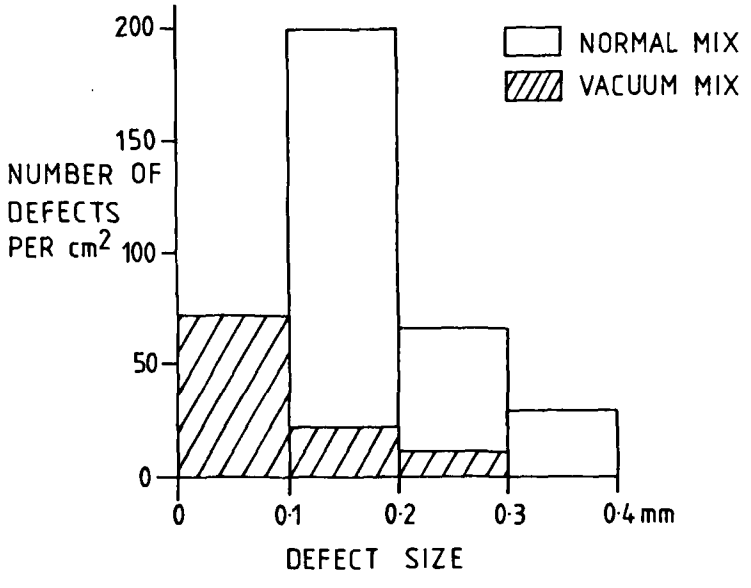

Figure 2 Population of Defects in Palacos R, Normal and Vacuum Mix.

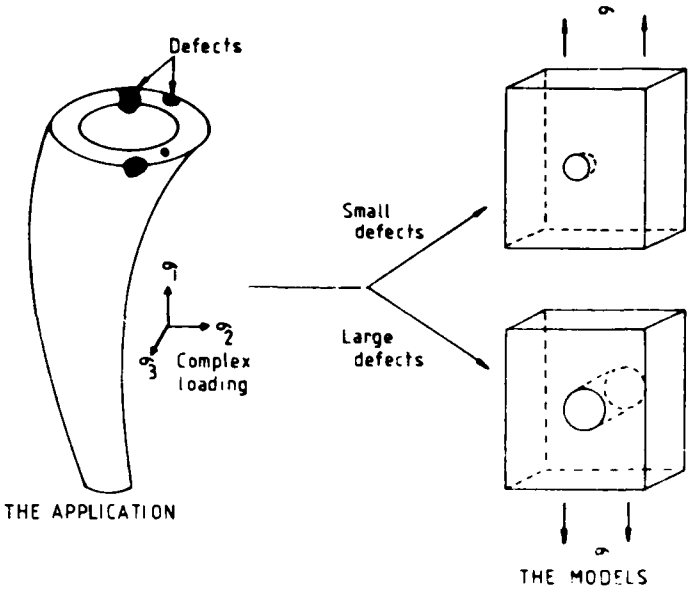

Figure 3 Methodology of the Defect Tolerance Analysis

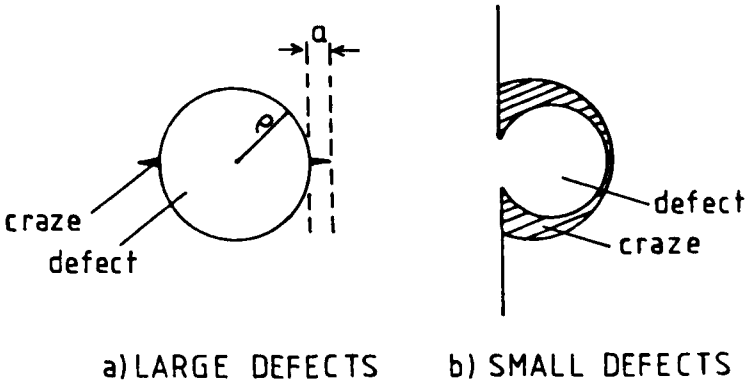

Figure 4 Defect-plus-craze Model for Large and Small Defects

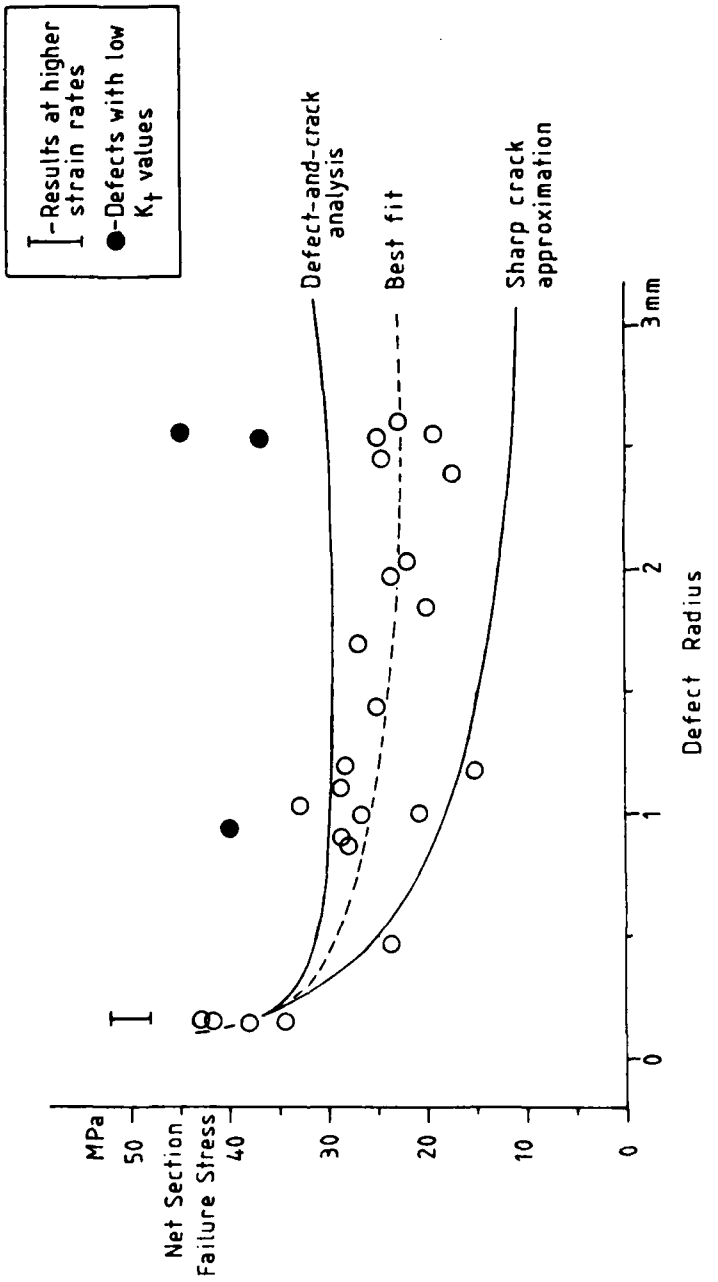

Figure 5 Comparison of Results and Analyses; Brittle Fracture.

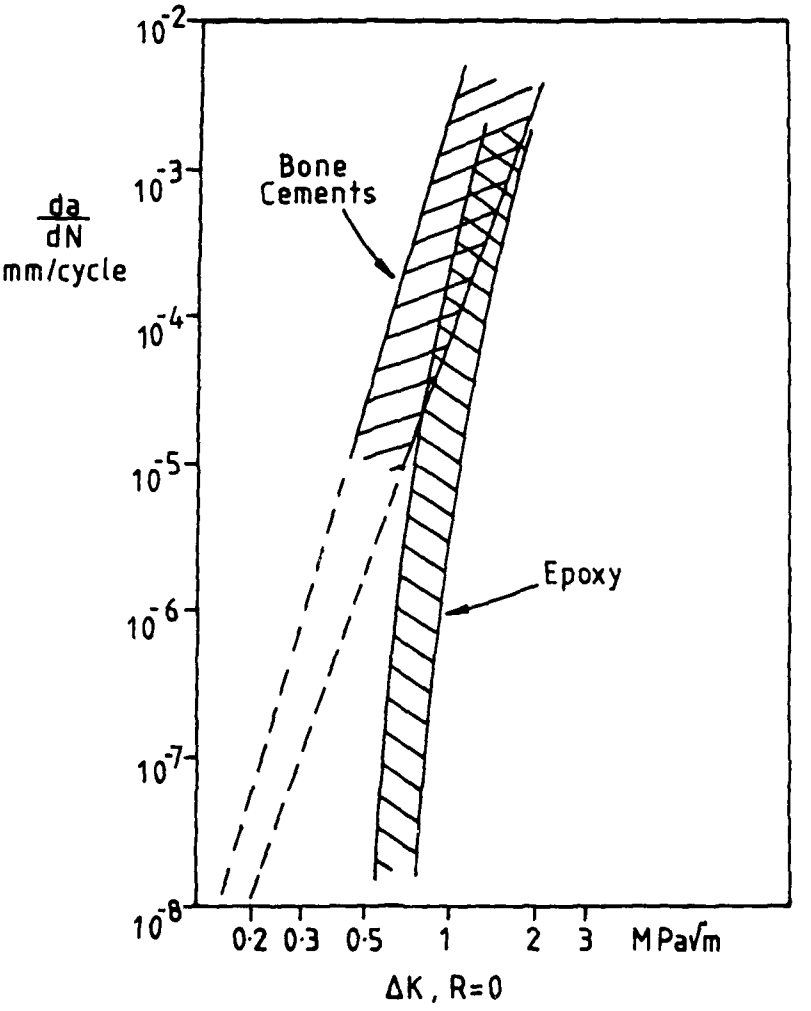

Figure 6 Available Crack Growth Data: Bone Cements and Epoxy.

MODELING AND EXPERIMENTAL TECHNIQUES

FATIGUE CRACK GROWTH: STATISTICAL CONSIDERATIONS

A.F. Blom* and B. Palmberg*

Statistical considerations of fatigue crack growth are presented. All the parameters of importance in a damage tolerance analysis are treated. A review of existing literature information on sources of scatter in fatigue crack growth during service loading is given. Various stochastic fatigue crack growth models are discussed. Present limitations in such models are pointed out and these are partly accounted for by modification of some existing models.

INTRODUCTION

Statistical techniques have been used to assess various fatigue related problems for a long time. While most of the work sofar has been concentrated on the scatter in total fatigue life of test specimens subjected to constant amplitude loading, there has recently become a large interest in the statistical aspects of fatigue crack propagation. This trend is obviously due to the fact that the design philosophies being used in primarily the aerospace field have changed from safe-life and fail-safe approaches to the damage tolerance concept.

The aim of the present paper is to discuss those parameters which are of importance in a probabilistic damage tolerance analysis with emphasis being put on the scatter in fatigue crack growth rates and on statistical models to predict fatigue crack propagation under general spectrum loading. Rather than going into excessive mathematical detail we intend to outline the demands on the statistical modelling from an engineering viewpoint. Limitations in existing models will be discussed and it will also be

* Structures department, The Aeronautical Research Institute of Sweden (FFA), P.O. Box 11021, S-161 11 Bromma, Sweden

emphasized that further experiments are required in order to improve on the present situation. Some calculations are performed in the last section of the paper, to illustrate how the described models can be used both for data reduction and for predictive purposes.

Before starting the discussion on probabilistic damage tolerance analysis and stochastic modelling of fatigue crack growth some historical reflections may be appropriate. It seems that most of the statistical techniques being employed today for these purposes are derived from ideas formulated a long time ago and consequently similar analyses have frequently been carried out in many disciplines within the areas of strength of materials and solid mechanics. Perhaps the first one to carry out such a study was Chaplin who treated the size effect phenomenon by means of a "weakest link" concept already more than a hundred years ago (1, 2). This particular work was long forgotten but another "weakest link" or "largest flaw" theory introduced by Griffith (3) in 1920 came to influence the work by scientists and engineers for a long time. However, although Griffith's theory, stating that the reduction of strength in isotropic materials was due to flaws, discontinuities or defects randomly distributed in the material, was generally accepted there was also a substantial confusion about the interpretation of results. This was due to lack of knowledge about the simultaneous developments in statistical extreme value theory, see Epstein (4) for more historical accounts. The people working with fracture problems did not realize that the analytical relationship between the strength of a specimen and its size would be dependent on the assumed distribution of strength close to flaws as the asymptotic behaviour of sample extremes essentially is determined by the tail behaviour of the assumed distribution. A more stringent approach was introduced by Weibull in his celebrated 1939 paper (5) where he showed how the fracture strength of materials could be represented by a probability distribution. However, Weibull introduced his distribution on an ad hoc basis and did apparently not recognize that it was one of three types of asymptotic distributions for suitably normalized minima (4). This was later clarified by Epstein (6, 7) who discussed the application of the asymptotic theory of extremes to problems of brittle fracture.

Extreme value distributions, and especially the Weibull distribution, have been widely used in fatigue life studies where the total number of load cycles, N, to failure is studied. Another very common distribution for fatigue life is the lognormal distribution which is very close to the Weibull distribution in the central range of the distribution, which is obviously the range where most observations are made. However, in the tail regions of the two distributions there is a significant difference. With a coefficient of variation, v, ($v = \mu/s$ where μ is the mean and s^2 is the variance) equal to 0.6, which is a typical value for N in

constant amplitude fatigue tests, probability estimates were compared using the Weibull and the lognormal models (8). It was pointed out that when N = 20% of the mean life there is almost an order of magnitude difference in failure probabilities.

In our treatment of probabilistic damage tolerance we will not only use both Weibull and lognormal distributions but several others as well. From the historical discussion and the numerical example above we see the importance of mathematicians and statisticans working together with engineers and applied scientists in order to make both physically and mathematically sound models of the complex problems we want to study. Hence, our approach in this paper is to start from what we believe are good existing statistical techniques, point out their engineering limitations and then, at least partly, modify them to better represent our understanding of the actual fatigue crack growth process.

As an end to this introduction it might be appropriate to briefly comment upon the risk levels we are considering. We have earlier stated that the probability of complete failure of a main structural part of an aircraft should be in the order of 10^{-3} to 10^{-5} during the whole life (9). It is interesting to compare these values to those of Ashby (10) who considers that the general public accepts a risk of 10^{-6} per annum, is prepared to fund safety measures if the risk reaches 10^{-4} per annum and insists on safety measures being taken if the rate rises as high as 10^{-3} per annum. Finally, it should also be pointed out, as shown in detail by Payne (11), that for most structures the actual failure rates tend to be two or three orders of magnitude higher than the predicted values due to errors in design. This is in contrast to aircraft structures where the design is verified with substantial amounts of testing including full-scale static tests to ultimate load, full-scale spectrum fatigue tests and in-flight load measurements, which altogether give a rather close agreement between predicted and actual failure rates.

DAMAGE TOLERANCE AND DURABILITY

Before we go into details about scatter considerations and stochastical modelling of fatigue crack growth it is necessary to briefly consider the deterministic approaches to damage tolerance and durability. Firstly, let us define what we mean with these two expressions.

Damage Tolerance

Basically, this approach which was developed by the United States Air Force (12), and which is now adopted with or without minor modifications by virtually all countries for both military and civil aircraft, differs from the original Fail-Safe philosophy in that it assumes cracks to exist in the structure already at the

very first load cycle. Also, a distinction is made between in service inspectable or non-inspectable structures. Presently, with the exception of landing gear, engines and engine mounts all fighter aircraft structures and all inspectable civil aircraft structures are considered as damage tolerant (12, 13). There is a trend to introduce the damage tolerance approach also for engines, e.g. (14).

Durability

While damage tolerance is the principal means to ensure structural safety, durability may be considered as a quantitative measure of the structure's resistance to fatigue cracking under specified service conditions. This means that the economic lifetime, including all inspections, replacements or repairs, should exceed or at least equal the design life based on damage tolerance.

Initial Flaw Size Assumptions

A damage tolerance analysis implies a thorough identification of all critical areas with due regard to the utilization of the aircraft and the impact of failure. According to the US Air Force Military Specification (12) these areas should be classified either as Slow Crack Growth, Fail Safe Multiple Load Path, or Fail Safe Crack Arrest structures. If it is possible to prove that the structure is Fail Safe due to Multiple Load Paths (i.e. load redistribution) or Crack Arrest capability, less stringent conditions have to be satisfied.

As a result of material and structure manufacturing and processing operations small imperfections equivalent to a 0.127 mm radius corner flaw shall be assumed to exist in each hole of each element in the structure. The flaws are assumed to be located in the most unfavourable orientation with respect to applied stresses and material properties. In addition it is assumed that initial flaws of sizes specified in Figure 1 can exist in any separate element of the structure. Only one initial flaw in the most critical hole and one initial flaw at a location other than a hole need to be assumed to exist. Interaction between these assumed initial flaws does not need to be considered. The flaw shape is assumed to be through the thickness (straight crack front), quarter circular or semi-circular. However, other flaw shapes with the same initial stress intensity factor are considered appropriate, particularly at locations in the structure where other shapes are more likely to occur.

Analysis Concepts and Testing

It should be emphasized that the damage tolerance evaluation essentially is analytical but that sufficient testing must be

performed to validate the analytical methodology. No strict requirements exist on how the analysis should be performed but the following steps are normally encouraged by authorities (13, 15).

- Based on structural analysis the most fatigue critical areas are identified.
- Stress intensity factors as function of crack geometries (length, depth - see Figure 1) and applied loading are computed for the identified areas.
- Fatigue crack growth is performed on a cycle-by-cycle basis preferably using tabulated constant amplitude fcg-data.
- If a retardation or retardation/acceleration model is used in the crack growth analysis, this model should be shown to be non-unconservative by relevant testing. For example, the original Willenborg model should not be used.
- In the definition of relevant load- and stress spectra, experimental truncation tests (of the scarce extreme loads) should be performed to obtain a spectrum which minimizes crack growth life for analysis.
- Extreme loads must be considered for residual strength calculations.
- A certain number of stiffened component tests should be performed to validate the prediction capability of crack growth in complex structures.
- Based on the analytical predictions of fatigue crack growth, relevant inspection invervals are defined.

These steps are usually complemented not only with full-scale static tests up to limit load but also with full-scale spectrum fatigue tests. The latter are typically carried out for two design life times in order to detect any cracking at locations which might have been overlooked in the analysis. If no cracking occurs during these two lives artificial flaws are introduced at critical areas and then the spectrum loading is carried out for two more design life times. During the latter phase crack growth is monitored and compared to analytical predictions. The testing is able to provide such comparisons for several locations as cracked components may either be repaired or replaced by new ones. Eventually, the test might end with a residual strength test of a major structural component.

It has to be realized that the original analysis is complemented also with in-flight load measurements and by the non destructive inspections carried out during service. Hence, the

original design life is not necessarily the actual life of the aircraft. It is recognized that individual aircraft in the fleet, especially for fighters, may have been subjected to much harsher load environment than the average aircraft and therefore may have to be taken out of service at an earlier date. During recent years it has been quite common to extend the life times of elder aircraft, originally designed by fail-safe principles, by going into damage tolerance analysis instead. It is in principle possible to extend the design lives even further, if after the nominal life no significant cracking has occurred. This is because the total life of the aircraft will depend on its durability (see definition above) while the damage tolerance ensures, at all stages, the structural safety of the aircraft.

An alternative analytical technique for crack growth predictions makes use of linearized spectrum fatigue crack growth data, e.g. (16). It has yet to be shown whether this method can be used for predictions in the general sense. Current experimental data, e.g. (17, 18), seem to indicate an effect of too many variables, to make this technique a serious alternative to the outline above. However, performing fatigue crack growth measurements during realistic spectrum loading and plotting the results as shown in Figure 2 (15) (crack growth per flight or flight hour, da/dF, versus the spectrum peak stress intensity factor, $\hat{K}$) is very useful in order to compare the predictive capabilities of various models. Figure 2 shows such comparisons for crack growth in Al 7010-T7 plate material subjected to a vertical fin spectrum. (Note the unconservative results when using the original Willenborg model.) This type of spectrum data presentation is also particularly relevant for ranking the fatigue resistance of various alloys, since it is well known that constant amplitude fatigue crack growth data does not necessarily reflect the actual behaviour in spectrum loading, e.g. (19, 20).

We have mentioned this latter technique because it has been adopted within statistical modelling by several workers. In a subsequent section we will come back to this formulation and explain the limitations in more detail.

VARIABILITY IN BASIC PARAMETERS

In this section we will briefly discuss sources of variability in the various input parameters for any damage tolerance analysis. Where enough data exist we will give typical values of scatter as represented by the most commonly used statistical distributions. It will also be discussed, for crack growth data, how raw data may be processed to give as much information as possible.

Load Spectra

The load acting on a complex structure such as an aircraft are related to various manoeuvres characteristic of the aircraft

type and include, for example, taxiing loads, ground-air-ground cycles, gust loads, flight manoeuvres, engine vibrations, cabin pressurization loads etc. For example, it can be mentioned that the full-scale fatigue test of the SAAB SF-340 commuter airliner involves 1543 unique load cases of 124 different kinds (as those mentioned above), (17). It should be emphasized that besides from these in-service loads, which may interact to give rise to multi-axial stresses, there may also exist loads due to manufacturing processes and also environmental load cycling such as varying temperatures and chemical influences.

Normally, some special type of loading is of most importance to the structure. For example, civil aircraft are most strongly influenced by ground-air-ground cycles whereas the flight manoeuvre loads are of most importance for a fighter aircraft. This obviously means that the load spectra being used for testing and analysis purposes are entirely different for civil and military aircraft. As an example we show a typical cumulative exceedance curve of the manoeuvre loads for a fighter aircraft in Figure 3.

Load interaction. It is well known that the information contained in Figure 3 not is quite sufficient since the sequential order of the loads in the spectrum is very important for the fatigue life. Models to account for this influence on the fatigue crack growth rates are normally based on plasticity considerations and as shown in Figure 2 they may predict rather different results, conservative or not, depending on the model chosen. In the flight sequence various parameters influence the crack growth with various amounts. The effect of spectrum variation on crack growth is shown in Figure 4 which is based on experimental results from 102 load spectra variations simulating the lower wing skin of the F-15 aircraft (21). The variations shown to have the greatest impact are those involving modifications of the maximum peak loads. These variations include mission mix, high and low load truncation, exceedance curve variations, and test limit load variations. Variations shown to have significant impact include those which modify all but the highest peak loads throughout the spectrum, such as sequence of missions, compression loads, and peak and valley coupling. Spectra variations shown to produce the least effect are those which modify lesser loads in each mission. These consist of reordering of loads within a mission and flight length variations.

Scatter considerations. In a similar study as the one above, by Dill and Saff (21), Abelkis (22) carried out testing to investigate the effect on crack growth due to a number of variations in the load spectrum. Results were obtained for three different transport aircraft lower wing surfaces which were also stated to be representative for similar bomber spectra. Using spectrum variations that could be expected in service, fleetwide crack

growth scatter by factors of 10 to 100 could be experienced, depending on whether a short-term or long-term spectrum variation was considered.

To further elucidate the scatter in load factors of individual aircraft in a fleet, consider the data in Figure 5 from Impellizzeri et al (23). Here is shown the scatter in load factor exceedances as a function of the average fleet aircraft flight hours at 6 g on the F-4 aircraft. It is readily seen that as an aircraft accumulates flight hours it becomes more likely that it will be subjected to a variety of load cases, and hence its load history will become more and more averaged to those of the other aircraft within the fleet. In order to study the impact of this usage variation on fatigue crack growth analysis was performed by Dill and Saff (21). They used upper and lower limits of the scatter data obtained at 4 g and 6 g, corresponding to 50% and 75% of the design limit load, respectively, to develop upper and lower bound cycle-by-cycle baseline stress spectra. Assuming an initial through the thickness crack of 0.05 inch to emanate from a 0.25 inch diameter hole they predicted crack growth, due to fleet usage scatter, by means of a crack closure related numerical model. The result of their analysis is shown in Figure 6 and it is particularly interesting to note that the crack growth scatter factor is decreasing (from about 13 at 1000 flight hours to about 3 at 2000 flight hours) as the fleet usage is increased. However, it was emphasized in (21) that this estimation was predicted without any consideration of material and geometric property variations or variations of load sequence and design limit stress. Thus, the result in Figure 6 is limited to represent the crack growth variations expected from fleet usage variation only. As all the other just mentioned parameters do indeed vary, the total crack growth range in a fleet is expected to be larger than what is predicted in Figure 6. Material property variations will be discussed in detail in a subsequent subsection.

Because of limited space more details on load variations can't be given here, but it is referred to Palmberg et al (9) and references therein. A very comprehensive review of spectrum test data is given by Schijve (24). Let it suffice to say here that when treating the ultimate failure due to a high load, an extreme value distribution should be used for the magnitude of that load. It should also be recognized that manoeuvre loads are only partly stochastic.

Stress Spectra and Stress Intensity Factors

Before any type of fatigue analysis can be performed, the determined load spectra have to be converted into stress spectra. Normally, load spectra are referred to the centre of gravity of an aircraft. Hence, it becomes necessary to firstly develop transfer functions for obtaining local load spectra for any part of the

structure. One way of doing this is to utilize a finite element model of the entire aircraft as illustrated in Figure 7 for the new swedish fighter JAS 39 Gripen. In such a model the aerodynamic loads are distributed over the entire model and inertia loads are calculated from a mass distribution in the finite element model. Local stress histories may be obtained by superposition of relevant internal load sequences. In the same analysis a rainflow count analysis can be performed to produce a matrix of associated peaks and troughs. This matrix can be used as input to the fatigue crack growth analysis. This concept of developing local load and stress spectra is further described by Jarfall (25).

The structural analysis is usually carried out in several steps by means of substructuring techniques. This enables the analyst to refine the finite element mesh size in regions which are assumed to be critical. Hereby, the stresses computed from the larger model are used as boundary conditions for the detailed models. An example of such a refined model is shown in Figure 8 which shows the structural model for stress intensity factor analysis of a fin attachment in the swedish fighter JAS-37 Viggen. It should be emphasized, though, that when cracking is introduced into substructures the boundary conditions may be violated, due to stress redistribution.

Although stresses have frequently been assumed to follow the Weibull distribution, relatively little is known about the accuracy in stress analysis predictions, and it appears that such distributions would mainly reflect the scatter in loads. Today it is, in our opinion, quite feasible to predict within any given accuracy stresses for any two-dimensional structure as long as the structural behaviour is linear. Complications arise if local plasticity occurs, e.g. at fastener holes, or large strain or displacement occurs, e.g. in bulging of fuselage structures. In the three-dimensional case it is usual to study phenomena as contact problems with or without frictional forces and further complications arise, when the stress state at, for example, joints is fully three-dimensional, in the very interpretation of the results. Spectrum fatigue crack growth under multiaxial loading is yet a virtually blank field, particularly in the predictive sense.

Stress intensity factors. While a multitude of techniques exist to determine K-factors, only a few are actually employed in analyses of cracks in large, complex structures. The most accurate results are obtained with 3-D finite element techniques using singular elements at the crack tip, see Figure 8. Hereby the stress intensity factors may be derived from the displacement or the stress fields or from the changes in potential energy and the error in K-values may be expected to be in the order of the errors in the stress analysis. Typically, errors less than about 5 per cent are possible to achieve. Because of the large costs involved in such analyses (note - the major cost is due to mantime in

structural modelling although the computing costs also may be prohibitive) other techniques are normally used as complements. This is particularly so when cycle-by-cycle fatigue crack growth analyses are performed and a very large no. of K-factors as function of specimen geometry, crack depth, crack width and loading are required. A usual approach is then to use a number of basic reference solutions, for example as obtained from handbooks or the archival literature, and to make use of the principle of superposition. This usually means that several over-simplifications concerning geometry etc. have to be made and consequently the errors in K-estimation may be rather large. For example, consider a stiffened panel where the fasteners are assumed to be rigid. The error in stress intensity factor can be up to 50% due to the neglection of fastener flexibility. It is also important to realize that there exist substantial scatter in the K-solutions found in the literature, even for rather basic cases. Consider a quarter-elliptical corner crack at a circular hole in a large plate subjected to uniform, uniaxial tension. Palmberg (26) compared fourteen different solutions, taken from the literature for this case, and found that by using the solution by Newman and Raju (27) as reference case (although not considered the best solution, but because it covers a wide range of crack sizes) differences of more than 65% existed with respect to the most extreme solution.

Verification of the accuracy of both stresses and stress intensity factors can to some extent be obtained from component and full-scale testing.

Special problems. When evaluating stress intensity factors in complex structures, it is frequently found that not only Mode I exists but also Mode II and less frequently also Mode III. To start with, it is not straight forward to separate these when the evaluation is based on energy concepts. Even if it is possible to do so, for example from the displacement fields, it is not clear how the data should be used for fatigue crack propagation predictions. Commonly, the total strain energy release rate is computed and converted into an effective stress intensity factor as if the loading would be in pure Mode I. This approach should give conservative results when used for predictions as any frictional effects due to other Modes of loading are neglected.

Residual stresses constitute a major problem in any fatigue analysis as they do inevitably exist in real structures and as they are still very difficult to estimate or measure without destroying the component (although X-ray diffraction studies sometimes give reasonable results the technique is not yet perfected). Generally, residual stresses are prevalent due to one of the following five reasons.

1) On purpose in order to obtain compressive stresses which are beneficial in delaying or preventing crack initiation. For example by shot peening or cold working.

2) By mismatch between different parts causing so called built-in stresses.

3) By different heat treatments during processing and construction (e.g. welding).

4) By material handling techniques (e.g. forgings, annealing procedures).

5) Overloading during service.

All these reasons have in common that the effect of residual stresses is to change the local mean stress while the stress range not is influenced. It should be realized that residual stresses may be redistributed during fatigue loading due to, for example, loads causing local plastic flow or by crack growth through the residual stress field. How the effect of residual stresses might be incorporated into fatigue crack growth predictions is discussed in (9), where stresses and K-factors are dealt with in more detail too, and references therein.

Imperfections and Inspections

While gross imperfections such as buckling of thin sheet may be introduced in the structure during manufacturing and assembly, we will here only consider flaws or crack like defects. The initial flaw size assumptions in the military specification for damage tolerance and durability have already been shown in Figure 1. Experimental work suggests that crack length should be exponentially or lognormally distributed and indicates that current NDT-techniques cannot detect crack lengths of only a few mm with any reasonable accuracy.

The latter point is amplified in Figure 9 where a statistical evaluation, made by Berens and Hovey (28) of the data collected by Lewis et al (29), of detection probability versus crack length is shown. The data include some 22 000 inspections, performed on 174 cracks by 107 different inspectors, and are representative of field inspection capability for selected aircraft structures. Since Figure 9 implies that statistical distributions of initial flaws not can be provided by NDT-techniques such distributions may instead be derived from the distributions of fatigue cracks of larger sizes occurring later on during the service life. Distributions so obtained are referred to as equivalent initial flaw size (EIFS) distributions.

The usual procedure of developing EIFS distributions is to make use of experimentally obtained crack growth curves by fitting a crack growth rate equation to them and then making a backwards extrapolation to find the crack length at time zero. These fictitious crack lengths are now defined as the equivalent initial flaw sizes. The EIFS distribution can be derived in the following way. Define the time to crack initiation (TTCI) as the time from the beginning of fatigue loading to some specified crack size a_o, which can be detected.

Let the three parameter Weibull distribution characterize the TTCI by:

$$F_T(t) = P\left[T < t\right] = 1 - e^{-\left(\frac{t-\varepsilon}{\beta}\right)^{\alpha}} \quad ; \quad t > \varepsilon \tag{1}$$

where T = TTCI, α = shape parameter, β = scale parameter and ε = = lower bound parameter. All these parameters are determined from test results. In the simplest case, the crack growth rate under spectrum loading may be written:

$$\frac{da}{dt} = C\,(\hat{K})^n \tag{2}$$

where $\hat{K}$ is the spectrum peak stress intensity factor, see Figure 2. Over relatively large crack length intervals it is possible to approximate the stress intensity factor by a power series of the crack length a as

$$\hat{K} = \hat{\sigma} \sum_{i=1}^{\infty} c_i a^{b_i} \tag{3}$$

In a region of small crack sizes a further approximation is to retain only the first term in Eq. (3). Substitution into Eq. (2) then yields,

$$\frac{da}{dt} = C\,(\hat{\sigma}\, c_1\, a^{b_1})^n = B\, a^{\gamma} \tag{4}$$

where $B = C(\hat{\sigma}\, c_1)^n$ and $\gamma = b_1 n$ are parameters which depend on load spectrum, material properties and structural geometry.

Assume that the crack length at time t_o is equal to a_o. Then Eq. (4) gives the crack length, a(o), at zero time by integration,

$$a(o) = \left[a_o^{1-\gamma} - (1-\gamma)\, B\, t_o\right]^{\frac{1}{1-\gamma}} \tag{5}$$

The relation between the TTCI distribution and the EIFS distribution can be visualized as in Figure 10.

Using Eqs. (1) and (5) the cumulative distribution of the initial crack size a(o) can be derived,

$$F_{a(o)}(x) = P\left[a(o) < x\right] = P\left[\left(a_o^{1-\gamma} + (\gamma-1)\, B\, t_o\right)^{\frac{1}{1-\gamma}} < x\right] =$$

$$= 1 - P\left[t_o < \left(\frac{x^{1-\gamma} - a_o^{1-\gamma}}{(\gamma-1)\, B}\right)\right] \qquad (6)$$

Substitution of Eq. (1) into Eq. (6) yields

$$F_{a(o)}(x) = e^{-\left[\frac{x^{1-\gamma} - a_o^{1-\gamma} - (\gamma-1)\, B\, \varepsilon}{(\gamma-1)\, B\, \beta}\right]^{\alpha}} \quad ; \; 0 < x < x_u$$

$$= 1 \quad ; \; x > x_u \qquad (7)$$

where x_u is the upper bound of the initial crack size,

$$x_u = \left[a_o^{1-\gamma} + (\gamma-1)\, B\, \varepsilon\right]^{\frac{1}{1-\gamma}} \qquad (8)$$

It is not necessary to use the simplified equation (2) in order to derive the EIFS distribution, Eq. (7). In fact, any non-negative crack growth rate formula can be used to derive EIFS distributions (9, 30).

It should be pointed out, though, that the equivalent initial crack size as given by Eq. (5) only is relevant for the specific conditions for which it is derived. That is, local behaviour such as material microstructure, reaming of holes, interference fit of fasteners, fretting etc. will influence the EIFS distribution. Also global parameters, such as the load spectrum and the sheet or plate thickness, will most likely influence the EIFS distribution. Besides from these restrictions the validity of linear elastic fracture mechanics is doubtful for very small flaws (15). Still, this concept is being extensively used in durability studies of airframes, see for example Manning et al (31), and as pointed out in some detail by Blom (15) will very likely have to be used for engine discs and blades if a damage tolerance concept is to be introduced for such components.

Inspection intervals based on fatigue crack propagation predictions are normally determined so that even if there is a crack that is not detected at one inspection this crack shall not become critical until the next inspection. Consequently, several inspections are carried out within the design life time. However, these inspections are not only determined from analytical results but also from the degree of inspectability of the particular structure. Besides from more casual but frequent inspections, carried out at every flight and in some more detail once every year, two other types of classifications exist. These are depot or base level inspectable and in-service non-inspectable. All slow crack growth structures have to be inspected according to either one of these two procedures.

Depot or base level inspectable. The extent of damage is to be detected utilizing any relevant NDT-technique, such as eddy current (see Figure 9), ultrasonics or X-rays. A typical inspection interval is a quarter of a life time. After the completion of such an inspection the extent of damage shall be assumed to that specified for a slow crack growth structure as shown in Figure 1. These damage sizes shall not grow to critical size, when applying the maximum load that is expected to occur once in 20 times the inspection interval, during twice the inspection interval. If this latter load is less than the design limit, the residual strength must at least equal the design limit load. If on the other hand this maximum load is larger than the design limit load, it does not have to exceed 1.2 times the maximum load expected in one life time.

In-service non-inspectable. The structure is in-service non-inspectable if either damage size or accessibility will preclude detection during one or more inspections. In this case, the initial damage size according to Figure 1 shall not grow to critical size during two service life times when subjected to the same maximum load as above.

It should be pointed out that Broek et al (32) recently have proposed an alternative method to determine inspection intervals, based on a re-analysis of the data in (29), see Figure 9. This method was developed so that the probability of crack detection is independent of the inspection technique, the crack growth curve, the specificity of the inspection and the accessibility of the location. It was claimed that no selection of detectable crack size is necessary and that the procedure is conservative, i.e. the actual probability of detection should be higher than what is predicted with the method (32).

Crack size distribution after multiple inspections. By using the randomized general crack growth relation introduced in the following section and the probability density function of time to crack initiation (TTCI), see Figure 10, the crack size distri-

bution at any time can be derived. This was done in our earlier work (9) where a similar derivation was also performed starting from EIFS distributions. Because of limited space those results are not rewritten here, instead it is referred to the initial derivation for such information.

Residual Strength

Limiting the discussion to linear elastic fracture mechanics we will assume that fracture occurs when the initiation criterion $K_I = K_C$ is fulfilled. Here K_I is meant to be the maximum applied stress intensity factor and K_C is the fracture toughness for the relevant thickness if known and is the plane strain fracture toughness K_{IC} otherwise.

Scatter in fracture toughness. There is likely to be more scatter in fracture toughness than in for example strength, due to the large influence on K_{IC} of small variations in heat treatment. Fracture toughness is usually assumed to be either normally distributed or Weibull distributed. Schütz (33) collected K_{IC}-data for several aerospace materials from the literature, and determined the coefficient of variation v from $v = s/\mu$ where s is the standard deviation and μ is the arithmetic mean of the fracture toughness, respectively. He determined values of v statistically for both Al-, Ti- and Fe-alloys and found generally that the coefficients of variation were lowest for Al-alloys where v became 0.03, 0.06 and 0.14 at 50, 90 and 100 per cent probability, respectively. It was also observed, as anticipated, that the coefficient of variation is larger for different heats than within the same batch. For example, for Al 7050-T73561 plate material the mean value of K_{IC}, obtained from 17 batches, was found to be 1195 $Nmm^{-3/2}$ and the coefficient of variation v = 0.1 at 50 per cent probability. The values given above should be applicable to all product types, i.e. plates, sheets and extrusions, with the exception of forgings which were not included in the study (and where scatter may be anticipated to be larger).

Probability of failure. Assuming that K_I and K_C are random variables the probability of failure is given by Eq. (9).

$$P_F = P\,[K_I > K_C] \tag{9}$$

While the probability density function f_{K_C} for the fracture toughness is assumed to be normal or Weibull it is more complicated to derive the corresponding function of K_I . This is because both crack length and peak stress are random variables. Assuming independence of crack length, peak load and fracture toughness it is possible to derive the probability density function f_{K_I} and then formulate the probability of failure as, according to (9):

$$P_F = P\,[D < 0] = \int_{-\infty}^{0} f_D(D)\, dD \tag{10}$$

where $D = K_C - K_I$ and its probability density function is

$$f_D(D) = \int_{-\infty}^{\infty} f_{K_C}(K_I + D)\, f_{K_I}(K_I)\, dK_I \tag{11}$$

where

$$f_{K_I}(K_I) = \int_{0}^{\infty} f_\Sigma(\sigma)\, f_G(K_I/\sigma)\, \frac{1}{\sigma}\, d\sigma \tag{12}$$

where $f_\Sigma(\sigma)$ is the probability density function of the extreme stresses which may be assumed to be extreme value distributed. The probability density function $f_G(g)$ is the function of the crack length and boundary correction together forming $g(a)$ in Eq. (13).

$$K_I = \sigma\, g(a) \tag{13}$$

If an inverse,

$$a = g^{-1}\,(g(a)) \tag{14}$$

exists, then $f_G(g)$ can be expressed as

$$f_G(g) = f_A(a(g))/(dg/da) \tag{15}$$

From the above equations it is possible to solve the probability of failure given in Eq. (10). It is also possible to express the probability of failure in terms of exceeding a critical crack length (9). Further on, the above discussion on residual strength requirements within the in-service inspection requirements may be incorporated into a similar probability expression as Eq. (10) but where the probability of the residual strength being lower than the maximum load considered at the inspections, as discussed before, is considered. For more information on this and for a complete derivation of relevant equations see Palmberg et al (9).

Fatigue Crack Growth Rates

During the past decade several workers have studied the variability in crack growth rates. Although it is now well recognized that environmental effects not only shift the entire crack growth curve but also influence the scatter in growth rates (34) we will here restrict the treatment to the inherent scatter in materials tested under nominally identical conditions. An estimate of such scatter is shown in Figure 11 where crack growth rates, tested at $R = \sigma_{min}/\sigma_{max} = 0$, in Al 2024-T3 obtained from 8

different sources are compared. The overall standard deviation became 0.35 for these data but only 0.15 for similar data obtained at R = 0.5. Using the larger value of the standard deviation (0.35) the crack growth rates for a 95% upper and lower bound were calculated (35) from Eq. (16).

$$\log \left(\frac{da}{dN} \right)_p = \log \left(\frac{da}{dN} \right)_m \pm STD \cdot t \qquad (16)$$

where p is the probability level, m is the mean, STD is the standard deviation in log da/dN and t is Student's multiplier.

A more stringent comparison has been carried out in a Round-Robin program reported by Clark and Hudak (36). They found that the intralaboratory scatter in crack growth rate was between 1.1 and 2.5, whereas the interlaboratory variability was between 2.5 and 5.5 depending on the stress intensity range. The scatter was defined as the ratio between maximum and minimum crack growth rate for constant ΔK-values. The material used in the investigation was 8Ni-8Co-1Mo steel. However, in the extensive work on Al 2024-T3 by Virkler et al (37) it was found that for 68 replicate specimens tested within the same laboratory at least a scatter factor of 4 was obtained. It is frequently assumed that the variability in crack propagation rate follows a lognormal distribution but also normal and Weibull distributions have been employed, e.g. (38).

Besides from the inherent material scatter all the above mentioned values also include artificially introduced scatter due to the precision of the experimental techniques and the curve fitting procedure which is used to convert raw data into crack growth rate data. In (36) it was concluded that the single most important source of variability in fatigue crack growth rate data was the experimental technique used to develop the raw test data, i.e. crack length versus no. of load cycles or some time measure. Perhaps more effort has been put into reducing the effect of the data processing on the variability in crack growth rates (36, 39). Hereby it has been common to assume that the best experimental evaluations should give the smoothest data and the least scatter. Such procedures as the incremental polynomial method (as used in the ASTM-standard) may, however, introduce statistically significant bias into the derived data and should therefore be exercised with care.

To isolate the scatter due to material variations from the scatter introduced by experimentation and data reduction is not a straight forward task, but there have been a few attempts. Virkler et al (37) started with the premise that the crack growth rate should be treated as a random variable and were able to show that a substantial part of the total scatter in growth rates indeed is due to local variations in the material. Inhomogeneous crack growth was not only indicated by the tendency for irregular crack growth within each test but also from the observation that tests

that started with unusually low growth rates tended to continue to grow slowly for most of the test. Recently, Ortiz and Kiremidjian (40) used the same set of data (37) to obtain parameters for a stochastic model of fatigue crack growth. Their approach is interesting in that it considers the reciprocal of the growth rate, dN/da, as the randomly varying material property, rather than da/dN. This reciprocal is modelled as a spatial stochastic process evolving along the path of the crack. Their stochastic model is composed by a random growth law, $f(\Delta K)$, and random noise. The random growth law is statistically characterized by the probability density function of its coefficients whereas the random noise (a zero mean Gaussian process) is characterized by its autocovariance function. The statistical analysis of model parameters is performed as a time series analysis of each individual record, of da/dN versus a, to obtain the coefficients of its growth law and the autocovariance of its noise process. Then the ensemble statistics is obtained by combining all the individual analyses. We find the approach in (40) of great interest although it suffers from a few drawbacks of which the most serious one is perhaps the requirement of having crack growth measurements taken at constant growth increments, Δa.

To end this subsection it should be emphasized that the vast majority, if not all, of the data intentionally produced to study scatter in growth rates have been produced within the Paris regime. This is, for example, true of the Virkler-data (37) that virtually all statisticians have relied on in the formulation of stochastic crack growth models. This, in turn, has led to unrealistic models as will be further clarified in the following section.

STOCHASTIC FATIGUE CRACK GROWTH MODELS

In this section we intend to formulate requirements on stochastic models for fatigue crack growth, to briefly review a few particularly interesting models and to introduce a novel technique incorporating several important engineering concepts.

Requirements on Stochastic Models

From an engineering point of view it is important that statistical models are similar to, and may be reduced to, the deterministic fatigue crack growth analysis technique incorporated in the damage tolerance concept as outlined above. An initial requirement, therefore, is that model parameters should be possible to estimate from crack growth rate data. Any model relying on crack size versus no. of load cycles or a time measure, to determine model parameters, is not consistent with fracture mechanics (since such data depends on the planar geometry of the specimens). Further, all the sources of variability as discussed in the preceeding section should be accountable for.

It is important to emphasize the necessity for expressing the crack growth rate as a general function of crack length, i.e. to use the full sigmoidal shape of the crack growth rate versus ΔK curve, rather than simply utilizing a straight line relationship of Paris type. The crack growth rate should be assumed to be a stochastic process rather than a stochastic variabale. This is to avoid the extreme case of a fully correlated crack growth rate for any two times, which yields unnecessarily large variations in fatigue life. Both the two latter requirements should be incorporated when a cycle-by-cycle stochastic analysis is carried out. This sort of integration technique is required in order to incorporate retardation models, accounting for load sequence effects, into the stochastic model.

We believe these latter requirements to be of large significance as any stochastic fatigue crack growth prediction has two major goals. These are, (1) to predict the mean crack growth curve and (2) to predict the variability from this mean value. It must be stressed that if the scatter is much larger in the predictions than in reality the analysis is not any more useful than a deterministic analysis. Also, self-evidently, correct scatter predictions around the wrong mean value is of no use at all in the predictive sense. Still, stochastical modelling, incorporating all the ingredients in a damage tolerance analysis, may be useful even if the initial predictions not are correct. This is because of the possibility to follow up, individually, the loading and possible cracking in the aircraft during actual operation. Hence, the models are not only used for initial predictions but, maybe more importantly, also for retirement for cause considerations. The last comment on requirements for stochastic models is that the predictive capabilities should be demonstrated and also compared to a deterministic analysis. This is, rather surprisingly, seldom done today.

Existing Stochastic Models

Several workers have proposed stochastic models for fatigue crack growth. It is beyond the scope of the present paper to present a complete review, instead we concentrate on a few promising models.

To start with, we note that a proper treatment of the problem leads to immense complex formulations for which the only way to obtain solutions seems to be by Monte Carlo simulations (9). Such calculations do, however, require more information than what is normally available and besides, the computer effort tends to be rather prohibitive (9, 41). Simplified solutions have therefore been suggested and we will comment on two different approaches. The first one, which has been developed by Bogdanoff and Kozin, see (30, 42, 43) and references therein, is the so-called B-model which is a unit jump state dependent process based on embedded

Markov chain theory. This model is physically appealing as it considers in each step the previous crack growth history (similar to cycle-by-cycle integration). This model has been shown to fit both constant amplitude and variable crack growth data. However, the model requires the first and second moment statistics of the time to reach various crack sizes as input information. Therefore, the model can't easily be applied to crack growth predictions and it won't be further considered here.

The other approach is to randomise the crack growth rate equation according to:

$$\frac{da}{dt} = q(a)\ X(t) \qquad (17)$$

where X(t) is a random process. This formulation has been the start for several researchers, e.g. (9, 44-49). There are two extreme cases for the random process X(t). At one extreme the process is fully uncorrelated for any two different times. This would correspond to a Gaussian white noise and the variability in time to reach a specific crack size would be minimum. The other extreme corresponds to a fully correlated process in which case the random process will become a random variable, X(t) = Z. This would yield the largest statistical dispersion in time to reach a specific crack size. Yang and Chen (44, 45) assumed Z to be a lognormally distributed random variable and derived the probability of failure for a component subjected to inspections.

Lin and Yang (46) developed a method to obtain the statistical moments of the time to reach a specific crack size when the random process X(t) was modelled as a random pulse train. They assumed that the crack size was close to a diffusive Markov process and obtained an iterative formula for the statistical moments of time to reach a specific crack size using Ito's differential equation and the Fokker-Planck equation. A similar formulation has recently been used by Sobczyk (47), in which he assumes X(t) to be a white noise.

However, it was pointed out that diffusion approximations could lead to physical impossibilities in that the crack growth increments could become negative, Lin and Yang (46), Kozin and Bogdanoff (30). To overcome this problem Lin et al (48) substituted the Markov approximation for a cumulant neglect closure model using the log-characteristic functions of a random process. Also Ford (49) assumed X(t) to be a random function, but ignored the diffusion term in the Fokker-Planck equation. By assuming X to be lognormally distributed he derived a moment generating function including a power law relation for the crack propagation time.

Models as these above have been used to study fatigue crack growth under general spectrum loading, see the work by Yang and Lin and their co-workers (44-46, 48) and references therein. However, without exception that work has utilized linearized spectrum fatigue crack growth data (see discussion above on Analysis Concepts and Testing and also Figure 2) instead of starting with constant amplitude data. The obvious advantage is that retardation effects due to load interaction is already included to start with, whereas the important disadvantage is the limited generality of the method. In fact, to perform predictions using such an approach on any other structure, or indeed on the same structure but for other loading, than for that one originally studied to determine model parameters does seem futile. On the other hand it might be possible to perform tests for various structures, such as wing panels, fin attachments etc., subjected to very different load histories and to collect and store statistical information in data banks, hereby making future predictions possible by chosing information from similar tests in the past. This latter comment does indeed seem similar to what would be required in order to use EIFS-distributions, as discussed in some detail before, for durability predictions of new structural components.

Cycle-by-Cycle Model

Considering such discussions as above the present authors have attempted to combine some of the existing models for probabilistic characterization of initial flaw sizes, fatigue crack growth and failure with the damage tolerance analysis technique (9). In essence, the model presented in (9) is based up the model of Yang and Chen (44, 45) with two major differences. The crack growth rate is expressed as a general function of the crack length and, secondly, the crack growth rate is assumed to be a stochastic process instead of a stochastic variable. These two differences are the result of introducing the cycle-by-cycle prediction technique and the model of Lin et al (48). The substitution of the stochastic variable in favour of the stochastic process is a result of trying to avoid the extreme case of a fully correlated crack growth rate for any two times, which may yield unnecessarily large variations in fatigue life. However, the substitution introduces a duration time of correlation, Δ, which currently is a practically unknown factor. Applying the model to known results will provide information for determining Δ.

Our model as given in (9) starts by expressing the general crack growth rate relation as in Eq. (17). The random process X(t) is modelled as a random pulse train;

$$X(t) = \sum_{k=1}^{N(t)} Y_k \, W(t, \tau_k) \qquad (18)$$

where N(t) is a homogeneous Poisson counting process giving the

total no. of pulses that arrive in the time interval $]-\infty, \tau_k]$, τ_k is the arrival time of the k:th pulse and Y_k is the random amplitude of the k:th pulse. For different k's the amplitudes are independent but they are drawn from the same statistical distribution, thus having the same probability density function as Y.

$$W(t, \tau_k) = W(t - \tau_k) = \begin{cases} 1 \text{ if } 0 < t - \tau_k \leq \Delta \\ 0 \text{ otherwise} \end{cases} \quad (19)$$

where Δ is the duration of correlation. All the necessary expressions to calculate expected value, covariance and higher cumulants of the random process X(t) are given in (9). The model which is explained in detail in (9) does include the entire probabilistic damage tolerance concept as discussed above. That is, initial flaws may be included in the form of EIFS-distributions or by otherwise known distributions. Service loading is characterized by two random variables describing the variations in load magnitudes (around the deterministic values) and variations in the sequential order of loads. The statistical distributions for these two random variables are not expressed explicitly, but they are included in the stochastic process X(t). The residual strength is statistically compared to the applied maximum load, assumed to be extreme value distributed. The entire model, incorporating effects of inspections, was used to carry out a statistical analysis of crack growth in a wing panel (9).

Numerical Example

In order to illustrate the application of stochastical fatigue crack growth models as the last one described (9), consider the following example. Crack growth from a riveted hole in a wing panel subjected to a flight-by-flight load spectrum, see Figure 12, is treated. An experimental study of 15 wing panels is used for comparison (50). A symmetric initial crack of length 2a = = 15 mm, see Figure 13, is assumed at a hole close to the edge of the specimen. The calculations are performed by repeating the load sequence, shown in Figure 12, over and over again until failure occurs. Using constant amplitude data as given in Figure 11 and arbitrarily chosing the duration time Δ = 2477 flights, it is possible to calculate the mean and variance of the process X(t) as:

$$E[X(t)] = E[Y] \lambda \Delta = e^{0.5(S_{\log da/dN} \cdot \ln 10)^2} = 1.3837 \quad (20)$$

$$\text{Var}[X(t)] = 0.5E[Y^2] \lambda \Delta =$$

$$= 0.5E[X(t)]^2 (e^{(S_{\log da/dN} \cdot \ln 10)} - 1) = 0.8755 \quad (21)$$

where $E[Y]$ is the ansemble average of Y, see Eq. (18), and λ is the arrival rate of the Poisson process. In the computation of Eqs. (20) and (21) it has been assumed that the crack growth rate is lognormally distributed for all ΔK-values.

The result of the prediction is shown in Figure 13 and it is seen that the obtained mean, $E[T]$, to obtain the critical crack length is slightly unconservative which is unusual. This is partly attributed to the use of recently produced material data, Figure 11, for predictions whereas the testing was performed quite a long time ago (50). Another reason might be the simplified assumption of symmetric crack growth from the hole. In the reality naturally occurring cracks did not grow symmetrically, which influences the utilized stress intensity factors. The predicted variations in crack propagation are shown to cover the experimental data although with a quite large span. This can be modified by altering the duration time Δ which, indeed, should be experimentally determined.

CONCLUSIONS

Based on a review of existing literature information on sources of scatter in fatigue crack growth during service loading a number of conclusions can be made.

The largest amount of scatter is due to the combined action of local variations, within a fleet of aircraft, in service loads and environment. Scatter in fatigue crack growth rate data is due to a combination of material inhomogeinity, batch-to-batch variations, experimental measurements and data processing techniques.

Stochastic fatigue crack growth models should be based on constant amplitude data incorporating the entire sigmoidal shape of the crack growth rate curve. The model should assume the crack growth data to be a stochastic process and predictions should be performed by cycle-by-cycle techniques similar to those presently being used for deterministic damage tolerance analysis.

Such a model, based on existing diffusion approximations, was introduced. It remains to study the influence of the duration of correlation on the predictions of crack growth.

ACKNOWLEDGEMENT

Financial support from the Swedish Defence Material Administration (FMV) and the Swedish Board for Technical Development (STU) is gratefully acknowledged. The authors wish to thank Mrs G. Ahlberg for help in preparing the manuscript.

REFERENCES

(1) Chaplin, W.S., Van Nostrand's Engineering Magazine, Vol. 23, 1880, pp. 441-444.

(2) Chaplin, W.S., "On the Relative Tensile Strengths of Long and Short Bars", Proceedings of the Engineer's Club, No. 3, Philadelphia, PA, U.S.A., 1882.

(3) Griffith, A.A., Philosophical Transactions of the Royal Society, Vol. 221 A, 1920, pp. 163-198.

(4) Epstein, B., "Applications of Extreme Value Theory to Problems of Material Behaviour", in "Probabilistic Methods in the Mechanics of Solids and Structures". Edited by S. Eggwertz and N.C. Lind, Springer-Verlag, Berlin, Germany, 1985.

(5) Weibull, W., "A Statistical Theory of the Strength of Materials", Ingeniörsvetenskapsakademiens Handlingar No. 151, Stockholm, Sweden, 1939.

(6) Epstein, B., J of Appl. Physics, Vol. 19, 1948, pp. 140-147.

(7) Epstein, B, J. of the American Statistical Association, Vol. 43, 1948, pp. 403-412.

(8) ASCE Committee on Fatigue and Fracture Reliability, J. of the Structural Division, ASCE, Vol. 108, 1982, pp. 3-88.

(9) Palmberg, B., Blom, A.F. and Eggwertz, S., "Probabilistic Damage Tolerance Analysis of Aircraft Structures", in "Probabilistic Fracture Mechanics and Reliability". Edited by J.W. Provan, Martinus Nijhoff Publishers, The Hague, The Netherlands, 1986.

(10) Ashby, Lord, New Scientist, 19 May, 1977, pp. 398-403.

(11) Payne, A.O., "Probabilistic Fatigue and Fracture Design", in "Advances in Fracture Research - ICF6". Edited by S.R. Valluri et al, Pergamon Press, Vol. 1, 1986.

(12) MIL-A-83444 (USAF), "Military specification airplane damage tolerance requirements", July 1974.

(13) Swift, T., "Verification of methods for damage tolerance - evaluation of aircraft structures to FAA requirements", in Proc. of the 12th ICAF Symposium, Centre d'Essais Aéronautique de Toulouse, France, 1983.

(14) Nethaway, D.H. and King, T.T., "F100 (3) Engine structural durability and damage tolerance assessment", Pratt and Whitney Aircraft Group, West Palm Beach, U.S.A. Report FR-10481-9, 1980.

(15) Blom, A.F., "Relevance of Short Fatigue Crack Growth Data for Durability and Damage Tolerance Analyses of Aircraft", in "Small Fatigue Cracks". Edited by R.O. Ritchie and J. Lankford, TMS-AIME, Warrendale, PA, U.S.A., 1986.

(16) Jarfall, L., "Prediction of fatigue life and crack growth using spectrum test data", SAAB-SCANIA, Linköping, Sweden, Report TKH R-3401, 1984.

(17) Blom, A.F. and Palmberg, B., "A Review of Investigations on Aeronautical Fatigue in Sweden During the Period May 1983 to April 1985", The Aeronautical Research Inst. of Sweden, Bromma, FFA Technical Note 1985-26, 1985.

(18) Palmberg, B., "Crack growth data for two Aluminum alloys 7050-T73651 and 2024-T3. The Aeronautical Research Inst. of Sweden, Bromma, FFA Technical Note 1984-51, 1984.

(19) Blom, A.F., "Effects of Fighter Wing Loads Spectrum Variation on Fatigue Crack Initiation and Propagation", in "Classical Fatigue". Edited by N.-G. Ohlson and H. Nordberg, Uddeholm Research, Hagfors, Sweden, 1985.

(20) Scarich, G.V. and Bretz, P.E., "Fatigue crack-growth resistance of Aluminum alloys under spectrum loading", Vol. 1 - Commercial 2XXX and 7XXX Alloys, Performed for Naval Air Systems Command by Northrop Corporation, Aircraft Division, Hawthorne, CA, U.S.A., Technical Report NOR 85-141, 1985.

(21) Dill, H.D. and Saff, C.R., "Effects of Fighter Attack Spectrum on Crack Growth", Performed by McDonnell Douglas Corporation for Air Force Flight Dynamics Laboratory, Wright-Patterson Air Force Base, Ohio, U.S.A., Report AFFDL-TR-76-112. 1977.

(22) Abelkis, P.R., "Effect of Transport Aircraft Wing Loads Spectrum Variation on Crack Growth", in "Effect of Load Spectrum Variables on Fatigue Crack Initiation and Propagation". Edited by D.F. Bryan and J.M. Potter, ASTM STP 714, American Society for Testing and Materials, Philadelphia, PA, U.S.A., 1980.

(23) Impellizzeri, L.F., Siegel, A.E. and MCGinnis, R.A., "Evaluation of Structural Reliability Analysis Procedures as Applied to a Fighter Aircraft". Air Force Materials Laboratory, Wright-Patterson Air Force Base, Ohio, U.S.A., Report AFML-TR-73-150, 1973,

(24) Schijve, J., "The Significane of Flight-Simulation Fatigue Tests", in "Durability and Damage Tolernace in Aircraft Design". Edited by A. Salvetti and G. Cavallini, EMAS Ltd., Warley, U.K., 1985.

(25) Jarfall, L., "Fatigue and Damage Tolerance Work During the Aircraft Design Process", Ibid.

(26) Palmberg, B., "A Review of the Stress Intensity Factors for Quarter-Elliptical Corner Cracks at Circular Holes", The Aeronautical Research Institute of Sweden, Stockholm, Report FFAP-H-719, 1984.

(27) Newman, Jr., J.C. and Raju, I.S., "Stress-Intensity Factor Equations for Cracks in Three-Dimensional Finite Bodies", in "Fracture Mechanics: 14th Symposium - Vol. 1". Edited by J.C. Lewis and G. Sines, ASTM STP 791, American Society for Testing and Materials, Philadelphia, PA. U.S.A., 1983.

(28) Berens, A.P. and Hovey, P.W., "Evaluation of NDE reliability characterization", University of Dayton Research Institute, Ohio, U.S.A., Report No. AFWAL-TR-81-4160, Vol. 1, 1981.

(29) Lewis, W.H., Dodd, B.D., Sproat, W.H. and Hamilton, J.M., "Reliability of nondestructive inspections - Final Report", Lockheed- Georgia Company, U.S.A., U.S. Air Force Report No. SA-ALC/MME 76-6-38-1, 1978.

(30) Kozin, F. and Bogdanoff, J.L., "Analysis of stochastic equation models of crack growth", in "Probabilistic Methods in the Mechanics of Solids and Structures". Edited by S. Eggwertz and N.C. Lind, Springer-Verlag, Berlin, Germany, 1985.

(31) Manning, S.D., Yang, J.N. and Rudd, J.L., "Durability of Aircraft Structures", in "Probabilistic Fracture Mechanics and Reliability". Edited by J.W. Provan, Martinus Nijhoff Publishers, The Hague, The Netherlands, 1986.

(32) Broek, D., Kalev, I., Davidson, A. and Shalev, D., "Inspection Intervals for Fixed Cumulative Probability of Crack Detection". FracturResearch, Inc. Columbus, Ohio, U.S.A., Report TN 8512, 1984.

(33) Schütz, W., "Treatment of Scatter of Fracture Toughness Data for Design Purposes", in "Practical Applications of Fracture Mechanics". Edited by H. Liebowitz, Advisory Group for Aerospace Research and Development, NATO, Neuilly sur Seine, France, Report AGARD-AG-257, 1980.

(34) Shaw, W.J.D. and LeMay, I., "Fractographic Studies and Statistical Scatter in Fatigue Crack Propagation Under Controlled Humidity Conditions", in "The Influence of Environment on Fatigue". IMechE Conf. Publ. 1977-4, The Institution of Mechanical Engineers, Bury St Edmunds, U.K., 1977.

(35) Palmberg, B., "Probabilistic Crack Propagation Using Cycle-by-cycle Technique", in "Probabilistic Methods in the Mechanics of Solids and Structures". Edited by S. Eggwertz and N.C. Lind, Springer-Verlag, Berlin, Germany, 1985.

(36) Clark, Jr.,W.G. and Hudak,Jr.,S.J., J. of Testing and Evaluation, Vol. 3, 1975, pp. 454-476.

(37) Virkler, D.A., Hillberry, B.M. and Goel, P.K., J. of Engng Mtrls and Techn., Vol. 101, 1979, pp. 148-153.

(38) Shaw, W.J.D. and LeMay, I., Fatigue of Engng Mtrls and Structures, Vol. 4, 1981, pp. 367-375.

(39) Wei, R.P., Wei, W. and Miller, G.A., J. of Testing and Evaluation, Vol. 7, 1979, pp. 90-95.

(40) Ortiz, K. and Kiremidjian, A.S., Engng Fracture Mech., Vol. 24, 1986, pp. 657-675.

(41) Nilsson, F.L., "Fatigue Crack Propagation under Random Loading", in "Probabilistic Methods in the Mechanics of Solids and Structures ". Edited by S. Eggwertz and N.C. Lind, Springer-Verlag, Berlin, Germany, 1985.

(42) Bogdanoff, J.L. and Kozin, F., J. of Applied Mech., Vol. 49, 1982, pp. 37-42.

(43) Bogdanoff, J.L. and Kozin, F., Engng Frac. Mech., Vol. 20, 1984, pp. 255-270.

(44) Yang, J.N. and Chen, S., "Fatigue Reliability of Gas Turbine Engine Components under Scheduled Inspection Maintenance", Proc. of 25:th AIAA/ASME/ASCE/AHS Structures, Structural Dynamics and Materials Conference, 1984.

(45) Yang, J.N. and Chen, S., "Fatigue Reliability of Structural Components under Scheduled Inspection and Repair Maintenance", in "Probabilistic Methods in the Mechanics of Solids and Structures". Edited by S. Eggwertz and N.C. Lind, Springer-Verlag, Berlin, Germany, 1985.

(46) Lin, Y.K. and Yang J.N., Engng Frac. Mech., Vol. 18, 1983, pp. 243-256.

(47) Sobczyk, K., Engng Frac. Mech., Vol. 24, 1986, pp. 609-623.

(48) Lin, Y.K., Wu, W.F. and Yang, J.N., "Stochastic Modeling of Fatigue Crack Propagation", in "Probabilistic Methods in the Mechanics of Solids and Structures". Edited by S. Eggwertz and N.C. Lind, Springer-Verlag, Berlin, Germany, 1985.

(49) Ford, D.G., "Coarsely Random Cracking in One-Crack Fatigue Models", Aeronautical Research Laboratories, Melbourne, Australia, ARL Structures Report 382, 1980.

(50) Eggwertz, S., "Investigation of Fatigue Life and Residual Strength of Wing Panel for Reliability Purposes", in "Probabilistic Aspects of Fatigue", ASTM STP 511, American Society for Testing and Materials, 1972.

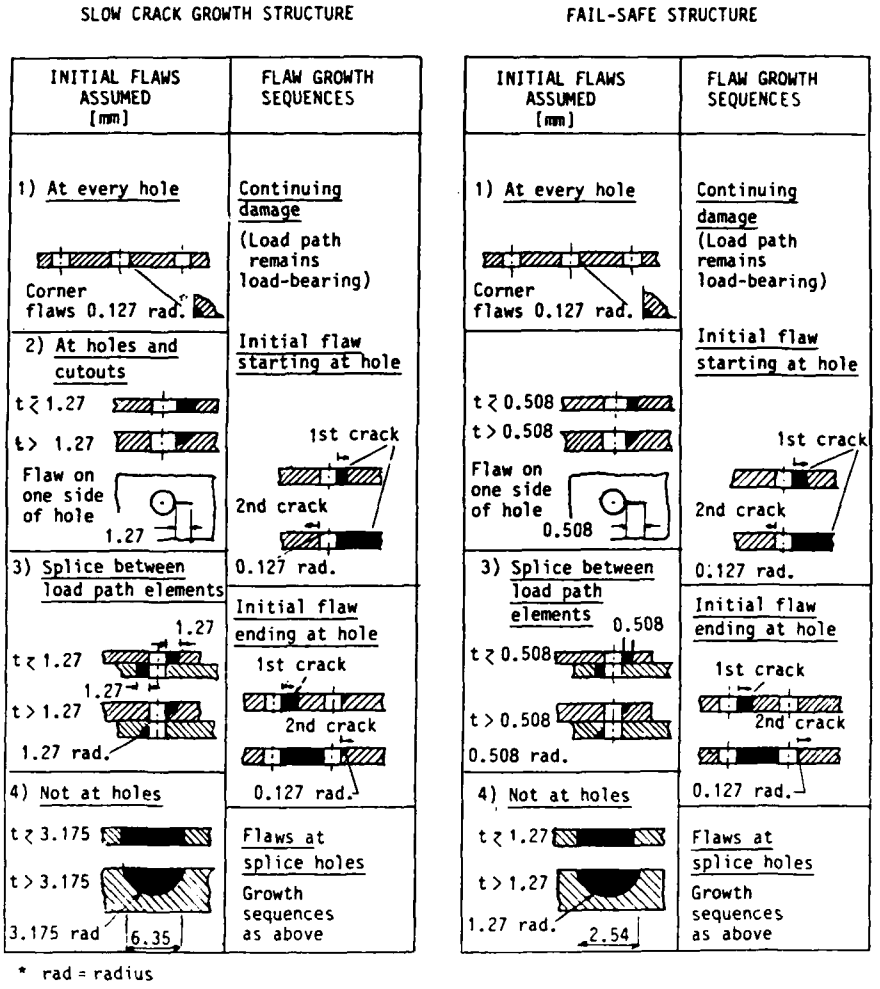

* rad = radius

Figure 1 Initial flaw size assumption

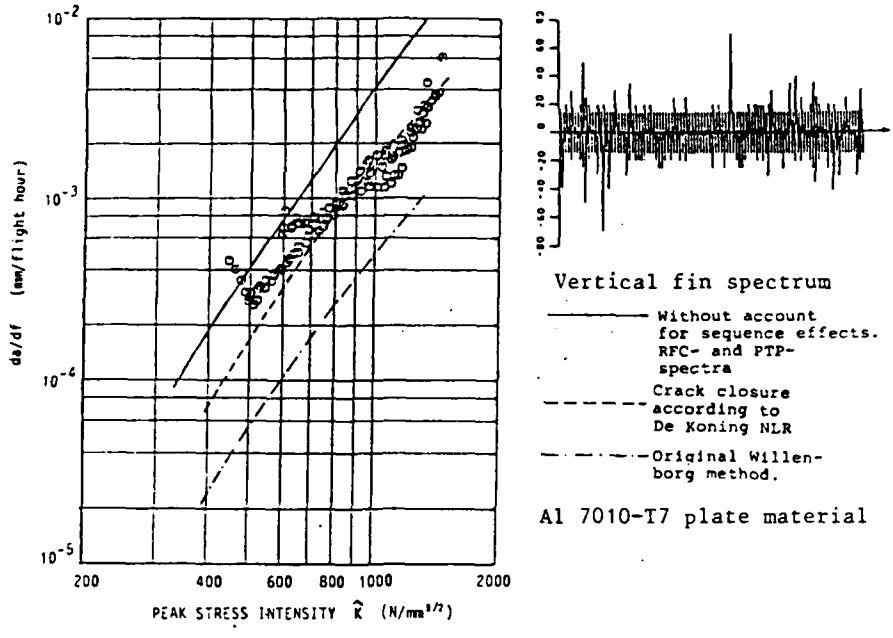

Figure 2 Prediction of spectrum fatigue crack growth rate using various models

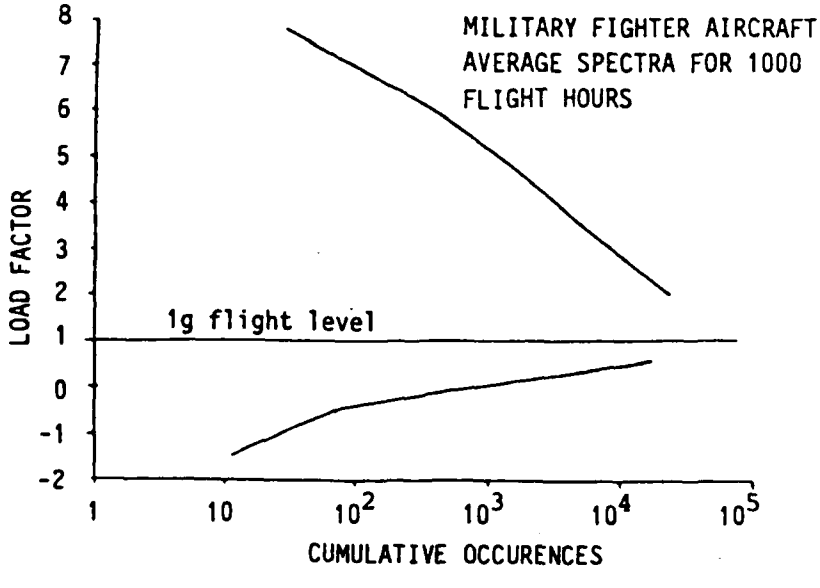

Figure 3 Cumulative occurrences of manoeuver load factors

Spectrum Variation Type	Range of Crack Growth Life		
	Less Than 10% Variation	Less Than 50% Variation	Greater Than 50% Variation
Reordering of Loads Within a Mission	√		
Sequence of Missions		√	
Mission Mix			√
Individual Flight Length	√		
High and Low Load Truncation			√
Compression Loads		√	
Exceedance Curve Variations			√
Coupling of Peaks and Valleys		√	
Test Limit Stress Level			√

GP76-0714-38

Figure 4 Effect of spectra variations on crack growth (21)

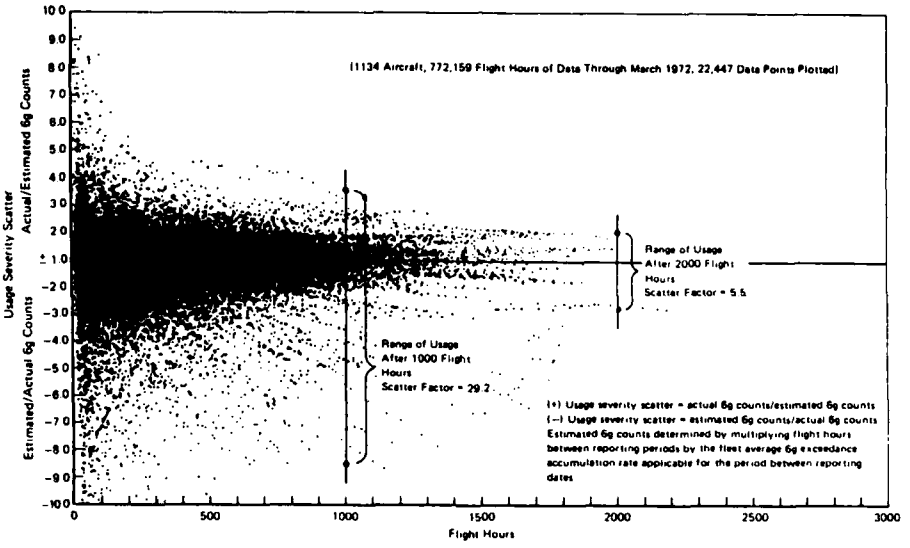

Figure 5 6 G usage severity scatter vs flight hours for air force F-4 aircraft reporting counting accelerometer data (23)

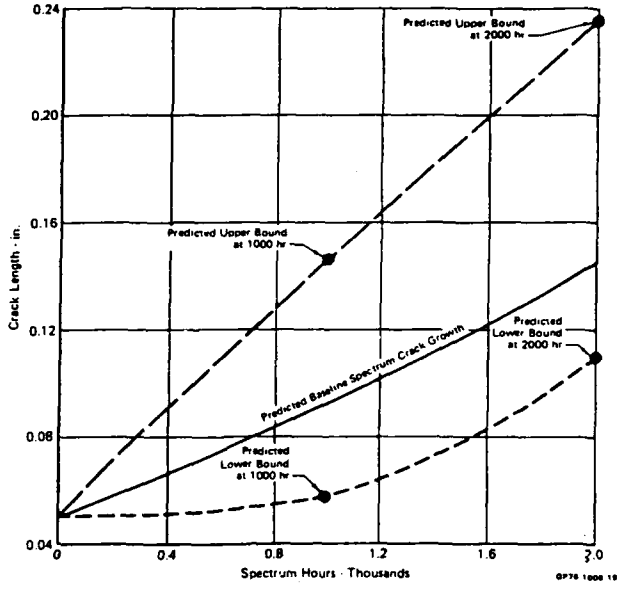

Figure 6 Range of crack growth predicted by contact stress model due to fleet usage scatter (21)

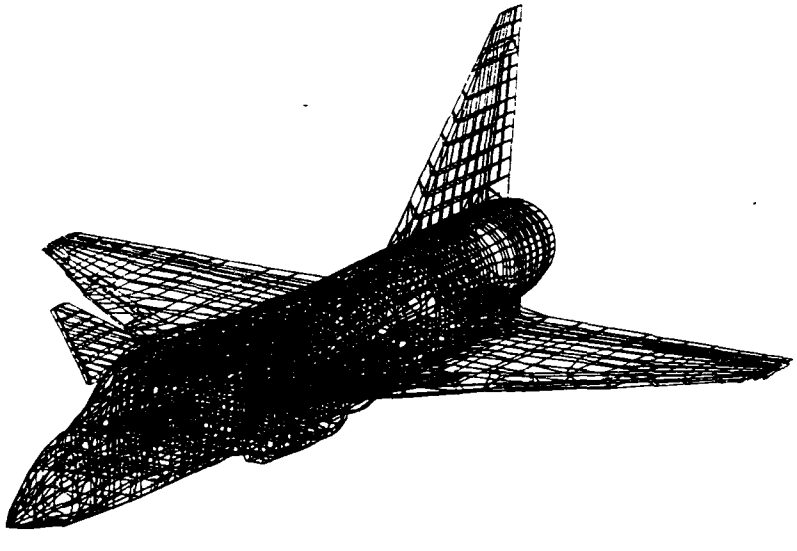

Figure 7 Finite element model of the JAS 39 "Gripen" (almost 10^5 degrees of freedom)

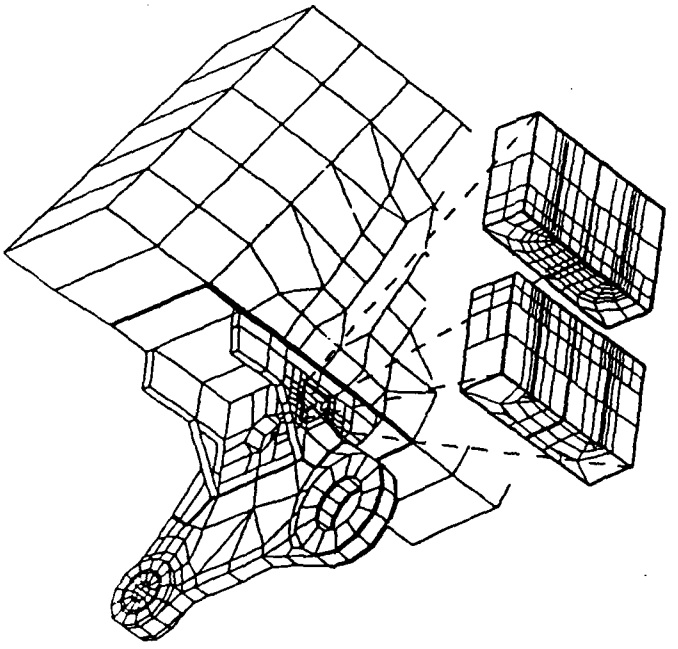

Figure 8 Structural model for stress intensity analysis of a fin attachment

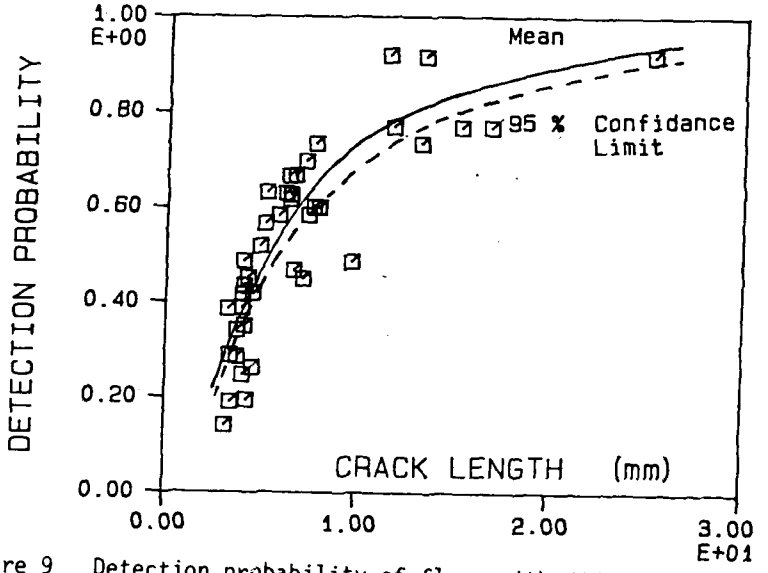

Figure 9 Detection probability of flaws with different lengths. From Berens and Hovey (28)

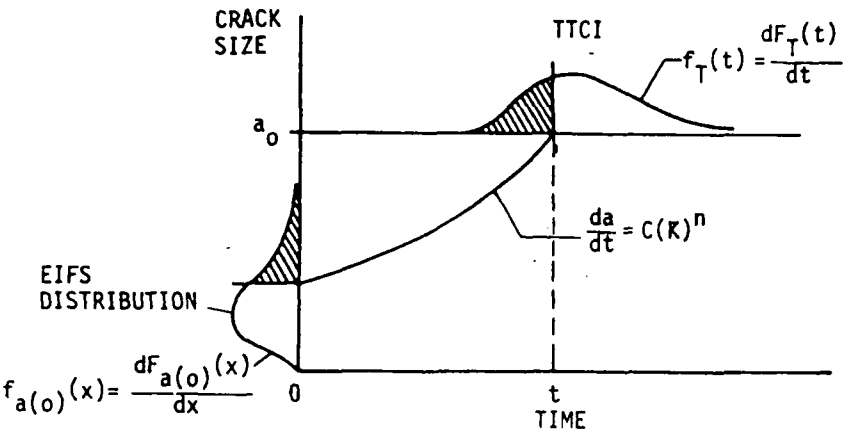

Figure 10 Relation between TTCI and EIFS

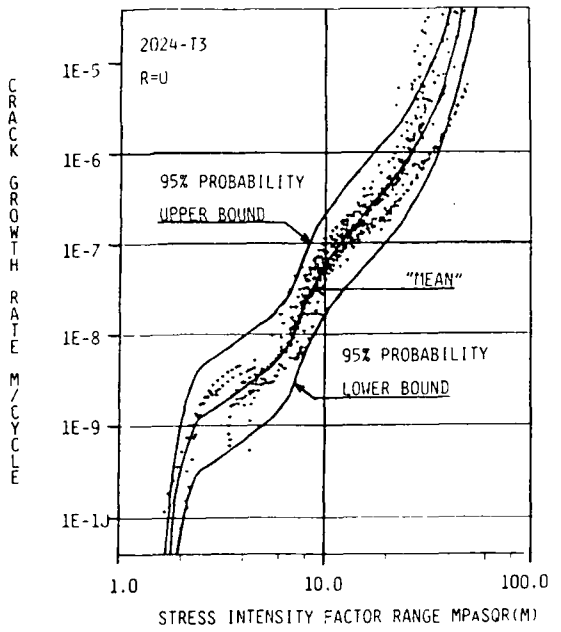

Figure 11 Crack growth rate in 2-4 mm thick test specimens of the aluminium alloy 2024-T3, R = 0

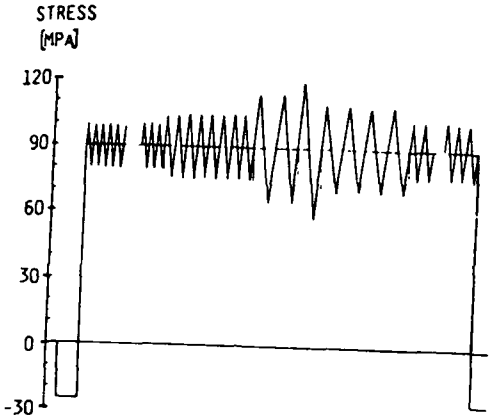

Figure 12 Load sequence for one flight, including 89 load cycles

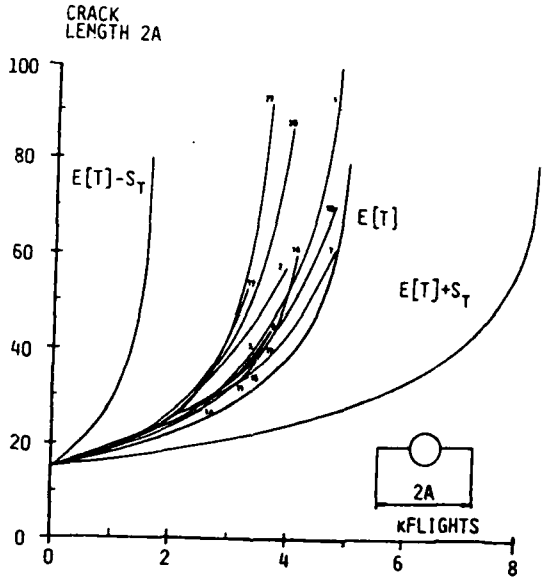

Figure 13 Comparison experimental result with computed result

CONSTRAINT EFFECTS IN FATIGUE CRACK GROWTH

R. C. McClung* and H. Sehitoglu*

Fatigue crack opening levels for different applied stress levels and stress states are determined with an elastic-plastic finite element simulation of fatigue crack growth. Both out-of-plane constraint (plane stress versus plane strain) and in-plane constraint (due to applied stress biaxiality) are shown to influence crack opening levels. These influences vary significantly with stress level. The trends in opening levels determined analytically compare favorably with experimental crack growth data from the literature on thickness effects and stress biaxiality effects. Changes in opening levels are interpreted in terms of the interaction between residual displacements and crack opening displacements.

INTRODUCTION

One of the classic problems in the study of fatigue crack growth is the effect of specimen thickness on crack growth rates. Typical reviews of the experimental literature (1,2) point out that under some conditions, growth rates are higher in thicker specimens; under other conditions, higher in thinner specimens; and under still other conditions, unchanged with thickness. No widely accepted explanation has emerged.

Variations in specimen thickness are typically associated with variations in the extent of out-of-plane constraint. Commonly this is described as a transition from "plane stress" conditions in thinner specimens to "plane strain" conditions in thicker specimens. Most proposed explanations for the thickness effect attempt to relate the stress state transition to changes in some key factor in fatigue crack growth such as plastic zone size, crack advance mechanism, or crack front orientation and shape.

*Department of Mechanical and Industrial Engineering, University of Illinois at Urbana-Champaign, Urbana, IL 61801.

Another key factor which is functionally related to changes in stress state is crack closure. Elber's pioneering experiments (3) were conducted with thin sheets, and early debate questioned whether closure was possible under plane strain. More recently it has become evident that closure does occur under practical plane strain conditions (4,5) although generally to a lesser extent. Experimental measurements of closure have been used in a few attempts to rationalize thickness effects with some success (6).

The purpose of this paper is to demonstrate that crack closure, properly understood, provides a successful explanation for a range of thickness effects. Furthermore, the effects of constraint on crack closure and hence on crack growth rates can be generalized to include also the effect of in-plane constraint, such as mode I biaxial loading. Finally, the interaction of in-plane and out-of-plane constraint in different specimen geometries is explored as a source of further variation in the data.

Crack opening levels presented in this paper are obtained from elastic-plastic finite element (FE) simulations of fatigue crack growth. The FE code (7,8) permits node release for cyclic crack extension and accounts for the changing boundary conditions associated with intermittent crack face contact. The mesh, composed of four-noded isoparametric elements, models a rectangular plate with symmetric cracks growing from a center hole. The hole has been shown to have a negligible effect on the behavior of the crack after some small amount of crack extension has occurred. Cracks are initiated at the notch root and grown to a maximum crack-length-to-specimen-width ratio (a/w) typically about 0.15. The material model employs kinematic hardening with a von Mises yield surface translating according to Ziegler's rule. The stress-strain curve is bilinear with E = 205140 MPa and plastic modulus C = 13700 MPa. Other material properties are yield stress σ_o = 430 MPa and ν = 0.3. These properties correspond to a 1070 class U railroad wheel steel at 20°C. Further details are available in references (7) and (8).

Out-of-Plane Constraint

Normalized crack opening levels as a function of the normalized maximum stress are shown in Fig. 1 for both plane stress and plane strain at an R-ratio of -1. Similar results have been obtained for R = 0. Note the significant difference between plane stress and plane strain, but also note the significant changes in opening levels with increasing maximum stress. The credibility of these results is enhanced in comparison with the data of Newman (9), which were derived from a fundamentally different modified Dugdale analysis. The quantitative differences in the two sets of results may be due in part to differences in the stress-strain models; Newman assumes a perfectly plastic material, while the FE analysis permits strain hardening.

At low stress levels, both analyses predict that crack opening levels will be lower (and hence crack growth rates higher) in plane strain. This result is in agreement with the majority of experimental data (2,6,10-13), which tend to exhibit faster growth in thicker specimens. On the other hand, a "crossover" occurs at higher stress levels such that earlier opening and faster growth is associated with plane stress conditions. This, too, is in keeping with experimental results: Jack and Price (14) and Griffiths and Richards (1) both found quicker growth in thinner specimens at maximum stresses approaching general yield. Finally, note that at a range of intermediate stresses, differences in closure behavior between plane stress and plane strain are negligible. This similarity may explain some null results in thickness effect data.

Plasticity-induced crack closure is caused primarily by residual tensile deformation in the wake of the growing fatigue crack. The crack opening event may be thought of as the crack opening displacements (COD) overcoming these residual displacements (δ_R) behind the crack tip. The crack opening level, then, will be determined by the "competition" between the COD and δ_R, both of which will change with geometry, material, applied loading, etc. This line of reasoning suggests that crack opening levels will tend to be higher when δ_R is a larger percentage of the maximum COD.

The relative magnitude of δ_R is roughly suggested by the difference between the CODs at maximum load of a fatigue crack and an ideal (stationary, monotonically loaded) crack. This difference may be easily estimated with the present FE formulation. The ideal crack is numerically modeled by releasing an appropriate number of nodes behind the crack tip and loading once from zero to maximum load. This comparison is not intended to provide an exact analysis or rigorous explanation of crack opening behavior, but only an aid to visualizing the possible interaction between COD and δ_R at different stress levels and stress states.

The CODs at maximum load for fatigue and ideal cracks at a low stress level under plane stress and plane strain are shown in Fig. 2. This figure suggests, as expected, that δ_R is considerably larger under plane stress than under plane strain. The COD for an ideal plane stress crack is only slightly larger than for plane strain (and actually less for fatigue cracks). We would expect, then, by comparing δ_R and COD, that crack opening levels are higher under plane stress at this stress amplitude. This was confirmed in Fig. 1.

The same COD information is shown in Fig. 3 for a considerably higher stress amplitude (note the change in vertical scale). Here the relationship between ideal and fatigue COD is considerably more complex. The difference between the two is

relatively smaller near the crack tip, especially in plane stress, and the fatigue COD even becomes larger than the ideal COD farther behind the crack tip. These phenomena are due, at least in part, to the reversed plasticity experienced by the fatigue crack at large compressive loads. We may roughly infer, however, that δ_R near the crack tip is only slightly larger under plane strain than under plane stress. Since the total COD for plane stress is considerably larger at this high stress amplitude, we expect lower opening levels under plane stress. This, too, is confirmed by Fig. 3.

The gradual decrease in normalized opening level with increasing stress amplitude (fixed stress state), which has been confirmed experimentally (15), can be rationalized with the same type of explanation. The residual displacements obviously increase with stress amplitude due to more severe plastic deformation at the crack tip, but apparently the COD values increase even more rapidly with stress amplitude. Simple models such as the Dugdale formulation, for example, suggest that COD values at the crack tip increase with the square of the remote stress. Another possible factor in the decrease of S_{open}/S_{max} with increasing S_{max} is the changing shape of the crack surfaces; the crack tip profile tends to be more blunted at higher stress levels.

A further note of interest is that, unlike previously published results (16,17), separation and intermittent contact of crack surfaces in plane strain was qualitatively similar to behavior in plane stress. Closure was generally continuous behind the crack tip (crack "zips" or "unzips" smoothly as it closes or opens) for both R = 0 and R = -1 in all cases where mesh refinement was sufficient.

In-Plane Constraint

It is clear that out-of-plane constraint and the accompanying changes in deformation behavior near the crack tip have a significant impact on crack opening behavior. It may also be true, then, that changes in near-tip deformation behavior caused by in-plane constraint, such as biaxial loading, will affect closure behavior. This was investigated by applying remote biaxial loads to the previous finite element mesh. Stresses transverse to the crack, σ_x, were chosen of equal magnitude to stresses normal to the crack, σ_y, and of either the same or opposite sign, so that $\lambda = \sigma_x/\sigma_y = \pm 1$. Equibiaxial loading corresponds to $\lambda = +1$, and pure shear loading to $\lambda = -1$. Only conditions of plane stress ($\sigma_z = 0$) have been considered to date.

Crack opening levels for conditions of R = 0, plane stress are shown in Fig. 4 for $\lambda = \pm 1$ in comparison with uniaxial ($\lambda = 0$) results. As expected, closure levels are a function of in-plane

constraint. Opening levels for pure shear (λ = -1) mode I cracks are consistently lowest, and the difference increases at higher stresses. Opening levels for equibiaxial loading are slightly higher than for uniaxial loading. Note that at lower stress levels, opening levels for all three conditions converge toward similar values.

These results are again consistent with the majority of experimental crack growth studies. Crack growth rates are generally observed to be highest for λ = -1 in comparison with λ = 0 or λ = +1 (18,19). When maximum stresses are lower, the differences in growth rates may become negligible (18,20,21).

Ogura et al. (22) previously reported elastic-plastic FE analysis which showed no change in opening levels with loading biaxiality for R = 0, but their results are suspect. Their crack growth increment/plastic zone size ratios are apparently larger than those found by Newman (9) to be insufficiently small for accurate results with identical constant strain triangle elements. Furthermore, the fatigue crack may not have been allowed to grow sufficiently far beyond the initial crack length to reach a stable opening value. The results of Ogura et al. for R = -1 loading, in which case mesh refinement requirements are less severe, are qualitatively very similar to the present results, suggesting significantly lower opening levels for λ = -1.

Crack opening displacement information for different biaxiality ratios is shown in Fig. 5. The intermediate case of λ = 0 has been omitted for clarity. The residual displacements do not seem to differ radically with , so the changes in opening levels may be attributable to the significantly larger COD for λ = -1. The variations in CODs and plastic zone sizes (not shown here) with stress biaxiality are in harmony with previous numerical results for ideal elastic-plastic cracks (23).

General Constraint

Since both in-plane and out-of-plane constraint have been shown to affect closure, it is possible that more complex interactions of constraint may affect closure in various specimen geometries. Leevers and Radon (24) have shown that implicit in-plane constraint, quantified as "T-stresses," varies widely from geometry to geometry. These nonsingular stress terms are most negative for a center-cracked panel (CCP) and most positive for a compact tension (CT) specimen. In some respects, a CT specimen generates a crack-tip stress field similar to a CCP specimen with applied biaxial loading corresponding to λ = + 1.5 (24). It is possible that the functional dependence of opening levels on maximum stress may change from geometry to geometry. Changes in opening levels could arise not only directly from changes in σ_R (due to variations in crack tip plasticity) but also indirectly

from changes in the COD (e.g., differences in COD shape between tension and bend geometries). This may also affect the relative contributions of out-of-plane constraint so that, for example, thickness effects could be different in a CT specimen than in a CCP specimen.

For these reasons, the term "general constraint" seems to be a more appropriate descriptor of the proper context in which to analyze constraint effects. This term suggests the simultaneous consideration of not only out-of-plane contributions but also explicit and implicit in-plane contributions. Other factors, such as extent of strain hardening, may also need to be taken into account. Research to investigate these behaviors is continuing.

CONCLUSIONS

Both out-of-plane constraint (plane stress versus plane strain) and in-plane constraint (variations in applied stress biaxiality) have been shown to influence crack opening levels in fatigue. These influences can be significantly different at different stress amplitudes. Trends in calculated crack opening levels are consistent with published experimental crack growth rate data demonstrating thickness effects and stress biaxiality effects.

Changes in crack opening levels with stress level and stress state can be interpreted in terms of the interaction between crack opening displacements and residual displacements. This interaction can be approximately visualized by comparing the crack opening displacements at maximum load of a fatigue crack and a corresponding ideal crack.

ACKNOWLEDGMENTS

Financial support was provided by the Fracture Control Program, College of Engineering, University of Illinois at Urbana-Champaign. Special thanks is extended to Mr. Paul Lalor for his extensive assistance with the numerical computations.

SYMBOLS USED

α = constraint factor used by Newman (9)

C = plastic modulus, $d\sigma/d\bar{\epsilon}_p$ (MPa)

δ_R = residual displacements along crack surface (μm)

λ = stress biaxiality ratio, σ_x/σ_y

S_{max} = maximum remote stress normal to the crack (MPa)

S_{open} = remote stress normal to the crack at which the crack first fully opens (MPa)

σ_o = yield stress (MPa)

REFERENCES

(1) Griffiths, J. R., and Richards, C. E., Mat. Sci. Eng., Vol. 11, 1973, pp. 305-310.

(2) Daiuto, R. A., and Hillberry, B. M., "Effect of Thickness on Fatigue Crack Propagation in 7475-T731 Aluminum Alloy Sheet," NASA CR 172367, June 1984.

(3) Elber, W., Eng. Frac. Mech., Vol. 2, 1970, pp. 37-45.

(4) Fleck, N. A., and Smith, R. A., Int. J. Fatigue, Vol. 4, 1982, pp. 157-160.

(5) Ewalds, H. L., and Furnee, R. T., Int. J. Fracture, Vol. 14, 1978, pp. R53-R55.

(6) Fleck, N. A., "An Investigation of Fatigue Crack Closure," Ph.D. Thesis, Cambridge University Engineering Department, May 1984.

(7) Lalor, P., Sehitoglu. H., and McClung, R. C., "Mechanics Aspects of Small Crack Growth from Notches--The Role of Crack Closure," The Behaviour of Short Fatigue Cracks, EGF Pub. 1, 1986, pp. 369-386.

(8) Lalor, P., and Sehitoglu, H., "Fatigue Crack Closure Outside Small Scale Yielding Regime," ASTM Int. Symp. on Fatigue Crack Closure, Charleston, SC, May 1986.

(9) Newman, J. C., Jr., ASTM STP 748, 1981, pp. 53-84.

(10) Broek, D., and Schijve, J., Aircraft Eng., Vol. 38, 1966, pp. 31-33.

(11) Fujitani, K., Sakai, T., Nakagawa, A., and Tanaka, T., Bull. JSME, Vol. 25, 1982, pp. 1195-1201.

(12) Bathias, C., Eng. Frac. Mech., Vol. 10, 1978, pp. 267-282.

(13) Sehitoglu, H., and McDiarmid, D. L., Int. J. Fatigue, Vol. 2, 1980, pp. 55-60.

(14) Jack, A. R., and Price, A. T., Acta Met., Vol. 20, 1972, pp. 857-866.

(15) McClung, R. C., and Sehitoglu, H., "Closure Behavior of Small Cracks under High Strain Fatigue Histories," ASTM Int. Symp. on Fatigue Crack Closure, Charleston, SC. May 1986.

(16) Fleck, N. A., and Newman, J. C., "Analysis of Crack Closure Under Plane Strain Conditions," ASTM Int. Symp. on Fatigue Crack Closure, Charleston, SC, May 1986.

(17) Fleck, N. A., Eng. Fract. Mech., Vol. 25, 1986, pp. 441-449.

(18) Brown, M. W., and Miller, K. J., ASTM STP 853, 1985, pp. 135-152.

(19) Smith, E. W., and Pascoe, K. J., ASTM STP 853, 1985, pp. 111-134.

(20) Miller, K. J., Metal Science, Vol. 11, 1977, pp. 432-438.

(21) Liu, A. F., Allison, J. E., Dittmer, D. F., and Yamane, J. R., ASTM STP 677, 1979, pp. 5-22.

(22) Ogura, K., Ohji, K., and Ohkubo, Y., Int. J. Fracture, Vol. 10, 1974, pp. 609-610.

(23) Miller, K. J., and Kfouri, A. P., Int. J. Fracture, Vol. 10, 1974, pp. 393-404.

(24) Leevers, P. S., and Radon, J. C., Int. J. Fracture, Vol. 19, 1982, pp. 311-325.

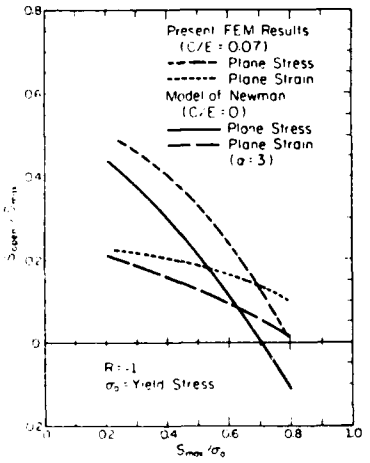

Fig. 1 Crack Opening Levels for Plane Stress and Plane Strain

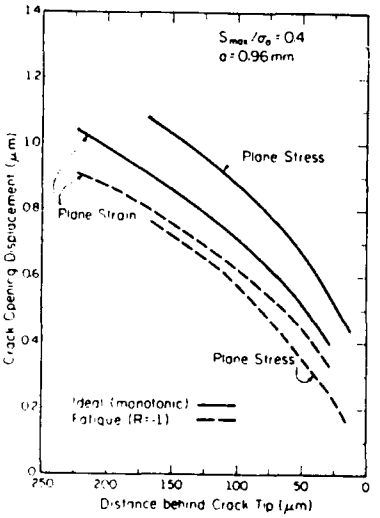

Fig. 2 Ideal and Fatigue COD at $S_{max}/\sigma_o = 0.4$

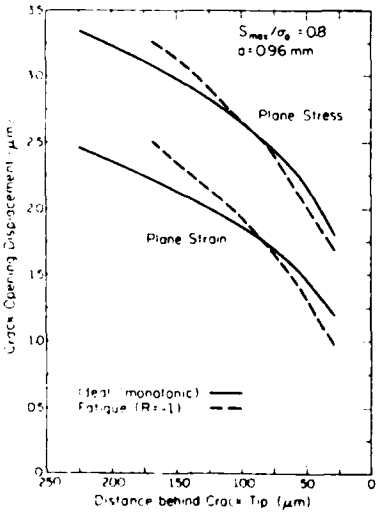

Fig. 3 Ideal and Fatigue COD at $S_{max}/\sigma_o = 0.8$

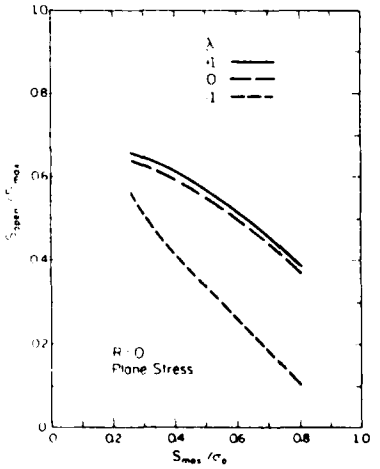

Fig. 4 Crack Opening Levels for Different Biaxiality Ratios

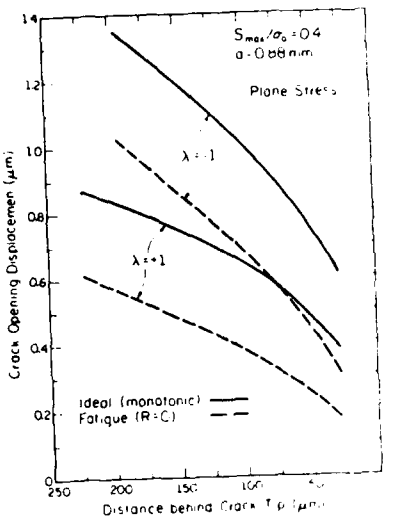

Fig. 5 Ideal and Fatigue COD for Different Biaxiality Ratios

COMPUTER AIDED MODELING AND FATIGUE FAILURE FORECAST UNDER STOCHASTIC LOADING

B.D. Notohardjono† and D.S. Ermer*

A methodology for an on-line fatigue failure forecast (FFF) for stocnastic loading is presented here. Autoregressive Moving Average (ARMA) models which are discrete representations of the underlying differential equations, are fitted to strain data for different times. Damping factors, that are estimated from the model parameters, decrease with time, and after generating a relationship between the normalized value of the damping factor, the remaining life or life ratio is found off-line. Several examples of on-line life prediction for the same kind of material that was tested off-line are given.

INTRODUCTION

Many service loads have irregular sequences containing complex variable amplitude and frequencies. Under this kind of loading the fatigue process can be viewed as a stochastic process.

When a material or product is subjected to variable loading, its "previous" condition or the "dependency" of the response of the fatigue process, is an important factor in determining fatigue life. As the fatigue process progresses the dependency of a response such as strain to its previous values becomes more prevalent. Thus, the response of the fatigue process, i.e., the stochastic data, is correlated data and can be modeled explicitly by a statistical time series function.

† IBM Corporation, Poughkeepsi, New York, 12602.

* Mecnanical Engineering Department, University of Wisconsin-Madison, Madison, Wisconsin 53706.

The fatigue life prediction method presented here is based on an analysis of the response and not on the input. In this output approach, an effective modeling technique that has been developed for system identification of different engineering system, is employed to find the adequate Auto Regressive Moving Average (ARMA) model of the strain response of a fatigue process (1). The purpose of the stochastic modeling is to estimate the key model parameter which can be used for failure process characterization, and later for on-line fatigue failure life predictions; i.e., for possible on-line monitoring of a critical machine/structure components. It has been shown in (2,3) that the damping factor after a given period of strain can be estimated from parameters of an adequate but simplified AR model and used as the key model criterion to assess the state of the fatigue process at a given time.

EXPERIMENTAL SET-UP, MATERIALS AND SPECIMENS

The fatigue testing machine used for the tests was a MTS servo-hydraulic model. The input to the servo controller was a signal from a Wavetek model 132 "noise generator", which was used to produce a stochastic force control command for all experiments. The stability limit of the testing equipment system dictated the maximum frequency and amplitude that could be realized for force control. In this case, the maximum number of peaks and valleys was about 10 per second. During a test the strain response was measured continuously by a 1 inch gage-length MTS extensometer. Next the analog strain data were digitized uniformly at a 20 millisecond sampling interval. This strain data was then fitted by ARMA models.

The material selected was SAE bolt steel, grade 2. The ultimate strength of this steel is 74 Ksi, its uniaxial stress is 57 Ksi, and the reduction in area is 40%. Four smooth cylindrical specimens were tested and the results were analysed off-line, whereas the other two cylindrical specimens were used for on-line analyses. In addition, two cylindrical specimens with a V-notch of 1/32 inch depth in the middle of the gage length were used for the on-line experiments to predict the fatigue life. The purpose of the notch was to show that the off-line analysis of smooth specimens can be used as a basis for effective on-line prediction of either notched or unnotched specimens.

MODELING THE STRAIN DATA

The purpose of the off-line analyses of the strain data is to form a data base for developing an on-line fatigue failure forecast. The first smooth specimen, CSA, was tested under a maximum stress of 69 Ksi, and a minimum stress of 12 Ksi. The test lasted three minutes. A typical strain response that was sampled uniformly at 20 milliseconds is given in Fig. 1.

The Autoregressive Moving Average model of order n,m, i.e., ARMA (n,m) model is given by

$$x_t = \sum_{i=1}^{n} \phi_i \, x_{t-i} + a_t - \sum_{j=1}^{m} \theta_j \, a_{t-j} \qquad (1)$$

$$E(a_t) = 0 \text{ and } E(a_t, a_{t-u}) = \delta_u \sigma_a^2$$

where the x_t's are the observed data after deducting their average, the ϕ's are the autoregressive parameters, the θ's are the moving average parameters, the a_t's are normally and independently distributed residuals with mean zero and variance equal to σ_a^2, and δ_K is the Kronecker Delta function. It should be noted that although ARMA (n,m) models can give better parameter estimation, the ARMA (n,0) is easier and faster to model, which make it suitable for on-line fatigue failure forecasting. Consequently ARMA (n,0) or AR(n) models, n = 2, 4, ..., were fitted to the recorded strain data until an adequate model was identified. A brief review of modeling technique is given in (1) and (3). The adequate models for all subsets of the CSA specimen are shown in Table 1 where only the real characteristic roots and the dominant modes are given. This table also gives the tabulated life ratio, t*, which is determined by the equation

$$t^* = \frac{t}{T} \qquad (2)$$

where t is the time the data was collected (minutes), and where T is the total duration of the test, i.e., the fatigue life of the specimen (minutes). From Table 1 it is clear that after fitting the CSA-3 data, the damping factor, ζ, decreased with time in general. However for the CSA-1 to CSA-3 data, the damping factor, ζ, increased from 0.35 to 0.42.

TABLE 1 - The Adequate AR(n) Models of CSA Data and Dynamic Characteristics [500 data pts].

	Life Ratio t*	Adequate Model n	Real Root λ	Percent Contribution P(%)	Damping Factor ζ
CSA-1	0.083	5	0.99	98.7	0.35
CSA-2	0.167	7	0.88	72.0	0.41
CSA-3	0.250	7	0.71	38.4	0.42
CSA-4	0.333	9	0.99	90.9	0.36
CSA-5	0.417	6	0.89	65.1	0.34
CSA-6	0.510	9	0.98	78.1	0.31
CSA-7	0.583	7	0.76	75.3	0.33
CSA-8	0.667	9	0.98	82.6	0.27
CSA-9	0.750	9	0.99	90.9	0.32
CSA-10	0.833	7	0.99	91.3	0.23
CSA-11	0.917	7	0.99	96.9	0.24
CSA-12	1.000	9	0.99	90.0	0.22

The reason for this increase could be cyclic hardening of the material. Also it should be noted that the initial period of the test can be considered as a "transition" period from zero force to complete dynamic loading. Therefore, it is assumed that the "initial stable condition" is actually through the CSA-3 data period, and therefore the decreasing trend of the damping factor from this "initial stable condition" is due to the fatigue process. Thus taking the damping factor at CSA-3 as the reference value, ζ_{ref}, the normalized damping factor, ζ^*, is given by

$$\zeta^* = \frac{\zeta}{\zeta_{ref}} \tag{3}$$

where ζ is the damping factor at a particular life ratio. For example, at CSA-7, the normalized damping factor is

$$\zeta^* = \frac{0.33}{0.42} = 0.79$$

The corresponding life ratio, is 0.583 (see column 2 of Table 1).

The second specimen, CSB, was tested under a maximum stress of 38 ksi and a minimum stress of -23.5 ksi. The test lasted 14 minutes. Whereas, the third (CSC) and fourth (CSD) specimens were fatigue tested

with maximum stresses of 45 ksi and 48 ksi, and minimum stresses of 9 ksi and 7 ksi respectively. The test lasted 24 minutes for the third specimen and 6 minutes for the fourth one. The normalized damping factors versus the life ratio for the four cases were combined to give an overall relationship and the plot is given in Fig. 2. Despite the scatter in this data the decreasing trend of the damping factor is obvious.

ON-LINE FATIGUE FAILURE FORECAST

The basis of the Fatigue Failure Forecast (FFF) is the correlation from plot of the normalized damping factor versus the life ratio as shown in Fig. 2. From this plot it can be seen that, despite some scatter, a decreasing exponential trend for the normalized damping factor versus time is obvious for all specimens, in terms of the life ratio. The normalized plots are used because the damping factor of the "initial" and "last" data set, for different kinds of specimens, can be different values, depending on the loading pattern input and the initial condition of the specimen. In general for the tests performed, the ratio of the normalized damping factors for the "last" to the "initial stable" condition is about 0.4-0.5. In other words, the decrease in value of the normalized damping factor could be used as a warning signal that failure was possible. Thus, by normalizing both the damping factor and the test time, the plots of normalized damping factor versus life ratio given a correlation in normalized form.

The decreasing trend of the normalized damping factor as a function of life ratio is considered as a deterministic trend. Consequently, the data was fitted by a deterministic exponential model and is given by

$$\ln \zeta^* = -0.0068 - 0.8310\ t^* \qquad (4)$$

This model can be used to estimate the fatigue life, and the forecasting process can be initiated when at least two sets of data have been analyzed. In this case, if ζ_1 is the damping factor of the "initial stable condition" obtained from the adequate AR model for data taken at time t_1, and ζ_2 is the damping factor for the next data set taken at time t_2, then the life ratio at time t_2 is given by

$$t_2^* = \frac{\ln \zeta_2/\zeta_1 + 0.0068}{-0.8310} \qquad (5)$$

The corresponding predicted life, t_{pred} of the specimen estimated at time t_2 is given by

$$t_{pred(t_2)} = (t_2 - t_1)\frac{1}{t_2^*} + t_1 \qquad (6)$$

After a specimen fails, its total life can be recorded, and then the prediction error, for the prediction made at time t is calculated from

$$\text{error} = \frac{t_{pred\ (t_2)} - \text{Actual Life}}{\text{Actual Life}} \times 100\% \qquad (7)$$

which can be used to estimate the accuracy of these methods.

To illustrate the on-line FFF, four cylindrical specimens were subjected to a stochastic loading. During the test, the strain data were measured continuously and transmitted to a computer for model fitting and specimen life predictions were conducted from time to time.

The predicted life of the first smooth specimen CSE, estimated after 20 minutes test time, was 428 minutes as shown in Table 2. The estimated life ratios and predicted lives for 50, 130, and 180 minutes and the corresponding errors are given in Table 2. The results show that updating the forecast will improve the life estimation considerably, since the method inherently takes into account the damage done by the previous loading condition. In addition, in the beginning of the life test the estimation of the damping factor is not the best because of the transient period from zero to full dynamic load, and because cyclic hardening or softening of the material may also take place during this time.

TABLE 2 **On-Line Life Prediction of Smooth Specimen CSE. Maximum engineering stress: 44.8 Ksi; Minimum engineering stress: 11.2 Ksi; Actual Life: 232 min. (Recorded after predictions).**

Time [min]	AR(n) Model	ζ	ζ^*	t^*	t_{pred} [min]	Error %
3	9	0.413				
20	9	0.398	0.96	0.04	428	84.5
50	10	0.375	0.91	0.11	430	84.2
130	11	0.246	0.60	0.61	209	9.7
180	10	0.220	0.53	0.75	239	3.1

It is also possible to take the estimated damping factor at 20 minutes as the reference point, and then the predicted life at 130 minutes for a normalized damping factor of 0.62 is 213 minutes. Next, when the 50 minute is taken as the reference at 130 minutes test time, the predicted life is 210 minutes, which is still very close to the prediction based on 3 minute or 20 minute references. This result shows the capability of the proposed on-line FFF method to predict the life at any time during the test period. In addition, this result also supports the choice of the "ln-linear" prediction model as the basis for on-line prediction, since the fatigue damage can be estimated based on any observed time period.

The second specimen (CSF) was tested on-line and the life predictions and their errors are given in Table 3. As before, a prediction at about 10% (20 minutes) of the total life, yielded a relatively high error of 72.5%. Whereas, the predictions estimated at 60 and 120 minutes had errors of only 36.6% and 13.4%, respectively. Other notched specimens, CSG and CSH, were analyzed on-line and the life predictions were very good - within 15.6% and 11.9%.

TABLE 3 **On-Line Life Prediction of Smooth Specimen CSF. Maximum Engineering Stress: 67.2 Ksi; Minimum Engineering Stress: 22.4 Ksi; Actual Life: 58 min. (Recorded after predictions made.)**

Time [min]	AR(n) Model	ζ	ζ^*	t^*	t_{pred} [min]	Error %
4	9	285				
20	10	220	772	303	57	72.5
60	10	196	688	442	131	36.6
120	10	186	653	505	233	13.4

CONCLUSIONS

This study was a new forecasting approach which used stochastic dynamic time series models of the system output or strain for improved fatigue process characterization. This study also showed a practical and effective methodology for on-line fatigue failure forecasts. It has the advantage that the current condition of the test piece is quantified by the damping factor estimated from the adequate AR model parameters of the strain response only. As a result of analyzing only the output, efforts to characterize the input and the previous loading history can be eliminated for reduced forecasting complexity and modeling costs.

The damping factor value depends on material, specimen geometries, existing flaws in the part, prior loading conditions, and the current loading condition, and it represents the system as measured by the strain response data. A relationship between the normalized damping factor value and the remaining life, or life ratio, was based on an off-line analysis and was given in terms of a 'ln-linear' equation. Although this correlation is material dependent, it does not depend on specimen geometries, existing flaws in the specimen, nor prior loading conditions. For the tests run, failure could be expected when the normalized damping factor value ζ^* decreased below 0.5 in value.

The AR model closely matches what physically happens as the fatigue process progresses; that is, the strain at a particular time is dependent on its previous value. Also the damping factor from the most dominant mode decreases with time, and this decreasing trend indicates the reduced capacity of the strain response to return its equilibrium condition. In other words the range of the strain amplitude increases with time as a result of the fatigue failure process. Furthermore, the increasing value of the real root λ represents the increasing mean of the strain response as a result of plastic strain accumulation, and could also be used to improve the FFF.

The on-line Fatigue Failure Forecast results presented here are considered very good, since the prediction error without updating is between 1% - 84.5% from the actual life. The final updated error ranged from only 3.1% - 5.2% for smooth cylindrical specimens, and from 11.9% - 12.8% for notched cylindrical specimens.

REFERENCES

(1) Pandit, S.M. and Wu, S.M., Time Series and System Analysis with Applications, John Wiley, 1983.

(2) Notohardjono, B.D. and Ermer, D.S., "On-line Fatigue Life Prediction of Steel Specimens Under Stochastic Loading by Time Series Modeling of the Output", The ASME Pressure Vessel and Piping Conference, San Antonio, Texas, 1984.

(3) Ermer D.S. and Notohardjono, B.D., "Fatigue Failure Identification by Time Series Model", Engrg. Fracture Mechanics J., Vol. 20, No. 516, 1984, pp. 705-718.

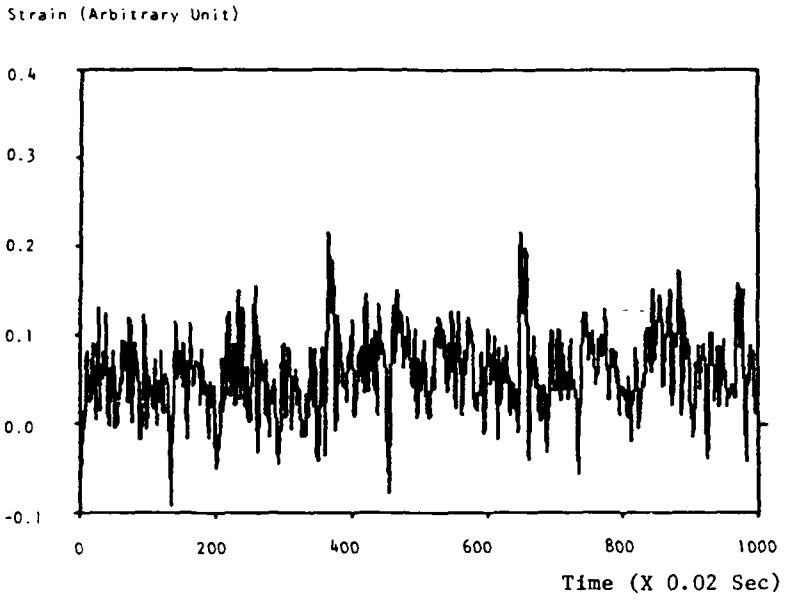

Figure 1 Typical strain data.

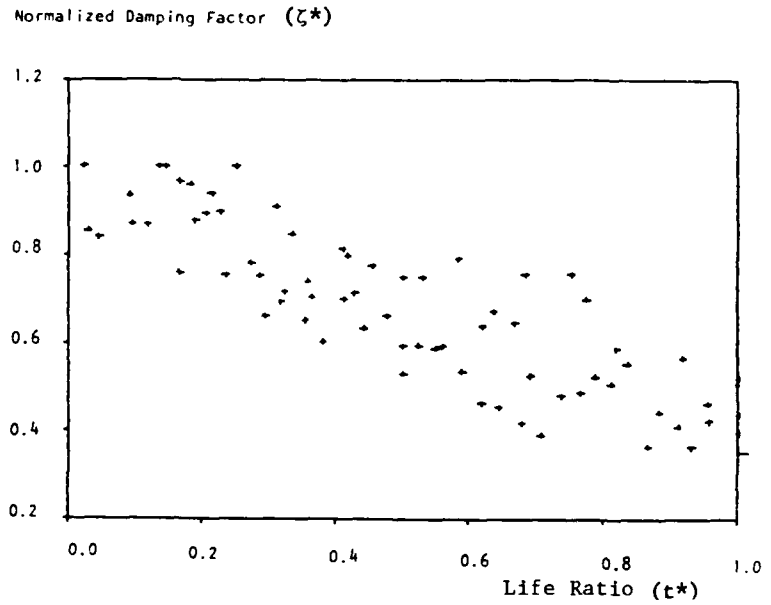

Figure 2 Normalized damping factor vs life ratio for cylinderical specimens CSA, CSB, CSC and CSD combined.

EMBRITTLING EFFECT OF THE PLASTIC ZONE

J. C. M. Li*

The plastic zone developed in Mode II and Mode III loading can shield the crack tip from the applied stress and increases the toughness of the material. However, upon unloading, it embrittles the material by providing the driving force for crack propagation. In Mode I loading, an asymmetric plastic zone can cause mixed mode crack propagation and crack branching and can also embrittle the material by the above Mode II effect. Plastic zones produced by chemical means such as hydrogen charging also can enhance crack propagation and may be the cause for hydrogen embrittlement.

INTRODUCTION

The ability of a material to develop a plastic zone at the crack tip is usually a sign of toughness. The larger the plastic zone, the tougher is the material because a crack cannot propagate without first expending part of its driving energy to develop the plastic zone. Another way of viewing this toughening effect is to say that the crack is "shielded" from the applied stress by the stress field of all the dislocations in the plastic zone(1-5):

$$K = K_a + K_s \qquad (1)$$

where K_a is the applied stress intensity factor without the plastic zone, K is that with the plastic zone, and K_s, when negative, is the shielding effect of the dislocations. The material is tough because K_a must first overcome K_s before it can propagate the crack.

*Materials Science Program, University of Rochester Rochester, New York 14627

However, under certain conditions, K_S may become positive. Then the plastic zone will enhance crack propagation. Several such conditions are described in this paper.

UNLOADING IN MODE II AND III

In Mode I loading, a positive K_I opens up the crack and propagates it and a negative K_I closes it so that the crack cannot propagate. In this case, the plastic zone developed during a positive K_I loading will shield the crack so that the effective K_I is less than the applied K_I. Upon unloading, the plastic zone closes the crack and reloading needs a minimum K_I equal to the shielding K_I before the crack can open. This is the whole idea behind the crack-closure theory of overloading effects. However, complications arise with unexpected consequences when the plastic zones are asymmetric. This will be discussed later.

The situations of Mode II and Mode III loadings are entirely different, since both positive K_{II} (or K_{III}) and negative K_{II} (or K_{III}) can propagate the crack. As a result, the plastic zone developed during a positive K_{II} or K_{III} loading can propagate the crack upon unloading. The effect is more pronounced when shielding is more effective. For example, if 90% of the applied K_{III} is shielded by the plastic zone, upon unloading 90% of the previously applied K_{III} is now available to propagate the crack.

An example (6) obtained by computer simulation is shown in Fig. 1. A Mode II or Mode III crack is propagating while emitting dislocations along the crack plane. Under an applied stress of $5A\sqrt{b/\ell}$ ($A = \mu/2\pi(1-\nu)$ for Mode II and $\mu/2\pi$ for Mode III, μ is shear modulus, ν is Poisson's ratio, b is the Burgers vector of the dislocations and ℓ is the crack length) or an applied stress intensity factor of $5A\sqrt{2\pi b}$, a crack emits a dislocation whenever its effective K exceeds $2A\sqrt{2\pi b}$ and in the meantime propagates with a velocity

$$v_c = bM_c \left(\frac{K}{A\sqrt{2\pi b}} \right)^3 \qquad (2)$$

where M_c is the crack mobility. The emitted dislocaitons move away according to a velocity-stress relation as follows:

$$v = M\left(\frac{\tau-\tau_F}{A}\right)^3 \qquad (3)$$

where τ_F is the lattice friction stress assumed to be $0.1A$ for this simulation, M is the dislocation mobility. The crack mobility is assumed to be smaller than dislocation mobility by a factor of $M_c/M = 10^{-7}$. Under these conditions, the crack propagates at

$$\Delta X_c/\Delta t = 7.6\times10^{-7}bM$$

during the development of the plastic zone and upon saturation when the plastic zone moves steadily with the crack. The effective K at the crack tip is $2A\sqrt{2\pi b}$ while the applied K is $5A\sqrt{2\pi b}$ so that $3A\sqrt{2\pi b}$ is shielded by the plastic zone.

Unloading during the steady state propagation causes the crack to surge forward at high speed. The distance covered before the crack stops at the end of the plastic zone is almost the same as that covered by crack extension during the development of the plastic zone. Sometimes there is some delay after unloading because the crack must go through the dislocation-free zone before the surge takes place. Even so the crack speed during this delay period may be faster than the speed during loading.

Asymmetric Plastic Zone in Mode I

As mentioned earlier, in Mode I loading, the K_I shielded by the plastic zone closes the crack during unloading and hence the plastic zone has no embrittling effect. However, when the plastic zone is asymmetric, while some K_I still may be shielded, there is some K_{II} developed by the plastic zone which can enhance crack propagation during loading or unloading. This effect is usually overlooked but it can explain crack branching, mixed mode propagation, shear band decohesion, and other effects of crack tip plasticity.

As an example (7), a Mode I crack is under an applied stress $\sigma = 10A\sqrt{b/\ell}$ where $A = \mu/2\pi(1-\nu)$, b is the Burgers vector and ℓ is the crack length. This applied stress creates a stress intensity factor K_a equal to $10A\sqrt{2\pi b}$. A number N of dislocations are allowed to be emitted along a slip plane oriented at an angle of $3\pi/8 = 67.5°$ very close to the maximum shear stress plane (70.5°). The lattice friction for the motion of these dislocations in terms of a resisting shear stress is $0.1A$. The distribution of these dislocations at equilibrium is shown in Fig. 2. It is seen that, when N is small, the dislocations are not gathered at the crack tip. The maximum linear density (number per unit length) is at some distance ahead of the crack tip. There is a "dislocation-free" zone at the immediate vicinity of the crack tip. The size of such a zone diminishes with increasing number of dislocations emitted until saturation. Under the loading conditions just described, 99 dislocations would saturate the slip plane, at which time the dislocation-free zone disappears and the location of maximum linear density approaches the crack tip.

The work done by the applied stress to emit these dislocations reduces the driving force for crack propagation. This is shown in Fig. 3. The applied stress intensity factor is $10A\sqrt{2\pi b}$ before the emission of any dislocations. The shielding effect of the emitted dislocations reduced the stress intensity factor as shown. The shielding is the most effective when the angle of the slip plane is closest to the maximum shear stress plane. However, it is noted that even at saturation there is still a residual stress intensity factor at the crack tip. Again, this residual stress intensity factor is the smallest when the slip plane is closest to the maximum shear stress plane.

While the emitted dislocations are protecting the crack tip from the applied stress so that the effective K_I is smaller than the applied K_I, they also produced a K_{II} which was not there before. This is shown in Fig. 4. The sign of K_{II} depends on the angle of the slip plane. The magnitude is seen to be the smallest when the angle is $3\pi/8$ and largest when the angle is $\pi/4$ or $\pi/2$.

Such effects on K_{II}, being created by the plastic zone, do not disappear upon unloading. Thus the plastic zone, instead of the usual toughening role, can embrittle the material by contributing to the driving force for crack propagation.

CHEMICAL PLASTIC ZONE AND HYDROGEN EMBRITTLEMENT

In addition to the mechanically produced plastic zones, chemically assisted dislocation emission from a crack tip with or without the presence of internal or external stresses can exert a stress intensity factor which can provide the driving force for crack propagation. This is a mechanism recently proposed (8) for hydrogen embrittlement. The dislocation emission is thought to be caused by the chemical driving force for hydrogen dissolution which is enhanced by dislocation pipe diffusion, similar to the phenomenon of DIGM (9). Of course, the chemical drivin- force can be combined with any stress intensity factor present at the crack tip to enhance the dislocatin emission process. The dislocations emitted by chemical means also can exert a stress intensity factor and if the sign is proper, can propagate the crack. So a crack can extend even without any mechanical stress simply because of the chemically produced dislocations.

For Mode I loading, the added chemical driving force can reduce the critical K_I for dislocation emission and, depending on the available slip systems, also can produce an asymmetric plastic zone. The plastic zone size could be much greater than that which can be produced by mechanical stress alone. Here the Mode II stress intensity factor produced by the plastic zone can cause crack extension that is otherwise impossible without the chemical

AD-A184 047 FATIGUE '87 VOLUME 3(U) VIRGINIA UNIV CHARLOTTESVILLE SCHOOL OF ENGINEERING AND APPLIED SCIENCE 46
R O RITCHIE ET AL. JUN 87 ARO-24134.3-MS-CF
UNCLASSIFIED N00014-87-G-0008 F/G 20/11 NL

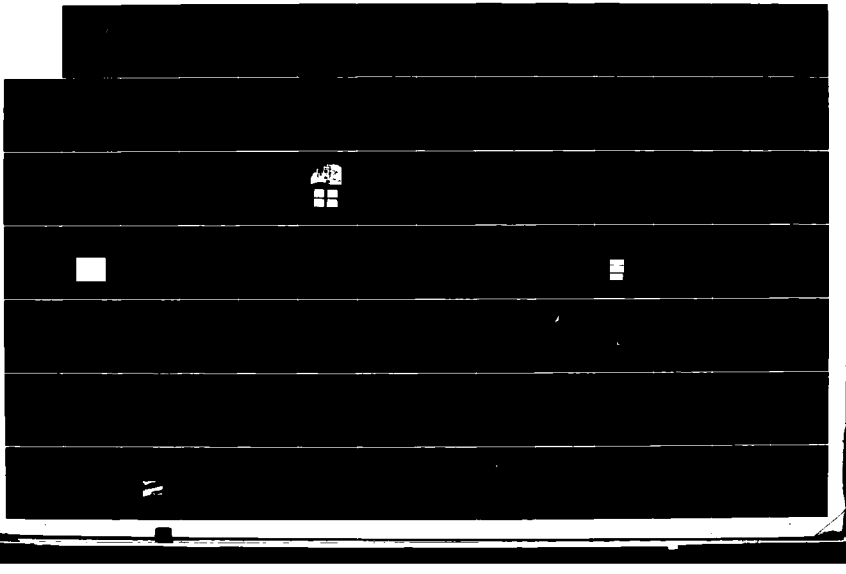

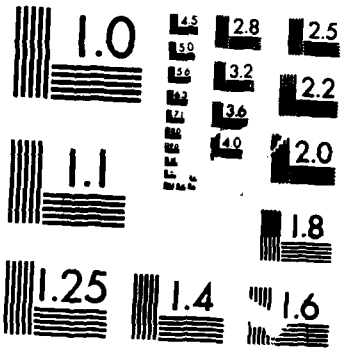

For Mode II loading, the added chemical driving force reduces the K_{II} required for dislocation emission and hence produces a greater shielding effect. Upon unloading or reverse loading the plastic zone will enhance crack propagation more than the situation without the chemical effect.

CONCLUSIONS

The plastic zone produced mechanically or chemically or both, sometimes can enhance crack propagation and hence, contrary to usual thinking, embrittles the material.

ACKNOWLEDGEMENT

Financial support by the US Department of Energy through DE-FG02-85 ER 45201is gratefully acknowledged.

REFERENCES

(1) B. S. Majumdar and S. J. Burns, Acta Met., Vol. 29, 1981, pp. 579 -588.

(2) R. Thomson, J. Mat. Sci. Vol. 13, 1978, pp 128 - 142.

(3) J. Weertman, Acta Met., Vol. 26, 1978, pp 1731 - 1738.

(4) E. W. Hart, Int. J. Solids Structures, Vol. 16, 1980, pp. 807 - 823.

(5) Shu-Ho Dai and J. C. M. Li, Scripta Met. Vol. 16, 1982, pp 183 - 188.

(6) Rui-Huan Zhao and J. C. M. Li, J. Appl. Phys. Vol. 58, No. 11, 1985, pp 4117 - 4124.

(7) V. Lakshmanan and J. C. M. Li, to be published.

(8) J. C. M. Li, C. G. Park and S. M. Ohr, Scripta Met. Vol. 20, 1986, pp. 371 - 376.

(9) P. G. Shewman, G. Meyrick, S. Mishra and T. A. Parthasarathy, Scripta Met. Vol. 17, 1983. pp 1231 -1235.

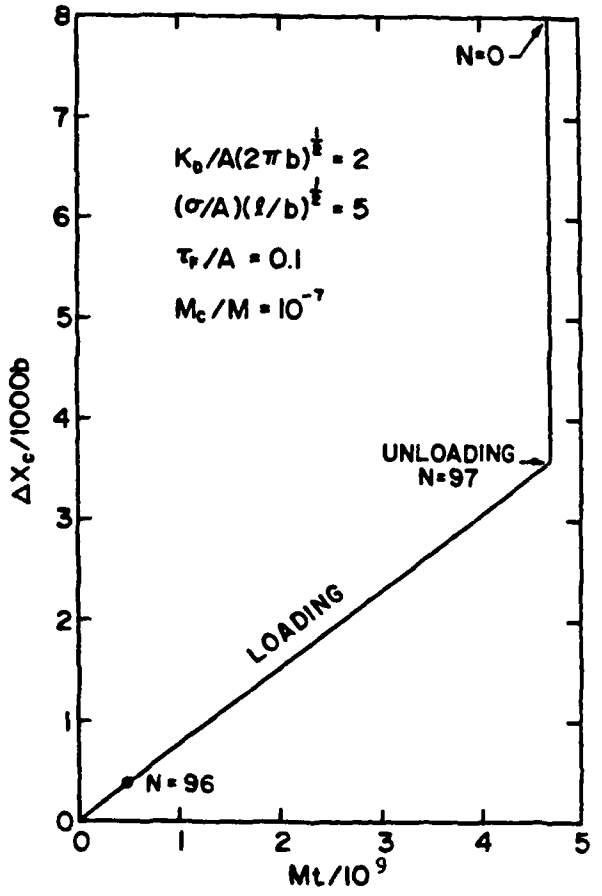

Fig. 1 Crack propagation during loading and unloading with simultaneous dislocation emission.

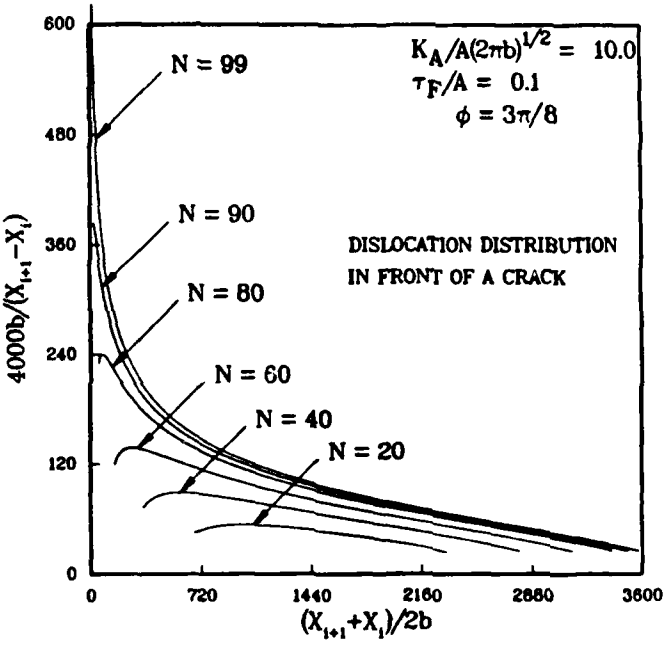

Fig. 2 Dislocation distribution from asymmetric Mode I emission along an inclined plane.

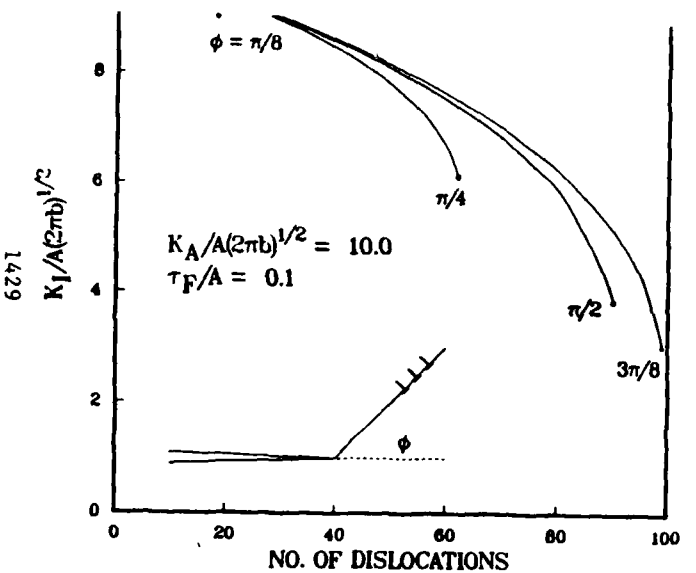

Fig. 3 Shielding effect of an asymmetric plastic zone developed in Mode I loading.

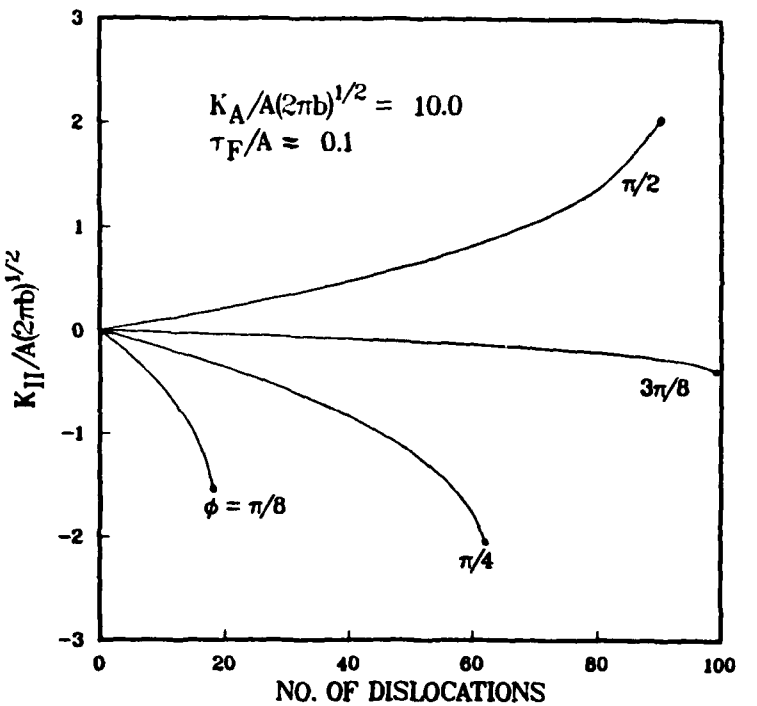

Fig. 4 K_{II} developed by an asymmetric plastic zone in Mode I loading.

A COMPARISON OF PLASTIC WORK ENERGY AND EXTERNAL ENERGY INPUT FOR FATIGUE CRACK PROPAGATION

C. Q. Bowles* and E. G. Wenski**

The plastic work, U, and the external energy input, W. required for fatigue crack propagation are discussed. Both energy values are experimentally determined for 2024-T35i Al. The values of plastic work are in agreement with those of Fine and coworkers (1-4). The external energy input to the specimen as determined from hysteresis loops measured by a load line clip gage is approximately three times larger than the plastic work.

INTRODUCTION

The concept of measuring the energy required for fatigue crack propagation has intrigued workers in the area of fatigue and fracture for some time. The following options exist.

1. Measure the energy input to the plastic zone ahead of the crack tip and attempt to correlate that energy with some critical energy required for crack propagation.
2. Measure the energy required to create two new fracture surface increments usually defined as t(da) where t is the specimen thickness and da is a crack growth increment.

* Associate Professor Mechanical & Aerospace Engineering, University of Missouri-Kansas City
** Formerly M.S. Graduate Student, presently with Allied Bendix Aerospace Corporation

3. Still another possibility is to measure the combined energies for creation of an increment of fracture surface and that input to the plastic zone ahead of the crack tip.

The more difficult of the above is item two which will not be discussed here.

CYCLIC PLASTIC WORK IN THE FATIGUE CRACK PLASTIC ZONE

Fine and co-workers (1-4) have developed an experimental technique to measure the energy input to the plastic zone associated with fatigue crack propagation. In particular small strain gages are attached to the sample near the tip of the fatigue crack and the hysteretic local strain-remote stress curve is recorded. The local stress is determined from a cyclic stress-strain curve of bulk material by finding the stress associated with the measured local strain. This local stress is then substituted for the originally measured remote stress. The total plastic work associated with each increment of crack growth is then determined as U and is defined as follows:

$$U = \frac{\int_{-Y_p}^{Y_p} \int_{0}^{X_p} \left(\int_{\varepsilon_1}^{\varepsilon_2} \sigma_u^2 d\varepsilon - \int_{\varepsilon_1}^{\varepsilon_2} \sigma_\ell^2 d\varepsilon \right) dX dY}{da/dN}$$

where ε_1 and ε_2 are the strains at the end points of the hysteresis loop, σ_u and σ_ℓ are the upper and lower local stresses for a single hysteresis loop in the plastic zone. The limits of integration are the boundaries of the plastic zone along X and Y directions with respect to the crack plane. The U measured by Fine and co-workers is formally defined by Weertman (5) and Mura and Lin (6) who suggest fatigue crack growth is governed by

$$\frac{da}{dN} = A \frac{(\Delta K)^4}{\mu \sigma_o^2 U}$$

where μ is the shear modulus, σ_o is a measure of the strength of the alloy and A is a constant of proportionality.

COMBINED PLASTIC ZONE ENERGY AND CRACK GROWTH ENERGY

Another approach to measuring the energy required for crack propagation was presented by Dowling (7) and Dowling and Begley (8) who used the concept of the cyclic J integral or ΔJ to characterize fatigue crack growth in pressure vessel steels. Rice (9) has pointed out that strictly speaking J should only be applied to two neighboring cracks of lengths a

and a+da and in such a case J is related to the potential energy difference between the two cracks. However, Dowling and Begley proposed an operational definition of J to account for cyclic deformation and incremental crack growth encountered in fatigue. The resulting ΔJ is shown in Fig. 1.

It is interesting to note that both U and ΔJ have the same units (Joules/sq.m) as a result of both being obtained from stress vs. strain and load vs. displacement plots respectively. However, Liaw (10) points out that the load vs. displacement plot is more appropriately related to W where

W = energy per cycle absorbed in the plastic zone + energy to extend an increment of crack length in one cycle

$$W' = \frac{W}{da/dN} = \frac{\text{energy/cycle absorbed in the plastic zone}}{dA/dN + \Delta V/(da/dN)}$$

$$W' = U + \Delta J$$

where W' is defined as the external energy input per cycle for a unit area of fatigue crack, dA. Using published literature data Liaw compared U for HY80 stees and ΔJ for A533B steel and finds U to be more than two orders of magnitude larger than ΔJ. The conclusion drawn is that external energy input to the sample during fatigue is primarily dissipated in the plastic zone and consequently $W \cong U$. In some similar work the authors of the present paper have attempted to compare the plastic work and the external energy input as measured by clip gage for the compact tension specimen.

EXPERIMENTAL DETAILS

Material selected for the experiments was 2024-T351 plate 1/2 in thick. ASTM compact tension specimens were fabricated with a modified notch to allow for load line displacement measurement. One face of each specimen was metallographicaly polished so that initial crack growth could be optically monitored. The ASTM Standard for decreasing ΔK was used to obtain a crack growth rate of 6.35E-06 mm/cycle with corresponded to a ΔK of 11 MPa. At the point of constant crack growth the specimens are removed from the test machine and 200x200 μm strain gages were glued to the specimen in the vicinity of the crack in the manner described by Fine (1) and as shown in Fig. 2. A standard clip gage was also mounted externally at the load line for the external work measurements.

When the tests were restarted reductions in load occurred every 0.125 mm in order to maintain constant ΔK. Testing was done at 10Hz except during measurement of hysteresis loops when the frequency was reduced to 0.1Hz. Cyclic stress strain data required for analysis of hysteresis loops was obtained from bulk specimens prepared from the 2024-T351 plate.

Two X-Y plotters were used so that hysteresis loops obtained from strain gages in the plastic zone and the load line mounted clip gage could be recorded simultaneously. All hysteresis loops were then digitized and stored for later analysis.

RESULTS

Cyclic Plastic Work

Data obtained from strain gages placed at the tip of the crack was analyzed in the manner described by Ikeda, et.al. Hysteresis loop areas were numerically summed in both the X and Y directions and that value divided by the crack growth increment per cycle. The resulting plastic work was

U = 2.06E05 Joules/sq.m

This result is in good agreement with that of Liaw, Kwun and Fine (3) who obtained for 2024-T4

U = 2.9E05 Joules/sq.m (average of two values)

Cyclic External Energy

The hysteresis loops obtained from a standard load line clip gage were first analyzed in the standard manner giving the following results:

J = 64.644 Joules/sq.m
J = 57.362 Joules/sq.m (corrected for crack closure)

The hysteresis loop data obtained with the clip gage was then analyzed by considering the area of each loop to be proportional to the external energy input into the sample. The area was then divided by the specimen thickness and the crack growth increment da. The results obtained in this manner are

W = 6.266E05 Joules/sq.m
W = 4.660E05 Joules/sq.m (corrected for crack closure)

DISCUSSION

The proposal by Liaw (10) that the external work as measured by a load line clip gage represents the energy input to the plastic zone plus the energy required to create new fracture surface appears to be correct. However, the further extension of that concept to define the external work as the sum of the plastic work U and ΔJ does not appear to be correct. In the present work the sum of U and ΔJ are approximately three times less than the calculated value of W.

The equation for ΔJ has been given by others as

$$J = 2A/Bb$$

where A is the area of the hysteristis loop, B is the specimun thickness and b is the remaining ligiment. The modification of this equation by dividing by the crack growth increment, da, instead of the remaining ligiment, b, no longer gives ΔJ in the strictest sense.

CONCLUSIONS

1. The value of the plastic work, U, obtained for 2024Al compact tension specimens in this work is in good agreement with that of Fine and coworkers for center cracked specimens.
2. The external energy input to a compact tension specimen as measured by load line mounted clip gage appears to be the sum of the energy input to the plastic zone and the energy required to create two new surfaces associated with the crack growth increment.
3. The value of the external energy input is three times the plastic work energy, U.

REFERENCES

1. Ikeda, S., Izumi, Y., and Fine, M. E., Engineering Fracture Mechanics, Vol. 9, 1977, pp. 123-136.
2. Izumi, Y., and Fine, M. E., Engineering Fracture Mechanics, Vol. 11, 1979, pp. 791-804.
3. Liaw, P. K., Kwun, S. I., and Fine, M. E., Metallurgical Transactions, Vol. 12A, 1981, pp. 49-55.
4. Izumi, Y., Fine, M. E., and Mura, T., International Journal of Fracture, Vol. 17, 1981, pp. 15-25.
5. Weertman, J., International Journal of Fracture, Vol. 9, 1973, pp. 125-131.
6. Mura, T., Lin, C. T., International Journal of Fracture, Vol. 10, 1974, pp. 284-287.
7. Dowling, N. E., ASTM STP 601, 1976, pp. 19-32.

8. Dowling, N. E., and Begley, J. A., ASTM STP 590, 1976, pp. 82-103.
9. Rice, J. R., Journal of Applied Mechanics, June 1968, pp. 379-386.
10. Liaw, P. K., Engineering Fracture Mechanics, Vol. 22, 1985, pp. 237-245.

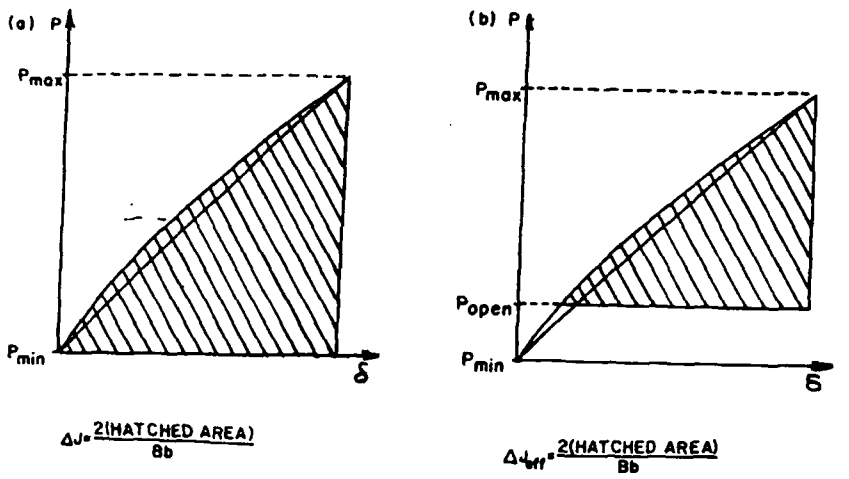

Figure 1 Operational definition of (a) cyclic J (ΔJ) and (b) effective cyclic J (ΔJ_{eff}).

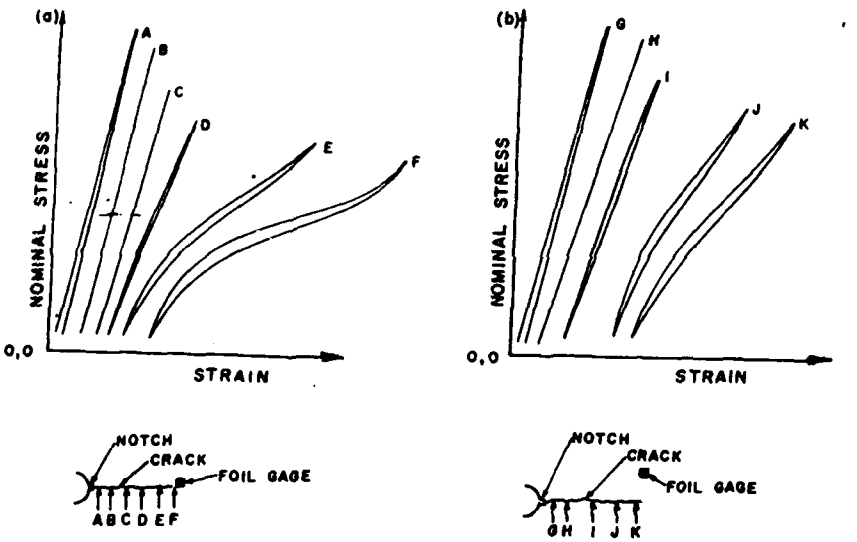

Figure 2 Typical nominal stress-strain hysteresis loops for (a) y = 0.020 in.

FATIGUE UNDER NONNORMAL RANDOM STRESSES USING MONTE-CARLO METHOD

H.J. Liu and S.R. Hu *

Abstract: A fatigue life prediction model is proposed for the structural elements subjected to a stress process, modeled as a stationary wide-band nonnormal process. This model is restricted to high cycle fatigue design and evaluation, uses available constant amplitude material fatigue data and Palmgren-Miner (PM) rule. The test results suggest that the model give a reasonable life estimates. Sencondly, Monte-Carlo method is discussed herein in some depth. The different time histories simulated by Monte-Carlo method for a given spectral density has been shown to be equivalent in the meaning of effects on fatigue damage in high cycle fatigue.

INTRODUCTION

Most of engineering structures, such as civil engineering structures, offshore platforms and flight vehicles, are subjected to the loads which vary in the random manner. Obviously, the loads are due to such environmental phenomena as earthquake, water waves, and wind. There are a lot of difficulties involved in predicting the time to fatigue failure in these so-called irregular loadings. This study concentrates on some aspects of the general problem of relating fatigue life. Other problems, which are not considered here, include uncertainty of material behavior and environmental factors etc, the factors which significantly influence fatigue behavior.

In many engineerings mentioned above, the conditions under which the engineering structures work are so complicated that the structural "hot-point" stress time histories are very difficulty to be got. In the other hand, an ergodic process is often too long to be expressed, the power spectral density needs only a piece of small paper to express enough information of loading. Maybe for these reasons the loading information for design purpose is often

*Dept. of Engineering Mechanics, Shanghai Jiao Tong University, Shanghai, P.R. China.

given in spectral form, such as sea force spectrum for offshore platform design, wind force spectrum for flight vehicle design. One can have the "hot-point" power spectral density (PSD) according to the structural transfer function H(jw). So we are sure that the PSD is known in any point of the structure. If the PSD is know, how do the fatigue analysis using cycle counting method and fatigue test be carried? The answer is simple. The fatigue analysis and test can be carried based on the simulated time histories which are generated by Monte-Carlo method. As we know, we can generate a series of different simulated histories from a given PSD. In this way another problem araises. It's known that different sequences make the different effects on the fatigue damage(1). Do all these simulated histories make the same effects on the fatigue damage?

Although many stress processes are normal, i.e. Gaussian(2)(3), there are many stress processes which are nonnormal. It is found that infleunces on the fatigue damage for normal and nonnormal processes are different(4). So the nonnormality of stress processes should be considered.

The general goal of this study is to develop an engineering model which can be used for design purpose and predicting fatigue damage under a stationary and ergodic random stress process X(t) which in general can be wide-band, nonnormal, and to make it clear whether the simulated time histories which often are used for fatigue analysis(4)(5)(6)(7) make the same effects on fatigue damage. Here high cycle fatigue only is considered. The fatigue behavior of material is described by an S-N curve which is assumed to be of the form

$$NS^m = C \quad \text{.....(1)}$$

in which S is the stress range, N is cycles to failure and m and C are empirical constants obtained from the constant amplitude experiments. All results presented relate to use of the Palmgren-Miner (PM) rule for calculating cumulative damage and rainflow algorithm is used to define cycles. The stress time history is considered to be a stationary. In general, the results included here may be considered to be appropriate to the crack initiation or both initiation and propagation period of fatigue and can be applied to structural systems.

FATIGUE UNDER NORMAL WIDE-BAND LOADING

In this section, X(t) is assumed to be stationary and normal, so the PSD W(f) exists, the typical PSD function is shown in Fig.1 Some important characteristics of process can be defined by PSD, list in Table 1. The general expression for the probability density of the peaks of the process can be obtained(8):

$$p(s)=\frac{1}{\sqrt{2\pi}\,\sigma}(1-\alpha^2)^{\frac{1}{2}}\exp\left[\frac{-s^2}{2\sigma^2(1-\alpha^2)}\right]+\frac{s}{2\sigma^2}\left[1+\operatorname{erf}\left(\frac{s}{\sigma(2\sqrt{\alpha^2-2})}\right)\right]*$$
$$*\exp\left(-\frac{s}{2\sigma^2}\right) \quad \text{.....(2)}$$

TABLE 1- Definition of Basic Terms of A Random Process

Definition	Term
K^{th} moment of PSD function, m_k	$\int_0^\infty f^k W(f)df$
Root-mean-square, σ	$\sqrt{m_0}$
Expected rate of zero crossings with (+) slope, f_0	$\sqrt{m_2/m_0}$
Expected rate of peaks, n_0	$\sqrt{m_4/m_2}$
Irregularity factor, α	f_0/n_0
Spectral width parameter, ϵ^2	$1-\alpha^2$

in which erf(.) is the error function. For the extreme case the probability density for peaks reduces to:

$$p(s)=\frac{s}{\sigma^2}\exp(-\frac{s^2}{2\sigma_2^2}),\ \text{for } \alpha=1,\ \text{narrow band} \quad \ldots\ldots\ldots\ldots\ldots\ldots(3)$$

$$\text{and } p(s)=\frac{1}{\sqrt{2\pi}\,\sigma}\exp(-\frac{s^2}{2\sigma^2}),\ \text{for } \alpha=0,\ \text{white noise} \quad \ldots\ldots\ldots\ldots\ldots\ldots(4)$$

where Eq.(3),(4) are called to have Rayleigh and Gaussian (normal) peak distribution respectively. In general, for most engineering structures the peak distribution will be neither Rayleigh nor Gaussian.

Palmgren-Miner cumulative damage rule is consistent with an assumption that the cumulative damage grows linearly with time. Although this rule is widely used, qustions are often raised regarding the degree of error that it introduces if damage grows nonlinearly. It is shown that PM rule is also consistent with a fairly broad class of theoretical models, which do give such nonlinear growth of damage(4). For this study PM rule is used. Assuming a linear damage rule, it has been shown that damage after n stress cycles can be written as(8),

$$D=nE[\frac{1}{N(s)}] \quad \ldots\ldots\ldots\ldots\ldots\ldots\ldots\ldots\ldots\ldots\ldots\ldots\ldots\ldots\ldots\ldots\ldots\ldots(5)$$

where N(s) is the number of cycles to failure at stress range S in the constant amplitude test and E(.) is the expected value. Fatigue failure is said to accur if $D \geq 1$. If the process is stationary, normal, and narrow band,

$$D_{NB}=\frac{n}{C}(2\sqrt{2}\,\sigma)^m\Gamma(\frac{m}{2}+1) \quad \ldots\ldots\ldots\ldots\ldots\ldots\ldots\ldots\ldots\ldots(6)$$

in which $\Gamma(.)$ is gamma function and n can be replaced by f_0T, T is desing life.

Fatigue stress cycles are easily identified in a narrow band process. If the process is wide band, it is not immediately obvious

how to count the fatigue stress cycles to be used with PM rule. A lot of cycle counting algorithms have been proposed. In these algorithms rainflow method is considered as one of the most accurate of predicting fatigue damage(1). Rainflow algorithm can identify cycles associated with closed hysteresis loops. Because of the complexity of the rainflow algorithm, it would be expectionally difficult to extract the distribution of stress cycles from the spetral density function W(f). Using Monte-Carlo approach, a sample function $X^d(t)$ of the process X(t) can be generated from a given PSD W(f) in a digital computer. Then the rainflow algorithm is used to the simulations to obtain a sample of rainflow stress cycles which can determine the degree of fatigue damage. Comparing rainflow damage with D_{NB}, the differences between them can be known. Wirsching and Light have proposed a model for wide band fatigue which is based on a modification of narrow band model(5).

Assume that fatigue damage under a wide band stationary process can be written as,

$$D_{WB} = \lambda \cdot D_{NB} \quad \text{.....(7)}$$

where λ is a correction factor for the narrow band assumption. Estimation of λ are obtained by computing D from a rainflow analysis of a sample from W(f) obtained by Monte-Carlo approach, damage can be estimated without simulating the stress processes for further analysis. This correction factor is simply,

$$\lambda = \frac{\text{damage rate by rainflow algorithm}}{\text{damage rate by narrow band assumption}} \quad \text{.....(8)}$$

To estimate λ for a given m and ϵ , great number of digital experiments have been done for four typical spectral shapes.(see Ref.5). From the experimental data, an empirical function of λ for a given m and ϵ can be written as,

$$\lambda(m,\epsilon)=a(m)+[1-a(m)](1-\epsilon)^{b(m)} \quad \text{.....(9)}$$

where

$$a(m)=0.926 - 0.033\ m$$
$$b(m)=1.587m - 2.323 \quad \text{.....(10)}$$

The model described by Eq.(7) can be to describe fatigue damage under wide band stress processes, and has been successfully used in the engineerings(9)(10).

SIMULATED STRESS TIME HISTORIES

For fatigue analysis using cycle counting method and test purposes Monte-Carlo approach is often used. Given an arbitrary one sided PSD function W(f), a sample of X(t) can be simulated using the following form(11),

$$X^d(t) = \sum_{j=1}^{M} [2W(\omega_j)\Delta\omega_j]^{\frac{1}{2}} \cos(\omega_j t + \phi_j) \quad \text{.....(11)}$$

where $W(\omega) = W(f)/2\pi$ in ω (rad/s). Frequency is defined over the interval (0, ω_u) with partition of length $\Delta\omega_j$ such that

$$\omega_u = \sum_{j=1}^{M} \Delta\omega_j \qquad \text{.....(12)}$$

Φ is a random phase angle, uniformly distribution in the (0, 2π) Using Eq.(11), a computer program for simulating time histories can be easily developed, and the computer can generate a series of different time histories for a given PSD W(f). One should easily find that the method of simulation of X(t) used for estimating and tests implies that these different histories for the same PSD make the same effects on the fatigue damage. No one has shown that this assumption is a fact. The situation is just opposite. Traditionally the sequences of stress histories influence the fatigue damage(1), if the larger stresses come first, the damage rate is less than unit when failure occurs, otherwise the rate is larger than unit. It is perplexing that the simulations from the same PSD have the same contributions to fatigue damage. If not, all the results using Monte-Carlo method priviously are incredible; If the same, we call them equivalent.

To make the problem clear, many experiments have been made. The procedure is shown in the flow chart, Fig.2. For a "real" stress history with a typical PSD function, three different histories can be simulated by using Eq. (11)(12). Input the four histories into MTS880 computer controlled electrohydro-servo system. Five specimens have been tested for each history. Comparing the life N or T for "real" history with N or T (i=1,2,3) for "simulated" histories, the conclusion can be made. The material behavior has been tested in the constant amplitude tests. The result is, m = 7.74 and $C = 1.15 * 10^{24}$. Table 2. lists all the experimental results, information of history, and rainflow results.

TABLE 2- Demonstration of Equivalent of the Simulated Histories

Classify*		"Real" History	Simu.1	Simu.2	Simu.3
f_o(HZ)		17.78	20.07	20.03	19.92
ϵ		.6	.61	.61	.61
σ(MPa)		130.1	125.6	126.4	128.5
λ		.67	.67	.67	.67
Life(PSD)		14685	17084	16297	14425
Life(RF.)		19613	28365	27468	24864
Test Life (sec)	1	20560	29659	16509	16482
	2	19961	16780	22364	18714
	3	16503	20395	20062	15805
	4	20809	20542	17890	13644
	5	21630	16609	18891	27814
Mean(sec)		19893	20797	19143	18492
S.D.(sec)		1778	4742	2224	5516

* For same PSD; All life in second.

The results of comparision between T_o and T_i (i=1,2,3) list in Table 3.

TABLE 3- Comparision between "Real" Life and Simulated Test Life

	"Real" History T_o	Simu.1 T_1	Simu.2 T_2	Simu.3 T_3
Mean Life	19893	20797	19143	18492
Error = $\left\| \frac{T_i - T_o}{T_o} \right\|$		4.5%	3.8%	7.0%

From Table 2 and 3, the conclusion may be got that the simulated histories generated by Monte-Carlo method for a given PSD W(f) make the same contributions toward the fatigue damage as the "real" history does, that is, the simulated histories are equivalent to the original history in the meaning of fatigue damage in the situation that only high cycle fatigue is considered.

FATIGUE UNDER NONNORMAL RANDOM LOADING

The results in the preceding section have all been based on the assumption that the process invlved are normally distributed. In the simulation procedures, for example, this normality results automatically from summation of a large number of independ random terms (as stated in the central limit theorem). In most situation, the nonlinearity in the behavior of a specimen may be presumed to be small, so that it is consistent to consider the response to be if the loading is normal. In structures, it may not be reasonable to consider either loading or response to be normal. For example, consider a offshore structure loaded by water waves, even if water velocities are normal, the nonlinearity of the drag force in Morison Equation can be expected to give a nonnormal loading on structure. The nonnormal and normal loading are significantly different(4). Lutes proposed a method to describe the nonnormality of processes.

Assume Y(t) is a zero mean stationary and ergodic random process. Kurtosis factor K is a simple measure for characterizing the nonnormality of a process, and defined as,

$$K = \frac{E[\, Y^4(t)]}{\sigma_Y^4} \qquad \text{.....(13)}$$

if K=3, Y(t) is normal; otherwise Y(t) is nonnormal. Simulation of a nonnormal process can be achieved by taking a nonlinear transformation of a normal process. That is, Let X(t) be a time history from a normal process, and let

$$Y(t) = G[\, X(t)] \qquad \text{.....(14)}$$

where G(.) is a monotonically increasing odd nonlinear function. Then Y(t) is not normal.

In order to emphasize the effect of nonnormality, the nonlinear

function have been scaled such that,

$$\sigma_Y = \sigma_X \quad \text{.....(15)}$$

Also, Y(t) has zero crossing and peaks at precisely those time when X(t) has them. Thus, Y(t) and X(t) are equivalent in terms of RMS, zero-crossing rate and irregularity factor---they link tightly with fatigue damage.

The particular nonlinear functions used are,

$$G_1(x) = a_1 \left(x + w_1 \frac{x^3}{\sigma_X^2} \right) \quad \text{.....(16)}$$

$$G_2(x) = a_2 \left(x + w_2 \cdot x \left(\frac{\sigma_X}{|x|}\right)^{\frac{1}{2}} \right) \quad \text{.....(17)}$$

Satisfying Eq.(15) requires that

$$a_1 = \left(1+6w_1 + 15w_1^2 \right)^{-\frac{1}{2}} \quad \text{.....(18)}$$

$$a_2 = \left(1.0 + 1.72w_2 + 0.798w_2^2 \right)^{-\frac{1}{2}} \quad \text{.....(19)}$$

Substituting Eq.(16), (17) into Eq.(13), we have,

$$K_1 = 3a_1^4 \left(1+20w_1 +210w_1^2 + 1,260w_1^3 +3,465w_1^4 \right) \text{ for } K \geq 3 \text{.....(20)}$$

$$K_2 = 3a_2^4 \left(1+2.87w_2 +3.19w_2^2 +1.64w_2^3 +0.333w_2^4 \right) \text{ for } K \leq 3 \text{.....(21)}$$

In order to predict the fatigue damage under nonnormal stress, we assume that the damage from nonnormal process can be modified accounting for nonnormality based on the model for predicting the damage from normal, narrow band process. That is,

$$D = L \cdot \lambda \cdot D_{NB} \quad \text{.....(22)}$$

$$L(K,m) = \frac{\text{Damage from Y(t) using rainflow method}}{\text{Damage from X(t) using rainflow method}} \quad \text{.....(23)}$$

L is called nonnormal correction factor. The procedure to determine L for a given m and K is similar to determination of λ . For a given K, one can easily get w or w from Eq(20) or Eq(21) and a or a from Eq. (18) or Eq.(19), then G(x) or G(x) is known. In the simulation study, an $X^d(t)$ was generated as in the preceding section, and Eq.(14) was used to generate a Y(t) history. From Eq.(23), L(k,m) can be determined.

The empirical relationship between L and K for a given m is demonstrated in Fig.3. The results are in accord with Lutes's results(4). It is shown that the effect of nonnomality may be quite significant.

To show whether the model Eq.(22) fits the experiments or not. The experiments have been made in MTS880 system for K=3.5 and K=2.5 nonnormal histories with the same spactral density W(f). The material behavior is the same in the previous section, i.e., m=7.74 and $C=1.15*10^{24}$. The results list in Table 4. Comparing the test results with analysis results from Eq(22), the conclusion may be made, i.e., the model for predicting fatigue damage under nonnormal loading is available for evaluation and design of engineering

TABLE 4- Test and Analysis Results For Nonnormal Loading

Classification*		History K=3.5	History K=2.5
f_o (HZ)		18.59	17.41
λ		.67	.67
L		2.45	.49
RMS σ (MPa)		122.4	129.3
Life (PSD)		9193	32123
Life (Rainflow)		11567	38392
Test Life (sec)	1	13894	44048
	2	13751	27754
	3	15088	29647
	4	15381	34746
	5	13039	42430
Mean Life (sec)		14231	35725
S.D. (sec)		978	7343

*For same PSD; All life in second
structures, in high cycle fatigue situation.

CONCLUSIONS

• An improved model for predicting high cycle fatigue under non-normal wide band random stress processes is processes is presented. The model is based on the rainflow cycle counting method and assumes a linear damage accumulation using Monte-Carlo approach. Using a closed form expression, fatigue damage can be predicted directly from spectral density W(f) without simulating. The nonnormal correction factor L herein is accord with Lutes's result(4). The experimental results suggest that the nonnormal model provide reasonable life estimates.

•Both theoretical and experimental analysis of Monte-Carlo approach have been presented here. The result is that the different time histories simulated by Monte-Carlo method for a given (th same) PSD W(f) contribute the same effects to fatigue damage, i.e., they are equivalent themselves in terms of fatigue damage. One should not hesitate to apply Monte-Carlo method to fatigue analysis and test.

REFERENCES

(1) Dowling, N.E.," Fatigue Failure Predictions for Complicated Stress-Strain Histories", J of Mater. Vol.7,No. 1, pp71-87
(2) Wirsching, P.H. & Prasthofer, P.H.," Preliminary Dynamics Assessment of Deepwater Platforms", J. of Struct. Div. Vol.102 1976
(3) Shin, G. S.,"Analysis of Random Vibration" (1977) (in Chinese)

(4) Lutes, L.D. et al, " Stochastic Fatigue Damage Accumulation" J. of Struct. Eng. Vol.110,No.11, 1984, pp2584-2601
(5) Wirsching, P.H. and Light, M.C., " Fatigue under Wide Band Random stress", J. of Struct. Div. Vol.106, No.ST7, 1980, pp1593-1607
(6) Wirsching,P.H. & Shehata, A.M., "Fatigue under Wide Band Random Stresses Using Rainflow Method", J. of Eng. Mater. & Tech. Vol. 99, No.3, ASME, 1977, pp205-211
(7) Chaudlhury,G.K. & Dover, W.D., "Fatigue Analysis of Offshore Platforms Subjected to Sea Wave Loadings", Int. J. Fatigue, No.1 (1985) pp13-19
(8) Lin, Y.K., Probabilistic Theory of Structural Dynamics, McGraw-Hall Book Co. Inc., N.Y., 1967
(9) Wirsching, P.H., "Fatigue Reliability of Welded Joints in Offshore Structures", OTC 3380, 1979, pp.197-206
(10) Hu,J., " A Study of Fatiue under Random Loading", the requirements for the degree of MS, Shanghai Jiao Tong Univ. 1985
(11) Yang, J.N.," Simulation of Random Envelope Precesses", J. of Sound and Vibration, Vol.21, pp.73-85

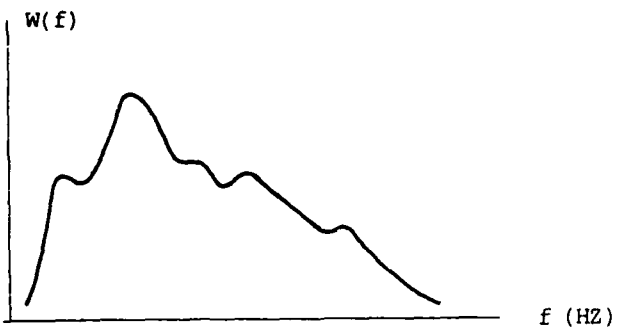

Fig.1 The Typical Power Spectral Density W(f)

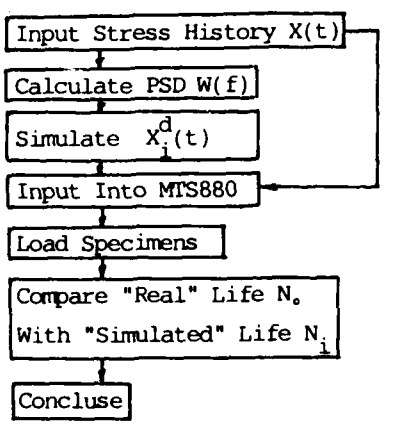

Fig.2 Flow Chart for Showing Equivalent

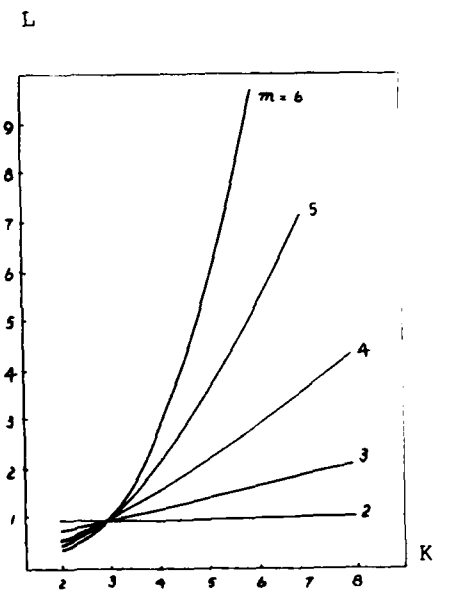

Fig.3 Nonnormal Correction Factor L

TELEMETRIC LASER EXTENSOMETRY TECHNIQUE FOR MONITORING DEFLECTIONS IN SMALL CRACKS

M. L. BARTLETT*, A. SAXENA*, AND R. C. BROWN*

Crack mouth opening displacements (CMOD) for small fatigue cracks were studied using a telemetric laser extensometry system. The resolution of measurement for this system was at least 1.27×10^{-7}m (.000005 in.). The measured compliances for small edge cracks in a uniformly stressed specimen were much larger than the analytically predicted values based on the assumption that K completely characterizes the crack tip stress field. These measurements suggest that for small cracks the strain energy release rate, G, is not equal to K^2/E and a crack driving force based on G may be more reasonable than K.

I. INTRODUCTION

Predictions of fatigue crack growth rates based on stress intensity parameter, K, have been shown to significantly underestimate the growth of small cracks (1,2). The full crack tip stress field solutions consist of several terms beyond the first singular term whose amplitude is characterized by K, as shown by Williams (3). For large cracks the crack tip stress field is essentially dominated by K, but in the case of small cracks, the other non-singular terms also contribute significantly to the crack tip stress field (4). Therefore, K alone cannot be expected to uniquely characterize the plastic zone size and perhaps the full driving force for small cracks (5).

* Fracture and Fatigue Research Lab
School of Materials Engineering,
Georgia Institute of Technology
Atlanta, GA 30332-0245

In order to focus on the contributions of the higher order non-singular terms to crack tip stresses, it was chosen to measure the crack-mouth-opening-displacement (CMOD) for small cracks. Since the expected deflections were small, a high resolution extensometer was required. Therefore, laser extensometers with resolutions on the order of 10^{-8}m were considered.

Recently, considerable success has been reported in measuring CMOD across small cracks using a laser Interferometric Strain Displacement Gage (ISDG) by Larsen and co-workers (6,7). This system requires a laser beam to shine onto two micro-hardness indentations on each side of the crack (6). As the crack opens, the relative motion of the indentations is monitored. However, no commercial systems of this type are currently available and building such a system is very intricate. Therefore, a commercially available telemetric laser extensometer (TLE) manufactured by ZYGO (Model no. 1532) was chosen for this study. The claimed resolution of this instrument is 2.5 x 10^{-8}m (10^{-6} in) which was adequate for this study. The set-up is described in detail.

II. DESCRIPTION OF THE TELEMETRIC LASER EXTENSOMETER

Experimental Set Up

Figure 1 is a picture of the laser system used for measuring CMOD. The system uses a thin band of scanning laser light, projected from the transmitter to the receiver. When a specimen is placed in the path of the beam, the object casts a shadow. The receiver detects the edges of this shadow and sends the data to a microprocessor, where the dimension is calculated. To perform these high resolution measurements, it was necessary to build an assembly to accurately align the laser on the specimen. This assembly is also shown in Figure 1. The elevator jacks allow for vertical flexibility, while the micrometer controlled linear translation tables allow for an accurate horizontal positioning. It was necessary to assure that the laser beamed squarely across the specimen. To ensure this, both the front and back micrometers were adjusted, until the smallest dimension was read. At this point, the laser beam was aligned at 90° to the edges of the specimen.

This procedure assured reproducibility of measurements from specimen to specimen.

It is of considerable interest to determine the highest loading frequency for which the TLE system can be used for on-line deflection measurements without interrupting the fatigue tests. Figure 2 shows a series of oscilloscope pictures of displacement vs. time (from the TLE System) as a function of load vs. time, at frequencies of 0.1, 0.5, 1.0, and 2 Hz. At 0.1 and 0.5 HZ, the load and displacement peaks match-up very well, indicating that the TLE system kept up with the deformation in the specimen. At 1 Hz, a noticeable phase shift exists between the two peaks and at 2Hz the phase shift becomes quite significant. With the present set-up, the dynamic response of the TLE system is therefore limited to 0.5 Hz. With proper computer interfacing, it may be possible in the future to pair load and displacement points and thereby improve the dynamic response of the TLE system beyond 0.5 Hz.

III. EVALUATION OF THE TLE SYSTEM

Two types of tests were performed to evaluate the TLE System. These included (i) the measurement of elastic compliance of specimens containing small edge cracks and (ii) measurement of over-all deflection of specimens fatigue cycled under strain controlled conditions, in other words the low cycle fatigue, LCF test. Same specimen geometry, test material, and experimental set-ups were used for both test types. The results of the LCF tests will be reported in a subsequent paper.

Test Material and Specimens

Test specimens were machined from a bar of AISI 1018 cold rolled steel, which was stress annealed prior to machining. The tensile properties of the material are summarized in Table 1.

TABLE 1 - Material Properties

Yield Stress	6.307 MPa	(43.5 Ksi)
Ultimate Tensile	10.15 MPa	(70.0 Ksi)
Percentage elongation	34%	
Grain Size (ASTM #)	8.2	(20.8 microns)

The geometry and size of the specimen are shown in Fig. 3. Flat specimens were selected so that two-dimensional cracks could be generated, thereby simplifying the data interpretation. These specimens were gripped in hydraulic pressure grips, which are capable of tension-compression loading while maintaining good alignment.

Elastic Compliance Tests

The TLE system was used to determine elastic compliance of specimens with various crack lengths. The laser was beamed vertically between two machined blocks which were attached to the shoulder of the specimen (Fig. 3). After the alignment check was performed, the compliance of an uncracked specimen was obtained. Subsequently, compliances were also measured in specimens containing cracks ranging from 2×10^{-4}m (0.008 in) to 2.64×10^{-3}m (0.104 in) in size. The procedure for obtaining specimens with different crack size is described below.

The smallest crack size, 2×10^{-4}m(0.008 in), was produced by electric discharge machining (EDM). The subsequent crack lengths were produced by extending the EDM notch by fatigue loading in a three-point bend fixture. By loading in three-point bending, ΔK values sufficiently large ($\approx$12 MPa m) to grow the crack at a reasonable rate could be produced, while maintaining dominantly linear elastic conditions in the test specimen. The bend fixture was set-up in one servo-hydraulic test machine with the TLE system on another. Thus, compliance measurements for several crack sizes could be made efficiently. In all, two specimens were employed in these measurements.

Figure 4 shows the typical load-deflection traces obtained. Several such traces were made for each crack size to obtain average compliances. In general, the reproducibility of compliance values was good. However, an occasional trace yielded a compliance which did not agree well with the overall results. The occurance of such a trace was about one in five or six. The reasons for this are not understood at this time. In order to minimize the contribution from such measurements, it is necessary to therefore average compliance over several measurements. The scatter

in the results presented in the next section is attributed to this behavior.

The resolution of the TLE system was 1.25×10^{-7} m (5×10^{-6} in) in our experimental set-up. We believe that this can be significantly improved by interfacing the TLE system with a computer.

IV. DISCUSSION OF THE COMPLIANCE MEASUREMENTS

Figure 5 shows the measured nondimensional compliance, CBE, as a function of the normalized crack size, a/W, where, C = compliance, B = specimens thickness, E = elastic modulus, a = crack size, and W = width of the specimen. These values are obtained after subtracting the compliance of the uncracked specimen. For comparison, the analytical compliance for the crack mouth opening and the load-line are also plotted in the figure. These were taken from the expressions given by Tada et al (8) as follows. For the crack-mouth-opening compliance (C_M), the following expression applies for $0 \leq a/W \leq 0.7$.

$$C_M BE = 4(a/W)\frac{1.46 + 3.42\ (1-\cos\ [(\pi/2)\ (a/W)])}{(\cos\ [(\pi/2)\ (a/W)])^2} \qquad (1)$$

For the load-point compliance (C_L), the following expression applies.

$$C_L BE = 4(a/W)\frac{(a/W)\{0.99-(a/W)[(1.3-1.2(a/W)+0.7(a/W)^2]\}}{(1-a/W))^2} \qquad (2)$$

For small crack sizes, the experimental compliance was considerably higher than both analytical compliances. For longer cracks, the experimental compliance correlated well with the crack mouth compliance rather than the load-line values. Considering that deflections were measured on the edge of the specimen containing the crack, it is reasonable to expect such a correlation. It should also be pointed out that Eq. (1) was derived for pin loading in which the specimen was free to rotate. Our gripping arrangement did not allow a completely free rotation. Nevertheless, at small a/W values, ($a/W < 0.2$), Eq. (1) is a reasonable representation of the analytical compliance, as is also borne out by the agreement with the experimental results.

For small cracks, the additional deflection due

to the crack as measured remotely across the shoulders of the test specimen is also equal to the additional load-point deflection. Since the measured deflection is much larger than the predicted load-point deflection based on K, it can be concluded that the crack tip stresses are higher than those calculated on the basis of K alone (4,5). Hence, second order terms in the Williams stress function must contribute significantly to the crack tip stress and deformation field. This could lead to the frequently observed trend of higher crack growth rates, as compared to those predicted on the basis of K for small cracks.

Obviously, there are several considerations other than the contribution to crack tip stress from the second order terms in completely rationalizing the small crack behavior. However, in the discussion which follows, we will focus only on this aspect.

We start the discussion by proposing the strain energy release rate G, as a candidate parameter for characterizing the crack driving force. Of course, when the cracks are large, this is equivalent to saying that K characterizes the crack driving force through the well known relationship $G = K^2/E$ (9). However, it should be kept in mind that in deriving this relationship between G and K it was assumed that the crack tip stress and displacements are completely specified by K. For small cracks, this assumption becomes questionable. In fact, it is not difficult to show that if the other non-singular terms in the Williams' series become significant, no unique relationship between G and K exists. Hence, strain energy release rate should no longer be used interchangeably with K. In other words, for small cracks, K no longer characterizes the strain energy release rate.

The following equation approximately describes the compliance of specimens containing small cracks.

$$CBE = 1.38(a/W)^{.285} \qquad (3)$$

The above equation was derived by conducting a regression analysis of the compliance data shown in Fig. 5. The trend represented by Eq. (3) is shown by a dotted line in Fig. 5. In conducting

the regression analysis, only data for crack sizes up to an a/W value of 0.125 were included. Also, one point which was in disagreement with the rest of the data was omitted from the regression analysis. The G for small cracks can be estimated as follows:

$$G=(p^2/2B)\frac{dC}{da} = \frac{P^2}{2B^2EW}\cdot\frac{d(CBE)}{d(a/W)} = \frac{\sigma^2 W}{2E}\frac{d(CBE)}{d(a/W)} \quad (4)$$

Substituting for d(CBE)/d(a/W) from Eq. (3) into Eq. (4), we get the following result.

$$G/(\sigma^2 W/2E) = \frac{.393}{(a/W)^{.715}} \quad (5)$$

Equation (5) is only valid for crack sizes smaller than 1.4×10^{-3}m (0.055 in). For longer crack sizes, Eq.(2) may be differentiated to derive an equivalent equation for estimating G. That expression is given below

$$G/(\sigma^2 W/2E) = a/W\,[8.446 - 14.85(a/W) + 304.64(a/W)^2 - 983.85(a/W)^3 + 1555.68(a/W)^4\,] \quad (6)$$

In Fig. 6 the values of $G/(\sigma^2 W/2E)$ are shown by dotted lines. The solid line shows the most likely behavior of the normalized strain energy release rate as a function of normalized crack size for single edge crack specimens. The shape of the normalized G curves resembles the commonly accepted trend for the behavior of small fatigue cracks. This implies that G may be a candidate for representing the crack driving force correctly in the linear elastic regime. This will be further explored in a forthcoming paper.

A word of caution is in order about the use of the compliance data for small cracks. In Figs. 5 and 6 the data is represented in a nondimensional form with crack sizes normalized by the width of the specimen. However, in the small crack regime, the only relevant length prameter is the crack length itself. In other words, the compliance values are not expected to scale-up (or down) for a specimen of identical geometry but a different value of W. Therefore, Eqs. (4) and (5) should not be used for specimens of other sizes without applying appropriate size corrections.

References

1. Leis, B.N., Kanninen, M.F., Hopper, A.T., Ahmad, J., and Broek, D., "A Critical Review of the Short Crack Problem in Fatigue," Report # AFWAL-TR-83-4019, 1983.

2. Ritchie, R.O. and Lankford, J., Small Fatigue Cracks, AIME publication, 1986, pp 1-5.

3. Williams, M.L., Journal of Applied Mechanics Vol. 24, No. 1, March 1957, pp 109-114.

4. Talug, A. and Reifsnider, K., "Cyclic Stress-Strain and Plastic Deformation Aspects of Fatigue Crack Growth - Symposium," STP637, American Society for Testing and Materials, 1977, pps 81-96.

5. Saxena, A., Wilson, W.K., Roth, L.D., and Liaw, P.K., International Journal of Fracture, Vol. 28, 1985, pps. 69-82.

6. Sharpe, Jr., W.N., "Applications of the Inter-ferometric Strain/Displacement Gage," Optical Engineering, Vol 21, No. 3, May/June 1982,pps 483-488.

7. Larsen, J.M., Jira, J.R., and Weerasooriya, T., "Crack Opening Displacement Measurements on Small Cracks in Fatigue," ASTM 18th National Symposium on Fracture Mechanics, Boulder, Co., June 1985, pps 7-12.

8. Tada, H., Paris, P., Irwin, G., The Stress Analysis of Cracks Handbook, Del Research Corporation, 1985.

9. Irwin, G.R., ASME Paper No. 57-APM-22, Presented at the Applied Mechanics Summer Conference, Berkely, CA, June 1957.

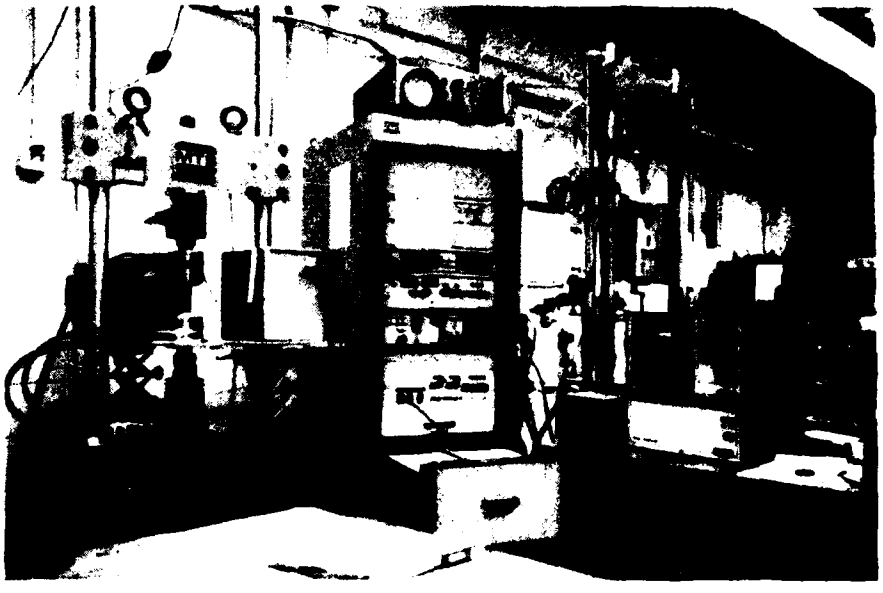

Figure 1 Telemetric laser extensometer setup

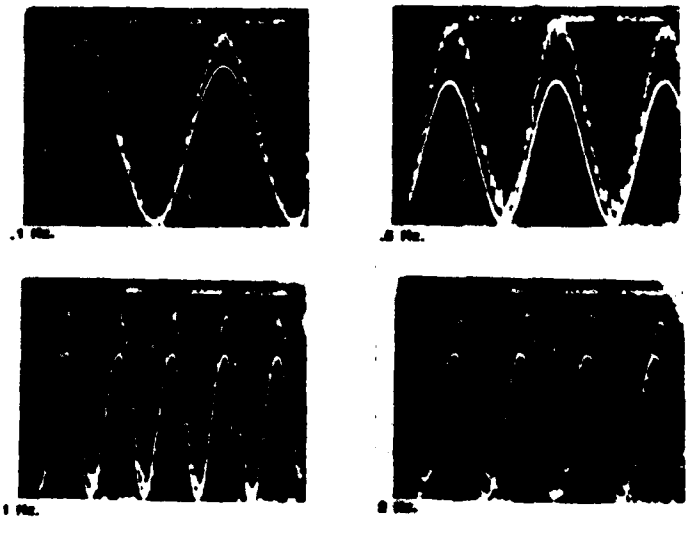

Figure 2 Oscilloscope traces of strain vs. time from the laser system compared with load vs. time

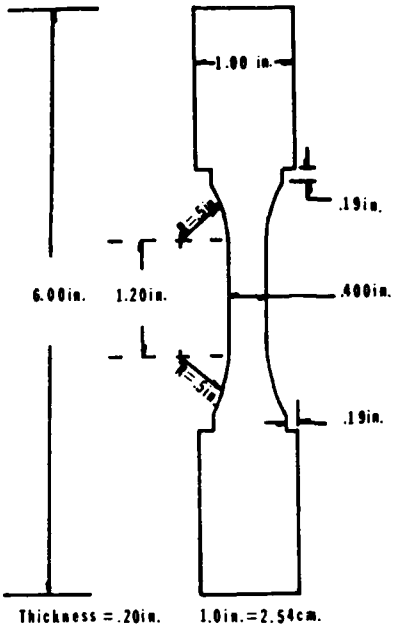

Figure 3 Small crack specimen geometry

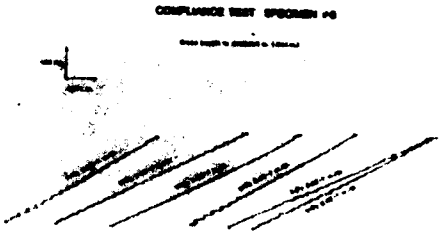

Figure 4 Typical compliances from the laser

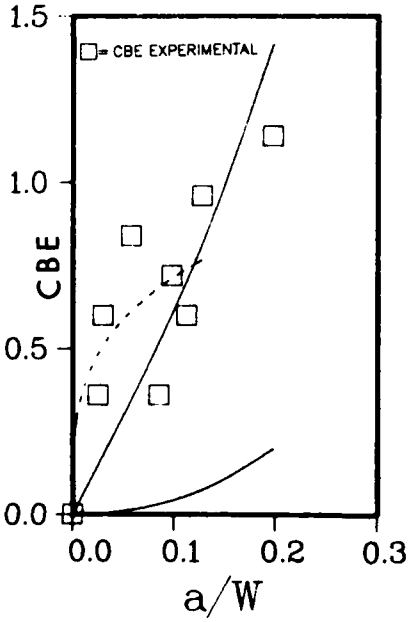

Figure 5 Nondimensional compliance, CBE vs. a/W

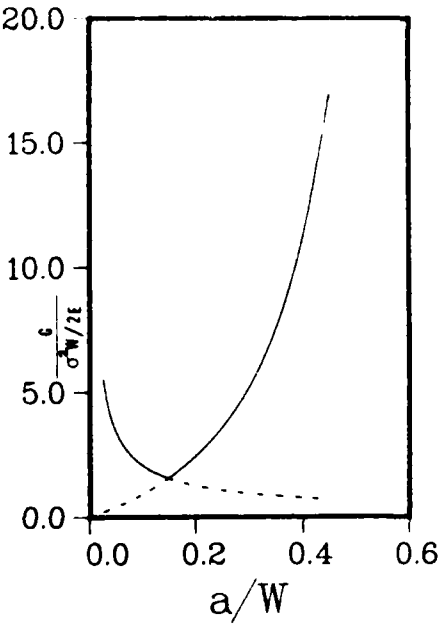

Figure 6 Strain energy release rate vs. a/W

X-RAY FATIGUE FAILURE PREDICTION BASED ON PLASTICITY RESPONSE TO MICROCRACKS

S. Weissmann*

Cyclic deformation of aluminum crystals and Al 2024 alloys gives rise to surface intrusions which develop into microcracks. Microplastic zones at the crack tips get strainhardened upon cycling and by impeding the advancing crack fronts induce new formation of surface intrusions. Associated with the strain hardened zones at the crack tips is a pronounced induced lattice misorientation which serves as an important criterion to predict fatigue failure in the alloys. The x-ray CARCA method is used to determine the critical lattice misalignment when catastrophic failure is imminent.

INTRODUCTION

Because of the realization that cyclic-induced surface intrusion represent microcracks,considerable attention has been focused on their detection, measurement and characterization (1-6). Lankford and Davidson (5) have shown that the plastic zone size of such small cracks is smaller than the average grain size and that the small cracks, despite retardation by obstacles which they may encounter, grow at a very fast rate. These stage I growth rates, being by orders of magnitude larger than those expected from extrapolation data of long cracks, were attributed to high cyclic strains at crack tips within grains of maximum crystallographic orientation. Ma and Laire (4) studying the frequency distributions of small cracks in copper single crystals cycled at plastic shear strain amplitudes of 2×10^{-3} and 4×10^{-3} up to one third of life, showed that they are skewed to very small crack depths and have long tails which become more extreme as the number of cycles increases. Consequently, and most significantly, small new cracks are continually nucleated at the surface as larger cracks propagate into the interior. In a series of papers, Tanaka and coworkers (8-10) developed

* Department of Mechanics and Materials Science, College of Engineering, Rutgers University, Piscataway, NJ 08854, USA

models for microcrack nucleation, based on slip dislocations blocked by grain boundaries and predicted the irregular propagation behavior of small fatigue cracks by making the growth rate directly dependent on the crack-tip displacement. The plasticity-induced closure model proposed by Budiansky and Hutchinson (11) for a large fatigue crack was extended to analyze the closure of a small fatigue crack formed in a smooth specimen. Criticizing the random slip model of microcrack initiation (4) Fine and Kwon (7) argued for crack models induced by vacancies and proposed a dislocation-vacancy dipole model. They chose copper for studies of fatigue crack initiation because, as stated by these authors, so much is known about fatigue of copper. Yet in a critical review of the current literature on experiments and theory of fatigue crack initiation, Fine and Kwon came to the conclusion "that the theory of fatigue crack initiation is still in a primitive (perhaps stone age) state." In the opinion of this author, such judgement appears a bit too harsh. In view of the believed accumulated knowledge based on fatigued copper crystals, an allusion to the bronze age may perhaps be a more apt comparison.

In an attempt to establish a bridge between the micro and macroscopic viewpoint of deformation, systematic studies of notch tip plasticity were carried out in the author's laboratory for several years on tensile deformed silicon crystals (12,13) and stainless steel (14). It became apparent that basic concepts which emerged from these investigations could be applied to cyclic-deformed metal crystals and alloys. The pertinent concepts applicable to the fatigue problem are: 1. characterization of crack tip plasticity by monitoring the induced lattice misalignment, 2. determination of fatigue failure by determining a critical lattice misalignment associated with strain hardening, beyond which the advance of the crack fronts can no longer be impeded.

Such studies have been performed on cycled Al crystals (15) and on smooth Al-2024-T4 alloys cycled in air (15,16) corrosive environment (17) resulting in successful failure prediction with an error range of about 5 percent (16,17). The results were obtained by x-ray rocking curve techniques, developed in the author's laboratory. These results, supported by recent SEM and TEM studies of cycled Al crystals and previous studies of AgZn (18), Al (1,19) and Ge(20) crystals invite a new, reinterpretation of the data, based on plasticity response to microcracks. This approach was taken in this paper with the aim of establishing a link between the microscopic aspects of small crack initiation and propagation, discussed above, and the macroscopic response of the material to cycling up to failure.

MONITORING OF CRACKTIP PLASTICITY BY X-RAY ROCKING CURVE MEASUREMENTS

Cracktip Plasticity Response in Single Crystals

As demonstrated by Pangborn et al, (15) x-ray rocking curve measurements of cycled aluminum crystals exhibited at the initial stages of cycling a rapid increase of the halfwidth value β at the surface and near-surface region, and a decreasing gradient from the surface into depth, x . As may be seen from Fig.1, a minimum in the curve was obtained at a depth of 100 μm from the surface and further in depth β increased again, attaining a plateau value at about 250μ which extended into the bulk. SEM correlation studies were carried out on aluminum crystals, cycled in tension-tension at constant strain, at a frequency of 15Hz with R=0.3.

Dimension, orientation and tensile direction are shown in Fig. 2. In order to examine the cracks, the Basinski method was used. The site parallel to the primary Burgers vector was first mechanically polished, followed by slight electropolishing and surface protection by non-conducting lacquer. Cracks shown in Fig. 3 emerged from the corner and side surface in the dashed line area.

For the sake of demonstration and because of the limited extent of this paper, only one fraction of the fatigue life of the crystal is presented here ($N=10^4$, about 0.1 N/N_F), giving a correlation between x-ray and SEM measurements. The complete correlation sequence covering the life span of the crystal will be given elsewhere. We shall concentrate now our attention on the dependence of β with depth distance from the surface in relation to crack-sizes. The large value of lattice misalignment at the surface, manifested by the large β value of the rocking curves in Fig. 1, results from the collective contribution of cracktip plasticity induced by very numerous small cracks (<5μm). The profile gradient of β reaching a minimum at a depth distance of about 100 μm is a manifestation of the cracktip plasticity response of a skewed size distribution of cracks with depth distance, that is with the largest number of small cracks located at and near the surface and only very few cracks of about 100μ extending into the interior.

The decline of β to its minimum value reflects the decreasing number of cracks contributing to the lattice misalignment. The observed skewed distribution of crack size is in good agreement with the detailed skewed histogram representation of stage I cracks in copper single crystals, reported by Ma and Laird (4). Of particular interest is the ascent of β to the plateau value at about 250μm. Current TEM studies and previous TEM investigations characterizing the microstructure at the intrusion tips (1) have shown a strain-hardened domain adjacent to the tips followed by a square-cell dislocation structure. Since the x-ray measurements deal with averages, the increase of β to the plateau value reflects, therefore, the strain hardened response of the microstructure to the collective crack front. It will be shown shortly that the cyclic strain hardened zone at the crack tip front plays in turn, an important role in subsequent crack nucleation at the surface so that there exist a dynamic interaction between crack initiation and

crack propagation.

Cracktip Plasticity Response in Alloy Al 2024-T3

Since the polycrystalline alloy consists of an aggregate of small crystals (the metallic grain) the double crystal diffractometer (DCD) method can analyze the defect structure by regarding each grain as a second crystal (test crystal) of a double crystal diffractometer. Consequently, for the investigation of microplasticity in Al 2024-T3, the method of computer-aided rocking curve analysis (CARCA) was employed which samples rapidly a large grain population and gives an accurate rocking curve analysis of the individual grains. Since the β values of the rocking curve is a measure of the local lattice curvature in the plastic zone, it can also be expressed by the excess dislocation density ρ of this zone. The data presented in Fig. 4, part A, were obtained from the rocking curve analysis of Al 2024-T3 cycled for various fatigue life fractions at $\pm$200 MPa, corresponding to the proportional limit. Analogous to the cyclically deformed single crystal (Fig. 1), the β-x profile revealed a higher excess dislocation density at the surface than in the bulk, a decline to minimum value and an ascent to a plateau value. With increase of life fractions the shape characteristic of the curve is maintained but shifted to larger ρ (or β) values and it will be noted that the large values at the surface approach rapidly saturation. This rapid increase at the surface upon cycling is caused by fresh nucleation of numerous intrusions which develop into microcracks giving rise to increased lattice misalignment. This nucleation process on the surface is the result of the resistance to crack propagation which the total crack front encounters by the cyclic strainhardened zone ahead of the crack front. The strain hardened zone is characterized by the ascending branch and plateau of the curve.

When a layer of 400μm was removed by electropolishing, containing most of the fatigue-induced cracks, the excess dislocation density declined rapidly during the initial cycles of renewed fatigue as shown in part B of Fig. 4. This behavior is attributed to the instability of the bulk dislocation structure when the crack front and strain hardened zone was removed. After reaching a minimum at 1 to 2 pct. of the life, the dislocation density began to increase again at approximately the same rate as in the original fatiguing and intrusions with concomitant crack development were again initiated. When cycling was again interrupted after 5 pct. to obtain a second depth profile, as exhibited in Fig. 4, part C, analysis of the specimen given 75 pct. prior cycling revealed, with the exception of the immediated surface, a low, uniform ρ value over the entire cross-section equal to the value of the undeformed virgin specimen. The instability of the bulk dislocation structure when cycling is resumed, after judicious, periodic removal of surface layers containing microcracks, contributes to the extension of fatigue life (2). It should be noted, however, that because of the

skewed distribution of crack sizes a sufficiently large surface layer has to be removed so as to eliminate also the few larger cracks. As may be seen from Fig. 4, the removal of 400 μm surface layer was adequate to accomplish this task.

DETERMINATION OF FATIGUE DAMAGE AND FAILURE PREDICTION

It has been shown that at the crack tips, cyclic strain hardening occurs and that with cycling the strain hardened zone at the crack front induces continual nucleation at the surface region. This dynamic interaction between the strain hardened zone at the crack front and the crack nucleation at the surface, leads to a skewed distribution of crack sizes; the highest frequency of crack size being located at or near surface sites ($\sim$<5μm) and the lowest frequency constituted by the larger cracks penetrating into the bulk (4). Indeed, the descending β values to the minimum in the depth profile curves of Fig. 1 and Fig. 4 reflect the contribution to lattice misalignment by the number of cracks.

The formation of PSB's on cycling with the concomitant generation of the skewed crack size distribution from the surface to the interior, results in a rapid increase and accumulation of lattice defects at the surface, thus causing surface roughening. This surface effect is particularly pronounced in polycrystalline materials and, therefore, the excess dislocation density at the surface, $\bar{\rho}_S$, reaches a saturation level early in life ($N/N_F \sim 0.25$) with a concomitant saturation for x-ray line broadening. It is because of the rapid surface roughening that in the past the assessment of accrued damage and fatigue failure prediction by x-rays was unsuccessful. Inspection of Fig. 4, part A shows the rapid increase of excess dislocation density ρ at the surface. By contrast, however, the buildup of ρ in the strainhardened region ahead of the crack front to the plateau level of the interior is much more gradual. The recognition of the gradual build up of plasticity in the interior of the material in response to the advance of the collective crack front originating from the surface leads to failure prediction. When upon cycling the plastic zone in the interior reaches a critical stage of cyclic strainhardening, beyond which the advance of the crack fronts can no longer be impeded, catastrophic failure is imminent. The critical stage of plasticity is quantitatively characterized by a critical lattice misalignment parameter, β_{cr}, obtained from x-ray rocking curve measurements and, therefore, can also be expressed in terms of a critical excess dislocation density, ρ_{cr}. Fig. 5 shows how ρ_{cr} can be predicted. Using the rapid CARCA method and employing radiation of different wavelength, the rocking curves of the grain population from surface and interior are obtained for different values of N/N_F. With copper radiation (λ=1.54A) the defect structure of the surface grain population of Al 2024-T3 is analyzed, while with molybdenum radiation (λ = 0.71A), owing to its greater depth penetration, essentially the grain population of the interior is analyzed, since the mass absorp-

tion coefficient of a material is proportional to the cube power of λ. As may be seen from Fig. 5, ρ_{cr} is obtained by extrapolation to the point of intersection. It will be noted that ρ_{cr} can be arrived at experimentally from data taken at low fractions of fatigue life and thus fatigue failure can be predicted at an early stage of fatigue life.

DISCUSSION

The difference in the development of $\bar{\rho}_S$ and $\bar{\rho}_B$ during fatigue cycling was recognized in our research work in the past and served as a basis for successful failure prediction of Al 2024-T4 cycled in air and corrosive environment, both for high and low cycle fatigue (15-17). It was, however, only as a result of a systematic study of notch tip plasticity (12-14) that the true nature of the buildup of $\bar{\rho}_S$ and $\bar{\rho}_B$ upon cycling became apparent. Previously, the formation of $\bar{\rho}_S$ was attributed to surface hardening and the formation of $\bar{\rho}_B$ as a bulk response reaction to surface hardening. The new perception which emerged recognizes that the development of $\bar{\rho}_S$ is associated with the formation of PSB's, extrusions and intrusions and that particularly the latter, with its contribution to microcrack formation has the greatest impact on $\bar{\rho}_S$. Above all, the important new perception which emerged is the mutual interaction between crack initiation at the surface via intrusions, and the strain hardened zone ahead of the crack front, impeding the crack front propagation. This mutual interaction results in a skewed size distribution of cracks with cracks of smallest size being most numerous and located at the surface. The few large cracks in the distribution spearhead the collective crack front and have the greatest impact on the strainhardening effect ahead of the crack front. The CARCA studies of notch tip plasticity have shown that the greatest strain hardening effect upon deformation does not occur immediately at the notch tip but some distance away from the tip along the direction of the maximum strainhardened trajectory of the plastic zone (12). Contour mapping of induced lattice misalignment in tensile-deformed, notched 304 steel exhibited the maximum lattice misalignment and dislocation interaction in contour zones two grain diameters removed from the tip (14). These effects appear to occur also in the strainhardened zones induced by cycling and have been observed experimentally by Tanaka who used this observation for the modelling of crack induction (10).

Acknowledgement. The support of this work by the Division of Material Research of NSF under grant DMR-8104985 is gratefully acknowledged.

REFERENCES

(1) Levine, E. and Weissmann, S., Trans. Q. ASM, Vol. 61, 1968, pp. 128-138.

(2) Basinski, Z.S. and Basinski, S.J., Scripta Met., Vol. 18,1984, pp. 161-175.

(3) Basinski, Z.S. and Basinski, S.J., Acta Met., Vol. 33, 1985, pp. 1307-1327.

(4) Ma, Bao-Tong and Laird, C., "Small Fatigue Cracks", Edited by R.O. Ritchie and J. Lankford, Met. Soc., AIME, Warrendale, Pa., USA, 1986.

(5) Lankford, J. and Davidson, D.L., "Small Fatigue Cracks", edited by R.O Ritchie and J. Lankford, Met. Soc., AIME, Warrendale, Pa., USA, 1986.

(6) Neumann, P. and Tönnessen, A., "Small Fatigue Cracks", edited by R.O. Ritchie and J. Lankford, Met. Soc., AIME, Warrendale, Pa., USA, 1986.

(7) Fine, M.E. and Kwon, I.B., "Small Fatigue Cracks", edited by R.O. Ritchie and J. Lankford, Met. Soc. AIME, Warrendale, Pa., USA, 1986.

(8) Taira, S., Tanaka, K., and Nakai, Y.,Mech. Res. Comm., Vol. 5, 1975, pp. 375-381.

(9) Tanaka, K. and Akinawa, Y., J. Soci. Mat. Sci., Japan, Vol. 34, 1985, pp. 1310-1316.

(10) Tanaka, K., "Small Fatigue Cracks", edited by R.O. Ritchie and J. Lankford, Met. Soc., Warrendale, Pa., USA.

(11) Budiansky, B. and Hutchinson, J.W., Trans ASME, J. Appl. Mech., Vol. 45, 1978, pp. 267-276.

(12) Liu, H.Y., Weng. G.J., and Weissmann, S., J. Appl. Cryst., Vol. 15, 1982, pp. 594-601.

(13) Liu, H.Y., Mayo, W.E. and Weissmann, S., Mat. Sci. and Eng., Vol. 63, 1984, pp. 81-90.

(14) Yazici, R. and Weissmann, S., "Fracture: Measurements of Localized Deformation by Novel Techniques", edited by W.W. Gerberich and D.L. Davidson, Conf. Proc. of Met. Soc. AIME, 1985.

(15) Pangborn, R.N., Weissmann, S. and Kramer, I.R., Met. Trans., Vol. 12A, 1981, pp. 109-120.

(16) Mayo, W.E. and Weissmann, S., "Fatigue 84", pp. 1161-1170. Editor, C.J. Beevers, Birmingham, U.K.

(17) Takemoto, T., Weissmann, S. and Kramer, I.R., "Fatigue, Environment and Temperature Effects", pp. 71-81. Editors: J.J. Burke and V. Weiss, Plenum Press, New York, USA, 1983.

(18) Shrier, A., Wallace, J.P., Slade, J.J. and Weissmann, S., Acta Met., Vol. 11, 1963, pp. 779-789.

(19) Weissmann, S., Shrier, A. and Greenhut, V., Trans. Q. ASM, Vol. 59, 1966, pp. 709-743.

(20) Scoble, W.R., Jr., and Wiessmann, S., Cryst. Lattice Defects, Vol. 4, 1973, pp. 1585-1593.

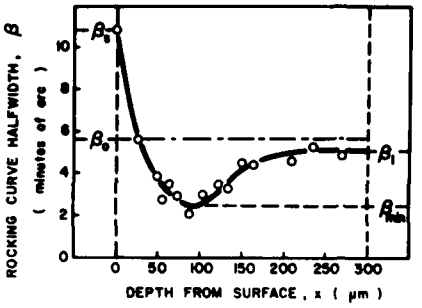

Figure 1. Profile of the measured half-width dependence on depth from the surface of a fatigued Al single at 10^4 cycles, [100]

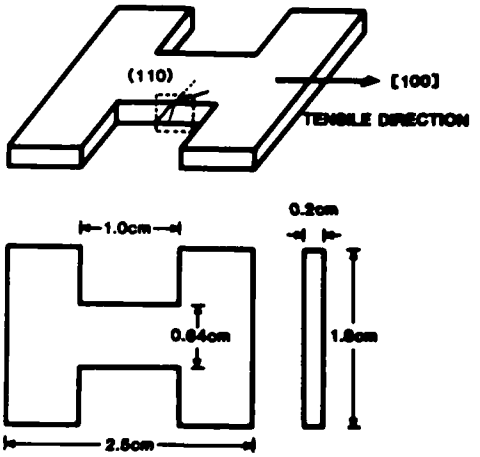

Figure 2. Al fatigue single crystal specimen emergence of cracks in dashlined area

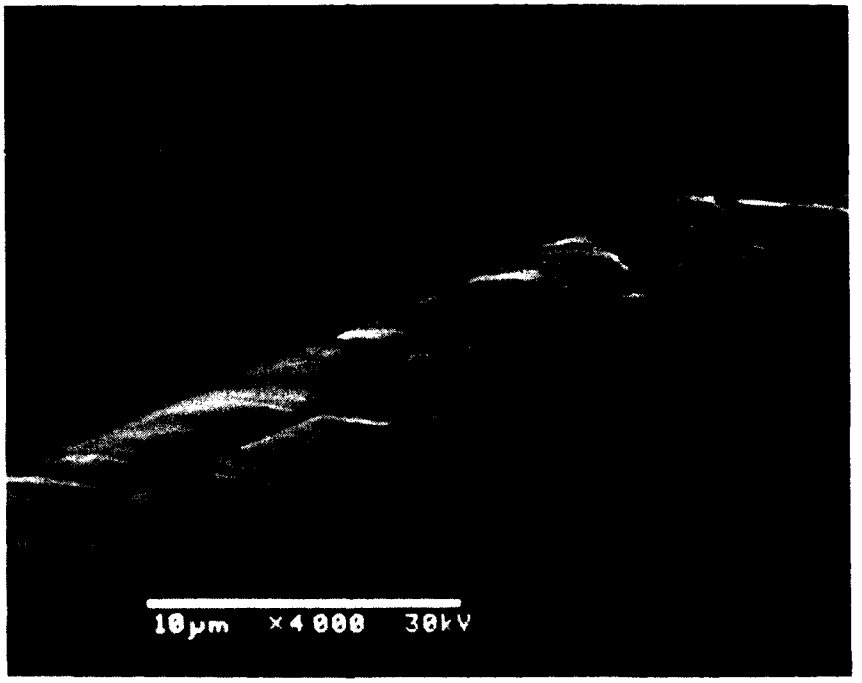

Figure 3. SEM observation of microcracks and intrusions

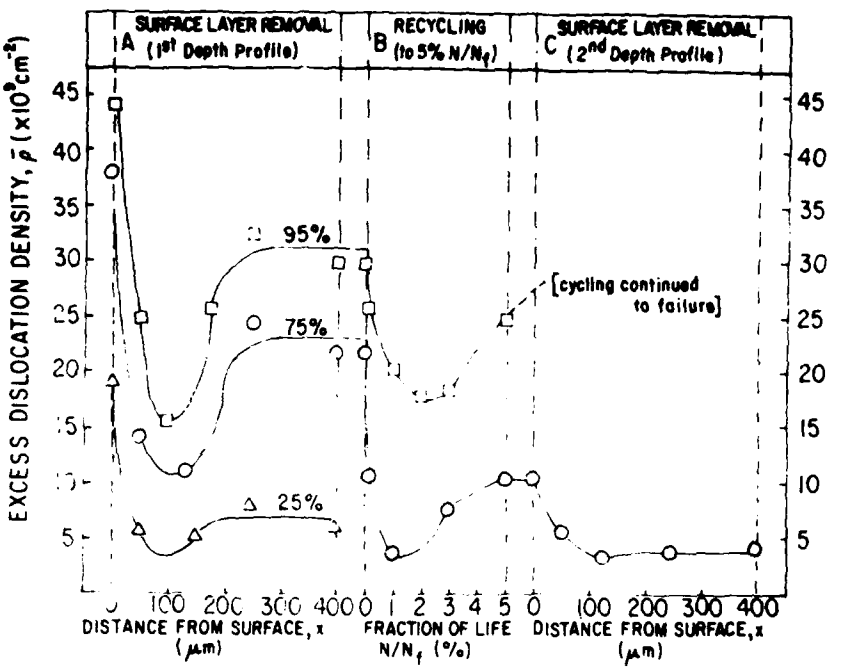

Figure 4. Composite diagram for Al 2024 given prior fatigue to 75 and 95 pct of their life at ± 200 MPa. Part A: depth profile; Part B: recycling; Part C: depth profile

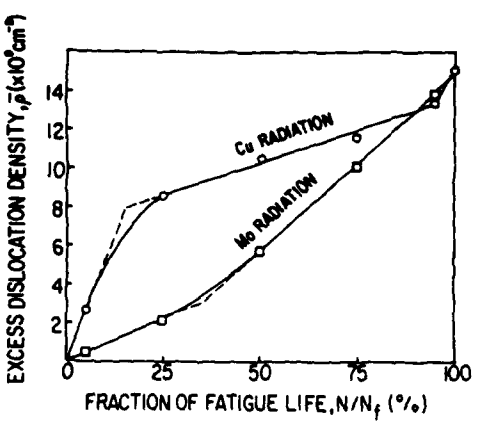

Figure 5. Dependence of $\bar{\rho}$ on N/N_F (%) of Al 2024 at ± 280 MPa by analysis with copper and molybdenum radiation

AN OPTICAL INTERFEROMETRY TECHNIQUE TO EVALUATE CLOSURE ALONG A CRACK FRONT

Angela A. Steffen and Paul F. Packman*

Fatigue crack closure was observed in PMMA SEN fatigue cracked three point bend specimens. Optical interference profiles indicate that a portion of the crack face can be approximated by a straight line and extended to obtain a rotation factor which indicated that the crack tip was open along the centerline for all loading conditions. The interference profiles along the edge showed that portions of the crack were closed for low loads and open under increasing loads. Crack opening profiles taken in the thickness direction indicate the closure of the crack faces extends into the thickness of the material at low loads. With increasing loads the interference profile indicates a transverse bending similar to anticlastic bending which vanishes at high applied loads.

INTRODUCTION

The behavior of an ideal crack under cyclic loading assumes that the crack tip is physically open under all positive external applied stresses. (1) Work conducted in recent years on fatigue crack growth, load interaction processes in fatigue crack growth and crack closure have demonstrated that fatigue cracks are closed for a portion of the loading cycle. Elber showed that for R=0 fatigue loading the closure stress is 50% of the maximum applied stress intensity K(fmax). Figure 1 shows the relationship between applied stress intensity, applied R ratio and the closure stress as given by Elber (2). Similar relationships were developed by Katcher and Kaplan (3). Observations for R=-1 fatigue loading show that the closure stress is relieved by the applied compressive loads, hence the crack growth rate should be the maximum for a given K range.

There are three fundamental features of fatigue crack closure;

*Civil/Mechanical Engr. Dept., Southern Methodist University, Dallas, TX 75275

(1) Physical touching of a portion of the adjacent crack faces for some portion of the load cycle (4) These may include oxide induced closure and roughness induced closure. (5)

(2) Residual compressive stresses associated with the plastic zone, which reduce the local stress intensity below the applied stress intensity factor (6)

(3) Plastic zone "wakes" which are the plastic zones associated with the crack tip plastic deformation in the previous positions of the crack.(7)

When one considers retardation of the fatigue crack growth associated with load interaction effects in fatigue spectrum loading, the interacting plastic zones should be added to this list.(8)

Following British Standard 5762, the crack tip opening displacement can be characterized as being made up of two factors; the elastic CTOD component given by:

$$\delta_e = K^2(1-\nu^2)/2\sigma_{ys}E) \qquad (1)$$

and a plastic component given by

$$\delta_p = r_p(W-a)v_p/r_p(W-a) + a + z) \qquad (2)$$

Of particular importance is the plastic rotation factor r_p which assumes the existance of a point of rotation beyond the crack tip about which the side of the crack rotate. The plastic rotation factors are given as approximately 0.4 (9), but "elastic" rotation values as low as 0.195 have been reported. (10) The presence of a rotation factor apriori implies that there is an opening at the crack tip since the value of $r_p(W-a)$ is the distance ahead of the crack tip where the adjacent faces of the crack, when extended are assumed to meet.

Figure 2 shows the variation in CTOD, COD and r for SEN bend tests on 0.36% C steel obtained by Ingham (11) itcan be seen that the linear extrapolated portion of the crack faces is extended to the crack centerline to obtain r(W-a). It can be observed further that the actual COD values near the crack tip are consistently lower than those determined by extrapolation of the straight line portions.

Optical interferometry techniques have also been used to demonstrate many of these phenomena in PMMA, aluminum and steels.-(12) Recent studies appear to indicate that an additional closure mechanism occurs in PMMA which may also be present in metallic systems as well. In this paper an optical interference technique was used to evaluate the contour of the crack opening displacements along the crack front, and for approximately 5.08 mm

back from the crack tip. The interference profile of the crack tip along the centerline of the crack front was used to evaluate the rotation factors necessary for the determination of CTOD, using specimens made from PMMA following BS5762.

Optical Interference Technique

Optical interference techniques have been used in fundamental studies of the fatigue and fracture behavior of materials for the past 10 years. (12) This high precision technique uses simple apparatus to measure shall displacements in regions associated with the crack tip. Multiple-beam optical interference has been used as a research tool since 1942 by Tolansky and others (13), for the study of a wide range of surface topographical characteristics.

A thin transparent wedge of refractive index m is necessary in order for interference to take place when a monochromatic light is reflected from the top and bottom surface of the wedge. The fringes formed represent a contour map of the surface examined and each fringe represents a contour of constant displacement. If the zero order fringe can be determined the exact magnitude of the displacement can be found. In transparent materials this technique can be used to determine COD's in the air wedge formed between adjacent crack surfaces. For metallic materials a transverse interference is used to determine the transverse surface displacements between the specimen and an optical flat.

For fracture and fatigue studies the air wedge between the top and bottom crack faces is considered the transparent wedge and the interference fringes obtained can be used to directly measure the crack opening displacement. The monochromatic light is directed perpendicular to the crack plane and then reflected from the top and bottom surfaces. An interference pattern is thus developed. The dark fringes indicate destructive interference and occur when the path difference between the crack faces is an odd number of half wavelengths.

$$V(r,\sigma) = \tfrac{1}{2}(n-\tfrac{1}{2})\lambda \quad n = 1,2,3,... \qquad (3)$$

Bright fringes indicate constructive interference and occur when:

$$V(r,\sigma) = \tfrac{1}{2}(n\lambda) \quad n = 1,2,3,... \qquad (4)$$

The fringe pattern can be used to analyze a crack under various loading conditions or under dynamic real time loading.

Optical interference techniques have been used in the analysis of stress intensity factors, CTOD, and fatigue crack growth and retardation. Closure studies have been performed by

Pitoniak etal (14) on PMMA compact tension specimens under overload conditions. Sharpe and Grandt (15) have used transverse interferometry to show significant surface closure at varying stress levels.

Experimental Technique (16)

Three point single edge notch bend specimens made from Polymethylmethacrylate (PMMA) corresponding to BS5762
CTOD dimensions were fatigue cracked to obtain valid test specimens. Photographs of sodium monochromatic light (λ=5889A^{o}) interference patterns were taken at various applied loads, and were digitized to obtain crack opening contours. Plots of the crack opening vs. distance back from the crack tip were taken along the centerline of the crack and used to obtain the rotation factor for the specimens. Plots of crack opening displacement parallel to the crack tip were made to evaluate the portions of the crack front that were physically closed for some portion of the loading cycle.

Experimental Results and Discussion

Figure 3 shows typical interference patterns obtained from the SEN PMMA bend specimens. The dark fringes correspond to constant displacement, destructive interference patterns used in the analysis. The fringe pattern represent contour lines of equal y-direction displacements, the vertical distance between contours is the wavelength of the sodium light. Examination of the low load photograph shows few fringes, typical of small values of COD, the maximum opening is approximately five fringes (0.0075mm). As the load is increased the number of visible fringes increases considerably as the COD increases. The low load patterns show a distinct curvature of the dark fringes that does not follow the contour of the curved crack front. It can be seen that two of the fringes are closed. This shows that there are portions of the crack whose COD diminishes with increasing distance back from the crack tip. These patterns are similar to those previously reported in compact tension specimens by Pitoniak etal.

The displacement pattern indicates that the COD at the edges of the specimen are smaller than those in the center of the specimen. The free surfaces at the edge are closed under zero load and low load as suggested by Elber.

As the load increases the contours move rapidly toward the crack tip, indicating the opening of the crack sides as expected. The relative movement of the contours near the free surfaces is more complex than that of the fringes near the center.

Figures 4 and 5 show plots of fringe order (COD) vs.

distance back from the crack tip. Four profiles are shown, one along the centerline, 30% and 60% of the half-thickness, and close to the edge. It can be seen that all four profiles have some straight line portions and then the actual COD decreases below the extended straight line as was observed by Ingham etal. The crack opening decreases as the profile moves from the centerline to the edge indicating that for this load level the edge COD is less than that at the center for all distances back from the crack tip.

Figure 6 shows a plot of the extrapolated CTOD vs. transverse distance from the centerline of the crack. These transverse crack profiles were taken at approximately 13 cross sections along the z direction. The transverse profile shows that the extrapolated CTOD and COD for some portions behind the crack tip is closed along the edge, and extending into the thickness of the specimen. The specimen CTOD is open in the center for all loads. As the applied load is increased the COD at the edges increases more rapidly than do the COD in the centerline. At the higher load examined, the transverse COD across the thickness is almost constant.

These transverse profiles at increasing load show that in addition to the opening of the longitudinal profile of the crack, a second "flexing" of the crack face is occurring with a radius of curvature perpendicular to the principal direction of the crack opening. It has been shown that the transverse cross section of a rectangular member in pure bending can have deformations within the plane of the cross section. (17) The neutral axis and free surface of the transverse section in pure bending is bent in a circle of radius $r' = r/\nu$. The curvature of this transverse cross section is called the anticlastic curvature. The transverse profile appears to take a shape indicative of the anticlastic curvature bending as an intermediate stage in the opening of the crack faces.

The opening of the crack faces under condition of closure associated with the crack tip and free edges is thus viewed as one that includes transverse bending and flexing of the material, and cannot be considered analogous to the opening and closing of a book with the rotation about the spine of the book. It appears that the couple moment necessary to remove the anticlastic curvature with increasing load decreases the available energy to the material in the vicinity of the crack tip.

Conclusions

The following conclusions can be made based upon the experimental work.

(1) The centerline profile of the fatigue cracks in SEN bend

specimens produced in PMMA have a straight line portion which can be extrapolated to obtain rotation factors following BS5762.

(2) The extrapolated rotation factors obtained in this investigation fall well within the data obtained by other investigators for tests within the elastic region, i.e. 0.198 etc.. These values of rotation factors, though in the elastic region imply the presence of a finite crack tip opening.

(3) The centerline profiles show the presence of a small but real crack tip opening under all loading conditions no-load as well as external load. These values of extrapolated crack tip opening are smaller than those obtained using the British Standards, etc..

(4) The interference profiles obtained for the regions of the crack near the edges of the specimen show that significant portions of the surface length of the crack is physically closed under no load and low load conditions. The crack opening displacements of the portions of the crack near these free surfaces rapidly open until they are equal to the openings observed at the center.

(5) Under no-load and low load conditions there is a transverse curvature of the crack faces, closed at each free surface, open in the middle, which increases as the load increases. The transverse curvature bears strong resemblance to the anticlastic curvature associated with a beam bending analysis.

REFERENCES

(1) Rice, J. "Mechanics of Crack Tip Deformation and Extension By Fatigue." Fatigue Crack Propagation. ASTM STP 415, ASTM, 1967, pp. 247-307.

(2) Elber, W. "Significance of Fatigue Crack Closure." Damage Tolerance In Aircraft Structures. ASTM STP 486, ASTM, 1971, pp. 230-242.

(3) Katcher, M. and Kaplan, M.. "Effects of R-Factor and Crack Closure on Fatigue Crack Growth for Aluminum and Titanium Alloys." Fracture Toughness and Slow-Stable Cracking, ASTM STP 559, ASTM, 1974, pp.264-282.

(4) Sharpe, W. etal. "Effects of Rest Time on Fatigue Crack Retardation and Observations of Crack Closure." Fatigue Crack Growth Under Spectrum Loads, ASTM STP 595, ASTM, 1976, pp.61-77.

(5) Schulz, K. "An Experimental Study of Fatigue Crack Retardation Under Tensile and Compressive Loading In PMMA." MS Thesis, Southern Methodist University, 1986.

(6) Jacoby, G. etal. "Experimental Results and a Hypothesis for Fatigue Crack Propagation Under Variable Amplitude Loading." Fatigue Crack Growth Under Spectrum Loads. ASTM STP 595, ASTM, 1976, pp.172-183.

(7) Banerjee, S. " A Review of Crack Closure." AFWAL-TR-84-4031 Air Force Wright Aeronautical Laboratories, Ohio, April 1984.

(8) Wheeler, O. "Spectrum Loading and Crack Growth." Trans. ASME J. Bas. Engr., Vol. 94, 1972, pp. 181-186.

(9) Dawes, M., "Elastic-Plastic Fracture Toughness Bases On the COD and J Contour Integral Concepts." Welding Institute Report 54/1978/E , 1978.

(10) Veerman, C. and Muller, T.." The Location of the Apparent Rotation Axis In Notched Bend Testing." Eng. Frac. Mech., Vol 4, 1972, pp. 25-32.

(11) Ingham, T. etal. "The Effects of Geometry On The Interpretation of COD Test Data." British Standards Institution Report C54/71, 1971, pp.200-208.

(12) Packman, P. "The Role of Interferometry In Fracture Studies." Experimental Techniques in Fracture Mechanics, 2. Iowa State University Press, 1975.

(13) Tolansky, S. "Multiple Beam Interferometry of Surfaces and Films." Dover Publications, New York, 1970.

(14) Pitoniak, F. etal. "Fatigue Crack Retardation and Closure in Polymethylmethacrylate." Eng. Frac. Mech., Vol 6, 1974, pp. 663-670.

(15) Sharpe, W., Jr. and Grandt, A., Jr.. " A Preliminary Study of Fatigue Crack Retardation Using Laser Interferometry to Measure Crack Surface Displacement." Mechanics of Crack Growth, ASTM STP 590, ASTM, 1976, pp. 302-320.

(16) Steffen, A. "An Experimental Study of Rotation Factors In An Elastic Material." MS Thesis, Southern Methodist University, 1985.

(17) Southwell, R. "An Introduction to the Theory of Elasticity." Dover Publications, New York, 1969.

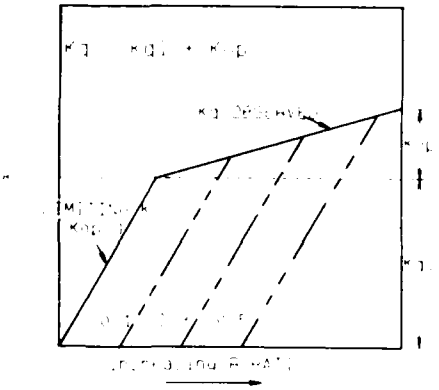

FIGURE 1: Relationship between applied K, R and K_{op}.

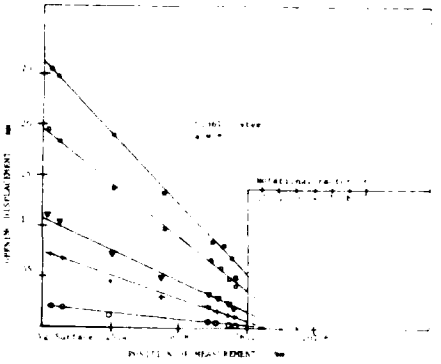

FIGURE 2: Variation of COD with position of measurement.

Please note figure 3 was supplied as a colour print by the authors. If the information from these figures is not clear please contact the authors directly for additional information.

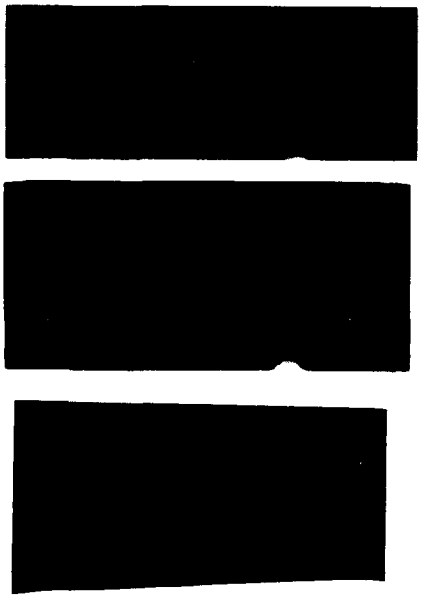

FIGURE 3: Interference fringe patterns for SENB specimen.

FIGURE 4: Plots of fringe order (COD) vs. distance back from tip.

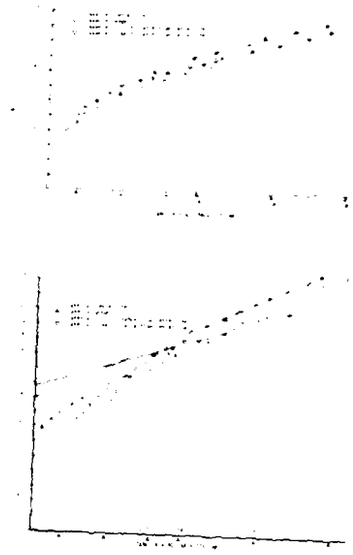

FIGURE 5: Plots of fringe order (COD) vs. distance back from tip.

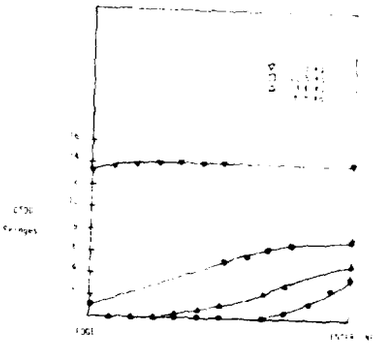

FIGURE 6: CTOD vs. crack front position for varying loads.

ON THE GEOMETRICAL DESCRIPTION OF FATIGUE CRACK SURFACES

B. Karlsson*, J. Wasén*, and K. Hamberg+

Fatigue crack surfaces generally have a stochastic character requiring statistical descriptions. The simple distributions often found are conveniently characterized by means and standard deviations. The fracture surfaces are effectively described by angular distributions, height distributions, and wavelength spectra. Such distributions develop during the fracture process as a result of the stochastic interactions between the stress field and the microstructure at the crack front.

A new model based on stochastic cracking is presented. The model describes the essential characteristics of the fracture surface geometry and naturally relates to the underlying microstructure.

INTRODUCTION

Characterization and quantification of fatigue fracture surfaces are often necessary in order to understand the fracture events. This may allow explanation of various effects related to the geometry of the fracture surface, as for instance the roughness induced crack closure. Such a geometrical quantification makes it possible to relate the fracture surface geometry to various microstructural parameters relevant for the fracture process (Hamberg et al. (1), Wasén et al. (2), and Coster and Chermant (3)). There are several difficulties associated with these descriptions. The technique of geometrical measurements on fracture surfaces is fairly complicated as regards the choice of suitable parameters and the resolution required. The aim of this paper is to discuss suitable descriptors and to evaluate these from real fatigue crack surfaces. Certain geometrical observations form the basis of a new, stochastic fracture model capable of reconstructing all essential characteristics of the real fracture surface, Wasén and Karlsson (4).

* Department of Engineering Metals, Chalmers University of Technology, S-412 96 Göteborg, Sweden.

+ AB Volvo, Technological Department, Laboratory for Metallic Materials, S-405 08 Göteborg, Sweden.

The geometrical situation is schematically shown in fig. 1, indicating the non-planar fracture surface as well as a projection of the surface and a section (profile) through it. Direct viewing in a single direction, as employed in conventional SEM techniques, only permits qualitative evaluations of details in the fracture surface. Still, relatively flat surfaces like grain boundary facets and transcrystalline cleavage allow approximate determinations of the surface geometry. A more exact account of the non-planar geometry requires stereoscopical recordings where image pairs with known tilt angles are photographed. Photogrammatical evaluation of such image pairs is then performed enabling a reconstruction of coordinates in the original fracture surface. The recording is operator demanding and permits only relatively few coordinates to be evaluated, Bauer and Haller (5). The application of automatic image analyzers is developing but still very limited due to substantial difficulties in finding reliable contrast and discrimination methods as well as the need for large computer capacity, e.g. Paul et al. (6). A more fundamental problem in stereometry is the shadowing effects occurring on overlapping or highly rugged surfaces. From a fractographical point of view the most serious limitation with this technique is the lack of microstructural, subsurface information needed to interpret the fractographic behaviour. The drawbacks of the non-destructive stereoscopical techniques are largely eliminated by coordinate analysis on fracture profiles taken from vertical sections through the fracture surface, e.g. Banerji and Underwood (7). Conventional metallographical preparation techniques followed by digitizing of the profile (directly in the metallographic mount or on photographs) then permit quantitative analysis of the profile in relation to the underlying microstructure. Overlapping is no problem in the profile analysis. In practice, computer support is necessary in both stereometry and profile analysis. The geometrical evaluations are basically the same in the two cases.

BASIC APPROACHES

The quantitative description of fracture surfaces is basically a problem of characterizing non-planar, localized surfaces. Classical stereology (Underwood (8)) has developed techniques to measure and quantify uniformly distributed surfaces. One usually assumes a uniform orientation of the normals to the surface elements (random normal orientation, RNO). The standard use of straight test lines to determine the surface density of uniformly distributed RNO surfaces is only to a limited extent applicable for localized surfaces (Wright and Karlsson (9)).

The microstructure in single phase or polyphase materials often controls the propagating crack. This may be due to inherent effects of the microstructure or may result from the extension and shape of the stress field at the crack tip. The exact geomety of the fracture surface is therefore rather complicated and in general not simply foreseeable from the microstructure.

Basically the fracture surface (and thus the fracture profile) has a stochastic or nonperiodic character. This irregularity has its roots in the stochastic local fracture events as well as in the nonrepetetive geometry of the microstructure. An additional reason may be nonsymmetries in the loaded specimens, even though the results of this paper clearly emphasize the former factors as being decisive. A consequence of such a stochastic fracture behaviour is that the fracture surface can be described only by geometrical distributions (mean values and deviations). The surface distribution in space is then conveniently described by the following quantities:

(i) Angular distributions or roughness indices.
(ii) Surface height distributions.
(iii) Spatial distributions via wavelengths (frequencies) or equivalent measures.

The analysis in this paper is mainly performed on profile contours. Evaluations of the surface quantities are possible in some cases; in others knowledge is still lacking to do so.

DIVIDING LINE (SURFACE), FILTERING

A problem in the profile or surface analysis is that a long-waved irregularity sometimes appears (Park and Fine (10), Wasén et al. (11)) and overlays the local fracture geometry created by the microstructure (fig. 2). A method to suppress non-averaged information from the measurements in order to get a suitable measure of the local, microstructurally induced roughness is to use a digital high pass filter technique (11). This technique uses a Fourier transformation of the crack profile from a length series to a frequency series, followed by cut-off of the low frequencies (i.e. the long-waved irregularity), and finally an inverse Fourier transformation of the remaining frequencies back to a length series.

The Fourier spectrum is suitably referred to a reference line defined by the line of least squares from the digitized points ("zero level" in fig. 2). In the filtering, the cut-off frequency can be chosen according to a geometric criterion, for example a frequency corresponding to a certain macroscopic irregularity or a microstructurally determined criterion. In fig. 2 (and in the model below), 50 grains were chosen as the cut-off wavelength. The dividing line is then identified with the filtered low-frequency (long wavelength) part and follows the macroscopic irregularity (fig. 2). Further details on the filtering technique have been discussed by Wasén et al. (11).

The two major arguments for the use of filtering are the following: Firstly, the width of the height distribution should not much exceed the grain size (or a corresponding, relevant microstructural unit), and secondly a comparatively short analysis

line allows a good averaging to be attained. A detailed analysis (11) on real fractographs has shown that the height distribution is strongly sensitive to the filtering out of the waviness whereas the angular distribution is rather insensitive to this procedure (cf. the scales of the profile in fig. 2).

In the experimental recordings, the fracture profile is digitized with a resolution of 0.5 μm. The coordinates for the Fourier transformation are produced in the following manner: The x-coordinates (with desired spacings) are selected by equidistant stepping along the reference line and the corresponding y-coordinates are calculated by successive regression based on the three nearest input points (Bengtsson et al. (12)) causing reduction of irrelevant "noise". Thereby the "real" profile is replaced by a chord chain accurately approximating the true line and defining the line of analysis (cf. fig. 10).

ANGULAR DISTRIBUTION

The angular distribution of the filtered profile can conveniently be described by weighting against the relative lenghts along the dividing line or by weighting against the length elements along the profile itself. The former weighting can simply be derived from the latter by the aid of the multiplying factor $1/\cos(\theta_i)$ (cf. fig. 10). Experimental data on fracture profiles in single phase materials reveal virtually Gaussian distributions (fig. 3). A suitable measure of the "average" local crack direction is then provided by the standard deviations of the two distributions, $\overline{\theta}$ and $\overline{\theta}_L$ respectively.

A different approach is the use of the linear roughness index R_L (9) and to define an equivalent orientation angle $\overline{\alpha}$ (11):

$$\overline{\alpha} = \arctan(1/R_L) \qquad (1)$$

Theoretical calculations on truncated, Gaussian angular distributions as well as experimental information show approximately pairwise proportionality between $\overline{\theta}$, $\overline{\theta}_L$ and $\overline{\alpha}$ (fig. 4) Therefore the linear roughness index R_L does contain equivalent information with the "mean" angular directions $\overline{\theta}$ and $\overline{\theta}_L$ (4). A comparison with corresponding values of the well-defined RNO-surface shows an excellent agreement (fig. 4). As an example, measurements on fracture profile in fig. 2 show close agreement with the theoretical predictions, fig. 4. Measurements on the fairly smooth fracture profiles found in pearlitic structures show typically $\overline{\theta} \approx 15^o$ (Hamberg and Karlsson (13)), whereas the extremely rugged fracture surface found in porous, sintered steels correspond to $\overline{\theta} \approx 35\text{-}40^o$ (14). Experimental recordings of a variety of fatigue fracture profiles from ferrous alloys in the authors' laboratory indicate a total span of approximately $\overline{\theta} \approx 12\text{-}40^o$, $\overline{\theta}_L$ ($= \overline{\alpha}$) $\approx 15\text{-}50^o$ and $R_L \approx 1.04 - 1.6$.

Area weighted angular distributions used as surface descriptors might be of interest. So far, no general theory seems to exist for the conversion of linear angular distributions to corresponding surface angular distributions. Under certain limiting geometrical assumptions such conversion functions have been derived (Scriven and Williams (15)) and expressed as equivalent multiplying factors for a stepwise transformation of the linear to the surface angular distributions. Computer modelling of different random surfaces (9) has been performed illustrating the character of such a transformation. For practical purposes a simple approach is to use averaging techniques as expressed by the surface roughness index R_S (9). The following relation between R_S and R_L relies on a simple step model but has proven as a very accurate predictor also for various random-type surfaces (9):

$$R_S = 1 + \pi/2\ (R_L - 1) \qquad (2)$$

The R_S-value can for instance be used to express true feature characteristics as linear size, perimeter lengths and interdistances from the corresponding quantities measured on single projections (Underwood (16)).

HEIGHT DISTRIBUTIONS

The height distributions, as referred to the dividing line, are expected to be symmetrical provided the measurements are statistically assured and the macroscopic load geometry is invariant. Measurements on single-phase ferrite indicate Gaussian-shaped height distributions (fig. 5). Thus the standard mean height deviation $\bar{H}$ is a sufficient descriptor of the height deviations. As indicated above $\bar{H}$ is sensitive to the exact cut-off value in wavelength in the filtering procedure. This has been tested experimentally (11) and reflects the stochastic character of the microstructure and the crack events. The choice of cut-off value is therefore a matter of judging the relevance of the information gained. A necessity in the experimental profile analysis is to achieve symmetry in the height distribution which could be followed by studying the gradual fading out of the skewness of the height distribution upon increasing the measuring statistics. The cut-off wavelength as well as the total length of analysis should be proportional to the grain size of the material.

SPATIAL CHARACTERIZATION

The spatial properties of the profile (height coordinates) can be exploited in various manners. Two descriptors will be briefly commented on: Fourier spectra and fractal properties.

Fourier spectra

A suitable characteristics of the profile geometry is given by decomposition in Fourier series (Passoja and Amborski (17)). Measurements on fracture profiles in single-phase materials (fig. 6) indicate a successively decreasing magnitude of high frequency components. The relatively smooth declining of the frequency spectrum and the presence of virtually all frequency components indicate an irregular character of the profile. This implies that the choice of cut-off frequency in the filtering process is arbitrary and has to be selected according to a suitable criterion (cf. above). By extending the filtering to lower wavelengths (higher frequencies) the height distribution is attained to a certain accuracy with a smaller length of analysis. In the example of fig. 6, the cut-off wavelength was chosen as a factor 50 times the mean intercept length (15 μm) and the total analysed length was approximately 2 mm. To ensure good averaging the length of the recorded profile should be several (say > 5) times the cut-off wavelength used. The exact choice of cut-off wavelength affects the width of the height distribution but hardly influences the angular distributions.

Fractal properties

Recently fractal analysis and the concept of fractal dimension have been applied in quantitative fractography (e.g. Wright and Karlsson (18), Underwood and Banerji (19)). This kind of analysis was originally developed in order to give some insight into the importance of measurement resolution (18). In addition, attempts to relate the appearance of the fractal plot of fracture profiles to the underlying microstructure have been made (3). Theoretical approaches (18) have been mainly concentrated on curves with self-similarity, while the experimental applications have been concerned with how the measured length of an irregular curve depends on the size of the measuring unit.

The measuring element may be designed in various ways (18). A common procedure is to substitute the real line with a chain of chords with constant length η (fig. 7). It is sometimes found (18, 19) that the estimated length of a line varies proportionately to some power of the measuring element so that

$$\ell = \ell_o \cdot \eta^{1-D} \qquad (3)$$

where D lies between 1 and 2. Lines with a single definable length are called fractal lines and D is the fractal dimension (fig. 9). Normalization allows the length ℓ to be replaced by the linear roughness index R_L (18).

In case of strictly regular shape patterns in the line there appear characteristic peaks in the fractal plot (18). Applied on fracture surfaces such peaks would correspond to a regular profile shape caused by a regular underlying microstructure. However, a thorough fractal analysis of two different fracture profiles - one transcrystalline and one intercrystalline crack respectively - has revealed that no possibility to reveal the characteristic microstructural size in the fractal plot exists, fig. 8 (18). This indeed follows from the stochastic character of the fracture profile (and of the microstructure) and has been mathematically confirmed by computer analysis (18). In addition, fig. 8 indicates a reversed sigmoidal fractal curve with varying D instead of an ideally linear fractal curve. In fact, this is partly a result of the measurement technique used and has recently been examined in detail (19). Fairly small differences in the fractal dimension of various fracture types are generally found suggesting a limited usefulness of fractal analysis as a means of quantifying fracture surfaces.

MODELLING

A suitable geometrical model should permit a reconstruction of the fatigue crack propagation process taking the relation to the underlying microstructure into consideration. The model suggested here is developed for single-phase materials and is given a fuller account elsewhere (4). The modelling concerns the fracture profile line.

The basis for the modelling is a detailed experimental analysis of fatigue cracks in ferritic steels. A process used to simulate the fracture surface must meet at least the following requirements:

1. It must regenerate the characteristic parameters and the character of the real fatigue crack profile.
2. The angular distribution should be independent of the height position relative to the dividing line. This statement is strongly supported by experimental findings (fig. 9).
3. The line segment distribution should be logarithmic-normal distributed and grain size dependent. This is in close accordance with experimental results (4).
4. The fracture process should be non-repetitive.

The assumptions above indicate that the crack can be approximated by a successive stepping process where each step is controlled by a stochastic angular direction (fig. 10). In the model a length weighted, normal distributed angular distribution is assumed with a standard deviation of 35 deg. corresponding to experimental data from ferritic steels (figs. 3 and 4). The mean distance between the deflection points is linearly dependent on to the grain size (4). In the results shown here, the lengths of the line

segments are assumed to be logarithmic normal distributed, in accordance with the linear intercept distribution (4) having a logarithmic standard deviation of 0.6.

Such a stochastic model analysed by a computerized Monte Carlo technique develops typical features corresponding to a real profile. For instance, a characteristic "irregular" waviness is found (fig. 11). By applying a filtering as above, various characteristics like a symmetric Gaussian shaped height distribution appear, fig. 12. Further, the frequency spectrum of the Fourier decomposed profile resembles that of the experimentally analysed profiles.

The proposed model thus regenerates a realistic fracture profile especially regarding nonperiodicity, waviness, the Fourier spectrum and the height distributions. In accordance with the real crack behaviour the model predicts a local propagation in random Gaussian distributed angular directions at the crack tip. The insensitivity to the height position of the crack tip means that the differential cracking is determined by the local strain field at the crack tip without any influence of the preceding profile geometry.

Experimental results prove a proportionality between the lengths of the approximating linear fracture elements and the mean intercept grain size of single-phase materials (cf. ref. 4). In addition, the recorded angular distributions are found to be independent of the grain size (4). A consequence would be that the standard mean height deviation $\bar{H}$ should be proportional to the fracture element size. Indeed, such a behaviour is predicted by the model and found in the experiments, fig. 13.

CONCLUDING REMARKS

The fracture surface created upon fatigue crack growth has a stochastic character requiring statistical descriptions. Frequently the distributions are simple and can be described by mean values and standard deviations. The following descriptors turn out to be most relevant:

1. Angular distributions. They are often Gaussian shaped around the main crack direction. Roughness indices can be used as alternatives to the standard mean deviation of the angular distribution. The linear directions along the profile are directly accessible, and conversion to surface angular distributions is theoretically possible under simplifying assumptions

2. Height distributions. These are easily attained from fracture profiles and are representative of the whole surface. Normal height distributions are often seen.

3. Spatial characterization. In particular, the Fourier spectrum is important. Presence of all components in the Fourier frequency spectrum indicates a stochastic character of the fracture surface.

The stochastic character of the surface invalidates a regular modelling and measurement techniques relied on such an assumption. The statistical descriptors can either be used on the whole fracture surface or in individual phases of polyphase materials (limitations in the spatial characterization). Experimental recordings of the fracture surface geometry generally require a filtering procedure due to the stochastic surface character.

Successful modelling of the fracture surface is possible by assuming stochastic local angular distributions at the crack tip. By such modelling it has been demonstrated that all essential characteristics of the surface are predictable. The statistical descriptors can be naturally related to the microstructure and be used in crack growth laws.

REFERENCES

(1) Hamberg, K., Wasén, J., and Karlsson, B., Chalmers Univ. Tech. To be presented at Fatigue '87, 1987.

(2) Wasén, J., Hamberg, K., and Karlsson, B., Chalmers Univ. Tech. To be published 1987.

(3) Coster, M., and Chermant, J.L., Intern. Metals Reviews, Vol. 28, 1983, pp. 228-250.

(4) Wasén, J., and Karlsson, B., Chalmers Univ. Tech. To be published, 1987.

(5) Bauer, B., and Haller, A., Pract. Metallogr., Vol. 18, 1981, pp. 327-341.

(6) Paul, J., Exner, H.E., Fripan, M., and Mehlo, H., Proceedings of the IV European Symposium for Stereology, Göteborg, 1985. Acta Stereologica, Vol. 5, 1986, pp. 127-131.

(7) Banerji, K., and Underwood, E.E., Acta Stereologica, Vol. 2, suppl. 1, 1983, pp. 65-70.

(8) Underwood, E.E., Quantitative Stereology, Addison-Wesley, Reading, 1970.

(9) Wright, K., and Karlsson, B., J. Microscopy, Vol. 130, pt. 1, 1983, pp. 37-51.

(10) Park, D.H., and Fine, M.E., In "Fatigue Crack Growth Threshold Concepts". Edited by D. Davidson and S. Suresh, AIME, New York, 1984, pp. 145-161.

(11) Wasén, J., Karlsson, B., and Hamberg, K., Proceedings of the IV European Symposium for Stereology, Göteborg, 1985. Acta Stereologica, Vol. 6, No. 1, 1987. In print.

(12) Bengtsson, S., Johannesson, B., and Warren, R. In Euromech 204 Colloqium "Structure and crack propagation in brittle matrix composite materials", Jablonna, Poland, 1985. To be published by Elsevier Applied Science.

(13) Hamberg, K., and Karlsson, B., Chalmers Univ. Tech. To be published, 1987.

(14) Bertilsson, I, and Karlsson, B., Chalmers Univ. Tech. To be presented at Fatigue '87, 1987.

(15) Scriven, R.A., and Williams, H.D., Trans. AIME, Vol. 233, 1965, pp. 1593-1602.

(16) Underwood, E.E., J. Metals, Vol. 38, 1986, pp. 30-32.

(17) Passoja, D.E., and Amborski, D.J. In Microstructural Science. Edited by J.E. Bennett, L.R. Cornwell, and J.L. McCall, Elsevier, New York, 1978, pp. 143-158.

(18) Wright, K., and Karlsson, B., J. Microscopy, Vol. 129, pt. 2, 1983, pp. 185-200.

(19) Underwood, E.E., and Banerji, K., Mater. Sci. Engin., Vol. 80, 1986, pp. 1-14.

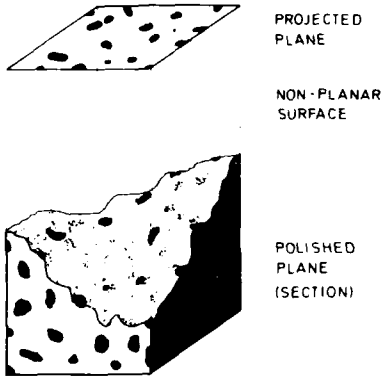

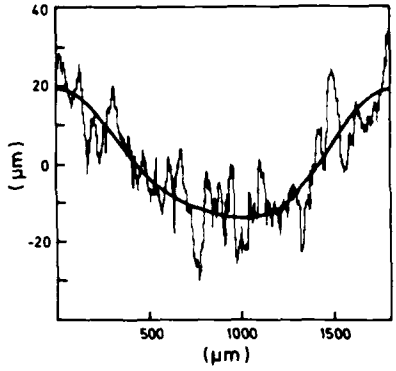

Fig. 1 Fig. 2

Fig. 1. Main surfaces encountered in quantitative fractography.

Fig. 2. Experimental fatigue fracture profile. Single phase ferrite; mean intercept length λ = 15 μm. Smooth curve defines the dividing line attained by filtering.

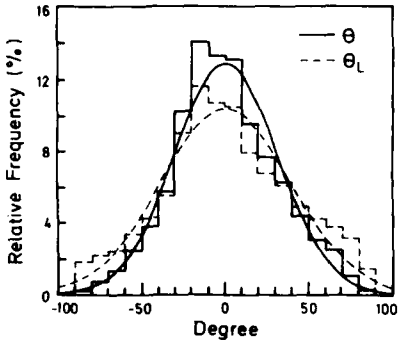

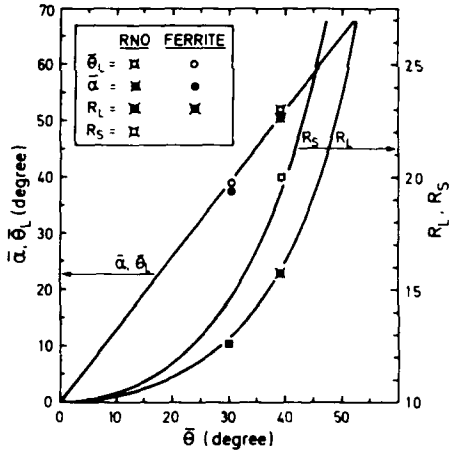

Fig. 3 Fig. 4

Fig. 3. Experimental angular distributions. Gaussian approximations included. Material as in fig. 2.

Fig. 4. Mean standard deviations of angles $\bar{\alpha}$ and $\bar{\theta}_L$ vs. $\bar{\theta}$. Theoretical R_L- and R_S-values included. Theoretical RNO-surface and experimental data added (ferrite as in fig. 2).

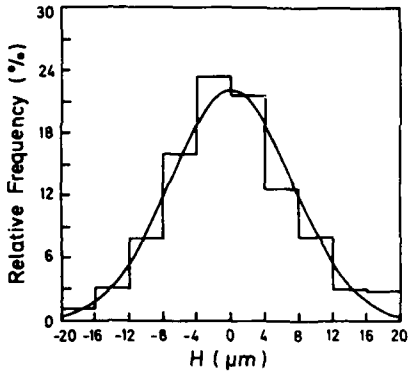

Fig. 5

Fig. 5. Experimental height distribution. Material as in fig. Filtered profile. Gaussian approximation included.

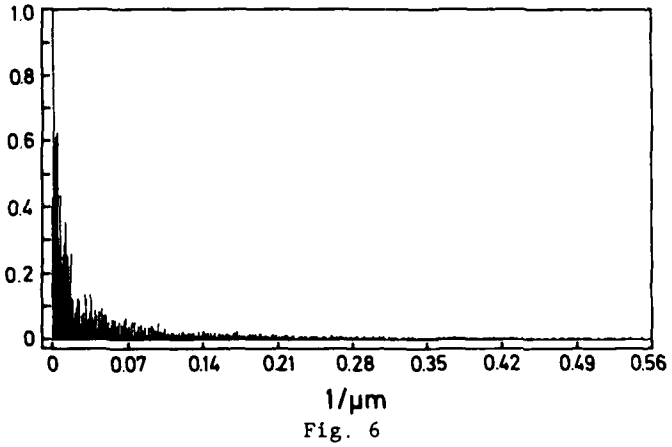

Fig. 6

Fig. 6. Normalized frequency spectrum of the profile in fig. Filtered profile (see main text).

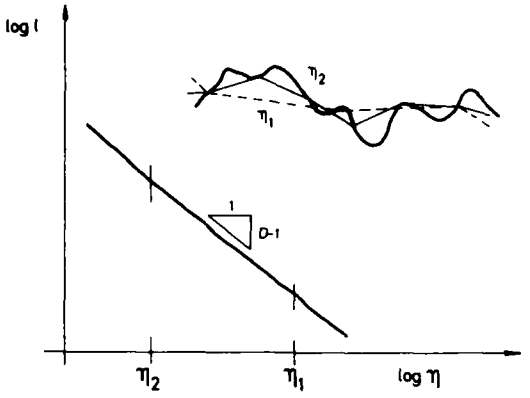

Fig. 7

Fig. 7. Fractal plot of a curved line. For a true fractal the log l - log η line is straight and unlimited.

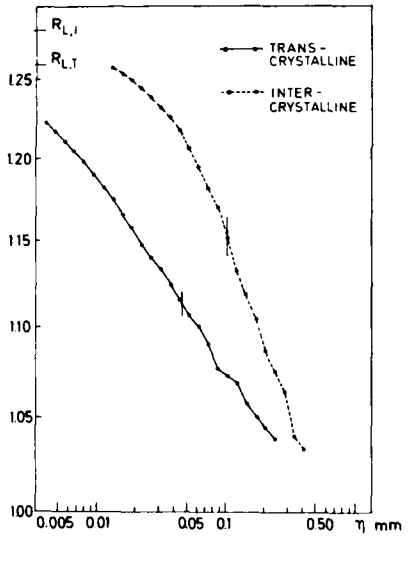

Fig. 8

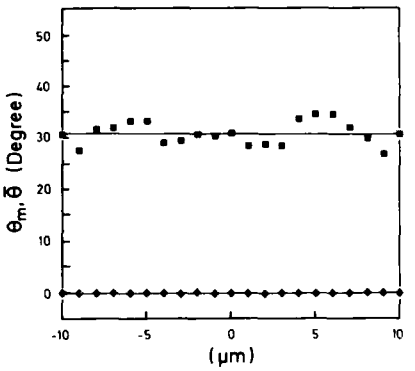

Fig. 9

Fig. 8. Fractal plot of typical transcrystalline and intercrystalline cracks in ferrous alloys (ref. 18).

Fig. 9. Mean angle (θ_m) and standard deviation ($\bar{\theta}$) of the line elements at various height levels along a fatigue crack profile. Material as in fig. 2.

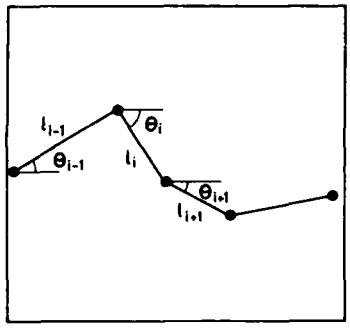

Fig. 10

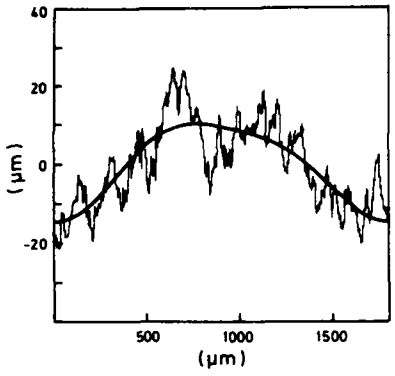

Fig. 11

Fig. 10. Modelling with a chain of successive chords with stochastic lengths and angular directions. Lengths and angles selectable from any desired distribution.

Fig. 11. Typical profile according to the theoretical model. Cf. the character of this profile with the experimental profile in fig. 2.

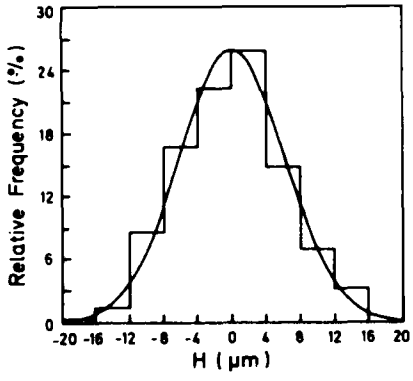

Fig. 12

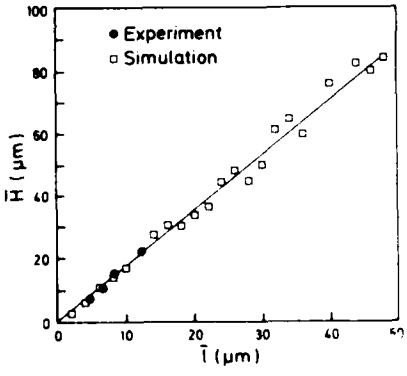

Fig. 13

Fig. 12. Typical height distribution from the model. Cf. experimental correspondence in fig. 5. Gaussian approximation included.

Fig. 13. Mean standard height deviation vs. mean step length from a logarithmic length distribution. Experimental and theoretical results.

Development of Research on Fatigue of Spot-Weld in Automobile Structures in Japan

Hideo KITAGAWA*, Tsugihiko SATOH** Satoshi NISHIJIMA***
Masao FUJIMOTO**** Nobuyuki MORI****

Abstract

Research in Japan on the fatigue strength or fatigue life of spot welds and/or spot welded automobile structures seems to be one of the most systematic and characteristic activities in this technical field world-wide, and a successful pioneer work too.

The trace of development of the research will be reviewed and discussed from a historical and technological viewpoint.

Experimental studies and pointing out of importance of the fatigue strength of spot welded joints for the automobile design appeared before 1965. Significance and necessity of the fatigue-of-spot-welds-study have been recognized by all of eleven Japanese automobile (body) companies at the beginning of the decade from 1970.

Co-operative and systematic research activities of the "Committee on Fatigue Strength and Structural Reliability" in the Society of Automotive Engineers in Japan started to work on this problem in 1972.

Three stages of the activities of the committee, 1972 to 1978, 1979 to 1981 and 1982 to the present will be stated, as summarized in Table 1 (referred from Mori's Report[1]).

Most of the fatigue S-N data in the first stage, 1972 to 1978, plotted on one figure are shown in Fig.1[2]. P_{max} is the peak value of the fatigue loads, and P_B is the tensile strength. A lot of scattering can be seen. The $P\text{-}P_{max}/P_B\text{-}N$ diagram for equi-variance by means of Nishijima's method is shown in Fig. 2[2].

In the second stage, 1979 to 1981, both high strength steels and low-carbon steel (in Table 2[3]) were tested, for investigating possibility of employing high-strength steels as the body panel for weight saving. The co-operative program of the fatigue tests in this stage is shown in Table 3[3]. Some of the results are summarized in Figs. 3 and 4[3].

In the third stage, 1982 to the present, classified typical spot-welded structure models were tested by five working groups. The working groups include most of automobile companies, larger steel manufacturers, relating universities and institutes. Structure models tested are shown in Fig. 5[4]. A lot of unexpected useful and comprehensive attainments and data were obtained. For examples, regidity of discontinuous thin plate structures[5], a new phenomena "buckling assisted fatigue' as shown in Fig. 6 [6] and 3-DK values of various joints[7] were anelized.

As the results of the comprehensive and systematic research activities, the following prediction methods have been proposed or selected.

(a) For the stage of design
  (a1) The prediction method based on loads acting to spot welds
  (a2) The prediction method by fracture mechanics
(b) For the stage of durability tests
  (b1) The prediction method using simulated specimens data transfered to members through the strain range.

---

* Professor, Department of Engineering, Yokohama National University
** Professor, Osaka Institute of Technology
*** Dr., National Research Institute for Metals
**** Dr., Toyota Central R. & D. Labs., INC

The method (a.) is schematically shown in Fig. 7[1]. The step (a) in this Fig. 7 is usually given by FEM computation. In the step (b)in Fig. 7 the standard spot-weld joint specimens' data are used. Minimum life of t· two in the step (b) is defined as the life of the spot. Some of the results are shown in Fig. 8.

In the (a2) method, all of the fatigue data for various types of spot-welded specimens under various types of loading (as shown in Fig.9) [7] are arranged with $\Delta K_{\phi max}$ and fell into one S-N band. Otherwise, different S-N curves were obtained for different types of specimens.

The (b1) method is illustrated in Figs. 10 and 11 [1]. Simulated specimens represent the strain distribution around a specified nugget in a given member.

Most of the activities and results reviewed and discussed above have been reported at the JSAE symposiums organized by this committee held every year or every other year. Proceedings were published.

The activity of the committee is still progressing, and now approaching our common problems. For examples,

(a) Economical and reliable analysis of K values (stress intensity factors).

(b) Fracture criteria for combined or more complex stress conditions.

(c) Evaluation methods in the case of employing new materials.

References

1 N. Mori,et al. ; Present Durobility Estimation and Fatigue Life ; Prediction of Automobile Bodies in Japan (1986).
2 K. Iwamoto ; JSAE Symp.(1978).
3 H. Kitagawa, T. Satoh and M. Fujimoto ; SAE 850371 (1985)
4 Fujimoto ; JSAE Symp (1985).
5 J. Niizawa, Tomioka,et al. ; JSAE Symp.(1985).
6 M. Oshima & H. Kitagawa ; SAE paper published in 1986
7 R. Yuuki, et al. ; JSAE Symp. (1985).

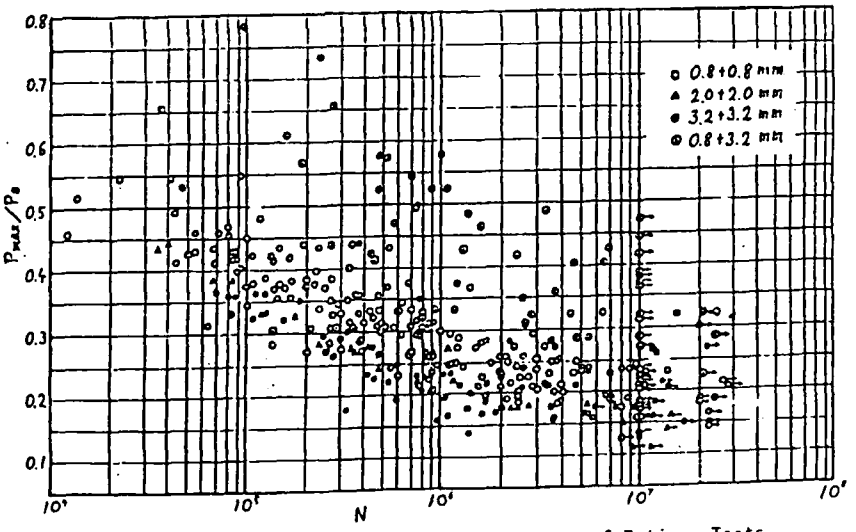

Fig.1 P_{max}/P_B Diagram for All of the Data of Fatigue Tests

Table ; CO - OPERATIVE ACTIVITIES OF COMMITTEE ON FATIGUE STRENGTH AND STRUCTURAL RELIABILITY OF JSAE

SUCCESSIVE CHAIRMEN

H.KITAGAWA : YOKOHAMA NATIONAL UNIVERSITY
T.SATOH : OSAKA INSTITUTE OF TECHNOLOGY
S.NISHIJIMA : NATIONAL RESEARCH INSTITUTE FOR METALS
M.FUJIMOTO : TOYOTA CENTRAL R. & D. LABS., INC.

(1) 1972 - 1978

" FATIGUE TESTS OF TENSILE SHEAR SPECIMENS "
(LOW - CARBON STEEL)

T. S. S.

→ THE EFFECT OF JOINT PARAMETERS ON FATIGUE STRENGTH WERE CLARIFIED.

(2) 1979 - 1981

" FATIGUE TESTS OF TENSILE SHEAR, CROSS TENSION AND PLANE BENDING SPECIMENS "
(LOW - CARBON AND HIGH - STRENGTH STEEL)

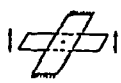

C. T. S.

BENDING

→ THE EFFECT OF MATERIALS AND LOADING TYPES ON FATIGUE STRENGTH WERE CLARIFIED.
(SAE PAPER 850371)

(3) 1982 - 1985

" FATIGUE TESTS OF STRUCTURAL COMPONENT MODELS "

THE DIFFERENCE FROM STANDARD JOINT SPECIMENS, AND FATIGUE LIFE PREDICTION METHODS WERE STUDIED.

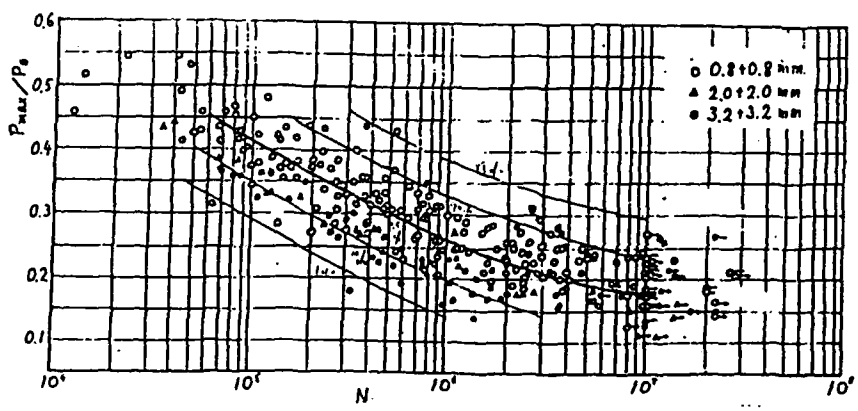

Fig.2 P-S-N Diagram Arranged by Nishijima's Method (except for Franged sp.)

Table 2 Kinds of steel sheets used

Steel	Thickness (mm)	Chemical composition (%)						Mechanical properties				
		C	Si	Mn	P	S	Al	Y.P. (MPa)	T.S. (MPa)	El (%)	$\bar{r}$ value	n value
Low-carbon (SPCE)	0.8	0.05	0.02	0.18	0.012	0.010	—	196	314	46	1.75	0.220
	1.2	0.043	0.012	0.273	0.012	0.021	0.056	182	328	44.3	1.68	0.225
	1.6	0.054	0.02	0.22	0.016	0.016	0.057	169	309	50.5	1.65	0.229
High-strength (Rephosphorized)	0.8	0.051	0.022	0.50	0.084	0.009	0.049	225	393	39	1.78	0.19
	1.2	0.057	0.003	0.27	0.074	0.017	—	223	367	39.8	1.45	0.226
	1.6	0.066	0.002	0.35	0.052	0.013	—	257	394	35.5	1.28	0.214

Table 3 Kinds of fatigue tests on co-operative program

Type of fatigue test	Tensile-shear fatigue test (Constant load amplitude)			Cross-tension fatigue test (Constant displacement amplitude)			Plane bending fatigue test (Constant displacement amplitude)		
Materials \	Specimen	Thickness T-T' (mm)	Co. in charge	Specimen	Thickness T-T' (mm)	Co. in charge	Specimen	Thickness T-T' (mm)	Co. in charge
Low-carbon & Low-carbon	A-1	0.8 - 0.8	ISZ	E-1	0.8 - 0.8	KAW	I-1	0.8 - 0.8	FHI
	A-2	0.8 - 1.2	ISZ	E-2	0.8 - 1.2	KAW	-	—	-
	A-3	0.8 - 1.6	ISZ	-	—	-	-	—	-
High-str. & High-str.	B-1	[0.8] - [0.8]	NMC	F-1	[0.8] - [0.8]	KAW & HIN	J-1	[0.8] - [0.8]	FHI
	B-2	[0.8] - [1.2]	NMC	F-2	[0.8] - [1.2]	HIN	-	—	-
	B-3	[0.8] - [1.6]	NMC	-	—	-	-	—	-
Low-carbon & High str.	C-1	0.8 - [0.8]	TMC	G-1	0.8 - [0.8]	HIN & TCL	K-1	0.8 - [0.8]	FHI
	C-2	0.8 - [1.2]	TMC	G-2	0.8 - [1.2]	TCL	-	—	-
	C-3	0.8 - [1.6]	TMC	-	—	-	-	—	-
	D-1	[0.8] - 0.8	MRD	-	—	-	-	—	-
	D-2	[0.8] - 1.2	MRD	H-2	[0.8] - 1.2	TCL	-	—	-
	D-3	[0.8] - 1.6	MRD	-	—	-	-	—	-

Notes; 1) The frame [ ] indicates high-strength steel.
2) The specimen D-1 is the same as C-1.
3) ISZ: Isuzu Motors, Ltd.
NMC: Nissan Motor Co., Ltd.
TMC: Toyota Motor Co., Ltd.
MRD: Honda R & D Co., Ltd.
KAW: Kanto Auto Works, Ltd.
HIN: Hino Motors, Ltd.
TCL: Toyota Central R & D Labs., Inc.
FHI: Fuji Heavy Industries, Ltd.

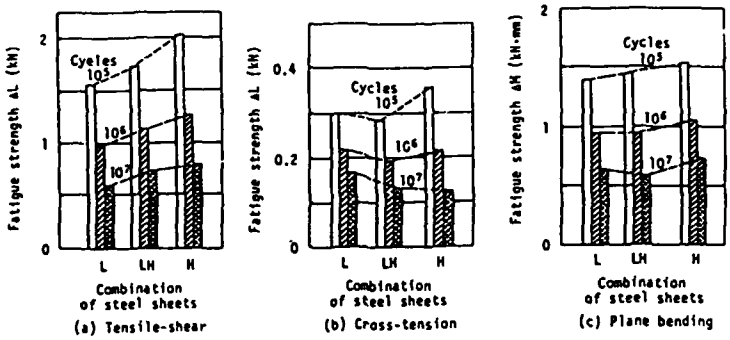

Fig. 3 Effect of combination of steel sheets on fatigue strength

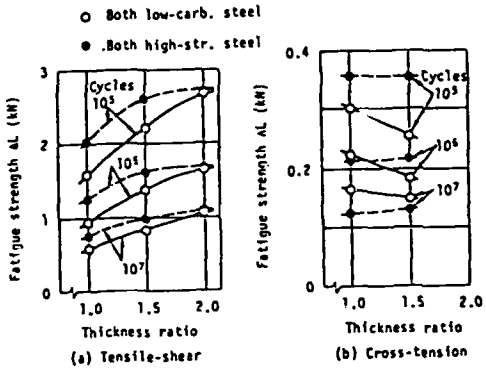

Fig. 4
Effect of thickness ratio on fatigue strength

	SHAPES AND LOADS		W/G LEADER
STRAIGHT MEMBERS		BENDING	M.OHSHIMA (NISSAN)
	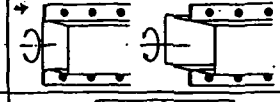	TORSION	A.MABUCHI (FUJI)
JOINTED MEMBERS	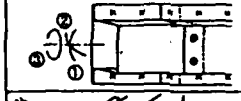	BENDING TORSION	A.TSUJIMURA (ISUZU)
	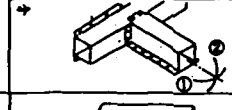	BENDING	N.MORI (TOYOTA C. L.)
MEMBER WITH BRACKET	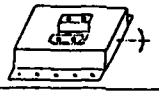	BENDING	H.NAGATA (TOYOTA)

Fig.5 Structural Models Studied

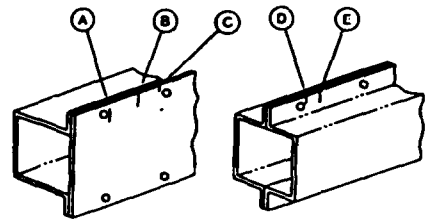

Fig.6 Fatigue Crack Mode in IN-plane Bending Fatigue Tests of Box Beam

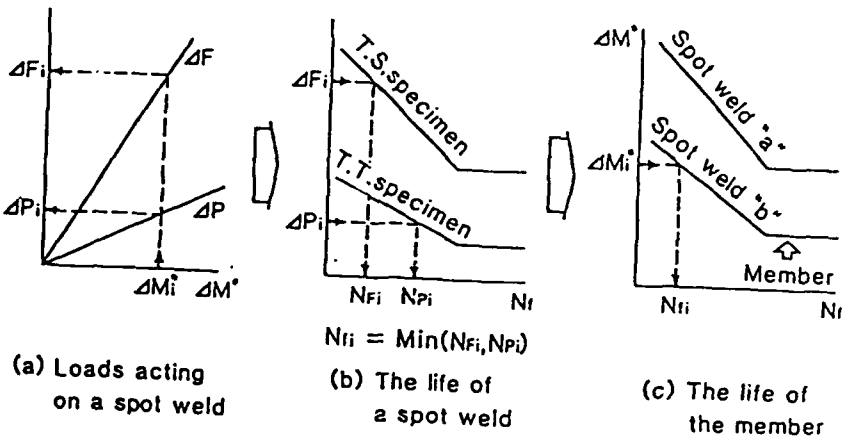

Fig.7 (a-1) The Method Based on Loads Acting to Spot Welds

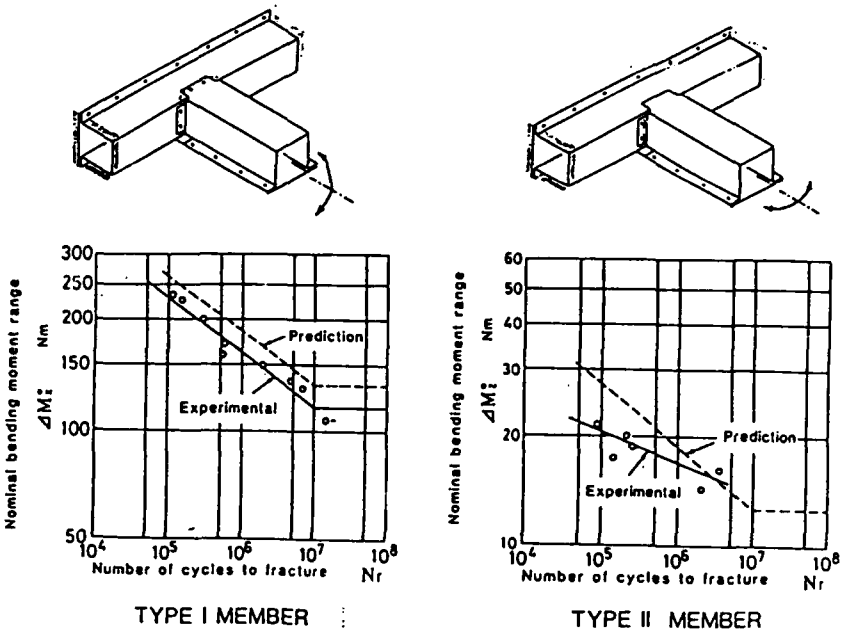

Fig.8 Results of Tests by Method(a-1)

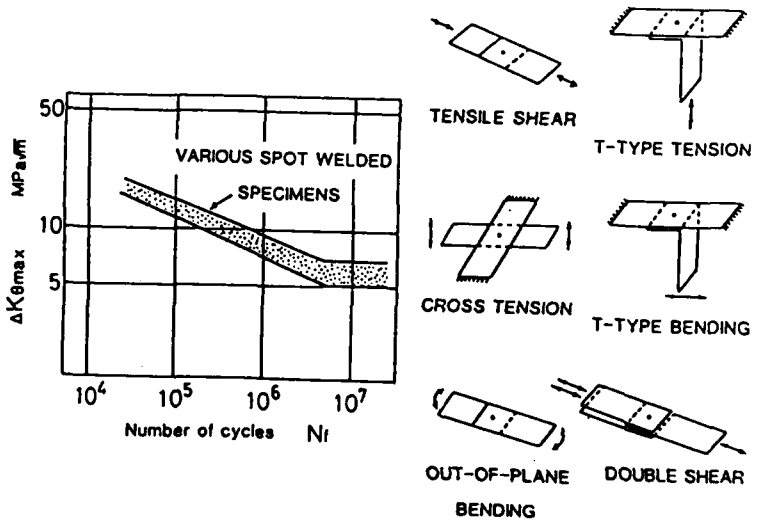

Fig.9 Method (a-2) (by Fracture Mechanics)

OVERVIEWS

AN OVERVIEW OF FATIGUE

A. J. McEvily*

In this introductory paper four topics are briefly discussed: fatigue crack initiation and growth in a nickel-base superalloy single crystal, the effect of the ambient environment on near-threshold fatigue crack growth behavior, the role of crack closure in load-interaction effects in fatigue crack growth, and the nature of creep-fatigue interactions, if any, during fatigue crack growth.

INTRODUCTION

The subject of fatigue continues to attract great interest from both the scientific and engineering communities as reflected in the current meeting which deals with not only fundamental considerations but, appropriately, with applied aspects as well. The papers to be presented summarize much of the research of recent years, research which has dealt with the problem of fatigue in a much more specific, less-speculative manner than heretofore. As a result of this research we have a much improved understanding of a variety of inter-related topics including crack closure, the role of microstructure, the effects of the environment, small and short crack behavior, anomalous crack growth, load-interaction effects, thresholds, mixed-mode fatigue, the effects of residual stresses, and creep-fatigue interactions. The present conference will serve to further advance our understanding of these areas as well as to elucidate the important questions that remain to be answered in future research. This particular presentation provides an

*Metallurgy Dept. and Institute of Materials Science, University of Connecticut, Storrs, CT 06268, U.S.A.

opportunity to discuss a number of topics of current interest in fatigue research and is intended to serve as a brief introduction to some of the more detailed presentations which follow.

CRACK INITIATION

Progress continues to be made in understanding the process of fatigue crack formation at slip bands as evidenced by recent papers presented in the symposium on Small Fatigue Cracks (1,2,3) where consideration was given to the transition from slip band intrusion to Stage I fatigue crack in copper. A particularly simple situation may occur in the case of single crystals of nickel-base superalloys(4). The slip process in these alloys is extremely planar and Mode II and III crack growth processes are favored over Mode I. Fig. 1 shows a schematic model, based upon Mott's cross-slip mechanism, for the formation of extrusions and intrusions at a corner. The formation of the intrusion, which is in essence a fatigue crack in this material, is facilitated by the proximity of the free surface at which the extrusion develops so that there is no net accumulation of material beneath the surface. This type of mechanism, with some modification to account for details of the fracture surface if it is not absolutely planar, can continue to operate across the thickness of a specimen and well into the depth. Several slip systems may be active but all slip vectors are in the plane of cracking, consistent with the Mode II and III deformation processes involved. Fig. 2 shows some of the detail of an actual fracture surface. The extrusions which form to enable the crack to advance as a large intrusion are evident. A main feature of the fatigue process in these planar glide alloys is that a distinction between crack initiation and crack propagation stages need not be made since they are both controlled by the same dislocation mechanisms.

ENVIRONMENTAL EFFECTS

In studies of fatigue crack growth in air in 304 stainless steel it has been observed (5) that the shape of the da/dN vs. ΔK plot can have a rather unusual form in the near threshold region, and this has been confirmed by our results, Fig. 3 (6). Since this alloy undergoes an fcc to bcc transformation during crack growth, the possibility was raised that the transformation might in some way be responsible for the shape of the crack growth plot (5). However when the alloy is tested in vacuum (10^{-3} Pa) a more usual form of the plot is obtained as shown in Fig. 3. We therefore conclude that the effect is related to the environment. As in the nickel-base alloy described above, glide in this low-stacking fault energy alloy is extremely planar. Fractographic evidence indicates that

Mode II operates extensively near threshold in air, a circumstance which promotes crack growth by the repeated rupture of oxide films formed at the crack tip (4).

There are nevertheless some interesting aspects of the fatigue crack growth process in 304 stainless steel which are indeed related to the metastable nature of the alloy. For example, the extent of transformation as determined by x-ray diffraction studies of the fracture surfaces is dependent upon the test environment and ΔK level as indicated in Fig. 4 where the results obtained from tests in air and vacuum are plotted. It is noted that the extent of transformation is of the order of 90% for tests in vacuum, whereas for tests in air the extent of transformation is of the order of 50% at the higher ΔK levels and gradually decreases to 10% at threshold. The lesser extent of transformation in air may be due to stabilization of the austenite by nitrogen. In addition since the threshold for the tests in air was lower than in vacuum, the lower stress intensities involved in air tests may be associated with a lesser degree of transformation.

Another interesting aspect of the crack growth behavior in 304 stainless steel was that the crack opening level in vacuum was found to be independent of ΔK level as measured by a front-face clip gauge, and was the same for increasing and decreasing ΔK testing. However in air the situation was quite different, for the increasing ΔK tests the closure level was less than for the decreasing ΔK tests at a given value of ΔK, with the disparity increasing with increase in ΔK, Fig. 5. This result is due to the variation in the extent of the transformation with ΔK level in air. The volume expansion on going completely from the fcc phase to the bcc phase is of order 2%, and this expansion tends to prop the tip open. However in a decreasing ΔK test in air since the % transformed falls off with decrease in ΔK, the residual expansion in the wake of the tip is higher than at the tip and closure due to this effect as well as to roughness-induced and oxide-induced closure remains fairly constant. On the other hand in the increasing ΔK test the residual expansion in the wake of the crack tip is less than at the tip and closure is reduced. It was noted that the fracture surface was dark in the decreasing ΔK test whereas it was bright in the increasing ΔK test. These observations are consistent with the degree of wake-related closure detected by the front-face clip gauge. However, despite these differences the rate of crack growth in the ΔK decreasing test was similar to that for the increasing ΔK tests. This indicates that closure did occur but over a very short distance behind the crack tip in the increasing ΔK tests and that the clip-gauge method was not sensitive enough to detect this closure.

The environment can exert other interesting influences on the shape of the da/dN plot. For example, Fig. 6 shows the appearance of a da/dN plot for fatigue cracks grown in a near-α titanium alloy in air and in vacuum (7), note that at the elevated temperature there is an abrupt transition to threshold in air which is absent for the other test conditions. Fig. 7 shows additional data for this type of alloy at an elevated temperature together with the crack opening behavior near threshold (8). It is seen that the crack opening level is fairly insensitive to ΔK level and is well below K_{max}, so that the sharp transition is not closure related. Rather it appears to be a reflection of the strength and thickness of the oxide formed at the crack tip at elevated temperature. Below the threshold the stressstrain state at the crack tip is insufficient to rupture this oxide film, which may be of the order of 10^{-5} mm in thickness, whereas above the threshold the crack tip strains are sufficient to rupture the oxide. The rupture of the oxide as well as the mechanical advance in the base metal contribute to the relatively rapid growth of the crack once threshold is exceeded. However at higher ΔK levels in air the relative contribution of the oxide rupture process decreases and the air and vacuum test results are closer together. Similar behavior has been observed in the case of a modified 9Cr-1Mo steel for which the threshold at 538°C in vacuum was in fact lower than that in air (9).

CREEP-FATIGUE INTERACTION

When smooth specimens are cycled under strain controlled conditions in air at elevated temperature the lifetimes are usually frequency dependent, but this frequency dependence is much less pronounced if the tests are carried out in vacuum. As Coffin has pointed out some so-called creep-fatigue interactions are really manifestations of environmental effects (10). If the testing is carried out under load control rather than strain control conditions creep-ratchetting may occur and there is no real creep-fatigue interaction with respect to failure mode (11). The absence of strong interaction effects at elevated temperature can also be seen with respect to fatigue crack propagation in ferritic steels. For example, Fig. 8 shows the da/dN plot for several ferritic alloy steels tested in vacuum at elevated temperature at frequencies of 30Hz or higher (9). It is noted that these steels, despite differences in mechanical properties, all behave in a similar manner in these tests. This suggests that the dislocation arrays at the crack tips which affect the crack opening and closing processes are similar and that these arrays reflect the cyclic history rather than the initial condition. It is further noted that there is no R-dependency, which is consistent with the absence of closure in these tests. We have recently repeated tests on a 9Cr-2Mo alloy in vacuum at 538°C

to study the effect of frequency (12). At a frequency of 0.3 Hz the crack growth rates were the same as at 30 Hz. Over this frequency range therefore there was no contribution to the crack growth process which might be associated with creep. Next we tested 1018 steel at this same temperature in vacuum. The results are shown in Fig. 8b. Even this low strength steel, tested well into its creep range, exhibited the same rate of crack growth as did the other ferritic steels. Further, although the rate of crack growth was independent of frequency over the range studied, the monotonic plastic zone size increased with decreasing frequency. Again the dislocations arrays developed in the cyclic plastic zone at a crack tip in these ferritic steels must be quite similar and independent of frequency. The absence of a frequency effect in the range studied indicates that the growth process in vacuum (in contrast to tests in air where oxidation occurs) is not thermally cally activated, i.e., the process is dominated by long range stress fields associated with group behavior of the multiplicity of dislocations at the crack tip. In fact the most important temperature dependent variable appears to be Young's modulus, for as Fig. 9 indicates, the results from both room temperature and elevated temperature experiments can be normalized through the use of Young's modulus (9).

LOAD-INTERACTION EFFECTS

Since crack growth in service rarely, if ever, occurs under constant amplitude loading it is important to understand how the material characteristics play a role in load-interaction, i.e. history, effects. We have recently determined the effects of R-changes and ΔK changes on fatigue crack growth processes and have found that in the absence of closure the crack opening load and the minimum load in a cycle under steady state conditions coincide (12). However if R of ΔK is changed transients can develop during which the K_{op} and K_{min} levels are again brought into coincidence by a process which we refer to as shakedown. Some of the features of the transient process are illustrated in Fig. 10. In this figure the appearance of a fatigue crack in PVC is shown under different loading conditions. The crack was initially cycled between a K_{max} of 4 MPa$\sqrt{m}$ and zero. At K_{max} the crack tip was open as in Fig. 10a. Upon unloading to only 2 MPa$\sqrt{m}$ the crack was as shown in Fig. 10b, partially closed. After a few cycles between 2 and 4 MPa$\sqrt{m}$ the crack tip at the maximum load was as in Fig. 10c. Note that the opening is now much less than in Fig. 10a, although K_{max} is the same. Such a result is unexpected on the basis of linear superposition. When the K_{min} level is maintained at 2 MPa$\sqrt{m}$ the crack tip which was formerly open at this level is now closed, i.e., crack closure is now occurring at or above the minimum of the new loading cycle (R=0.5), Fig. 10d. Then when the load is reduced to zero the crack closes over its

entire length, Fig. 10e, and in fact there is more closure now than for a simple R=0 cycle. After each transition the material establisher a new closure level and during this transition upon reduction in R or ΔK a retardation in crack growth rate can occur. For example, Fig. 11 shows the results of tests in which R was changed but ΔK was held constant. Crack opening levels during the transition period were determined by examining replicas in a scanning electron microscope. During the transition the closure levels gradually changed and as ΔK_{eff}, $(K_{max}-K_{op})$, increased the rate of crack growth also increased until the steady state growth rate was achieved.

We have also recently studied the effect of a reduction of ΔK at constant K_{min} on the subsequent crack growth rate. This type of test is in effect an overload test with multiple overloads being applied. As with single overloads the crack growth rate undergoes a transient period during which the rate is retarded, but in contrast to the case of a single overload, crack closure levels through the full thickness are affected. This comes about because as in the case of the PVC when the mean load is reduced an additional clamping effect is experienced by the crack so that in effect the opening load is initially higher than it would have been in the absence of the prior loading overload history. The through thickness type of closure associated with multiple overloads is considerably different from the surface related closure associated with single overloads.

CONCLUDING REMARKS

It is clear that this brief introduction has not been able to touch upon many aspects of current interest in the field of fatigue. This shortcoming will be remedied by the papers that follow.

ACKNOWLEDGEMENT

The support received for this study from the U.S. Department of Energy, Office of Basic Energy Sciences, Division of Material Sciences, Grant DE-FG02-84ER45109 is gratefully acknowledged.

REFERENCES

(1) Ma, B. and Laird, C., in "Small Fatigue Cracks", ed. by R. O. Ritchie and J. Lankford, Met. Soc. AIME, Warrendale, Pa., 1986, p. 9.

(2) Fine, M. E. and Kwon, I. B., ibid., p. 29.

(3) Neumann, P. and Tonnesen, A., ibid., p. 41.

(4) Chen, O. and McEvily, A. J., U. of CT., to be published.

(5) Matsuoka, S., Nishijima, S., Masuda, C., and Ohtsubo, S., in "Advances in Fracture Research", Proc. of ICF6, Vol. 3, 1984, Pergammon Press, Oxford, p. 1561.

(6) Zagrany, W. and McEvily, A. J., U. of CT., to be published.

(7) Ruppen, J. R., and McEvily, A. J., Fatigue of Eng. Mater. Struct., Vol. 2, 1979, p. 63.

(8) Minakawa, K., U. of CT, unpublished results.

(9) Nakamura, H., Murali, K., Minakawa, K., and McEvily, A. J., in Proc. Int. Conf. on Microstructure and the Mechanical Behavior of Materials, Xian, China, 1985, ed. by Gu and He, to be published by EMAS, Warfield, England.

(10) Coffin, L. F., In Fatigue at Elevated Temperatures, ASTM STP 520, 1973, p. 5.

(11) Bunch, J. O., and McEvily, A. J., to be published.

(12) McEvily, A. J., and Yang, Z., Scripta Met., Vol. 20, 1986, p. 1781.

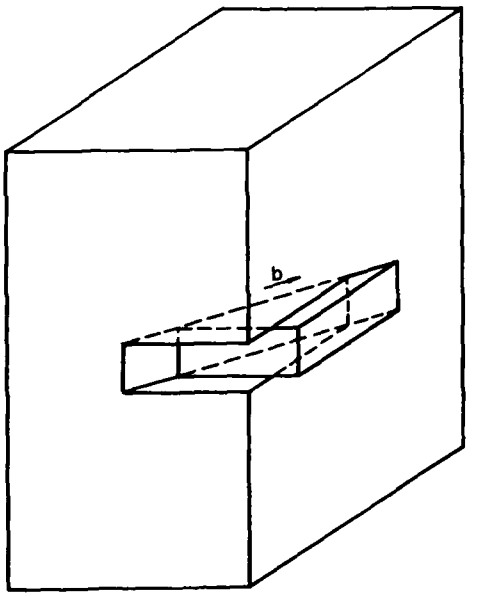

Fig. 1 Schematic of intrusion-extrusion process at a corner.

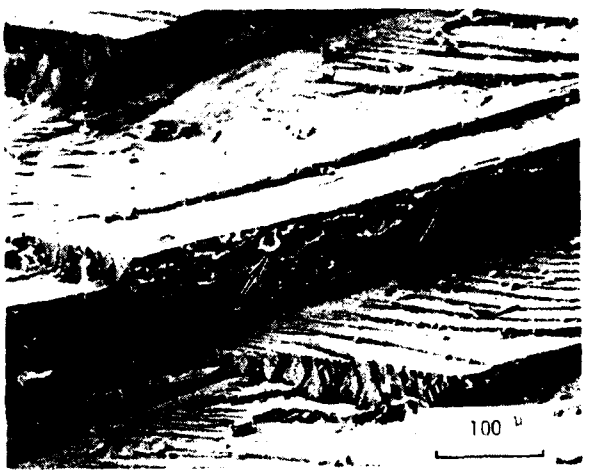

Fig. 2 Appearance of fatigue fracture surface in a nickel-base superalloy single crystal (4). Arrows indicate extrusions.

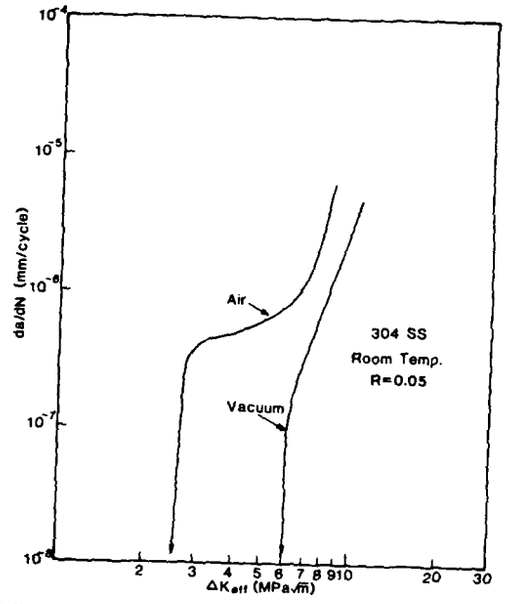

Fig. 3 da/dN vs. ΔK plots for 304 Stainless steel for R=0.05 in air and in vacuum (6).

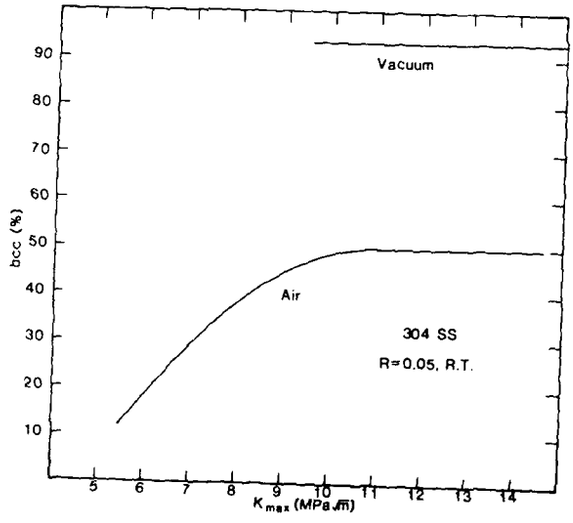

Fig. 4 % bcc phase formed on fatigue fracture surface of 304 stainless steel in air and in vacuum as a function of ΔK (6).

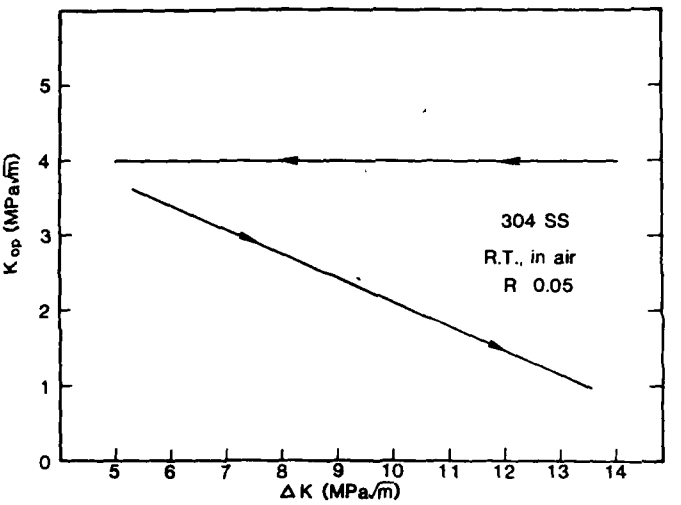

Fig. 5 Crack opening behavior of 304 stainless steel in air for ΔK decreasing and ΔK increasing conditions (6).

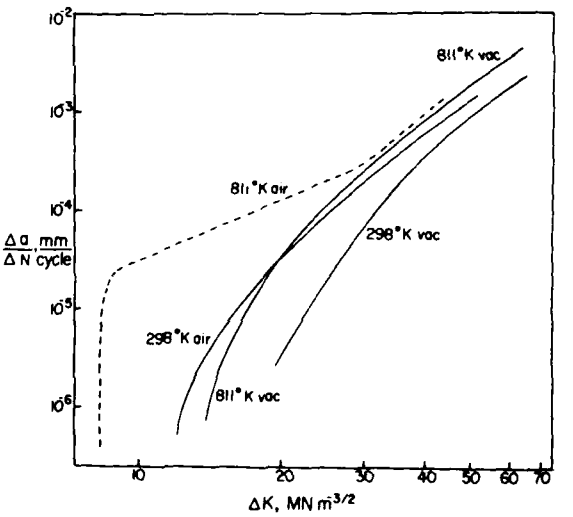

Fig. 6 da/dN vs. ΔK plots for Ti-6Al-2Sn-4Zr-2Mo-0.1Si alloy at R=0.05 at room and elevated temperatures in air and in vacuum (7).

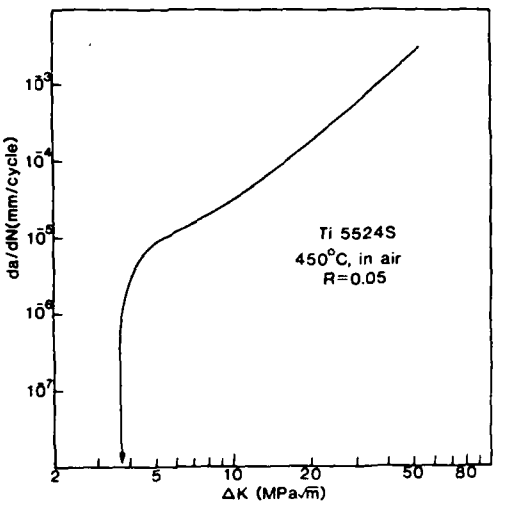

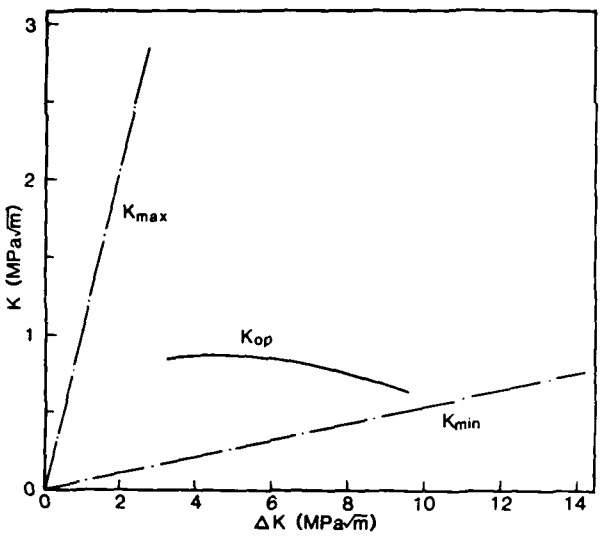

Fig. 7 da/dN and crack opening behavior for Ti 5Al-5Sn-2Zr-4Mo-0.25Si in air at elevated temperature (8).

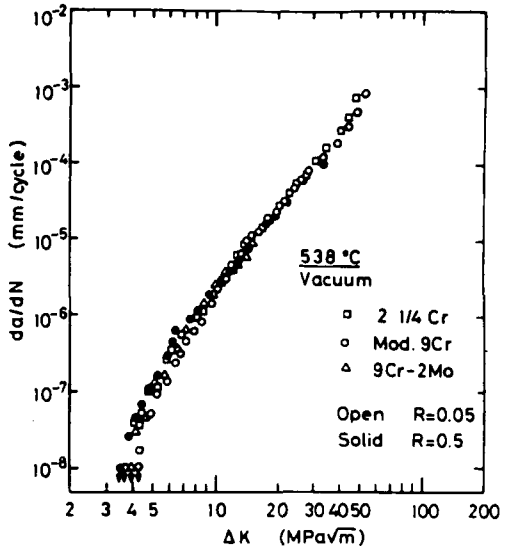

Fig. 8a da/dN vs. ΔK plot for three ferritic steels in vacuum at 538°C as a function of R (5).

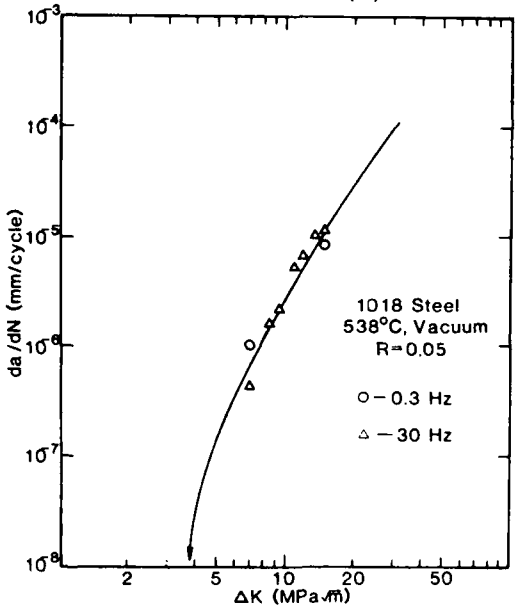

Fig. 8b da/dN data for 1018 steel as a function of frequency compared with behavior of ferritic steels shown in Fig. 8a, solid line.

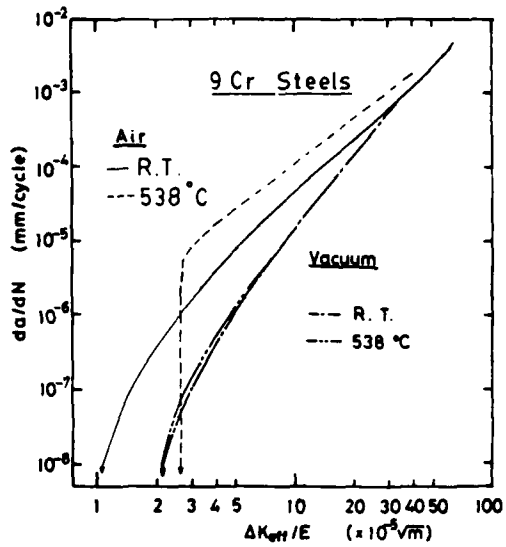

Fig. 9 da/dN as a function of ΔK/E for a modified 9Cr-1Mo steel tested in air and in vacuum at room temperature and 538°C (9).

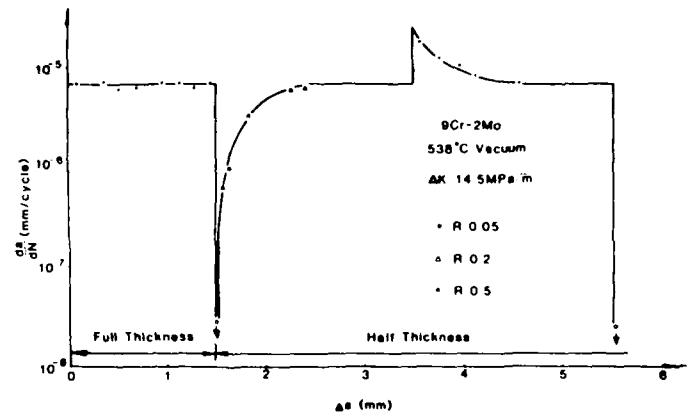

Fig. 11 Effect of a change in R at constant ΔK on the rate of fatigue crack growth (12). Note that in steady state there is no R-dependency for this alloy in range of tests shown.

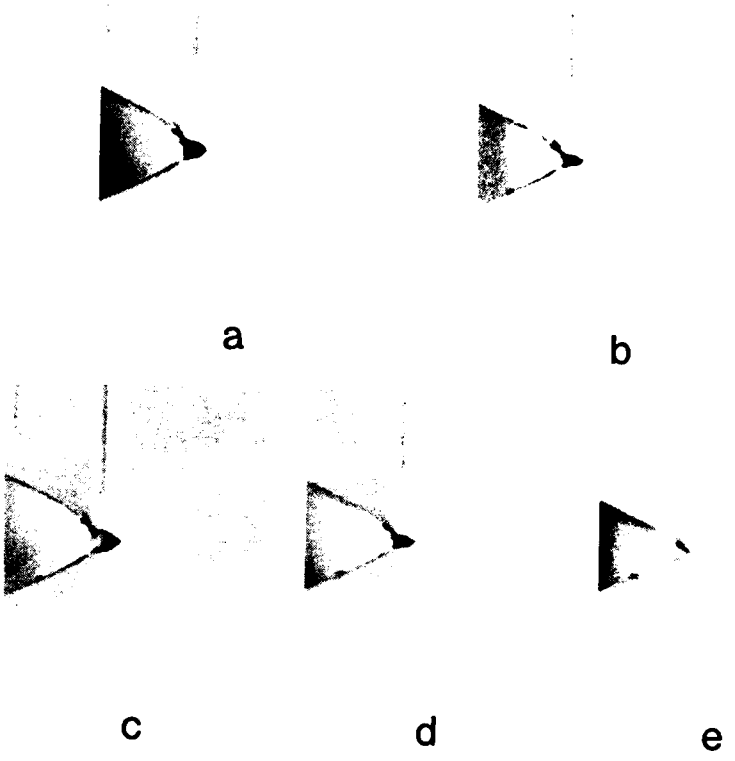

Fig. 10 Fatigue crack opening and closing behavior in PVC. (a) at K=4MPa$\sqrt{m}$, R=0, (b) at K=2MPa$\sqrt{m}$ after unloading from 4MPa$\sqrt{m}$ during R=0 test, (c) at 4MPa$\sqrt{m}$ in R=0.5 test, (d) at K=2MPa$\sqrt{m}$ in R=0.5 test, and (e) after reduction in load to zero X15.

DEFORMATION MECHANISMS AND CRACK INITIATION IN FATIGUE

V. Gerold and B. Meier*

Fatigue crack initiation of metals and alloys as the onset of failure is a very complex phenomenon which is influenced by many interacting parameters such as microstructure, loading conditions, environment, etc.. At first, fatigue deformation mechanisms preceeding crack initiation will be discussed. A review is given on recent research on fcc material on both single phase and precipitation-hardened single and polycrystals. It is followed by a survey on new results in the area of crack nucleation. Because of the outstanding importance of fatigue crack initiation in common service, the initiation mechanisms in commercial aluminium-based alloys are included in this review.

INTRODUCTION

Fatigue failure of structural components is one of the major failure mechanisms which limits the lifetime of construction parts. Therefore, it is very important to have a basic understanding of the deformation and failure mechanisms occuring in metals and alloys. The purpose of this paper is a review of recent progress in this field. It will describe basic research on model single and polycrystals which has been performed in order to understand the deformation mechanisms which finally may lead to the nucleation of cracks. In addition to these results the very important different mechanisms of crack nucleation on commercial aluminium alloys will be discussed in detail. In order to limit the presentation it is restricted on the properties of fcc materials.

In the following Chapter the deformation mechanisms for single phase materials will be reviewed both for single and for polycrystals. Recent results on planar slip material are included. The next Chapter summarizes research on precipitation-hardened material

* Max-Planck-Institut fuer Metallforschung, Institut fuer Werkstoffwissenschaften, and Institut fuer Metallkunde, Universitaet Stuttgart, D-7000 Stuttgart 1, FRG

and the final Chapter discusses the crack initiation mechanisms for the different types of material.

Other recent review papers have appeared in the field of fatigued single phase single crystals (1), precipitation-hardened crystals (2,3) and crack initiation in single phase material (4,5). In addition, another paper has reviewed precipitation-hardened aluminium alloys (6).

FATIGUE DEFORMATION MECHANISMS IN SINGLE PHASE MATERIALS

Plastic deformation in fcc single phase materials is mainly influenced by its stacking fault energy which marks the ease of cross slip of screw dislocations. Materials with medium or high stacking fault energies result in so-called wavy slip since it is very easy for the screw dislocations to leave the active slip planes and to distribute slip into broader bands on parallel slip planes. In contrast, materials with low stacking fault energy deform in planar slip where plastic shear is concentrated mainly on single active slip planes. Most of the papers published in the last years are concentrated on pure copper which belongs to the wavy slip materials. In spite of the fact that this has already a long tradition, quite new and interesting results have emerged very recently by many authors. In contrast to this there exists only a single recent contribution to planar slip material. At first the results on wavy slip materials will be presented.

Wavy Slip Materials, Single Crystals

Cyclic Stress-Strain Curve and Dislocation Structures. In low cycle fatige (LCF) experiments where the plastic shear strain amplitude γ_{pl} is kept constant during the cycling, single crystals oriented for single slip show a final saturation shear stress amplitude τ_s after hardening which depends on the applied strain amplitude. Since the well-known papers by Winter (7) and Mughrabi (8) it is accepted that there exist three regimes I to III as shown in Fig. 1 for the case of copper.

Regime I exists up to a strain amplitude $\gamma_{pl} \approx 6 \cdot 10^{-5}$. In this range the saturation stress increases steadily with increasing strain amplitude and the deformation is homogeneous. The saturation state is characterized by the vein structure where irregular veins contain dislocation multipoles of a high density of primary edge dislocations. They are also called loop patches (9) since they consist of many small loops. These veins are surrounded by dislocation-poor channels with a very low density of screw dislocations. Both structures have about the same volume fraction of 50 %. The hard veins contribute only by elastic polarization to the plastic deformation (8). According to Kuhlmann-Wilsdorf (11) a flip flop

mechanism has to be assumed in the veins in order to understand the size of the back stress which can be determined from the shape of the hysteresis loops.

Regime II reaches up to $\gamma_{pl} \simeq 7.5 \cdot 10^{-3}$. It is characterized by a constant plateau value of the saturation stress which is about 28 MPa for copper single crystals. In this range the plateau stress amplitude is caused by the localized deformation in persistent slip bands (PSBs) which form out of the vein structure. These bands have a width of one to several microns and are characterized by the so-called ladder structure where narrow primary edge dislocation walls normal to the Burgers vector occupy only 10 % of the band volume while 90 % of it is occupied by channels which allow the screw dislocations to move to and fro. The walls have a distance of ca. 1 µm from each other. Compared to the vein structure the PSBs are capable of a much larger shear amplitude which reaches an average value of about 1 %. According to Mughrabi (10) the reason for the structural change from veins to PSBs is caused by the incapability of the vein structure for larger shears and not by the onset of secondary glide as suggested by Kuhlmann-Wilsdorf and Laird (12). The volume fraction of the PSBs increases linearly with the applied plastic shear amplitude and reaches 100 % at the upper end of regime II.

The nucleation of PSBs out of the vein structure depends on the details of this structure. For higher strain amplitudes $\gamma_{pl} \geq 10^{-3}$ the cyclic hardening coefficient increases drastically with increasing γ_{pl}. This is connected with a change in the dislocation vein structure. As a result the nucleation stress τ_n for the first PSBs decreases below the plateau stress τ_p and can reach values as low as 0.6 τ_p (8). In regime III ($\gamma_{pl} \geq 7 \cdot 10^{-3}$) the plastic deformation is so high that secondary dislocations are necessary. In this range the stress amplitude increases again. Gradually a cell structure is developing from the wall structure.

Similar types of cyclic stress-strain curves have been obtained in several fcc metals and solid solutions (10). For copper, nickel and silver a plateau stress of 6.5 to $6.6 \cdot 10^{-4}$ G has been found (13). TEM investigations of fatigued nickel single crystals (15) resulted in the same dislocation structures as has been found in copper. The same value was observed for Cu-2 at.% Co whereas for Cu-2 at.%Al the value was substantially higher by 20 % (14).

Based on experimental observations Essmann et al (16) presented a model for the deformation mechanisms in the PSBs. It describes the irreversible part of the glide process originating from dislocation annihilation in both the dislocation walls and the channels. The annihilation of edge dislocations in the walls occurs by climb processes on short distances which create large amounts of vacancies. The vacancy concentration increases with cycling and reaches a saturation value of the order of 10^{-4}. In the same time this

leads to a volume expansion of the PSBs into the direction of the Burgers vector which results in the formation of extrusions at the surface of the crystal.

Secondary Cyclic Hardening. During fatigue experiments in the plateau regime large plastic strains can be accumulated after the plateau stress amplitude is reached. During this cycling a slight hardening by less than 10 % is observed which has been first investigated by Abel (17). With the beginning of secondary hardening the hysteresis loop becomes more pointed (Wang and Mughrabi (18)). A detailed TEM investigation revealed a gradual formation of sharp boundary layers of secondary dislocations between matrix and PSBs. During further fatiguing the old PSBs gradually change their structure to dislocation cells which have a larger resistance against shear. As a result the band ceases to contribute to plastic deformation and new bands have to be created.

Influence of the Deformation Mode on PSB Initiation. The onset of PSB nucleation depends on the details of the vein structure which can be considerably influenced by the deformation history. Already in 1968 Neumann (19) reported on the occurence of strain bursts if copper single crystals are fatigued under ramp-loading conditions where the controlled load amplitude is gradually increased. The strain bursts indicate instabilites of the developing dislocation structure which changes discontinuously step by step to more stable ones depending on the applied stress. Each burst can be observed to last for several cycles before the new dislocation structure has stabilized itself.

The final dislocation structures obtained this way have more difficulties to transform into PSBs. As has been found recently by Yan et al (20) the crystal could be loaded up to a shear stress amplitude of 32 MPa without PSB formation at fatigue frequencies of 34 Hz (Fig. 2). If at a constant stress amplitude of 32 MPa the frequency is lowered to 2 Hz fatigue softening starts at this frequency indicating the nucleation of PSBs. From these findings the authors conclude that thermally activated processes such as vacancy formation by dislocation climbing must be essential for PSB nucleation.

Strain Avalanches During Cycling in the PSB Regime. Deformation instabilities do not only occur in the vein structure but also during PSB deformation. Very recently, Yan and Laird (21) published hysteresis loops which have been registered with a digitizing oscilloscope (Fig. 3). The sudden increase of plastic strain due to strain avalanches causes the machine control to reduce the elastic strain which leads to the observed sudden stress reduction. Thereafter, the stress recovers leading to the streaks. From this explanation an interruption of the loop contours is expected which is not shown in the figure. This effect is quite different from the strain bursts since it occurs several times within a single loop.

A first interpretation of these results in combination with those of other authors have been presented by Buchinger et al (21a). They point to similarities to the deformation behavior of neutron-irradiated Cu crystals where the first dislocations sweep out obstacles leading to a decrease of the friction stress which then gives rise to the observed strain avalanches. In the case of PSB deformation such obstacles may be a high concentration of vacancies which are produced during PSB deformation. For more details the reader is referred to the original paper (21a).

Wavy Slip Material, Polycrystals

In this chapter the main results on copper and other polycrystals will be summarized. Since there are many similarities to the behavior of edge oriented single crystals they will be discussed also.

In the literature there exists a controversy about the question if the cyclic stress-strain curves of polycrystals show also a plateau. Obviously, the grain size plays an important role. While for grain sizes above 100 μm there seems to be at least an indication of a plateau (22-27) it fully disappears for smaller grain sizes (28). In addition, the observed stress response strongly depends on the loading history (29) and a plateau may not be observed for constant strain amplitude tests. For [111] oriented single crystals there seems to exist either no or only a very short plateau region (26). This is caused by the increased influence of multiple slip for both the edge-oriented single crystals and the polycrystals which drastically reduces the range of strain amplitudes where only single slip occurs.

Various authors have investigated the dislocation structure for multiple slip oriented single crystals as well as for polycrystals. New dislocation structures such as large areas of walls or of so-called labyrinth structures have been found. The latter consist of two sets of nearly perpendicular wall structures which interact in a characteristic way as shown in Fig. 4. Rasmussen and Pedersen (23) and Charsley (30) were the first who reported on labyrinth structures in polycrystals of pure Cu and a Cu-Ni alloy. The orientations were given as two sets of either {110} (23) or {100} walls (30).

Labyrinth structures could be found even in nickel (15) and in copper crystals oriented for single slip (31) if the plastic shear strain amplitude is greater than $2 \cdot 10^{-3}$. At this amplitude secondary slip becomes more active. A carefull analysis by Ackermann et al (31) gave two {210} orientations for the walls both containing the direction of the primary edge dislocations. The authors suggest that the {100} walls observed by other authors could as well be interpreted as {210} walls. However, this would not be the case for the investigation of an [001] oriented Cu single crystal by Jin and

AD-A184 047 FATIGUE '87 VOLUME 3(U) VIRGINIA UNIV CHARLOTTESVILLE 5/6
SCHOOL OF ENGINEERING AND APPLIED SCIENCE
R O RITCHIE ET AL. JUN 87 ARO-24134.3-MS-CF
UNCLASSIFIED N00014-87-G-0008 F/G 20/11 NL

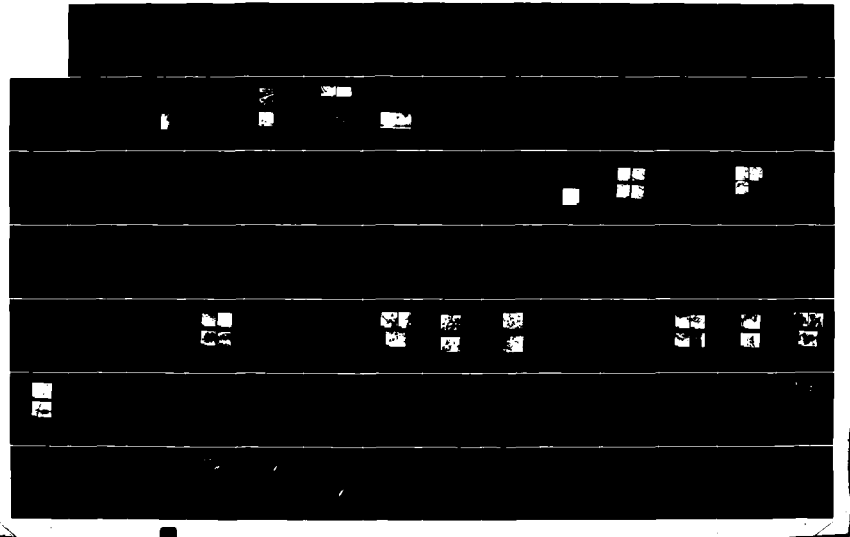

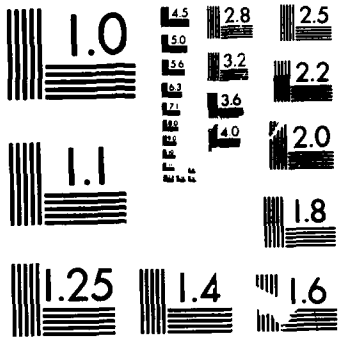

Winter (32) who clearly found very thin (010) and (001) walls with a wall spacing of 0.5 μm (Fig. 4). The majority were (001) walls normal to the loading direction. In another investigation on Cu crystals oriented for double slip the same authors found a variety of dislocation structures depending on the kind of the second slip system (33).

Very recently, Dickson et al (34) presented a simple model to explain the occurence of several wall orientations. According to these authors the walls consist of stackings of dislocation loops from two slip systems. These loops are elongated into the direction L_1 resp. L_2 of the corresponding edge component. The stackings occur into the directions $(L_1 + L_2)$, $(L_1 - L_2)$ and the direction normal to them. In this way the authors could predict {100} and {210} walls but not the combination of walls observed by Ackermann et al (31). The frequent observations of L and T type joints in the walls of labyrinth structures led Charsley and Kuhlmann-Wilsdorf (35) to suggest that their formation is favored because stresses are screened at the wall ends, lowering the strain energy of the system.

Planar Slip Material, Single Crystals

In contrast to the large amount of research on wavy slip single crystals the efforts on planar slip single crystals such as Cu-Al with a large content of aluminium are less pronounced. Several older papers have appeared in a time where the existence of a plateau stress has not been known. For example, Desvaux (36) has reported the existence of strain bursts in Cu-Al single crystals containing 12 at.% Al if the crystal is ramp-loaded as it has been found in pure Cu (19). In plastic strain-controlled experiments Abel et al (37,38) did not find a saturation stress for crystals containing more than 10 at.% Al. These crystals continuously harden up to final failure. In addition, strain bursts which were due to the formation of new slip bands were reported to occur during cycling. These bands gradually harden until new ones take over the plastic deformation. Obviously, these bands are no more persistent. As an example, Fig. 5 shows the stress response of a crystal containing 16 at.% Al which was fatigued with a constant plastic strain range of 0.27 %.

Only very recently new interesting results have been reported by Laird and co-workers (39) which are also reviewed in (1). In contrast to the foregoing results they reported a saturation stress for crystals containing 16 at.% Al. Such a curve is also shown in Fig. 5. The corresponding cyclic stress-strain curve is reproduced in Fig. 1 where it can be compared with the curve for pure copper. It shows a narrow plateau at the same stress level as that for copper. From these and additional TEM results the authors concluded that below the plateau level there exist mainly edge-dominated planar dipolar arrays, i.e., two closely arranged active slip

planes with extended edge dislocations of opposite sign. In the plateau region again a second type of dislocation structure appears as bands of high dislocation density in the primary slip system which cannot be resolved by TEM.

The different fatigue behavior found by Abel et al probably is caused by the soft machine they used for the experiments. The strain bursts they observed exceeded the controlled strain range and may have led to a different dislocation structure which was more stable against formation of a second one as it has been reported for pure copper (20) in one of the foregoing chapters. This effect seems to be much more pronounced for Cu-Al. Since the plateau range is rather small it can not be expected that the plastic deformation is only controlled by the bands which are assumed to be persistent.

FATIGUE DEFORMATION MECHANISMS IN PRECIPITATION-HARDENED MATERIALS

Precipitation-hardened alloys differ in their mechanical behavior from single phase alloys in so far as the additional interaction between dislocations and precipitated particles play now a dominant role. This considerably alters the fatigue properties. The alterations can best be observed in single crystal studies since the crystal can respond macroscopically to alterations of the deformation mechanism whereas this effect often is smeared out in polycrystals due to the different behavior of differently oriented grains.

Single Crystal Behavior

At first it should be mentioned that the atomic order of the precipitates plays a dominant role which influences the particle-dislocation interaction. Secondly, for the overaged state the particles are by-passed by the Orowan mechanism which again influences the deformation mechanisms in fatigue. In well-ordered precipitates the shearing of particles occurs by groups or pairs of dislocations on the same slip plane for minimizing the amount of antiphase boundaries. This results in a planar slip behavior where the deformation is located in single slip planes isolated from each other. For disordered particles usually wavy slip is observed where the slip is distributed over neighboring planes since the dislocations are able to leave the slip plane by local cross slip. Most research has been done for the latter type and this will be reported first.

Stress Response and Cyclic Stress-Strain Curves. The stress response of precipitation-hardened crystals differs considerably from that of single phase crystals. As an example, Fig. 6 gives the stress response of Cu-Co crystals heat-treated to obtain three different precipitation states (40,41). The controlled plastic strain amplitude was about 10^{-3} where the formation of PSBs can be expected. The supersaturated solid solution shows an increase of the

stress amplitude until saturation in a similar way as the pure copper crystal. In contrast, the underaged crystal (as well as the peak-aged one) shows a much faster hardening followed by a considerable softening which finally may reach a constant stress amplitude τ_s'. This saturation range can be reached for underaged alloys if the test is conducted in high vacuum (dashed line in Fig. 6). For this alloy it has been shown that the amount of softening is about 80 % of the original precipitation hardening (40). For the overaged crystal the stress level is low again and does not alter very much during cycling. This behavior is typical for alloys hardened by precipitates having no long-range order.

In Fig. 7 the cyclic stress-strain (CSS) curves of various alloys have been collected from the literature. For the three underaged cases Al-Cu (θ") (42), Cu-Co (43) and Cu-Ti (44) a pseudo-plateau range is found which describes the position of the peak stress τ_m which is followed by a marked softening. Both the plateau and the softening are caused by the formation of PSBs in which the plastic strain is localized during further cycling. For strain amplitudes below the plateau range the curve describes the saturation stress τ_s since no softening and no PSBs have been observed. Compared to the two copper alloys the plateau for Al-Cu (θ") is shifted to smaller plastic shear strain amplitudes but the reason is not known yet. It should be mentioned that the precipitation state of the strongly hardened Cu-Ti crystal is described by spinodal decomposition. The CRSS has about the same value as the pseudo-plateau stress whereas for Cu-Co the CRSS is only 45 MPa and therewith much smaller than the plateau stress.

In contrast to the underaged and peak-aged crystals the overaged ones do not show much variation of the saturation stress level for different plastic shear strain amplitudes as it is shown in Fig. 7 for Al-Cu (θ') (45).

Dislocation Structures. In precipitation-hardened alloys PSBs are nucleated for all strain amplitudes in the plateau region (Fig. 7) shortly before the peak stress is reached. However, their appearance is quite different and their influence on the stress response is much more drastic than in the case of single phase crystals. Usually, these bands are formed inside of large deformation bands of primary dislocations (thickness ca 5 μm) which develop during the hardening stage inside the vein structure (46,47). The PSBs are very narrow, their width is below 100 nm (46) compared to 1 to 2 μm for single phase material. Fig. 8 shows a typical TEM micrograph taken from an Al-Ag alloy containing spherical G.P. zones (47). The primary dislocations are out of contrast and the PSB can be seen because of lack of particle contrast. The particles have been sheared off several times by the heavy to and fro dislocation motion inside the PSB (48) since the strain concentration can amount to an average shear amplitude of 30 to 60 % (49). In the case of an Al-Zn-Mg single crystal containing the semicoherent η' phase it

could be demonstrated by TEM that the particle contrast reappears after re-aging the foil in the hot stage of the microscope. This demonstrates that the band does not deplete on solute atoms (48). The same result was obtained for Al-Ag by local chemical analysis using a scanning TEM (50).

Recently, that shearing off has been demonstrated by computer simulation (3,5). In assuming random slip a simple estimate gives the number of cycles needed for this process as $N = (R/b)^2/\gamma_{PSB}$ (51). In this equation γ_{PSB} is the mean shear amplitude in the PSB, R the particle radius and b the length of the Burgers vector. Assuming R = 4.7 nm, b = 0.26 nm and $\gamma_{PSB} = 0.1$ it results N = 3 100 which corresponds to the softening range shown in Fig.6. More sophisticated calculations lead to similar results (5).

The development of the dislocation structure depends on both the amount of precipitation hardening and the controlled plastic strain amplitude. The first is a measure of the interaction between dislocations and particles which reduces the effect of dislocation-dislocation interaction. With increasing strain amplitude the latter interaction is improved. Both effects on the resulting dislocation structure are schown schematically in Fig. 9 (52,41). With increasing strength of the particles the vein structure gradually changes to a more homogeneous one while the dislocation density increases. In addition the PSBs decrease in their width from about 1 μm to 50 nm.

A totally different dislocation structure is found in alloys containing a well ordered intermetallic phase as, for example, the γ' phase in nickel-based alloys. In that case the dislocation particle interaction causes the formation of pair dislocations on the same slip plane. Therefore, cross slip becomes much more difficult and a planar arrangement of dislocations is the result. Thus, high shear activities occur on individual slip planes with no deformation in between. The cumulative shear occuring in individual planes can be observed in alloys containing particles with a bimodal size distribution (53). The small fraction of very large particles (100 nm) serves only as indicator for the cumulative shear which can amount to more than 100 nm on an individual slip plane which is much more than the usual diameter of the strengthening particles (10 nm). In the case of a polycrystalline Nimonic 80 A alloy very often the cumulative shear of two neighboring active slip planes was found to be exactly opposite to each other (54,41). The narrow band between the two planes was tilted against the remaining matrix resulting in a TEM orientation contrast as shown in Fig. 10. In that case the particle contrast has disappeared because of orientation changes and not by particle shearing. This can be seen at position D where the contrast of small particles is still visible inside the band.

It seems that the two different cases described here are two limiting cases. For Al-Cu crystals containing the θ" phase, Lee and Laird (42) also reported an orientation contrast for the PSBs and stated no shearing-off of the particles inside the bands. On the other side, the authors found shearing inside the bands and assumed a disordering of the particles as cause for the softening.

Polycrystal Behavior

In the underaged and peak-aged state the polycrystals also show hardening and softening stages during cycling the latter being not so well developed as in the case of single crystals. The question of the existence of a pseudo plateau has also been discussed in the literature. At first such an existence has been claimed for underaged Al-Cu (56) but a more careful investigation clearly showed that such a plateau is observed only for very coarse-grained material (57) as shown in Fig. 11. In this diagram the results of pure Cu (28) and of an underaged Cu-Co alloy (59) have been included. In order to compare the results with those of the corresponding single crystals the transformations $\tau = \sigma/M$ and $\gamma_{pl} = M \cdot \Delta\varepsilon_{pl}/2$ were applied. For the orientation factor M the Sachs factor 2.24 has been used which is only applicable if mainly single slip does occur in both single and polycrystals. Obviously, this is the case for small strain amplitudes since for all three materials the data for single and polycrystals agree with each other.

CRACK INITIATION MECHANISMS

In most cases fatigue damage starts with the nucleation of cracks at distinct sites on the surface of the specimen. In order to improve the fatigue properties it is very important to understand the various crack initiation mechanisms. Generally, the cracks are initiated at sites of large deformation inhomogeneities. Such sites are PSBs, grain boundaries and finally brittle inclusions which are common for most commercial alloys.

Single Phase Material

Single Crystals. In single crystals with smooth surfaces fatigue cracks initiate only at surface roughnesses which form during cycling. This process has been described in detail by Mughrabi et al (60) for planar slip and wavy slip material. In the first case the roughness is introduced by the relatively large slip steps caused by localized shear on individual slip planes. This case will not be discussed further. In the second one it is due to the formation of PSBs. At first these bands form smooth extrusions which gradually roughen during further cycling (61) forming narrow intrusions as nucleation sites for cracks.

In a more thorough study on the crack nucleation mechanisms in copper single crystals Hunsche and Neumann (62,63) used a new sec-

tioning technique which reveals undistorted surface profiles with a resolution of 20 nm. They ramp-loaded the crystals up to a stress amplitude of 32 MPa and hardened it at this amplitude. Thereafter, they switched to plastic strain control with a larger strain amplitude (typically $\gamma_{pl} = 0.2$ %) which forced the crystal to form PSBs. The experiments were stopped after different cycling periods and sections parallel to the Burgers vector and to the load axis were prepared for SEM investigations. In this way the authors could clearly demonstrate that the nucleation of a crack at the tip of an intrusion is really a nucleation process influenced by the environment. While the intrusions show a vertex angle of about 30° the corresponding angle for a crack is zero. Fig. 12a represents a typical example.

The experiments also reveal the existence of large protrusions as shown in Fig. 12 b. They typically have a height of about 20 and a width of 40 microns. Their profile is asymmetric and is roughened by extrusions and intrusions of PSBs which have grouped together (63), probably because of the special fatigue hardening experiments. The first larger stage I cracks (20 μm) nucleate at the smooth end of the protrusion but after half of the lifetime a fatal crack has developed from an intrusion in the steep slope region (Fig. 12 b). It already has left the stage I orientation after a length of only 3 μm.

Further investigations (62) showed that crack nucleation is mainly enhanced by oxygen while the PSB topography is not affected by this agent. The vacuum experiments revealed the existence of re-welded cracks which may retard the effective crack nucleation and early growth rate by a factor 20 to 100 compared to experiments in air or oxygen. Chemisorption of oxygen at newly created surfaces may be the reason for the observed differences.

Polycrystals. As in the case of single crystals the intrusions formed by the PSBs seem to be nucleation sites of cracks. However, the grain boundaries play also an important role. In copper polycrystals, even at low plastic strain amplitudes more than 50 % of the cracks are initiated at boundary sites where PSBs impinged (4,60). The interaction between PSBs and grain boundaries probably leads to earlier crack nucleation compared to the case of single crystals, especially for coarse-grained samples. This may be the reason why the cyclic lifetime of such samples is much shorter than those of single crystals (4).

In the literature it is often suggested that the fatigue limit is defined by such a stress level where the nucleation of PSBs is no more possible because no cracks can be formed in that case (64,65). According to Müllner et al (66) this is not quite true at least at high frequencies. These authors used ultrasonic resonance techniques at 20 kHz and found the stress level for PSB formation in polycrystalline copper (54 MPa) distinctly below the fatigue

limit which was 60 to 75 MPa depending on the grain size. Below the fatigue limit the PSBs were restricted to single grains and showed microcracks inside the bands which did not propagate, however, for cycle numbers up to $5 \cdot 10^8$.

This result may be caused by the extremely high cyclic frequency. In single crystal experiments the same authors (66) found a much higher plateau shear stress amplitude (τ_s = 35 MPa compared to 28 MPa (8)) but the onset of PSB formation occured already at very low γ_{pl} where τ_s is much lower. These findings may have their explanation in the difficulty for the dislocations to form a stable vein structure at the ultrasonic frequency. The less stable this structure the lower the stress level for PSB formation as it has been discussed in one of the foregoing chapters. On the other side, the full plastic activity of the PSBs is reached only at higher stress levels because thermally activated processes are necessary to keep the PSBs mobile. The change to high frequencies has a similar effect as a change to low temperatures where an increase of the plateau stress level has been observed (67). Thus, the PSBs found below the fatigue limit in the ultrasonic experiments with polycrystals may not have reached their full activities.

Precipitation-Hardened Material

Crack Initiation at PSBs or Slip Steps. As pointed out in one of the foregoing chapters in precipitation-hardened materials the PSBs are very narrow and show a much larger plastic shear compared to those in single phase materials. Thus, their efficiency as nucleation sites is much more pronounced than in the former case (49,68,69). Careful investigations showed that such bands and slip steps act as preferred nucleation sites which show the highest slip offset on the specimen surface. For example, in Al-Cu crystals containing θ" particles the cracks initiate at higher slip offsets which occurred during softening and had reached 5 times the mean value (49). However, such a critical slip offset for crack nucleation does not seem to be a necessary condition. In a careful experiment on Ni-Al polycrystals, Anton and Fine (70) found the first microcracks with a size of 50 nm at slip lines without a distinct slip offset already after a few cycles.

As has been shown in Fig. 6 the localized deformation in PSBs always leads to a softening process which may end at a stress amplitude level τ_s'. This raises the question below which stress level the nucleation of the PSBs can be circumvented. A detailed investigation with underaged Cu-Co single crystals led to the conclusion that τ_s' (≈60 MPa) is a critical stress level above which PSBs can be formed. But even below this level down to the CRSS value (50 MPa) the nucleation of very small micro-PSBs could be observed which had only a length of several ten microns (71,58) and did not grow. Such micro-PSBs were also observed in Cu-Ti crystals

where they were found even at stress amplitudes far below the CRSS value (80 MPa compared to a CRSS of 150 MPa which is much higher than for Cu-Co) (72).

Crack Initiation at Grain Boundaries. Polycrystals usually show the stable phase occuring at grain boundaries and, in addition, a precipitation free zone (PFZ) is observed. In this case the crack initiation site depends on the slip distribution. For example, Sanders and Starke (73) investigated two binary Al-Li alloys with different volume contents of the δ' phase. For the alloy with a higher content planar slip takes place and cracks are initiated at the slip lines. For the other alloy wavy slip did occur and at higher strain amplitudes the crack initiated at grain boundaries where the slip bands impinge. The latter was observed also for an underaged Cu-Co alloy (59) where the effect was more pronounced for coarse-grained samples. Crack initiation at grain boundaries may be even more important for peakaged or slightly overaged samples where the PFZ is more developed (74,75).

Influence of the Grain Size on Residual Stresses. Residual stresses are very important for crack nucleation phenomena. In this paragraph only such stresses will be discussed which develop during fatigue. Since in a polycrystal the surface grains are less restrained than those in the interior they should have a lower flow stress. X-ray measurements of the line broadening from a surface layer of an Al 2024-T3 alloy revealed a steadyly increasing dislocation density with increasing cycling (76). This density value decreased if a thicker layer was investigated indicating the different behavior of the surface compared to the interior. Residual stress measurements in the surface layer of fatigued alloys by X-ray line shifts indicated that in tension-tension tests (R=0) compressive residual stresses can be built up even if the maximum stress is less than the yield point (77). These stresses increase with increasing grain size.

An interesting method has been reported by Morris et al (78). These authors used ultra-thin mica flakes on the surface as reference gauges to measure local plastic strains. After unloading from the compression half-cycle they measured dimensional changes occuring during the following tensile half-cycle. For Al 2219-T851 specimens fatigued in fully reversed bending with a stress amplitude of $0.85 \cdot \sigma_y$ they found a residual tensile strain only in large grains exceeding about two times the average grain size. The situation in the surface layer is described by plastically deformed large grains embedded in a fine-grained matrix which is strained only elastically. The same research group developed a "dual domain model" (79) which enabled the authors to calculate the flow stresses within the plastically deformed large grains. The result is an *increasing softening with increasing grain size*. From their model the authors concluded that for grains larger than fourfold the average size the local yield strength after fatiguing is drasti-

cally reduced to about a third of the bulk yield stress. Therefore, the fatigue lifetime is mainly determined by the cracks which initiate earlier in the large grains.

If this is true the effect of coaxing would need a new explanation. Instead of localized hardening during cyclic preloading at low amplitudes the total input of hysteric energy deposited in the grain might be the parameter controlling crack initiation (79).

Commercial Aluminium Alloys

In this chapter the fatigue crack initiation in commercial age-hardenable aluminium alloys will be summarized. For more details the reader is referred to the paper by Starke and Lütjering (80). These alloys usually contain three different types of second phase particles: (i) The hardening particles with sizes of several nm, (ii) the dispersoids with a size of typically 100 nm as grain refiners and (iii) large inclusions of intermetallic phases from impurities like Fe or Si with sizes up to several μm. While the dispersoids tend to have a beneficial effect in homogenizing slip processes, the inclusions serve as additional nucleation sites. The results of various authors on Al-Cu-based alloys are compiled in Fig.13. S-N resp. S-N_i curves are given and the preferred nucleation sites for cracks are shown as a function of the applied stress amplitude (R = -1) and the cycle numbers.

With the exception of Al 2219 which has been investigated in the overaged state (81) all other alloys showed crack initiation at PSBs for high stress amplitudes which changed to initiation at the interface between matrix and inclusion in lowering this amplitude (82-84). This seems to be typical for most of the alloys and has been reported also by many other authors. For Al 2219 the cracks initiated at grain boundaries while at higher stress amplitudes at first fracture of inclusions is observed followed by slip band cracking and finally grain boundary cracking with increasing cycle numbers.

In order to study the influence of slip distribution and grain size on crack initiation behavior the alloy AlMgSi1 (close to Al 6170) has been investigated in two different heats where the dispersion of the dispersoids was altered resulting in a fine-grained and a coarse-grained version of the alloy. In addition, the grain size at the surface was altered by different surface treatments (85.86). The results are summarized in Fig. 14. For a fine distribution of dispersoids the microstructure consists of unrecrystallized small subgrains. At low stress amplitudes the cracks initiate in the transverse interface inclusion-matrix like stage II cracks whereas at large amplitudes the inclusions start to fracture. This behavior does not change even if the surface layer is changed to a recrystallized larger grain size by special treatments.

For a coarse dispersoid distribution the resulting grains are large and pancake-shaped. At low stress amplitudes slip bands initiate again mainly at the transverse interface where they finally develop into slip band cracks. This is shown in Fig. 15a where two cracks have been initiated at such interfaces of two inclusions. The very interesting fact is that cracks initiate always in this interface independently of the type of slip behavior. With increasing stress amplitude other initiation sites can be observed, too, as grain boundaries or fractured inclusions. Fig. 15b shows a micrograph of the surface from a specimen which was overloaded during cycling. Besides a fractured inclusion a decohesion is observed at the transverse interface of another inclusion. If for this microstructure a fine-grained surface layer is produced the crack initiation is delayed compared to the other structures (86).

Further Developments. The possible improvements to delay crack initiation consist of measures to homogenize the slip distribution in the material. For aluminium alloys these measures have been listed already by Starke and Lütjering in their excellent report (80). They are (i) the reduction of inclusion content, (ii) the presence of dispersoids or unshearable precipitates (overageing) and (iii) the improvement of the grain boundary areas by thermomechanical treatment. The improving effect of these measures is limited, however, for conventionally produced alloys. Other processing techniques as the rapid solidification powder metallurgy seem to lead to better material. Recently, Grant and co-workers (87) have reviewed the properties of such alloys. For a 7075 type material they reported a considerable increase of the fatigue limit from 160 to 260 MPa (88). Further research is necessary in order to understand the reasons for this considerable improvement.

CONCLUSIONS

In spite of the fact that the principal micromechanisms of cyclic deformation and the reasons for crack initiation are known quite well, there is still lack in the fundamental understanding why these mechanisms operate. Future research in this field will be directed to this deeper understanding but more efforts will be undertaken to research on new types of alloys and materials.

ACKNOWLEDGEMENTS

The authors are indepted to W.L Morris and his co-workers for sending their manuscript prior to publication. They also thank P. Neumann and A.T. Winter for leaving their micrographs for reproduction.

REFERENCES

(1) Laird, C., Charsley, P., Mughrabi, H., Mater. Sci. Eng., Vol.81, 1986, pp. 433-450.
(2) Laird, C., Metallurgical Treatises, Ed. J.K.Tien and J.F.Elliott, Metallurg. Soc. AIME, 1981, 505-527.
(3) Mughrabi, H., 4th Risø Int. Symp. on Metallurgy and Materials Science. Risø Nat. Laboratory, Roskilde, Denmark, 1983, pp. 65-82.
(4) Mughrabi, H., Proc. 7th Int. Conf. on Strength of Metals and Alloys, Montreal, Canada 1985, Pergamon Press, Vol. 3, 1985, pp. 1917-1942.
(5) Mughrabi, H., Conf. Proc. on Dislocations and Properties of Real Materials, Book No. 323, The Institute of Metals, London, 1985, pp. 244-262.
(6) Gerold, V., 4th Int. Conf. on Age-Hardenable Aluminium Alloys, Materials Science Forum, Trans Tech Publ., Aedermannsdorf, Switzerland, 1987, in press.
(7) Winter, A.T., Phil. Mag., Vol.30, 1974, pp. 719-738.
(8) Mughrabi, H., Mater. Sci. Eng., Vol.33, 1978, pp. 207-223.
(9) Kuhlmann-Wilsdorf, D., and Laird, C., Mater. Sci. Eng., Vol.27, 1977, pp. 137-156.
(10) Mughrabi, H., Proc. 5th Int. Conf. on the Strength of Metals and Alloys, Aachen 1979, Pergamon Press, Vol.3, 1979, pp. 1615-1638.
(11) Kuhlmann-Wilsdorf, D., Mater. Sci. Eng., Vol. 39, 1979, pp. 127-139.
(12) Kuhlmann-Wilsdorf, D., and Laird, C., Mater. Sci. Eng., Vol.46, 1980, pp. 209-219.
(13) Mughrabi, H., Ackermann, F., and Herz, K., Proc. of ASTM-NBS-NSF Symposium on Fatigue Mechanisms, ASTM-STP 675, 1979, pp. 69-105.
(14) Wilhelm, M., Everwin, P., Proc. 5th Int. Conf. on the Strength of Metals and Alloys, Aachen 1979, Pergamon Press, Vol.2, 1979, pp. 1089-1094.
(15) Mecke, K., and Blochwitz, C., Crystal Res. & Technol., Vol.17, 1982, pp. 743-758.
(16) Essmann, U., Gösele, U., Mughrabi, H., Phil. Mag., Vol.A44, 1981, pp. 405-426.
(17) Abel, A., Mater. Sci. Eng., Vol. 36, 1978, pp. 117-124.
(18) Wang, R., Mughrabi, H., Mater. Sci. Eng., Vol. 63, 1984, pp. 147-163.
(19) Neumann, P., Z. Metallkunde, Vol. 59, 1968, pp. 927-934.
(20) Yan, B., Hunsche, A., Neumann, P., Laird, C., Mater. Sci. Eng., Vol. 79, 1986, pp. 9-14.
(21) Yan, B.-D., Laird, C., Acta metall., Vol.33, 1985, pp. 2023-2031.
(21a) Buchinger, L., Yan, B.-D., and Laird, C., Mater. Sci. Eng., Vol. 70, 1985, pp.161.168.
(22) Bhat, S.P., Laird, C., Scripta metall., Vol.12., 1978, pp. 687-692.

(23) Rasmussen, K.V., Pedersen, O.B., Acta metall., Vol. 28, 1980, pp. 1467-1478.
(24) Figueroa, J.C., Bhat, S.P., Veaux, de la, R., Murzenski, S., Laird, C., Acta metall., Vol. 29, 1981, pp. 1667-1678.
(25) Cheng, A.S., Figueroa, J.C., Laird, C., Lee, J.K., 2nd Risø Int. Symp. on Metallurgy and Materials Science, Risø Nat. Laboratory, Roskilde, Denmark, 1981, pp. 405-415.
(26) Kettunen, P., Lepistö, T., Kuokkala, V.-T., Scand. J. Metallurgy, Vol. 14, 1984, pp. 121-126.
(27) Kuokkala, V.-T., Kettunen, P., Acta metall., Vol. 33, No.11, 1985, pp. 2041-2047.
(28) Mughrabi, H., Wang, R., 2nd Risø Int. Symp. on Metallurgy and Materials Science. Risø Nat. Laboratory, Roskilde, Denmark, 1981, pp. 87-98.
(29) Buchinger, L., Laird. C., Mater. Sci. Eng., Vol. 76, 1985, pp. 71-76.
(30) Charsley, P., Mater. Sci. Eng., Vol. 47, 1981, pp. 181-185.
(31) Ackermann, F., Kubin, L.P., Lepinoux, J., Mughrabi, H., Acta metall., Vol. 32, No. 5, 1984, pp. 715-725.
(32) Jin, N.Y., Winter, A.T., Acta metall., Vol. 32, No.8, 1984, pp. 1173-1176.
(33) Jin, N.Y., Winter, A.T., Acta metall., Vol. 32, No.7, 1984, pp. 989-995.
(34) Dickson, J.I., Handfield, L., L'Espérance, G., Mater. Sci. Eng., Vol. 81, 1986, pp. 477-492.
(35) Charsley, P., and Kuhlmann-Wilsdorf, D., Phil. Mag. A, Vol. 44, No.6, 1981, pp. 1351-1361.
(36) Desvaux, M.P.E., Z. Metallkunde, Vol. 61, 1970, pp. 206-213.
(37) Abel, A., Wilhelm, M., and Gerold, V., Mater. Sci. Eng., Vol. 37, 1979, pp. 187-200.
(38) Abel, A., Wilhelm, M. and Gerold, V., Z. Metallkunde, Vol.70, H.9, 1979. pp. 577-581.
(39) Buchinger, L., Cheng, A.S., Laird, C., Stanzl, S., and Yan, B.D., unpublished research on the cyclic deformation of a Cu-Al alloy, University of Pennsylvania, U.S.A., pp. 1981-1985.
(40) Gerold, V., and Steiner, D., Scripta metall., Vol.16, 1982, pp. 405-408.
(41) Gerold, V., Lerch, B., Steiner, D., Z. Metallkde., Vol.75, 1984, pp. 546-553.
(42) Lee, J.-K., and Laird, C., Mater. Sci. Eng., Vol. 54, 1982. pp. 39-51 and 53-64.
(43) Wilhelm, M., Mater. Sci. Eng., Vol.48, 1981, 91-106.
(44) Sinning, H.-R., and Haasen, P., Scripta metall., Vol. 15, 1981, pp.85-90.
(45) Horibe, S., Laird, C., Acta metall., Vol. 31, 1983, pp. 1567-1579.
(46) Vogel, W., Wilhelm, M., Gerold, V., Acta metall., Vol.30, 1982, pp. 21-30.

(47) Köhler, E., Steiner, D., Gerold, V., 4th Risø Int. Symp. on Metallurgy and Materials Science. Risø Nat. Laboratory, Roskilde, Denmark, 1983, pp. 345-350.
(48) Vogel, W., Wilhelm, M., Gerold, V., Proc. 5th Int. Conf. on the Strength of Metals and Alloys, Aachen 1979. Pergamon Press, Vol.2, 1979, pp. 1175-1180.
(49) Lee, J.-K., Laird, C., Phil. Mag., Vol.A47, 1983, pp. 579-597.
(50) Köhler, E., Bischoff, A. and Gerold, V., Scripta metall., Vol.18, 1984, pp. 699-702.
(51) Steiner, D., Beddoe, R., Gerold, V., Kostorz, G., Schmelczer, R., Scripta metall., Vol.17, 1983, pp. 733-736.
(52) Maier, D., Gerold, V., Z. Metallkde., Vol. 70, 1979, pp. 775-781.
(53) Clavel, M., Pineau, A., Mater. Sci. Eng., Vol. 55, 1982, pp. 157-171.
(54) Lerch, B., Doctoral Thesis, University Stuttgart, 1983.
(55) Frick, K., Diplomarbeit, University Stuttgart, 1985.
(56) Cheng, A.S., Figueroa, J.C., Laird, C., Lee, J.-K., 2nd Risø Int. Symp. on Metallurgy and Materials Science. Risø Nat. Laboratory, Roskilde, Denmark, 1981, pp. 405-415.
(57) Horibe, S., Lee, J.-K., Laird, C., Fatigue Engng. Mater. Struct., Vol.7, 1984, pp. 145-154.
(58) Steiner, D., Müller, W., Gerold, V., Scripta metall., Vol.18, 1984, pp. 693-698.
(59) Choe, J.S., Gudladt, H.-J., Gerold, V., Z. Metallkde., Vol.77, 1986, pp. 739-745.
(60) Mughrabi, H., Wang, R., Differt K. and Essmann, U., ASTM STP 811, 1983, pp. 5-45.
(61) Differt, K., Essmann, U., and Mughrabi, H., Phil. Mag. A, Vol. 54, 1986, pp. 237-258.
(62) Hunsche, A. and Neumann, P., Int. ASTM Symp. on Fundamental Questions and Critical Experiments on Fatigue, Dallas-Fort Worth, Texas USA, 1984.
(63) Hunsche A., and Neumann, P., Acta metall., Vol.34, 1986, pp. 207-217.
(64) Laird, C., Mater. Sci. Eng., Vol. 22, 1976, pp. 231-236.
(65) Mughrabi, H., Proc. 2nd Int. Symp. on Defects, Fracture and Fatigue. Martinus Nijhoff Publ., The Hague, Boston and London, 1983, pp. 139-146.
(66) Müllner, H., Weiss, B., Stickler, R., Lukas, P., and Kunz, L., Proc. 2nd Conf. on Fatigue and Fatigue Threshold, Birmingham, 1984, pp.423-434.
(67) Basinski, Z.S., Korbel, A.S., and Basinski, S.J., Acta metall., Vol.28, 1980, pp.191-207.
(68) Hornbogen, E., Verpoort, C., Superalloys, 1980, pp. 585-593.
(69) Hornbogen, E., Verpoort, C., 5th Int. Conf. on Fracture, ICF5, Cannes, France, 1981, pp.315-322.
(70) Anton, D.L., Fine, M.E., Mater. Sci. Eng., Vol. 58, 1983, pp. 1187-1198.

(71) Steiner, D., Gerold, V., Proc. 2nd Int. Symp. on Defects, Fracture and Fatigue. Martinus Nijhoff Publ., The Haag, Boston, London 1983, pp. 53-62.
(72) Sinning, H.-R., Acta metall., Vol.30, 1982, pp. 1019-1026
(73) Sanders, J.T.H., and Starke, E.A., Acta Metall., Vol. 33, 1982, pp. 927-939.
(74) Lee, J.K., Bhat, S.P., Veaux de la, R. and C. Laird, Int Journ. of Fracture, Vol. 17, No. 2, 1981, pp. 121-141.
(75) Lütjering, G., Hamajima, T. and Gysler, A., Fracture 1977, ICF4, Waterloo, Canada, Vol. 2, 1977, pp. 7-16.
(76) Pangborn, R.N., Weissmann, S., and Kramer I.R., Metall. Trans.A, Vol. 12A, 1981, pp. 109-121.
(77) James , M., and Morris, W.L., Scripta metall., Vol 17 1983, pp. 1101-1104.
(78) Morris, W.L., Inman, R.V., James, M.R., J. Mater. Sci., Vol. 17, 1982, pp.1413-1419.
(79) Morris, W.L., Cox, B.N., James, M.R., Acta metall., 1986, in press.
(80) Starke, E.A., and Lütjering, G., Fatigue and Microstructure, Proc. of 1978 ASM Materials Science Seminar, Amer. Soc. for Metals, 1979, pp. 205-243.
(81) James , M.R., Morris, W.L., "The Role of Microplastic Deformation in Fatigue Crack Initiation", Fatigue Mechanisms: Advances in Quantitative Measurement of Physical Damage. Eds. J. Lankford, D.L. Davidson, W.L. Morris, and R.P. Wei, ASTM STP 811, 1983, pp. 46-70.
(82) Kung, C. Y., and Fine, M. E., Met. Trans.A, Vol. 10A, 1979. pp. 603-616.
(83) Grosskreuz, J.C., Shaw, G.G., "Critical mechanisms in the development of fatigue cracks in 2024-T4 aluminum", Proc. 2nd Int. Conf. on Fracture, Brighton, U.K., 1969, pp. 620-629.
(84) Sigler, D., Montpetit, M.C., Haworth, W.L., Metall. Trans.A, Vol. 14A, 1983, pp. 931-938.
(85) Ruch, W., and Gerold, V., Proc. 4th Europ. Conf. on Fracture, Leoben/Austria, 1982, Vol.II, pp.383-390.
(86) Meier, B., Gerold, V., "The Influence of Microstructure and Residual Stresses on the Initiation and Propagation of Short Surface Cracks on AlMgSi1", this Conference.

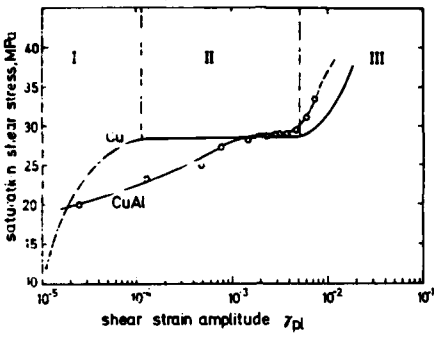

Fig. 1. Cyclic stress-strain curves from Cu and Cu-6 at.% Al single crystals. After Mughrabi (8) and Buchinger et al (39).

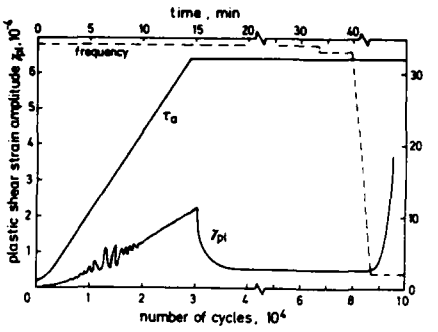

Fig. 2. Shear stress and plastic shear strain response of a copper single crystal. Ramp loading at 34 Hz to a constant stress level. Final reduction of the frequency leads to marked softening (formation of PsBs). After Yan et al (20).

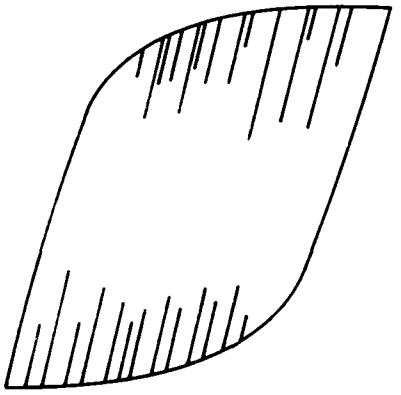

Fig. 3. Hysteresis loop from an copper single crystal showing deformation instabilities during cycling in the plateau range. After Yan and Laird (21).

Fig. 4. Labyrinth structure of an [001] oriented copper single crystal showing (100) and (001) walls and a PSB. Courtesy of Yin and Winter (32).

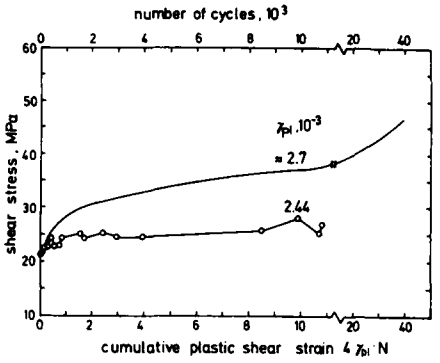

Fig. 5. Stress response of Cu-16 at.% Al single crystals fatigued at constant γ_{pl}. Upper scale shows the cycle numbers. Upper curve: after Abel et al (37). Upper scale shows the cycle numbers. Lower curve: after Buchinger et al (39).

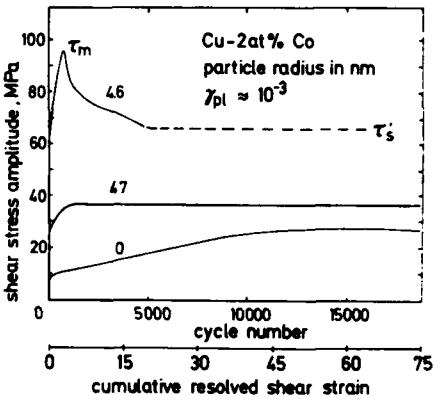

Fig. 6. Stress response of Cu-Co single crystals with different particle sizes. After Gerold and Steiner (40).

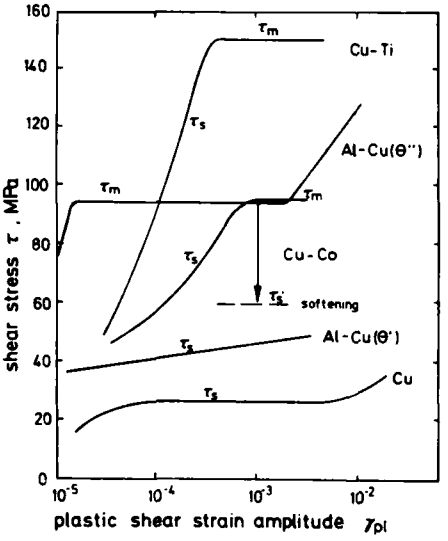

Fig. 7. Cyclic stress-strain curves for various age-hardened single crystals:
Underaged states:
Cu-4 at.% Ti after Sinning (44)
Cu-2 at.% Co after Wilhelm (43)
Al-1.8 at.% Cu (θ")
after Lee and Laird (42)
Overaged state:
Al- 1.6 at.% Cu (θ')
after Horibe and Laird (45)
τ_s = saturation stress
τ_m = peak stress
τ_s' = saturation stress after softening

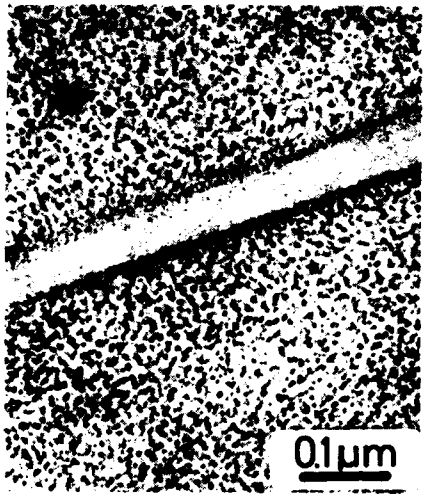

Fig. 8. TEM micrograph of a PSB in an Al-Ag alloy containing spherical G.P.Zones. Dislocations are out of contrast. From Köhler et al (47).

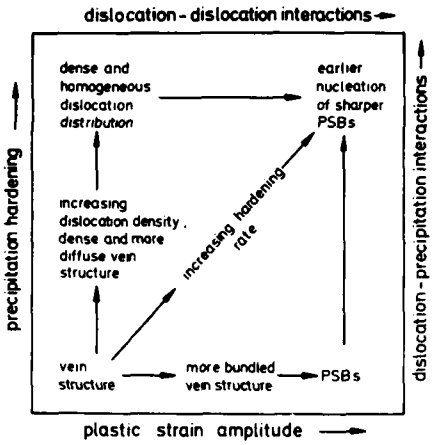

Fig. 9. Influence of the amount of precipitation hardening and plastic strain amplitude on the dislocation structure. After (53, 41).

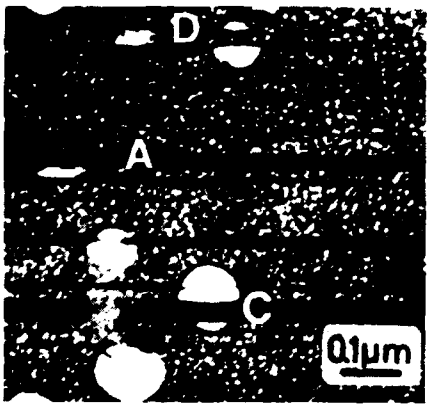

Fig. 10. Dark field TEM micrograph of an fatigued Nimonic 80A alloy. Dark bands are no PSBs but tilted areas between two active slip planes with opposite cumulative shear (55).

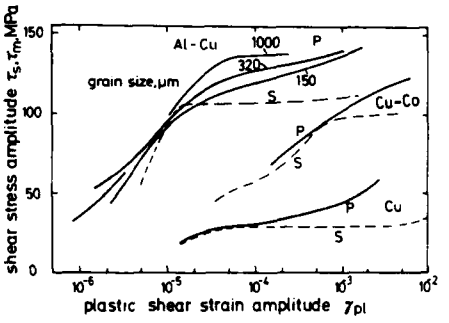

Fig. 11. Comparison of cyclic stress - strain curves from single and polycrystals of Al-Cu containing θ" (58) underaged Cu-Co (60) and pure Cu (26). For stress and strain correction the Sachs factor 2.24 has been used.

Fig. 12. SEM micrographs of longitudinal sections of fatigued Cu single crystals (undistorted view) and part of the surface (20 Hz, γ_{pl} = 0.2%). Courtesy of Hunsche and Neumann (62)
a) Stage I crack (arrow) at the notch root of an intrusion after 30 000 cycles.
b) Stage II crack after 60 000 cycles.

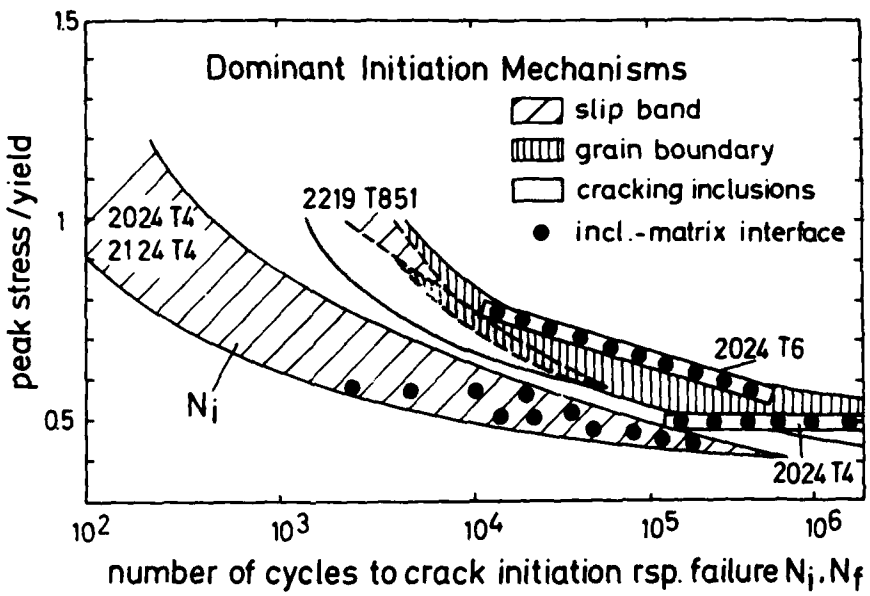

Fig. 13. Dominant crack initiation mechanisms in Al-Cu-based alloys (R = -1).
2024/2124 after Kung and Fine (82),
2219 after James and Morris (81),
2024 T6 after Sigler et al (83),
2024 T4 after Grosskreuz and Shaw (83).

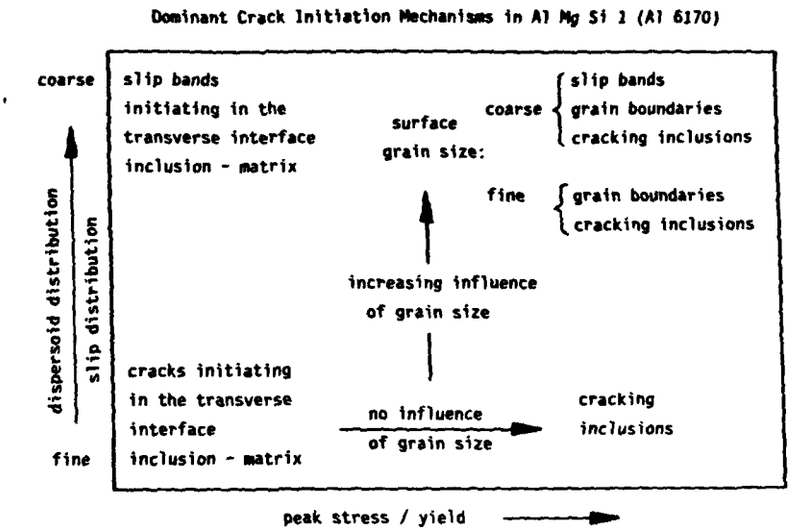

Fig. 14. Dominant crack initiation mechanisms in AlMgSi1 (Al 6170) samples heat treated for different dispersoid distributions and surface grain sizes fatigued with constant stress amplitude.

(a) (b)

Fig. 15. SEM micrograph from the surface of fatigued AlMgSi1 samples (coarse dispersoid distribution).
a) Cracks initiated in the transverse interfaces of two inclusions.
b) Overloaded specimen showing a cracked inclusion and another one with decohesion of the transverse interface.

ENVIRONMENTALLY ASSISTED FATIGUE CRACK GROWTH

R. P. Wei*

A framework is presented for understanding the role of environmental variables and of microstructure through modeling of environmentally assisted fatigue crack growth. The principal features of fatigue crack growth response and the current state understanding are illustrated by data on structurally important alloys. The interactions between environment and microstructure are illustrated by recent results on a high-strength steel and an aluminum alloy. The need for environmental control in studies of fatigue mechanisms is emphasized.

INTRODUCTION

Metal fatigue is well recognized as an important cause for failure or early retirement of engineering structures. The performance of structures can be further degraded by the interactions of fatigue loading with the external (service) environment, or with an environment (e.g., hydrogen) that is internal to the material. The influence of environment on fatigue (that is, corrosion fatigue) was recognized some 70 years ago by Haigh (1) and later by Gough and Sopwith (2). Much of the work that followed focused on the reduction of fatigue lives by both gaseous and aqueous environments without distinguishing between the crack initiation and crack growth phases of fatigue (McEvily and Wei (3)).

Beginning in the 1960's, more systematic investigations of environmentally assisted (corrosion) fatigue crack growth were initiated; for example, the work of

* Professor of Mechanics, Department of Mechanical Engineering and Mechanics, Lehigh University, Bethlehem, PA 18015, USA.

Hartman (4), Bradshaw and Wheeler (5), and Wei et al (6). Work during this period was reviewed by McEvily and Wei (3) and by Wei (7), and is also summarized in (8). A considerable amount of work followed over the past 20 years to characterize corrosion fatigue crack growth response in terms of the pertinent environmental, geometrical and loading variables. These efforts have provided not only basic understanding, but also a framework for further understanding and for design.

In this paper, modeling of corrosion fatigue crack growth is briefly reviewed, and is discussed in terms of a framework for understanding the role of environmental variables and of microstructure. The principal features of fatigue crack growth response and the current state understanding are illustrated by data on structurally important alloys. The interactions between environment and microstructure are illustrated by recent results on a high-strength steel and an aluminum alloy. The need for environmental control in studies of fatigue mechanisms is emphasized.

MODELING OF ENVIRONMENTALLY ASSISTED CRACK GROWTH

Environmentally assisted (corrosion) fatigue crack growth involves complex interactions between the material, its internal and external environment, and the applied load. Depending on the nature of these interactions, the crack growth response can be very different. Understanding and utilization of data, therefore, require mechanistic understanding of the processes that control crack growth. Such understanding has begun to be developed through identification of the underlying chemical processes and modeling of fatigue crack growth response in terms of the rate controlling process in both gaseous and aqueous environments. The modeling effort serves as a basis for further fundamental understanding, and provides a formalized framework for the interpretation and utilization of crack growth data. Although the considerations are limited to the case of fatigue crack growth, these same considerations are also relevant for crack initiation.

Mechanical (Microstructural) Modeling

A superposition model was proposed by Wei and Landes (9), and Wei (10) to decouple the mechanical and environmental components of crack growth rate. This model has been modified by Wei and Gao (11) to recognize the fact that mechanical (or "pure") fatigue and cycle-dependent corrosion fatigue proceed by different micromechanisms and occur concurrently or in parallel (6)(9).

Modeling was based on the proposition that the rate of crack growth in a deleterious environment, $(da/dN)_e$, is composed of the sum of three components according to Eqn. (1).

$$(da/dN)_e = (da/dN)_r (1 - \phi) + (da/dN)_c \phi + (da/dN)_{scc} \quad (1)$$

In this equation, $(da/dN)_r$ is the rate of fatigue crack growth in an inert (reference) environment, and is interpreted as the mechanical fatigue (or "pure" fatigue) crack growth rate; $(da/dN)_{scc}$ is the contribution by sustained-load crack growth; $(da/dN)_c$ represents the cycle-dependent contribution which requires synergistic interaction of fatigue and environmental attack, and is identified as the "pure" corrosion fatigue crack growth rate; and ϕ is the fractional area of crack that is undergoing pure corrosion fatigue. It should be noted that the rates themselves may be composed of contributions from several concurrent micromechanisms.

For simplicity, the sustained-load growth or stress corrosion cracking (SCC) term, which is considered as a sequential contribution, is not included in the subsequent discussions, and Eqn. (1) may be rewritten into the following form:

$$(da/dN)_{cf} = [(da/dN)_e - (da/dN)_r]$$

$$= [(da/dN)_c - (da/dN)_r]\phi \quad .....(2)$$

Equation 2 indicates that, in the limit, for $\phi = 0$ or for a test in an inert environment, $(da/dN)_e$ is equal to $(da/dN)_r$, which corresponds to pure fatigue. For $\phi = 1$, $(da/dN)_e$ is equal to the maximum or "saturation" growth rate, $(da/dN)_{e,s}$, and is equal to $(da/dN)_c$, the pure corrosion fatigue growth rate.

In essence, the parameter ϕ represents the material's response to changes in environmental conditions. It is directly related to its counterpart (the fractional surface coverage, θ) in chemical modeling; namely, $\phi = \theta$ (11). The maximum in corrosion fatigue crack growth rate, therefore, corresponds to saturation or the maximum extent of chemical reaction ($\theta = 1$) (11)(12)(13). A more detailed discussion follows.

Chemical Modeling

Important understanding of corrosion fatigue crack growth response in gaseous environments has been developed through chemical modeling (12,13) and through experimental verification of the role of gas transport and

surface reactions on $(da/dN)_{cf}$ by Wei et al (14), Shih and Wei (15), and Brazill et al (16). Similar understanding is being developed for the aqueous environments and is illustrated by the work of Wei and Shim (17), Wei and Shim (18), Wei (19), Alavi et al (20), and Thomas et al (21).

The modeling effort considers the processes that can be involved (in part or in total) in the enhancement of fatigue crack growth. These processes include (10)(22): (i) transport of the deleterious environment to the crack tip; (ii) reactions of the environment with newly produced crack surfaces to evolve hydrogen or to effect localized dissolution; (iii) hydrogen entry; (iv) diffusion of hydrogen to the fracture (or embrittlement) site; (v) partitioning of hydrogen among the various microstructural sites; and (vi) hydrogen-metal interactions leading to embrittlement. These processes operate consecutively or in sequence. The overall crack growth response is governed by one or more of these processes in conjunction with the mechanical driving force for crack growth (or ΔK).

The actual processes would depend on the mechanism of crack growth enhancement; namely, active path dissolution or hydrogen embrittlement. For a dissolution mechanism (see (8)), only the first two steps in the sequence need to be considered, where the anodic (dissolution) reactions in the second step are directly responsible for crack growth enhancement. On the other hand, if hydrogen embrittlement is the responsible mechanism, then the reaction step serves only as the source for hydrogen. All of the remaining processes (3 through 6) must be considered. It should be noted that these steps would be identical for aqueous and gaseous environments.

Assuming that environmental enhancement of fatigue crack growth results from embrittlement by hydrogen that is produced by the reactions of hydrogenous gases with the freshly produced crack surfaces, models for transport and surface reaction were proposed (12)(13). An analogous model for electrochemical reaction controlled crack growth has been proposed for steels in aqueous environments, where the kinetics of reaction are deemed to be slow (17)(19). In these models, the environmental contribution is assumed to be proportional to the extent of reaction per cycle, which is given by the fractional surface coverage θ, and the crack growth rate $(da/dN)_{cf}$ is given as follows:

$$(da/dN)_{cf} = [(da/dN)_c - (da/dN)_r]\theta \quad \text{.....(3)}$$

A model for diffusion controlled growth (23) and one involving strain induced hydride formation (24)(25)(26) have also been suggested. The latter model relates to metallurgical changes and the consequent effect on crack growth rates, and will be considered separately later. Diffusion controlled crack growth occurs when the preceding transport and surface reaction processes are more rapid, and needs to be considered outside of the context of limited surface coverage per cycle.

Transport controlled growth. For highly reactive gas-metal systems, crack growth is controlled by the rate of transport of the gases to the crack tip (12)(13). The surface coverage (θ) is linearly proportional to pressure (p_o) and inversely proportional to frequency (f). The environmental contribution to fatigue crack growth is given by the following relationships (24)(25):

$$(da/dN)_{cf} = [(da/dN)_c - (da/dN)_r]\cdot[(p_o/f)/(p_o/f)_s] \quad (4a)$$

$$\text{for } (p_o/f) < (p_o/f)_s$$

$$(da/dN)_{cf} = [(da/dN)_c - (da/dN)_r] = \text{constant} \quad .....(4b)$$

$$\text{for } (p_o/f) \geq (p_o/f)_s$$

The terms in the second set of square brackets in Eqn. (4a) correspond to the fractional surface coverage (θ), or extent of surface reaction, and are identified with the fractional area of crack that undergoes pure corrosion fatigue (ϕ). The term $[(da/dN)_c - (da/dN)_r]$ is the maximum enhancement in the rate of cycle-dependent corrosion fatigue crack growth, and is a consequence of the observation that the extent of reaction is limited, or $\theta \rightarrow 1$ (14)(16). The saturation exposure $(p_o/f)_s$ is a function of gas pressure, temperature, and molecular weight of the gas, and of K level, load ratio, yield strength and elastic constants; through their influences on crack geometry and gas transport (12)(13).

A growth rate dependence upon ΔK^2 is implicitly assumed to reflect the expected proportionality between the size of the "hydrogen damaged" zone and the crack-tip plastic zone size (13)(23)(26). The temperature dependence is reflected through its influence on the fatigue process, the mechanical properties and on gas transport (24)(25).

Surface and electrochemical reaction controlled growth. With less reactive systems, crack growth is controlled by the rate of surface reactions at the crack tip. For

simple first-order reactions, the crack growth rate in gaseous environments is given by Eqn. (5) in terms of pressure, frequency and the reaction rate constant k_c (12)(13).

$$(da/dN)_{cf} = [(da/dN)_c - (da/dN)_r]\cdot[1 - \exp(-k_c p_o/f)] \quad (5)$$

A more general interpretation of surface coverage can be made, however, to accommodate multi-step reactions. The actual form of the crack growth response would reflect the nature and kinetics of the individual reaction steps, and would be more complex.

For corrosion fatigue in an aqueous environment, the extent of surface reaction per cycle is identified with the fractional amount of electrical charge transferred by the reactions at the crack tip; that, is with q/q_s, where q is the amount of charge transferred per cycle; q_s is the "saturation" amount or that required to complete the reactions. The amount of charge transferred (q) is assumed to be directly proportional to the amount of hydrogen produced each cycle. As an analogue to Eqn. (5), $(da/dN)_{cf}$ may be expressed as follows (26):

$$(da/dN)_{cf} = [(da/dN)_c - (da/dN)_r]\cdot[q/q_s] \quad \ldots\ldots\ldots\ldots (6)$$

Temperature dependence is reflected in part through its influence on the fatigue process; that is, on the reference rate $(da/dN)_r$. More importantly, it is manifested through its influence on the reaction rates. If the reaction mechanisms remain unchanged, the maximum enhancement in rate (or $(da/dN)_c$) is expected to remain constant. The temperature dependence for corrosion fatigue would be reflected principally through its frequency dependence, with the maximum remaining constant.

Diffusion controlled growth. When the transport and surface reaction processes are sufficiently rapid, crack growth rate is then determined by the rate of diffusion of hydrogen from the crack tip to the "fracture process zone". According to Kim (23), $(da/dN)_{cf}$ would become proportional to the square-root of hydrogen diffusivity (D) and inversely proportional to the square root of frequency.

$$(da/dN)_{cf} = A_o \exp(-H_B/RT)\cdot(p_o D/f)^{1/2}\Delta K^2 \quad \ldots\ldots\ldots\ldots (7)$$

where A_o is an empirical constant, H_B is the binding enthalpy of hydrogen to dislocations, and R is the universal gas constant. The model includes an explicit dependence on ΔK^2.

CURRENT UNDERSTANDING

The current state of understanding of corrosion fatigue crack growth may be conveniently considered in two parts. The first part consists of the understanding of crack growth response in terms of the controlling chemical processes, and the second, the influence of microstructural variables.

Chemical Aspects

The transport and surface (and electrochemical) reaction controlled models have been examined by coordinated studies of the kinetics and mechanisms of gas-metal reactions, and of corrosion fatigue crack growth response as functions of pressure, temperature, and time (or frequency). Good agreement between these models and the experimental data on crack growth and surface and electrochemical reactions has been obtained (see Figs. 1 to 3, for example) (14)(16)(21)(27). The transport controlled case is represented by aluminum and titanium alloys in water vapor (Fig. 1), and steels in hydrogen sulfide (Fig. 2) at low pressures; the reaction controlled case, by high strength steels in aqueous electrolytes (see Fig. 3, for example (27)).

Good correlations have been obtained between the cycle-dependent component of corrosion fatigue crack growth rate and the amount of charge transferred in the electrochemical reactions with bare steel surfaces for the NiCrMoV steel in sodium sulfate solution (27) and for X-70 and HY130 steels in sodium chloride solution (21). The temperature and frequency dependence is consistent with the model predictions.

It is recognized that the form of the response would depend on the kinetics and on the specific nature and mechanism(s) of the reactions, and may reflect both transport and reaction control. For the case of reaction controlled crack growth, the response may reflect the fact that the reactions do not follow simple first-order kinetics, and the presence of more than one reaction step. For example, for the case of 7075-T651 aluminum alloy (Fig. 2), the additional enhancement at the higher pressures is surface reaction controlled and is attributed to a slow step in the reactions of water with segregated magnesium (28). Similarly, the increase in rate observed on the 2-1/4Cr-1Mo steel in hydrogen sulfide at the higher pressures is surface reaction controlled, and is identified with the slower second step in the reactions of H_2S with iron (16)(29). A similar situation exists for crack growth of high-

strength steels in water vapor and in aqueous solutions. The situation in water vapor may be further complicated by capillary condensation at the crack tip (17)(18)(30).

Evidence for diffusion-controlled crack growth is provided by the data on the titanium alloys (see Fig. 4, for example). At the higher frequencies, $(da/dN)_{cf}$ was found to be inversely proportional to the square root of frequency (Chiou and Wei (31)). This dependence, coupled with the known reactivity of titanium, is consistent with diffusion control. The abrupt decrease in growth rates at the lower frequencies is attributed to the operation of a hydride mechanism that depends on both strain and strain rate (24)(25)(26)(31). There is no quantitative model for hydride induced crack growth, however, at this time.

Microstructural Aspects

The importance of considering the role of different micromechanisms was discussed by Gerberich and Peterson (32). The role of micromechanism (or of microstructure) is explicitly incorporated in the modified superposition model by Wei and Gao (see Eqns. (1) and (2)) (11). The implications of the model are as follows: (i) the partitioning of hydrogen to the various microstructural sites would not be uniform (11)(33), and (ii) the fractional area of fracture surface (ϕ) produced by pure corrosion fatigue would be equal to the fractional surface coverage (θ) for chemical reactions. The relationship between the microstructural and environmental parameters (ϕ and θ) has been examined by Ressler (34) and by Gao et al (35).

Following the work of Pao et al (36), Ressler (34) studied the micromechanical aspects of corrosion fatigue crack growth in an AISI 4340 steel, tested in water vapor (585 Pa) at room temperature. The cycle-dependent component of corrosion fatigue crack growth rate is shown as a function of inverse frequency (or period) in Fig. 5. Fractographic data show a change in fracture surface morphology with decreasing frequency from a predominantly transgranular mode (relative to the prior-austenite grains) to one that is predominantly intergranular (see Figs. 6 and 7).

By identifying the intergranular failure mode with pure corrosion fatigue and the transgranular mode with mechanical fatigue, the fraction of pure corrosion fatigue (ϕ) is identified approximately with the fraction of intergranular failure and can be estimated from the microfractographs. A comparison was then made be-

tween ϕ and θ, which is obtained from independent surface reaction measurements, Fig. 8 (Simmons et al (37)). This comparison is shown in Fig. 9, and required an adjustment for exposure to account for capillary condensation in the fatigue crack growth experiments. The agreement is seen to be excellent.

A similar comparison has been made by Gao et al (35) for a 7075-T651 aluminum alloy. Typical morphology of fatigue fracture surfaces produced in water vapor is shown in Fig. 10. The pure corrosion fatigue micromechanism is typified by Fig. 10(b), and that for mechanical fatigue by Fig. 10(c). A comparison between ϕ and θ is given in Table 1, and shows reasonable agreement.

TABLE 1 - Comparison of Areal Fraction of "Corrosion" Fatigue Component with Fractional Surface Coverage for a 7075-T651 Aluminum Alloy.

Environmental Condition	ϕ	θ
Pure oxygen, 267 Pa	0	0
Water vapor, 1.3 Pa	0	0.28
Water vapor, 2.7 Pa	0.78	0.58
Water vapor, 4.7 Pa	0.94	1.0
Water vapor, 67 Pa	1.0	1.0
Water vapor, 670 Pa	1.0	1.0

These results indicate the important role of microstructure, and of the interactions between the environmental and microstructural variables. Much more work is needed to broaden the scope of this understanding, and to provide statistically reliable support. Nevertheless, the framework for understanding has been set in place.

DISCUSSION

Clearly, a more complete understanding and modeling of corrosion fatigue crack growth response is needed. This understanding would require detailed information on the kinetics and mechanisms of the relevant surface/electrochemical reactions. In addition, information on the various other processes (including diffusion and distribution of hydrogen, and the physio-chemical processes of embrittlement) is needed to complete the understanding and to allow for the "prediction" of actual crack growth rates, in a manner analogous to that described by Gao and Wei (33) for sustained-load crack growth. The appropriateness and efficacy of models depend on proper modeling in terms of the controlling processes and of the possible transfer of control with changes in environmental conditions.

Prediction of service lives, which involves extrapolations well beyond the range of available data, requires modeling (both statistical and probabilistic) to identify additional key variables and to provide quantitative assessments of risk. The key variables that affect corrosion fatigue crack growth include stress intensity range, load ratio, frequency, and temperature, plus a host of environmental and metallurgical variables (such as, solution composition, pH, electrode potential, gas composition and partial pressure, alloy composition, and microstructure). For improved predictions, other factors must be considered as well. These factors include corrosion product blockage, which can alter the crack-tip environment; corrosion product wedging, which affects the effective crack driving force; and short crack effects, that reflect altered driving force and local chemistry.

So far, the environmental conditions at the crack tip are presumed to be known and well characterized. In fact, the chemical and electrochemical conditions near the crack tip can be different from those of the external (bulk) environment, and depend on the kinetics of the transport processes and of the reactions with the crack surfaces. Suitable models, therefore, must address (i) the formation of the crack-tip electrochemical environment, and (ii) the kinetics of reactions with the crack-tip environment, as discussed by Wei et al (22), and by Turnbull (38). Additional work in this area is needed.

It is to be recognized that temperature and frequency are two of the most significant variables. They should be utilized for broadening the scope of under-

standing, and as screening variables to critically assess proposed models and mechanisms. Despite the well established importance of environmental influences and the efforts at understanding corrosion fatigue, the fatigue community, by and large, has chosen to ignore this problem both in its design of experiments and in the interpretation of results. As a minimum, a well-controlled inert reference environment (not laboratory air, for it can be deleterious) should be used, so that the resulting data can be meaningfully interpreted in terms of the purely mechanically or metallurgically based models.

SUMMARY

Based on available experimental results and models, a formalized basis for understanding corrosion fatigue crack growth has been established. Corrosion fatigue crack growth is believed to result from embrittlement by hydrogen that is produced by the reactions of the environment (both gaseous and aqueous) with newly created surfaces at the crack tip. These reactions are localized to the crack tip region. The crack growth rate is proportional to the extent of reaction per cycle, with the actual growth rates determined by the interactions of the microstructure with the environment (namely, with hydrogen).

Corrosion fatigue crack growth response is governed by the response of the controlling chemical and electrochemical processes, and can be different for the various material-environment systems and for a given system when the conditions are changed. These changes in response must be properly taken into account in design, and for understanding fatigue mechanisms. As a minimum, an inert reference environment should be used to mitigate the influences of deleterious external environments in "mechanistically" oriented research.

ACKNOWLEDGEMENT

This work is supported in part by the Office of Basic Energy Sciences, Department of Energy, under Grant DE-FG02-84ER45138.

REFERENCES

(1) Haigh, B. P., J. Inst. Metals, Vol.18, 1917, p.55.

(2) Gough, H. J. and Sopwith, D. G., J. Inst. Metals, Vol. 49, 1932, p. 93.

(3) McEvily, A.J. and Wei, R.P., in "Corrosion Fatigue: Chemistry, Mechanics and Microstructure", NACE-2, eds. Devereux, O. F., McEvily, A. J. and Staehle, R. W., Nat. Assoc. Corro. Engrs., 1972, pp.381-394.

(4) Hartman, A., Intl.J.Fract.Mech., Vol.4, 1965,p.167.

(5) Bradshaw, F. J. and Wheeler, C., Appl. Mat. Res., Vol. 5, 1966, p. 112.

(6) Wei, R. P., Talda, P. M. and Li, C. Y., ASTM STP 415, Am. Soc. Testing & Matls., Philadelphia, PA, 1967, p. 460.

(7) Wei, R .P., Engr. Fract. Mech., Vol. 1, 1970, pp. 633-651.

(8) Corrosion Fatigue: Chemistry, Mechanics and Microstructure, NACE-2, eds. Devereux, O. F., McEvily, A. J. and Staehle, R. W., Nat. Assoc. Corro. Engrs., 1972.

(9) Wei, R. P. and Landes, J. D., Mater. Res. Stand., Vol. 9, No. 7, 1969, pp. 25-28.

(10) Wei, R. P. in "Fatigue Mechanisms", ASTM STP 675, ed. Fong, J. T., Am. Soc. Testing Matls., Philadelphia, PA, 1979, pp. 816-840.

(11) Wei, R. P. and Gao, M., Scripta Met., Vol.17, 1983, pp. 959-962.

(12) Weir, T. W., Simmons, G. W., Hart, R. G. and Wei, R. P., Scripta Met., Vol. 14, 1980, pp. 357-364.

(13) Wei, R.P. and Simmons, G.W., in "FATIGUE: Environment and Temperature Effects". Edited by Burke, J. J. and Weiss,V., Sagamore Army Materials Research Conference Proceedings, Vol. 27, 1983, pp. 59-70.

(14) Wei, R. P., Pao, P. S., Hart, R. G., Weir, T. W. and Simmons, G. W., Met. Trans. A, Vol. 11A, 1980, pp. 151-158.

(15) Shih, T. H. and Wei, R. P., Engr. Frac. Mech., Vol. 18, No. 4, 1983, pp. 827-837.

(16) Brazill R. L., Simmons, G. W. and Wei, R. P., J. Engr. Matls. & Tech., Trans. ASME, Vol. 101, July 1979, pp. 199-204.

(17) Wei, R. P. and Shim, G., in "Corrosion Fatigue", ASTM STP 801, eds. Crooker, T. W. and Leis, B. N., Am. Soc. Testing & Mater., Philadelphia, PA, 1983, pp. 5-25.

(18) Shim, Gunchoo, and Wei, R. P., "Corrosion Fatigue and Electrochemical Reactions in Modified HY130 Steel," Mats. Sci. & Engr., Vol. 86, 1986, pp. 121-135.

(19) Wei, R. P., "Corrosion Fatigue Crack Growth", Proceedings of International Symposium on Microstructure and Mechanical Behaviour of Materials, 21-24 Oct., 1985, Xi'an, People's Republic of China, E.M.A.S., Warley, England (to be published).

(20) Alavi, A., Miller, C. D. and Wei, R. P., "A technique for measuring the kinetics of electrochemical reactions with bare metal surfaces", Corrosion, 1987 (in press).

(21) Thomas, J. P., Alavi, A. and Wei, R. P., Scripta Met., Vol. 20, 1986, pp. 1015-1018.

(22) Wei, R. P., Shim, G. and Tanaka, K., in "Embrittlement by the Localized Crack Environment", ed. Gangloff, R. P., The Metall. Soc. of AIME, Warrendale, PA, 1984, pp. 243-263.

(23) Kim, Y. H., Speaker, S. M., Gordon, D. E., Manning, S. D., and Wei, R. P., Naval Air Development Center (604), Warminster, PA, Report No. NADC-83126-60, Vol. I, March, 1983.

(24) Pao, P. S. and Wei, R. P., in Titanium: Science and Technology, eds. Lutjering, G., Zwicker, U. and Bunk, W., FRG: Deutsche Gesellschaft Fur Metallkunde e.V., 1985, p. 2503.

(25) Birnbaum, H. K., "On the mechanisms of hydrogen related fracture in metals", Proc. of ONR Workshop on Environment-Sensitive Fracture of Metals and Alloys, Washington, DC, June 3, 1985 (to be published).

(26) Peterson, K. P., Schwanebeck, J. C., and Gerberich, W. W., Met. Trans. A, Vol. 9A, 1978, p. 1169.

(27) Nakai, Y., Alavi, A., and Wei, R. P., "Effects of Frequency and Temperature on Short Fatigue Crack Growth in Aqueous Environments", Submitted for publication in Met. Trans. A.

(28) Wei, R. P., Gao, M. and Pao, P. S., Scripta Met., Vol. 18, 1984, pp. 1195-1198.

(29) Lu, M., Pao, P. S., Weir, T. W., Simmons, G. W. and Wei, R. P., Met.Trans.A, Vol.12A, 1981, pp.805-811.

(30) Dwyer, D. J., Simmons, G. W. and Wei, R. P., Surf. Sci., Vol. 64, 1977, pp. 617-632.

(31) Chiou, S. and Wei, R. P., "Corrosion Fatigue Cracking Response of Beta Annealed Ti-6Al-4V Alloy in 3.5% NaCl Solution", Report No. NADC -83126-60 (Vol. V), U. S. Naval Air Development Center, Warminster, PA, 30 June 1984.

(32) Gerberich, W. W. and Peterson, K. A., in "Micro and Macro Mechanics of Crack Growth", eds. Sadanada, K., Rath, B. B. and Michel, D. J., The Metall. Soc. of AIME, Warrendale, PA, 1982, pp. 1-17.

(33) Gao, M. and Wei, R. P., Met. Trans. A., Vol. 16A, 1985, pp. 2039-2050.

(34) Ressler, D., "An Examination of Fatigue Crack Growth in AISI 4340 Steel in Respect to Two Corrosion Fatigue Models", M.S. Thesis, Dept. of Mech. Engg. & Mechanics, Lehigh University, Bethlehem, PA, 1984.

(35) Gao, M., Pao, P. S. and Wei, R. P., in "FRACTURE: Interactions of Microstructure, Mechanisms and Mechanics", eds. Wells, J. M. and Landes, J. D., The Metall. Soc. of AIME, Warrendale, PA, 1985, pp. 303-319.

(36) Pao, P. S., Wei, W. and Wei, R. P., in "Effect of Frequency on Fatigue Crack Growth Response of AISI 4340 Steel in Water Vapor", ed. Foroulis, Z. A., The Metall. Soc. of AIME, Warrendale, PA, 1979, pp. 565-580.

(37) Simmons, G. W., Pao, P. S. and Wei, R. P., Met. Trans. A, Vol. 9A, 1978, pp. 1147-1158.

(38) Turnbull, A., in "Embrittlement by the Localized Crack Environment", ed. Gangloff, R.P., The Metall. Soc. of AIME, Warrendale, PA, 1984, pp. 3-31.

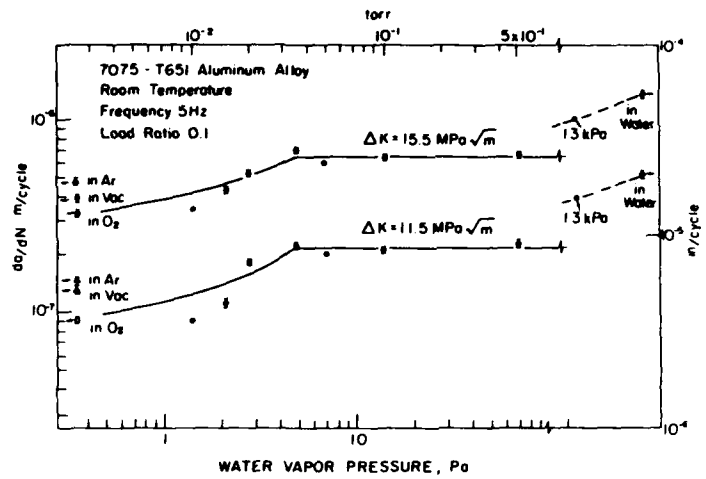

Figure 1 The influence of water vapor pressure and of other environments on fatigue crack growth in 7075-T651 (AlMgZn) alloy at room temperature. The solid lines represent predictions of a model for transport-controlled crack growth. The dashed lines indicate surface-reaction-controlled growth and reflect the influence of segregated magnesium (14)(35).

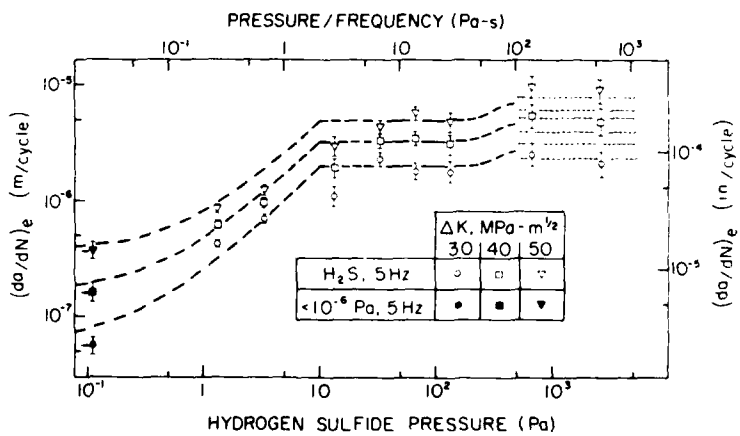

Figure 2 The influence of hydrogen sulfide pressure on fatigue crack growth in a 2-1/4Cr-1Mo (A542 Class 2) steel at room temperature. The solid lines represent predictions of a model for transport-controlled crack growth. The dashed lines indicate surface-reaction-controlled growth and reflect the second step of hydrogen sulfide-iron surface reactions (16).

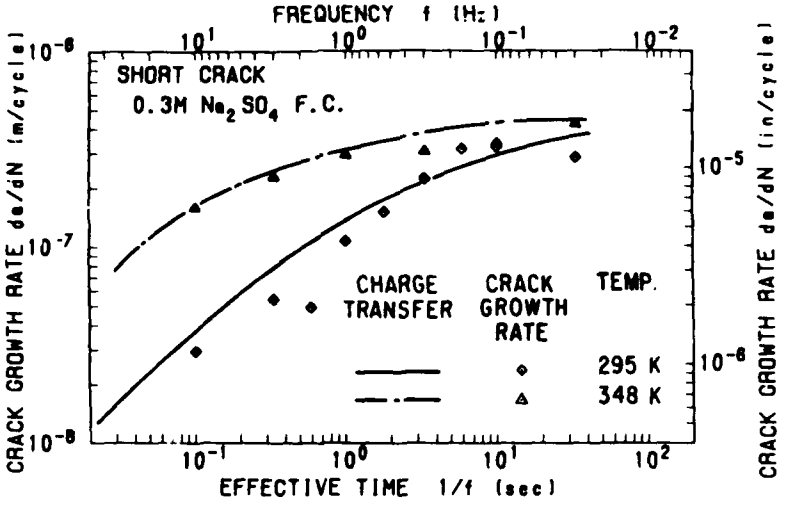

Figure 3 Influence of frequency and temperature on fatigue crack growth for NiCrMoV steel in 0.3N Na_2SO_4 solution (27).

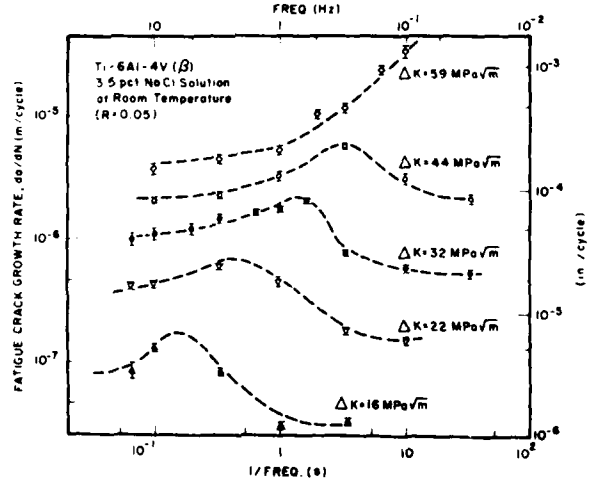

Figure 4 Influence of frequency on fatigue crack growth in a Ti-6Al-4V alloy exposed to 0.6M NaCl solution at room temperature and R = 0.1 (31).

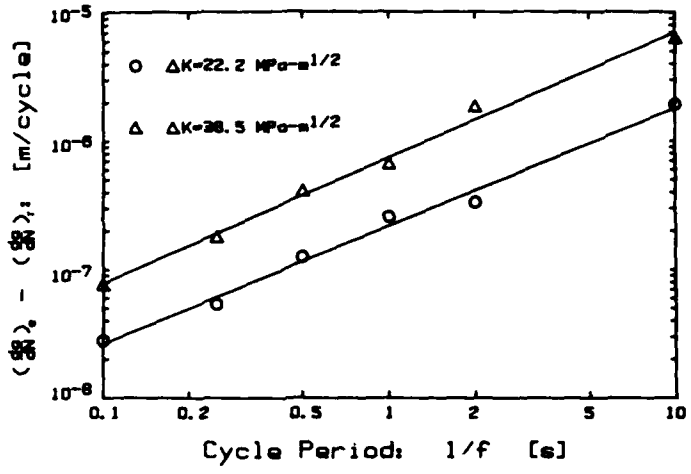

Figure 5 Influence of frequency on fatigue crack growth rate for an AISI 4340 steel in water vapor at 585 Pa at room temperature (34).

Figure 6 Microfractograph of fatigue fracture surface for AISI 4340 steel showing predominantly transgranular failure at 8 Hz and intergranular failure at 0.1 Hz(34).

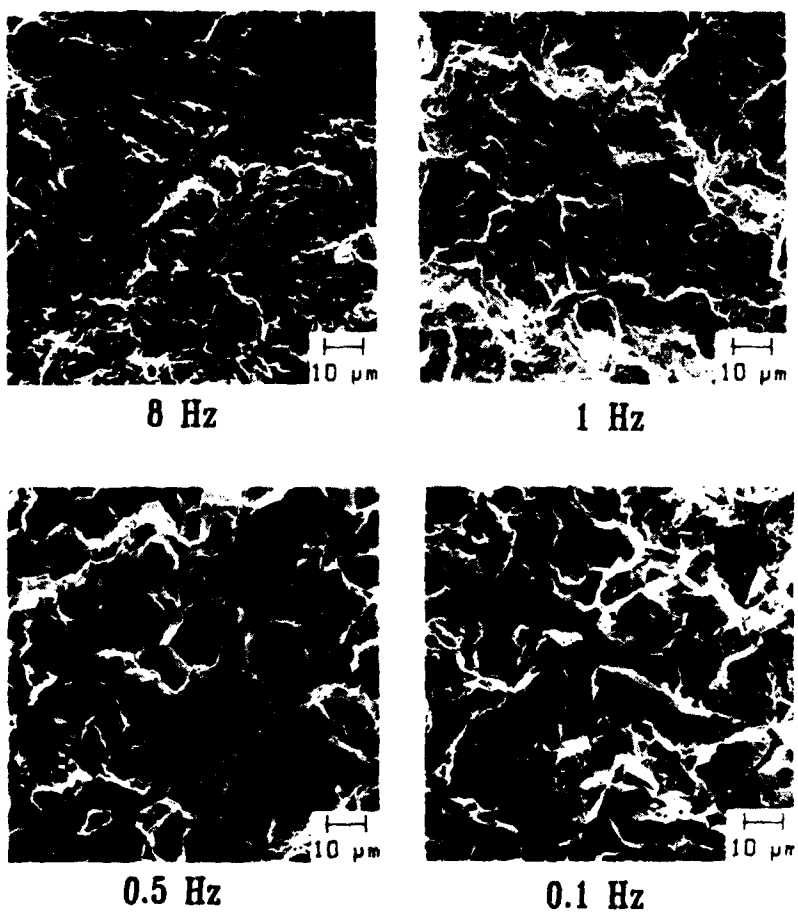

Figure 7 Microfractographs of AISI 4340 steel showing changes in fracture surface morphology with frequency (34).

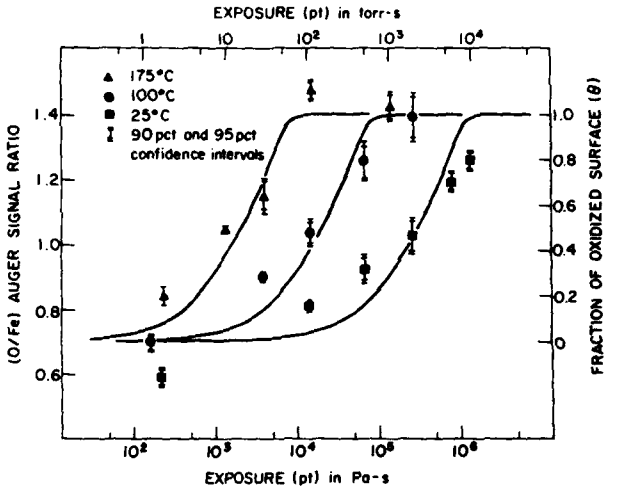

Figure 8 Oxygen Auger electron signal from AISI 4340 steel surface as a function of exposure to water vapor at three temperatures (37).

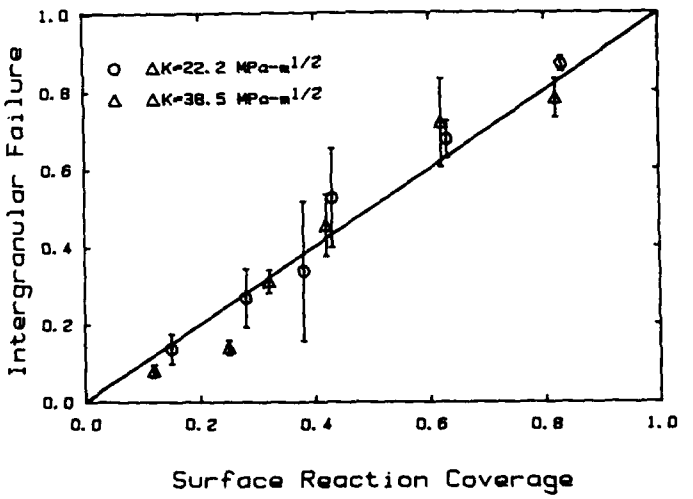

Figure 9 Correlation between surface coverage and fraction of intergranular failure (or ϕ) for AISI 4340 steel.

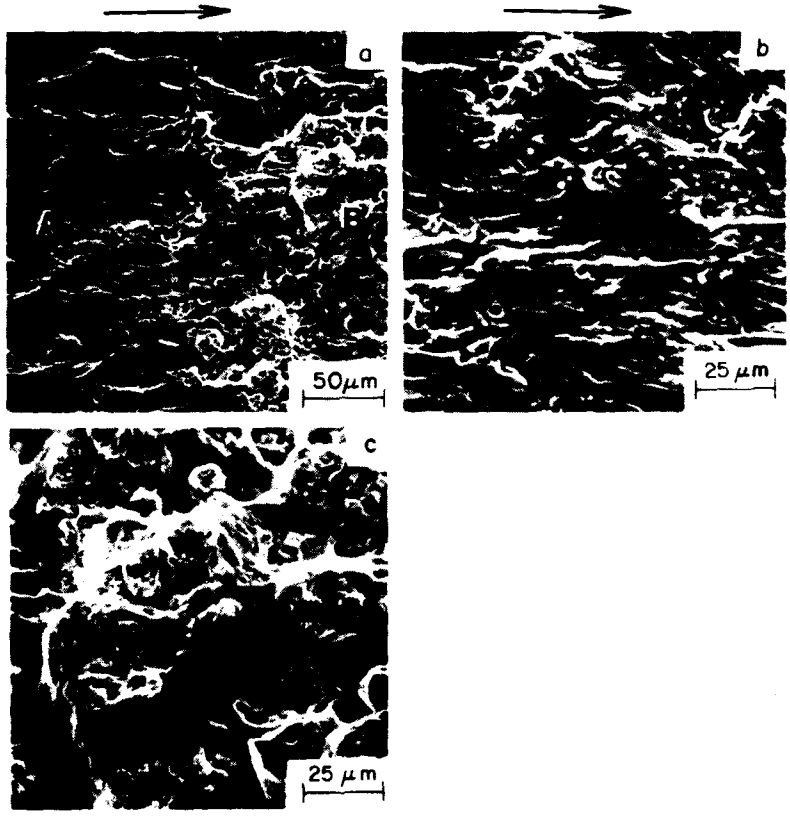

Figure 10 Microfractographs of I/M 7075-T651 specimen tested in water vapor at 1.3 Pa and 670 Pa (ΔK = 11 MPa-$m^{\frac{1}{2}}$, R = 0.1 and f = 5 Hz) showing differences in fracture surface morphology. a) Region A tested at 670 Pa and Region B at 1.3 Pa; b) corrosion fatigue component, Region A, and c) near "pure" mechanical fatigue component, Region B (35).

DEFORMATION, FATIGUE AND FRACTURE BEHAVIOR OF TWO CAST ANISOTROPIC SUPERALLOYS

Walter W. Milligan*, Eric S. Huron**, and Stephen D. Antolovich*

Tensile and low cycle fatigue (LCF) tests were conducted on two cast anisotropic superalloys. The effects of temperature, strain rate and stress range were investigated. Deformation behavior was extensively characterized and modeled. LCF and fracture behavior were studied and correlated with deformation behavior.

INTRODUCTION

In recent years, advancements in precision casting have allowed the introduction of directionally solidified and single crystal turbine blades in gas turbine engines and advanced rocket engines. Currently, the turbopump blade in the Space Shuttle Main Engine (SSME) is fabricated from Directionally Solidified Mar-M 246 + Hf. A possible replacement for this alloy is single crystal PWA 1480.

Both alloys show substantial improvements in creep strength and high temperature fatigue strength over conventionally cast alloys, due to the lack of transverse grain boundaries. However, their use presents an analytical problem, because of anisotropic elastic and plastic properties. Consequently, the

* Fracture and Fatigue Research Laboratory, School of Materials Engineering, Georgia Institute of Technology
** Pratt and Whitney, Government Products Division

conventional continuum-mechanical approach is frequently inadequate. This has lead designers and analysts to try to incorporate the fundamental deformation and damage mechanisms which are active in these alloys.

In addition to the complicated anisotropic properties, the microstructures and deformation mechanisms in these alloys are also complex. Deformation mechanisms depend on temperature, strain level, strain rate, and stress state. In the directionally solidified (DS) material, an additional complicating factor is introduced by the longitudinal grain boundaries, and the associated rotational freedom of the grains. Metallurgical analysis is clearly needed in order to fully understand the behavior of these alloys.

The results reported in this paper are part of a long term project in which the constitutive behavior of the two alloys is being studied. The variables are temperature, strain level, strain rate, orientation, and number of cycles. Additionally, the behavior of the alloys under non-isothermal cyclic loading will be studied. The main focus of the project involves documenting fundamental metallurgical deformation mechanisms, and using this knowledge to develop physically-based constitutive models. To date, interrupted tensile tests and low cycle fatigue (LCF) have been conducted on PWA 1480, and the associated deformation analysis has been completed. Fully reversed, strain-controlled fatigue tests have been completed on DS Mar-M 246, and tensile tests have also been conducted. The analysis of the deformation behavior has recently begun for this material.

MICROSTRUCTURES

The alloys are similar, in that they are based on the two-phase γ/γ' structure, and both contain a large volume fraction of γ'. However, there are significant differences in chemistry and microstructure due to the grain boundaries which are present in the DS material. The alloy compositions are given in Table I.

PWA 1480

PWA 1480 is the simpler of the two, due to the lack of grain boundaries and the subsequent lack of need for grain boundary strengthening phases. The material is single crystalline, with the tensile axis

within 10° of <001>. The alloy contains a fine dispersion of ordered, cuboidal γ' particles in a disordered γ matrix, Figure 1(a). The γ' size was fairly uniform, ranging from 0.25 to 1.0 μm, with an average γ' size of 0.5 μm. There were isolated areas in the interdendritic regions which contained larger primary γ'particles. The average γ' volume fraction was 55-60%.

As shown in Figure 1(b), the alloy contained a residual dendritic structure with micropores and large interdendritic eutectic pools. The volume fraction of microporosity was 0.15-0.20%, and most pores were less than 50 μm in diameter. The volume fraction of eutectic was about 5%, with an average diameter of about 150 μm. Due to a low carbon content of 42 ppm, very few carbides were observed. As shown in Figure 1 (a), the initial dislocation density was also very low.

Mar-M 246

The γ' structure of the alloy is shown in Figure 1(c). The volume fraction γ' was 60%, and the average γ' size was also about 0.5 μm in this alloy. In contrast to the low lattice parameter mismatch of 0.28% for PWA 1480, the mismatch between the lattice parameters of the γ and γ' in Mar-M 246 was high, about 0.65%.[1] This high misfit influenced the γ' morphology, as seen by the sharp cube corners of the γ' and the relatively high initial dislocation density in the precipitate/matrix interface. Note that some stacking faults were present in the starting microstructure.

As shown in Figure 1(d), the microstructure consisted of elongated, columnar grains which were parallel to <001>. The grain diameters varied, but were on the order of 100 μm. The grain boundaries were serrated and irregular, and some transverse boundaries and tapered grains were observed. Similar to PWA 1480, the γ' was finer near the dendrite cores and larger in the interdendritic regions. MC and $M_{23}C_6$ carbides, as well as eutectic pools were present at grain boundaries and interdendritic boundaries, and the MC carbides exhibited a slight "script" morphology. Some scattered micropores were observed, but the level of porosity was not considered to be significant, as subsequent mechanical testing revealed no initiation or failure due to micropores.

TENSILE BEHAVIOR

Mechanical Properties

For PWA 1480, tests were conducted at 20, 705, 760, 815, 871, 982, and 1093°C. For Mar-M 246, tests were conducted at 20, 704, 927, and 1093°C. Tests were conducted at 0.5%/min and 50%/min. The tests on PWA 1480 were interrupted after the yield point, while most Mar-M 246 tests were conducted to failure. References [2] and [3] should be consulted for the data.

The behavior of both alloys was quantitatively similar. As shown in Figure 2, the yield strength was the same at 20 and 705°C. Above 760°C, the strength began to drop off rapidly, and strain rate began to have an effect on the strength. The temperature where the strain rate began to have an effect on the strength was a function of strain rate. At the lower strain rate, the strength began to drop off above 760°C, while at the higher strain rate, the strength did not begin to fall until above 815°C. Such behavior is typical of high volume fraction superalloys.

The stress-strain curves for Mar-M 246 are shown in Figure 3. (Note that the upper endpoints of the curves do not correspond to specimen failure, because the extensometer was removed prior to failure in order to prevent damage to it). The shape of the stress-strain curves indicates a change in strain hardening behavior. At room temperature and 704°C at 50%/min, the curves were approximately horizontal after yielding. For all other test conditions, a steeper stress-strain curve was observed. This indicates that the deformation was much more homogeneous at higher temperatures, and this hypothesis was supported by TEM observations which will be discussed later in the paper.

Yield Strength Analysis

As indicated by the strain rate and temperature dependence of the yield strength, yielding at elevated temperatures is a thermally activated process. It is therefore appealing to present the data in the form of an Arrhenius-type relationship. Rate-controlling mechanisms may then be deduced as a function of temperature. Figure 4 is a plot of the modulus-normalized yield strength vs inverse temperature for PWA 1480, which can be represented by an equation of the form:

$$\sigma/E = A \exp (Q'/RT) \qquad ...(1)$$

where σ = Yield strength,
E = Elastic modulus at temperature, T,
Q' = Apparent activation energy,
A = A constant.

There are three distinct temperature regimes when the data are represented in this way:

a) At low temperatures (below 760°C), Q' was almost zero, so thermal activation was not a factor in the range of strain rates tested.

b) At high temperatures (above 927°C at 50%/min and above 815°C at 0.5%/min), Q' was constant and equal to 50 kJ/mol, and was independent of strain rate. The true activation energy was calculated to be 500 kJ/mol, which is indicative of a diffusion controlled process [2].

c) At intermediate temperatures, a transition from the low to the high temperature behavior occurred. It is evident from the shape of the curves that the transition region boundaries and functional forms were a strong function of strain rate.

Deformation Structures

Analysis of the deformation substructures at yield resulted in the same three temperature regimes as the Arrhenius analysis for PWA 1480, and the boundaries of the three regimes were the same. As discussed below, low temperature deformation at yield was dominated by γ' shearing, high temperature deformation was dominated by γ' by-pass, and intermediate temperatures exhibited a transition from shearing to by-pass.

Low Temperatures. Deformation substructures at yield at 20, 705, and 760°C (high strain rate only) were qualitatively similar for PWA 1480. The dominant deformation mechanism was shearing of the γ' by pairs of a/2<110> dislocations on octahedral planes. At 20°C, relatively few dislocations were present at yield, and the spacing between dislocations was large. However, the dislocation density at yield was significantly higher than it was in the as heat-treated material. There was also evidence of γ' shearing,

including the presence of dislocation pairs and residual loops within the γ'. At 705 and 760°C, the dislocation density at yield was very high, and the structure consisted of intense slip bands which contained closely spaced dislocations, Figure 5. It is possible that this type of structure may have been formed but was not observed at 20°C, due to extremely localized, non-homogeneous slip.

Through systematic analysis of the dislocation Burgers vectors and line directions, it was determined that the vast majority of dislocations observed after deformation at low temperatures were of the type {111} a/2<110>. Dislocations travelled through the γ' as closely-spaced pairs in order to minimize the anti-phase boundary (APB) area created by the a/2<110> displacement of the superlattice. This is demonstrated by Figure 5(b), in which those portions of the dislocations within the precipitate are constricted due to the high APBE, while those portions of the same dislocations which had exited the precipitates are split due to the elastic repulsion.

Dislocation structures observed at failure in Mar-M 246 at low temperatures followed the same trends. At 20 and 705°C, precipitate shearing occurred, and many dislocations were present in the γ' and at the interface (Figure 5 (c)).

High Temperatures. The boundary separating the high and low temperature regimes was a function of strain rate for PWA 1480. At the low strain rates, high temperature behavior was dominant at 815°C and above. while at the high strain rates. high temperature behavior did not manifest itself until 927°C and above.

In contrast to the shearing which was observed at low temperatures, deformation during yielding at high temperatures occurred primarily by dislocations moving between and around the precipitates. Figure 8 shows a typical substructure in PWA 1480 consisting of dislocation loops left in the γ/γ' interface and in the γ matrix. Dislocations were only infrequently observed within the γ' after interrupted tests conducted at the low strain rates above 815°C. Although a few slip bands were observed to have cut the γ' even at 1093°C. the dominant mechanism at low strain levels at 927°C and above was particle by-pass for all strain rates. As seen in Figures 6 and 7, this leads to a very homogeneous substructure for both alloys. which is

consistent with the observed high degree of strain hardening.

While dislocations were not observed within the γ' after interrupted tests at the low strain rate in PWA 1480, the specimens which were tested to failure at 871 and 982°C contained a high density of dislocations within the γ', Figure 8. This indicates that the first step in deformation was by-pass of the γ', which was followed by shearing of the γ' later in the test. Shearing occurred only after large increases in the matrix dislocation density and significant strain hardening had occurred.

At very high temperatures and low strain rates, the γ' coarsened, and the substructure consisted of interfacial hexagonal networks of dislocations, Figure 9. Under these conditions, the γ' was not sheared, and a large amount of dynamic recovery had occurred. Consequently, the strain hardening exponent was lower at 1093°C (n=.221) than it was at 927°C (n=.371).

Intermediate Temperatures. Not surprisingly, a transition from shearing to by-pass was observed at yield in the range from 760 to 927°C (depending on strain rate). Slip bands were only observed at the high strain rate, and the slip band density decreased as the temperature increased.

Discussion of Tensile Behavior

Both the activation energy analysis and the analysis of the deformation substructures at yield divided the tensile behavior into three regimes. At low temperatures, deformation during yielding occurred by γ' shearing. At high temperatures, deformation during yielding occurred by γ' by-pass. The intermediate temperature regime exhibited transitional behavior. Attempts to model the yielding behavior must therefore be divided into these three regimes. However, the intermediate temperature regime exhibited complex transitional behavior which would be difficult to model with the available data.

As discussed in ref. [2], currently available models of yielding in high volume fraction superalloys are based on the premise that dislocation penetration into the particle is the rate-limiting step. The following type of expression for the Critical Resolved Shear Stress (CRSS) results from such an analysis [4]:

$$\tau_c = (\gamma_o/2b) - (T/br_o) + \tfrac{1}{2}(\tau_m + \tau_p) \quad ...(2)$$

where
- τ_c = CRSS,
- γ_o = Antiphase Boundary Energy,
- b = Dislocation Burgers Vector,
- T = Dislocation Line Tension,
- r_o = Radius of Particles in Slip Plane,
- τ_m = CRSS of the Precipitates,
- τ_p = CRSS of the Matrix.

However, the results of this study [2] indicated that penetration was not the rate-limiting step in the yielding process at all temperatures in the shearing regime. This implies that current theories are not valid for all conditions. Further work in this area is underway.

At high temperatures, deformation during yielding occurred by γ' by-pass. The rate limiting step in these alloy systems during by-pass is climb of dislocations over the precipitates. A model [5] is available for this phenomenon which fits the experimental data very well. The CRSS is given by:

$$\tau_c = \tau_o + K_1 Q_o - K_2 T [\ln(k_3 \dot{\varepsilon})] \quad ...(3)$$

where
- τ_o = Threshold Stress
- Q_o = Activation energy of the rate-limiting diffusion process,
- k's = Constants which include micro-structural parameters,
- T = Temperature,
- $\dot{\varepsilon}$ = Strain Rate.

It is observed that the CRSS should be a linearly decreasing function of temperature, and this agrees with the data fairly well.

FATIGUE BEHAVIOR OF DS MAR-M246

Life Correlation

The LCF test results are shown in Fig. 10. The data was first fitted to the well-known Coffin-Manson Law:

$$\Delta\varepsilon_p = C(N_f)^{-\beta} \quad ...(4)$$

where $\Delta\varepsilon_p$ is the plastic strain range (usually at half-life), C is a constant, N_f is the number of cycles to failure, and β is the Coffin-Manson exponent. The

resulting Coffin-Manson equations were:

$$\begin{aligned} 704°C: \Delta\varepsilon_p &= .08\ N_f^{-.783} \\ 927°C: \Delta\varepsilon_p &= .11\ N_f^{-.676} \\ 1093°C: \Delta\varepsilon_p &= .80\ N_f^{-.762} \end{aligned} \qquad \ldots(5)$$

The correlation coefficients were 0.996, 0.986, and 0.999 respectively. Life was also plotted and correlated against stress range (Figure 10 (b)). The effects of strain rate on fatigue life can be noted by examining Figures 10 (a) and 10 (b). At 704°C, the 1.0%/minute strain rate resulted in shorter lives, on the basis of plastic strain range. On the basis of stress range, the lives were approximately equal for 1.0% and 100%/min. At 927°C and 1093°C, oxidation was an important factor in determining life. The slow strain rate lives were longer on the basis of plastic strain range, but when lives were plotted against stress range (Figure 10 (b)), they were shorter at the slower strain rates.

It has been shown [6] that LCF life for single crystal 7-14-6 (Ni-6.8Al-13.8Mo-6W) could be correlated well with either ($\Delta\varepsilon_t$ x E) or the Neuber parameter ($\Delta\varepsilon_t$ E $\cdot$ s_{max})$^{\frac{1}{2}}$, even for different orientations. The present data for 100%/min were analyzed with these parameters and the correlations were higher than those for σ_{max} or $\Delta\varepsilon_t$ alone. This confirmed that elastic modulus, which varies in DS materials due to misorientation, is obviously significant in determining fatigue life in the strain-controlled LCF tests, through its effect on stress.

Cumulative Glide Behavior

The LCF tests were conducted using total strain control. Representative cumulative glide curves, plotting stress vs. cycle, are given in Figure 11. At 20°C the stress range increased to a maximum, followed by a gradual decrease over the remainder of the test. Similar behavior has been observed in MAR-M200 [7] and Waspaloy [8, 9] and is consistent with precipitate shearing. At 704°C, 100%/minute strain rate, the stress range was essentially constant throughout the test. At 927°C, 1.0%/minute, and at 1093°C, marked softening was observed. Although the softening might at first seem to be due to particle shearing, TEM studies (which are discussed in subsequent paragraphs) revealed that particle coarsening was taking place with relatively little or no shearing.

Fracture Character

SEM examination of LCF fracture surfaces revealed marked differences dependent on test condition. At room temperature and 704°C, initiation was due to cracking at carbides in the interdendritic regions, and subsequent formation of slip bands (Figure 12 (a)). The slip band spacing was wider at 704°C. Fracture surfaces were perpendicular to the stress axis and were highly crystallographic at 20°C, less crystallographic at 704°C, 100%/minute (Figure 12 (b)), and only marginally crystallographic at 704°C, 1.0%/minute. Optical examination revealed that at both 20°C and 704°C cracks followed transgranular paths along interdendritic regions, which are to be more brittle due to the eutectic and carbides in those regions. Only slight deflection was observed at vertical grain boundaries.

At 927°C the fracture character was quite different. The fracture surfaces were still perpendicular to the stress axis, but the initiation region was flat and featureless and not crystallographic (Figure 12 (c)). As expected, the surface was heavily oxidized. Optical microscopy (Figure 12 (d)) confirmed the formation of cracks perpendicular to the stress axis (Stage II) due to oxidation of eutectic constituent in interdendritic regions. The oxidation was more severe at the slow strain rate tests, which caused reductions in lives at 927°C and 1093°C. The initiation region at 1093°C was similar to 927°C: flat and featureless and resulting from Stage II initiation at oxide spikes. However, behind the flat initiation region, the crack changed direction slightly and deviated from a plane normal to the stress axis.

Dislocation Substructures

The dislocation substructures, along with the observations concerning fracture character and cumulative glide behavior, show that the LCF behavior of this material is highly dependent on the precipitate/matrix relationship.

At 20°C, there were linear dislocation segments throughout the microstructure with a significant amount of dislocation debris at the precipate-matrix interface (Figure 13(a)). The overall dislocation density was quite high. The dislocation character was a/2<110> (111). At 704°C, the overall dislocation density was lower. Dislocations were present on the interface and

there was evidence of precipitate shearing (Figure 13(b)). Most of the dislocations were of type a/2<110> {111}. However, some a/2<110> {110} dislocations were found. These dislocations were pure edge, and near the precipitate/ matrix interfaces, where the strong component of the Burger's vector in the direction of the cube face would serve to accomodate the lattice mismatch. Despite the strong strain rate effect on life, there was little qualitative difference in the substructures as a function of strain rate with the exception of slightly more "wavy" dislocations in the low strain rate tests, especially in the interface regions. On the basis of plastic strain range, the lives at 704°C were much shorter than for other test conditions. This has been explained elsewhere [10] as being due to the maximum γ' strength (high stress) and an aggressive environment.

At 927°C, 100%/min, some shearing of γ' by a/2 <110> {111} dislocations was observed, but the dislocation density in the precipitates was very low (Figure 14 (a)). The most significant structural feature observed at 927°C and above was precipitate coarsening, with formation of hexagonal networks of dislocations at the interfaces. Trace analysis showed that the networks were composed of near-edge a/2 <110> dislocations on {111} planes with some dislocations on {110} planes. The interfacial networks were quite well developed at the slow strain rate, and coarsening was extensive.

At 1093°C, 1.0%/min, no dislocations were present in the matrix or precipitate interiors (Figure 14(b)). All dislocations were stored in arrays on the precipitate-matrix interfaces, with the same character as observed at 927°C. The γ' coarsened significantly, in an irregular manner, even at 100%/minute strain rate. Similar coarsening was observed at 927°C at 1.0%/minute strain rate, but was absent at higher strain rates. At 1.0%/minute at 1093°C, the degree of coarsening was severe (Figure 14 (b)). Note that the mean free path between precipitate particles has increased greatly.

Precipitate coarsening is obviously very important in the high temperature deformation of MAR-M246+Hf. In DS Rene 80, coarsening has been shown to be accelerated by stress. To investigate the stress effect in MAR-M246+Hf, undeformed samples were held for 49 hours at 927°C and 1093°C with no applied stress. The resulting γ' structure for 1093°C is shown in Figure 14

(c). Some coarsening has occurred. The 1093°C, 100%/min. LCF tests coarsened to a greater extent after test times of only 30 minutes, and at 1093°C, 0.5%/min., the structure coarsened even in a tensile test. Thus in MAR-M246+Hf, the high mismatch provides a driving force for coarsening without deformation; however, deformation does increase the rate of coarsening significantly as observed for other systems [10, 11].

Cyclic Deformation of PWA 1480

Fatigue tests conducted at room temperature and 927°C resulted in the same types of substructures as those observed in simple tension. At room temperature, intense, inhomogeneously distributed slip bands cut the γ'. At 927°C, the dominant deformation mechanism was γ' by-pass, even at a strain rate of 50%/min and a plastic strain range of 0.2%. Further work is in progress.

Grain Boundary Slip Behavior

For the low temperature tests, slip behavior on the surface could be studied by EM. The slip behavior across boundaries varied considerably; a typical example is given in Figure 15. In Figure 15 (a), the grain at the right showed primary slip with slip traces present on the entire grain surface. The grain on the left contained only short slip traces, adjacent to the grain boundary. In Figure 15 (b), both grains exhibited primary slip. In the grain on the left, secondary slip was observed on two additional slip systems. These effects are similar to the results of bicrystal studies [12 - 17] and indicate that stresses can arise at the boundary due to incompatibility effects. This topic will be considered in more detail in the discussion.

Discussion of Fatigue Behavior

Factors Influencing Life. As shown in Figure 10, the effect of strain rate on life for the DS MAR-M246 changed with temperature. The reduction in life at 704°C for the slow strain rate, for a given plastic strain range, could be due to the difference in strain hardening behavior. For a given amount of strain the higher degree of strain hardening at the 1.0%/minute strain rate resulted in a higher stress range. Note that in terms of stress range there is little strain rate effect.

At 927°C and 1093°C, oxidation was an important factor in determining life, and the slow strain rate lives were longer on the basis of plastic strain range. This result was due to the fact that, for a given number of cycles, increased time was available for softening due to precipitate coarsening. This caused a beneficial reduction in stress, although increased time was available for oxidation. However, in terms of stress range, life was shortened at the slow strain rate. Although beneficial coarsening did occur to a greater extent, more time was available (in a given number of cycles) for detrimental oxidation, so the life was reduced.

Antolovich, Baur, and Liu [10, 18] have presented a model for the effect of oxidation on life. The model assumes parabolic oxidation kinetics and relates the depth of oxide spikes to the time of the test. The relative depth, l_i of an oxide spike, is given by:

$$l_i = (t/t_0)^{\frac{1}{2}} \qquad ...(6)$$

where t is the time to failure. For oxide-induced failure, the maximum stress at initiation was proportional to $t^{\frac{1}{2}}$, or $l^{\frac{1}{4}}$. Figure 16 shows a plot of maximum stress at initiation vs. the relative oxide depth for the present study. Visually, the correlation appears to be best for 1093°C, and the horizontal slope at 704°C implies little or no dependence of failure on oxidation.

Cumulative Glide Behavior

The cumulative glide behavior of the MAR-M246 was strongly dependent on temperature due to changes in the deformation mode. At 20°C, the structure was indicative of heterogeneous, planar slip and precipitate shearing, consistent with the surface slip lines, the gradual drop in life over the last portion of the test, and the highly crystallographic fracture behavior. The initial hardening during the test corresponded to hardening in the matrix, which is relatively strong at 20°C. At the point of maximum stress the dislocation density at the precipitate/matrix boundaries and associated stress concentration was sufficiently high to initiate precipitate shearing. It should be noted that the TEM substructure was taken from the failed specimen. A worthwhile experiment would be to run an interrupted test, to a point before the maximum stress is reached, and study the deformation substructure. The completion of the

present study will involve a complete matrix of interrupted testing.

At 704°C, at both strain rates, edge dislocations on {110} planes were present after deformation. This is a significant result, because such dislocations in the FCC structure are sessile, would act as strong barries, and would cause hardening. Note that at 704°C, at both strain rates, the stress range of all tests is stable almost immediately. The stability of the stress range may be due to a balance of precipitate shearing, which would eventually soften the material, and strengthening from the immobile dislocations on {110} planes. Again, completion of interrupted tests will help to clarify these results.

At 927°C, 100%/min., the stress range was also stable. Note that although coarsening and the formation of interfacial networks had begun to occur, some precipitate shearing was still occurring at the high strain rate. At 927°C, 1.0%/min. and 1093°C, a drop in stress over the life of the test was observed, due to coarsening of the γ'. This coarsening, with the resultant interfacial network of dislocations, and the low observed dislocation density in the matrix and precipitate are important in determining fatigue life. First, the low dislocation density is indicative that recovery processes can occur easily. Thus, the damage due to dislocations is probably minimal. The interfacial networks are not actually damage, because they serve to accomodate the mismatch. Also, the interfacial networks themselves can accomodate large strains by serving as sources and sinks for dislocations, and the coarsening increased the mean free path between precipitates. The effects explain the observed increase in fatigue on the basis of plastic strain range at 927°C and 1093°C. Coarsening has been discussed in studies on Rene' 80 [10], and it was shown that at 871 and 982°C, life was determined by a balance between beneficial coarsening and detrimental oxidation. Essentially the formation of oxide spikes or regions of higher oxygen content constitute damage to the extent that they nucleate stable cracks. The formation of cracks at these defects depends on the stress level, which is determined by the amount of coarsening. The more coarsening, the lower the stress and the longer the life. As discussed earlier, when the present data (100%/min.) was fitted to the Antolovich model, the correlation was best at 1093°C. The lower fit at 927°C could be explained by the fact that some shearing (a mechanism not related to

oxidation) was occuring at 927°C.

Grain Boundary Slip Behavior

The final topic of discussion concerns the grain boundary slip behavior observed at 20°C and 704°C in the MAR-M246 LCF tests. Studies of bicrystal deformation have provided fundamental information on the role of grain boundaries. As discussed by Hook and Hirth [16, 17], the grain boundary is a source of constraint on deformation, because to remain compatible at the boundary, each grain must contribute to the strains in the grain boundary plane in a like manner. In an ideal DS structure, because of rotational freedom, the grains will possess different compliance matrices relative to a common spatial coordinate system. This leads to elastic incompatibility. In addition, deformation on the operative slip systems will not be geometrically continous and consequently will cause plastic incompatibility. In an actual DS structure the situation is even more complicated because of a small allowable degree of tilt misorientation. The tilt misorientation will result in changes in modulus (and therefore stress) and changes in Schmid factors for any given slip system.

A detailed analysis of the slip patterns shown in Figure 15 could be made following the methods of Margolin [15]. However, such an analysis would require knowledge of the exact crystallographic orientations of each grain. Because of the grain size, the available X-ray equipment could not be used for these determinations due to the width of the beam. Following the analysis of Prakash [19], the observed slip pattern can be rationalized based on misorientation. The following equation defines an incompatibility parameter ϕ, as a function of degree of misorientation,

$$\phi = -h/(h_2 + k_2) \cdot (1 - \cos\theta - h/k \sin\theta) \quad ...(7)$$

This equation predicts increasing incompatibility with increasing rotation difference. The misorientations of the grain in Figure 15 were measured by examining the grains structure on transverse planes. The secondary dendrites arms are aligned along <001> directions and may be used to measure orientation differences. The misorientation between the grains was 7° in Figure 15 (a) and 28° in Figure 15 (b), correlating well with the observed degree of incompatibility slip. Greater rotational differences lead to higher local stresses which cause slip concentration in the boundary.

CONCLUSIONS

Strain rate, temperature, time, and microstructure had strong effects on the mechanical properties of both alloys, and physical damage mechanisms have been correlated with these effects. This is the first step toward characterizing the constitutive behavior of the alloys from the physical point of view. In the remaining portion of the program, these relationships will be further explored to develop constitutive models based on actual microstructural deformation mechanisms in the alloys.

ACKNOWLEDGEMENTS

The authors gratefully acknowledge the financial assistance of NASA-Lewis Research Center under Grant NAG3-503, and helpful discussions with Dr. Robert C. Bill, grant monitor.

REFERENCES

1. Bowman, Randy, M.S. Thesis, Georgia Tech, 1986.

2. Milligan, W. W., NASA CR-175100, 1986.

3. Huron, E. S., NASA CR-175101, 1986.

4. Copley, S. M. and Kear, B. H., Trans TMS-AIME, 239, 1967, p. 984.

5. Brown, L. M. and Ham, R. K., "Dislocation-Particle Interactions," in "Strengthening Methods in Crystals," A. Kelly and R. B. Nicholson, eds., Wiley, New York, 1971, pp. 9-134.

6. Dalal, R. P., Thomas, C.R. and Dardi, L. E., in "Superalloys 1984," M. Gell et. al., eds., AIME, New York, 1984, p. 185.

7. Gell, M. and Leverant, G. R., Trans. TMS-AIME, 242, 1968, p. 1869.

8. Lerch, B., Jayaraman, N. and Antolovich, S. D., Mater. Sci. Eng., 66, 1984, p. 151.

9. Stoltz, R. E. and Pineau, A. G., Mater. Sci. Eng., 34, 1978, p. 275.

10. Antolovich, Stephen D., Liu, S. and Baur, R., Metall. Trans., 12A, 1981, p. 473.

11. Antolovich, Stephen D., Rosa, E. and Pineau, A., Mater. Sci. Eng., 47, 1981, p. 47.

12. Aust, K. T. and Chen, N. K., Acta. Metall., 2, 1954, p. 632.

13. Hauser, J. J. and Chalmers, B., Acta. Metall., 9, 1961, p. 802.

14. Chuang, Y. and Margolin, H., Metall. Trans., 4, 1973, p. 1905.

15. Lee, T. K. and Margolin, H., Metall. Trans. A, 8A, 1977, p. 157.

16. Hook, R. E. and Hirth, J. P., Acta. Metall., 15, 1967, p. 535.

17. Hook, R. E. and Hirth, J. P., Acta. Metall., 15, 1967, p. 1099.

18. Antolovich, S. D., Baur, R. and Liu, S., in "Superalloys 1980," J. K. Tien et. al., eds., ASM, Metals Park. Ohio, 1980, p. 605.

19. Prakash, A., Ph.D. Thesis, University of Cincinnati, 1981.

TABLE I - Alloy Compositions

ELEMENT	PWA 1480	D.S. MAR-M 246
Cr	10	9
Co	5	10
Al	5	6
Ti	1.3	1.5
W		10
Mo		2.5
Ta	12	1.5
Hf		1
C	42 ppm	0.15
B		0.015
Zr		0.05
Ni	Bal.	Bal.

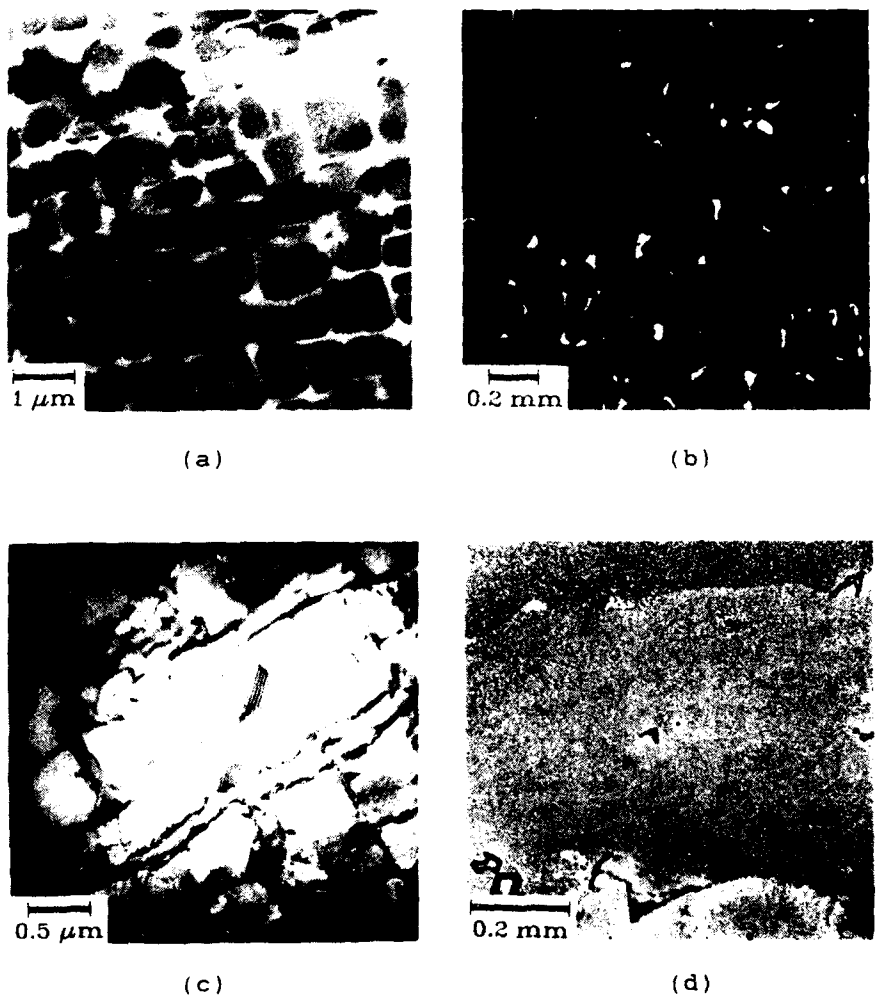

Figure 1. Initial Microstructures. (a) PWA 1480, TEM, g=<200>, (b) PWA 1480 Optical Micrograph, (c) Mar-M 246 TEM.g=<200>, (d) Mar-M 246 Optical Micrograph.

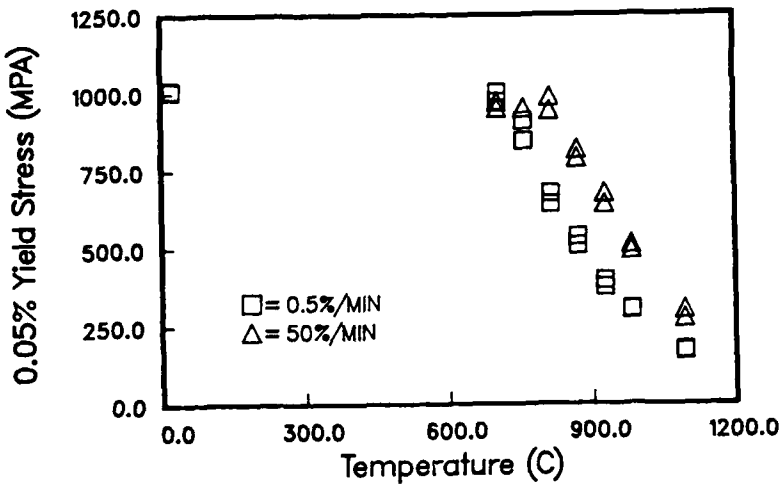

(a)

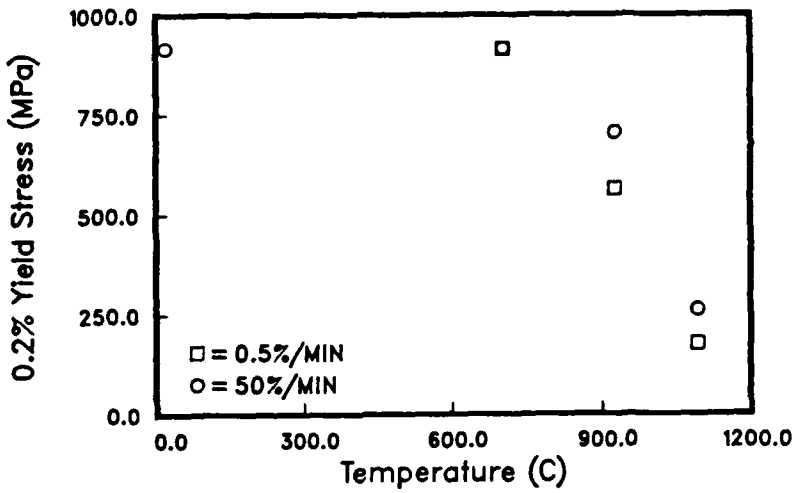

(b)

Figure 2. Yield strength vs. Temperature. (a) PWA 1480. (b) MAR-M 246.

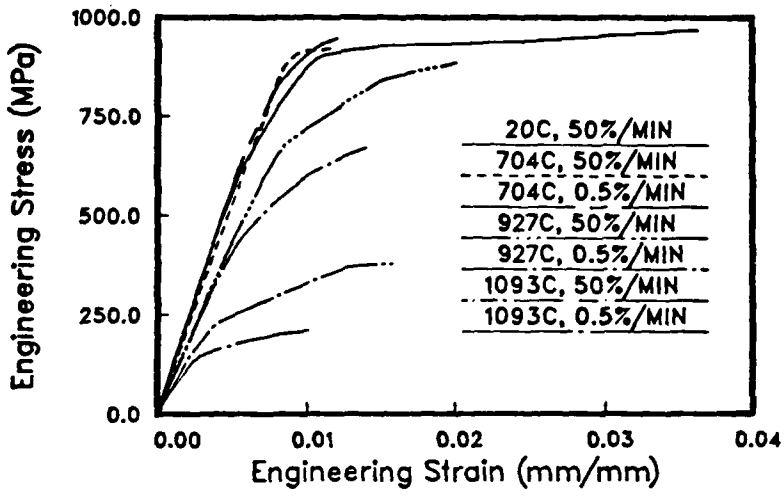

Figure 3. Representative tensile test curves for MAR-M 246.

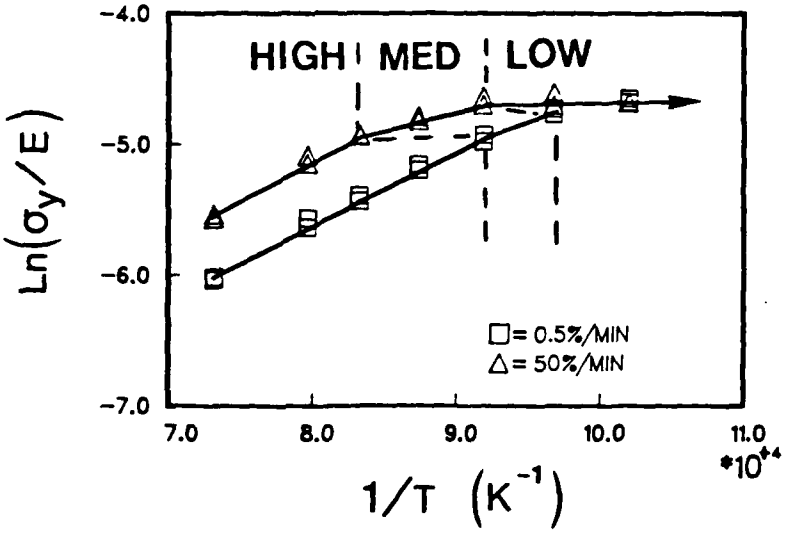

Figure 4. Arrhenius representation of PWA 1480 yielding data.

(a) (b)

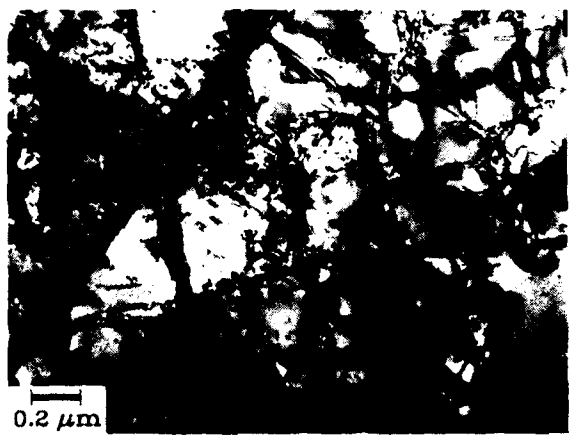

(c)

Figure 5. Shearing of γ' at Low Temperatures. (a) PWA 1480, 705°C, 50%/min, (b) same, showing dislocation pairs which split in matrix (arrow), (c) Mar-M 246, 20°C, 50%/min.

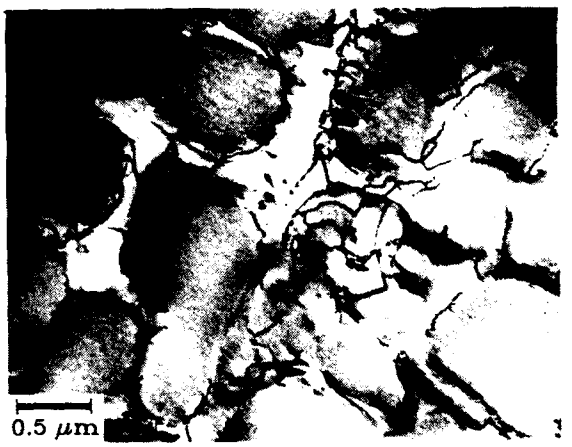

Figure 6. γ' by-pass at yield at high temperature. PWA 1480, 982°C, 0.3% plastic strain, 0.5%/min.

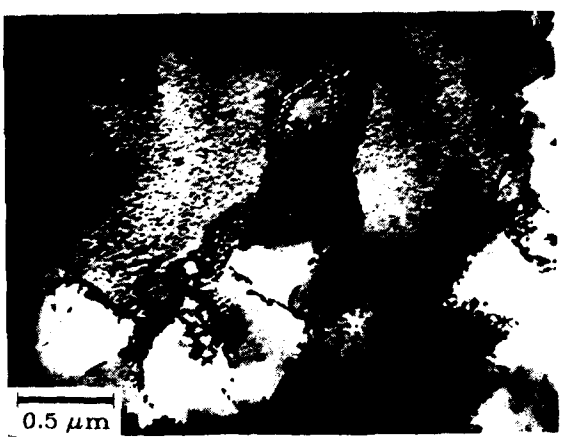

Figure 7. γ' by-pass and coarsening after tensile test to failure MAR-M 246, 1093°C, 0.5%/min.

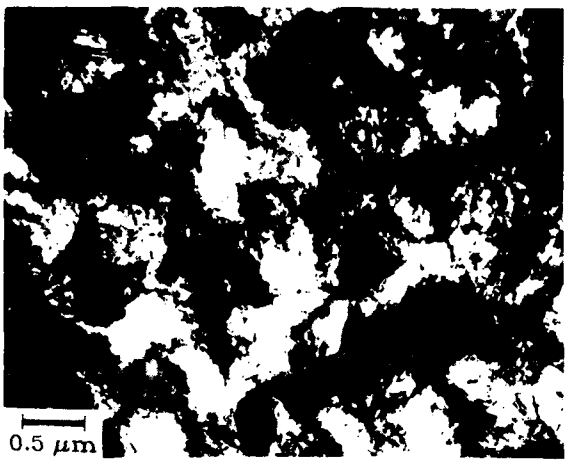

Figure 8. γ' shearing during late stages of tensile test in PWA 1480 at 871°C and 0.5%/min.

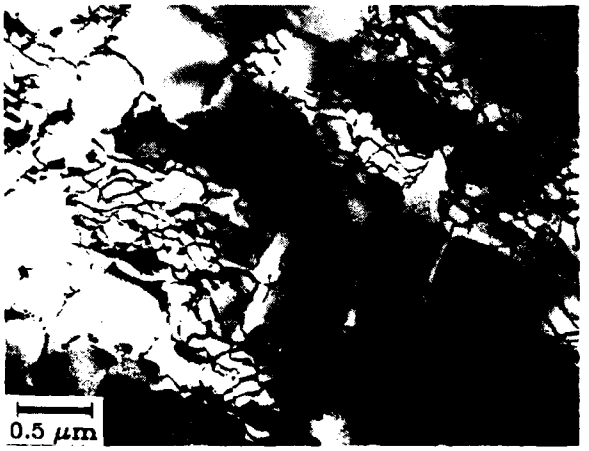

Figure 9. Interfacial networks developed at yield at high temperature. PWA 1480, 1093°C, 0.3% plastic strain,0.5%/min.

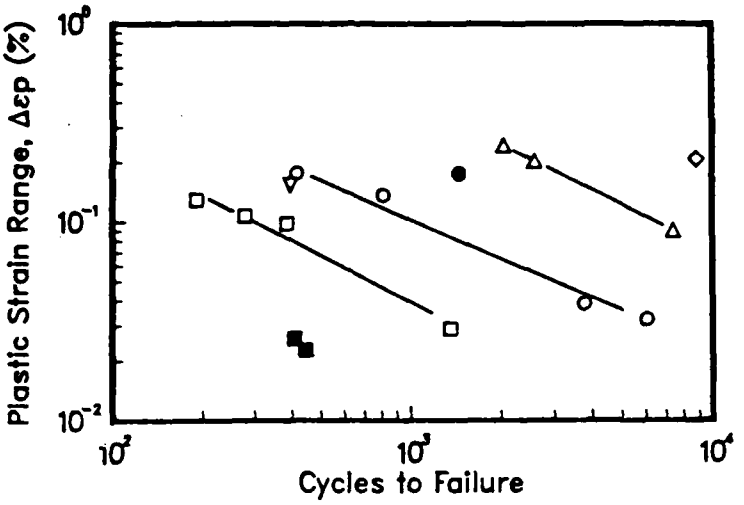

(a)

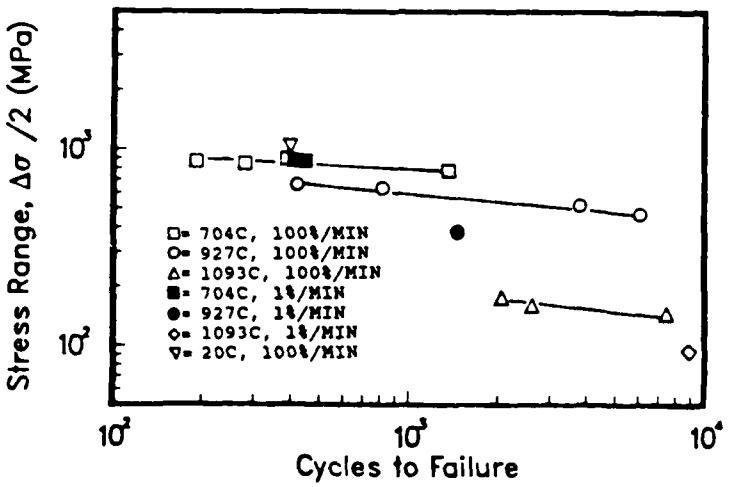

(b)

Figure 10. Fatigue behavior of MAR-M 246. (a) Coffin-Manson plot. (b) Stress Range vs. Life.

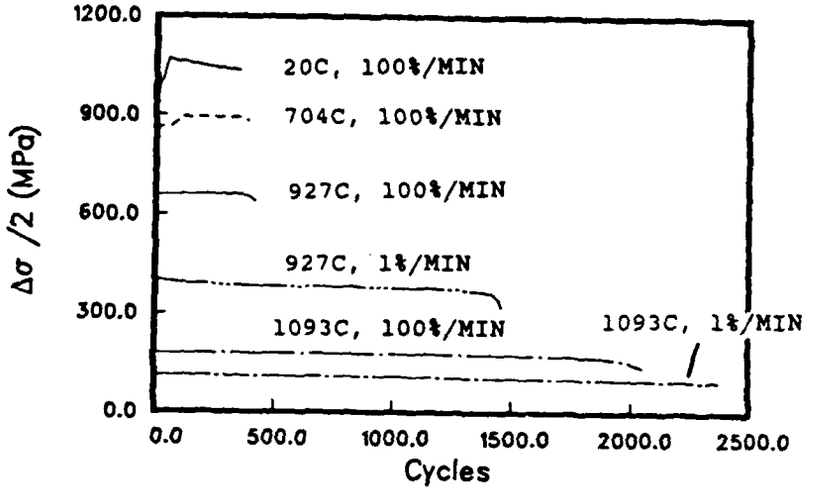

Figure 11. Representative cumulative glide curves for MAR-M 246.

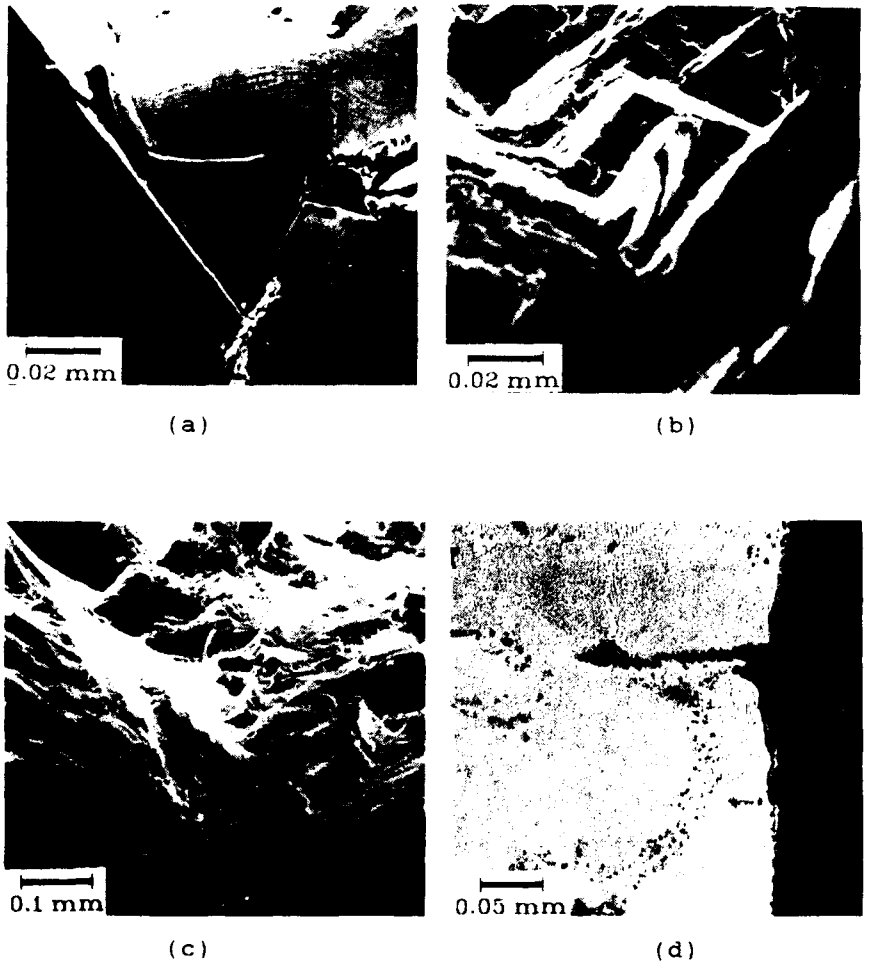

Figure 12. LCF fracture behavior of MAR-M 246. (a) Initiation and crystallographic propagation at 20°C. (b) Less crystallographic fracture at 704°C, 100%/min. (c) Initiation due to oxidation at 927°C. (d) 927°C oxide spikes.

(a)

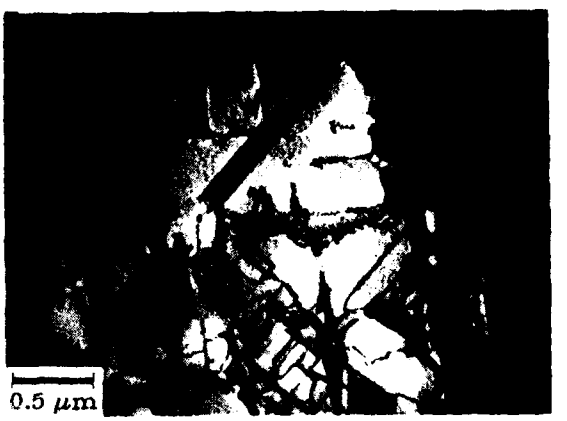

(b)

Figure 13. LCF dislocation structures at low temperatures. (a) 20°C, 100%/min, showing remnants of shearing. (b) 704°C, 100%/min Note stacking faults indicative of shearing.

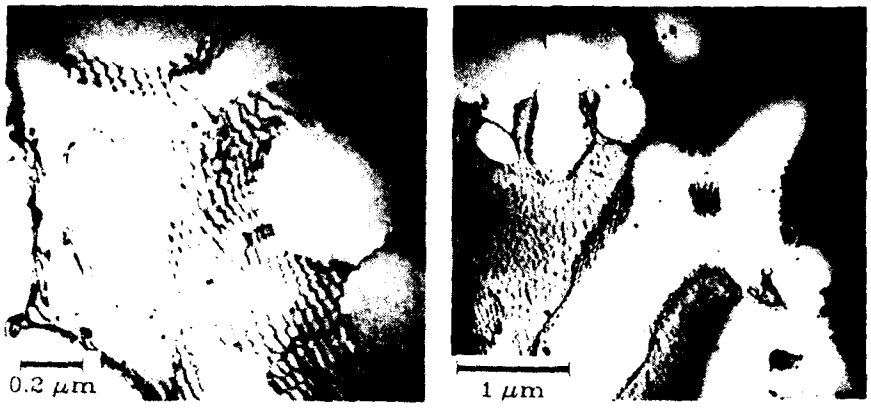

(a) (b)

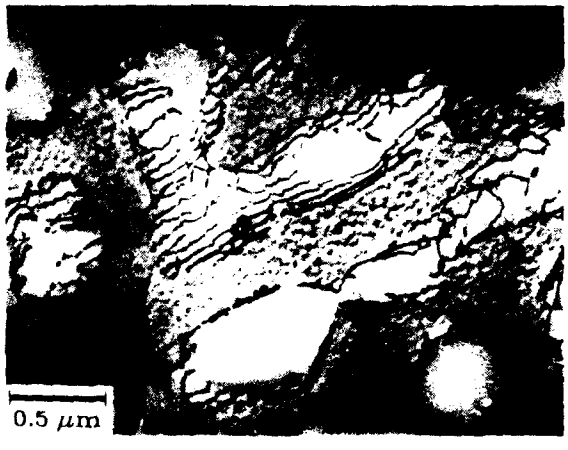

(c)

Figure 14. High Temperature Substructures. (a) Mar-M 246, 927°C, 100%/min LCF, (b) Mar-M 246, 1093°C, 100%/min LCF, (c) Untested Mar-M 246, aged at 1093°C for 49 hrs.

(a)

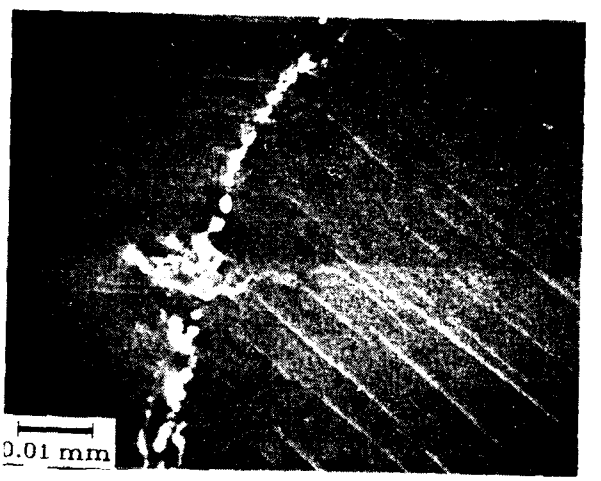

(b)

Figure 15. Grain Boundary Slip Behavior in 20°C LCF test. (a) Primary slip has occurred in both grains, with secondary slip on two systems in the grain on the left. Misorientation is approximately 28°. (b) Primary slip has occurred only in the grain on the right, with some secondary slip in the grain on the left in the grain boundary area. Misorientation is approximately 7°.

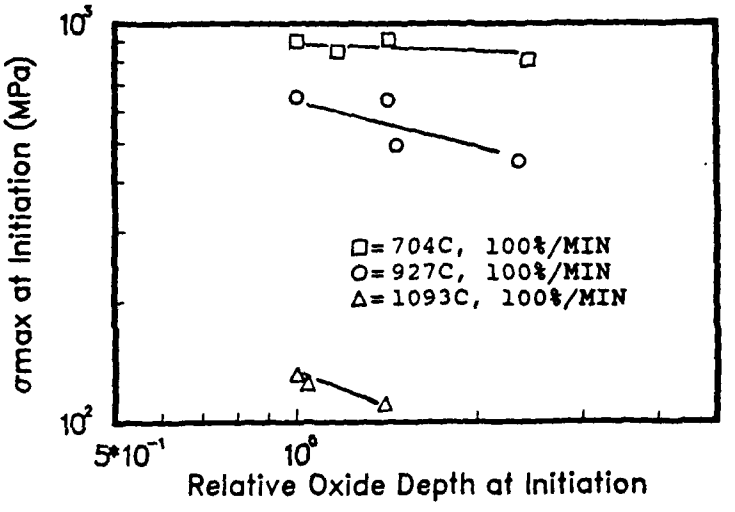

Figure 16. Stress at Initiation *vs.* Oxide Depth. This plot is based on the model proposed by Antolovich and coworkers [10, 18]. The slopes of the data at 704°C and 927°C is are nearly horizontal, indicating little dependence of life on oxidation, while a stronger dependence is noted at 1093°C.

APPLICATIONS OF FATIGUE ANALYSES: TRANSPORTATION

R. W. Landgraf*

Progress in the implementation of modern fatigue methodology in ground vehicle design is reviewed in the context of recent advances in data acquisition, computer modeling and laboratory simulation testing technologies. A fatigue analysis program, designed specifically for ground vehicle problems, is described and example applications presented. The trend towards integration of this methodology into computer workstation environments is discussed and future needs and refinements are identified.

INTRODUCTION

The assurance of adequate fatigue performance in ground vehicle structures, while never an easy task, has taken on new complexities with the unprecedented rate of new product development to meet the demands for lighter, more efficient and durable vehicles. Examples include: the substitution of a variety of stronger and lighter materials throughout vehicles, the employment of new structural design concepts to achieve more optimized structures, and an ever accelerating product cycle time.

These trends have forced designers to rely increasingly on a wide array of computer-based design and testing tools to assist in product development and evaluation by allowing rapid consideration of a wider range of design and performance criteria than was previously possible. These design aids include:

- computer-aided drafting and solid modeling,
- finite element modeling of components and sub-systems,

* Research Staff, Ford Motor Co., Dearborn, Mich.

- full-scale structural modeling for vehicle dynamics and durability studies,
- small, microprocessor-based field data acquisition devices,
- extensive computer databanks for material properties and service loads,
- sophisticated laboratory simulation systems for structural evaluation,
- new life prediction routines for assessing product durability at various stages throughout the design process.

Although not yet optimally linked into integrated design procedures, considerable progress has been made in applying these new technologies to the special problems of the ground vehicle industry. With respect to fatigue analysis, the increasing availability of detailed load and stress information early in the design process provides an excellent opportunity to implement modern life prediction methodology as part of the product development procedure. This is a departure from the traditional approach entailing extensive testing of prototype hardware. The most immediate challenge in this regard is to accelerate the implementation of new methodology in engineering design by packaging life prediction routines in easily used formats that are properly interfaced with related computer-based design tools (1).

This paper will review current efforts to incorporate modern fatigue methodology in ground vehicle design practice. After a brief overview of ground vehicle durability issues, approaches for generating the necessary input information for fatigue analyses are outlined. Features of a recently developed, interactive fatigue program, developed specifically for ground vehicle problem solving, are then described and example applications presented. Finally, some future trends and emerging needs are discussed.

DURABILITY DESIGN OF GROUND VEHICLES

In order to gain insight into the nature of typical ground vehicle structures, key fatigue critical components of two major automotive systems, a front suspension and an engine, are shown in Fig. 1. Suspension componentry entails a wide range of materials and processes including formed and welded sheet metal, high-performance forgings and castings, and heat treated and surface processed steels. Further, suspension systems are subjected to extremely variable service loadings under a variety of usage patterns.

Engine components likewise involve a range of cast, forged and heat treated members. To achieve greater powerplant efficiencies,

a great deal of effort is currently directed at reducing the weight of reciprocating components by substituing higher performance materials, such as aluminum and titanium alloys, ceramics and metal-matrix composites, for more traditional engine materials. Attention here is primarily on high cycle fatigue resistance as influenced by temperature and often hostile environments - e.g. combustion gases.

The automotive engineer, because of the nature and use of the product, faces some unique challenges. Among these are:

- automobiles are a high volume item and must be amenable to mass production techniques; manufacturing feasibility and cost are major considerations.

- structures tend to be non-redundant, single load-path configurations of relatively thin sections.

- there is no periodic inspection of components in service.

- ground vehicles are subjected to extreme variations in service loads due to driver-to-driver variables and differences in driving conditions between regions and countries.

All of these issues require the designer to take a somewhat different view of mechanical durability than, say, the aerospace industry. Emphasis is primarily on crack intiation and early growth. Classical fracture mechanics analyses have yet to find wide application for the thin (plane stress) sections and lower strength materials normally used; they have been applied, however, to cast metals and welded joints. Further, probabilistic design strategies must be employed with a view to anticipating the "worst scenario" service case as a design objective.

The general procedure for performing fatigue analyses is shown by the flow chart in Fig. 2. Using component load and stress information, a local stress-strain analysis is performed at potential failure locations, damage is determined for each event in a history, and a initiation life projected. For propagation life, the local stress-strain analysis is used to determine stress intensity factors for subsequent crack growth analysis.

As indicate in Fig. 3, a number of technical activities and specialties are involved in assuring the mechanical durability of a vehicle. These involve the applicacion of both analytical and experimental techniques that rely heavily on computers as tools for accomplishing specific tasks and as communication links between related activities. Early in the design process, road-load information is developed either from previous vehicles or by using surrogate vehicles run on selected durability routes. Full vehicle computer moodels can then be used to determine load paths through

the structure and, hence, the design loads for subsystems and individual components (2). Finite element modeling then provides indications of highly stressed areas in a component and establishes relations between applied loads and local stresses - a "component calibration." At this point fatigue calculations can be made, using material property data and historical service usage profiles, to obtain early indications of probable structural integrity.

While the ultimate test of any vehicle remains the successful completion of a carefully planned durability test on a proving ground, increased emphasis is being put on the use of laboratory road-load simulation systems to more quickly identify potential problem areas and correct them before getting to the costly and time-consuming proving ground tests (3). Fatigue analyses are used extensively in these studies for making life projections from strain histories obtained from instrumented componentry.

The accuracy, and hence utility, of any fatigue analysis is highly dependent on the nature and quality of input information. Thus the acquistion and manipulation of the appropriate loads, stress analyses and material property data into suitable formats is crucial to successful fatigue analysis. Fortunately, a variety of new tools and techniques are becoming available to assist in this important task. The next section provides an overview of current trends in generating the input information for fatigue studies.

FATIGUE ANALYSIS - INPUT INFORMATION

SERVICE DATA ACQUISITION AND ANALYSIS

Road-load data, acquired under a variety of service usage conditions, provide a major input in establishing durability design and performance objectives. Traditionally, service history data has been recored on FM tape for post-processing on a central computer facility. Alternatives to this rather cumbersome approach are provided by a new generation of small, self-contained microprocessor-based devices that acquire and digitally store information in a variety of formats (4, 5). Some devices can be left unattended on vehicles for periods of several weeks while others have the capability of making life estimates in the field. The expanded use of these new recorders/analyzers promises to provide for greatly improved documentation of vehicle usage profiles.

VEHICLE ANALYSIS

A prime purpose for gathering road-load information is to develop load paths and levels through critical parts of the structure so that individual components can be properly sized. Some of the complexities associated with such analyses are indicated in Fig. 4 where three force vectors, measured by a wheel

force transducer as the vehicle negotiates a rectangular chuckhole, are displayed on a time base. It is immediately apparent that the peak forces in each direction occur at different times thus necessitating a detailed time increment analysis to determine the forces acting at other points in the structure - e.g. the ball joints. Such loading patterns also result in complex mutiaxial stress states in components that must be accounted for in fatigue calculations.

Computer modeling schemes are becoming available to handle these rather complex structural dynamics calculations (6). These programs allow a vehicle to be "driven" over a road profile at specified speeds and determine the resulting load levels at critical points throughout the structure. Such information provides more realistic performance objectives for early design studies and provides a basis for structural optimization exercises.

COMPONENT ANALYSIS

Once the loads experienced by various components have been determined, stress (strain) analysis techniques are employed to identify potential failure sites and to provide inputs to damage analysis routines. Finite element modeling, as shown for an automotive wheel assembly in Fig. 5, is a particularly powerful technique for early design studies. Three high stress areas, with the associated stress excursions during one wheel revolution, are indicated in the figure. Component sizing and material selection exercises can be carried out using this information. When prototype hardware becomes available, such studies also assist in strain gage placement for experimental verification of component performance.

MATERIAL PROPERTIES

Materials information plays a key role in any durability analysis and has evolved over the past century from simple life diagrams, defining safe ranges of operating stresses, to detailed portrayals of a material's resistance to fatigue crack initiation and propagation as well as complete cyclic constitutive relations for use in structural analysis. As indicated in Fig. 6, modern material characterization methods include strain cycling of smooth specimens, to obtain cyclic deformation relations and life curves for damage analysis, and cycling of precracked specimens to obtain crack growth rates as a function of stress intensity range.

The lack of availability of materials data and properties in readily accessible data bases remains a serious problem and continues to restrict the wide-spread use of the newer life prediction methodologies. This situation is currently receiving attention and efforts are underway to develop large, central

repositories of material propery information (7, 8).

DAMAGE ANALYSIS AND LIFE PREDICTION

Armed with the necessary input information outlined in the previous section, a designer can perform a fatigue analysis using available life prediction methodologies. The features of a procedure based on local stress-strain concepts are shown in Fig. 7. Combining service loading, material and component information, the local deformation response at the potential failure location is modeled. Individual events are then identified for which damage is assessed, summed, and a lifetime estimated.

A general purpose fatigue analysis program, incorporating this methodology, has been developed for ground vehicle applications (9); a program overview is provided in Fig. 8. Program coordination is handled by a central control module that interacts with the user through a set of question and answer sets in order to compile the basic problem description file, activate the correct damage analysis, and display results. Help routines are available to assist the inexperienced practitioner in assembling information necessary for a life prediction. Finally, an extensive material property data bank, with built-in search and sort routines, and a service history data bank are available through the control module.

A more detailed portrayal of the damage analysis of a notched member is given in Fig. 9. After the local stress-strain response at the notch root is determined, individual events in the history are identified based on the occurrence of closed hysteresis loops for which a strain range and a maximum stress can be determined. A parameter based on these values is then used in conjunction with the appropriate material life curve to assess damage which is summed, linearly, to predict initiation life. Crack growth predictions are based on stress intensity factors, determined from the local stress-strain analysis, used with material crack growth curves. The program also provides a variety of graphical outputs as will be demonstrated in the next section.

APPLICATIONS

Fatigue analyses can be effectively employed at various stages in a product design cycle. Of particular value is the ability to perform design studies prior to prototype development. The combination of finite element and damage analysis routines allow a designer to carry out a wide variety of "what if . . ." scenarios that can often reduce the number of prototype iterations.

At later stages, experimental data from instrumented prototype hardware can be quickly analyzed to identify marginal designs, or material choices, without having to perform extensive testing.

Finally, such tools can be used during validation testing, to project service performance based on early durability results, and in developing and interpreting accelerated laboratory simulation tests.

Example outputs from the durability analysis of an induction hardened transmission shaft are shown in Figs. 10 and 11. Because of the existence of hardness gradients and residual stresses resulting from component processing, it is necessary to consider both surface and subsurface behavior in such problems. Figure 10 represents a computer stress-strain simulation of the surface of the shaft under a prescribed durability history. The simulation was run both without and with a compressive residual stress; the fatigue life was projected to be about a factor-of-three to -four longer with the residual stress.

In Fig. 11 is shown a simulation of the material at the case:core interface for the same history; the history is represented in the form of a strain range-mean-occurrence plot to the left. Because of the much lower interior hardness, the subsurface response displays considerable plasticity and, in fact, failure would be expected to occur here. This plastic deformation would also lead to relaxation of the surface residual stresses. Performance improvements could be realized by deepening the case.

Shown above the strain-occurrence plot is a related plot indicating the percent of total damage associated with each strain level. This information is of use in setting up accelerated laboratory simulation tests for product evaluation and quality control. Because, in this instance, the bulk of the damage is associated with the largest strain levels, a great deal of cycle compression is possible. That is, the measured service history of over 100,000 events can be reduced to a few hundred events in the laboratory with little effect on life.

As demonstrated in the previous example, component processing can have major effects on fatigue performance. Formed sheet metal parts provide another case in point. Computer modeling of forming operations is finding increased application and, because of similar methodologies, provides an opportunity for a coordinated approach to design and manufacturing. The concept is shown in Fig. 12 using a finite element model of a wheel spider. If the strain path information from the forming analysis were accessible, it could be incorporated into a subsequent fatigue analysis allowing the material properties to be suitably altered to account for the prior deformation. In general, the complete processing history of a component must be considered in order to reliably assess its expected service performance.

A final example of fatigue analysis, again using an automotive wheel assembly, is shown in Fig. 13. Here usage spectra obtained

from a cross-section of customers are displayed as bending moment - frequency of occurrence distributions for various percentile drivers. Wheel bending moments have been normalized to the levels obtained by a professional driver (100%). These usage profiles were combined with finite element results, relating applied moment to local wheel stresses (Fig. 5), to obtain fatigue life estimates for different percentile loading profiles. Results of this analysis, plotted on probability scales on the right, provide indications of the expected service performance of this component. Two candidate steels are compared using both mean and lower bound properties. Such calculations provide a convenient way to incorporate both material and usage variability in design analysis.

FUTURE TRENDS AND NEEDS

It is clear that the continuing development of a wide variety of computer-based design, analysis and testing aids is having a major impact on ground vehicle product development. A significant emerging trend for the next decade is the integration of these separate technologies into powerful engineering work station environments in which a designer, or design team, will have ready access to the complete spectrum of analysis capabilities. Since mechanical durability issues remain a prime concern, fatigue methodology can be expected to play a crucial role in these activities.

With this integration into computer networks, the development of more systematic design philosophies can be anticipated. For example, decision path guidelines, to assist engineers in choosing and applying appropriate tools at particular points in design evolution, are becoming available. In this regard, the computer becomes a natural repository for all information and experience attained in a design exercise. This provides a growing technical data base that should aid greatly in refining and optimizing future designs in a minimum of time.

The most pressing need now is for the packaging of currently available technology into easily used computer routines that can be included in large libraries of design aids - i.e. getting into the hands of the designers what we already know. The fatigue program described is a first attempt to provide ground vehicle engineers with the latest developments in material and stuctural fatigue methodology in an interactive, self-instructive package. Results to date have been encouraging; a number of engineering groups are using the routines for problem solving with little or no assistance.

It has further become evident that such a program, in addition to analysis capabilities, provides unique educational opportunities; it can serve as an effective teaching resource for engineers, or students, with limited experience in fatigue

analysis. By having to carefully define the various problem solution components, the user gains an appreciation for the nature of fatigue analysis procedures. Further, the variety of graphical outputs available provides useful portrayals of the physical realities of a particular problem and also serve to alert the engineer to the sensitivity of fatigue calculations to relatively minor variations in input data. These features help to insure against the use of such a tool as a "black box" device.

In the longer term, a number of further developments and refinements can be envisioned. Examples include:

- improved methods for handling the multiaxial stress-strain fields commonly encountered in structures
- improved crack growth models incorporating plasticity and spectrum loading effects
- libraries of stress intensity solutions for use with finite element analyses
- extensive crack growth data bases for automotive materials
- development of damage and failure criteria for advanced materials such as ceramics and composite systems (particularly at elevated temperature)
- improved methods for predicting the durability of welds and adhesively bonded joints.

As this technology becomes available, it can be easily incorporated into existing program architecture, thus further extending analysis capabilities.

REFERENCES

(1) Landgraf, R. W. and Conle, A., "Trends in Assuring the Mechanical Durability of Automotive Structures," Proceedings, XX FISITA Congress, P-143, SAE, Warrendale, PA, 1984, pp. 4.124-4.130.

(2) Bickerstaff, D. J., Birchmeier, J. E. and Tighe, W. R., "Overview of Design Approaches for Optimizing Fatigue Performance of Suspension Systems," Proceedings, SAE Fatigue Conference, P-109, SAE, Warrendale, PA, 1982, pp. 1-10.

(3) White, K. J., "The Road Simulator - A Practical Laboratory Approach," Prediction and Simulation of In-Service Conditions, IMechE Conf Publ. 1985-5, Inst. Mech. Engrs., London, 1985, pp. 69-80.

(4) Socie, D. F., Shifflet, G. and Berns, H. in Service Fatigue Loads Monitoring, Simulation and Analysis, ASTM STP 671, ASTM, Phila., 1978.

(5) Schaefer, R. A., Transactions, Soc. Auto. Engrs., Vol. 91, Sect. 3, 1983, pp. 2761-2771.

(6) Birchmeier, J. E., "Computer Simulation of Nonlinear Vehicle Response to Generalized Road Inputs at Ford Light Truck," Proceedings, Fifth Int'l. Conf. on Vehicular Structural Mechanics, P-144, SAE, Warrendale, PA, 1984, pp. 161-176.

(7) Kaufman, J. G., Standardization News, STDNA, Vol. 14, No. 2, 1986, pp. 28-33.

(8) Landgraf, R. W. and Conle, F. A., "Material Property Data: A Ground Vehicle Perspective," Materials Property Data - Applications and Access, MPD-Vol.1/PVP-Vol.111, ASME, New York, 1986.

(9) Conle, A., and Landgraf, R. W., "A Fatigue Analysis Program for Ground Vehicle Components," Proceedings, SEECO '83, Int'l. Conf. on Digital Techniques in Fatigue, Soc. Environ. Engrs., London, 1983, pp. 1-28.

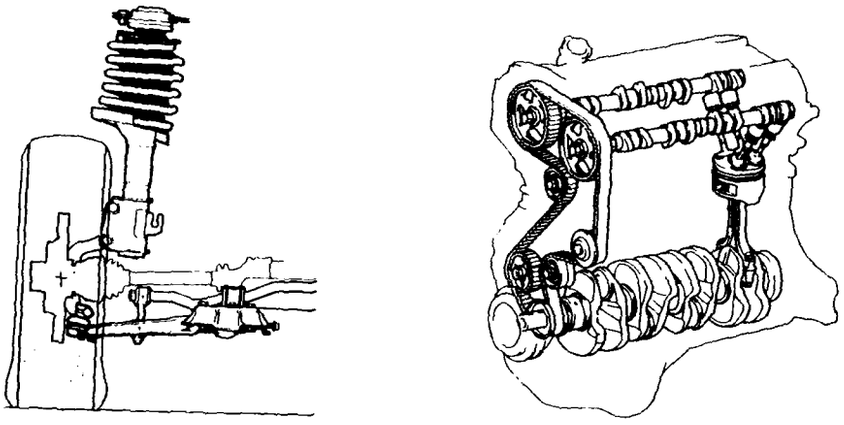

Suspension

Engine

Figure 1 Examples of fatigue critical componentry

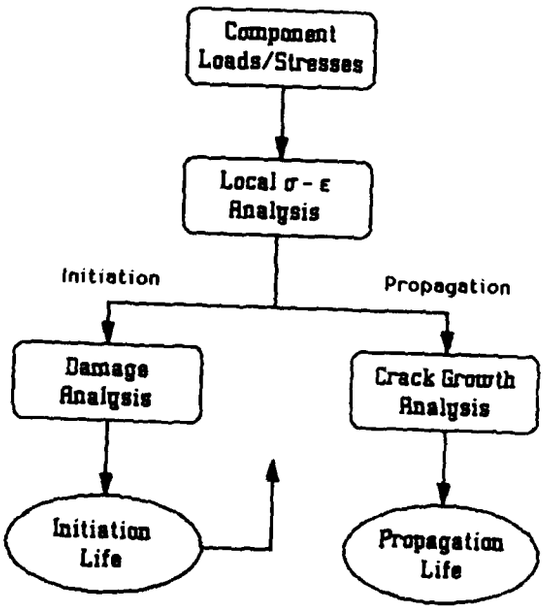

Figure 2 Steps in performing a fatigue analysis

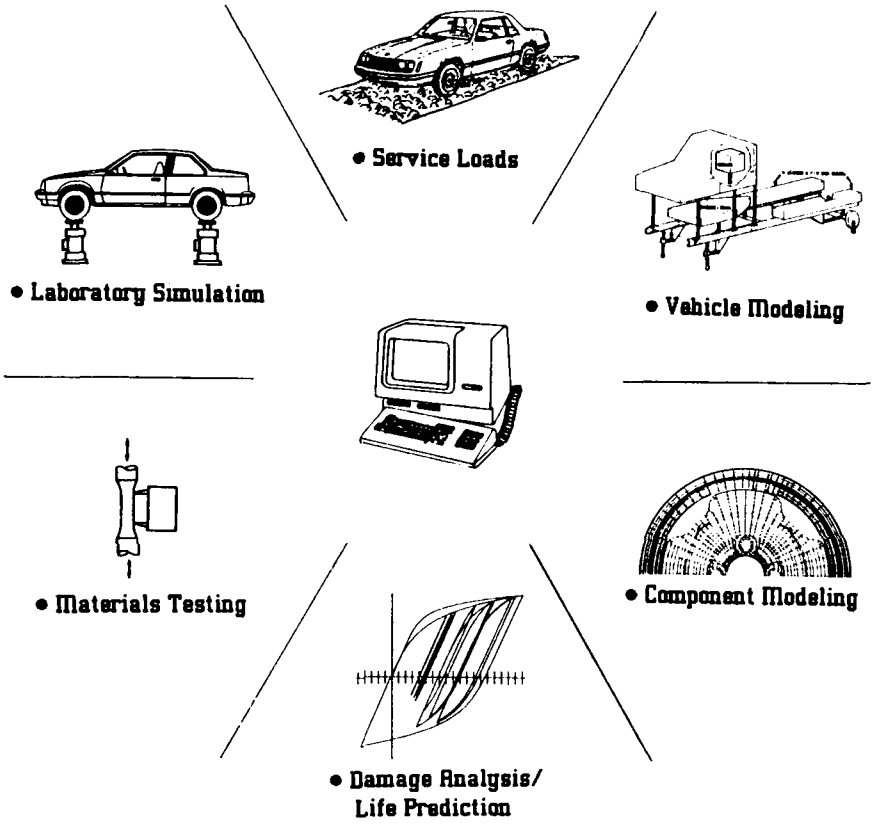

Figure 3 Durability assurance technologies

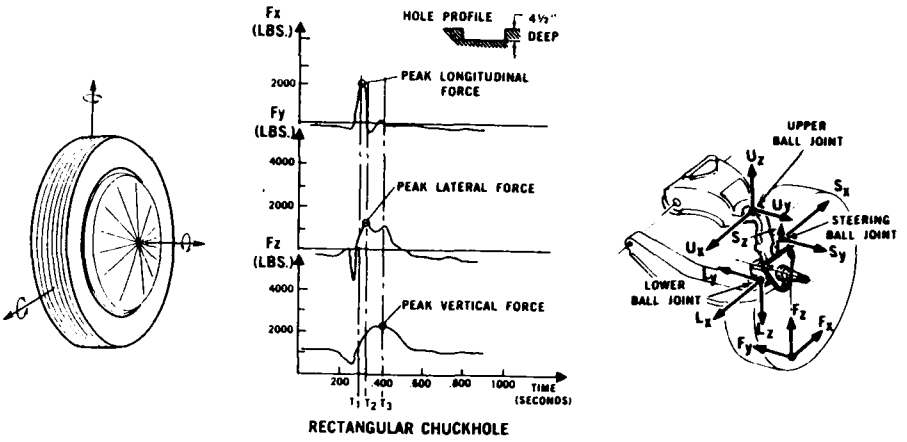

Figure 4 Wheel force transducer measurements

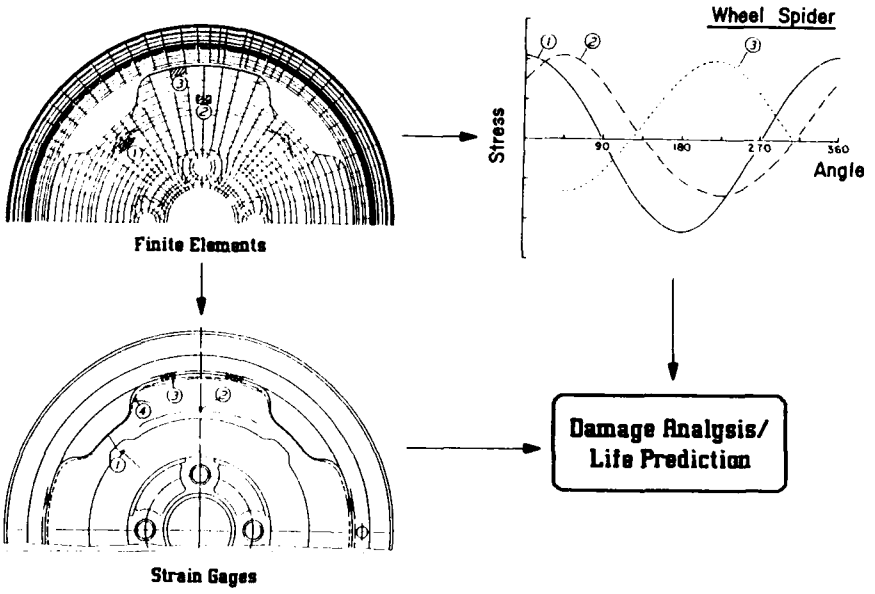

Figure 5 Component analysis by finite elements and strain gages

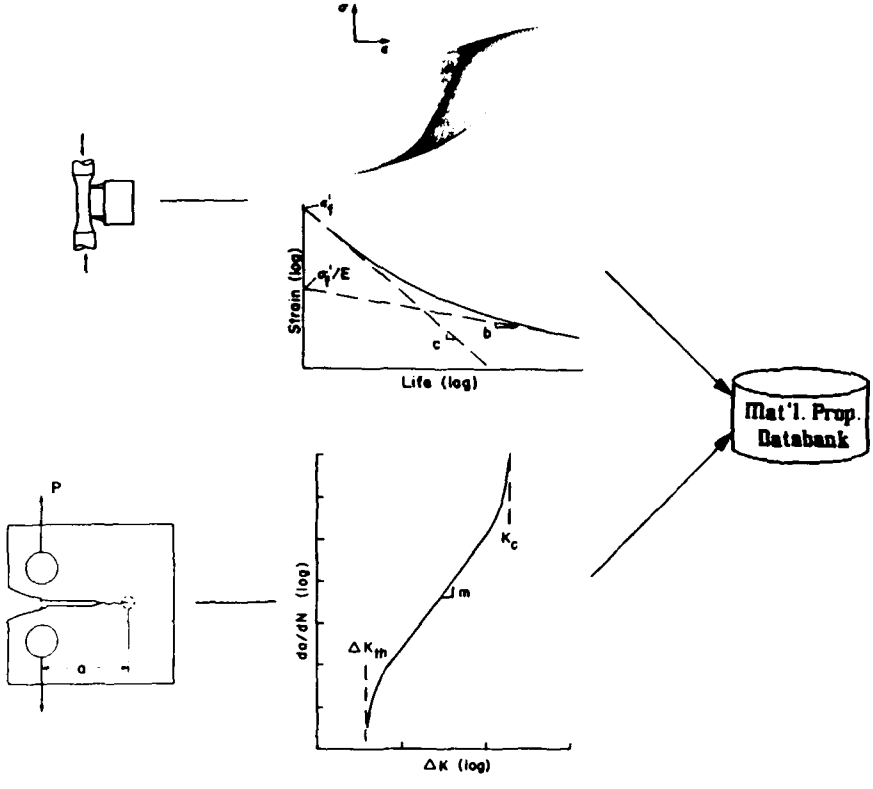

Figure 6 Materials information for fatigue analysis

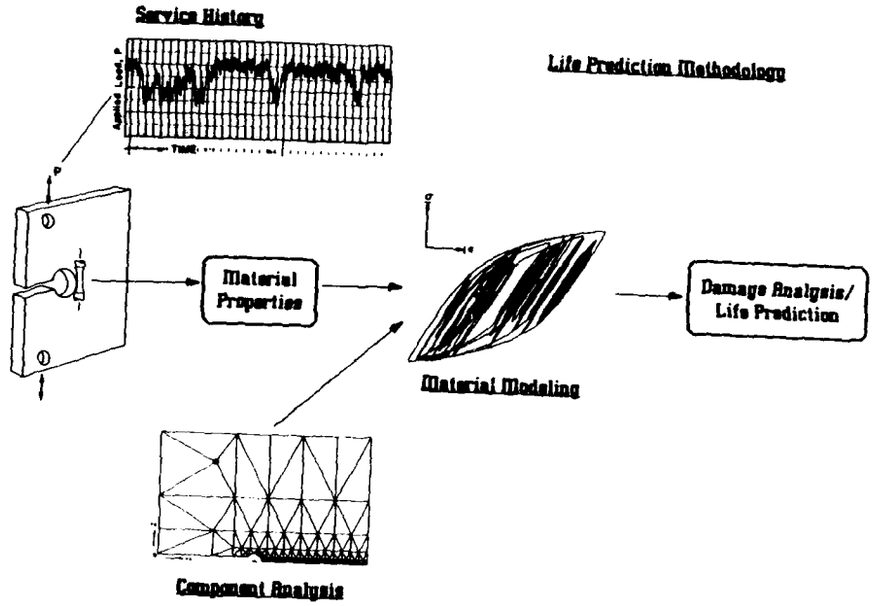

Figure 7 Local stress-strain fatigue methodology

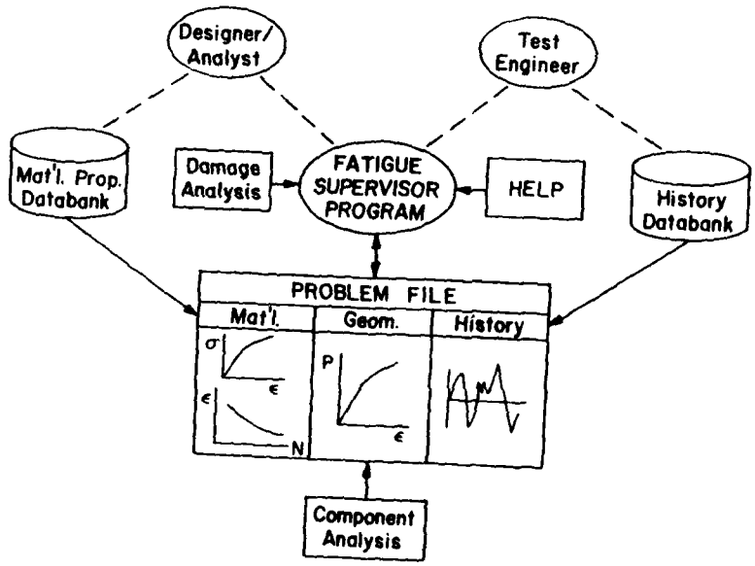

Figure 8 Features of general purpose fatigue analysis program

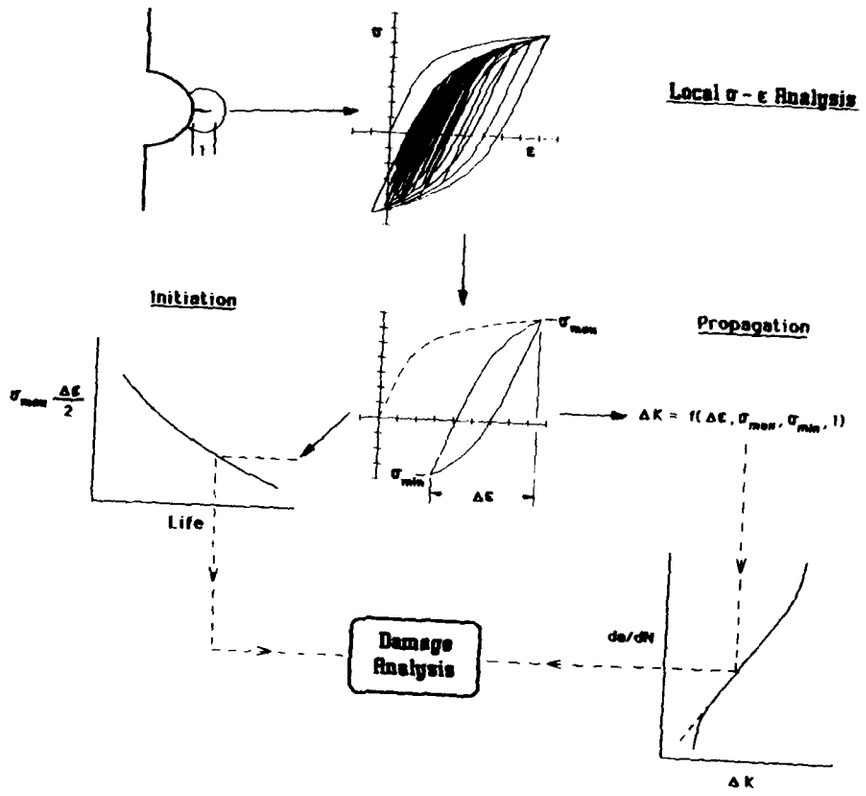

Figure 9 Details of local stress-strain and damage analysis

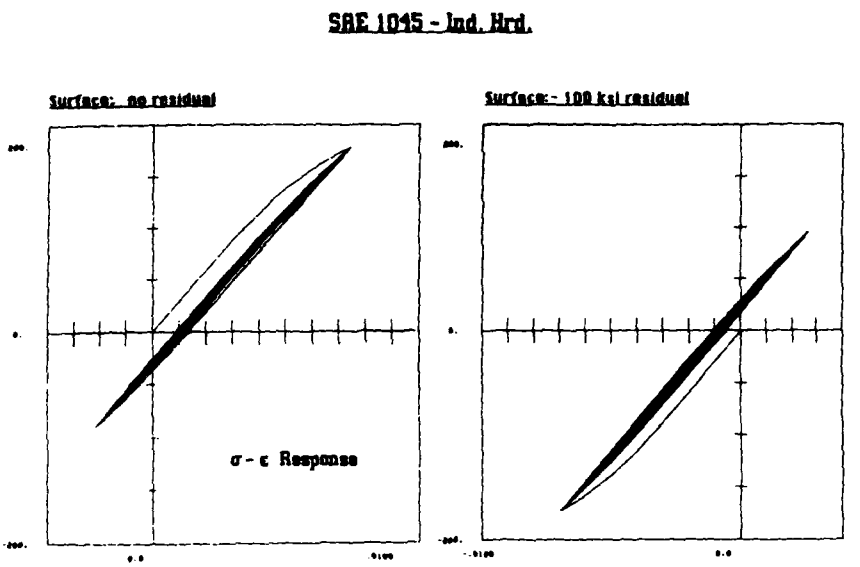

Figure 10 Stress-strain simulation of shaft - surface

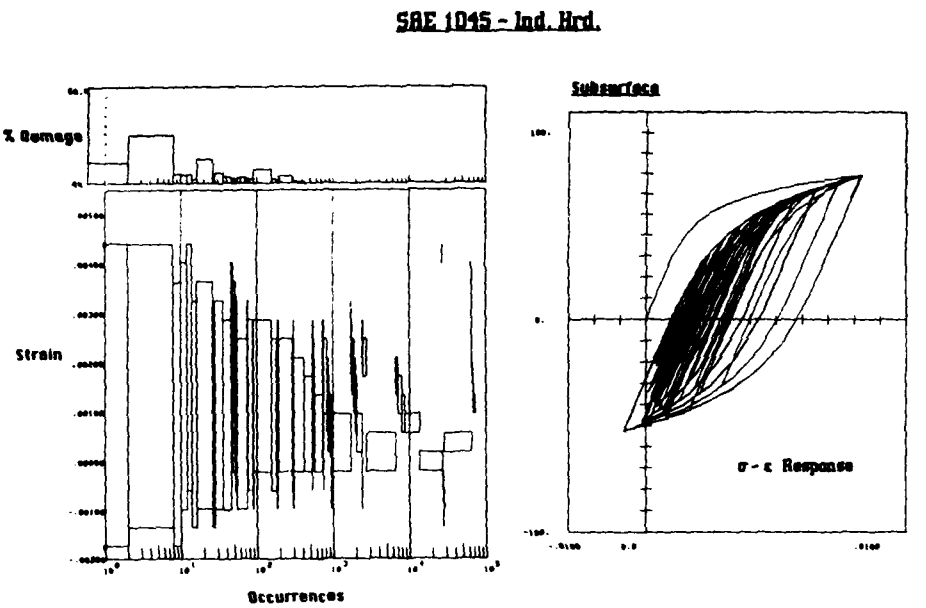

Figure 11 Stress-strain simulation of shaft - subsurface

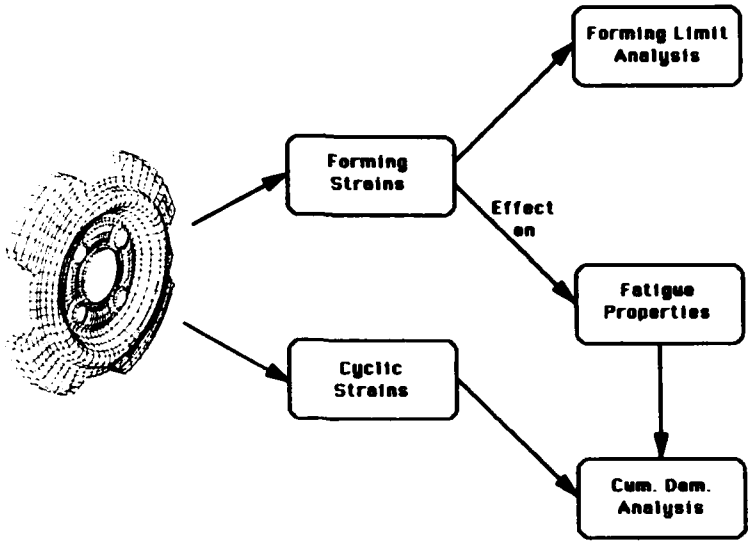

Figure 12 Technique to account for forming effects on fatigue

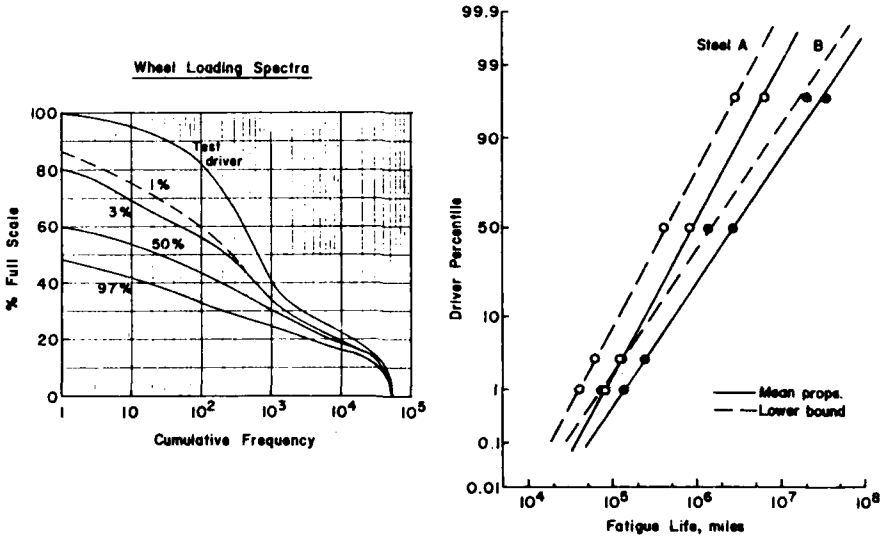

Figure 13 Fatigue analysis of a wheel assembly

FATIGUE CRACK GROWTH

C.J. Beevers*

In broad terms the paper considers the growth of both small and long fatigue cracks in a range of engineering metals and alloys. Both intergranular and transgranular modes of small crack growth in aluminium alloys are reported and analysed. The relationship between small and long crack growth are considered and these lead to the conclusion that the ΔK_{eff} curve for long cracks can present an upper bound range of growth rates for both small and long cracks when the crack length is greater than the grain size or the basic microstructural element.

INTRODUCTION

There is a continuing requirement to improve our understanding of the damage which results from the cyclic loading of materials, components and structures.

Whilst definitive progress has not always been achieved, there is now available a wide range of information on such topics as fatigue crack growth rates, fatigue thresholds, the influence of variable amplitude loading, environmental effects and to some extent the area of small crack behaviour.

In the following sections some recent observations from our laboratory are presented in the context of the more general advances which have been achieved in recent years.

The fatigue crack growth process involves many interactive processes but can be considered in terms of two major components ΔK^i and ΔK^c. If the crack extension process can be represented in terms of a crack growth rate da/dN which responds to a driving force ΔK then the applied or global ΔK may have two components ΔK^i and ΔK^c. ΔK^i is the intrinsic component and is concerned with the crack tip and the creation of new fatigue fracture surfaces. Microstructure, slip character and environment play a significant

* Department of Metallurgy and Materials,
University of Birmingham, Birmingham, B15 2TT, U.K.

role in determining the magnitude of ΔK^i, in relation to particular growth rates. The extrinsic component ΔK^c is a reflection of the interactions which develop between fatigue fracture surfaces and the extent to which this leads to load transfer and modification of the stress fields in the crack tip region. This load transfer can result from the development of microstructural or oxide induced asperities, hydrodynamic wedging of the crack faces and the formation of an extended plastic wake leading to plasticity induced crack closure. The specific behaviour of a range of engineering metals and alloys will be considered in the following sections and fatigue crack growth response will be examined in terms of both the extrinsic and intrinsic contributions to fatigue crack growth.

FATIGUE CRACK GROWTH IN LOW ALLOY STEELS

A study of the fatigue crack growth characteristics of a quenched and tempered low alloy steel, En 19, revealed several features relating to the source and magnitude of crack closure, fatigue threshold hysteresis and the relationship between long and small crack behaviour. The low alloy steel was oil quenched from 900°C and tempered at 550°C to produce a fully tempered martensitic structure with a yield stress of ∿1020 MPa. Tests on three point bend specimens (20 mm by 50 mm by 250 mm) were carried out at 19°C at a frequency of 100 Hz with an R ratio in the range 0.1 to 0.7 and in a laboratory air environment with a relative humidity of 60%. In any one test the R ratio was kept constant but load shedding and load increments were applied to approach and depart from the threshold region. Strain gauge attached close to the crack tip region were used to obtain load-displacement curves and a measure of the fatigue crack closure present during test.

The results of such tests are illustrated in Figure 1 and show the expected R ratio dependence of both fatigue crack growth rates and fatigue thresholds. The data also shows a considerable difference between the approach and departure from threshold. The results from test T2 (T2 refers to the test number not to the temper condition) where crack closure measurements were made are presented in Figure 2. The results indicate that the R ratio effect and the fatigue threshold hysteresis can be attributed to the occurrence of fatigue crack closure. From previous studies (1, 2, 3) crack closure would be expected to result from the presence of microstructural or oxide originated asperities. Examination of the surface of the test specimens prior to final fracture revealed the extent of oxide build up during test.

The illustrations in Figure 3 show the build up of oxide debris for the R = 0.3 test and its absence in the R = 0.7 test. A more detailed examination of the surface revealed the results shown in Figure 4. Extensive oxide debris was present on the specimen surface and substantial agglomeration of the oxide had occurred to result in oxide nodules which were in close proximity to the fatigue fracture surfaces. The implication of Figures 3 and 4 is

that extensive non mode I crack face interactions occurred during the tests leading to continued oxide generation and nodule formation. The squeezing of the oxide between the fatigue fracture faces is an indication of the low strength and rigidity of the freshly formed oxide. The oxide only becomes an effective load transfer medium following substantial compaction to create the nodule form of the oxide (Figure 4).

The essential features of fatigue crack closure models (4,5) is that load transfer occurs behind the crack tip as a consequence of the presence of rigid asperities. The present observations show that the crack faces were kept apart both close to and well behind the crack tip. In view of the general trend to measure closure forces via clip gauges or back face strain gauges away from the crack tip the effects of load transfer along the crack path may well be worthy of further consideration.

The threshold hysteresis is characteristically observed when extended load cycling is carried out in the threshold region, usually with a view to establish ultra low fatigue crack growth rate behaviour. Subsequent to this activity substantial load increments can be required to effect further fatigue crack growth. A scanning electron micrograph of the crack tip region where threshold hysteresis had occurred is presented in Figure 5. The development of these nodules can explain the form of the results in Figures 1 and 2 where ΔK_{th} was raised from $\sim$6 $MNm^{-3/2}$ to $\sim$8 $MNm^{-3/2}$ by increases in the fatigue crack closure contribution to ΔK_{th}.

Small crack tests were carried out on the En 19 steel with prior austenite grain sizes of 10 and 40 μm. The specimens (36 mm by 15 mm by 3 mm) were subjected to three point bending at room temperature with R = 0.1 and at a frequency of $\sim$100 Hz. Results for long crack growth in compact tension specimens for En 19 with a 10 μm prior austenite grain size and at an R ratio of 0.1 and 0.7 are included in Figure 6. The small crack data showed a widespread of growth rates for both the 10 and 40 μm prior austenite grain size material. The growth rates of the small cracks exhibited rates both faster and slower than the R = 0.1 long crack curve but with one or two exceptions, were contained by the R = 0.7 or ΔK_{eff} curve. Detailed examination of the specimen surfaces revealed inter-lathe separation to be a dominant feature of the fatigue crack growth process.

The data points lying outside the R = 0.7 curve resulted from crack growth in particularly large prior austenite grains with extended lathe formation. Thus where the crack length was greater than the prior austenite grain size the R = 0.7 or ΔK_{eff} curve represented an upper bound range of values for growth of both small and long cracks.

In contrast to the long crack observations in Figures 3 and 4 there was no evidence of oxide formation on the specimen surfaces or on the fatigue fracture surface of the contained (semi-elliptical) small crack specimens.

SMALL FATIGUE CRACKS

Substantial improvements in the understanding of small fatigue crack characteristics have been achieved over the past five years (6, 7, 8). The overall programme has undoubtedly provided substantial benefits in terms of the development and selection of new materials and the assessment of component reliability.

Some recent developments in the small fatigue crack area are outlined below. The small fatigue crack is often represented schematically as shown in Figure 7a. In this case the primary variables are presented as crack growth rate da/dN and ΔK. A fatigue crack growing in a single grain can be retarded or arrested at a grain boundary. The presence of fatigue cracks with substantial growth rates can be attributed to failure associated with intermetallics or inclusions. The view of small crack behaviour can be extended to a more general statement as illustrated schematically in Figure 7b. This view is based on the observations of small fatigue cracks in a Astraloy, a powder route nickel base superalloy. Small pores (5-10 μm) were the source of fatigue crack initiation (Figure 7c). The cracks grew in a shear mode from the pore for 1 to 2 μm and subsequently grew as a dominantly Mode I crack through the rest of the grain. With a grain size of 50-100 μm it was possible to monitor in detail the growth of individual cracks. At a distance of the pore diameter away from the pore surface the cracks exhibited increasing growth rates before retardation or arrest occurred at the grain boundary. The observations in Figure 7 provide an example of this behaviour in nickel alloys and a more detailed study in a wider range of materials is clearly desirable. As the tendancy to more homogeneous, high strength nickel and titanium alloys develops a more detailed understanding of the early stages of small crack growth becomes more desirable.

The small crack growth characteristics of a range of alloys have been studied. Three point bend specimens (36 mm by 15 mm by 3 mm) were subjected to cyclic loading at 19°C, with R = 0.1 and a test frequency of 100 Hz. The details of the mechanical properties and maximum cyclic stress are presented in Table 1. Detailed metallographic studies showed that the α/β titanium alloy (Ti 6Al 4V) and the aluminium alloy (a mechanically alloyed Mg/Li alloy) exhibited transgranular crack growth. The low alloy steel exhibited a fatigue crack growth process based on inter-lathe separation. The 18, 4, 1 bearing steel (18W 4Cr 1V) has a tempered bainite matrix with substantial carbides up to 40 μm in diameter. The fatigue crack growth in the bearing steel tended to be dominated by cracking associated with the carbides.

TABLE 1 - Mechanical Properties of Materials: with Fatigue Data Presented in Figure 8

Material	Yield Stress σ_y MPa	Youngs Modulus E GPa	Maximum stress in the load cycle MPa
Bearing Steel	2,200	286	680
Low Alloy Steel	1,080	200	810
α/β Titanium Alloy	950	115	860
Aluminium Alloy	490	79	500

The data obtained from testing these four materials is presented in Figures 8(a-c). The fatigue crack growth rate da/dN is presented as a function of a, ΔK and $\Delta CTOD$. The value of "a" was determined from replica observations where the surface breaking crack length was designated 2a. The value of $\Delta CTOD$ was obtained from the relationship

$$\Delta CTOD = \frac{\Delta K^2}{2E\ \sigma_y}$$

where $\Delta K \simeq \Delta\sigma\ 1.2(\pi\ a)^{\frac{1}{2}}$

It was initially thought that the large range in yield stress 490 MPa to 2,200 MPa would result in relatively wide ranges of response for both growth rate and thresholds of these small cracks. The data in Figure 8a and 8b show no marked trend in the results when presented in terms of 'a' or ΔK. The results in 8c show that the bearing steel exhibits higher crack growth rates for a particular $\Delta CTOD$ than the low alloy steel or α/β titanium alloy. This result is consistent with a crack growth mode dominated by the cracking associated with the massive carbides in the bearing steel.

In the absence of substantial closure contributions to ΔK_{th} for small cracks do we have to accept an upper bound of 3-4 $MNm^{-3/2}$ for ΔK_{th} or can this be substantially improved by manipulation of micro or macro structure?

INTERGRANULAR SMALL CRACK GROWTH

The observations to be presented in this section were obtained from a study of a high purity Al 4.5% Cu alloy cast and rolled under controlled laboratory conditions. In the solution treated,

quenched and aged condition, a TEM study showed that a precipitate free zone and elongated θ precipitates were associated with the grain boundaries. With a grain size of 40–100 μm the peak aged strength was ∿280 MPa.

Fatigue crack growth studies were carried out on plane bar specimens (6 mm by 15 mm by 36 mm) using three point bending at an R ratio of 0.1 and at a frequency of ∿100 Hz in laboratory air. The application of a cyclic stress resulting in a maximum surface stress of 80% of the tensile yield stress produced intergranular cracks in the range 5 to 50 μm in $\sim 10^5$ cycles.

For over 30 specimens tested and examined the initiation and growth of small fatigue cracks was dominantly intergranular in character. Detailed studies showed that the intergranular fatigue cracks were retarded and arrested like their transgranular counterparts but the processes involved were somewhat different. Three distinct retardation and arrest procedures were observed for intergranular small cracks. a) The interaction with a large inclusion located on the grain boundary, b) by the approach of the crack to a triple point and c) the change of crack mode from intergranular to transgranular. These features are illustrated schematically in Figure 9(A, B and C). The initial crack in Figure 9A is retarded by the approach to the inclusion and triple point in Figure 9B. The inclusion and the triple point offer resistance to the slip accommodation required for crack extension. In Figure 9C the crack has been retarded at the second triple point and has also undergone a transition from intergranular to transgranular crack growth. The change in the mode of crack growth accompanied by a substantial change in crack growth direction can lead to crack closure. An example of an arrested crack which has changed from an intergranular to a transgranular mode of growth is illustrated in Figure 10. An example of such an intergranular-transgranular transition as viewed on the fatigue fracture surface is shown in Figure 11.

As the contained crack developed from the surface the extent of transgranular failure increased. Examples of ductile and brittle striation formation are presented in Figure 12.

Long fatigue crack growth and threshold studies were carried out on the Al 4.5% Cu alloy using compact tension specimens. The fatigue crack growth mode was dominantly transgranular and similar in character to observations for small contained cracks in Figure 12.

The results from an R=0.1 test on the Al 4.5% Cu alloy and the small crack data are presented in Figure 13. The results show that the small cracks exhibited a wide range of growth rates but that the ΔK_{eff} curve offered a range of upper bound growth rates for both the small and long crack response of the aluminium alloy.

THE SMALL-LONG CRACK RELATIONSHIP

Small cracks can exhibit growth rates substantially lower than their long crack counterparts. The data presented in Figures 14 and 15 refers to two mechanically alloyed aluminium alloys where small contained crack growth data is compared with long crack data obtained from CT tests. In the In9021 alloy significant oxide induced closure occurred whilst in the In9052 there was no detectable closure.

The mechanically alloyed aluminium alloys exhibit good resistance to the initiation of fatigue cracks and as a consequence the small crack growth was only obtained with surface stresses approaching the yield stress. As a consequence substantial plasticity was observed in association with the small cracks. The resultant plasticity dominated closure of the small cracks produced growth rates for the small contained cracks substantially lower than for the long crack counterpart. In the In9021 alloy the long crack closure was more effective than the plasticity induced closure in the small cracks. In both cases the ΔK_{eff} curve presented an upper bound range of growth rates for both small and long cracks.

The results in Figures 16 and 17 show the relationship between small and long crack growth in two titanium alloys (9, 10). The results for the Ti 6Al 4V alloy show that the small crack growth rates lie close to the ΔK_{eff} curve. For the IMI 685 which had a coarse grain size and was tested at relatively high stresses, the small crack growth rates were substantially higher than the long crack data.

In the preceding parts of this paper results have been presented regarding the relationship between small and long crack growth behaviour for a range of metals and alloys. The low alloy steel with a quenched and tempered microstructure exhibited a dominantly inter-lathe separation mode of crack growth, the aluminium 4.5% copper alloy exhibited intergranular small crack growth and the mechanically alloyed aluminium and titanium alloys had a dominantly transgranular mode of separation. These results combine to suggest that in circumstances where the small crack is larger in size than the basic microstructural unit then the long crack ΔK_{eff} curve provides an upper bound range of growth rates for both small and long cracks.

THE EVALUATION OF FATIGUE DAMAGE ASSOCIATED WITH FASTENER HOLES

This section presents information about the development and application of an eddy current method for monitoring fatigue at holes. In particular, it brings together the results of small crack growth in microstructurally [illegible] non-destructive eddy current techniques.

AD-A184 047 FATIGUE '87 VOLUME 3(U) VIRGINIA UNIV CHARLOTTESVILLE SCHOOL OF ENGINEERING AND APPLIED SCIENCE 6/6
R O RITCHIE ET AL. JUN 87 ARO-24134.3-MS-CF
UNCLASSIFIED N00014-87-G-0008 F/G 20/11 NL

END
DATE FILMED
8 87

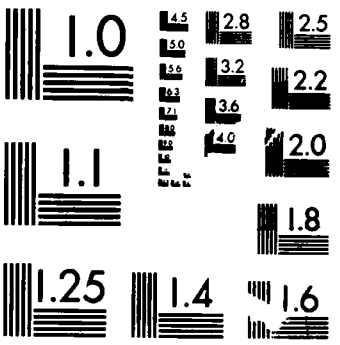

MICROCOPY RESOLUTION TEST CHART
NATIONAL BUREAU OF STANDARDS-1963-A

component-related test pieces to be continually assessed for the development of fatigue damage under the action of uniform and random loading conditions. The equipment is currently being used to measure the growth of cracks during fatigue of plate tensile specimens of aluminium alloys of length 250 mm, width 38 mm and thickness 10 mm with a 6.5 mm diameter through-thickness hole at mid-width. Cracks of the order of 0.1 mm deep and over are being measured.

The Crack Size Measurement System

A Nortec model NDT-25L eddyscope is being used in conjunction with a Nortect PS-2M probe scanner and a 1/4 inch diameter type SD-16 differential probe.

The scanner allows a probe to be rotated and translated along a hole in a helical motion or to be rotated only. The probe scanner is intended, when used in its rotation + translation mode, to enable examination of the bores of holes. The translation is 0.635 mm for each rotation but this is too great a movement for the resolution required. In consequence, the probe scanner has been mounted on a stepper-motor driven table which allows small, reproducible translational movements of the probe to be made. During inspection of a hole the scanner is run in its rotation only mode and, for each rotation of the probe, the probe body is moved on average 0.106 mm along the axis of the hole. This movement is produced by the stepper-motor driven rotation of a lead screw which moves the table. For this work, the translational movement was chosen not to be continuous over the period of a rotation but is step-wise and arranged to occur when the probe coils are at a region of the hole surface where tensile stresses are absent and cracking will not be present.

Fatigue loading has been carried out on an Amsler Vibrophore machine and an Instron servo-hydraulic machine. An Apple IIe microcomputer has been interfaced to the Eddyscope, the probe scanner, the stepper-motor driven table and the test machine to give computer control of all items of equipment. This degree of control has been utilised in the development of a fully automated fatigue test program which allows fatigue load cycling of a test specimen and the detection, positioning and sizing of cracks growing at the hole as a function of load cycles. The sizing is currently in terms of crack signal because suitable calibration data is presently being obtained. Data analysis is on-line and hard copy of the results is provided both in tabular form and graphically. Key data are stored initially on a 1 M byte RAM card within the microcomputer before being transferred to disk at the end of test. A block diagram of the experimental set-up is shown in Figure 18.

Automated Fatigue Testing

In outline, a fatigue test with the equipment involves fatigue cycling a specimen for a selected number of cycles, examining the hole for cracking with the Eddyscope and then repeating the sequence. The program for running an automatic test first requests that set-up data be input at the keyboard. This is printed out on the test record and includes the required load range and R ratio, the number of load cycles between examinations of the hole, the depth of the hole and the width and thickness of the plate. The probe must be aligned with the hole in the specimen when the specimen is first placed in the grips of the test machine.

The test starts with the probe clear of the specimen and the requested number of load cycles are performed. Fatigue loading is halted and the probe is advanced towards the hole by the stepper motor until the surface of the specimen is detected. Detection of the surface of the specimen serves as a zero point of reference for positioning cracks within the hole and for comparing signals from different scans of the hole. Whilst the probe is rotated and moved step-wise along the hole, the Y component of the Eddyscope output signal is input to the microcomputer via an A/D converter and is analysed to reveal cracks. This sequence of loading, cracking and inspection is shown schematically in figure 19. A crack is identified by the rate of change of the Eddyscope output signal, by the symmetry of the signal and by the amplitude of the signal. The crack signals during each probe rotation are stored in terms of the amplitude of the signal, the angular position around the hole and the position along the hole. When the probe has moved completely through the specimen thickness it is rapidly retracted and the key data of crack signal and position are output on the printer in tabular form. The table is separated into data for the left-hand and right hand side of the hole. The data is also presented graphically in terms of crack signal versus distance through the hole. The x and y coordinates of each point on the graphs are also printed out and stored to disk for future analysis.

Fatigue Crack Growth Data

A sequence of three graphical data outputs is shown in figure 20 for the development of cracking at a hole in a plate of 2024 T351 aluminium alloy. The remote applied stress range was 145 MPa with R = 0.1. In the initial stages of the test, more than one crack nucleated as shown by figure 20a and these then grew and merged together as shown in figure 20b. After 59000 cycles, further crack nucleation occurred between about 1 mm and 4 mm into the hole as shown in figure 20b and these new cracks then grew and

merged with the earlier ones as indicated in figure 20c. Cracking extends almost through the thickness in figure 20c with the crack intersecting one side-face. The maximum crack depth was measured after test from the fracture face to be 1.99 mm.

Clearly this innovative technique makes a significant contribution towards a further understanding of the processes involved in the early stages of crack growth. It allows a quantitative assessment of the rate of growth of an individual crack contained within the bore of a hole and also provides information on the interactions between multiple cracks. This technique has applications in the examination of damage sensitive regions associated with fastener holes and bore holes in a wide range of materials including aluminium, titanium and nickel alloys and stainless steel.

CONCLUSIONS

1) Nodules formed by the compaction of oxides formed on the fatigue fracture faces of low alloy steels can induce substantial closure effects and lead to threshold hysteresis.
2) Intergranular small cracks in aluminium alloys are observed to be retarded and arrested as a result of a) interactions of the crack with grain boundary inclusions, b) the approach of the crack to a grain boundary triple point, and c) the transition in fatigue crack growth mode from intergranular to transgranular.
3) In materials with ultra fine microstructures such as mechanically alloyed aluminium alloy the small crack growth rates can be substantially lower than their long crack counterpart.
4) In some metals and alloys where the small crack length is greater than the basic microstructural unit then the ΔK_{eff} long crack curve can offer a range of upper bound growth rates for both small and long cracks.
5) The development of fatigue damage associated with fastener holes can now be analysed in terms of crack length and shape using recent advances in eddy current techniques.

ACKNOWLEDGEMENTS

I wish to thank my research colleagues for their discussions and to acknowledge the contribution of results to the paper of Dr. L. Grabowski, Dr. P. Mulvihill, Mr. A. Tack, M. Birt and Dr. M. Halliday.

REFERENCES

(1) Walker, N.J. and Beevers, C.J. Fatigue Crack Closure in Titanium Fatigue of Engineering Materials and Structures, Vol. 1, 1979, pp. 135-148.

(2) Beevers, C.J. Micromechanisms of Fatigue Crack Growth at Low Stress Intensities. Metal Science J. 1980, pp. 418-423.

(3) Ritchie, R.O. Near Threshold Fatigue. An Overview of the Role of Microstructure and Environment. Fatigue '84, 1984, pp. 1833-1863.

(4) Beevers, C.J. et al. A Model for Fatigue Crack Closure. Engineering Fracture Mechanics, 1984, pp. 93-104.

(5) Carlson, R.L. and Beevers, C.J. Mixed Mode Fatigue Crack Closure Model. Engineering Fracture Mechanics, 1985, pp. 651-659.

(6) Ritchie, R.O. and Lankford, J. "Small Fatigue Cracks". pub. The Metallurgical Society Inc, 1986.

(7) Miller, K.J. and de los Rios, E.R. "The Behaviour of Short Cracks". pub. Mechanical Engineering Publications, London, 1986.

(8) Schijve, J. The Practical and Theoretical Significance of Small Cracks - An Evaluation. Fatigue '84, pub. EMAS, U.K. 1984.

(9) Hicks, M.A. and Brown, C.W. A Comparison of Short Crack Behaviour in Engineering Alloys, Fatigue '84, 1984, pp. 1337-1347.

(10) Hicks, M.A., Jeal, R. and Beevers, C.J. Slow Fatigue Crack Growth and Thresholds of IMI 685, Fatigue of Engineering Materials and Structures, Vol. 6, 1983, pp. 51-65.

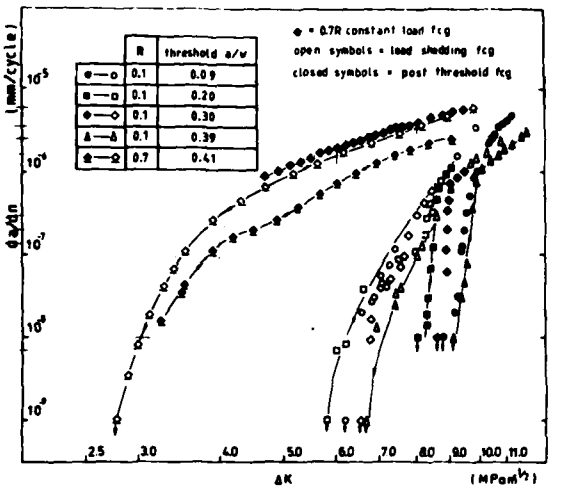

Figure 1. The influence of R ratio on the fatigue crack growth and threshold characteristics of a low alloy steel En 10

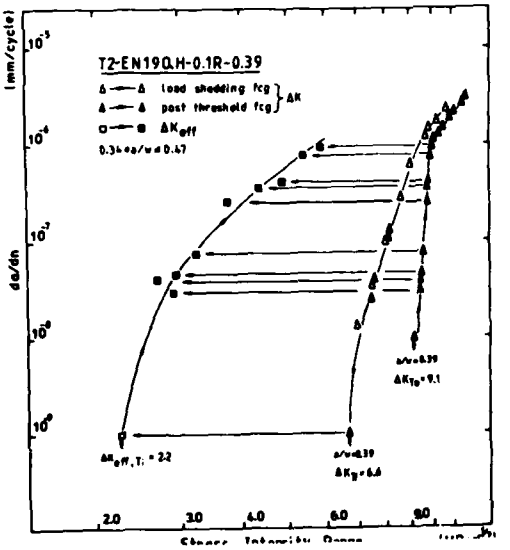

Figure 2. A ΔK_{eff} plot of the data obtained from an approach to and departure from threshold. The threshold hysteresis affect can be attributed to fatigue crack closure.

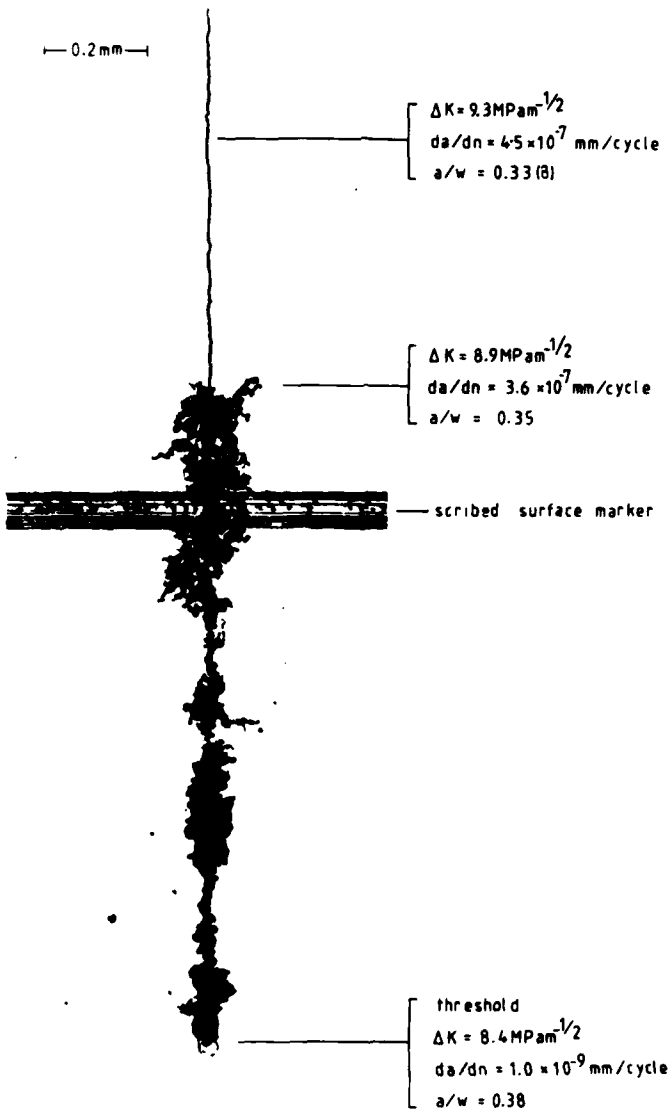

Figure 3a. A macroscopic view of the surface of an En 19 test specimen prior to final fracture shows extensive oxide debris R = 0.3.

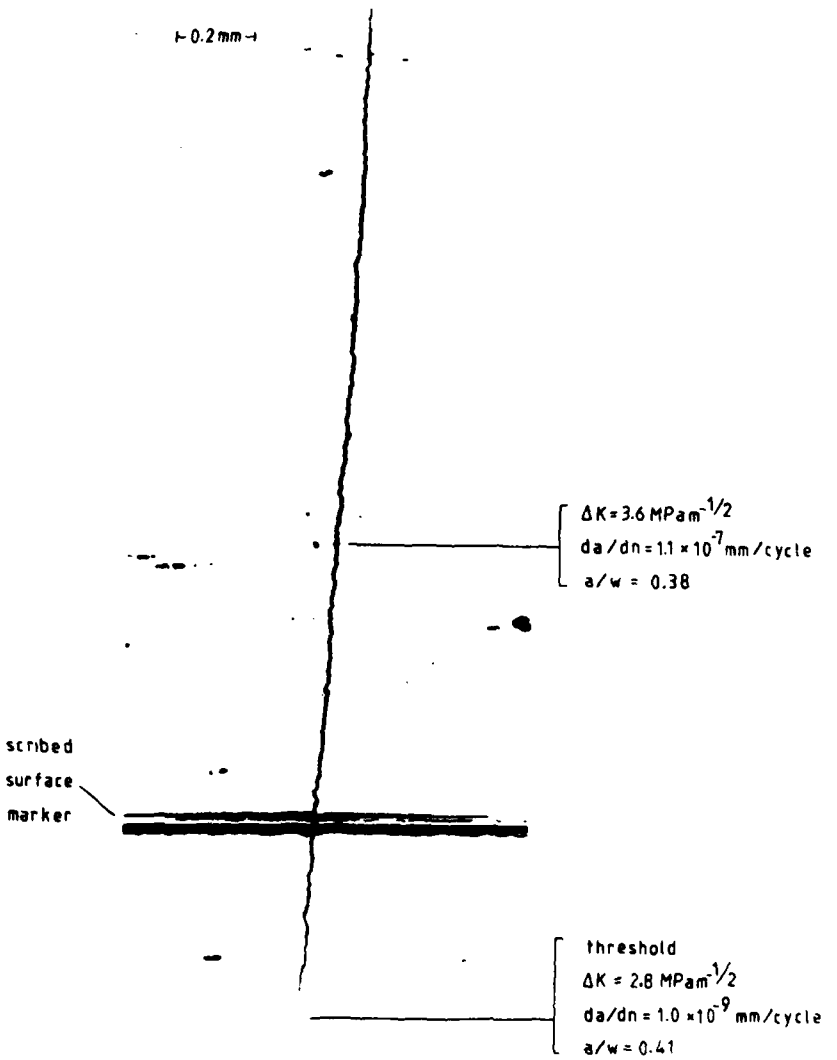

Figure 3b. A macroscopic view of the surface of an En 19 test specimen prior to final fracture exhibiting little evidence of surface debris R = 0.7.

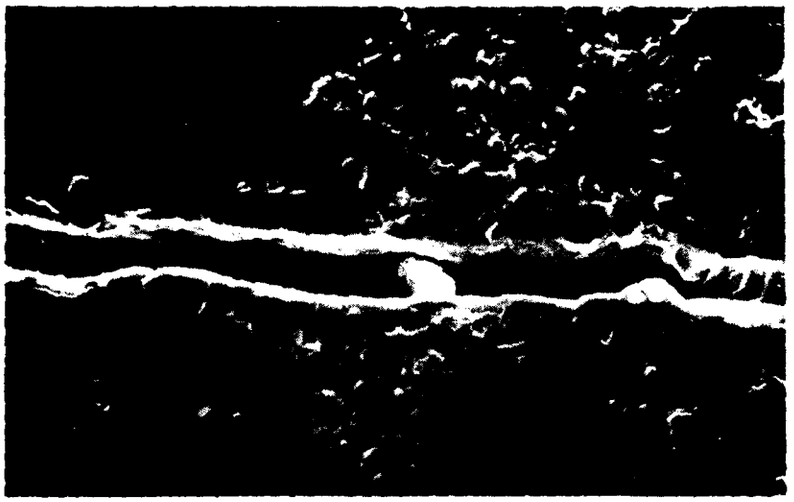

(a)

(b)

Figure 4. The distribution of oxide debris on the specimen faces and between the fatigue fracture faces of a low alloy steel tested at R = 0.3 at room temperature in laboratory air. a) x 460, b) x 5000.

Figure 5. Nodules of oxide formed in the threshold region of a low alloy steel En 19. x 2,500

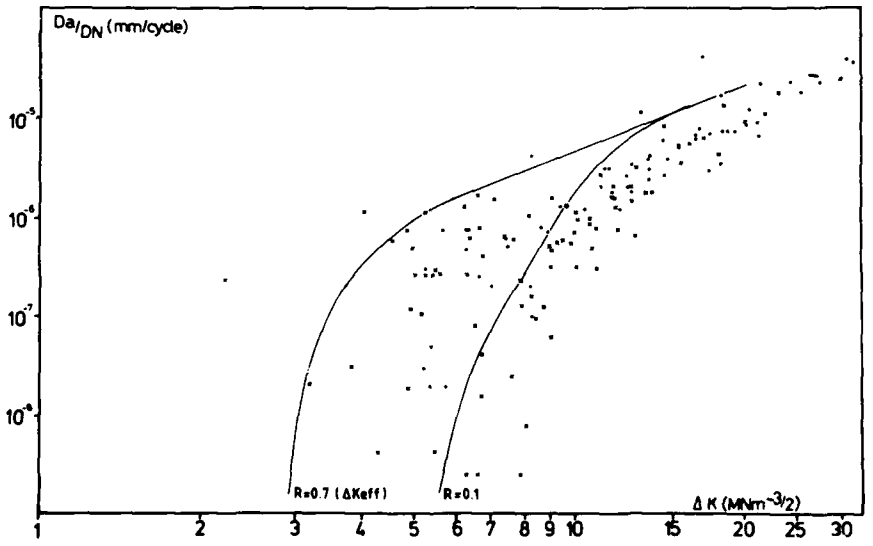

Figure 6. Data for long crack growth (solid lines) from CT tests and small cracks in a low alloy steel En 19. Prior austenite grain size + 40 μm • 10 μm

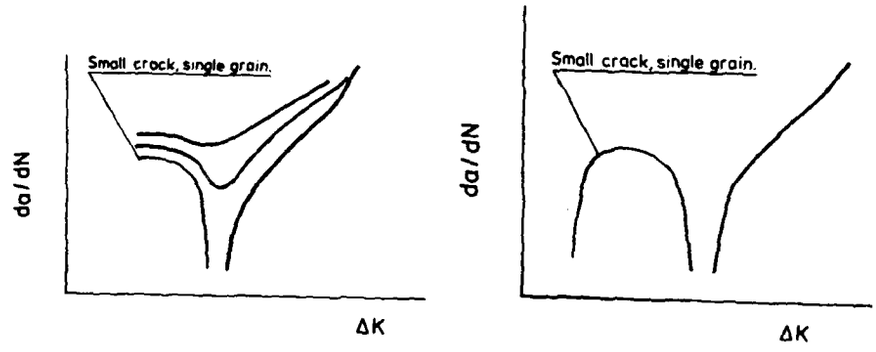

(a) (b)

(c)

Figure 7. An illustration of the growth of a small fatigue crack in an individual grain of a nickel base superalloy. Initiation from a pore was followed by increased growth rates prior to retardation at the first grain boundary.

(a)

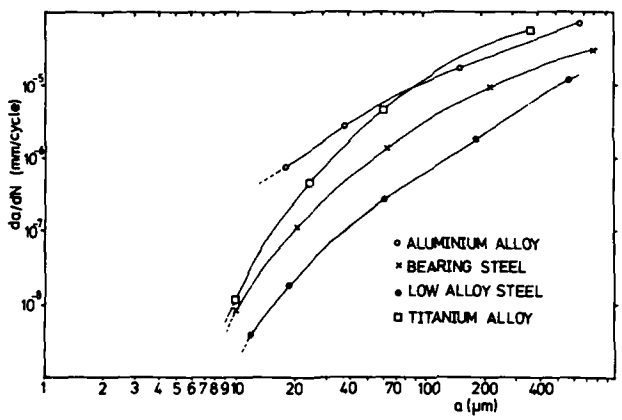

(b)

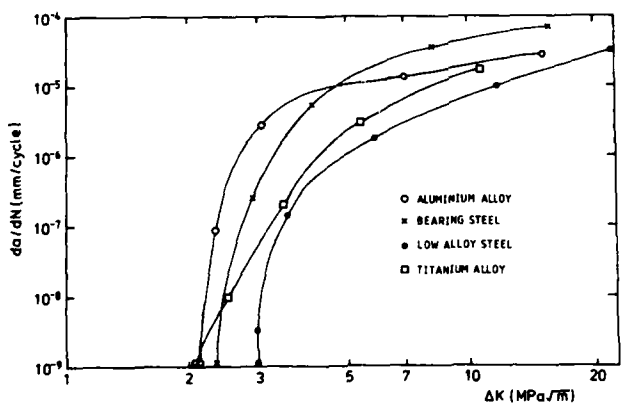

(c)

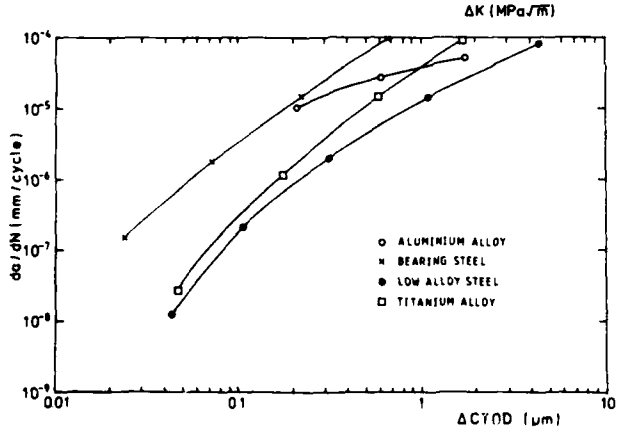

Figure 8. Data for small crack growth in a rnage of materials with proportions presented in Table 1.

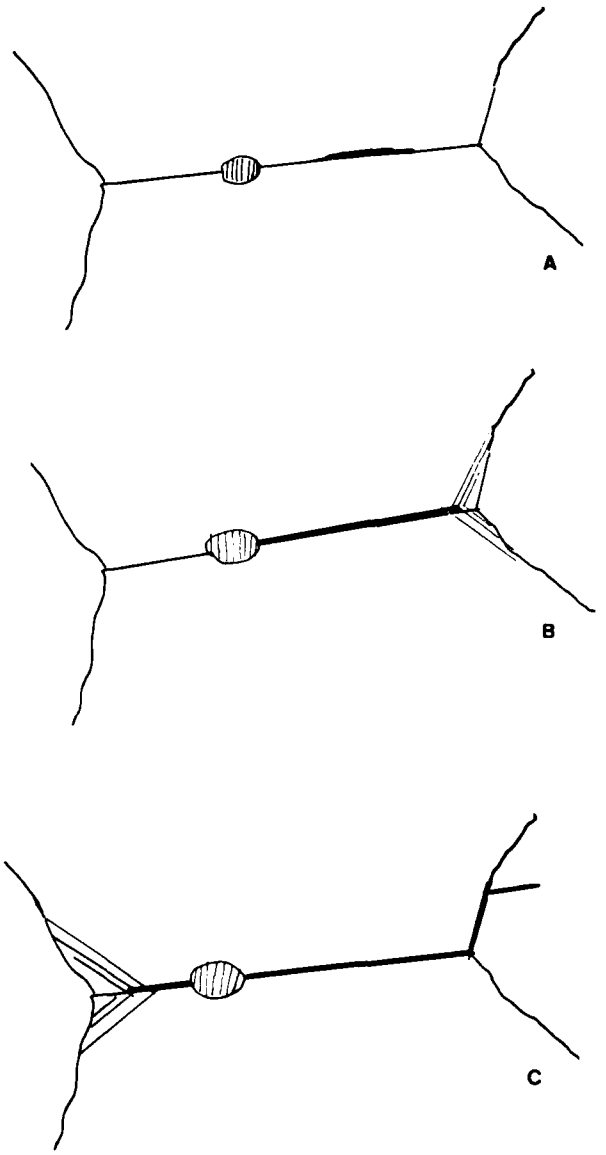

Figure 9. A schematic illustration of retardation and arrest mechanisms of intergranular small cracks in aluminium alloys.

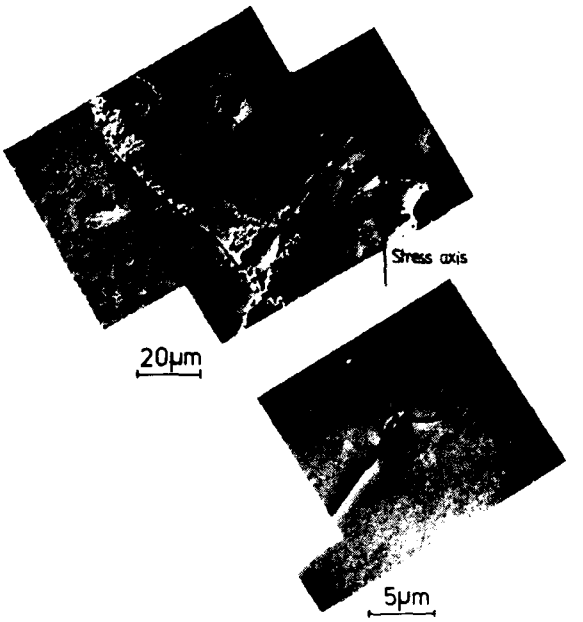

Figure 10. An example of the arrest of a small crack in an aluminium alloy following a transition in crack growth mode from intergranular to transgranular.

Figure 11. An illustration of the transition from intergranular (left) to transgranular (right) for a fully aged aluminium-copper alloy.

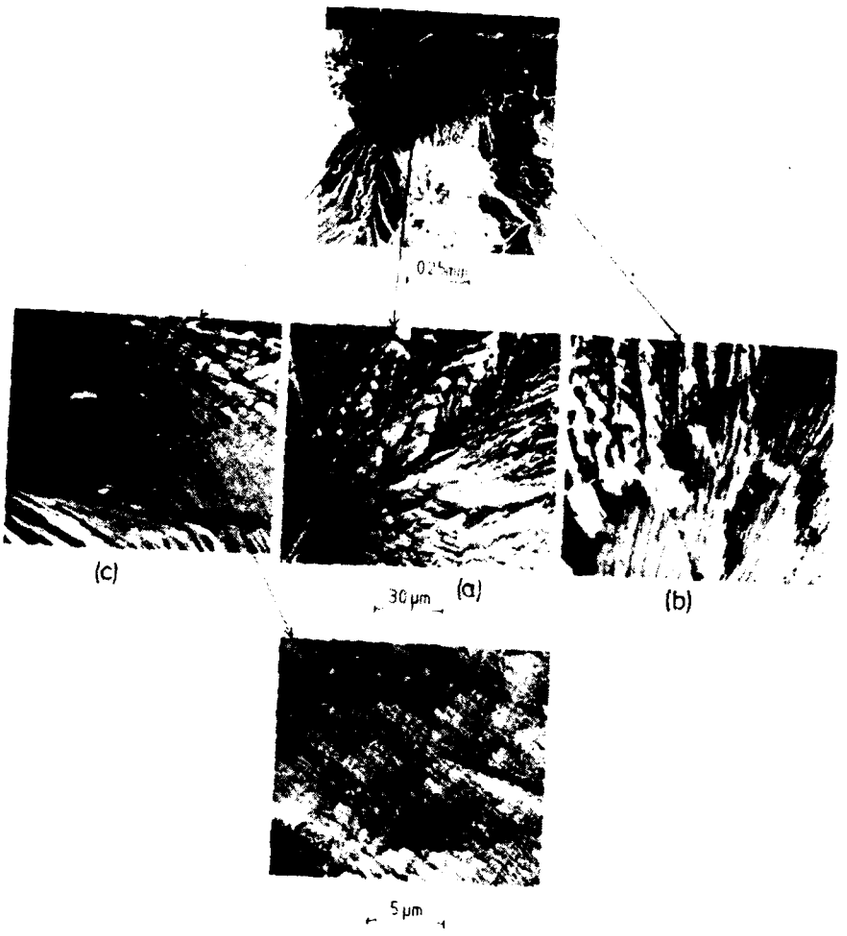

Figure 12. An SEM view of a contained small crack and the modes of transgranular fatigue failure for an Al 4.5%Cu alloy tested in a peak aged condition at room temperature.

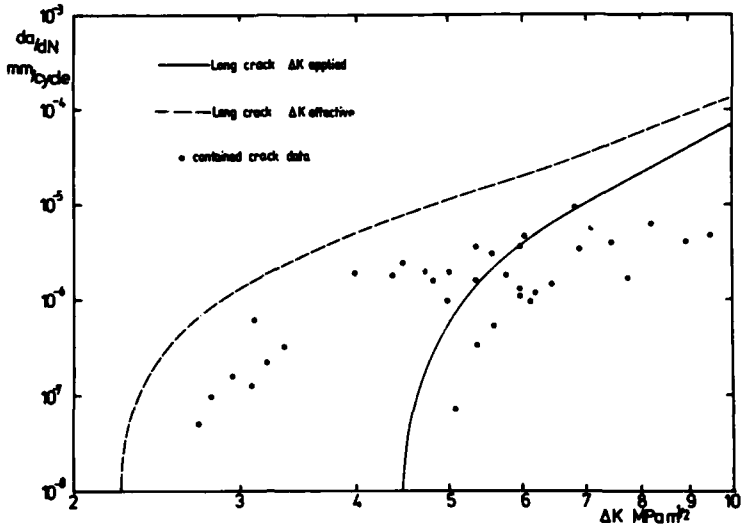

Figure 13. The data for small and long crack growth tests in an Al 4.5% Cu alloy. The long crack data was obtained using CT specimens and the short crack data from three point bed tests.

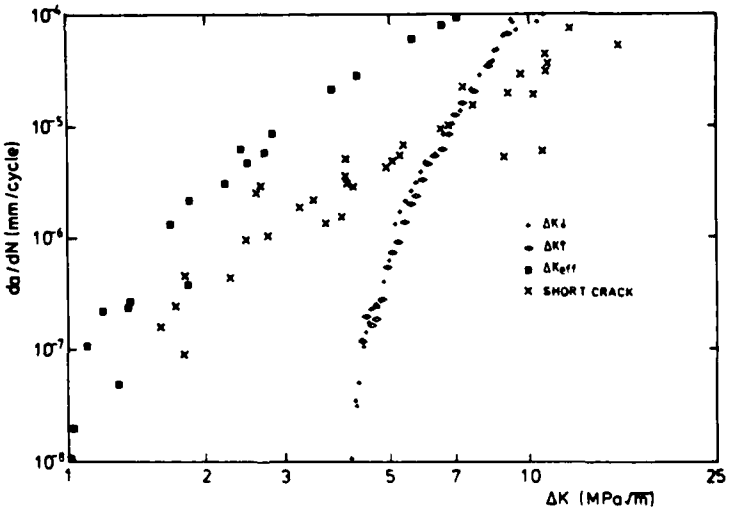

Figure 14. Small and long crack data obtained from the point bend tests and CT specimens respectively of a mechanically alloyed aluminium alloy In 9021.

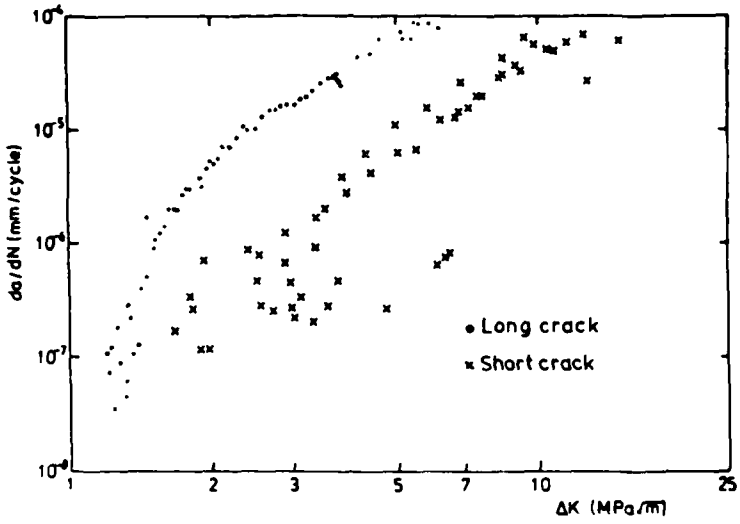

Figure 15. Small and long crack data obtained from three point bend tests and CT specimens respectively for a mechanically alloyed aluminium alloy In 9052.

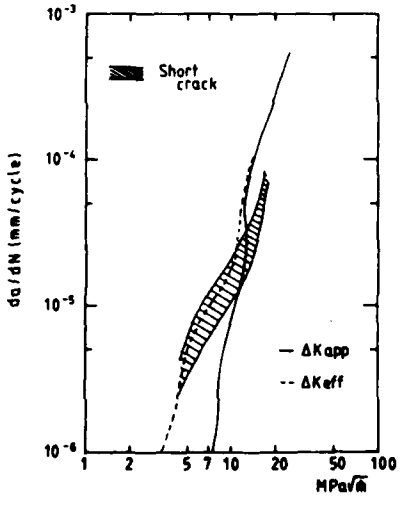

Figure 16. Small and long crack fatigue crack growth for the titanium alloy Ti 6Al 4V.

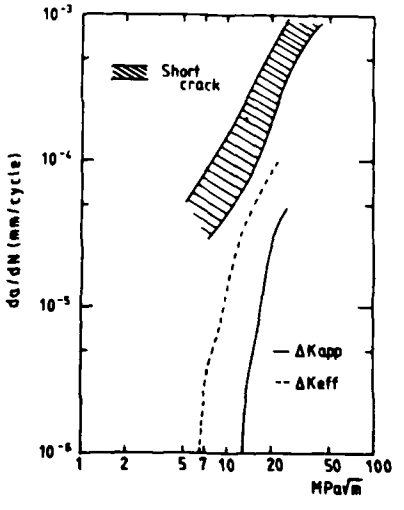

Figure 17 Small and long fatigue crack growth for the titanium alloy IMI 685.

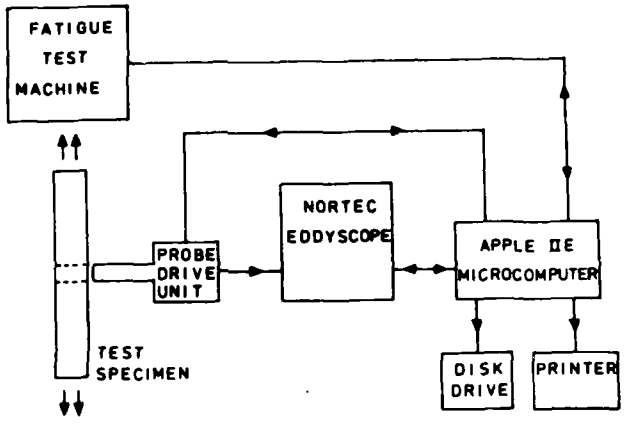

Figure 18 Schematic illustration of the link-up between the Eddyscope, test machine and control system.

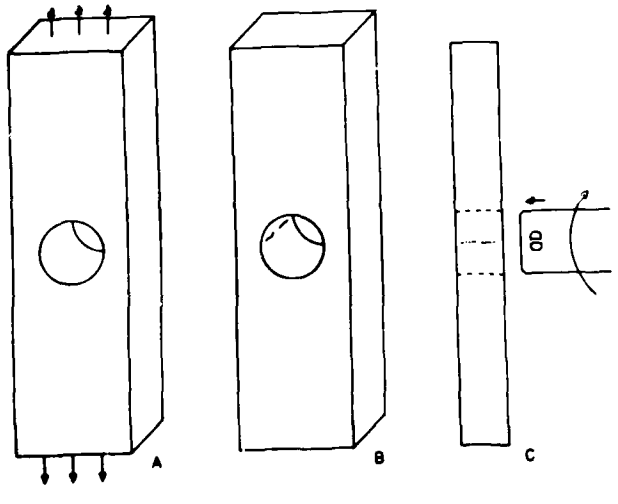

Figure 19 Specimen geometry and probe location. Specimen dimensions, 250 mm by 38 mm by 10 mm.

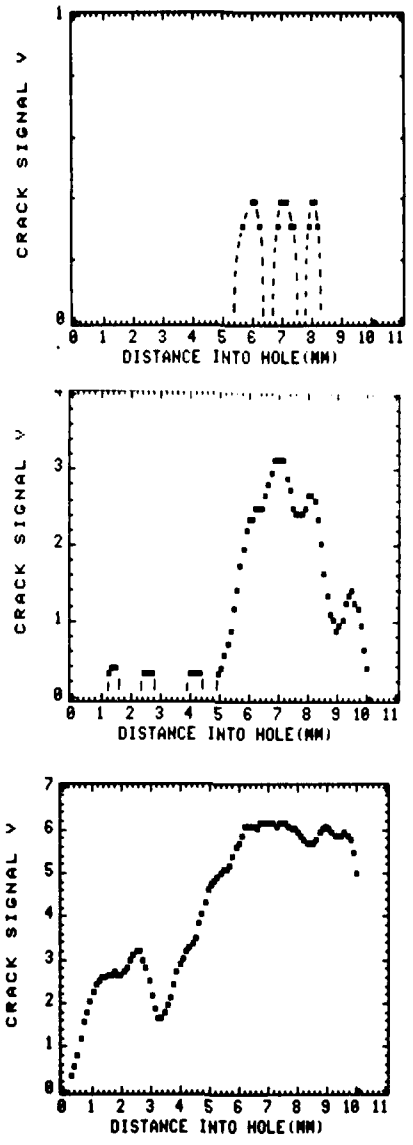

Figure 20 Examples of the signals associated with fatigue crack development in a single specimens subjected to the fatigue loading described in text.

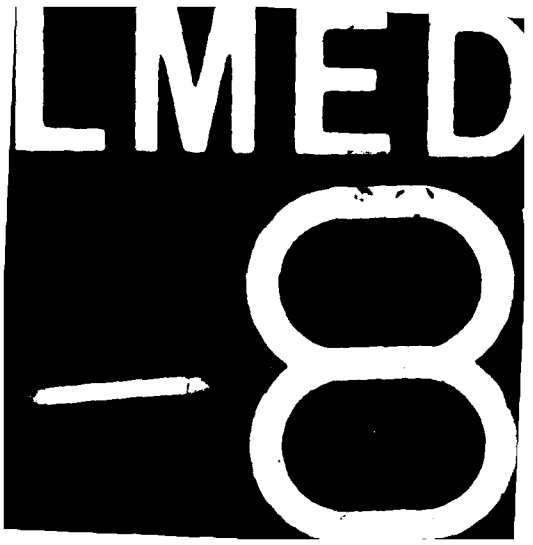
LMED
8